UNIVERSITÀ
DEGLI STUDI
FIRENZE

DOTTORATO DI RICERCA IN
SCIENZE CHIMICHE

CICLO XXXI

COORDINATORE Prof. Piero Baglioni

Multitechnique Investigation for Rational Design of Molecular Spin Qubits

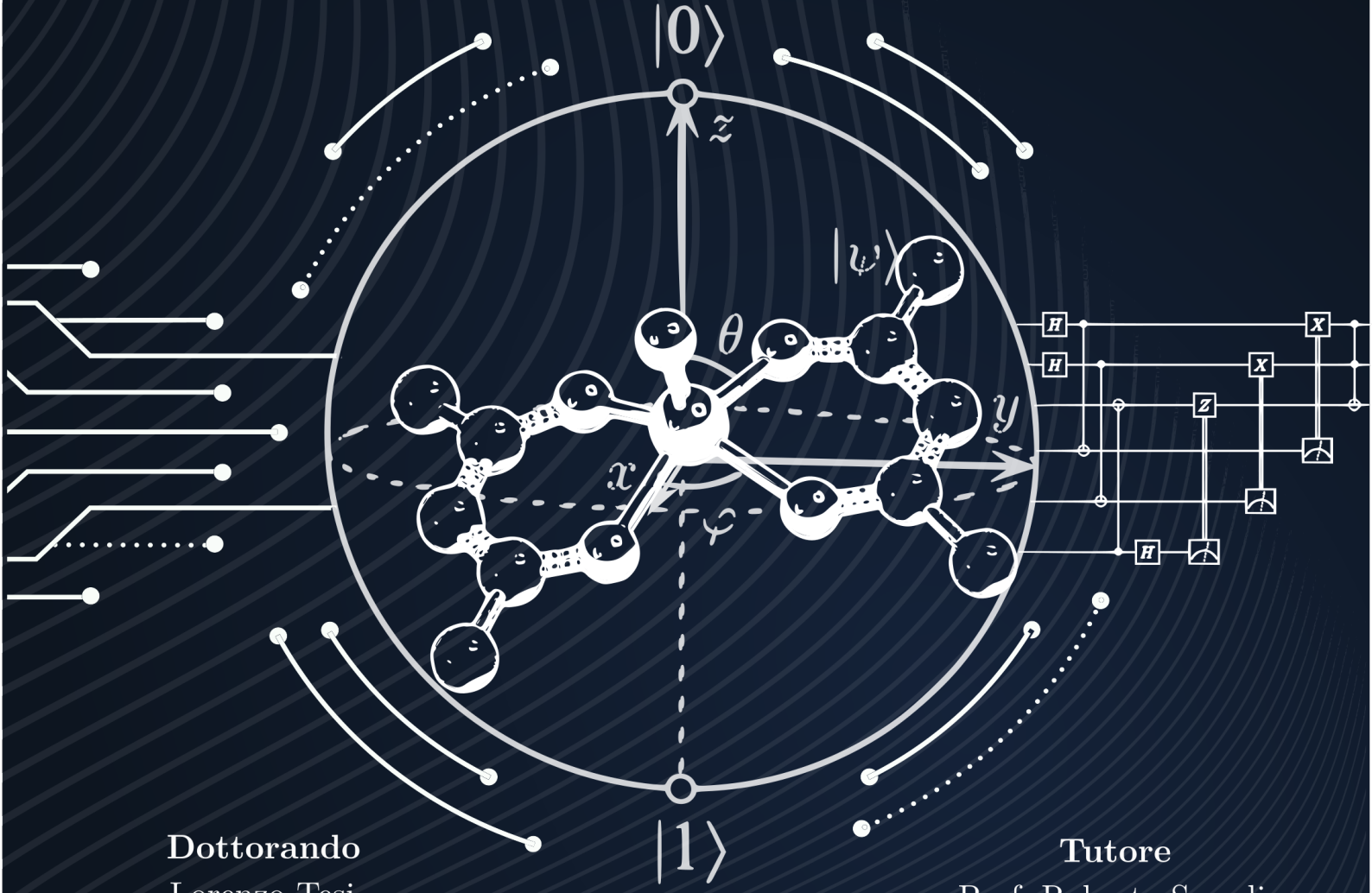

Dottorando
Lorenzo Tesi

Tutore
Prof. Roberta Sessoli

UNIVERSITÀ
DEGLI STUDI
FIRENZE

DOTTORATO DI RICERCA IN
SCIENZE CHIMICHE

CICLO XXXI

COORDINATORE Prof. PIERO BAGLIONI

MULTITECHNIQUE INVESTIGATION FOR RATIONAL DESIGN OF MOLECULAR SPIN QUBITS

Settore Scientifico Disciplinare CHIM/03

Dottorando
Dott. Lorenzo Tesi

_____
(firma)

Tutore
Prof. Roberta Sessoli

_____
(firma)

Coordinatore
Prof. Piero Baglioni

_____
(firma)

Anni 2015/2018

Cover: Classic becomes Quantum

2018, *Lorenzo Tesi*

PhD in Chemical Science, November 2018

Coordinator: Prof. Piero Baglioni

Tutor: Prof. Roberta Sessoli

University of Florence

Piazza San Marco, 4

50121 Firenze

Alla mia famiglia,
a Eleonora.

C'è una teoria che afferma che,
se mai qualcuno riuscisse a scoprire esattamente
a che scopo esiste l'Universo e perché esso esiste,
allora questo sparirebbe immediatamente
e sarebbe sostituito da qualcosa di ancora
più bizzarro e incomprensibile.

C'è un'altra teoria secondo la quale
ciò è già accaduto.

-Douglas Adams-

Contents

Summary

Reproducing the quantum properties of matter is a difficult task for our (classical) computers and this problem is increasingly relevant as quantum technologies develop. For this reason, in 1982 R. Feynman proposed the realization of quantum computers, *i.e.* devices based on the laws of quantum mechanics physics, capable of naturally modelling the quantum phenomena. A quantum computer exploits the *superposition* of two states of a quantum bit (*qubit*), and the *entanglement* between two or more qubits. Several systems have been proposed to realize qubits: ion traps, superconductors, photons, nuclear and electron spins, etc. and, in principle, any system that satisfies the Di Vincenzo's criteria could be used as a qubit. Among the various proposals, we have decided to focus on the electronic spin of molecules. Indeed, molecules with spin $S = 1/2$ under an applied magnetic field provide a two-levels system, manipulable through microwave pulses in order to create the required superposition. The main advantage of molecules lies in coordination chemistry that offers boundless possibilities for designing molecular structures. For example, entanglement between qubits can be achieved in a controlled way by exploiting coordination chemistry to finely tune the magnetic interactions between the magnetic centres. With respect to other proposed platforms, the ease of realizing multi-qubit systems makes molecules very appealing. Other advantages in the use of molecules concern their scalability and the possibility to address them individually once isolated on a surface. On the other hand, the major limit of molecular spin qubits is the coherence time of the superposition state, which reduces the exploitability of the quantum properties of the qubit. When referring to spins, the coherence time corresponds to the *spin-spin relaxation time*, T_2, which experimentally can be estimated by using the phase memory time T_m. The coherence time determines the duration after which the quantum information of the qubit is loss. Another figure of merit is the *spin-lattice relaxation time*, T_1, which refers to the 'classical' memory time of the qubit. Controlling T_1 is of crucial importance: if too long it limits the speed of initialization of the qubit, whereas, if too short it induces a collapse of T_2, especially as the temperature increases. While the protocol to directly enhance the coherence time is quite clear, though demanding from the synthetic point of view, the strategies for a further and significant lengthening of T_2 provided by a corresponding increase of T_1 are still not sufficiently understood. The main source of the relaxation processes affecting T_1 originates from molecular and lattice vibrations. Such relaxation processes may occur in many different ways, but all of them indirectly involve the spin through the spin-orbit

coupling (the displacement of ions, caused by vibrations, produces a variation of the electrostatic potential around the reference ion).

In this respect, the wide-ranging investigation carried out in my PhD work and here presented, has been aimed at the increasing of the molecular qubits performances through a rational chemical design. In particular, it has been useful to identify the necessary ingredients to lengthen T_1 and to shed lights on the relation between structural effects and spin dynamics. The investigation has been developed on several vanadyl-based molecular systems by exploiting a multi-technique approach based on: direct-current (dc) magnetometry and continuous-wave (cw) Electron Paramagnetic Resonance (EPR) to determine the static spin properties, alternate-current (ac) susceptometry and pulsed Electron Paramagnetic Resonance (EPR) to characterize the spin dynamics in concentrated and diluted molecular systems, and Time-Domain Terahertz (TD-THz) spectroscopy to have access to the low-energy vibrational spectrum. However, other techniques have been employed within this work: low temperature μ-Hall magnetometry, calorimetric measurements, Cantilever Torque Magnetometry (CTM), 4D-Inelastic Neutron Scattering (4D-INS) and Muon Spin Resonance (μSR) spectroscopy. Moreover, the close collaboration with theoreticians has been fundamental for the modelling and rationalization of the experimental results obtained.

From these studies we established that long relaxation times are provided by using: *i)* molecules with a single magnetic centre, *ii)* principally based on vanadium(IV), which is a light element with $S = 1/2$ and small spin-orbit coupling, *iii)* in a square pyramidal geometry, which strongly stabilizes the d_{xy} ground state, *iv)* with as little as possible nuclear spins in the paramagnetic ion neighbourhood, *v)* and in a highly diluted solid crystalline matrix. Under these conditions, T_1 reaches values of the order of hundreds of milliseconds at the liquid ^{4}He temperature, while T_2 is of the order of few microseconds at the same temperature. Strikingly, coherence times of the order of few microseconds have been observed at the remarkable temperature of 300 K for these vanadyl-based molecular systems. The possibility to perform quantum manipulation experiments on these systems at room temperature has been also proven by recording *Rabi oscillations*.

The investigation also points out that long coherence times, T_2, can be reached at 300 K only when T_1 exhibits a weak temperature dependence. Indeed, it has been shown that an abrupt decrease of T_1 causes a consequent pronounced decrease of T_2, thus hindering quantum manipulation at room temperature. In this work, we have suggested that variations on the temperature dependence rely on the composition of the low-energy vibrational spectrum of the concerned molecule. Indeed, spin-lattice relaxation for a two-levels $S = 1/2$ system occurs through the one-phonon direct process and the two-phonons Raman process. It has also been shown that these processes involve low-energy

vibrational modes, whose characterization becomes fundamental for a full understanding of the spin-lattice relaxation nature.

A more accurate optical characterization has been devoted to a specific molecule of formula $[VO(acac)_2]$, which has been taken as a vanadyl-based molecular spin qubit prototype to achieve a complete rationalization of their spin dynamics. Moreover, since THz spectroscopy is limited to the Γ-point of the Brillouin zone, this prototype molecule has been investigated through 4D-INS. Thanks to this, the acoustic and optical low-energy phonons in all the main directions of the reciprocal space have been directly measured. The entire spectroscopic investigation has been flanked by theoretical calculations based on *ab initio* and DFT methods. Indeed, only a virtuous interplay between several experimental approaches and a theoretical modelling of these systems allows to shed light on the relation between the vibrational structure and spin dynamics.

Usually, in the analysis of magnetic data, it is assumed that the lattice system is well-coupled to the thermal bath. However, when the lattice is not able to dissipate the excitation transferred from spins, a significant depart from equilibrium may occur. This effect, which is known as *spin-phonon bottleneck*, becomes more dramatic in highly concentrated systems and when large crystals are used. Such a phenomenon has been found to affect many of the vanadyl-based molecules here investigated, with a noticeable efficacy in $[VO(acac)_2]$. A comparative study has been performed by considering the results obtained for this molecule and those obtained of two other vanadyl-based molecules also coordinated by β-diketonate ligands. Moreover, heat capacity experiments were performed on a single crystal of $[VO(acac)_2]$ and the results compared to those extracted by ac susceptibility measurements. These findings have been successfully rationalized by means of simple thermodynamic considerations, supported by theoretical DFT-based calculations.

In this work we have also proposed to use Muon Spin Resonance spectroscopy for investigating molecular spin qubits. Indeed, this technique offers a unique point of view for detecting the spin dynamics of molecular magnets. However, before applying μSR to potential qubits, preliminary studies have been carried out. In this frame, μSR experiments were performed on two isotopically enriched samples of a Dy-based Single Molecule Magnet (SMM). The isotopes that have been used, ^{161}Dy and ^{164}Dy, have nuclear spin $I = 5/2$ and $I = 0$, respectively. Muon experiments were performed at zero magnetic field and in the 2-300 K temperature range, conditions for which muons are effective local probes of the molecular spin dynamics. In this frame, we have demonstrated the capability of this technique to capture fine details of the spin dynamics of molecular systems, down to isotopic effects in the tunneling of magnetization. Moreover, deviations of the μSR results from the ac susceptibility outcomes can be explained as a consequence

of the muon ability to detect not only specific dynamics processes but all the sources of spin fluctuations.

A further preliminary study has been performed by using Low Energy μSR (LEM) on a self-assembled monolayer of the same Dy-based SMM previously investigated. The spectroscopic characterization of the sample through X-Ray Photoelectron Spectroscopy (XPS) and X-Ray Absorption Spectroscopy (XAS) synchrotron-based techniques has confirmed the grafting of the molecules on surface and it has suggested several arrangements of the molecules on surface. In this study, μSR experiments have been performed in presence of a transverse magnetic field and demonstrate that muons can probe the presence of paramagnetic ions close to the surface. Further μSR studies in zero-field are expected to give access to the spin dynamics of this monolayer of Dy-based SMM. Moreover, in a future perspective we think that such investigations will provide useful information also for molecular addressable spin qubits deposited on surface.

Finally, the characterization of the static and dynamics magnetic properties of a system with $S > 1/2$ is described. The inclusion of this study in the dissertation provides a useful example to highlight which aspects need more care when dealing with multi-levels spin systems. The study has been performed on a cobalt(II)-based SMM in a pseudo-octahedral geometry, which results in three unpaired electrons and a non-completely quenched orbital contribution. The multi-technique approach has been necessary even in this case, though involving different techniques. Indeed, we have employed a combination of dc and ac magnetometry, cw-EPR and CTM. Once more, the study has been supported by theoretical calculations. This approach has evidenced that the spin Hamiltonian well-reproduces the experimental data at low temperatures, but when the latter is increased the model is not valid anymore. In these cases, more accurate models must be used and *ab initio* calculations represent the best solution. Finally, the spin-lattice relaxation of systems with $S > 1/2$ may involve further relaxation processes that complicate the analysis, such as quantum tunneling of the magnetization and Orbach process. The analysis of magnetic data for this system has shown the key role of the quantum tunneling at low temperature, whereas at higher temperatures the Raman process has been found to dominate over the Orbach one.

The work carried out and described in this dissertation cannot be considered concluded. Indeed, we have pointed out the fundamental importance of considering the vibrational structure in the rational design of more performant molecular spin qubits. These achievements represent a solid starting point for further investigations. It should be stressed that the great tunability provided by coordination chemistry enable us to cover many still unexplored possibilities for the future development of molecular qubits.

Chapter 1

Introduction

The birth of modern computer science dates back to 1936 with a breakthrough paper of the great mathematician Alan Turing.[1] In that work, Turing developed in detail an abstract notation about a model for computation, nowadays known as *Turing machine*. Few years later, John von Neumann developed a simple theoretical model concerning how to put together all the components required for implementing the Turing machine in a practical fashion. The hardware development became a reality in 1947, when John Bardeen, Walter Brattain, and (secondarily) William Shockley built up the first transistor, for which they were awarded the Nobel Prize. Since then, computer hardware has grown in power at an impressive pace. In 1965 such a growth was codified by Gordon Moore, who stated that computer power would double for constant cost roughly every two years. Strikingly, Moore's law has approximately held true in the decades since, and it is expected to end as soon as the quantum effects will begin to interfere in the functioning of the smaller and smaller electronic devices. This poses a limitation on the increasing power of computers. A possible solution to this problem might be the use of a different computing paradigm. A paradigm as such is provided by the theory of quantum computation, which is based on the idea of using a quantum physics approach to perform calculations, instead of a classical physics one. The In 1985, the theory was developed by David Deutsch, who questioned whether the laws of physics could be used to derive a stronger version of the Universal Turing machine, *i.e.* to define a computational device that would be capable of efficiently simulating any physical system.[2] In particular, since the laws of physics are ultimately quantum mechanical, Deutsch was naturally led to consider computing devices based upon the principles of quantum mechanics. This laid the foundations of *Quantum Computation*. Following the studies of Deutsch, a quantum

[1] A. M. Turing. On computable numbers, with an application to the Entscheidungsproblem. *Proc. Lond. Math. Soc. 2*, 1936, **42**, 320.

[2] D. Deutsch. Quantum theory, the Church-Turing Principle and the universal quantum computer, *Proc. R. Soc. Lond. A*, 1985, **400**, 97.

computer is expected to have computational power largely exceeding that of a classical computer, *i.e.* a computer based on a classical physics. The enhancement of computational power of a quantum computer derives from the possibility to increase the number of problems that can be solved in an *efficient* way, with a consequent significant speed advantage over classical computers. In the context of computer science, an algorithm is defined *efficient* if it runs in a time which is a polynomial expansion of the size of the problem solved, whereas an *inefficient algorithm* requires super-polynomial, typically exponential, time. The inability of a classical computer to solve certain problems efficiently is one of the main driving forces for the implementation of quantum computers.

The heuristic vision of Deutsch was improved by many people, and in particular by Peter Shor, who demonstrated that two enormously important problems, *i.e.* the problem of finding the prime factors of an integer number and the 'discrete logarithm' problem, could be solved efficiently on a quantum computer. The importance of such a demonstration relies on the fact that no efficient solution to these two problems exists in classical computation. In the following years, many other algorithms, for example the Deutsch-Jozsa's or the Grover's, were theorized to work efficiently for a quantum computer, thus supporting the claim that a quantum computer was inherently more powerful.

The power of a quantum computer relies also on another key idea, suggested by Richard Feynman during a talk and then published the following year, in 1982.[3] Such an idea is summarized in the Feynman's keynote concluding words:

> "…nature is not classical, and if you want to make a simulation of nature, you would better make it quantum mechanical, and it is a wonderful problem because it does not look so easy."

Since then, several teams of researchers have begun fleshing this idea out, evidencing that it is indeed possible to use quantum computers to efficiently simulate systems that have no known efficient simulation on a classical computer.

A research field that will certainly benefit from the capability of quantum computers in simulating the properties of nature is chemistry, or, more in general, material science. Indeed, even the most advanced computational methods can only provide a crude approximation of the quantum rules that govern the behaviour of atoms and molecules, as the calculators that are currently available are based on classical physics. Nowadays, only few quantum problems can be solved analytically, such as for example the hydrogen

[3] R. P. Feynman. Simulating physics with computers, *Int. J. Theor. Phys.*, 1982, **21**, 467.

atom since it contains only one electron. When the studied system presents more electrons, the problem can be solved only by adopting many approximations. In this frame, researchers in quantum chemistry have developed iterating self-consistent methods, the most famous being the Hartree-Fock one, which can often predict molecular properties with great accuracy. However, such methods are limited by the demanding computational time to rather small chemical systems.

These problems may be overcome by recalling the Feynman's idea to exploit specific characteristics of quantum-mechanics, like *superposition* and *entanglement* of quantum states, to simulate quantum problems. Experimentally, performing quantum computation implies to control the dynamics of the quantum system q under the action of an external stimulus. Here, the quantum system q is the fundamental unit of the quantum computer, which, in analogy to the classical bit, is called *quantum bit*, or *qubit*. Thus, defining the input of the calculation means to prepare the qubit in a given quantum state, while processing data means to let the qubit evolve under the action of a given stimulus, and finally reading the output stands for measuring the final quantum state of the qubit. Since qubits are quantum objects themselves, they can be used to represent quantum systems like electrons. Therefore, no approximation is required for a system of qubits to represent exactly electrons in a complex molecule. This may enable us to determine the ground-state energies of molecules, from which their stability and reactivity can be predicted, including the elucidation of reaction mechanisms and calculation of reaction pathways and rates. Moreover, the simulation of quantum phenomena would help to understand the catalytic action of an organometallic complex, or to predict the rate and stability of drug binding, which is a fundamental step to develop new drugs. Further applications can be imagined also in condensed-matter physics, since accurate simulations of the electronic structure of molecules are crucial to obtain materials with improved properties suitable for batteries, solar cells or, in general, electronic devices. These are only few examples concerning what quantum computers are expected to do. We may wonder which further problems could be solved more efficiently on a quantum computer rather than a classical one: "One of the most exciting things about quantum computation and quantum information is how *little* is known about the answers to this – and not only this – question! This is a great challenge for the future".[4]

However, it is well-known that quantum phenomena can be very elusive. Indeed, in order to exploit the quanto-mechanics properties of our qubit in calculations, it is of fundamental importance to keep its quantum state coherent. This is because a quantum state does not live infinitely but after a certain time, called *coherence time*, it returns

[4] M. A. Nielsen and I. L. Chuang. Quantum computation and quantum information, 10th ed., Cambridge University Press, 2011

classical. The environment interacting with the qubit disrupts its quantum state and accelerates this process, which is referred to as *decoherence*. One could think to isolate the qubit from the environment, but this would preclude its manipulation (given by an external stimulus), observation (to read out the results) and scalability (the computational power depends on the number of connected qubits that can be individually manipulate). Moreover, to really exploit the power of quantum mechanics, it is necessary to have one or more qubits coupled together. For this reason, a realistic implementation of the qubit must achieve a delicate balance between these constraints.

Nowadays, finding suitable, robust, and scalable systems as potential qubits represents one of the main challenges in chemistry, physics, and materials science for the development of these technological applications. As an example, the company D-Wave has realized a prototype of a quantum computer that performs some specific task sufficiently fast to attract the interest of companies such as NASA and Google, which have invested amazing sums of money in this device. Separately, Google has also built up a prototype with 22-qubits, whereas IBM has recently announced other two prototype devices with 16 and 17 qubits. In all these prototypes, the qubit is implemented in superconducting circuits, also called transmons. The main problems of such devices are the very low temperatures of working (15 mK) that complicate their physical realization, the scalability that limits the number of integrated qubits and the quantum error correction that strongly reduces their efficiency. For this reason, these systems are far from being considered as real quantum computers, and the challenge is still open.

Many systems were proposed for realizing qubits, and, among these, the electronic spin of molecular systems represents a very promising candidate for this purpose. The main advantage of molecules is that coordination chemistry offers boundless possibilities for the design of molecular structures. A prototype molecular spin qubit is composed of one or more metal centres coordinated through ligands, which allow to obtain a specific environment for the spin carrier. A wise choice of the ligands allows, for example, to realize multi-qubits architectures, which are required to exploit entanglement between qubits.

On the other hand, molecular spin qubits often suffer from relatively short coherence times compared to other potential systems. This loss of information is related to the *transverse relaxation time* (T_2), or spin-spin relaxation time, which corresponds to the coherence time discussed above. For experimental reasons, it should be noted that usually the coherence time is estimated by measuring the phase memory time (T_m), corresponding to a lower limit of T_2. Another characteristic time for molecular spin qubits is the *longitudinal relaxation time* (T_1), or spin-lattice relaxation time, which defines the classical memory time, i.e. the time required for the magnetization to recover its

equilibrium value. After this time, the system loses completely the initial information. Following their definitions, it is evident that $T_1 \geq T_2$, for which T_1 represents an upper limit for the coherence time. Controlling T_1 is of crucial importance: if it is too long, it limits the speed of initialization of the qubit, whereas if it is too short, it induces a collapse of T_2, especially as the temperature increases.

The three main sources of decoherence arise from the interaction between the spin qubit with: the nuclear spin bath (hyperfine interactions), the neighbouring electronic spins (dipolar interactions) and the thermal vibration of the molecule and/or the extended lattice (phonons). Both hyperfine and dipolar interactions mainly affect T_2, and, in principle, they may be controlled by a careful design of the ligands and counterions of the molecular spin qubit and by its dilution in a non-magnetic host. This requires the control of both its chemical composition and its electronic structure, *i.e.* the control of the coordination environment around the metal ion embodying the spin qubit. On the other hand, the phonons are the principal source of relaxation for T_1. Besides effects such as the tumbling of methyl groups in solution that can be reduced through several precautions, the coherence time is mainly affected by lattice vibrations only indirectly, due to the reduction of T_1. Such vibrations, whose efficiency is mediated by the spin-orbit coupling, may affect the spin carrier by means of several different relaxation processes. The identification of the active processes, as well as the knowledge about how such processes cause relaxation is mandatory to enhance the relaxation times T_1 and T_2.

In this respect, the intense investigation carried out in my PhD work has been aimed at increasing the performances of molecular qubits through chemical design. In particular, the investigation proceeded by identifying the necessary ingredients to lengthen T_1. The molecular systems studied are based on vanadium(IV) that belongs to the first row of the transition metals in the Periodic Table of Elements ($[Ar]3d^1$). Since it has one unpaired electron, the resulting spin value is simply $S = 1/2$. However, the most abundant isotope for vanadium is ^{51}V (rel. ab. 99.75%), which also has a nuclear spin $I = 7/2$. The use of this element is motivated by its small spin-orbit coupling, for which the effect of phonons is limited. The coordination chemistry of the investigated systems is dominated by the vanadyl centre VO^{2+}, which stabilizes and well isolate the electronic ground state d_{xy}, thus further reducing the orbital contribution to the spin-lattice relaxation. Several different ligands were used in order to address specific structural effects on the spin relaxation times and shed lights on the nature of the relaxation processes. For this purpose, the combination of several magnetometric and optical techniques has been fundamental. The multi-technique approach adopted includes direct-current (dc) magnetometric and alternate-current (ac) measurements, continuous-wave (cw-) and

pulsed Electron Paramagnetic Resonance (EPR) measurements and Time-Domain Terahertz (TD-THz) spectroscopy. However, further techniques were employed in this work: μ-Hall device magnetometry to record magnetization decays and hysteresis, calorimetric measurements and cantilever torque magnetometry (CTM). More exotic techniques have also been employed, such as 4D-Inelastic Neutron Scattering (4D-INS) and Muon Spin Resonance (μSR) measurements. Theoretical calculations have also been useful to rationalize the obtained results. The use of such different techniques has resulted in a wide interdisciplinary collaboration with many chemists and physicists. The results here described are thus the fruit of the work of the author as well as that of many collaborators.

The thesis is organized in six chapters. In Chapter 2 the basic concepts about qubits will be presented, including a more specific outlook on the molecular spin qubits. In Chapter 3, I have personally reviewed the principal spin relaxation processes focusing, in particular, on the processes active for a spin ½ system. The chapter has been written by covering a wide range of literature of condensed-matter physics from 1930 until recent years. In Chapter 4 the results of the multi-technique investigation performed on the several different vanadium-based molecular systems will be illustrated. The chapter is organized by combining all the outcomes obtained for these systems within my PhD work and separately published. In doing this, such results are integrated with further experimental data. The comparative analysis of data for the different vanadium-based systems has been carried out so that, thanks to the comparison, new conclusions could be reached. Chapter 5 is devoted to a specific vanadyl-based molecule that, thanks to its simplicity and the possibility to grow large single-crystals, has become a suitable prototype system to investigate the spin dynamics from many different points of view, both experimental and theoretical, in order to reach a full comprehension of the processes that are involved in the relaxation. In Chapter 6 the use of μSR in investigating the spin dynamics of molecular spin qubits is encouraged. Preliminary studies are shown for a dysprosium(III)-based Single Molecule Magnet (SMM), firstly as bulk material and secondarily as monolayer grafted on a gold surface. Finally, in Chapter 7 the magnetic investigation of a cobalt(II)-based system with spin value higher than $S = 1/2$ is reported since it provides a nice example of how the multi-technique approach changes when systems with higher spin values are investigated. The chapter also contains the study performed on lanthanides-based 1D spin helices, in which the capability of cantilever torque magnetometry to resolve the spin structure is demonstrated, even in case of complex systems and spin non-collinearity.

Chapter 2

Magnetic Molecules as Spin Qubits

The first part of the chapter exposes the fundamental aspects of the quantum computation and, through the postulates of quantum mechanics, introduces the main properties of the *qubit*. A closer look is devoted to the electronic spin of molecular magnets as platform to implement qubits. The second part of the chapter briefly presents the more recent results achieved in this research area. The aim of this section is not to cover the entire literature but to provide an overall view of the state-of-the-art.

The books (Quantum Computation and Quantum Information, M. A. Nielsen and I. L. Chuang, 2011)[1] and (A Short Introduction to Quantum Information and Quantum Computation, M. Le Bellac, 2006)[2] are an inescapable introduction to the basics of Quantum Computation and have been fundamental for writing this chapter. The chapters (Molecular Magnets for Quantum Information Processing, K. van Hoogdalem et al., 2014)[3], (Quantum Computation with Molecular Nanomagnets: Achievements, Challenges, and New Trends, A. Ghirri et al., 2014)[4] and (Magnetic Molecules as Spin Qubits, P. Santini et al., 2017)[5] contain more specific indications about the use of Molecular Magnets in Quantum Information Processing and have also been useful for writing this chapter. As a further reading, an excellent discussion on the reasons why building of a quantum computer is difficult can be found in (D. DiVincenzo, 1995)[6].

2.1 Qubits and how to use them

In analogy to the bit, which is the fundamental unit of the classical computation, the qubit is the fundamental concept of the quantum computation. The qubit can be briefly defined as a two-level quantum system representing the simplest elementary building block for a quantum computer. Like the classical bit, which can assume two values (either 0 or 1), a qubit can be prepared in two possible states $|0\rangle$ and $|1\rangle$, where the symbol '$|\ \rangle$' is the standard notation for states in quantum mechanics by using the *Dirac notation*. However, contrary to the classical bit, the qubit can be prepared in a state *other* than

states $|0\rangle$ or $|1\rangle$. Indeed, for a qubit it is possible to form linear combinations of states, usually indicated as *superpositions*

$$|\psi\rangle = \alpha|0\rangle + \beta|1\rangle \tag{2.1}$$

where α and β are complex numbers. Thus, the state of a qubit is a vector in a two-dimensional complex vector space, called *Hilbert* space. The two states $|0\rangle$ and $|1\rangle$ are known as *computational basis states* and form an orthonormal basis for this vector space. This follows from the first postulate of quantum mechanics.

> **Postulate 1:** Associated to any isolated physical system is a complex vector space with inner product (that is, a Hilbert space) known as the *state space* of the system. The system is completely described by its *state vector*, which is a unit vector in the system's state space.

The first postulate does not define the state space or the state vector, which depends on the chosen system. The simplest quantum mechanical system is the qubit, which has a two-dimensional state space, and whose state vector can be written as in eq. (2.1).

One useful picture in thinking about qubits is given by the *Bloch sphere* geometric representation, which is shown in Figure 2.1. In this frame, eq. (2.1) can be rewritten as

$$|\psi\rangle = \left(\cos\frac{\theta}{2}|0\rangle + e^{i\varphi}\sin\frac{\theta}{2}|1\rangle\right) \tag{2.2}$$

where θ and φ are real numbers, and they define a point on the unit sphere, as shown in Figure 2.1. This provides a useful means of visualizing the state of a single qubit, and it is useful as testbed for ideas about quantum computation.

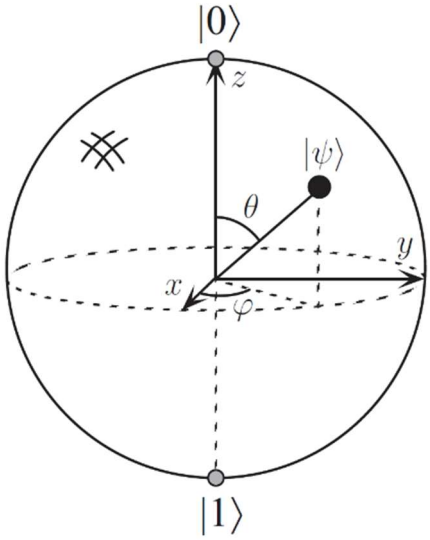

Figure 2.1. Bloch sphere representation of a qubit. The image has been taken from ref[1].

The time evolution of the qubit state $|\psi\rangle$ is described by the second quantum mechanics postulate

> **Postulate 2:** The evolution of the state $|\psi\rangle$ for a *closed* quantum system is described by a *unitary transformation*. That is, for every evolutive process of the system, it can be always defined an operator $U(t)$ for which
> $$|\psi'\rangle = U(t)|\psi\rangle.$$

Once more, the postulate does not specify the unitary operators U that describes the evolution of the system and that will vary from case to case. Each unitary operator represents the operation performed by a so-called *quantum gate*, of which there exists a rich variety. Just to provide some examples, the only non-trivial classical single bit gate is the *NOT-gate*, which takes either $|0\rangle$ to $|1\rangle$ or $|1\rangle$ or $|0\rangle$. An important one-qubit gate that has not classical analogues is the *Hadamard gate*, for which $H|0\rangle \equiv (|0\rangle + |1\rangle/\sqrt{2})$ or $H|1\rangle \equiv (|0\rangle - |1\rangle/\sqrt{2})$, shown in Figure 2.2. An example of two-qubits gate is the *CNOT-gate*, which acts as a NOT-gate on the second qubit (target qubit) if and only if the first one (control qubit) is in the state $|1\rangle$, and does nothing otherwise (Figure 2.2). It is proven that arbitrary single-qubit rotations, coupled with the CNOT-gate, are sufficient to implement any two-qubits unitary evolution exactly.[7] However, this statement does not consider the efficiency of the algorithm.

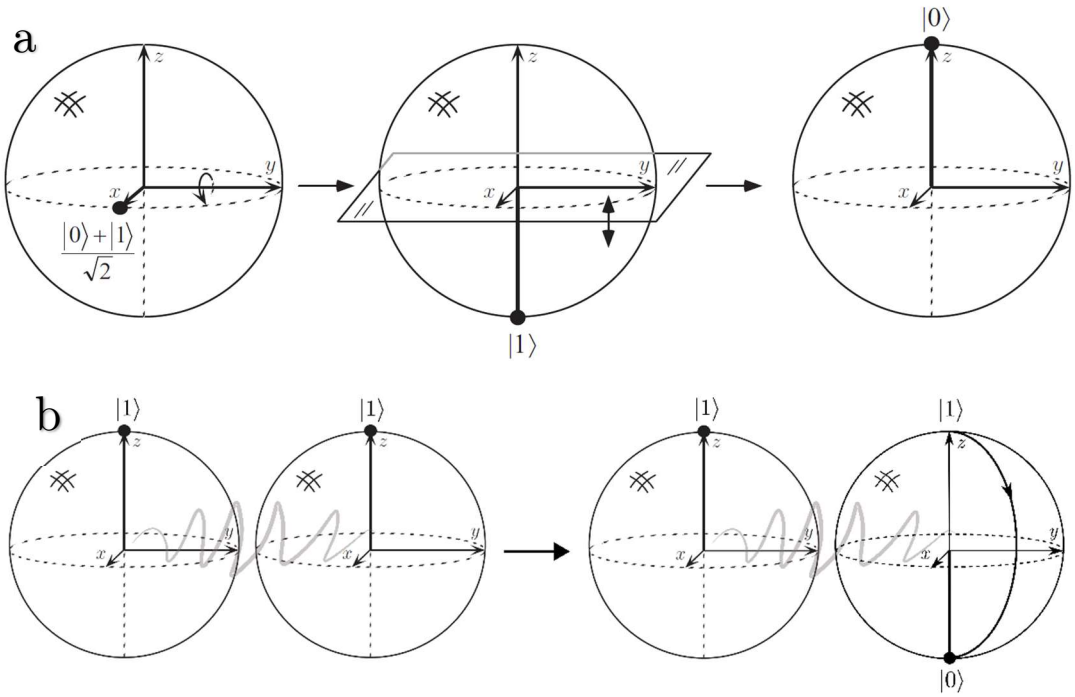

Figure 2.2. Visualization of the Hadamard gate (a) and C-NOT (b) on the Bloch sphere. The Hadamard gate is given by a rotation of the sphere about the y axis by 90°, followed by a rotation about the x axis by 180°. The C-NOT gate inverts the state of one qubit if and only if the other one is in the $|1\rangle$ state. Image (a) has been taken by ref[1].

In a more general context, to identify the physical interactions that realize specific single-qubit gates it is possible to refer to the time-dependent Schrödinger equation

$$i\hbar\frac{d|\psi\rangle}{dt} = \mathcal{H}(t)|\psi\rangle \tag{2.3}$$

where $\hbar$ is the Planck constant and $\mathcal{H}(t)$ is the *Hamiltonian* of the system. The latter is a Hermitian operator that describes the total energy of the system; if this operator is known the dynamics of the system is fully determined. Indeed, $U(t) = \exp(-i\mathcal{H}t/\hbar)$, and then the temporal evolution of $|\psi\rangle$ can be described as

$$|\psi'\rangle = e^{-\frac{i}{\hbar}\mathcal{H}t}|\psi\rangle. \tag{2.4}$$

However, the second postulate requires the described system to be closed, *i.e.* not interacting in any way with other systems. As a matter of facts, all systems interact with an environment. The requirement of an isolated system is not satisfied, for example, in case of evolution due to measurement. In this case, indeed, the system interacts with the experimental equipment used to observe the system. This interaction makes the system no longer closed, and thus not necessarily subject to unitary evolution. The third

postulate provides a means for describing the effects of measurements on quantum systems,

> **Postulate 3:** Quantum measurements are described by a collection $\{M_m\}$ of *measurement operators*. These are operators acting on the state space of the system being measured. The index m refers to the measurement outcomes that may occur in the experiment. If the state of the quantum system is $|\psi\rangle$ immediately before the measurement, then the probability that the result m occurs is given by $p(m) = \langle\psi|M_m^\dagger M_m|\psi\rangle$ and the state of the system after the measurement is $M_m|\psi\rangle/\sqrt{\langle\psi|M_m^\dagger M_m|\psi\rangle}$.

An example of the third postulate is represented by the measurement of a qubit in the computational basis described in eq. (2.1). In that case, the probability of obtaining 0 as the measurement outcome is

$$p(0) = \langle\psi|M_0^\dagger M_0|\psi\rangle = \alpha\langle\psi|M_0|\psi\rangle = |\alpha|^2 \tag{2.5}$$

and, similarly, the probability of obtaining the measurement outcome 1 is $p(1) = |\beta|^2$. Naturally, $|\alpha|^2 + |\beta|^2 = 1$, since the probabilities must sum to one.

By recalling the Bloch sphere of Figure 2.1, it could be noted that since there are an infinite number of points on the Bloch sphere, in principle one could store the entire *Divina Commedia* using an extremely large binary expansion of θ. This is however misleading, since by measuring the qubit state, the output will be always either 0 or 1. Indeed, measurement changes the state of a qubit, which collapses from its superposition states $|0\rangle$ and $|1\rangle$ to the specific state, $|0\rangle$ or $|1\rangle$, consistent with the measurement result. Thus, from a single measurement one obtains only a single bit of information about the state of the qubit.

It is not possible to examine a qubit to determine its quantum state, that is, the values of α and β. Indeed, when a qubit is measured, the output which is obtained can be either the result $|0\rangle$, with probability $|\alpha|^2$, or the result $|1\rangle$, with probability $|\beta|^2$. However, the outcome of the measurement, after the qubit has been manipulated and transformed, depends distinctly on the different properties of its state. Thus, though they are not accessible, the quantum states have real and experimentally verifiable consequences.

For realizing a true quantum computer it is not sufficient to exploit the quantum superposition state, but it is necessary to have a composite quantum system made of at least two qubits in order to perform two-qubits gates. The fourth postulate describes how

the state space of a composite system is built up from the state spaces of the component systems,

> **Postulate 4:** The state space of a composite physical system is the tensor product of the state spaces of the component physical systems. Moreover, if we have systems numbered 1 through n, and system number i is prepared in the state $|\psi_i\rangle$, then the joint state of the total system is $|\psi_1\rangle \otimes |\psi_2\rangle \otimes ... \otimes |\psi_n\rangle$.

This postulate also enables us to define one of the most interesting and puzzling ideas associated with composite quantum systems: *entanglement*. By considering the two qubits state

$$|\psi\rangle = \frac{|00\rangle + |11\rangle}{\sqrt{2}} \tag{2.6}$$

this state has the remarkable property that there are no single qubit states $|a\rangle$ and $|b\rangle$ such that $|\psi\rangle = |a\rangle \otimes |b\rangle$. A state of a composite system having this property, *i.e.* which cannot be written as a product of states of its component system, is an *entangled* state. The entanglement is a natural occurrence of quantum systems when they are correlated by some weak interaction, and it is a necessary property to realize two-qubits gate. This, in addition to the possibility to exploit the superposition state in performing quantum operation, gives access to the *quantum parallelism*, which is expected to enormously increase the potential of information processing.[8]

Notwithstanding its strangeness, qubits are real objects and they can be realized with many different physical systems. Examples of systems proposed for the realization of qubits are: quantum dots,[9, 10] cold trapped ions,[11] cavity quantum electrodynamics,[9, 12] bulk nuclear magnetic resonance,[13] low-capacitance Josephson junctions,[14] donor atoms,[15, 16] linear optics,[17] colour centres in diamond,[18-20] carbon nanotubes,[21] nanowires[22] and molecular spins.[23-28]

The challenge of experimental realization of a quantum computer is a delicate balance between constraints. For example, a quantum computer must be well isolated in order to retain its quantum properties, but at the same time its qubits have to be accessible so that they can be manipulated to perform a computation and to read out the results. A key concept which emerges from this is the *decoherence*, or *quantum noise*. The length of the longest possible quantum computation is roughly given by the ratio between τ_Q, *i.e.* the time for which a system remains quantum-mechanically coherent, and τ_{op}, *i.e.*

the time necessary to perform elementary unitary transformations. Both times are related to each other, since they are determined by the strength of the coupling between the system and the external world, and they vary depending on the type of system chosen for implementing the qubit (and consequently on the corresponding setup used). For example, for molecular electronic spins the ratio $\lambda = \tau_Q/\tau_{op}$ should be about 10^4; the time τ_{op} necessary to manipulate electronic spin by using microwave pulses is about 10^{-8} s, for which coherence times in the range of tens of microseconds are needed.

The basic requirements that the chosen system must fulfil to efficiently work as qubit can be collected together and correspond to the abilities of the system to:

1. **Robustly represent quantum information.**

   Quantum computation is based on the transformation of the quantum state of a qubit. To avoid accumulation of error during the transformation and evolution of the quantum state, the decoherence must be minimized. For this purpose, it is crucial to choose a system with a finite number of accessible states; indeed, if the choice of representation is poor, then decoherence will result in destroying the qubit superposition states. A well-isolated qubit is also a possible strategy to reduce decoherence. In this frame, the figure of merit for a qubit is the minimum lifetime of the arbitrary superposition states, the *coherence time*. In addition to a long coherence time, it should be chosen a system that can be scalable and that can provide multi-qubits architectures.

2. **Perform a universal family of unitary transformation.**

   Closed quantum systems evolve unitarily as determined by their Hamiltonians. Quantum algorithms can be implemented by controlling the Hamiltonian of the chosen system so that it is possible to make an arbitrary selection from a universal family of unitary transformations. Two important parameters for a unitary transformation are the minimum achievable fidelity ($\mathcal{F}$), which quantifies the ability of the system to provide as output the state given as input, and the maximum time τ_{op} required to perform elementary operations.

3. **Prepare a fiducial initial state.**

   One of the most important requirements for being able to perform a useful computation, even classically, is to be able to prepare the desired input. This means to produce repeatedly one specific quantum state with high fidelity, since a unitary transformation can turn it into any other desired input state. However, in some systems this can be achieved by working with very low temperatures.

4. **Measure the output result.**

   One key aspect of the measurement process for quantum computation is the collapse of the superposition state. The output of a good quantum algorithm is a

superposition state which gives a useful answer with high probability when measured.

Satisfying all these requirements in a single system simultaneously is very hard. Notwithstanding the huge progresses achieved in the several research areas, it is not yet clear which system will turn out to be most suitable for qubit implementation.

The more intuitive idea of qubit is provided by the two-levels of a single spin 1/2. Spins are excellent quantum systems since, in most cases, mathematical descriptions and experimental tools for their manipulation are already largely developed. In this frame, the first candidate that one could imagine for implementing a qubit is the single spin of an atom. However, experimentally it would be very challenging to control this single spin, since the length scale on which this control would take place is prohibitively small. On the contrary, solid-state implementations of qubits, such as quantum dots,[10] require fields on a scale of several tens of micrometres only, making control of the state easier. The increased size, however, means additional sources of decoherence, and enormous efforts have been done in recent years to reduce its effects. Molecular magnets are in between these two extremes. The typical sizes of molecules mean that the requirements on the spatial scale on which control can be possible are lost with respect to those for a single spin. However, molecules are still small as compared to other solid states implementations of qubits. This aspect, in addition to the possibility of chemically engineering molecular magnets with a wide variety of properties, may make one hopeful that sources of decoherence in molecular magnets can be reduced.

Compared to other types of qubit realization, molecular magnets offer important advantages: they are scalable, and their structure can be tuned with chemical methods, for example by coupling more qubits together so that two-qubit gates can be implemented. Moreover, it is not strictly necessary to use systems with spin 1/2, but the two state levels may be embodied by any spin system that in a certain regime exhibits two effective states. In this sense, if the system exhibits more than two effective states, it represents the so-called *qudit* system. It has been recently shown that the multilevel structure of the qudit can be exploited to efficiently encode and operate a qubit with embedded quantum error correction.[29] This aspect results paramount considering that nowadays it is the strongest limitation of the operating quantum computers, which are based on superconducting circuits.

The basic requirements previously listed can be now discussed on the basis of the choice of the electronic spin of molecular magnets as platform to realize qubits. Moreover, they will be here presented following the five criteria proposed by DiVincenzo[8] for realizing a quantum computer:

i. **Properly defined and scalable qubits.**

In molecular spin-systems, this means that each spin qubit is sufficiently isolated within the molecule to exhibit a proper two-level qubit basis, indicated as the spinors $|\downarrow\rangle$ and $|\uparrow\rangle$, well separated from any possible excited state. Examples of true spin ½ are the transition metals Cu^{II}, V^{IV}, Cr^{V} or Ti^{III}, and, as mentioned later, lanthanide ions within a strong crystal field. Scalability is a key factor to build quantum computers and it is one of the most challenging aspects at the moment. Scalability requires an array of connected logical building blocks and the capability to individually manipulate them by an external potential. By exploiting chemical methods, macroscopic arrays of identical molecules can be obtained by addressing molecules on surface. The individual manipulation of them can be achieved by using scanning probe microscopy techniques. However, other strategies are under investigation, such as the implementation of hybrid molecular spin-superconductor devices, which require large ensembles composed of identical molecular spin systems (easily achievable by using chemical methods).

ii. **Easy and efficient initialization.**

There must be the possibility to set each qubit in a well-defined initial state at any time and in an efficient manner, otherwise quantum noise occurs. For a molecular spin this can be done by placing it into its ground state, for example by cooling it under an external magnetic field or by means of external stimuli.

iii. **Implementing universal quantum gates.**

Single- or two-qubits gates can be performed by manipulating the electronic spin of molecular magnets with pulses of microwave radiation, such as those used in pulsed Electron Paramagnetic Resonance. Indeed, the superposition state can be obtained by applying on the sample an oscillating magnetic field B_1, perpendicular and with intensity smaller than the external static magnetic field B. By exposing the qubit to pulsed microwave fields for suitably time intervals, *Rabi oscillations* can be measured. An example is reported in Figure 2.3.

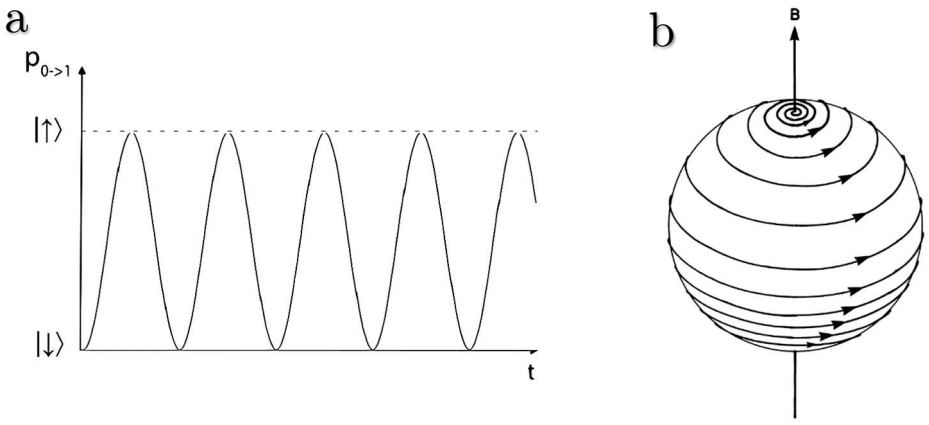

Figure 2.3. (a) Example of Rabi oscillations for a generic spin 1/2. (b) Evolution of the superposition state into the Bloch sphere in case of Rabi oscillations. Image (b) has been taken by ref[30].

This can be expressed mathematically by writing the Hamiltonian of the system

$$\mathcal{H}(t) = -\frac{\hbar}{2}\begin{pmatrix} \omega_0 & \omega_1 e^{i\omega t} \\ \omega_1 e^{-i\omega t} & -\omega_0 \end{pmatrix} \tag{2.7}$$

where ω_0 is the Larmor frequency of the spin induced by B, ω_1 the spin precession frequency related to B_1 and ω the frequency of the spin. The evolution of the system can be expressed as follows: if at time $t = 0$ the qubit is in the state $|\downarrow\rangle$, at a time t it will have a probability $p_{\downarrow\to\uparrow}(t)$ of being found in the state $|\uparrow\rangle$ given by

$$p_{\downarrow\to\uparrow}(t) = \left(\frac{\omega_1}{\Omega}\right)^2 \sin^2\frac{\Omega t}{2} \tag{2.8}$$

where $\Omega = \sqrt{(\omega - \omega_0)^2 + \omega_1^2}$ is known as *Rabi frequency*. The oscillations between the two levels have maximum amplitude at the resonance condition, that is, for $\omega = \omega_0$, for which

$$p_{\downarrow\to\uparrow}(t) = \sin^2\frac{\omega_1 t}{2}. \tag{2.9}$$

The resonant transition between the two levels can be simply achieved by adjusting the time t during which the rotating field acts. For example, $(\omega_1\ t)/2 = \pi/2$ is called π-pulse, whereas the superposition state can be obtained by using $t = \pi/2\omega_1$ that is called $\pi/2$-pulse. This can be visualized

as moving the superposition state in a screw-like motion back and forth between the bottom pole and the top pole of the Bloch sphere (Figure 2.3). At this point it should be clear that Rabi oscillations are the basic process used to manipulate qubits, and their observation in nutation pulsed EPR spectroscopy is a proof of the feasibility of such a quantum manipulation.

iv. **Readout of qubits.**

The state of the target qubits in output must be determined once the computation is finished. This implies that any qubit must be addressed selectively, either spatially, spectrally, magnetically or by any other means. This is a very challenging task for implementing qubits with molecular magnets. In this frame, the addressing of individual molecules deposited on a surface, as in scanning probe microscopies, seems the more plausible direction.

v. **Long enough coherence times compared to the 'clock time' of the quantum computer.**

As mentioned before, the information content in the qubit is not infinitely long-lived, contrary to what would emerge considering a unitary transformation acting on a closed quantum system, as stated by postulate 2. This occurs since in practical a qubit cannot be completely isolated from the environment, whose fluctuations result in decoherence, *i.e.* the process whereby information about a quantum state is lost. In molecular magnets, decoherence of the electron spin mainly arises from its coupling to phonons and nuclear spins. It is important to specify that decoherence of a single qubit takes place on two different time scales. For molecular magnets, the longitudinal (spin-lattice) relaxation time, T_1, describes the average time in which the environment induces random transition from $|\downarrow\rangle$ to $|\uparrow\rangle$, and vice versa. The time T_1 sets on upper limit on the time a system can be used as a classical bit. The transverse (spin-spin) relaxation time, T_2, describes the time in which the system loses its information about the superposition state. This coincides with the coherence time previously mentioned and corresponds to the time for which the transition from the quantum- into the classical regime occurs. The two relaxation times are related to each other, and in particular T_1 represents the upper limit of T_2. Pulsed EPR is the primary tool for investigating and characterizing the spin dynamics, *i.e.* the evolution of such relaxation times, of molecular spin qubits.

The control of decoherence represents a key challenge for the implementation of quantum-information processing using the electronic spin of molecular magnets, since it would maximize the coherence time. In this frame, it is necessary to achieve a detailed

understanding of the decoherence processes, which can be reached by exploiting the great variability of coordination chemistry. The primary aim is hence the identification of the degrees of freedom that are more robust with respect to decoherence and that are thus more suitable for encoding quantum information.

2.2 Molecular spin qubits

The discovery of the quantum tunneling of magnetization in the 1990s represents the first breakthrough towards this research area. Indeed, this demonstrated that molecular spins are real systems on which quantum effects can be controlled and studied in laboratory conditions.[31, 32] From this achievement, many chemists and physicists started to study the so-called *Single Molecule Magnets* (SMMs), *i.e.* polynuclear molecular cluster based on *d*-block metals and showing magnetic hysteresis at low temperatures, for implementing super-dense memory storage. This application is still based on the classical protocol (0 or 1), for which the figure of merit is T_1. In the 2000s, a second breakthrough occurred, with the rise of the second generation of molecular nanomagnets based on mononuclear complexes containing a single magnetic ion, generally based on *f*-block metals.[33] This research area kept growing and most recently a third breakthrough has pushed the applicability temperature limit of these systems from few tens of Kelvin to the remarkable temperature of 80 K, *i.e.* close or above to the liquid N_2 temperature limit.[34, 35]

In parallel to this approach, the interest in using these systems for quantum technologies applications has grown. Indeed, the first proposal date back to 2001, with the idea to perform Grover's algorithm in ensembles of high-spin nanomagnets such as Mn_{12} or Fe_8,[24] exploiting the non-equispaced multilevel energy pattern of these molecules and a multifrequency pulsed EPR spectrometer.

The first measurements to investigate the coherence were performed on the Fe_8 SMM.[36-38] However, the real breakthrough in this field occurred in 2007, when Rabi oscillations and coherence times of the order of few microseconds have been experimentally observed in 2007 for Cr_7Ni rings at liquid helium temperatures, demonstrating the potentialities of polynuclear molecular clusters for Quantum Computing applications.[39] This complex is an heterometallic ring with antiferromagnetic coupling among the constituent ions, resulting in a nearly isotropic doublet ground state well isolated from the states of higher multiplicity lying at higher energy. Today such kinds of systems are still investigated as building blocks for more complex architectures.[5, 40] A year later, Rabi oscillations were measured also for Fe_4 (with a ground-state $S = 5$) and V_{15} (with a ground-state $S = 1/2$) nanomagnets at the same low temperatures,

evidencing coherence times of the order of few hundreds of microseconds.[41, 42] While optimization strategies for improving the coherence times were actively looked for polynuclear transition metal clusters, an alternative involving the use of mononuclear molecular systems was proposed in 2013 by investigating the coherence time of CuPc, which showed coherence time values around a few microseconds at 80 K.[43] Following this strategy, the optimization of structural features, such as the reduction of methyl groups and spin-active nuclei, has led to coherence times of 68 μs at low temperature and, remarkably, 600 ns at room temperature for the molecular system $(Ph_4P)_2[Cu(mnt)_2]$.[44] However, the complete exclusion of nuclear spins from the ligands and environment of the molecular system (but not from the metal ion) was reached with the synthesis of $[V(C_8S_8)_3]^{2-}$ and its measurement in CS_2 solution. Strikingly, these foresights resulted in coherence times at 10 K of 675 μs, demonstrating the power of synthetic chemistry in extending coherence times to values that are comparable to those of other solid state qubits.[45] A series of detailed investigations on this type of molecular systems, both varying metal ion and ligands, have been useful to identify the key features for enhancing the coherence times of molecular spin qubits.[46-55]

A further strategy investigated in the recent years focused on the use of lanthanide ions instead of transition metals. Lanthanide ions allow a great control over the energy level structure and electro-nuclear hyperfine interaction. The use of these systems as potential solid-state qubits have been proposed in the first decade of the millennium,[56, 57] but molecular based materials were only investigated in the past few years.[58-60] Interesting systems were obtained by using inorganic polyoxometalate cages or organic sp^2 structures. In the former case, among the investigated systems,[61-63] the molecular system $[HoW_{10}O_{36}]^{9-}$ is particularly appealing since it showed a high insensitivity to magnetic noise. This is, indeed, possible by exploiting avoided level crossings between qubits states, also known as *clock transitions*.[64]

While the previously discussed studies were essentially aimed to find complexes with suitably long coherence times, large efforts have been also devoted to fulfilling the other above-mentioned criteria for the development of suitable qubits. In this respect, recently many studies have been focused on realizing two-qubits molecular systems. In particular, two strategies have been actively pursued: the connection of Cr_7Ni derivative rings either through ligands or mononuclear metal complexes,[40, 65] and the synthesis of binuclear heterometallic lanthanides systems.[58, 66] Most recently, a bi-metallic vanadyl-based molecular system has been also proposed as a potential two-qubits gate, exploiting an hybrid approach based on electron-nuclear interaction.[67] The use of nuclear degrees of freedom has indeed been shown to be particularly powerful in the case of $TbPc_2$. This represents an example of sp^2-coordinated molecular spin qubit, and in this case quantum

manipulation can be performed by exploiting four sub-states created by the strong hyperfine coupling between the electronic ground state and nuclear spin.[68, 69] It is on this system, indeed on a single molecule of it, that the first realization of the Grover's quantum algorithm has been achieved.[70]

In this context, the research presented in this dissertation, started in 2015 and mainly based on exploring vanadyl molecules, has been carried out.

2.3 Bibliography

1. M. A. Nielsen and I. L. Chuang, *Quantum Computation and Quantum Information: 10th Anniversary Edition*, Cambridge University Press, 2011.
2. M. Le Bellac, *A Short Introduction to Quantum Information and Quantum Computation*, Cambridge University Press, Cambridge, 2006.
3. J. Bartolome, F. Luis and J. F. Fernandez, *Molecular Magnets*, Springer-Verlag Berlin Heidelberg, 2014.
4. A. Ghirri, F. Troiani and M. Affronte, *Struct Bond*, 2015, **164**, 383-430.
5. P. Santini, S. Carretta and G. Amoretti, in *Molecular Magnetic Materials*, eds. B. Sieklucka and D. Pinkowicz, 2017.
6. D. P. DiVincenzo, *Science*, 1995, **270**, 255.
7. A. Barenco, C. H. Bennett, R. Cleve, D. P. DiVincenzo, N. Margolus, P. Shor, T. Sleator, J. A. Smolin and H. Weinfurter, *Phys. Rev. A*, 1995, **52**, 3457-3467.
8. D. P. DiVincenzo, *Fortschritte der Physik*, 2000, **48**, 771-783.
9. A. Imamoglu, D. D. Awschalom, G. Burkard, D. P. DiVincenzo, D. Loss, M. Sherwin and A. Small, *Phys. Rev. Lett.*, 1999, **83**, 4204-4207.
10. D. Loss and D. P. DiVincenzo, *Phys. Rev. A*, 1998, **57**, 120-126.
11. J. I. Cirac and P. Zoller, *Phys. Rev. Lett.*, 1995, **74**, 4091-4094.
12. Q. A. Turchette, C. J. Hood, W. Lange, H. Mabuchi and H. J. Kimble, *Phys. Rev. Lett.*, 1995, **75**, 4710-4713.
13. N. Gershenfeld and I. Chuang, *Science*, 1997, **277**, 1689-1690.
14. A. Shnirman, G. Schon and Z. Hermon, *Phys. Rev. Lett.*, 1997, **79**, 2371-2374.
15. B. E. Kane, *Nature*, 1998, **393**, 133-137.
16. R. Vrijen, E. Yablonovitch, K. Wang, H. W. Jiang, A. Balandin, V. Roychowdhury, T. Mor and D. DiVincenzo, *Phys. Rev. A*, 2000, **62**, 012306.
17. E. Knill, R. Laflamme and G. J. Milburn, *Nature*, 2001, **409**, 46-52.
18. R. Hanson and D. D. Awschalom, *Nature*, 2008, **453**, 1043-1049.

19. F. Jelezko and J. Wrachtrup, *Physica Status Solidi a-Applications and Materials Science*, 2006, **203**, 3207-3225.

20. P. Maletinsky, S. Hong, M. S. Grinolds, B. Hausmann, M. D. Lukin, R. L. Walsworth, M. Loncar and A. Yacoby, *Nat. Nanotechnol.*, 2012, **7**, 320-324.

21. D. V. Bulaev, B. Trauzettel and D. Loss, *Physical Review B*, 2008, **77**.

22. M. Trif, V. N. Golovach and D. Loss, *Physical Review B*, 2008, **77**.

23. J. Lehmann, A. Gaita-Arino, E. Coronado and D. Loss, *Nat. Nanotechnol.*, 2007, **2**, 312-317.

24. M. N. Leuenberger and D. Loss, *Nature*, 2001, **410**, 789-793.

25. F. Meier, J. Levy and D. Loss, *Phys. Rev. Lett.*, 2003, **90**, 047901.

26. J. Tejada, E. M. Chudnovsky, E. Del Barco, J. M. Hernandez and T. P. Spiller, *Nanotechnology*, 2001, **12**, 181-186.

27. F. Troiani, A. Ghirri, M. Affronte, S. Carretta, P. Santini, G. Amoretti, S. Piligkos, G. Timco and R. E. P. Winpenny, *Phys. Rev. Lett.*, 2005, **94**, 207208.

28. M. Trif, F. Troiani, D. Stepanenko and D. Loss, *Phys. Rev. Lett.*, 2008, **101**, 217201.

29. R. Hussain, G. Allodi, A. Chiesa, E. Garlatti, D. Mitcov, A. Konstantatos, K. S. Pedersen, R. De Renzi, S. Piligkos and S. Carretta, *J. Am. Chem. Soc.*, 2018, **140**, 9814-9818.

30. J. A. Weil and J. R. Bolton, in *Electron Paramagnetic Resonance*, John Wiley & Sons, Inc., 2006, pp. 357-384.

31. R. Sessoli, D. Gatteschi, A. Caneschi and M. A. Novak, *Nature*, 1993, **365**, 141-143.

32. D. Gatteschi, R. Sessoli and J. Villain, *Molecular nanomagnets*, Oxford University Press, Oxford, UK, 2006.

33. N. Ishikawa, M. Sugita, T. Ishikawa, S. Koshihara and Y. Kaizu, *J. Am. Chem. Soc.*, 2003, **125**, 8694-8695.

34. F.-S. Guo, B. M. Day, Y.-C. Chen, M.-L. Tong, A. Mansikkamäki and R. A. Layfield, *Science*, 2018, **362**, 1400-1403.

35. F.-S. Guo, B. M. Day, Y.-C. Chen, M.-L. Tong, A. Mansikkamäki and R. A. Layfield, *Angew. Chem. Int. Ed.*, 2017, **56**, 11445-11449.

36. M. Bal, J. R. Friedman, Y. Suzuki, K. M. Mertes, E. M. Rumberger, D. N. Hendrickson, Y. Myasoedov, H. Shtrikman, N. Avraham and E. Zeldov, *Physical Review B*, 2004, **70**, 100408.

37. M. Bal, J. R. Friedman, M. T. Tuominen, E. M. Rumberger and D. N. Hendrickson, *J. Appl. Phys.*, 2006, **99**, 08D103.

38. S. B. K. Petukhov, W. Wernsdorfer, A.-L. Barra, and V. Mosser, *Phys. Rev. B* 2007, **75**, 064408.

39. A. Ardavan, O. Rival, J. J. L. Morton, S. J. Blundell, A. M. Tyryshkin, G. A. Timco and R. E. P. Winpenny, *Phys. Rev. Lett.*, 2007, **98**, 057201.

40. A. Fernandez, J. Ferrando-Soria, E. M. Pineda, F. Tuna, I. J. Vitorica-Yrezabal, C. Knappke, J. Ujma, C. A. Muryn, G. A. Timco, P. E. Barran, A. Ardavan and R. E. P. Winpenny, *Nature Communications*, 2016, **7**.

41. C. Schlegel, J. van Slageren, M. Manoli, E. K. Brechin and M. Dressel, *Phys. Rev. Lett.*, 2008, **101**, 147203.

42. S. Bertaina, S. Gambarelli, T. Mitra, B. Tsukerblat, A. Muller and B. Barbara, *Nature*, 2008, **453**, 203-U205.

43. M. Warner, S. Din, I. S. Tupitsyn, G. W. Morley, A. M. Stoneham, J. A. Gardener, Z. Wu, A. J. Fisher, S. Heutz, C. W. M. Kay and G. Aeppli, *Nature*, 2013, **503**, 504-508.

44. K. Bader, D. Dengler, S. Lenz, B. Endeward, S.-D. Jiang, P. Neugebauer and J. van Slageren, *Nat Commun*, 2014, **5**, 5304.

45. J. M. Zadrozny, J. Niklas, O. G. Poluektov and D. E. Freedman, *ACS Central Science*, 2015, **1**, 488-492.

46. K. Bader, S. H. Schlindwein, D. Gudat and J. van Slageren, *Phys. Chem. Chem. Phys.*, 2017, **19**, 2525-2529.

47. K. Bader, M. Winkler and J. van Slageren, *Chem. Commun.,* 2016, **52**, 3623-3626.

48. M. J. Graham, M. D. Krzyaniak, M. R. Wasielewski and D. E. Freedman, *Inorg. Chem.*, 2017, **56**, 8106-8113.

49. M. J. Graham, C. J. Yu, M. D. Krzyaniak, M. R. Wasielewski and D. E. Freedman, *J. Am. Chem. Soc.*, 2017, **139**, 3196-3201.

50. M. J. Graham, J. M. Zadrozny, M. Shiddiq, J. S. Anderson, M. S. Fataftah, S. Hill and D. E. Freedman, *J. Am. Chem. Soc.*, 2014, **136**, 7623-7626.

51. C. J. Yu, M. J. Graham, J. M. Zadrozny, J. Niklas, M. D. Krzyaniak, M. R. Wasielewski, O. G. Poluektov and D. E. Freedman, *J. Am. Chem. Soc.*, 2016, **138**, 14678-14685.

52. S. Lenz, K. Bader, H. Bamberger and J. van Slageren, *Chem. Commun.*, 2017, **53**, 4477-4480.

53. J. M. Zadrozny and D. E. Freedman, *Inorg. Chem.*, 2015, **54**, 12027-12031.

54. J. M. Zadrozny, M. J. Graham, M. D. Krzyaniak, M. R. Wasielewski and D. E. Freedman, *Chem. Commun.*, 2016, **52**, 10175-10178.

55. Z. Liu, B.-W. Dong, H.-B. Meng, M.-X. Xu, T.-S. Wang, B.-W. Wang, C.-R. Wang, S.-D. Jiang and S. Gao, *Chem. Sci.*, 2018, **9**, 457-462.

56. S. Bertaina, S. Gambarelli, A. Tkachuk, I. N. Kurkin, B. Malkin, A. Stepanov and B. Barbara, *Nat. Nanotechnol.*, 2007, **2**, 39-42.

57. R. M. Rakhmatullin, I. N. Kurkin, G. V. Mamin, S. B. Orlinskii, M. R. Gafurov, E. I. Baibekov, B. Z. Malkin, S. Gambarelli, S. Bertaina and B. Barbara, *Physical Review B*, 2009, **79**, 172408.

58. D. Aguila, L. A. Barrios, V. Velasco, O. Roubeau, A. Repolles, P. J. Alonso, J. Sese, S. J. Teat, F. Luis and G. Aromi, *J. Am. Chem. Soc.*, 2014, **136**, 14215-14222.

59. F. Luis, A. Repolles, M. J. Martinez-Perez, D. Aguila, O. Roubeau, D. Zueco, P. J. Alonso, M. Evangelisti, A. Camon, J. Sese, L. A. Barrios and G. Aromi, *Phys. Rev. Lett.*, 2011, **107**, 117203.

60. K. S. Pedersen, A. M. Ariciu, S. McAdams, H. Weihe, J. Bendix, F. Tuna and S. Piligkos, *J. Am. Chem. Soc.*, 2016, **138**, 5801-5804.

61. J. J. Baldovi, S. Cardona-Serra, J. M. Clemente-Juan, E. Coronado, A. Gaita-Arino and H. Prima-Garcia, *Chem. Commun.*, 2013, **49**, 8922-8924.

62. M. J. Martinez-Perez, S. Cardona-Serra, C. Schlegel, F. Moro, P. J. Alonso, H. Prima-Garcia, J. M. Clemente-Juan, M. Evangelisti, A. Gaita-Arino, J. Sese, J. van Slageren, E. Coronado and F. Luis, *Phys. Rev. Lett.*, 2012, **108**, 247213

63. S. Ghosh, S. Datta, L. Friend, S. Cardona-Serra, A. Gaita-Arino, E. Coronado and S. Hill, *Dalton Trans.*, 2012, **41**, 13697-13704.

64. M. Shiddiq, D. Komijani, Y. Duan, A. Gaita-Arino, E. Coronado and S. Hill, *Nature*, 2016, **531**, 348.

65. J. Ferrando-Soria, E. Moreno Pineda, A. Chiesa, A. Fernandez, S. A. Magee, S. Carretta, P. Santini, I. J. Vitorica-Yrezabal, F. Tuna, G. A. Timco, E. J. McInnes and R. E. Winpenny, *Nat Commun*, 2016, **7**, 11377.

66. G. Aromi, D. Aguila, P. Gamez, F. Luis and O. Roubeau, *Chem. Soc. Rev.*, 2012, **41**, 537-546.

67. M. Atzori, A. Chiesa, E. Morra, M. Chiesa, L. Sorace, S. Carretta and R. Sessoli, *Chem. Sci.*, 2018, **9**, 6183-6192.

68. R. Vincent, S. Klyatskaya, M. Ruben, W. Wernsdorfer and F. Balestro, *Nature*, 2012, **488**, 357-360.

69. S. Thiele, F. Balestro, R. Ballou, S. Klyatskaya, M. Ruben and W. Wernsdorfer, *Science*, 2014, **344**, 1135-1138.

70. C. Godfrin, A. Ferhat, R. Ballou, S. Klyatskaya, M. Ruben, W. Wernsdorfer and F. Balestro, *Phys. Rev. Lett.*, 2017, **119**, 187702.

Chapter 3

Theory of Spin Relaxation

The theory of spin relaxation is a wide topic that covers almost one century of researches. The aim of this chapter is to provide a background useful to understand the main processes that drive the magnetic relaxation of the ions investigated in this dissertation, rather than provide an exhaustive discussion about the spin relaxation theory. For this reason, the chapter is focused on: *i)* the spin-lattice relaxation, for which other types of relaxation will be considered only as perturbations of it; *ii)* paramagnetic ions of transition metals, being the dissertation principally based on the investigation of single ion vanadyl-based molecules; *iii)* Kramers doublets, though non-Kramers systems will be mentioned; *iv)* solid-state systems, neglecting effects related to the liquid state. Emphasis will be placed on side effects as the spin-phonon bottleneck, whereas other effects, such as the cross-relaxation or the relaxation through impurities, are not interesting for this dissertation and they are overlooked. It is useful to remember that the dissertation (and so this chapter) is mainly focused on the strategies to lengthen the spin-lattice relaxation time T_1, because it represents a hindrance for increasing the coherence time T_2, in particular as the temperature is increased. However, the main processes acting on T_2 will be also briefly presented for completeness.

The chapter has been written according to a wide literature about Spin Relaxation. In particular, the following reviews have been fundamental for this purpose: (The establishment of thermal equilibrium in paramagnetic crystals, J. C. Gill, 1975),[1] (Spin-lattice relaxation in rare-earth salts, R. Orbach, 1961)[2] and (The theory of paramagnetic relaxation, K. W. H. Stevens, 1967)[3], in addition to the book (Electron Spin Relaxation Phenomena in Solids, K. J. Standley and R. A. Vaughan, 1969)[4].

3.1 From the free ion to the spin Hamiltonian

Starting from the free ion, the electronic states are degenerate because of the non-zero total angular momentum, $\boldsymbol{J}$. For the lighter ions this is the resultant of a total orbital momentum $\boldsymbol{L}$ and spin $\boldsymbol{S}$, $\boldsymbol{J} = \boldsymbol{L} + \boldsymbol{S}$, coupled by the spin-orbit interaction $\lambda \boldsymbol{L} \cdot \boldsymbol{S}$. This degeneracy is then partially or totally removed by including the free ion in an environment generating a crystalline field, which is the electrostatic field of the ion's neighbour atoms corrected for the covalent character of the interaction.[5] In certain cases, however, other perturbations can remove the degeneracy, *e.g.* when Jahn-Teller effects occur.[6] Interestingly, ions having half-integer spin value, $\boldsymbol{S}$, and without additional interactions that breaks the time-reversal symmetry will be at least doubly degenerate, as stated by the Kramers degeneracy theorem.[7] This means that even the low symmetry of the crystal field cannot separate the two states, named *Kramers doublets*. The application of a magnetic field breaks the time-reversal symmetry and removes this degeneracy. Consequently, this theorem identifies two classes of ions, one with integer and the other with half-integer spin values, having notable differences in the magnetic properties. A further small separation of each electronic state may result from the interaction between electronic and nuclear spin, whose strength depends on the hyperfine coupling.

The relative influence of crystal field and spin-orbit coupling is different in *f*-orbital and *d*-orbital ions because of their inherent nature, as shown in Figure 3.1. Indeed, *f*-orbitals are internal to the electronic shell, for which they feel a crystal field weaker than the spin-orbit coupling λ, typically 10^2 cm^{-1} against 10^3 cm^{-1}. In the crystal, the total angular momentum $\boldsymbol{J}$ of the free ion is widely retained, and the $(2J+1)$-fold degeneracy of the ground state is split in a series of levels, doublets if Kramers ion, spaced in many cases by a few tens of cm^{-1}. The opposite situation is encountered for *d*-orbital open shell ions, for which the crystal field can remove the free ion degeneracy with separations, around 10^4 cm^{-1}, larger than λ. The crystal field can leave a singlet or a multiplet as lowest orbital state. In the first case, the orbital momentum is quenched by a factor $\sim\lambda/\Delta$ and the spin $\boldsymbol{S}$ gives rise to a lowest group of $(2S+1)$ levels split. In the second case, the orbital reduction is of the order of λ^2/Δ or less. Finally, the application of 1 T of magnetic field will separate the Kramers doublets of few cm^{-1}, whereas the hyperfine splitting is of the order of 10^{-2} cm^{-1}.

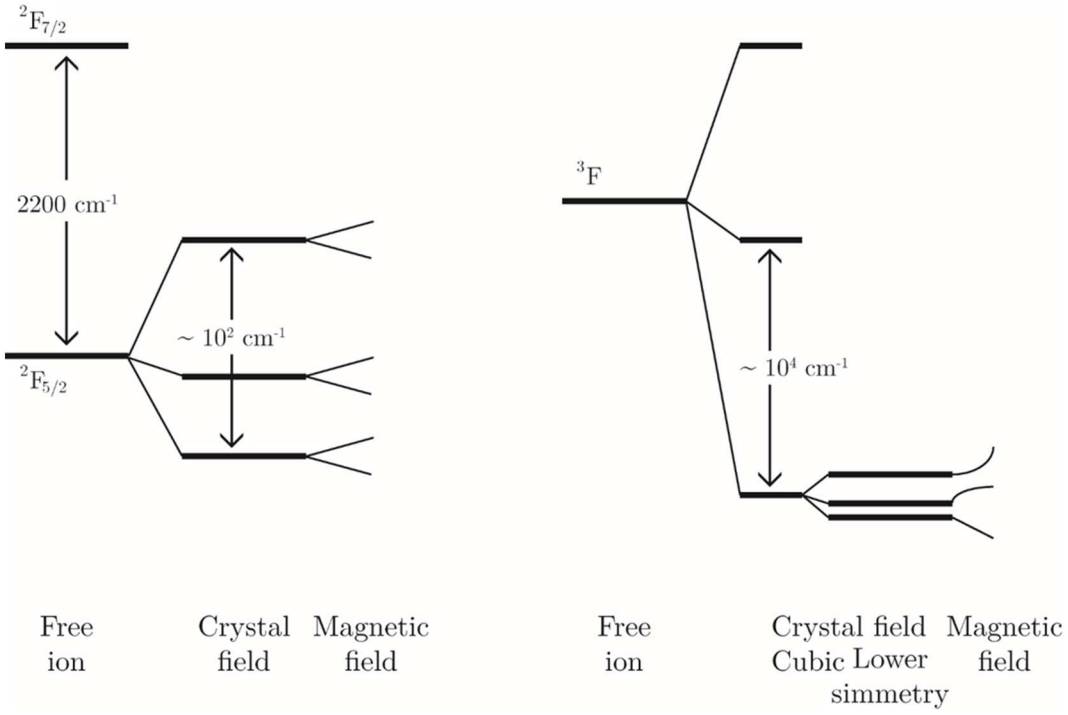

Figure 3.1. Effect of crystal and magnetic fields on (left) a lanthanide ion: Ce^{3+} ($4f^1$) in trigonal symmetry) and (right) a transition metal of the iron group: Ni^{2+} ($3d^8$) in a distorted octahedral symmetry. The image has been readapted starting by ref[1].

Well-defined spin level groups with large energy separation, when compared to their internal splittings, are usually produced by the crystal field and spin-orbit coupling terms. Such groups, each one deriving from a specific orbital state, will contain $(2S+1)$ spin levels and are more conveniently described by using the *Spin Hamiltonian approximation*. In this case, $\boldsymbol{S}$ is an effective spin whose value can differ from that of the free ion. A generic Spin Hamiltonian can be written as

$$\widehat{\mathcal{H}} = \beta \boldsymbol{H} \cdot g \cdot \hat{\boldsymbol{S}} + \hat{\boldsymbol{S}} \cdot \boldsymbol{D} \cdot \hat{\boldsymbol{S}} + \hat{\boldsymbol{S}} \cdot \boldsymbol{A} \cdot \hat{\boldsymbol{I}} + \hat{\boldsymbol{I}} \cdot \boldsymbol{Q} \cdot \hat{\boldsymbol{I}} \qquad (3.1)$$

where the first term corresponds to the *Zeeman interaction* in an applied field $\boldsymbol{H}$. The contribution of the orbital momentum is parametrized within g, which in general becomes a tensor with values more different from the spin-only value 2.0023 the larger is the orbital contribution. The second term is the *Zero Field Splitting* contribution that disappears for systems with $S = 1/2$. The two remaining terms respectively accounts for the *hyperfine interaction* between $\boldsymbol{S}$ and the nuclear spin $\boldsymbol{I}$, and the *quadrupolar coupling* between $\boldsymbol{I}$ and the electric field gradient within the ion. This approximation is often valid, however in certain cases it may fails, for example when the orbital momentum is non-completely quenched, for which a more accurate model must be used.

3.2 A simple model of relaxation

The spin can be perturbed in several ways, for example by the application of a magnetic field, and after the disturbance it returns to the equilibrium. This phenomenon is called *relaxation* and can involve the exchange of energy, in which case it is called *spin-lattice relaxation* (§3.3), or it can be adiabatic, and it is called *spin-spin relaxation* (§3.4). The former phenomenon involves the energy exchange between the crystal lattice, which surrounds the spin carrier, and the spin system mediated by the *spin-orbit coupling*. Whenever the spin is out of equilibrium, thermal vibrations of the crystal lattice restore the equilibrium dissipating the energy with the thermal bath. The entire process of dissipation from spin to bath occurs with the characteristic time T_1, or *spin-lattice relaxation time*. Usually, this time is related to the spin-lattice energy transfer, since this is the rate determining step, and it depends on which relaxation process is affecting the spin relaxation. In this frame, the *lattice-lattice* and *lattice-bath* transfers are faster, and consequently do not influence the characteristic relaxation time. However, an exception is represented by the *spin-phonon bottleneck* (§3.3.8), in which the lattice vibrations are not-well connected to the bath, for which they are not able to establish the equilibrium between the spin-lattice system and thermal bath, with noticeably repercussions on the spin relaxation.[8]

Concerning the second phenomenon, the *spin-spin relaxation*, the interaction is internal to the spin system, with the consequent conservation of the total energy. This effect is evident in the broadening of the linewidths of the resonance absorption spectra recorded by EPR measurements or measuring directly T_m, or *phase memory time*. The broadening of these peaks corresponds to the loss of coherence of the transversal magnetization.

An elementary description of these relaxation phenomena can be done considering individual paramagnetic ions making transitions between the accessible spin states $|p\rangle$. Considering T the temperature of the bath, the population of the state $|p\rangle$ with energy E_p is given according to the Boltzmann condition by

$$n_p^0 = \exp\left(-\frac{E_p}{kT}\right) Z^{-1} \tag{3.2}$$

where $Z = \sum_p \exp(-E_p/kT)$ is the partition function. Any perturbation corresponds to the variation of the level populations, for that $n_p - n_p^0 = \delta n_p$. It should be noted that in expression eq. (3.2) the strength of the coupling with the perturbation is not present, which instead appears in the rate at which the equilibrium is approached. The return to the equilibrium is indeed described by the rate equation of the process, whose form depends on the type of process involved. In the simplest case the spin-lattice relaxes due

to the van Vleck mechanism,[9] in which spins make transitions independently to each other, and the detailed balance is given by the fact that the probability of the transition from the state $|p\rangle$ to the state $|q\rangle$ is related to the reverse transition by

$$P_{pq} = P_{qp} \exp\left(\frac{E_p - E_q}{kT}\right) \tag{3.3}$$

and the rate equations may be written as

$$\delta\dot{n}_p = \sum_q (\delta n_q P_{qp} - \delta n_p P_{pq}). \tag{3.4}$$

Their formal solutions can be expressed as

$$\delta n_p = \sum_\lambda A_{p\lambda} \exp(-t/\tau_\lambda) \tag{3.5}$$

that are series of exponential decays with amplitude $A_{p\lambda}$ and characteristic relaxation times τ_λ with which the equilibrium is approached. It appears clear that, in general, the recovery of an out-of-equilibrium population can be analysed into sums of exponential decays. However, in many experiments the recoveries are not observed until all exponentials except one have decayed to zero, in which case the recovery can be reproduced by a single exponential. Examples of relaxation processes are shown in Figure 3.2. For instance, for a simple two-levels system

$$\begin{aligned} \dot{n}_1 &= -n_1 P_{12} + n_2 P_{21} \\ \dot{n}_2 &= -n_2 P_{21} + n_1 P_{12} \end{aligned} \tag{3.6}$$

and because $n_1 + n_2 = N$, these can be rearranged to give

$$\dot{n}_1 - \dot{n}_2 = 2n_2(P_{12} + P_{21}) - 2NP_{12} \tag{3.7}$$

from which follows that $n_1 - n_2$ recovers exponentially at a rate determined by $2(P_{12} + P_{21})^{-1}$.

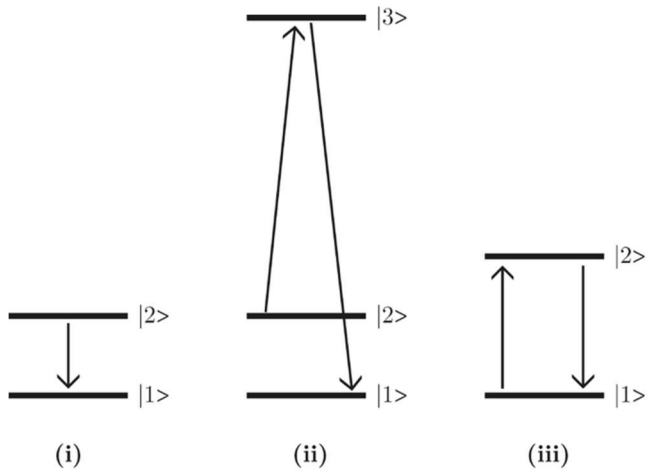

Figure 3.2. Relaxation processes represented as transitions between states of individual spins. Examples of spin-lattice relaxation are shown in (*i*) and (*ii*). A simplified view of the spin-spin relaxation resulting from coupling between identical spins is given in (*iii*). The image has been readapted starting from ref[1].

Some of the main transition processes, nowadays corresponding to the direct and Raman, were firstly identified by Waller, who also established the quantum mechanical framework for the calculation of the transition probabilities.[10] However, in his model the connection between the spin and lattice systems depends on the modulation of the magneto-dipolar interactions caused by the vibrational modes, but this mechanism is nowadays considered of secondary relevance. The principal mechanism was recognized by van Vleck as the modulation of the electrostatic fields (*i.e.* the electrostatic potential of the crystal field) produced by the distortion of the atoms surrounding the paramagnetic ion. The calculations of van Vleck culminated with the famous work about the relaxation times of Cr^{3+} and Ti^{3+} in alums.[11] However, the unsatisfactory agreement between theory and experimental data discouraged further exploration for almost two decades, when the academic subject assumed practical importance with the development of masers. It is around the early 1960s that it is possible to find the major activity in this area, with the extension of the research to lanthanide and actinide elements, and rapid advancements in several parallel aspects like the study of the relaxation in nuclear spin systems, or the improvement of microwave-based techniques. However, like a flame that burns too quickly, the spin relaxation research slowed down already in the early 1970s, when the superiority of the laser prototypes, with respect to masers, was doubtless.

The spin relaxation theories have remained far from the universality for which many experimental features are still unsolved.

3.3 The spin-lattice relaxation

The thermal vibration of a crystal can be seen as the analogue of the black-body electromagnetic radiation. In the same way, the transition processes concerning the spin-lattice relaxation have their counterparts in the emission and absorption of photons. The three most important types of process are presented in Figure 3.3.

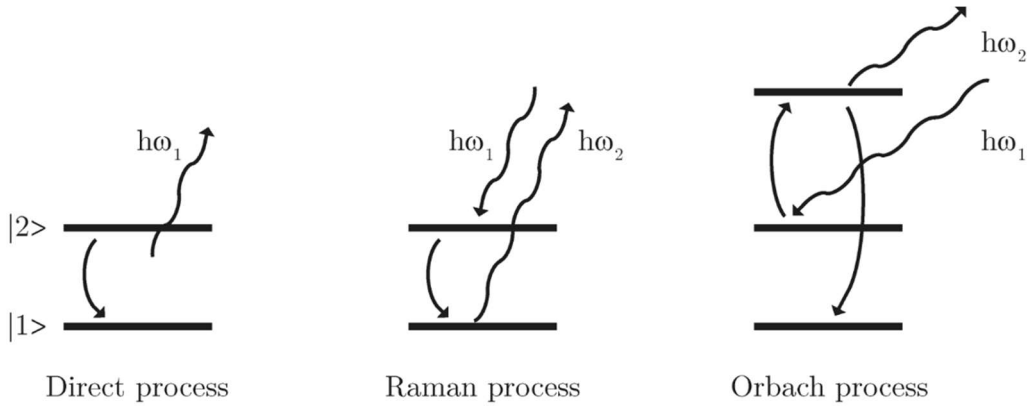

Figure 3.3. The three principal types of processes for the spin-lattice relaxation: direct, Raman and Orbach. Such processes are discussed in detail in this chapter.

By considering transition metals, the direct relaxation process arises from terms in the so-called *effective Hamiltonian* that are linear with the strain. Such a Hamiltonian is produced by mixing the spin-orbit and orbit-lattice terms, which couple the spin magnetic moment to the lattice vibrational modes. Only phonons of energy $\hbar\omega$ are utilized in this process, because only these phonons have the proper energy (*i.e.* equal to the energy separation of the spin states). These phonons are thus on 'speaking terms' with the spin system. The direct process consists in a spin transition between states $|p\rangle$ and $|q\rangle$ induced by one lattice vibration with resonant frequency $\omega_{pq} = (E_p - E_q)/\hbar$, in analogy to the radiative transitions involving single photons. This process dominates the spin-lattice relaxation at temperature sufficiently low, usually below the liquid hydrogen temperature.

At higher temperatures the two-phonons processes are responsible of a more pronounced relaxation. In such processes, spin transitions are induced by the absorption of one phonon accompanied by the emission of another whose frequencies differ by ω_{pq}. For the two-phonons Raman processes the effective Hamiltonian is built up in much the same way of the direct term, but using higher order of perturbation, being the orbit-lattice terms taken twice. Thus, the strain will appear in the second order, allowing all phonons to take part to the relaxation process. The equivalent of the Raman scattering, and named accordingly, involves transitions to and from virtual excited states. The Orbach process is a particular case of Raman that involves real transitions to and from

almost unoccupied excited states. This process is the analogue of the resonance fluorescence in spectroscopy.

The direct process matrix element of the effective Hamiltonian may be larger than the two-phonons processes. In general, at very low temperatures the direct process dominates because the density of the thermally excited phonons is not sufficiently high to produce second order processes. However, increasing the temperature more phonons can take part to the two-phonons relaxation, making the correspondent processes generally more effective at higher temperatures.

3.3.1 The harmonic lattice

Unless the temperature is exactly 0 K, the lattice of a crystal is never motionless.[12] The atomic displacement produced by an elastic wave propagating inside the crystal is

$$\boldsymbol{u}(\boldsymbol{r}) = u_0 \cos(k\boldsymbol{r}) \cos(\omega t) \tag{3.8}$$

where u_0 is the amplitude, k the propagation vector, $\boldsymbol{r}$ the atomic position in a three-dimensional crystal and $\cos \omega t$ accounts for the periodic behaviour. The energy of this lattice vibration is quantized, corresponding to the quasi-particle phonon, and it is

$$q = \left(n + \frac{1}{2}\right) \hbar\omega. \tag{3.9}$$

A standard simplification in the theory of crystal vibrations leads to the idea of independent modes of vibration, which can be described by the lattice Hamiltonian

$$\boldsymbol{\mathcal{H}}_l \equiv \sum_i \left\{ \begin{array}{l} \frac{1}{2}\hbar\omega_{i1}(\alpha_i^*\alpha_i + \alpha_i\alpha_i^*) \\ +\frac{1}{2}\hbar\omega_{i2}(\beta_i^*\beta_i + \beta_i\beta_i^*) \\ +\frac{1}{2}\hbar\omega_{i3}(\gamma_i^*\gamma_i + \gamma_i\gamma_i^*) \end{array} \right\} \tag{3.10}$$

where the α_i, β_i and γ_i are Bose annihilation operators: α, β, γ annihilate phonons, whereas $\alpha^*, \beta^*, \gamma^*$ create phonons. Expression (3.10) is written in this particular way to highlight that for each value of i there are three distinct modes, one longitudinally polarized mode and the other two orthogonal transverse modes. The harmonic lattice Hamiltonian can also be expressed as

$$\mathcal{H}_l \equiv \sum_i \{\hbar\omega_i\alpha_i^*\alpha_i + \hbar\Omega_i(\beta_i^*\beta_i + \gamma_i^*\gamma_i)\} \tag{3.11}$$

where $\hbar\omega_i$ is the angular frequency of the ith longitudinal mode and Ω_i is that one related to the ith transverse mode. Usually $\omega_i > \Omega_i$, though in the Debye model $\omega_i = \Omega_i$. Furthermore, the Debye model assumes that the dispersion relation is written as $\omega = vk$, where v the constant velocity of sound. Given these two assumptions, the Debye model provides the density of states $\rho(\omega) = 3V\omega^2/2\pi^2\hbar v^3$. Moreover, in this model the heat capacity is given by an increasing number of acoustic modes with cut-off frequency ω_D, known as Debye frequency.

Lattice vibrations vary the interatomic spacings in a time-dependent way, thus modulating the crystal field. If one could have an instantaneous picture of the lattice, it would show distortions from the regular lattice symmetry. The rate at which the picture changes depends on the vibrational frequencies, but as these are less than the Debye frequency ω_D, electrons in any ions follow the displacements of the nucleus of that ion instantaneously. In a crystal, the paramagnetic ion is surrounded by neighbour ions, each of which produces an electrostatic potential. When the ion is displaced its electrons will be displaced accordingly to it and thus without producing any resultant potential. However, consequently to such a displacement, the potential that electrons experience from the other ions changes since they have been moved to a different position relative to the neighbours. In the general case, considering the (x, y, z) reference framework and (X_0, Y_0, Z_0) the initial position of the ion that is displaced in the new position (X_1, Y_1, Z_1), the ion-lattice interaction can be expressed as

$$V(x,y,z) = \sum \left[\begin{array}{c} (X_n - X_0)\dfrac{\partial V_n}{\partial x} + (Y_n - Y_0)\dfrac{\partial V_n}{\partial y} + (Z_n - Z_0)\dfrac{\partial V_n}{\partial z} \\ + \dfrac{1}{2!}\left\{ (X_n - X_0)^2 \dfrac{\partial^2 V_n}{\partial x^2} + \cdots \right\} + \cdots \end{array} \right] \tag{3.12}$$

where the nth neighbour sets up a crystal-field potential energy V_n and the sum is over all the neighbours and over all the electrons of the ion. Each $\partial V_n/\partial \boldsymbol{r}$ can be considered as an operator of the atomic strain ϵ. It appears now evident that the spin-lattice relaxation is caused by an orbit-lattice interaction, and that the spin of the ion is only aware of the lattice via terms already present in the free-ion Hamiltonian, which couple spin and orbit. Among these, the most important is the spin-orbit coupling.

A different approach considers spherical waves instead of planar waves, thanks to which the potential in polar coordinates (r, θ, ϕ) can be written as

$$V(x,y,z) = \sum_{n=0} A_n^0 r^n Y_n^0(\theta, \phi) \tag{3.13}$$

where A_n^0 are constants determined by the charge distribution and distance of the neighbour, and $Y_n^m(\theta, \phi)$ are spherical harmonics. This approach has been used for the

first time by Stevens[13] and, though generic, it is particularly suitable for rare-earth ions.[2] For this reason, it is not further discussed here, and an in-depth description can be found in (Stevens, 1967).[3]

Once the perturbation term of the Hamiltonian is written, the Fermi's golden rule can be used to calculate the transition probability

$$P_{p\to q} = \frac{2\pi}{\hbar}\ |\langle q|\mathcal{H}_{sl}|p\rangle|^2\rho \tag{3.14}$$

in which $\mathcal{H}_{sl}$ is the spin-lattice Hamiltonian, and ρ the density of the vibrational states.

In the next sections the essential features of this relaxation process will be described assuming the crystal as a continuous, isotropic and non-dispersive medium, and adopting the Debye model.[12] Moreover, lattice vibrations will be considered as travelling plane elastic waves that displace the neighbour ions of the paramagnetic ion. A more rigorous treatment can however be made replacing these approximations step by step.

3.3.2 The one-phonon transition: direct process

The displacement of a neighbour ion distant $\boldsymbol{r}$ from the paramagnetic ion, due to a wave α with frequency ω_α, is

$$\boldsymbol{u}_\alpha(\boldsymbol{r}) \simeq \boldsymbol{A_\alpha K_\alpha}\cdot\boldsymbol{r}\cos(\omega_\alpha t) = \epsilon_\alpha \boldsymbol{r}\cos(\omega_\alpha t) \tag{3.15}$$

where $\boldsymbol{A_\alpha}$ is the amplitude of the wave and $\boldsymbol{k_\alpha}$ its wavevector, and it is also assumed that $\boldsymbol{k_\alpha}\cdot\boldsymbol{r} \ll 1$. Such an approximation is valid since for the direct process ω_α is far below the Debye limit and neighbours distant by more than a few lattice spacings are ineffective on the paramagnetic ion. The effect of the alternating strain $\epsilon_\alpha\cos\omega_\alpha t$ can be represented, in first order to ϵ_α, by adding to the Spin Hamiltonian of the ion the term

$$\mathcal{H}^\alpha_{sl} = \epsilon_\alpha V_\alpha\cos(\omega_\alpha t) \tag{3.16}$$

where the operator V_α acts on the spin states. The probability for a wave with frequency ω_α close to ω_{pq} to induce transition from $|p\rangle$ to $|q\rangle$ is calculated from the first-order time dependent perturbation theory

$$P^\alpha_{pq} = \frac{2\pi}{\hbar}|\langle Q_\alpha|\ \epsilon\ |Q_\alpha+1\rangle|^2\ |\langle q|V_\alpha|p\rangle|^2\ \rho(\delta) \tag{3.17}$$

where Q_α is the number of phonons at energy α. During the transition the energy is conserved by increasing the number of phonons of a unity. By defining δ_{pq} as the energy

of the transition, the occupation number of the phonon mode is assumed to have its thermal equilibrium value

$$Q_\alpha = [\exp(\delta_{pq}/kT) - 1]^{-1} \tag{3.18}$$

while the density of states $\rho(\delta)$ is given by the classical expression from the Debye model

$$\rho(\delta) = \frac{3V\delta_{pq}^2}{2\pi^2\hbar^3 v^3} \tag{3.19}$$

where the crystal has volume V and velocity of sound v.

By considering that

$$|\langle Q_\alpha|\ \epsilon\ |Q_\alpha + 1\rangle|^2 = \frac{(Q_\alpha + 1)\ \delta_{pq}}{2Mv^2} \tag{3.20}$$

where M is the mass of the crystal, the probability $P_{pq}^{\ D}$ for the transition to be induced by the thermal vibration of the lattice at the temperature T is

$$\begin{aligned} P_{pq}^{\ D} &= \frac{2\pi}{\hbar}\left[\frac{(Q_\alpha + 1)\ \delta_{pq}}{2Mv^2}\cdot\frac{3V\delta_{pq}^2}{2\pi^2\hbar^3 v^3}\right]\ |\langle q|V_\alpha|p\rangle|^2 \\ &= \frac{3}{2\pi}\left(\frac{\delta_{pq}}{\hbar}\right)^3\frac{(Q_\alpha + 1)}{\rho_c\hbar v^5}W_D^2 \end{aligned} \tag{3.21}$$

where D refers to the direct mechanism, W_D^2 is the average of $|\langle q|V_\alpha|p\rangle|^2$ over the concerned lattice mode and ρ_c is the crystal density.

It should be underlined that such a result is obtained without using semiclassical arguments by treating $\mathcal{H}_{sl}^{\alpha}$ as an operator, for which every spin transition is followed by the destruction or creation of a phonon of frequency ω_α.

Recalling the procedure used in §3.2, the spin-lattice relaxation time for the direct process results to be

$$\frac{1}{T_1^D} = \frac{3}{2\pi}\left(\frac{\delta_{pq}}{\hbar}\right)^3\frac{\coth(\delta_{pq}/2kT)}{\rho_c\hbar v^5}\ W_D^2 \tag{3.22}$$

and when $\delta_{pq} \ll 2kT$, then $\coth(\delta_{pq}/2kT) \to 2kT/\delta_{pq}$ and eq. (3.22) takes the form

$$\frac{1}{T_1^D} = \frac{3\delta_{pq}^2 kT}{\pi\hbar^4 v^5\rho_c}\ W_D^2 \tag{3.23}$$

From eq. (3.23) it follows that the spin-lattice relaxation time for the direct process becomes roughly proportional to T^{-1}. In the opposite condition, when $2kT \gg \delta_{pq}$, T_1 tends

to be temperature independent, though this dependence hardly occurs. In order to compute a value for T_1, the properties of the system like density and velocity of sound, as well as the elements of the matrix W_D^2 should be known.

At this point, the main problem concerns the evaluation of the V_α elements that couple the spin system to the lattice. Two coupling mechanisms were proposed. In the first, proposed by van Vleck,[9] transitions are induced by modulating crystal electric fields. The second, proposed by Waller,[10] considers the spin-lattice relaxation dominated by the modulation of any spin-dependent interaction between paramagnetic ions such as the magnetic-dipolar or spin-spin interactions. However, nowadays it is known that the Waller mechanism is a secondary effect that may become important only for high concentrated systems. The two coupling mechanisms appear to embrace all practical possibilities. Hereafter the van Vleck mechanism is the one discussed.

Although the coupling mechanism now is defined, the choice of the interaction term V_α is still not straightforward. Indeed, several approaches and approximations can be contemplated depending on the concerned system.[4]

When $|p\rangle$ and $|q\rangle$ are states of a Kramers doublet they cannot be coupled by the crystal field, unless some other interaction lifts their degeneracy. Accordingly, W_D inevitably vanishes. The application of an external magnetic field H splits the doublet making the states susceptible to lattice strains through modulation of the splitting tensor g. Indeed, the magnetic field modifies the two states by the mixing with contributions from the excited doublets. If it is considered just the first excited pair of states $|p_1\rangle$ and $|q_1\rangle$ at energy Δ from the ground state doublets, the original states $|p\rangle$ and $|q\rangle$ take the form

$$\begin{aligned} |p'\rangle &= |p\rangle + \frac{\beta H}{\Delta}|p_1\rangle \\ |q'\rangle &= |q\rangle + \frac{\beta H}{\Delta}|q_1\rangle. \end{aligned} \tag{3.24}$$

The resulting $W_D = \langle q'|V_\alpha|p'\rangle$ is now proportional to H, for which, when $H \propto \delta_{pq} < kT$, the relaxation time in eq. (3.23) becomes proportional to $H^{-4}T^{-1}$. This field dependence may be further modified in presence of electron-nuclear interactions. Indeed, δ_{pq} ceases to be proportional to H when the Zeeman splitting is small (eq. 3.22). In addition, a modulation of the hyperfine tensor, A, contributes to W_D with an amount which, if H is not too small, is independent of H and leads to transition probabilities varying as H^2T.[14, 15] The relaxation in this case can be affected by other phenomena, such as internal fields (§3.3.7). This dependence is also observed when dealing with non-Kramers ions, whose states can be displaced by electric fields alone, and, consequently, W_D can be non-zero even without applying a magnetic field. However, in general, the values of W_D will result

reduced for a Kramers system since the transitions between the doublet states can occur only because of the admixture between ground and excited orbital states. More specifically, the transitions are the result of a modulation that does not depend on g, but only on its small orbital contribution $g-2$. This term is of the order of λ/Δ when the lowest excited state is a singlet, and of λ^2/Δ when a multiplet is left. In both cases, $W_D \sim \beta H(g-2)$ strongly activates the relaxation processes.[16, 17]

3.3.3 The two-phonons transition: Raman process

The Raman process in not unique, but it may change significantly depending on the investigated system. However, all the possible Raman processes involve two lattice waves, whose frequencies differ by ω_{pq}, that combined non-linearly cause the spin transition. The interaction between the spin and two vibrations α, β may be formally represented by

$$\mathcal{H}_{sl}^{\alpha\beta} = \epsilon_\alpha V_\alpha + \epsilon_\beta V_\beta + \epsilon_\alpha \epsilon_\beta V_{\alpha\beta} \tag{3.25}$$

where V_α, V_β and $V_{\alpha\beta}$ operate on the spin states, and the lattice strains $\epsilon_\alpha, \epsilon_\beta$ create and destroy phonons in the respective modes. Raman transitions can arise both from the quadratic term $V_{\alpha\beta}$ in first-order of perturbation, and from the linear terms V_α and V_β combined in second-order of perturbation. The matrix element appropriate to describe a transition $|p\rangle \rightarrow |q\rangle$, in which a phonon of frequency ω_α is destroyed, $Q_\alpha - 1$, and one of frequency $\omega_\beta = \omega_\alpha - \omega_{pq}$ is created, $Q_\beta + 1$, is

$$\langle q|W_{\alpha\beta}|p\rangle = \langle q|V_{\alpha\beta}|p\rangle + \sum_s \left(\frac{\langle q|V_\beta|s\rangle\langle s|V_\alpha|p\rangle}{E_p - E_s + \hbar\omega_\alpha} + \frac{\langle q|V_\alpha|s\rangle\langle s|V_\beta|p\rangle}{E_p - E_s - \hbar\omega_\beta} \right) \tag{3.26}$$

where $|s\rangle$ is an intermediary excited state that may correspond to any state of spin, whether thermally accessible or not. It should be also noted that the resonant case, $\hbar\omega_\alpha = E_s - E_p$, corresponds to the Orbach process, which will be discussed later (§3.3.4). The lattice is considered by using the same assumptions adopted previously for the direct mechanism, for which the Raman transition probability may be written as

$$P_{pq}^R = \frac{9}{8\pi^3 \rho_c^2 \, v^{10}} \int W_R^2 \, \omega_\alpha^3 \, \omega_\beta^3 \, Q_\alpha (Q_\beta + 1) \, d\omega_\beta \tag{3.27}$$

where Q_α and Q_β are the average numbers of phonons per mode respectively of frequency ω_α and ω_β, W_R^2 is the appropriate average of $|\langle q|W_{\alpha\beta}|p\rangle|^2$, and the integration covers all possible lattice frequencies.

Usually, the onset of the Raman process occurs at temperatures for which kT is large in comparison with $\hbar\omega_{pq}$, but lower than the Debye energy $k\theta_D$. Given that the main contribution to P_{pq}^R derives from the region where $\hbar\omega_\beta$ is several times kT, it is possible to ignore the existence of an upper limit to ω_β and neglect the difference between ω_α and ω_β. Expression (3.27) then becomes

$$P_{pq}^R = \frac{9}{8\pi^3\rho_c^2\ v^{10}} \int_0^\infty W_R^2\ \omega^6\ \frac{\exp(\hbar\omega/kT)}{[\exp(\hbar\omega/kT)-1]^2}\ d\omega. \tag{3.28}$$

It turns out, according to (J. C. Gill, 1975)[1], that three main cases may occur, in which W_R is independent of ω, or is proportional to ω or to ω^{-1}. These different situations depend on the order of perturbation, but also on the energy of $|s\rangle$ compared to $k\theta_D$. If it is assumed that $W_R = F\omega^m$, then

$$P_{pq}^R = \frac{9}{8\pi^3\rho_c^2\ v^{10}} \left(\frac{kT}{\hbar}\right)^{7+2m} F^2 I_{6+2m} \tag{3.29}$$

where the integral over ω assuming a Debye spectrum[12] is

$$I_n = \int_0^\infty \frac{x^n \exp x}{(\exp(x\ -1))^2} dx \tag{3.30}$$

which is called *Transport Integral*. Commonly, at low temperatures a variation of the relaxation time as T^{-5}, T^{-7} or T^{-9} is to be expected, according to whether W_R is proportional to ω^{-1}, ω^0 or ω, respectively. Temperature dependences close to these are indeed usually observed, although the failure of the assumption $\boldsymbol{k}\cdot\boldsymbol{r} \ll 1$ and that one for which the lattice frequencies obey to the Debye law is already noticeable for temperatures corresponding few per cents of θ_D. Interestingly, according to eq. (3.29), at higher temperatures P_{pq}^R varies with a weaker temperature dependence and ultimately, when $kT \gg \hbar\omega$ for all lattice modes capable of coupling to the spins, a temperature dependence close to T^{-2} is expected to occur.

It is now clear that Raman process may assume several forms depending on whether expression (3.26) is dominated by the term in $V_{\alpha\beta}$ or by those in V_α, V_β and, in the latter case, on the energy of the intermediate virtual state $|s\rangle$. It should be noted that although usually one type of Raman process dominates over the others, in some cases more than one processes may occur simultaneously. When this happens, all the relative contributions must be considered in $\left|\langle q|W_{\alpha\beta}|p\rangle\right|^2$.

The main possibilities, which are shown in Figure 3.4, are now discussed in detail. In (*i*), the transition $|p\rangle \to |q\rangle$ is induced by terms in $V_{\alpha\beta}$ and consequently W_R is substantially independent of the phonon frequencies ω, so that at low temperature the

relaxation time is proportional to T^{-7}. A dependence on H^{-2} occurs when $|p\rangle$ and $|q\rangle$ belong to the same Kramers doublet and are coupled by $V_{\alpha\beta}$ in presence of an external magnetic field. In (*ii*) and (*iii*) are shown two cases in which the transition results from the linear terms V_α, V_β and the intermediate states $|s\rangle$ are not thermally accessible. In the non-Kramers system (*ii*) one may neglect $\hbar\omega$ in the energy denominators of expression (3.26), for which W_R is independent of ω and the relaxation times are proportional to H^0T^{-7}. A similar conclusion applies to Kramers systems, in (*ii*), when the relaxation is between states belonging to different doublets.

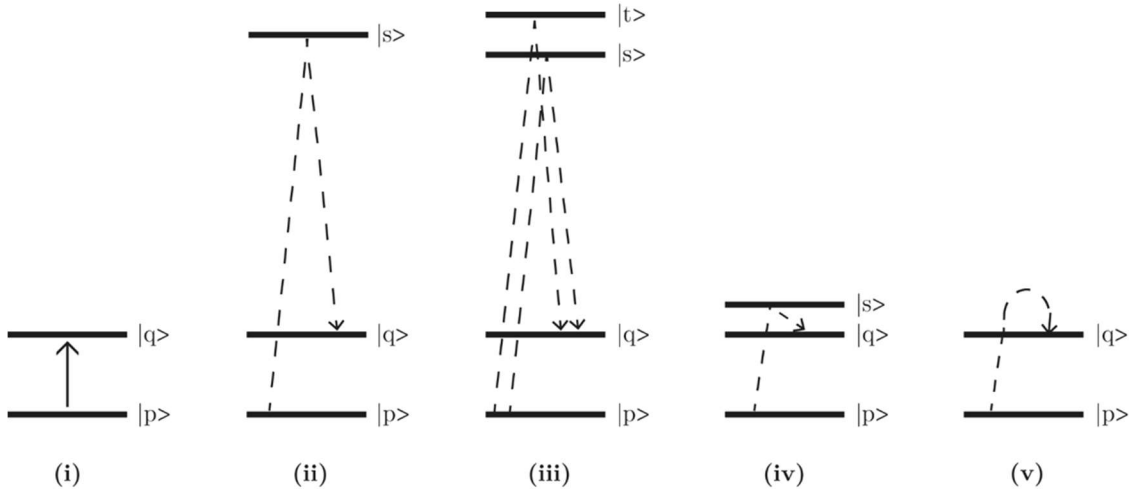

Figure 3.4. Possible Raman processes: (*i*) due to terms in $\mathcal{H}_{sl}$ quadratic in lattice strain; (*ii*) through virtual transitions in non-Kramers ions when the intermediate spin state $|s\rangle$ has energy $E_s \gg kT$; (*iii*) in Kramers ions, similarly; (*iv*) when the intermediate state $|s\rangle$ has energy $E_s < kT$; and (*v*) when $|s\rangle$ is identical with one of the terminal spin states $|p\rangle, |q\rangle$. The image has been readapted starting from ref[1].

When the states $|p\rangle$ and $|q\rangle$ belong to the same Kramers doublet, as in (*iii*), it must be considered in eq. (3.26) that $|s\rangle$ is accompanied by its Kramers conjugate $|t\rangle$. If the crystal field operators V_α, V_β represent static strains, by virtue of the Kramers theorem they would be incapable of coupling $|p\rangle$ and $|q\rangle$ in any order of perturbation when a magnetic field is absent. This implies that, if ω_α and ω_β are zero, the contributions to $|\langle q|W_{\alpha\beta}|p\rangle|^2$ from $|s\rangle$ and $|t\rangle$ would cancel exactly to each other. There are two main ways for which the *van Vleck cancellation* (*i.e.* this vanishing of crystal-field matrix elements in Kramers systems) is avoided in the dynamics situation of Raman relaxation. Even in the static case, the presence of a magnetic field modifies the energies and wavefunctions of the states so that the contributions from $|s\rangle$ and $|t\rangle$ fail to cancel, by an amount proportional to H. The resulting relaxation time is at low temperature proportional to $H^{-2}T^{-7}$. However, the presence of the phonon energies in the denominators of eq. (3.26)

are almost always more important in preventing the cancellation. From this it follows that $|s\rangle$ and $|t\rangle$ contribute to W_R with an ω^2 term, so that the relaxation time varies as H^0T^{-9}. The latter situation is the most relevant for our case. In addition, in the previous cases the transition probabilities were obtained neglecting in expression (3.26) the term $\hbar\omega_\alpha$ in the denominators. Now, for $|p'\rangle$ and $|q'\rangle$ belonging to the same Kramers doublet, the final value of the probability is reduced by a factor $(\beta H/\Delta)^2$. It is therefore relevant to see what happens if $\hbar\omega_\alpha$ is not neglected. In this case, indeed, the energy term can be expanded as

$$\frac{1}{E_p - E_s \pm \hbar\omega_\alpha} \simeq \frac{1}{E_p - E_s} \mp \frac{\hbar\omega_\alpha}{(E_p - E_s)^2} \tag{3.31}$$

and it is necessary to consider the contributes that originate from the second term on the right. When explaining this treatment in his review[3], Stevens says that it is "rather complicated matter to do in detail", but he points out to a relevant aspect: these terms cannot be reproduced in a distorted-lattice problem, and their existence is only due to the vibration of the lattice. The van Vleck cancellation is here avoided. However, the inclusion of crystal-field matrix elements is not sufficient, and a combination of crystal fields and lattice dynamics is required. This results in considering a new system in which $|q, Q_1, Q_2, \ldots\rangle$ and $|p, Q_1 + 1, Q_2 - 1, \ldots\rangle$ are not Kramers conjugate states anymore. Indeed, detailed calculations have shown that these elements do not have the van Vleck cancellation, and when quantities like $\langle p'|(\hbar\omega_\alpha/(E_p - E_s)^2 \ldots |q'\rangle$ are evaluated they do not vanish, even if $|p'\rangle$ and $|q'\rangle$ are approximated by the Kramers pair from which they derive. An immediate consequence is that the associated relaxation process is independent of the magnetic field. The temperature dependence is also changed since now W_R contains an extra factor of type $\hbar\omega_\alpha/(E_p - E_s)$, and the integral over ω becomes

$$I_8 = \int \omega^8 \frac{\exp(\hbar\omega/kT)}{[\exp(\hbar\omega/kT) - 1]^2}\, d\omega \tag{3.32}$$

resulting in a T^9 dependence. This type of Raman process will have the general form

$$P_{pq}^R \sim 8! \left(\frac{kT}{\hbar}\right)^9 \frac{W_R^2}{\Delta^2} \left(\frac{2V}{4\pi^2 M v^5}\right)^2. \tag{3.33}$$

For a Kramers ion, the process with dependence T^9H^0 will probably dominate over the H^2T^7 term, since the latter is $(\beta H/kT)^2$ times lower. Moreover, for this dominant process, eq. (3.26) is approximatively $W_R \sim (2V^2/\Delta)(\hbar\omega/\Delta)$, where the matrix elements V of the strain are likely to be similar in order of magnitude to the energies Δ of the low excited doublets.

Up to here it has been described the principal Raman processes that occur both for Kramers and non-Kramers systems. However, other Raman processes can arise depending on the boundary conditions of the problem, from which very different temperature and magnetic field dependences can be obtained. For more details, brave readers are invited to refer to (K. N. Shrivastava, 1983).[18] Moreover, the processes (*iv*) and (*v*) of Figure 3.4 are not related to the systems that are investigated in this dissertation and they are not discussed; they can be found in (J. C. Gill, 1975)[1].

3.3.4 Resonant Raman: Orbach process

The description of this process as a resonant version of the Raman was given for the first time by (R. Orbach, 1961)[2]. Expression (3.27) for the Raman transition is extended to provide the Orbach process by including the resonant peak in the integration in the vicinity of $\hbar\omega_\beta = E_s - E_q$. After a series of calculations that are here omitted, the contribution to the spin-lattice relaxation time of the Orbach process is

$$\frac{1}{T_1^{\,O}} = \frac{3W_O^2}{2\pi\hbar\rho_c v^5}\left(\frac{\delta_{sp}}{\hbar}\right)^3 \exp\left(-\frac{\delta_{sp}}{kT}\right) \tag{3.34}$$

where δ_{sp} is the energy difference between the lowest lying state $|p\rangle$ and a third 'real' excited level $|s\rangle$, and $k\theta_D \gg \delta_{sp}$. The temperature variation of the relaxation time from this process is very rapid, and it roughly varies as $\exp(\delta_{sp}/kT)$. The same dependence can be obtained by considering this mechanism as produced by two separate direct processes.

3.3.5 Another case of Raman: Local modes process

Starting from the Raman processes, another important mechanism can be derived: the local mode process.[19-23] Expression (3.27) can be viewed as a complicate sum over all the lattice modes for which the strain factor has a peak in the region of each of the characteristic frequencies. In a simplified description, this sum can be replaced by a series of simple definite integrals where, in the region of each characteristic frequency, the strain factor is replaced by its peak value for the appropriate frequency interval. If the peak of the local strain is enhanced sufficiently, the integral involving it dominates the sum. In this case the Raman relaxation will have the form

$$\frac{1}{T_1^{\,R}} = B\frac{\exp(\hbar\omega_i/kT)}{(\exp(\hbar\omega_i/kT)-1)^2} \tag{3.35}$$

where B contains various constant parameters. The form of eq. (3.35) is simple because the process of relaxation involves the creation and destruction of phonons at $\hbar\omega_i$ only. The temperature dependence for this process corresponds roughly to T^3. For this process, the same assumptions previously used for the Raman process apply.

It should be stressed that the local mode process occurs only in the limited temperature range for which the local strain dominates the relaxation. When increasing the temperature, other contributions of the strain factor become important, for which the entire sum of eq. (3.27) must be considered. Finally, it is worth to underline the difference between the Orbach process and this one. The former process only depends on the spin levels structure, whereas the latter only depends on the vibrational structure of the system.

3.3.6 The Waller mechanism

The van Vleck mechanism previously described is definitely the more accurate model to explain the spin-lattice relaxation. However, this mechanism does not account for the concentration dependence of the relaxation rates that often occurs experimentally. An explanation of this type of dependence can be given by considering the Waller mechanism, for which the relaxation is due to the modulation of magnetic-dipolar or spin-spin interactions. It should be remarked that both the van Vleck and Waller mechanisms may be simultaneously involved in the relaxation of the system, though with different importance.

Usually, the magnetic-dipolar coupling is weak in comparison with splittings such as the Zeeman effect, for which it can be neglected, and the relaxation is described assuming the spins uncoupled. However, if this coupling is not neglected, for example in a system with only Zeeman splitting $g\beta H$, the modulation of such a coupling between two spins S_i, S_j leads to transitions with involved energies of the order of either $g\beta H$ (corresponding to reversal of one spin) or $2g\beta H$ (corresponding to both changing state). Moreover, the values of W_D and W_R can be estimated on the order of $(g\beta)^2 r^{-3}$. The theory of Waller was improved by (S. A. Al'tshuler, 1956)[24], who found in the latter term, *i.e.* the one corresponding to the transition in which two spins change state simultaneously, an important contribution to the direct process. Furthermore, the d-orbital paramagnetic ions that have well-isolated Kramers doublets, resulting in a little orbital momentum, have been identified as systems that may result more affected by this process. This type of relaxation is also more important when small magnetic fields are applied, and in highly

concentrated systems. Magnetic dilution, indeed, reduces its effectiveness, for which it is expected that relaxation times will be roughly proportional to c^{-1}.

For what concern the other type of modulation, *i.e.* the spin-spin interaction, it should be noted that several types of spin-spin interactions can exist between paramagnetic ions in crystals, however only the exchange interaction should be strong enough to affect the spin-lattice relaxation. Indeed, this type of relaxation process is accepted as one of the main active in magnetically ordered systems. On the other hand, evidences of its importance in the relaxation of paramagnetic crystals have been rather elusive. For this reason, this mechanism lies outside the scope of this dissertation and is not further discussed.

3.3.7 Magnetic field dependence of T_1

The description of the variation of T_1 with the applied field H is of general character and can be analysed separately. Indeed, by focusing on Kramers systems, in the previous sections it has been shown that the Raman process is independent from H and the dependence of the direct process, varying as H^4, is effective only at high values of applied magnetic fields. For values of H smaller or comparable to the internal fields, these will induce spin relaxation. Brons and van Vleck[9] firstly described phenomenologically this dependence as

$$T_1 = T_1{}^0 \frac{(1 + d^2H^2)}{(1 + c^2H^2)} \tag{3.36}$$

where T_1^0 is the relaxation time for zero field strength and d, c are adjustable parameters.

Successively Orbach[2] developed a complete theory of the field dependence for rare-earths ethylsulfates molecules, in which internal fields are due to dipolar and hyperfine interactions according to

$$T_1^{-1} = \frac{1}{T_1{}^0} \frac{\left(H^2 + \mu H_{hyp}^2 + \frac{1}{2}\mu' H_{dip}^2\right)}{(H^2 + H_{hyp}^2 + \frac{1}{2}H_{dip}^2)} \tag{3.37}$$

where the parameter μ solely depends on the orbit-lattice parameters, while μ' depends also on the temperature and concentration. In presence of exchange interactions, (C.-Y. Huang, 1967)[25] extended the Orbach model replacing H_{dip} with H_{exch}. These expressions were used to reproduce the experimental results for both rare-earths and transition metals. However, due to its inherent complexity, the simpler form of eq. (3.38) was preferred to analyse the experimental data[16]

$$T_1^{-1} = \frac{1}{T_1^{\,0}} \frac{c(b_0/C_0 + H^2)}{(cb_0/C_0 + H^2)} \tag{3.38}$$

where c is the spin concentration and b_0/C_0 represents the square of the internal fields, caused by the dipole-dipole, hyperfine and exchange interactions. The last term can, in principle, be deduced by magnetic specific heat measurements.[26]

3.3.8 The spin-phonon bottleneck

So far, it was assumed that the spin-lattice relaxation was the rate-determining step in the de-excitation process. However, if the lattice is not able to dissipate the energy transferred from spins to the thermal bath, a noticeably depart from the equilibrium, which is defined as the temperature of the bath, may occur. At low temperature, where the heat capacity of spins is commonly much larger than that of the lattice modes involved in the relaxation, this assumption is valid only if the energy can be transferred rapidly from the lattice modes to either the bath or the remaining modes of the lattice. It was pointed out by van Vleck[8, 27] that these transfers can be so slow as to limit the rate of spin-bath relaxation when induced by the direct process. This occurs because the energy released by spins is carried only by the narrow band of the lattice modes whereby the two spin levels are resonant. This impediment becomes more important in systems with high spin density, or when a voluminous crystal is used, being increasingly probable that a spin resonant vibration will be absorbed by another spin before it is dissipated to the bath. This restriction of spin-lattice relaxation by a 'phonon bottleneck' has been observed in many systems, including those relaxing through the Orbach process.[28-30]

The simplest model of spin-phonon bottleneck treats the spin system as affecting equally all lattice modes within a narrow band of frequency $\Delta\omega$, centred at the frequency of a spin resonance line and corresponding roughly to its width. If this spin resonance band results from transitions between a spin state $|p\rangle$ and a higher state $|q\rangle$, with populations respectively N_p and N_q, the net rate at which phonons are created in those modes in single-phonon (direct) transitions is

$$R_{sl} = -N_p P_{pq} + N_q P_{qp}. \tag{3.39}$$

If the average number of phonons per mode is n, eq. (3.39) can be written

$$R_{sl} = \frac{P_{pq}^0}{n_0}[(n+1)N_q - nN_p] \tag{3.40}$$

where P^0_{pq} and n_0 are the values that would occur in absence of any bottleneck effect, *i.e.* when the system is at the thermal equilibrium.

The net rate at which phonons escape from the band $\Delta\omega$, either into the bath or into other modes, is

$$R_{lb} = (n - n_0)\ \rho(\omega_{pq})\ \Delta\omega\ \tau_p^{-1} \tag{3.41}$$

where $\rho(\omega_{pq})\Delta\omega$ is the number of modes resonant with spins, and τ_p is the excited phonon lifetime within the band $\Delta\omega$. The energy stored by those modes may almost always be neglected, and R_{sl} set equal to R_{lb} for the entire relaxation. Rearranging (3.40) and (3.41), a further relaxation term due to bottleneck appears evident and it can be written as

$$R_{sl} = R^0_{sl}\ \left[1 + A\left(\frac{N_p - N_q}{N}\right)\right]^{-1} \tag{3.42}$$

where R^0_{sl} is the net transition rate in absence of bottleneck effects, N the total number of spins in the crystal, and

$$A = \frac{N\ \tau_p\ P^0_{pq}}{\rho(\omega_{pq})\ \Delta\omega\ n_0} = \frac{\pi W_D^2\ \delta_{pq}\ N\tau_p}{\hbar^2 \Delta\omega\ M\ v^2}. \tag{3.43}$$

where the various parameters have been already used to define for example eq. (3.23).

The effect of bottleneck is thus equivalent to the reduction of the transition probabilities P_{pq}, P_{qp} by a factor $[1 + A(N_p - N_q)/N]^{-1}$, in which the quantity A is not inherently temperature dependent.

In the case of relaxation by the ordinary direct process, the dependence of R_{sl} on spin populations makes it impossible to specify a unique characteristic time, even for a two-levels system. This can be overcome defining an 'effective' relaxation time, τ_e, which changes as the recovery proceeds as

$$\tau_e = -s/\dot{s} \tag{3.44}$$

where the term s is a saturation parameter that links the out-of-equilibrium term $N_p - N_q$ to its value at the thermal equilibrium; this is expressed as

$$s = 1 - \frac{N_p - N_q}{N_p^0 - N_q^0}. \tag{3.45}$$

Then, for two levels

$$\tau_e = \tau_0[1 + \sigma(1 - s)] \tag{3.46}$$

where τ_0 is the characteristic time of the unrestricted relaxation, and $\sigma = A(N_p^0 - N_q^0)/N$ specifies the severity of the spin-phonon bottleneck.

It is evident, that if $s = 1$, corresponding to the initial excitation, then $\tau_e = \tau_0$ and the rate at which spins relax is unaffected by the finite disturbance of lattice equilibrium. As recovery proceeds, however, τ_e increases and approaches $\tau_0(1 + \sigma)$ for $s \ll 1$. Thus, bottleneck increases by a large factor the relaxation time, even when the system is only slightly deviating from the thermal equilibrium. Since both τ_0 and $N_p^0 - N_q^0$ are proportional to $\tanh(\delta_{pq}/2kT)$, when $\sigma \gg 1$ the relaxation τ_e is proportional to $\tanh^2(\delta_{pq}/2kT)$ and varies approximately as T^{-2} when $kT \gg \delta_{pq}$. Moreover, the tendency of A, and thus of τ_e, is to increase with paramagnetic concentration and with the size of the crystal. However, the latter dependence is introduced only when τ_p is limited by energy dissipation through the surface of the crystal.

The above treatment, made by (J. C. Gill, 1975)[1], is close to that made by (B. W. Faughnan and M. W. Strandberg, 1961)[31], which is the most common treatment accounted for spin-phonon bottleneck. Moreover, it has provided a starting point for further developments of the theory. It is also worth to mention the work of (P. L. Scott and C. D. Jeffries, 1962)[29], who applied the model to rare-earths, and that of (A. M. Stoneham, 1965)[30], who derived a more general alternative model based on a thermodynamic approach. A common ground to such studies is the main role of the phonon relaxation mechanisms, which are reflected in the phonon excitation lifetime τ_p. Indeed, the above-mentioned authors have pointed out that different types of bottleneck effects can occur. These can be divided either in 'spatial bottleneck', where the rate-determining process is the transfer of energy in space, or in 'spectral bottleneck', where the transfer of energy in frequency is the rate-determining step. Depending on the type of mechanism, τ_e may exhibit a dependence on temperature within T and T^6, on spin concentration between c and $c^{-1/3}$, and on the crystal radius linearly.

We have here discussed the case in which spin-phonon bottleneck effects influence the direct relaxation process. It should be stressed that these are not expected to influence the Raman process, since it involves a wide spectrum of lattice frequencies. However, the Orbach process, which in a simplified view corresponds to a double-step direct process, uses two narrow bands of lattice modes, for which bottleneck effects may be present. This case is, however, not discussed in the dissertation since Orbach mechanisms are not expected to be active in the relaxation of the investigated molecules.

3.4 The spin-spin relaxation

Belong to this category all phenomena that adiabatically decrease the transverse magnetization, *i.e.* which affect the spin-spin relaxation time T_2. These processes originate from dipolar interactions between electronic and/or nuclear spins surrounding the reference electronic spin. In discussing this type of relaxation, it is useful to employ the Electron Paramagnetic Resonance terminology.[32]

In general, every electronic spin flip affects the coherence of other electronic spins through the dipolar interaction. This decoherence phenomenon can be reduced by increasing the distance among spins, *i.e.* by diluting the magnetic system, for example with an isostructural diamagnetic molecule. However, even in this case, when magnetically diluted electron spins are surrounded by magnetically concentrated nuclear spins, spin-echo dephasing is dominated by *nuclear spin diffusion*. Such a process consists in nuclear spin flips that modulate the electron-nuclear dipolar interaction, with the consequent loss of spin coherence in the xy-plane. Even though the nuclear spin flips are relatively slow, the large number of nuclei that are dipole-coupled with the electron spin makes this effect the major contribution to the coherence time.[33] This has been demonstrated by replacing ligand and/or solvent protons with deuterons or with elements spin nuclei free, which have smaller or no magnetic moments. Indeed, this has led to an enhancement of the relaxation time T_2. The nuclear spin diffusion process exhibits weak or no temperature dependence and it is independent from the magnetic field.

Spin coherence in the xy-plane cannot be longer than the relaxation along the z-axis, and thus T_1 represents an upper limit of T_2. This introduces a temperature dependence on T_2, which becomes temperature dependent according to the thermal variation of T_1. However, this is not the only phenomenon that can provide a temperature dependence for T_2. Indeed, the spin-spin relaxation depends on temperature when dominated by motional processes. These can be either tumbling of the molecule that averages $\boldsymbol{g}$ and $\boldsymbol{A}$ anisotropy, or internal motions such as rotation of methyl groups or ring inversions that interchange axial and equatorial substituents. Such effects are reduced when working in solid-state matter rather than in solution.

It should be noted that usually, instead of the spin-spin relaxation time T_2, the spin-echo dephasing time T_m is measured, since it is easier to obtain. This encompasses all processes that disturb electron spin phase coherence and can be considered a lower limit of T_2.[34, 35]

3.5 Picking up the pieces

The main processes affecting the spin-lattice and spin-spin relaxation have been described in this chapter, with emphasis for $S = 1/2$ Kramers systems of transition metal ions. The spin-spin relaxation is mainly dominated by nuclear spin diffusion and spin-lattice relaxation. Indeed, the spin-spin relaxation time, T_2, is independent of temperature. However, as temperature is increased, T_1 reduces and introduces a temperature dependence on T_2. A lengthening of the latter can thus be achieved only reducing the number of nuclear spins, since it decreases nuclear spin diffusion, and weakening the processes that cause spin-lattice relaxation.

The spin-lattice relaxation time is affected by lattice vibrations mainly through the modulation of the crystal field, which is accounted for by the spin-orbit coupling, according to the van Vleck mechanism. Two principal types of processes were distinguished depending on whether the number of phonons involved in the transition is one or more. The first case corresponds to the direct process, where a phonon matching the energy of two spin levels causes spin transition. The spin-lattice relaxation time dependence on temperature and magnetic field is $T_1^{-1} \propto TB^4$ for Kramers systems. This process is dominant at low temperature, usually between the liquid helium and liquid hydrogen temperatures. Phonons involved in the spin-lattice relaxation are then dissipate to the thermal bath, for which the thermal equilibrium is maintained. However, when the lattice is not able to dissipate the spin excitation to the thermal bath, spin-phonon bottleneck effects may occur. Since a rigorous theory of this phenomenon is still missing, the produced effects remain hard to predict and control. Commonly the temperature dependence, when phonon bottleneck occurs, is $T_1^{-1} \propto T^2$, but large deviations from this temperature dependence may be expected. Moreover, its effects on the magnetic field dependence of the spin-lattice relaxation are still unclear.

As the temperature is increased more high-energetic phonons are available and two-phonon processes dominate the relaxation. The Raman and Orbach processes belong to this category. These occur with the simultaneous involvement of two phonons whose energy difference corresponds to the spin levels separation. Several types of Raman processes exist, but every case involve a virtual excited state. According to literature, the Raman process produces, for Kramers doublets, a dependence as $T_1^{-1} \propto B^0T^9$. However, given the great variety of possible Raman processes, other temperature and magnetic field dependences may occur. The Orbach process is a specific case of Raman process in which the virtual state corresponds to a real magnetic excited state; this provides a dependence as $T_1^{-1} \propto \exp(-\Delta/kT)$. The local mode process is another specific case of Raman process that involves low energy vibrational modes.

The above description is valid when assuming the phonon spectrum according to the Debye model. In this treatment, acoustic modes are only considered, and no distinctions between longitudinal and transverse modes are made. Moreover, the crystal is approximated to an elastic solid with a continuum of phonons and a cut-off frequency, known as Debye temperature, above which no more phonons are present. Although it is well known that this approximation is very rough for molecular solids, more accurate models are seldom employed.

The relaxation processes can be reconsidered in view of this model. The direct process is dominant as long as the temperature is much lower than the Debye temperature, and the phonon density of states is such that the transition probability for this process increases linearly with temperature. The Raman processes take place with the transfer of energy through a virtual excited state, which can be at any energy lower than the Debye temperature. These processes depend upon the transport integral from zero to the cut-off temperature. The local modes process occurs when a distinct mode is effective enough to produce the collapse of the transport integral, which depends on all the possible modes, into only that term.

Picking up the pieces, the spin-lattice relaxation time depends on temperature according to

$$T_1^{-1} = A_{dir}T + A_{Ram}\left(\frac{T}{\theta_D}\right)^9 J_8\left(\frac{\theta_D}{T}\right) + A_{loc}\left[\frac{e^{\Delta_{\mathrm{loc}}/kT}}{(e^{\Delta_{\mathrm{loc}}/kT}-1)^2}\right] + A_{Orb}\, e^{-(\Delta_{Orb}/kT)} \qquad (3.47)$$

where $A_{dir}, A_{Ram}, A_{loc}, A_{Orb}$ are the coefficients of the various processes; J_8 is the transport integral and θ_D the Debye temperature; Δ_{loc} is the frequency of the local mode and Δ_{Orb} the energy of the magnetic excited state.

The magnetic field dependence of the spin-lattice relaxation can be easily described by the expression

$$T_1^{-1} = A_{dir}B^4 + d\left(\frac{1+eB^2}{1+fB^2}\right) \qquad (3.48)$$

where the first term accounts for the direct process, while the second is a simple version of the phenomenological Brons-van Vleck law, which considers the effect of the internal magnetic fields in inducing spin relaxation. In this model d represents the relaxation at zero field, f the ability of the external magnetic field to suppress the internal relaxation mechanisms, and e the attitude of the internal magnetic moments to induce relaxation and is inversely proportional to the number and strength of the internal spins.

The relaxation processes described in this chapter represent a small part of pieces of the relaxation puzzle and many others may occur. Indeed, the discussion has been limited to the principal mechanisms that will be useful to describe the relaxation processes of the molecules investigated in the next chapters.

3.6 Bibliography

1. J. C. Gill, *Reports on Progress in Physics*, 1975, **38**, 91.
2. R. Orbach, *Proceedings of the Royal Society of London. Series A. Mathematical and Physical Sciences*, 1961, **264**, 458.
3. K. W. H. Stevens, *Reports on Progress in Physics*, 1967, **30**, 189.
4. K. J. Standley and R. A. Vaughan, *Electron Spin Relaxation Phenomena in Solids*, Plenum Press, New York, 1969.
5. A. Abragam and B. Bleaney, *Electron Paramagnetic Resonance of Transition Ions*, Dover, New York, 1986.
6. H. A. Jahn and E. Teller, *Proc. R. Soc. Lond. A*, 1937, **161**, 220-235.
7. H. A. Kramers, *Proc. K. Akad. Amsterdam*, 1930, **33**, 959-972.
8. J. H. van Vleck, *Physical Review*, 1941, **59**, 724-729.
9. J. H. van Vleck, *J. Chem. Phys.*, 1939, **7**, 72.
10. I. Waller, *Z. Phys.*, 1932, **79**, 370-388.
11. J. H. van Vleck, *Physical Review*, 1940, **57**, 426-447.
12. C. Kittel, *Introduction to Solid State Physics*, John Wiley & Sons, Inc., New York, 1986.
13. K. W. H. Stevens, *Proc. Phys. Soc.* , 1952, **65A**, 209.
14. A. J. van Duyneveldt, C. L. Pouw and W. Breur, *Physica* 1972, **57**, 205-214.
15. J. M. Baker and N. C. Ford, *Phys. Rev.*, 1964, **136**, A1692-1701.
16. A. C. De Vroomen, E. E. Lijphart, D. Y. H. Prins, J. Marks and N. J. Poulis, *Physica*, 1972, **61**, 241-249.
17. T. Chang and G. C. Yang, *J. Chem. Phys.*, 1968, **48**, 2546-2549.
18. K. N. Shrivastava, *physica status solidi (b)*, 1983, **117**, 437-458.
19. J. G. Castle, D. W. Feldman, P. G. Klemens and R. A. Weeks, *Phys. Rev.* , 1963, **130**, 577-588.
20. D. L. Mills, *Phys. Rev.*, 1966, **146**, 336-343.
21. D. W. Feldman, J. G. Castle and G. R. Wagner, *Phys. Rev.*, 1966, **145**, 237-240.
22. J. Murphy, *Phys. Rev.*, 1966, **145**, 241-246.

23. J. G. Castle and D. W. Feldman, *Phys. Rev.*, 1965, **137**, A671.

24. S. A. Al'tshuler, *Izv. Akad. Nauk. SSSR*, 1956, **20**, 1207-1214.

25. C.-Y. Huang, *Phys. Rev.*, 1967, **161**, 272-277.

26. G. Ablart and J. Pescia, *Phys. Rev. B*, 1980, **22**, 1150-1162.

27. J. H. van Vleck, *Phys. Rev.*, 1941, **59**, 730-736.

28. W. J. Brya and P. E. Wagner, *Phys. Rev.*, 1966, **147**, 239-241.

29. P. L. Scott and C. D. Jeffries, *Phys. Rev.*, 1962, **127**, 32-51.

30. A. M. Stoneham, *Proc. Phys. Soc.*, 1965, **86**, 1163-1177.

31. B. W. Faughnan and M. W. Strandberg, *J. Phys. Chem. Solids*, 1961, **19**, 155-166.

32. Arthur Schweiger and G. Jeschke, *Principles of Pulse Electron Paramagnetic Resonance*, Oxford University Press, 2001.

33. S. Lenz, K. Bader, H. Bamberger and J. van Slageren, *Chem. Commun.*, 2017, **53**, 4477-4480.

34. S. S. Eaton and G. R. Eaton, in *eMagRes*, DOI: doi:10.1002/9780470034590.emrstm1507.

35. S. K. Misra, in *Multifrequency Electron Paramagnetic Resonance*, 2011, DOI: doi:10.1002/9783527633531.ch10.

Chapter 4

The Vanadyl story

In this chapter the results of the investigation about the static and dynamic magnetic properties of a series of V^{IV} complexes are discussed.

The investigation of these molecules has been useful to understand the chemical and structural features required to achieve long relaxation times, with particular attention for the spin-lattice relaxation time. Furthermore, they confirmed the effects of T_1 in limiting the coherence time T_m, underlining the importance of shedding light on the nature of the spin-lattice relaxation in order to lengthen the coherence time. Thanks to a multi-technique approach based on ac susceptometry and both cw- and pulsed EPR, several ingredients have been identified as necessary to increase T_1. These include the use of a metal ion with small spin-orbit coupling, the attention to the energy structure of the *d*-orbitals and the type of coordination provided by the ligand. Moreover, the analysis of magnetic measurements evidenced the main role of low-energy vibrational modes in the spin-lattice relaxation. This has led to investigate more in detail the vibrational spectrum of these molecules through time-domain THz spectroscopy with the support of DFT and *ab initio* theoretical calculations.

The molecules investigated are:

- $[VO(dpm)_2]$, where *dpm = dipivaloylmethanate*, hereafter **VOdpm**;
- [VO(Pc)], where *Pc = phthalocyaninate*, hereafter **VOPc**;
- $[(Ph)_4P]_2[VO(dmit)_2]$ and $[(Ph)_4P]_2[V(dmit)_3]$, where *dmit = 1,3-dithiole-2-thione-4,5-dithiolate*, hereafter **VOdmit** and **Vdmit**, respectively;
- $[VO(Et_2dtc)_2]$, where *Et_2dtc = diethyldithiocarbamate*, hereafter **VOdtc**;
- $[(Ph)_4P]_2[VO(cat)_2]$ and $[(Ph)_4P]_2[V(cat)_3]$, where *cat = cathecolate*, hereafter **VOcat** and **Vcat**, respectively;
- $[(Ph)_4P]_2[VO(naph\text{-}cat)_2]$ and $[(Ph)_4P]_2[V(naph\text{-}cat)_3]$, where *naph-cat = naphthalene-catecholate*, hereafter **VOnaphcat** and **Vnaphcat**, respectively;
- [VO(TCPP-Zn_2-bpy)], where *TCPP = tetracarboxylphenylporphyrinate*; *bpy = 4,4'-bipyridyl*, hereafter **VOTCPP**;
- [VO(TPP)], where *TPP = tetraphenylporphyrinate*, hereafter **VOTPP**.

An additional molecule, of formula [VO(acac)$_2$] has been studied.[1] The latter has been chosen as a prototype to investigate in detail the properties of such vanadyl-based molecules and a separate chapter has been dedicated (Chapter 5).

The chapter is organized collecting all the results provided by a specific characterization of the investigated molecules, rather than the temporal order whereby the various studies have been designed and performed. Thanks to this comparative approach, the author hopes that the discussion can profit of a more comprehensive view on the properties of all the investigated systems and allow the drawing of more sound conclusions.

In the first section the crystallographic structure, as well as the static magnetic properties obtained by cw-EPR, are briefly exposed. The second and third sections are devoted to the spin dynamics characterization performed through ac susceptibility and pulsed EPR experiments. The fourth section reports the results obtained by THz spectroscopy and, in conclusion, in the fifth section the results previously shown are analysed and discussed.

The Chapter is based on the following publications:

Papers in Appendix

VOdpm: Quantum coherence in a processable vanadyl complex: new tools for the search of molecular spin qubits.
L. Tesi, E. Lucaccini, I. Cimatti, M. Perfetti, M. Mannini, M. Atzori, E. Morra, M. Chiesa, A. Caneschi, L. Sorace and R. Sessoli. In: *Chemical Science* **7** (2016), pp. 2074–2083.

VOPc: Room-temperature quantum coherence and Rabi oscillations in vanadyl phthalocyanine: toward multifunctional molecular spin qubits.
M. Atzori, L. Tesi, E. Morra, M. Chiesa, L. Sorace and R. Sessoli. In: *Journal of the American Chemical Society* **138** (2016), pp. 2154-2157.

VOdmit/Vdmit: Quantum coherence times enhancement in vanadium(IV)-based potential molecular qubits: the key role of the vanadyl moiety.
M. Atzori, E. Morra, L. Tesi, A. Albino, M. Chiesa, L. Sorace and R. Sessoli. In: *Journal of the American Chemical Society* **138** (2016), pp. 11234-11244.

VOdtc: Spin dynamics and low energy vibrations: insights from vanadyl-based potential molecular qubits.
M. Atzori, L. Tesi, S. Benci, A. Lunghi, R. Righini, A. Taschin, R. Torre, L. Sorace and R. Sessoli. In: *Journal of the American Chemical Society* **139** (2017), pp. 4338-4341.

VOcat/Vcat/VOnaphcat/Vnaphcat : Structural effects on the spin dynamics of potential molecular qubits.
M. Atzori, S. Benci, E. Morra, L. Tesi, M. Chiesa, R. Torre, L. Sorace and R. Sessoli. In: *Journal of the American Chemical Society* **57** (2018), pp. 731-740.

VOTCPP/VOTPP: Scaling up electronic spin qubits into a three-dimensional metal-organic framework.
T. Yamabayashi, M. Atzori, L. Tesi, G. Cosquer, F. Santanni, M.-E. Boulon, E. Morra, S. Benci, R. Torre, M. Chiesa, L. Sorace, R. Sessoli and M. Yamashita. In: *Journal of the American Chemical Society* **140** (2018), pp. 12090-12101.

4.1 Static properties

The investigated molecules can be divided in two groups: those containing the vanadyl moiety and those containing tris-chelate V^{IV} ions. The former ones, reported in Figure 4.1, have square pyramidal geometry: deviation from the tetragonal symmetry often occurs due to a rhombic distortion in the equatorial plane.

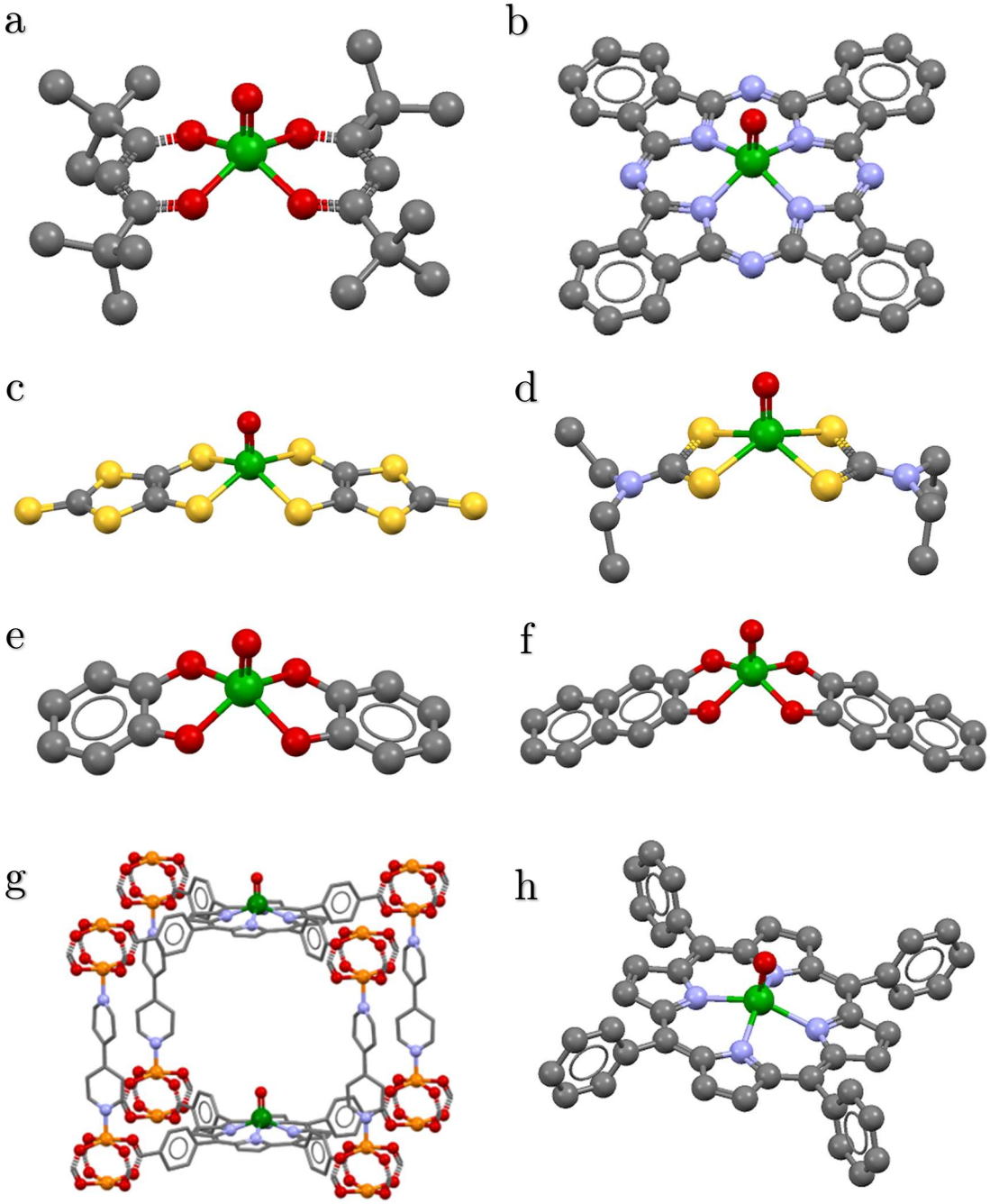

Figure 4.1. Molecular structures of the investigated molecules containing the vanadyl moiety: (a) **VOdpm**, (b) **VOPc**, (c) **VOdmit**, (d) **VOdtc**, (e) **VOcat**, (f) **VOnaphcat**, (g) **VOTCPP** and (h) **VOTPP**. Colour code: V=green, O=red, S=yellow, N=blue, C=grey, Zn=orange. Hydrogen atoms are omitted for clarity.

The molecules **VOdpm**, **VOcat** and **VOnaphcat** feature two bidentate ligands with oxygen donor atoms, **VOdmit** and **VOdtc** feature two bidentate ligands with sulphur donor atoms, while **VOPc**, **VOTPP** and **VOTCPP** have coordinating macrocyclic ligands with nitrogen donor atoms. The last system differs from the others because of its covalent structure extended in three-dimensions, forming a 3D Metal-Organic Framework (MOF). This is composed by [VO(TCPP)] units connected in their basal plane through $[Zn_2(COO)_4]$ subunits to form 2D layers, which are then connected by pillar-like bpy ligands through an axial coordination between pairs of $[Zn_2(COO)_4]$ subunits.[2-5] The obtained structure has 3D channels with a pore dimension of 1.66 x 1.38 nm^2 along the crystallographic *a* and *b* axes. Since the [VO(TCPP)] monomer has the tendency to form complex long-range structures through a network of hydrogen bonds, **VOTPP** has been considered as the MOF's building block to perform a comparative study of the spin dynamics properties.

For all complexes in this group, the V=O bond is the shortest one in the vanadium coordination sphere, and the metal ion is always found slightly above the basal plane. For these vanadyl-based molecules, the crystallographic space and point groups, as well as bonds distances and closest metal-metal distances, are reported in Table 4.1.

Data reported in Table 4.1 clearly show that the V=O distance is unaffected by the choice of the ligand. On the other hand, the bond distances in the basal plane of the coordination sphere obviously depend on the donor atom: V-O is the shortest and the most variable, whereas V-N and V-S are more symmetric. The latter type of bond is also the longest, in agreement with a major ionic radius of the sulphur atoms. The distance of the metal centre from the basal plane is similar for all systems. This feature of the vanadyl molecules may be important in the perspective of depositing them on surfaces since it may help in keeping the paramagnetic unit well-separated from the surface, thus preserving its magnetic properties.[6, 7] It is also important to consider the shortest V···V distances, since the electronic spins influence each other through dipolar interactions. In this respect, it is remarkable to note the relatively long distances between the metal ions within **VOTCPP**.

It is worth to underline the inherent asymmetry of **VOdtc**. The terminal methyl groups of one Et_2dtc^- ligand are oriented, as expected, above and below the S_2CN plane of the ligand. Curiously, the methyl groups of the other ligand of the molecule are both oriented in the same direction. This feature is inherent to the molecule since the homogeneity of the sample has been confirmed by X-ray analysis. Such a sterically unfavourable distortion may be due to the presence of short-contacts involving the terminal methyl groups.[8]

Table 4.1. Main parameters of the crystal structure for the molecules containing the vanadyl moiety.

Molecules/ Features	space group	point group	V=O distance	V-L distance	V···V shortest distance	distance from basal plane
VOdpm	monoclinic *P2₁*	C_1	1.59 Å	V-O 1.963-1.980 Å	7.95 Å	0.55 Å
VOPc (Type II)	triclinic *P-1*	C_1	1.58 Å	V-N 2.008−2.034 Å	6.18 Å	0.57 Å
VOdmit	monoclinic *C2/c*	C_2	1.59 Å	V-S 2.386-2.387 Å	10.50 Å	0.68 Å
VOdtc	monoclinic *P2₁/c*	C_1	1.59 Å	V-S 2.395−2.414 Å	8.01 Å	0.75 Å
VOcat	monoclinic *P2₁/c*	C_1	1.61 Å	V-O 1.960−1.980 Å	11.95 Å	0.62 Å
VOnaphcat*	hexagonal *P6₅22*	C_2	1.60 Å	V-O 1.927−1.975 Å	7.31 Å	0.67 Å
VOTCPP	tetragonal *P4*	C_4	1.60 Å	V-N 2.09 Å	13.9 Å	0.59 Å
VOTPP	tetragonal *I4*	C_4	1.58 Å	V-N 2.11 Å	10.9 Å	0.58 Å

In addition to the synthesis and crystallization of these compounds, the isostructural analogues of **VOPc**, **VOdmit**, **VOTCPP** and **VOTPP** have been synthetized to obtain a solid-state magnetic dilution. This type of spin dilution is mandatory to measure the magnetic dynamics properties by pulsed EPR up to room temperature (298 K) and to correlate the relaxation times to the structural features, *i.e.* the vibrational modes of the crystalline lattice.[9] For **VOPc**, the high stability of the diamagnetic TiOPc allows the preparation of crystalline materials with different percentage of paramagnetic component diluted in the diamagnetic host; two compounds were thus prepared with dilution percentage 10 and 0.1%, hereafter indicated as **10%-VOPc** and **0.1%-VOPc**, respectively. Concerning **VOdmit**, the EPR experiments were performed on a $5 \pm 1\%$ crystalline dispersions in $[(Ph)_4P]_2[MoO(dmit)_2]$, and hereafter labelled as **5%-VOdmit**.[10] The same co-crystallization was done using the deuterated cation d_{20}-$(Ph)_4P^+$, in order to evaluate the decoherent contribution provided by the ^1H nuclei;[11, 12] the obtained

compound is identified hereafter as ***d*$_{20}$-5%-VOdmit**. The porphyrinate compounds were diluted with the isostructural analogues based on Ti^{IV}, by using a $5 \pm 1\%$ dilution for **VOTCPP** and a $2 \pm 1\%$ dilution for **VOTPP**; namely obtaining [$VO_{0.05}TiO_{0.95}$(TCPP-Zn_2-bpy)] (labelled as **5%-VOTCPP**) and [$VO_{0.02}TiO_{0.98}$(TPP)] (labelled as **2%-VOTPP**), respectively. For **VOTPP**, a milder dilution (30%) was also prepared to study the dilution effects through ac susceptometry, hereafter labelled as **30%-VOTPP**.

The X-band cw-EPR spectra for these vanadyl molecules show the 8-fold hyperfine splitting due to the coupling between the $S = 1/2$ electronic spin of V^{IV} and the $I = 7/2$ nuclear spin of its most abundant isotope (^{51}V, abundance 99.76%). The signals are further split by the anisotropic component of the hyperfine coupling. The cw-EPR spectra exhibit very similar features for all the systems: two examples are reported in Figure 4.2.

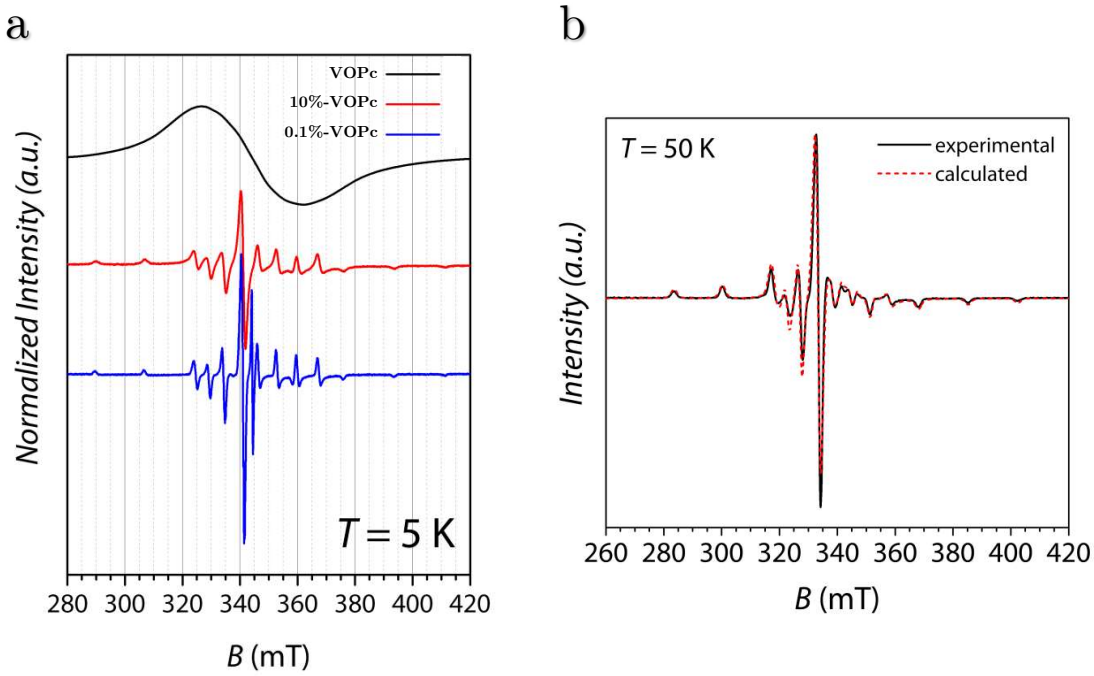

Figure 4.2. (a) X-band ($\nu = 9.47$ GHz) cw-EPR spectra of **VOPc** in its pure form and diluted 10% and 0.1% in solid matrix of the diamagnetic TiOPc. (b) X-band ($\nu = 9.39$ GHz) cw-EPR spectra of **VOnaphcat** in frozen solution (1.0 mM in 3:1 CH_2Cl_2:C_6H_6), and its simulation using the software package EasySpin for Matlab.[13]

It is evident from Figure 4.2 that the dilution either in crystalline solid or frozen solution matrix is necessary to increase the spin-spin relaxation time T_2, which is responsible of the homogeneous linewidth, and to obtain a resolved spectrum. Indeed, the pure form of **VOPc** exhibits a unique broad band due to dominant dipolar interactions between paramagnetic centres, whereas the 10% dilution already allows to detect the hyperfine structure. Spectral simulations[13] in agreement with the experimental data were obtained on the basis of the following spin Hamiltonian:

$$\mathcal{H} = \mu_B \hat{\boldsymbol{S}} \cdot \boldsymbol{g} \cdot \boldsymbol{B} + \hat{\boldsymbol{I}} \cdot \boldsymbol{A} \cdot \hat{\boldsymbol{S}} \tag{4.1}$$

The best-simulation parameters for all the cw-EPR spectra of the vanadyl complexes are reported in Table 4.2.

Table 4.2. Best-parameters of the cw-EPR spectra simulation for the vanadyl-based molecules.

Molecules/ Parameters	g_x	g_y	g_z	A_x **(MHz)**	A_y **(MHz)**	A_z **(MHz)**
VOdpm	1.9880(2)	1.9815(3)	1.949(1)	167.9(1)	190.4(2)	509.6(3)
VOPc/type II	1.987(1)	1.987(1)	1.966(1)	167.9(1)	167.9(1)	476.7(2)
VOdmit	1.988(1)	1.986(1)	1.970(1)	128(2)	138(2)	413(2)
VOdtc	1.989(1)	1.985(1)	1.969(1)	135(2)	153(2)	440(2)
VOcat	1.988(1)	1.980(1)	1.956(1)	126(2)	159(2)	465(2)
VOnaphcat	1.988(1)	1.979(1)	1.955(2)	127(2)	156(2)	465(4)
VOTCPP	1.9865(1)	1.9865(1)	1.963(1)	168(2)	168(2)	477(2)
VOTPP	1.9865(1)	1.9865(1)	1.963(1)	169(2)	169(2)	480(2)

The experimental spectra are satisfactorily reproduced by assuming an axial model ($x = y \neq z$) for the systems coordinated by macrocyclic ligands, *i.e.* **VOPc** (despite the C_1 point symmetry of the molecule), **VOTCPP** and **VOTPP**. Instead, a rhombic model ($x \neq y \neq z$) must be adopted for those derivatives with bidentate ligands. However, in general, the electronic spin is not highly affected by the change of ligand, since the values in Table 4.2 are all similar to each other. Remarkably, quasi-identical parameters are obtained for **VOTCPP** and **VOTPP**, thus confirming the validity of the building block assumption. The obtained spin-Hamiltonian parameters can be explained considering the presence of a short V=O bond that is responsible for a *d*-orbital splitting of the metal centres. This lead the d_{xy} orbital lowest in energy and well-separated from the other orbitals (Figure 4.5). Furthermore, the *g*-factor values are close to the free-electron value, *i.e.* 2.0023, thanks to the small spin-orbit coupling characteristic of a light transition metal such as vanadium. These features, in addition to the single unpaired electron of the V^{IV} ion, resulting in an electronic spin value $S = 1/2$, make these systems good candidates for realizing molecular spin qubits.[14]

The other class of V^{IV} based molecules discussed in this chapter is composed of tris-chelate complexes, based on some of the ligands already used for the previously discussed vanadyl derivatives. The resulting molecular geometry is octahedral with a slight trigonal

distortion; the graphical representation of their molecular structures is reported in Figure 4.3.

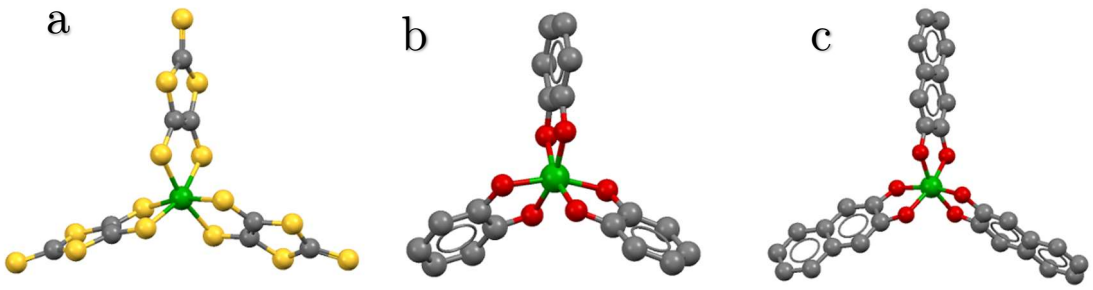

Figure 4.3. Molecular structure of the investigated tris-chelated vanadium-based molecules: (a) **Vdmit**, (b) **Vcat** and (c) **Vnaphcat**. Colour code: V=green, O=red, S=yellow, C=grey. Hydrogen atoms are omitted for clarity.

Their crystal structures consist of homoleptic tris-chelated $[V(dmit)_3]^{2-}$, $[V(cat)_3]^{2-}$ and $[V(naph\text{-}cat)_3]^{2-}$ anions showing Λ and Δ chirality and tetraphenylphosphonium cations. The space and point groups, as well as the bonds distances and closest metal-metal distances, are reported in Table 4.3.

Table 4.3. Main parameters of the crystal structure for the vanadium-based tris-chelated molecules.

Molecules/ Features	space group	point group	V-L distance	V···V shortest distance	twist angle	chelate fold angle
Vdmit	monoclinic *P2₁/c*	*C₁*	V-S 2.380-2.394 Å	9.75 Å	∽41.0°	∽7.2°
Vcat	monoclinic *C2/c*	*C₂*	V-O 1.939-1.958 Å	10.12 Å	∽41.5°	∽0°
Vnaphcat	monoclinic *P2₁/n*	*C₁*	V-O 1.925-1.956 Å	11.20 Å	∽38.6°	∽0°

The V-S, V-O and V-V distances are consistent with those found for the vanadyl-based molecules. The twist angles, *i.e.* the angle between the two medians of two parallel triangular faces of the octahedron, are similar to each other. Finally, it is noted that the plane of the ligand forms a non-zero chelate fold angle with the metal donor atoms plane only for V-S complexes (Table 4.3).

An isostructural diamagnetic analogous based on Ti^{IV} has been prepared only for the **Vdmit** complex with a dilution percentage of $6 \pm 1\%$, close to that used for **VOdmit**, and namely $[(Ph)_4P]_2[V_{0.06}Ti_{0.94}(dmit)_3]$ (labelled as **6%-Vdmit**).

The cw-EPR spectra of these systems agree with the presence of a vanadium ion with the 8-fold splitting due to the hyperfine coupling between the electronic spin $S = 1/2$ and the nuclear spin $I = 7/2$. Again, these features emerge after the dilution either in crystalline solid or frozen solution matrix, but the observed linewidths are larger than for vanadyl derivatives due to a shorter T_2; the experimental spectra and their simulations are shown in Figure 4.4.

The simulations were performed by using the spin Hamiltonian expressed in eq. (4.1) and assuming an axial model for **Vcat** and a rhombic one for **Vnaphcat** and **Vdmit**.[13] The best-simulation parameters obtained by simulating cw-EPR spectra are reported in Table 4.4.

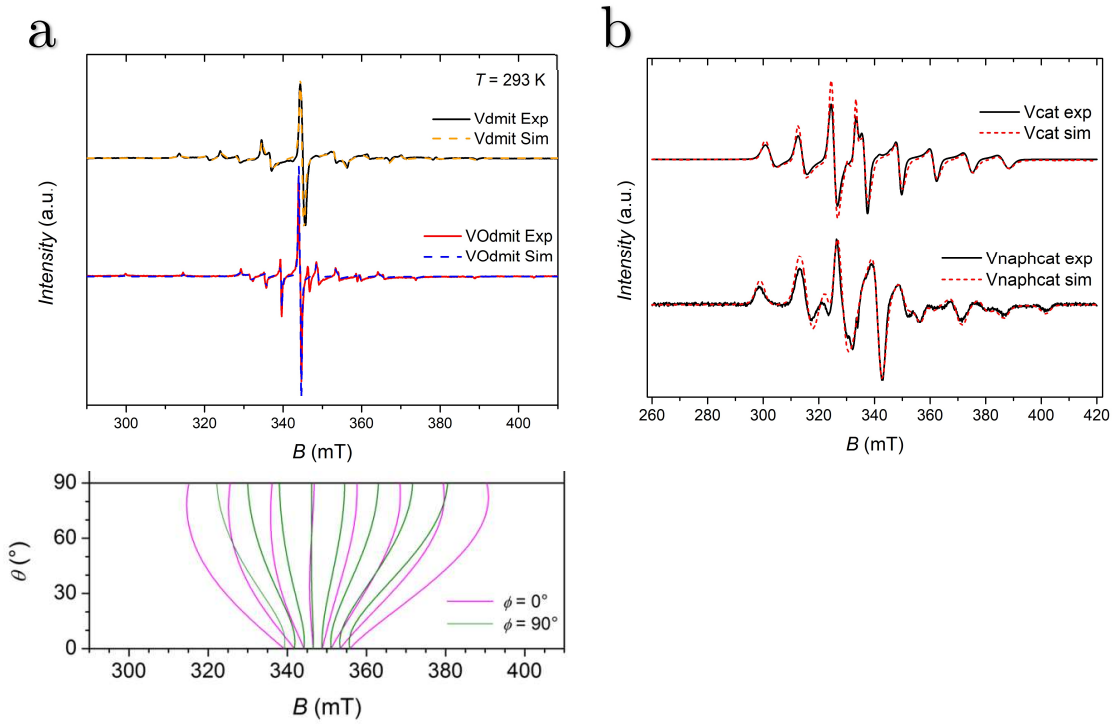

Figure 4.4. Experimental and simulated (a) X-band ($\nu = 9.7$ GHz) cw-EPR spectrum of **Vdmit** diluted in solid state matrix with above shown the angular dependency profile (θ vs magnetic field) for two values of ϕ, corresponding to the rotation in the zx ($\phi = 0$) and zy (ϕ =90) planes; and for (b) X-band ($\nu = 9.39$ GHz) cw-EPR spectra of **Vcat** and **Vnaphcat** in frozen solution (1.0 mM in 3:1 CH_2Cl_2:C_6H_6).

Table 4.4. Best-simulation parameters of the cw-EPR spectra for the vanadium-based tris-chelated molecules.

Molecules/ Parameters	g_x	g_y	g_z	$\lvert A_x \rvert$ (MHz)	$\lvert A_y \rvert$ (MHz)	$\lvert A_z \rvert$ (MHz)	α, β and γ (°)
Vdmit	1.961(1)	1.971(1)	1.985(1)	299(2)	230(2)	40(5)	-20, -10, 0
Vcat	1.945(1)	1.945(1)	1.989(2)	330(6)	330(6)	65(5)	-
Vnaphcat	1.914(1)	1.927(1)	2.001(2)	394(2)	245(3)	30(7)	-

Compared to the parameters obtained for the vanadyl molecules, a higher variability in the $\boldsymbol{g}$ and $\boldsymbol{A}$ constants is encountered due to the more flexible coordination geometry of the tris-chelated molecules. Moreover, from the analysis of the cw-EPR spectrum of **Vdmit** it emerges the non-collinearity of the $\boldsymbol{A}$ and $\boldsymbol{g}$ tensors. This feature, which is consistent with the triclinic point symmetry[15] (Table 4.3) of the complex anion **Vdmit**, was not previously recognized for tris-dithiolene V^{IV} complexes, and it has been here identified thanks to the improved resolution of the solid crystalline spectra together with the multifrequency EPR approach (X-band and Q-band).[11, 16] The angles reported in Table 4.4 are the Euler angles that define the passive rotation of the hyperfine principal axes system into the $\boldsymbol{g}$-matrix principal axes system, $\boldsymbol{A} = R(\alpha,\beta,\gamma)A_{diagonal}R^{+}(\alpha,\beta,\gamma)$.

For the tris-chelate molecules, the ligand field symmetry is responsible for a *d*-orbital splitting that leaves the d_{z^2} orbital (where z is the trigonal axis of the distorted octahedron)[16] lowest in energy with respect to the other orbitals; this is shown in Figure 4.5.

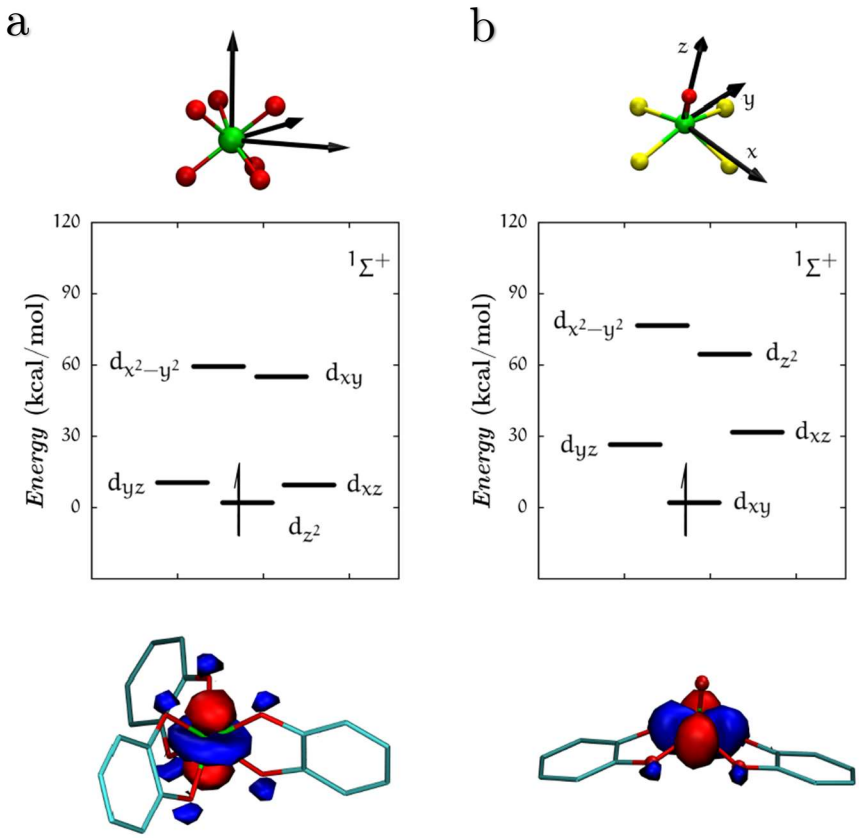

Figure 4.5. From the top: system of reference chosen for the orbital labelling; electronic structure around the SOMO-LUMO gap; SOMO orbital for pseudo-octahedral (a) and square pyramidal (b) geometries. The image has been taken by ref[17].

4.2 Ac susceptibility studies

These studies were performed for all the molecules previously presented in order to get deeper insights on their magnetization dynamics. The thermal variation of the magnetic susceptibility in a zero-static magnetic field reveals no imaginary component of the susceptibility (χ'') for every investigated temperature, as expected from the theory (§3.3).[18, 19] When a small static magnetic field (>30 mT) is applied, slow magnetic relaxation is observed with appearance of a peak in the imaginary component of the susceptibility and a concomitant decrease of the real part (χ'). The real and imaginary components of the susceptibility can be fitted according to the Debye model[20]

$$\chi'(\omega) = \chi_S + (\chi_T - \chi_S)\frac{1 + (\omega\tau)^{1-\alpha}\sin(\pi\alpha/2)}{1 + 2(\omega\tau)^{1-\alpha}\sin(\pi\alpha/2) + (\omega\tau)^{2-2\alpha}}$$
$$\chi''(\omega) = (\chi_T - \chi_S)\frac{(\omega\tau)^{1-\alpha}\cos(\pi\alpha/2)}{1 + 2(\omega\tau)^{1-\alpha}\sin(\pi\alpha/2) + (\omega\tau)^{2-2\alpha}} \quad (4.2)$$

where τ is the relaxation time, α represents the distribution in relaxation times, χ_T and χ_S are the thermal and adiabatic susceptibility, respectively. By using eq. (4.2) it is possible to extract values of τ as a function of the temperature or the applied magnetic field. Examples of frequency dependences of the real and imaginary components of the susceptibility either varying the temperature or the magnetic field are reported in Figure 4.6, together with their fits.

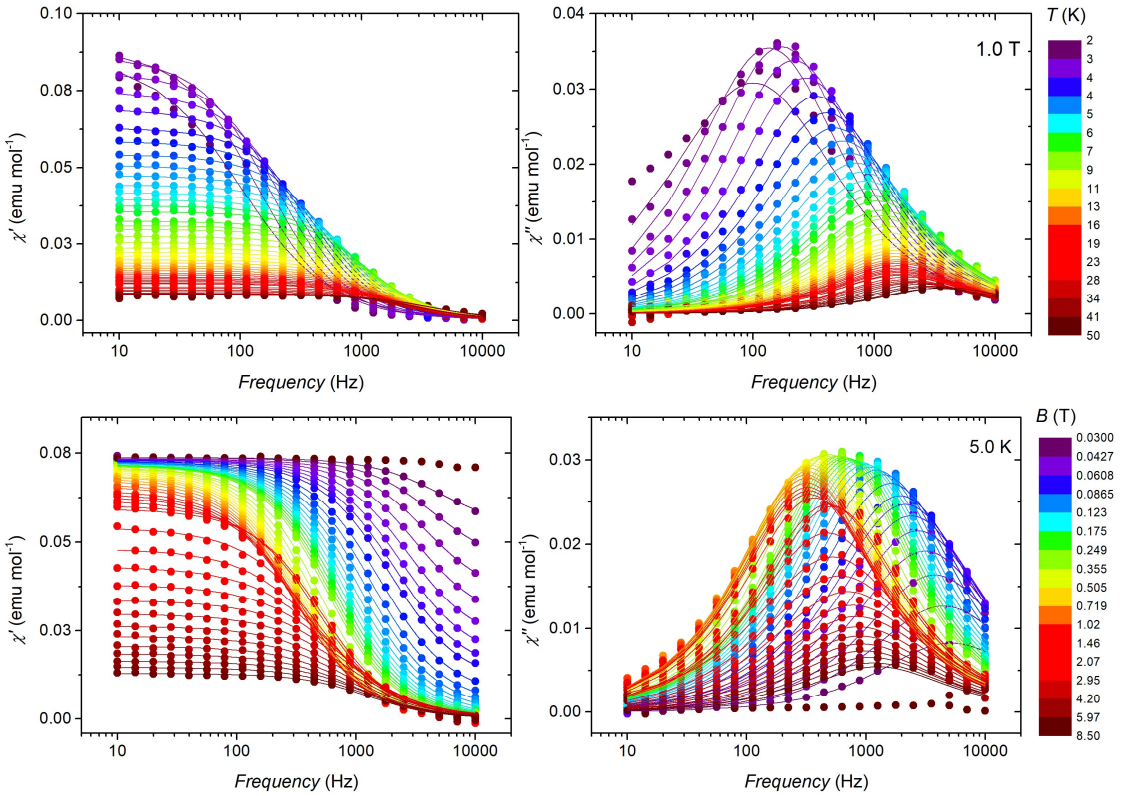

Figure 4.6. Frequency dependence of the real component χ' and the imaginary component χ'' of the magnetic susceptibility of a microcrystalline powder sample of **VOTPP** as a function of the temperature (2.0-50.0 K range) under an applied magnetic field of 1 T (up); and as a function of the magnetic field (30-8500 mT) at the temperature of 5.0 K (down). The solid lines represent the best-fit obtained by simultaneously fitting χ' and χ'' through the generalized Debye model equations.

The ac susceptibility of all the molecules described in this chapter has been investigated both as a function of temperature and magnetic field for microcrystalline powders of pure compounds, but only the extracted relaxation times will be reported in the following. In first approximation, and if concentration dependent effects such as cross-relaxation or spin-phonon bottleneck are absent, this characteristic time, τ, corresponds to the spin-lattice relaxation time T_1.[20] Furthermore, being this relaxation time related to the frequency of the maximum of χ'' by $\tau = 1/2\pi\nu_{max}$, by following the shift of such maxima, the corresponding variation of τ is easily evaluated, at least qualitatively. The temperature dependence of τ for all the vanadyl derivatives will be firstly exposed; this is reported in Figure 4.7a. The measurements were performed using a static magnetic field of 1 T for all molecules except for **VOdpm**, which is reported in Figure 4.7b for different crystalline sizes and under a static magnetic field of 200 mT. The vanadyl systems reported in Figure 4.7a present relaxation times between 0.03 and 10 ms with different temperature dependences. The general trend of τ is to decrease as the temperature is increased. Analogies can be observed between **VOcat** and

VOnaphcat, which are quasi-superimposed, and between the three macrocyclic coordinated systems **VOPc**, **VOTPP** and **VOTCPP**. At low temperature, the latter systems show a strong temperature dependence up to 10 K that weakens increasing the temperature and slowly start to decrease again above 30 K. It should be noted that dipolar effects may play a key role in pure systems for which a reduction of the spin density may produce a rigid upward shift of the absolute values of τ. This has been observed, for example, by slightly diluting in crystalline solid-state matrix **VOTPP** in order to obtain a spin density similar to that of **VOTCPP**. In this case, indeed, their τs result quasi-superimposed, as one could be expected by considering the remarkable similarity of their electronic properties (see Table 4.2) and spin dynamics behaviour (Figure 4.7a). On the other hand, it is interesting to include in this comparison also **VOPc**, whose electronic properties are close to those of **VOTPP** and **VOTCPP**. The relaxation time of **VOPc** is the lowest and even the solid-state dilution **10%-VOPc** does not seem to increase significantly τ (see Figure 4.8). However, **VOPc** has the shortest V···V distances (Table 4.1), suggesting that a higher dilution should be performed to obtain comparable V···V distances and thus comparable relaxation times with those of **VOTPP** and **VOTCPP**. On the other hand, this would reduce the number of spins below the detection limit of the ac susceptometer instrument. The relaxation times of other vanadyls are instead more regular, and they share a similar variation of the temperature dependence increasing the temperature. This can be attributed to the passage from a region where the direct relaxation process is more effective to another one, at higher temperatures, where the Raman process dominates. However, among the several possible reasons in differentiating the temperature dependence of the spin dynamics, one of the most important can be certainly attributed to the different low-energy vibrational spectrum. For example, the long relaxation times of **VOcat** and **VOnaphcat** could be explained by considering the high rigidity introduced by the catecholate-like structure. These aspects are discussed in more detail in the following section, with the support of the spectroscopic investigation.

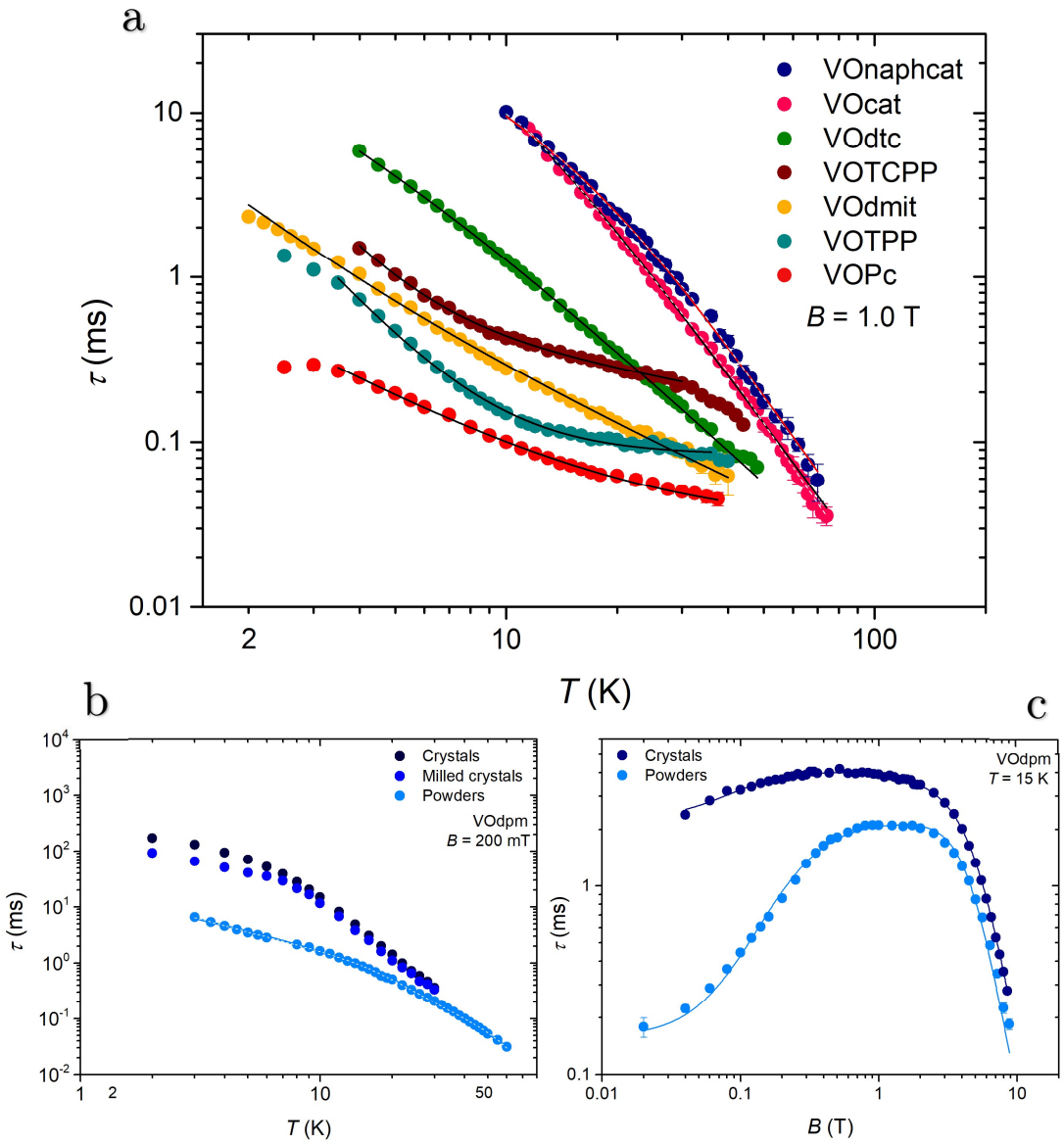

Figure 4.7. Temperature dependence of τ extracted from ac susceptibility measurements for: (a) microcrystalline powders of all vanadyl systems here investigated, except **VOdpm**, under a static magnetic field of 1.0 T. (b) **VOdpm** at different crystalline sizes (from quasi-millimetric crystals to quasi-micrometric powders) under 200 mT. (c) Magnetic field dependence of τ for **VOdpm** at different crystalline sizes at 15 K. Solid lines represent the best-fit using different models (see infra). Dashed lines correspond to the fits of τ for **VOcat** and **VOnaphcat** by using the local mode model eq. (4.7).

The presence of spin-phonon bottleneck effects (§3.3.8) is observed for **VOTPP** and **VOTCPP** at low temperature. These effects are shown more in detail in Figure 4.7 where the temperature and magnetic field dependence of the **VOdpm** relaxation times are reported for different degrees of crystals grinding. The phonon bottleneck, which is more effective in bigger crystals, appears to lengthen τ; decreasing the crystalline sizes the relaxation times shorten from ca. 130 to ca. 6 ms at 3 K. Since the bottleneck affects only the direct process, by increasing the temperature it gradually becomes less effective. Consequently, at higher temperatures smaller deviations are observed between different

crystallite sizes. It should be specified that in Figure 4.7 the temperature dependence of τ for **VOdtc** appears similar to that of **VOdpm**, but this is misleading since different magnetic field values were used in the measurements.

The magnetic field dependence of τ for the investigated vanadyl-based molecules are reported in Figure 4.8. The relaxation times cover three orders of magnitude, from 0.01 to 10 ms, in agreement with the values shown in Figure 4.7. For all systems, there is a rapid increase of τ at low fields, which then reaches a maximum and remains almost unchanged in a variable field range, to finally decreases at higher fields. Although the low field region where τ initially increases and its extent can be very different from system to system, at high fields all systems behave in the same way. This non-monotonous behaviour reflects two antagonist effects of the magnetic field: at low fields spin-spin and spin-nuclei interactions promote rapid relaxation, but their strength reduces as the external magnetic field is increased. On the other hand, by increasing the magnetic field the energy separation between the two spin levels grows, with the consequence that a greater number of phonons can match this energy difference. This produces a more efficient spin-phonon direct process of relaxation with the characteristic magnetic field dependence $\tau \propto B^4$ (§3.7). The role of the internal fields is underlined in Figure 4.8b where the comparison of τ between pure and solid-state diluted compounds of **VOTPP** and **VOPc** is reported. Such fields contribute in two different ways: the relaxation times for **30%-VOTPP** are rigidly shifted upwards without changes in the magnetic field dependence. Instead, for **10%-VOPc** the only modification appears in the low-fields shape, which is the region dominated by internal fields. The presence of a peculiar dip at 2.0 T for both **VOPc** and **VOTPP** is well evident in Figure 4.8b, and it is also visible for **VOTCPP** in Figure 4.8a, however its origin is still unclear.

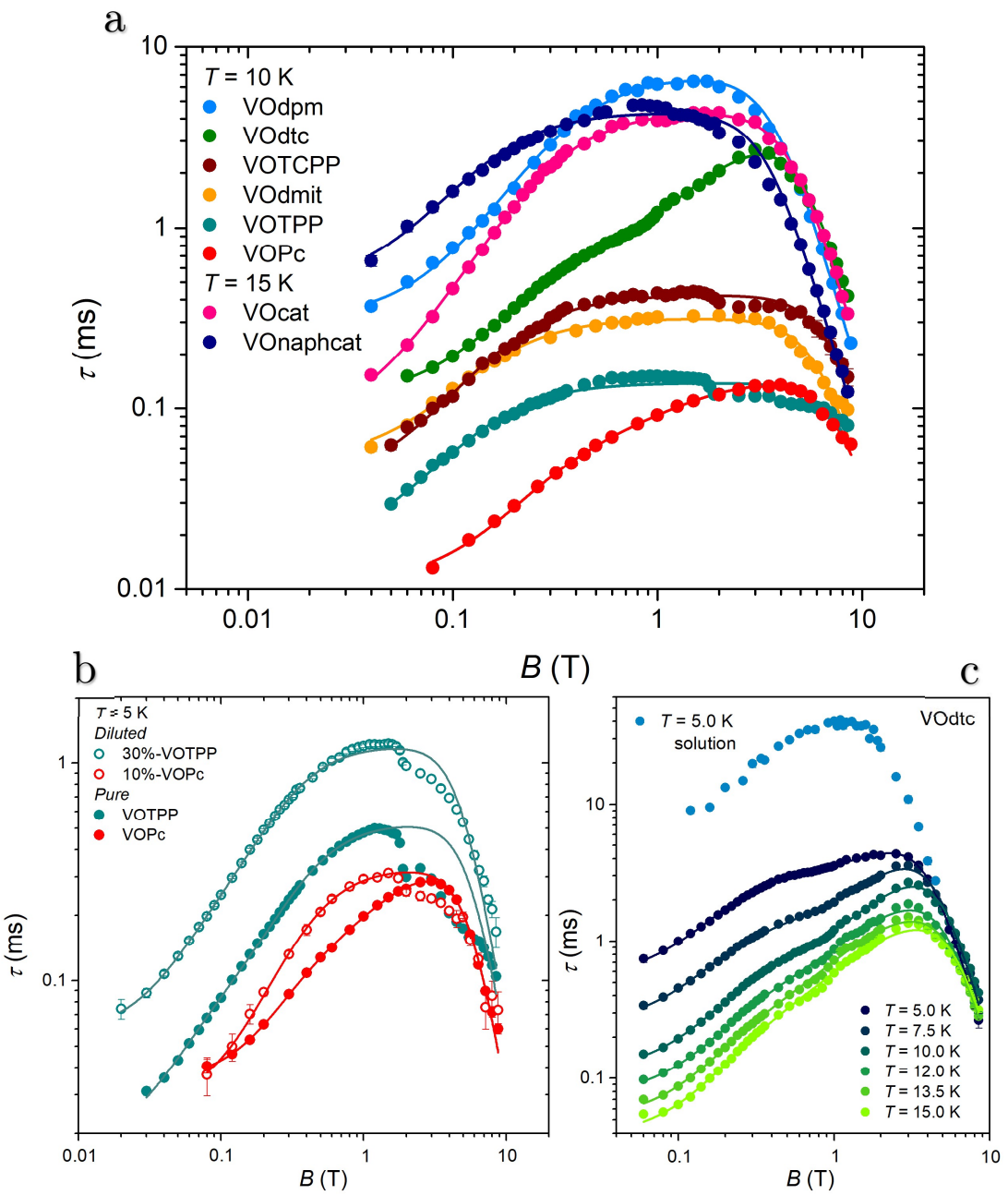

Figure 4.8. Magnetic field dependence of τ extracted from ac susceptibility measurements (a) for microcrystalline powders of all vanadyl systems here investigated, at different temperatures (see legend); (b) for the pure and solid-state diluted compounds of **VOTPP** and **VOPc** at the temperature of 5 K; (c) for **VOdtc** at different temperatures, both as microcrystalline powders and frozen solution. Solid lines represent the best-fits obtained using the Brons-van Vleck models.

Another peculiar feature is evident in the field dependence of τ for **VOdtc** (Figure 4.8c), which exhibits a shoulder at ca. 500 mT for all the investigated temperatures of the pure compound. Such a feature is lost in frozen solution matrix (CH_2Cl_2/toluene) where it relaxes even slower. This can be explained by considering that such a complex magnetic field dependence is related to the crystalline structure of **VOdtc**, which is clearly lost in an amorphous environment such as the one obtained working in frozen

solution matrix. Furthermore, the enhancement of τ can be easily explained considering again the different spin density between the powder microcrystalline and frozen solution compounds. To take into account this variable in explaining the results, the spin densities of the investigated compounds are shown in Table 4.5, from which it is evident that molecules with counterions have lower spin densities. However, the lowest spin density is achieved for **VOTCPP**, thanks to its MOF structure, for which a further dilution is not expected to play a major role.

Table 4.5. Spin densities of the vanadyl compounds investigated by ac susceptibility for the pure samples (up) and their dilutions (down).

	VOdpm	VOPc	VOdmit	VOdtc	VOcat	VOnaphcat	VOTPP	VOTCPP
Spin density $\left(\frac{spin}{nm^3}\right)$	1.62	1.65 ↓ (10%) 0.16	0.75	2.48 ↓ $3 \cdot 10^{-5}$	0.84	1.33	1.14 ↓ (30%) 0.34	0.26

The same analysis has been performed on the vanadium tris-chelated molecules: **Vdmit**, **Vcat** and **Vnaphcat**. The relaxation times as a function both of temperature and magnetic field are reported in Figure 4.9.

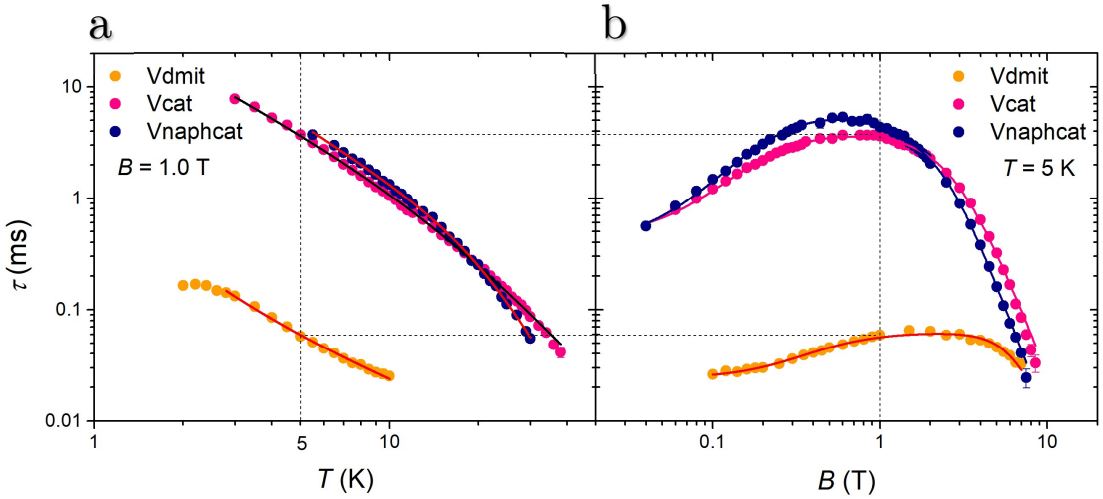

Figure 4.9. Temperature (a) and magnetic field (b) dependences of the relaxation time τ for powder crystalline compounds of **Vdmit**, **Vcat** and **Vnaphcat**. The dashed lines highlight the correspondence of the relaxation times in the two different measurement conditions. The solid lines in (a) correspond to the best fits obtained by using the simple power-law model. The solid lines in (b) are the best fits obtained by using the Brons-van Vleck models.

The relaxation times of these tris-chelate molecules show a behaviour similar to that of the vanadyl molecules previously described. However, the inspection of τ values at 10 K shows that there is almost one order of magnitude of difference between those of the tris-chelated species (Figure 4.9) and of their vanadyl analogues (Figure 4.7a). This

shortening of τ for the tris-chelate species cannot be explained by considering the spin density (Table 4.6), which should result in longer relaxation times. Two different hypothesis may be done: the strongest spin-orbit coupling contribution, as evidenced by the g anisotropy in Table 4.4, which promotes the energy transfer between the spin and lattice systems, and the different low-energy vibrational spectrum, which will be discussed in section (§4.4).

Table 4.6. Spin densities of the vanadium-based tris-chelate compounds investigated by ac susceptibility for the pure samples.

Spin density $\left(\frac{spin}{nm^3}\right)$	Vdmit	Vcat	Vnaphcat
	0.69	0.80	0.68

4.3 Pulsed EPR studies

Ac susceptometry is a non-resonant technique that provides useful information about the temperature and magnetic field dependence of the magnetization relaxation time τ, which corresponds to T_1 in a first approximation, for concentrated or moderately-diluted samples. Instead, pulsed EPR spectroscopy is a resonant technique that allows to characterize both T_1 and T_m in a wide temperature range of highly diluted samples. Indeed, the investigated samples must have narrow resonance lines (see cw-EPR) and, to fulfil this condition, a dilution either in a crystalline matrix or in a frozen solution is required. Whenever possible the former should be preferred since it maintains unaltered the crystalline structure, and thus the phononic structure of the system, and it allows to reach higher temperatures.

Pulsed EPR measurements were performed in the Laboratories of the University of Turin in collaboration with Dr. E. Morra and Prof. M. Chiesa. As preliminary measurement, the X-band and/or Q-band Echo-Detected Field-Swept (EDFS) EPR spectra were recorded at different temperatures by using a standard Hahn echo sequence. As an example, the EDFS spectra of **5%-VOdmit** and 6**%-Vdmit** are shown in Figure 4.10a. The observation of spin-echo is already an indication that the quantum coherence of the investigated molecule can be observed.[21] Furthermore, the spin Hamiltonian parameters found by simulating the cw-EPR spectra allow to obtain high-quality EDFS spectra simulations, confirming that the entire paramagnetic component of the sample is experiencing the detected coherence.

Then, inversion recovery experiments were performed by fixing the static magnetic field at the value corresponding to a specific transition and varying the temperature.[22]

Usually, two transitions are chosen: *i*) the so-called powder-like position, $m_I = -1/2$ (OP1), where all molecules are excited due to the negligible angular dependency of the resonance field, and *ii*) the single-crystal-like position, $m_I = -7/2$ (OP2), where only molecules with their z axis within 10° from the field direction are selected (Figure 4.10a).

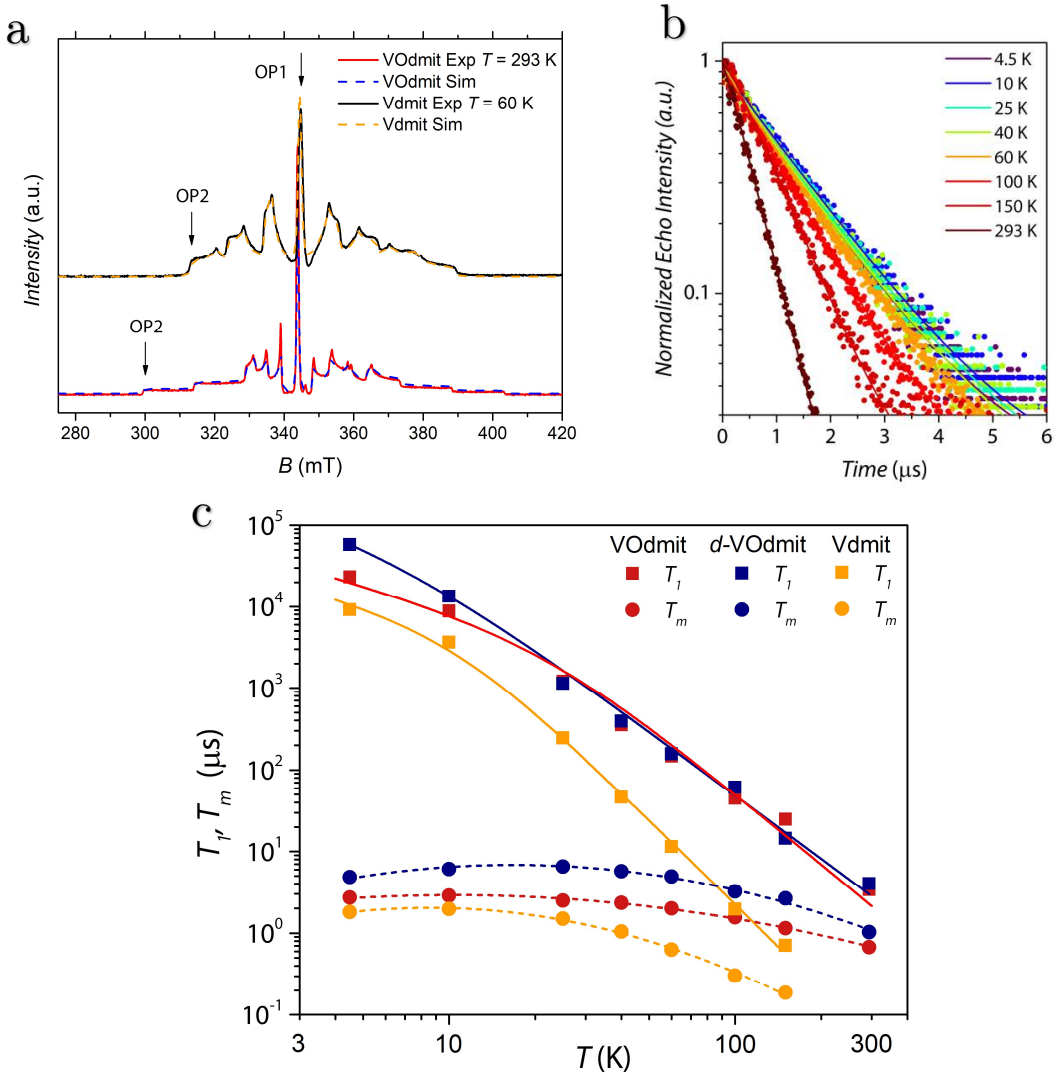

Figure 4.10. (a) Experimental EDFS EPR spectra for **5%-VOdmit** (red line) and **6%-Vdmit** (black line) at X-band frequency ($\nu = 9.7$ GHz). The spectral simulations obtained using the spin Hamiltonian parameters reported in Table 4.4 are also reported. The arrows indicate the two spin transitions chosen to perform EPR experiments. (b) Echo decay traces recorded at the OP1 (X-band) for **5%-VOdmit** at different temperatures (see legend). (c) Temperature dependence of T_1 and T_m for **5%-VOdmit**, ***d*$_{20}$-5%-VOdmit** and **6%-Vdmit** obtained measuring at the powder-like transition OP2. Solid and dashed lines represent a guide for the eyes. Error bars are within the size of the symbols.

In this case, experiments were performed on OP2, and the resulting saturation recovery traces were fitted, as usually done for transition metal-based systems, with a stretched mono-exponential expression[23]

$$I = I_0 + k_1 \exp[-(t/T_1)^{\beta_1}] \quad (4.3)$$

where I indicates the echo intensity, t is the time delay between the initial pulse and echo detection, and β_1 is the stretch factor. Examples of the extracted spin-lattice relaxation times T_1 for **5%-VOdmit** and **6%-Vdmit** are reported as a function of temperature in log-log plots in Figure 4.10c.

The quantum coherence time is usually investigated and quantified through the phase memory time, T_m, which is obtained by performing echo decay experiments. The decay traces (Figure 4.10b) were fitted using the stretched exponential equation

$$I = I_0 + k_m \exp[-(2t/T_m)^{\beta_m}] \quad (4.4)$$

and T_m is reported as a function of temperature in log-log plots in Figure 4.10c.

Thus, Figure 4.10c contains the relaxation times T_1 and T_m for **5%-VOdmit**, ***d*$_{20}$-5%-VOdmit** and **6%-Vdmit** using the transition OP2 (no major differences with OP1 were observed). The two vanadyl compounds have similar T_1 values in almost the whole investigated temperature range, except for the very low temperatures where T_1 for the deuterated sample is longer. This increase can be related either to the different dipolar coupling[24] or to the isotope mass effect[25]. Furthermore, T_1s of the vanadyl species are higher than that of **6%-Vdmit** in the entire investigated temperature range, in agreement with what observed in ac susceptometry. The thermal variation of T_1 for **5%-VOdmit** shows a slow decrease from the maximum value of ca. 23 ms at 4.5 K to the lowest but still remarkable value of 3.37 μs at 293 K. Instead, the thermal variation of T_1 for **6%-Vdmit** shows a slow decrease from the maximum value of ca. 9 ms at 4 K up to ca. 15 K, after which a more pronounced decrease is observed as the temperature increases. Consequently, the lowest detectable value of T_1 for **6%-Vdmit** is 0.71 μs at 150 K.

The relaxation time T_m shows an almost temperature-independent behaviour in the 4.5-100 K range, with values between 6.5-3.2 μs and 2.9-1.6 μs for ***d*$_{20}$-5%-VOdmit** and **5%-VOdmit**, respectively. This behaviour suggests that in this temperature range decoherence is essentially dominated by nuclear spin diffusion (§3.4).[26] Then, T_ms slowly decrease as the temperature increases, due to the contribution of T_1, reaching remarkable values of 0.68 and 1.0 μs at room temperature. The thermal variation of T_m for **6%-Vdmit** also shows an almost temperature-independent behaviour in a limited temperature range (4.3-25 K) with values of T_m within the 2.0-1.5 μs. However, unlike the coherence time of the other two vanadyl-based molecules, it decreases more abruptly as the temperature increases, reaching 0.19 μs at 150 K. This value is already close to the detection limit of pulsed EPR spectrometer, hindering the room temperature

measurements. This is due to the strong temperature dependence of T_1 which, at high temperatures, limits T_m. Enhancing T_1 and reducing its temperature dependence appears thus mandatory to obtain long and weak temperature dependent coherence times.

The same procedure above described has been used to obtain the relaxation times T_1 and T_m of the other vanadyl-based molecules; these are reported in Figure 4.11. The molecules diluted in solid state matrix, that are **0.1%-VOPc**, **5%-VOdmit**, **2%-VOTPP** and **5%-VOTCPP**, are grouped in Figure 4.11(a,b), whereas those diluted in frozen solutions, that are **(1mM)-VOdpm**, **(1mM)-Vcat** and **(1mM)-Vnaphcat**, are reported in Figure 4.11(c,d). The frozen solutions consist of 1 mM solutions in a mixture of 2:3 of CH_2Cl_2/toluene for **VOdpm** and 3:1 of CH_2Cl_2/C_6H_6 for the others two. The resulting spin densities for the molecules here investigated are reported in Table 4.7, from which it is possible to compare the densities obtained by the different types of dilution. Indeed, the spin densities within the same type of dilution are similar to each other, thus excluding dipolar effects as the cause of possible differences in the relaxation times.

Table 4.7. Spin densities of the diluted compounds investigated by pulsed EPR.

	1 mM VOdpm	0.1% VOPc	5% VOdmit	6% Vdmit	1 mM VOcat	1 mM VOnaphcat	2% VOTPP	5% VOTCPP
Spin density $\left(\frac{spin}{nm^3}\right)$	(Liq.)	(Solid)	(Solid)	(Solid)	(Liq.)	(Liq.)	(Solid)	(Solid)
	$6 \cdot 10^{-7}$	0.016	0.037	0.041	$6 \cdot 10^{-7}$	$6 \cdot 10^{-7}$	0.023	0.013

It is worth noting the differences between the relaxation time τ extracted by ac susceptibility measurements and T_1, measured by pulsed EPR. Indeed, the relaxation times of **VOdmit**, **Vdmit** and **VOPc** increase significantly and become similar to each other. The relaxation time of **VOTPP** shows some improvements for which it crosses the relaxation time of **VOTCPP**. The latter two relaxation times are not affected by spin-phonon bottleneck anymore, but they maintain the same weak temperature dependence. All these effects have to be attributed to the passage from pure to highly diluted compounds, thus strongly reducing the dipolar interaction.

Focusing on the solid state diluted systems (Figure 4.11a,b), **5%-VOdmit** has the longest T_1 in the entire temperature range. **0.1%-VOPc** is very similar: T_1 has a slightly weaker temperature dependence at low temperature and a slightly stronger variation above 30 K; in any case its value at room temperature is remarkably of 1.1 μs. For **2%-VOTPP** T_1 at the lowest temperature is one order of magnitude lower than that of **0.1%-VOPc**, and it is 1.5 ms at 5 K. Concerning the behaviour, T_1 is almost temperature independent up to 30 K, after which a more pronounced decrease begins and it reaches 0.4 μs at room temperature. A further weaker temperature variation of T_1 is exhibited

by **5%-VOTCPP**, which has, however, also the shortest T_1 of the series. Indeed, at 5 K it is worth 0.35 ms, that is two orders of magnitude lower than that of **0.1%-VOPc**, while at room temperature T_1s of the two derivatives coincide.

The phase memory times T_m for all the investigated systems are initially temperature independent and then they slowly decrease increasing the temperature. The temperature value at which T_m starts to decrease is related to the absolute value of T_1. The phase memory time of **2%-VOTPP** begins to decrease at 60 K, whereas for **5%-VOTCPP** it starts to decrease at ca. 200 K, reflecting the relative temperature dependence of T_1. At their lowest temperature values, T_ms of **0.1%-VOPc** and **5%-VOdmit** are superimposed and equal to 2.7 μs. They differ for their thermal variation that is constant for the former system up to 150 K, whereas it is slightly decreasing for the latter one. Thanks to the general small temperature variations of T_m, all these systems have measurable coherence times at room temperature, and they are worth 0.83, 0.68, 0.14 and 0.12 μs for **0.1%-VOPc**, **5%-VOdmit**, **5%-VOTCPP** and **2%-VOTPP**, respectively.

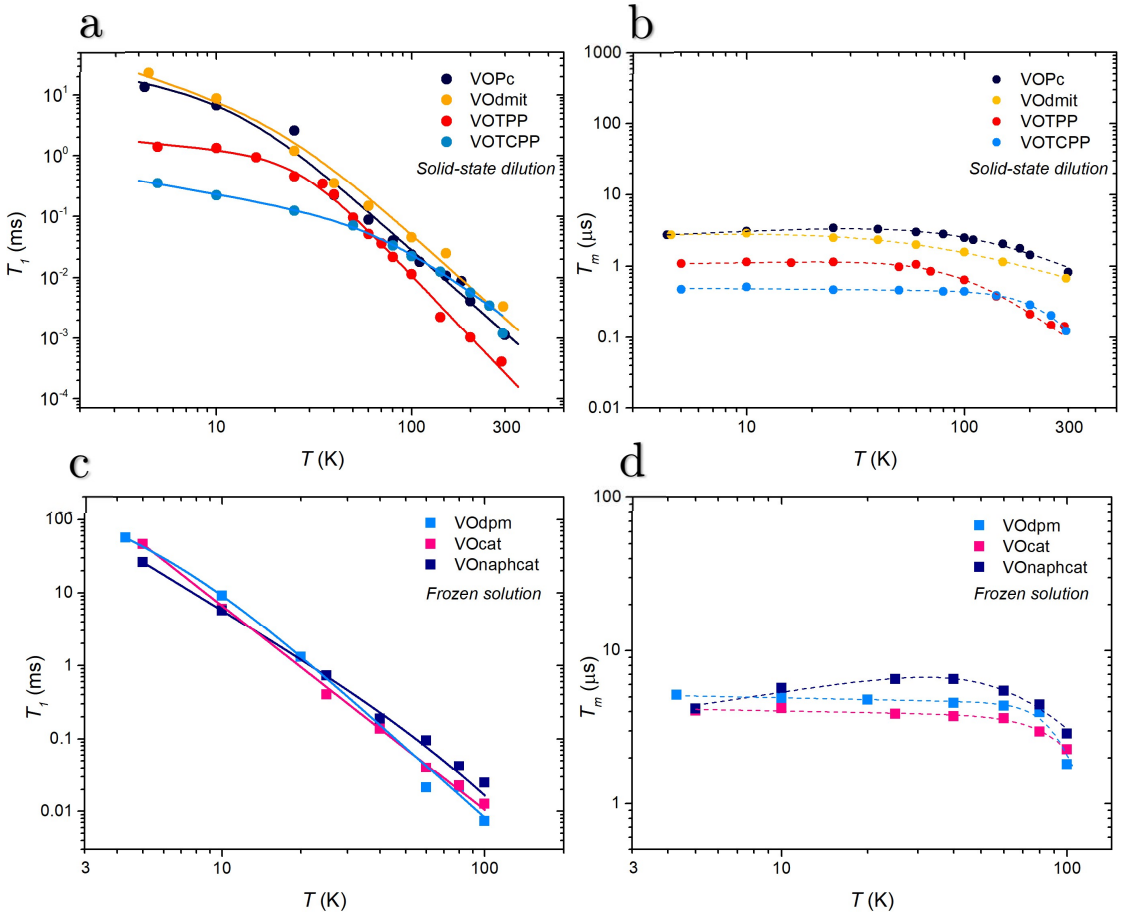

Figure 4.11. Temperature dependence of T_1 (a) and T_m (b) for solid state diluted compounds **0.1%-VOPc**, **5%-VOdmit**, **2%-VOTPP** and **5%-VOTCPP**; and of T_1 (c) and T_m (d) for frozen solution diluted compounds **(1mM)-VOdpm**, **(1mM)-VOcat** and **(1mM)-VOnaphcat**.

The outcomes for the vanadyl-based molecules diluted in frozen solutions, reported in Figure 4.11(c,d), indicate that T_1s are higher than those in solid state dilution, and they are very similar to each other. For **(1mM)-VOdpm** and **(1mM)-VOcat** T_1 is equal to 46 ms at 5 K, whereas it is 26 ms for **(1mM)-VOnaphcat**. The distinction between the two different temperature regions, clearly observed for the solid-state diluted compounds, is here less evident, and the thermal variation of T_1 appears to vary with a power-law of ca. $n = 3$, reaching 25, 13 and 7 μs at 100 K for **(1mM)-VOcat**, **(1mM)-VOnaphcat** and **(1mM)-VOdpm**, respectively. The melting of the frozen solutions has limited the investigated temperature range to 100 K.

The phase memory times of the vanadyl-based molecules diluted in frozen solution matrix are longer than those relative to the solid-state diluted derivatives: T_m is worth 5 μs for **(1mM)-VOdpm** and 4.1 μs for **(1mM)-VOnaphcat** and **(1mM)-VOcat**. Once more, T_ms of **(1mM)-VOcat** and **(1mM)-VOdpm** show a temperature-independent behaviour up to 60 K, after which they rapidly decrease. The thermal variation of **(1mM)-VOnaphcat**, instead, shows an increment up to 40 K, which probably is due to effects induced by the dynamics of counterion active nuclei, reaching 6.6 μs, and then it decreases like those of the other systems. At 100 K there is an inversion, for which the highest T_m of 2.88 μs belongs to **(1mM)-VOnaphcat**, followed by 2.2 and 1.8 μs of **(1mM)-VOcat** and **(1mM)-VOdpm**, respectively. Comparison between these values and those found for the solid state diluted systems are not adequate since the pronounced acceleration of the frozen solution T_ms is consequent to the softening of the solvent glassy matrix.

To prove that the observed coherence times are long enough to allow coherent spin manipulations at room temperature, nutation experiments were performed at different microwave powers (§2.1). Remarkably, Rabi oscillations were clearly observed with the expected linear dependence of the Rabi frequency (Ω_R, see §2.1) as a function of the microwave magnetic fields; as example, the Rabi oscillations and Rabi frequency for **5%-VOdmit** are reported in Figure 4.12.

More specific pulsed EPR studies were performed to fully characterize the local environment of the V^{IV} ions and to estimate the dipolar contribution of nuclear spins contained in the ligands. Q-band Mims Electron Nuclear Double Resonance (ENDOR) experiments, however, show very similar proton rich environment for **5%-VOdmit** and **6%-Vdmit**. This excludes the dipolar nuclear fields as the cause of the abruptly temperature decrease of T_1 for **6%-Vdmit** when increasing the temperature (Figure 4.10c). Furthermore, Hyperfine Sublevel Correlation (HYSCORE) experiments were also performed for **2%-VOTPP** and **5%-VOTCPP**, once more evidencing quasi-identical nuclear environment around the paramagnetic centres. For further details, see refs[27, 28].

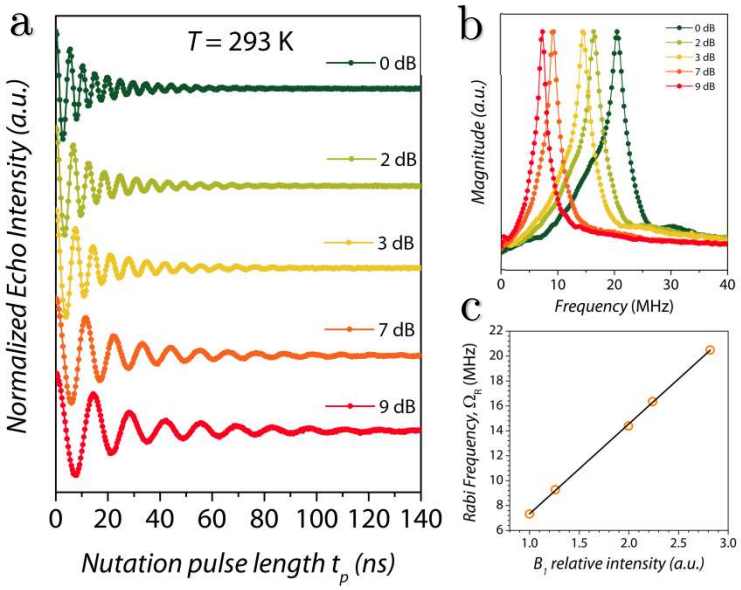

Figure 4.12. (a) Rabi oscillations recorded for **5%-VOdmit** at 293 K for different microwave attenuations (Q-band). (b) Fourier transform of the Rabi oscillations. (c) Linear dependence of the Rabi frequency (Ω_R) as a function of the relative intensity of the oscillating field B_1.

4.4 THz STUDIES

An accurate characterization of the low-energy vibrational modes active in these compounds is crucial for a better understanding of the correlation between structural features and spin dynamics. This has been done by using Time-Domain Terahertz (TD-THz) spectroscopy in collaboration with S. Benci of the group of Prof. R. Righini and Prof. R. Torre in LENS (Florence). It is underlined that this investigation is also part of the PhD thesis work of S. Benci. The measurements were performed on microcrystalline powder samples of the pure compounds embedded in a pellet of polyethylene. The home-built set-up that has been used allows to investigate the Far-IR frequency region between 0.3 and 4.0 THz, corresponding to 10-133 cm^{-1}, as well as to vary the temperature between 10 and 300 K.[29, 30] Vibrational spectra were recorded for **VOdmit**, **Vdmit**, **VOcat**, **Vcat**, **VOdtc**, **VOTPP**, **VOTCPP** and **VOPc** at several temperatures, and for **VOnaphcat** and **Vnaphcat** at room temperature; all the spectra are reported in Figure 4.13. It is worth to note that for **VOTCPP** only the spectrum at 300 K is reported since it does not show any signal in the entire investigated temperature range.

Focusing on the spectra of **VOdmit** (Figure 4.13a) the more intense vibrational modes are already visible at 300 K, but the spectrum becomes clearer decreasing the temperature because of the narrowing of the bands. Indeed, most broad and structured bands visible at room temperature separate in a set of narrower bands with slightly different energies at 10 K, though some of them are still resulting from the overlap of two or more modes. In addition, with decreasing the temperature the modes often shift

at higher frequencies. The rate at which this occurs can be in principle attributed to the specific composition of the vibrational modes. Indeed, it is reasonable to assume that, in the 10-100 cm^{-1} range, vibrational modes with a large contribution of external component (reticular and translational) will have a greater shift with respect to those modes having stronger internal character.

The THz spectra of the bidentate-based molecules are quite complex, since they exhibit many features. The first vibrational mode for **VOdmit**, at 30 cm^{-1}, is also the most intense. This is followed by several other modes of lower intensity between 46 and 91 cm^{-1}, and a more intense one at 105 cm^{-1}. Instead, for **Vdmit** the lowest vibrational mode is at 18 cm^{-1}, and the subsequent modes are closer to each other up to 64 cm^{-1}. After this group, only two broad bands are distinguishable, at 85 and 95 cm^{-1}. The spectra of **VOcat** exhibit a dense group of low-intense modes between 30 and 40 cm^{-1} followed by a group around 60 cm^{-1}. However, the most intense vibrational mode is at 74 cm^{-1}. Similarly, **Vcat** has a dense group of low-intense modes between 25 and 30 cm^{-1}, and the more intense modes are at 48 and 70 cm^{-1}. The room temperature spectra of **VOnaphcat** and **Vnaphcat** have the lowest vibrational modes at 20 cm^{-1}. Then, the former has an intense broad band between 25 and 60 cm^{-1}, whereas the latter shows other peaks at 32 and 45 cm^{-1} plus an intense broad band between 60 and 85 cm^{-1}. The spectrum of **VOdtc** is similar to that of **VOcat**, with a group of low-intense modes between 28 and 41 cm^{-1} and a group of more intense modes between 60 and 76 cm^{-1}.

If we restrict the analysis to the bidentate-based ligand molecules, we see that qualitatively the sulphur-based systems (**VOdmit**, **Vdmit** and **VOdtc**) have vibrational modes at lower energies with respect to the oxygen-based systems (**VOcat**, **Vcat**, **VOnaphcat** and **Vnaphcat**). Moreover, for a given ligand, the vanadyl-based molecules have vibrational modes at higher energies.

The THz spectra of the macrocycle-based molecules are simpler. Indeed, **VOTPP** has only one vibrational mode at 67 cm^{-1}, which does not reveal other features on decreasing the temperature, but shows a pronounced narrowing and shifting to higher frequencies, up to 67 cm^{-1} at 20 K. This behaviour is close to that observed for **VOPc**, which has one vibrational mode at 52 cm^{-1} that does not change significantly by decreasing the temperature. A further vibrational mode can be found at 75 cm^{-1}, but the very weak absorption of **VOPc** makes its THz spectrum very noisy. A particular case is represented by **VOTCPP** that does not present any vibrational mode for all the investigated temperatures, probably due to the strong stiffening produced by its three-dimensional covalent lattice. The first vibrational modes for this system are expected at frequencies higher than the available instrumental spectral range.

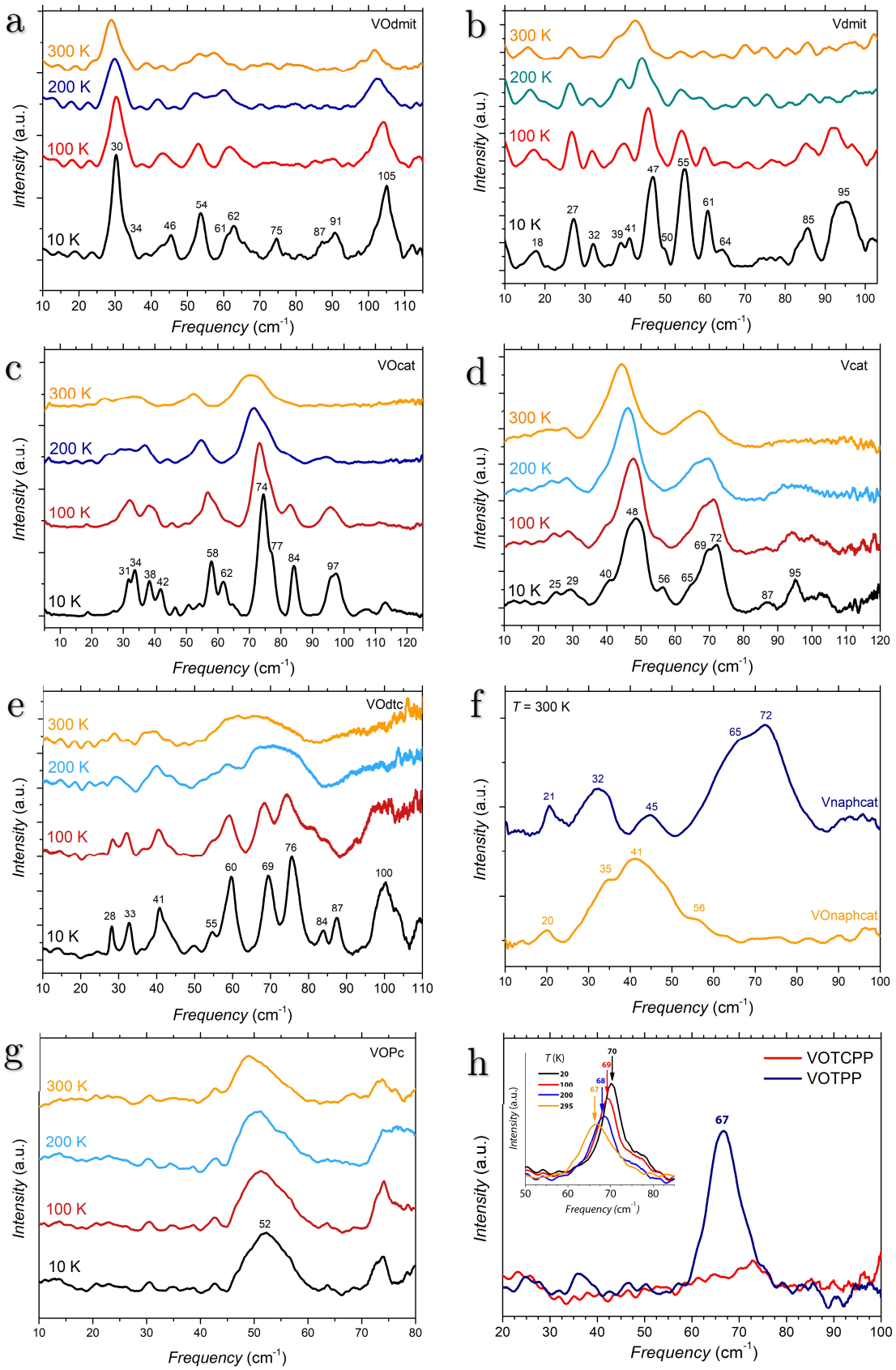

Figure 4.13. Low-energy Far-IR vibrational spectra at several temperatures recorded by TD-THz spectroscopy for **VOdmit** (a), **Vdmit** (b), **VOcat** (c), **Vcat** (d), **VOdtc** (e), **VOnaphcat** and **Vnaphcat** (f), **VOPc** (g), **VOTPP** and **VOTCPP** (h). The frequency values of the main vibrational modes are indicated for the lowest temperature spectrum.

Being all the investigated molecules centrosymmetric, for the rule of the mutual exclusion, only a subset of vibrational modes is IR-active, whereas the other must be Raman active. Thus, the recording of Raman spectra in the terahertz regime is also important to exclude relevant low-energy vibrational modes that might have remained undetected in the IR absorption spectra. A modification of the set-up to record Raman spectra in such a frequency range is in progress.

4.5 Analysis and discussion of the results

A few approximated models can be taken into account to reproduce the magnetization relaxation times obtained by ac susceptometry and the spin-lattice relaxation times obtained by pulsed EPR measurements. Such models are already described in Chapter 3. All the fits were performed by using the Matlab's script FMinuit[31] and the results of the analysis are reported and discussed in the following sections.

4.5.1 Temperature dependence of τ

The principal relaxation processes affecting the spin dynamics of these molecular systems are expected to be the direct process at low temperatures (§3.3.2), resulting in a linear thermal variation, and the Raman process at higher temperatures, which according to the theory should provide a power-law temperature dependence scaling as T^9 (§3.3.3). In addition, spin-phonon bottleneck effects, which are characterized by a power-law temperature dependence, x, between 1 and 2, can be very important when working with pure compounds and when the direct process is dominant (§3.3.8). In this frame, the simplest model that can be considered to fit the temperature dependence is

$$\tau = (a_{dir}T + a_{Ram}T^n)^{-1} \qquad (4.5)$$

where a_{dir} and a_{Ram} are the coefficients related to the direct and Raman processes, respectively. This model has been used to fit the data obtained by ac susceptometry for the molecules reported in Table 4.8, in which the corresponding best-fit parameters are also included.

Table 4.8. Best-fit parameters obtained using the model in eq. (4.5) to reproduce the temperature dependence of τ obtained by ac susceptibility data under a static magnetic field of 1 T.

Eq. (4.4)	a_{dir} **(ms^{-1} K^{-1})**	a_{Ram} **(ms^{-1} K^{-n})**	n
VOnaphcat	$7.8(4) \cdot 10^{-3}$	$1.6(3) \cdot 10^{-5}$	3.2(1)
VOcat	$3.9(5) \cdot 10^{-3}$	$5.1(7) \cdot 10^{-6}$	3.0(1)
Vnaphcat	$4.9(2) \cdot 10^{-2}$	$4.9(2) \cdot 10^{-5}$	3.7(1)
Vcat	$5.1(1) \cdot 10^{-2}$	$3.8(1) \cdot 10^{-4}$	3.0(1)
VOdtc	$2.18(8) \cdot 10^{-2}$	$4.6(3) \cdot 10^{-3}$	2.1(1)
VOdpm (0.2T)	$5.23(5) \cdot 10^{-2}$	$7.9(1) \cdot 10^{-5}$	3.1(1)

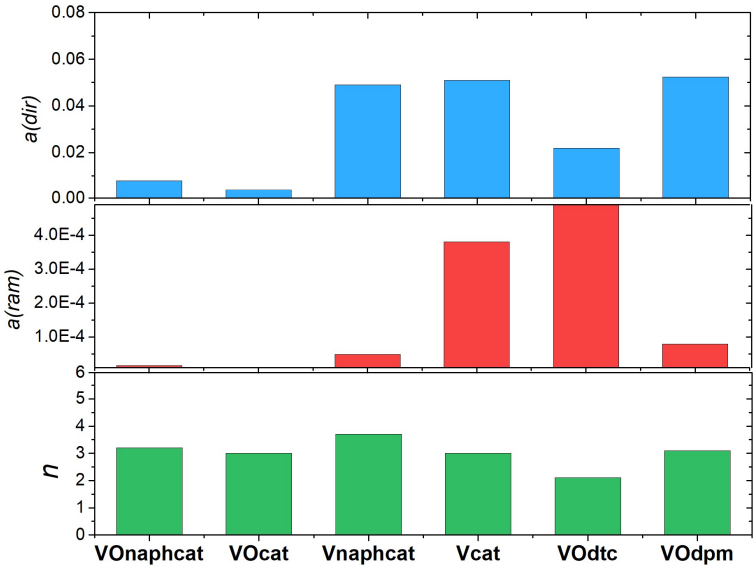

The relaxation coefficients of the tris-chelated molecules **Vnaphcat** and **Vcat** are higher than those of the vanadyl analogous (Table 4.8), in agreement with the longer τs of the latter (Figure 4.7 and Figure 4.9). This is a consequence of the different electronic orbital ground state, which is the well-isolated d_{xy} orbital for vanadyl molecules, and the mixed d_{z^2} for the tris-chelate molecules. Indeed, a stronger orbital contribution means a greater spin-orbit coupling that promotes the spin relaxation. Coefficients similar to those of **Vnaphcat** are shown by **VOdpm**, though it has a lower exponent of the Raman power-law ($n = 3.1$ vs $n = 3.7$). It should be noted that **VOdpm** was measured at 200 mT, instead of 1 T. Moreover, care should be taken when comparing the relaxation coefficients of **VOcat** and **VOnaphcat** with those of the other systems, since their low temperature τs are not available. Indeed, they were measured only between 10 and 70 K, which is a temperature region higher than that investigated for the other molecules.

Interestingly, the temperature dependence of the Raman process for all the investigated molecules is described by power-laws with exponents between $n = 2.1$ and $n = 3.7$, values strongly differing from the expected $n = 9$ (eq. 3.33).[32]

However, not all the temperature dependences of the investigated molecules can be reproduced by using eq. (4.5), either because of spin-phonon bottleneck effects or because of unexpected weaker temperature dependences of τ. The latter case appears to be characteristic of molecules coordinated by macrocyclic ligands such as **VOPc**, **VOTPP** and **VOTCPP**. Their temperature dependences have been reproduced by considering a model in which the relaxation time is the sum of two different relaxation times, according to eq. (4.6):

$$\tau = 1/(a_{dir}T^{x}) + 1/(a_{pb}T^{y}) \qquad (4.6)$$

where a_{dir} is again the coefficient related to the direct process, but now a power-law lower than $x = 1$ can occur; instead, a_{pb} is related to the direct process when it is affected by spin-phonon bottleneck effects. The best-fit parameters are reported in Table 4.9. It should be noted that the description of the relaxation time either by considering the sum of two different relaxation times (eq. 4.6) or the sum of the relaxation rates (eq. 4.5) is analogous to consider an electric circuit composed by resistances either in parallel or in series.[33]

Table 4.9. Best-fit parameters obtained using the model in eq. (4.6) to reproduce the temperature dependence of τ obtained by ac susceptometry measurements.

Eq. (4.5)	a_{dir} (ms^{-1} K^{-x})	x	a_{pb} (ms^{-1} K^{-y})	y
VOdmit	0.44(1)	1.0(1)	0.14(1)	2.1(1)
Vdmit	4.9(5)	1.0(1)	1.14(3)	2.4(3)
VOPc	32(30)	0.0(4)	0.85(7)	1.2(1)
VOTPP	12(2)	0.0(3)	$5.3(8) \cdot 10^{-2}$	2.4(1)
VOTCPP	1.0(1)	0.4(1)	$2.0(1) \cdot 10^{-2}$	2.8(1)

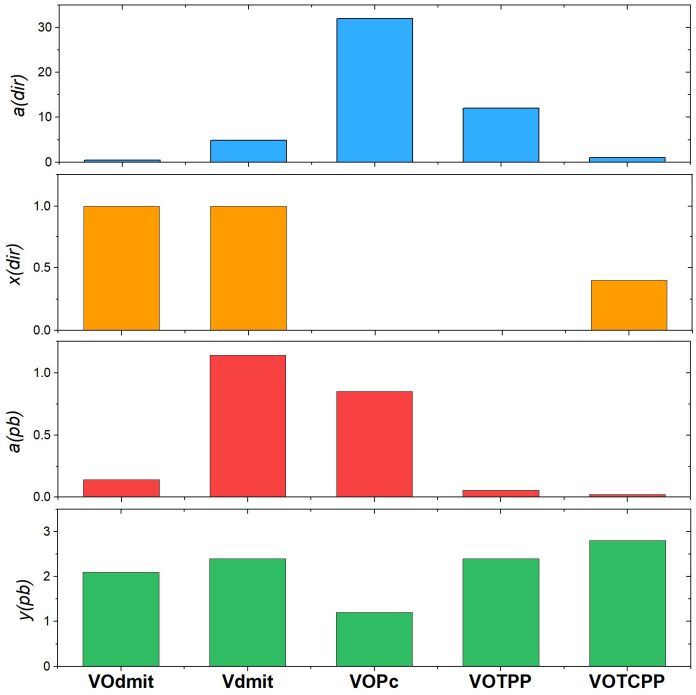

From Table 4.9 it is possible to note again the higher coefficients of the tris-chelate molecules, in this case **Vdmit**, with respect to the vanadyl analogous, here **VOdmit** (Figure 4.7 and Figure 4.9). Weak phonon bottleneck effects are present at low temperature but, as the sample is heated, the characteristic linear dependence of the

direct process comes out. Instead, the relaxation times of **VOPc**, **VOTPP** and **VOTCPP** exhibit an initial decrease attributed to the phonon bottleneck, $y \sim 2$, and a quasi-temperature independent region, which is accounted by $x \ll 1$. This behaviour, according to what described in (§3.3.2), may occur when $kT \ll \hbar\omega$. Such a dependence is consistent with the very low number of vibrational modes present in their low-energy vibrational spectrum (Figure 4.13). However, the observed weak temperature dependence remarkably extends up to 30 K, which is certainly unexpected. At 30 K, indeed, the acoustic modes out the Γ-point should be enough populated to produce spin-lattice relaxation through direct process. It is then reasonable to ask: is this weak temperature dependence a consequence of spin-phonon bottleneck effects? Or can it derive from cross-relaxation processes? Or, further, are the acoustic modes insufficient to produce relaxation without the "help" of the low-energy optical modes? These questions are still open.

Notwithstanding their simplicity, these two models succeed to point out specific features from the general behaviour of the temperature dependence of τ, such as the presence of two different processes and the efficiency whereby they influence the spin dynamics. A more rigorous model for the Raman process was described in (§3.3.3) and is the Debye Transport Integral. However, this model can be applied to reproduce the experimental data only when they are investigated in a wide temperature range, such as that provided by pulsed EPR. A further way to account for the Raman process that can be applied also to reduced temperature ranges, such as those provided by ac susceptometry, is the local mode model (§3.3.5). This has been employed to reproduce the relaxation times of **VOcat** and **VOnaphcat**. The model used is expressed as

$$T_1 = \left(a_{dir} T^x + a_{loc} \frac{\exp\left(\frac{\hbar\omega_1}{kT}\right)}{\left(\exp\left(\frac{\hbar\omega_1}{kT}\right) - 1\right)^2} + b_{loc} \frac{\exp\left(\frac{\hbar\omega_2}{kT}\right)}{\left(\exp\left(\frac{\hbar\omega_2}{kT}\right) - 1\right)^2} \right)^{-1} \qquad (4.7)$$

where, in addition to the direct process already described, a_{loc} and b_{loc} are the coefficients for the two local mode processes and $\hbar\omega_1$ and $\hbar\omega_2$ are their respective low-energy phonons involved in the spin-lattice relaxation. The results are reported in Table 4.10.

Table 4.10. Best-fit parameters obtained using the model in eq. (4.7) to reproduce the temperature dependence of τ for **VOcat** and **VOnaphcat** obtained by ac susceptometry measurements.

Eq. (4.6)	a_{dir} (ms^{-1} K^{-x})	x	a_{loc} (ms^{-1})	$\hbar\omega_1$ (cm^{-1})	b_{loc} (ms^{-1})	$\hbar\omega_2$ (cm^{-1})
VOcat	$9.0(5) \cdot 10^{-3}$	1.0(1)	10(1)	47(2)	734(270)	200(15)
VOnaphcat	$9.0(6) \cdot 10^{-3}$	1.0(1)	4(1)	40(4)	240(80)	160(13)

As shown in Figure 4.7a, the best-fits obtained using eq. (4.7) are identical to those obtained by the previous models and, accordingly, the parameters obtained for the direct process are similar (Table 4.10). Concerning the Raman process, both the investigated molecules require the use of two local modes: the first between 40-50 cm^{-1} and the second between 160-200 cm^{-1}. The first vibrational mode of **VOnaphcat**, at 40 cm^{-1}, coincides with the maximum of the broad band visible in its THz spectrum (Figure 4.13). Instead, the parameter obtained for **VOcat** may correspond to the low-intensity vibrational mode at 47 cm^{-1}, probably because of a more intense spin-phonon coupling. However, it may also be produced by an average between the vibrational modes grouped at 30-40 cm^{-1} and those grouped at 60 cm^{-1}. The second vibrational modes extracted by the fit are beyond the instrument spectral range. Unfortunately, these parameters have a considerable uncertainty, probably due to the limited temperature range investigated, for which it is impossible to make any correlation. Finally, it should be noted that the frequency value of the two local modes are in both cases higher for **VOcat** than for **VOnaphcat**, thus suggesting a higher rigidity of the structure for the former molecule.

4.5.2 Temperature dependence of T_1

The spin-lattice relaxation times measured by pulsed EPR have been fitted, as done in the previous section, by considering the direct and Raman processes. The latter has been reproduced by using three different models: the simple power-law, the local mode (§3.3.5) and the Debye Transport Integral model (§3.3.3). The Debye transport integral is the more rigorous model and it is particularly accurate when the Raman process is produced by the sum of many vibrational modes that can be described by the Debye approximation (§3.3.1). However, if only one or few phonons are responsible for the Raman-type relaxation, the transport integral collapses in single terms as expressed in eq. (4.7), corresponding to the local modes model. Important hints may, however, be provided also by applying the simple power-law model. The use of these three models to reproduce the temperature dependence of T_1 has been restricted to the compounds diluted in solid state matrix. In doing so, the analysis is not limited by the temperature at which the frozen solution melts and, more important, the information extracted can be related with the low-energy vibrational spectrum. The fits were performed on **0.1%-VOPc**, **5%-VOdmit**, **2%-VOTPP**, **5%-VOTCPP** and **6%-Vdmit**. It should also be remarked that the investigated samples are highly diluted, for which no phonon bottleneck effects are expected. The simple power-law model used is expressed as

$$T_1 = (a_{dir}T^x + a_{ram}T^n)^{-1} \tag{4.8}$$

which is identical to eq. (4.5) except for the exponent of the direct process. The last has been introduced to reproduce also the weak temperature dependence observed for the macrocyclic-based vanadyl molecules. The best-fit parameters are reported in Table 4.11, while the fits are visible in Figure 4.11.

Table 4.11. Best-fit parameters obtained using the simple power-law model in eq. (4.8) for T_1, derived by pulsed EPR results.

Eq. (4.9)	a_{dir} (ms^{-1} K^{-x})	x	a_{Ram} (ms^{-1} K^{-n})	n
5%-VOdmit	$1.2(4) \cdot 10^{-2}$	1.0(1)	$1.9(5) \cdot 10^{-5}$	3.0(1)
6%-Vdmit	$1.9(5) \cdot 10^{-2}$	1.0(1)	$6(4) \cdot 10^{-5}$	3.5(1)
0.1%-VOPc	$2.5(9) \cdot 10^{-2}$	0.6(4)	$7(6) \cdot 10^{-4}$	2.8(1)
2%-VOTPP	0.4(1)	0.3(3)	$1.5(8) \cdot 10^{-5}$	3.4(1)
5%-VOTCPP	1.2(1)	0.54(6)	$3(2) \cdot 10^{-4}$	2.5(1)

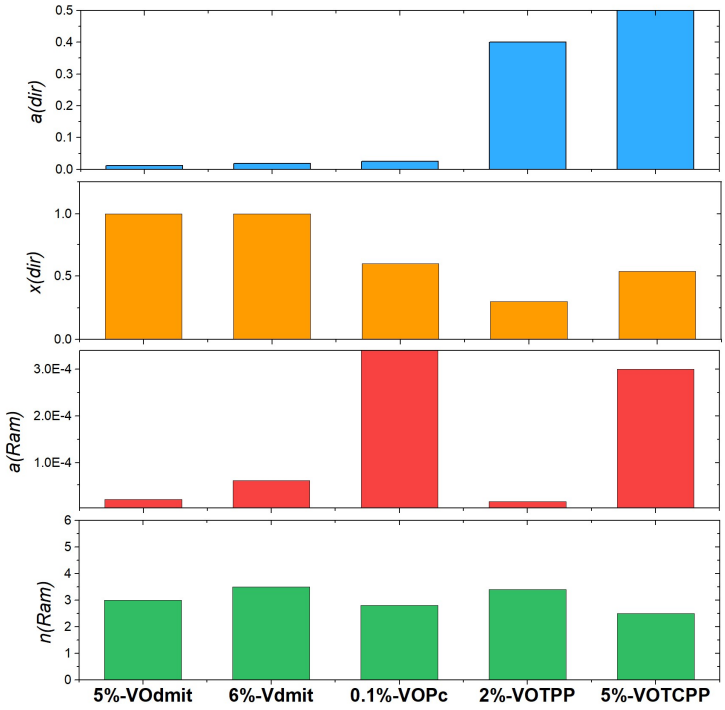

This model evidences the presence of a direct process with linear temperature dependence for T_1s of **5%-VOdmit** and **6%-Vdmit**, and a quasi-independent variation ($x < 1$) for those relative to **0.1%-VOPc**, **2%-VOTPP** and **5%-VOTCPP**. On increasing the temperature, for every system the Raman process causes a more pronounced thermal variation of T_1, with a temperature dependence of ca. T^3. The relaxation time of **5%-VOTCPP** has the lowest value of n, that is 2.5, whereas those of **6%-Vdmit** and **2%-VOTPP** have almost the same value, $n = 3.5$. However, it is

important to note that they are graphically very different (Figure 4.11a), and this is due to their Raman coefficients that are four times lower for **2%-VOTPP** with respect to **6%-Vdmit**. This corresponds to the onset of the Raman process at higher temperature.

The fit by the Debye Transport Integral model has been done using the expression

$$T_1 = \left(a_{dir} T^x + a_{ram} \left(\frac{T}{\theta_D} \right)^9 I_8 \left(\frac{\theta_D}{T} \right) \right)^{-1} \tag{4.9}$$

where θ_D is the Debye temperature and I_8 is the Transport Integral, which is defined in eq. (3.30). The best-fit parameters are reported in Table 4.12, while the fits are shown in Figure 4.14.

Table 4.12. Best-fit parameters obtained using the Debye Transport Integral model in eq. (4.9) for T_1, derived by pulsed EPR.

Eq. (4.10)	a_{dir} (ms^{-1} K^{-x})	x	a_{Ram} (ms^{-1})	θ_D (K)
5%-VOdmit	$1.0(2) \cdot 10^{-2}$	1.0(1)	179(21)	105(2)
6%-Vdmit	$2.6(5) \cdot 10^{-2}$	1.0(1)	$1.4(5) \cdot 10^{4}$	186(21)
0.1%-VOPc	$3(3) \cdot 10^{-2}$	0.6(4)	$1.4(2) \cdot 10^{3}$	185(9)
2%-VOTPP	0.4(1)	0.4(3)	$1.1(1) \cdot 10^{4}$	280(10)
5%-VOTCPP	1.0(1)	0.64(4)	$2.7(8) \cdot 10^{3}$	304(37)

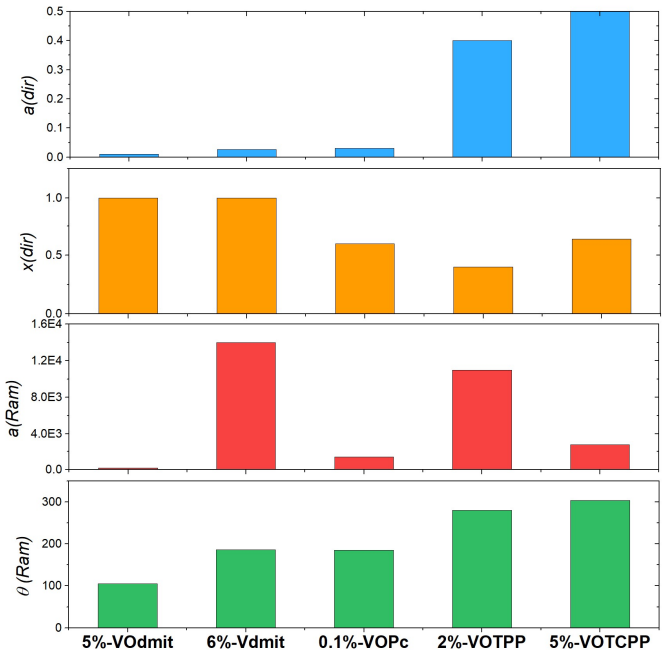

The direct coefficients and exponents agree with the previous findings, whereas the Raman process can be analysed from another point of view. Indeed, the Debye temperature θ_D indicates the cut-off temperature over which the Debye approximation

fails: higher is this value and higher is the temperature at which optical phonons will affect the relaxation. However, high values of θ_D appears in conflict with what pointed out by the THz measurements and by the analysis of the local modes discussed for τ, from which emerged that the optical phonons cannot be neglected already at the liquid hydrogen temperatures. Despite the major rigorousness of the Debye model, it is evident that it still contains too many approximations to fully describe the Raman relaxation process. On the other hand, the Debye temperature remains an average parameter that accounts for the importance of the optical phonons involved in the magnetic relaxation. For example, the Raman coefficient for **5%-VOdmit** is the lowest (Table 4.11), however, as pointed out by its θ_D, the optical phonons play a key role already at low temperature. **6%-Vdmit** and **0.1%-VOPc** have values of θ_D slightly higher than that of **5%-VOdmit**, but with Raman coefficients two and one orders of magnitude higher, respectively. Consequently, the relaxation time of **6%-Vdmit** is the first that abruptly decreases (Figure 4.14). Higher values of θ_D are shown by **2%-VOTPP** and **5%-VOTCPP**, but again with Raman coefficients one order of magnitude different to each other. Consequently, T_1 for **2%-VOTPP** is more similar to that of **6%-Vdmit**, whereas T_1 for **5%-VOTCPP** is comparable to that of **0.1%-VOPc**. Thus, the combination of high values of a_{Ram} and small values of θ_D corresponds to a strong temperature variation of T_1, as shown by **6%-Vdmit**, whereas the opposite leads to the very weak temperature dependence of **5%-VOTCPP**.

As evidenced by the results shown above and considering the approximations of the Debye model, the use of eq. (4.9) is equally informative with respect to the simple power-law model, and it allows to see the problem from another point of view. Moreover, since it well reproduces the experimental data, it confirms that the process involved in the spin relaxation is the Raman process as theoretically described (§3.3.3).

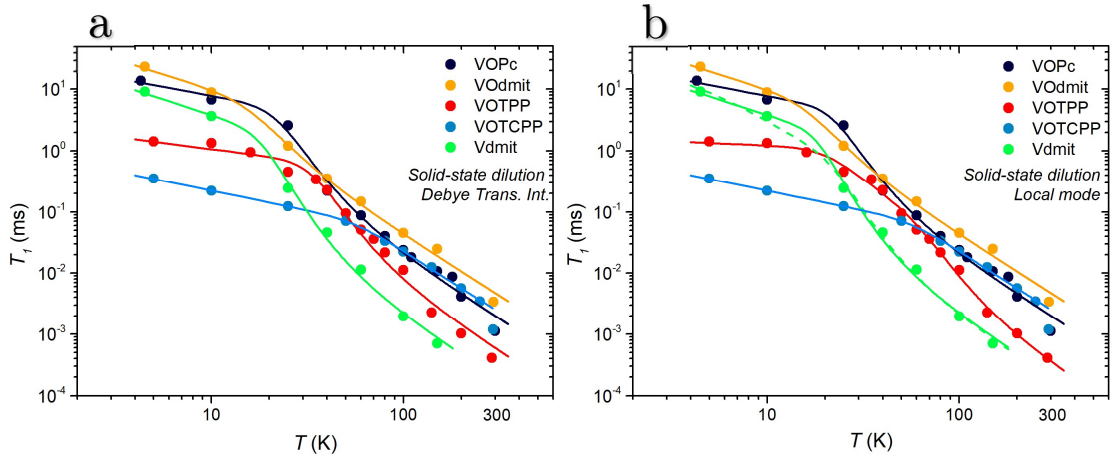

Figure 4.14. Temperature dependence of T_1 for solid state diluted compounds **0.1%-VOPc**, **5%-VOdmit**, **6%-Vdmit**, **2%-VOTPP** and **5%-VOTCPP** reproduced by the Debye Transport Integral model (a) and the local modes model (b).

The third model used is the local modes. The use of this model is reasonable by recalling the presence of low-energy vibrational modes in the experimental THz spectra. The expression used to perform the fits is the same reported in eq. (4.7); the best-fit parameters are reported in Table 4.13, while the fits are shown in Figure 4.14.

Table 4.13. Best-fit parameters obtained using the local modes model in eq. (4.7) for T_1, derived by pulsed EPR.

Eq. (4.6)	a_{dir} (ms^{-1} K^{-x})	x	a_{loc} (ms^{-1})	$\hbar\omega$ (cm^{-1})
5%-VOdmit	$1.0(2) \cdot 10^{-2}$	1.0(1)	19(2)	63(3)
6%-Vdmit	$2.6(6) \cdot 10^{-2}$	1.0(1)	$1.3(2) \cdot 10^{3}$	108(4)
6%-Vdmit (two phonons)	$2.1(8) \cdot 10^{-2}$	1.0(1)	1(1) $2(1) \cdot 10^{3}$	18(fixed) 123(37)
0.1%-VOPc	$3(3) \cdot 10^{-2}$	0.6(4)	$1.4(5) \cdot 10^{2}$	110(15)
2%-VOTPP (two phonons)	0.4(2)	0.3(2)	34(7) $6(2) \cdot 10^{3}$	67(fixed) 303(35)
5%-VOTCPP	1.01(1)	0.65(1)	$2.95(9) \cdot 10^{2}$	184(2)

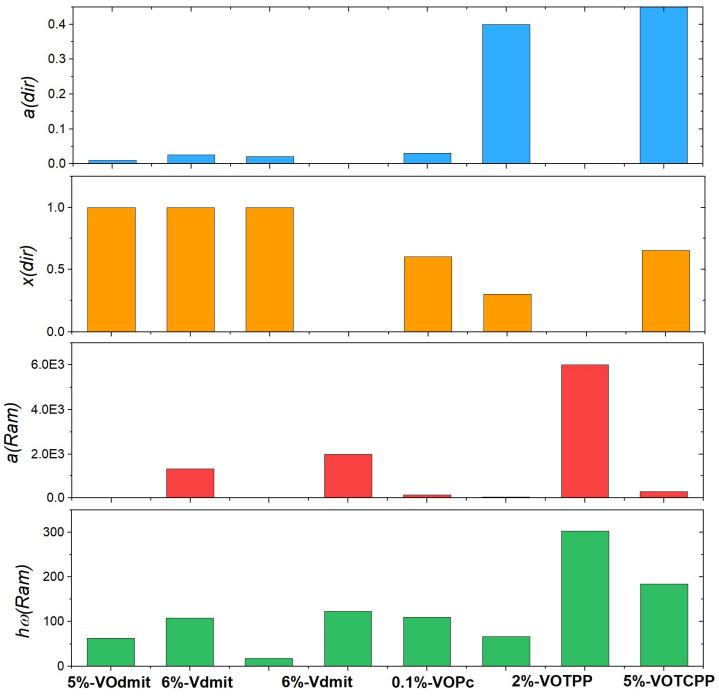

Once more, the parameters of the direct process agree with the previous findings (Table 4.11 and Table 4.12). The trend of the local modes coefficients also reflects the Raman coefficients extracted from the previous models; the peculiarity here is that it is possible to obtain hints on the phonons that are more relevant for the spin relaxation.

Unfortunately, the limited number of points of T_1 collected for the investigated molecules does not allow to obtain precise results about the active vibrational modes. For example, the relaxation time of **6%-Vdmit** is equally well reproduced using either one or two low-energy local modes. In the former case, a single mode at 108 cm^{-1} appears to be the only phonon responsible of the spin relaxation, which is certainly a rough approximation of the real situation. Indeed, according to the THz spectrum of **6%-Vdmit** (Figure 4.13), it is reasonable to think that this value is averaged on many vibrational modes affecting the relaxation. This because, as the temperature increases, phonons at higher energies populate and contribute to the spin-lattice relaxation.

In this frame, the temperature dependence of T_1 for **5%-VOdmit** can be satisfactorily reproduced by an average effective phonon, *i.e.* a parameter that is resulting from the mixing of many different low-energy modes, at 63 cm^{-1}. This corresponds to an extracted value slightly lower with respect to all the other investigated molecules, in agreement with the θ_D values shown in Table 4.12. The macrocyclic molecules are more interesting because of their very simple THz spectrum: the temperature dependence of T_1 for **2%-VOTPP** is well reproduced using the phonon mode at 67 cm^{-1} and a more energetic one that is probably averaged. The relaxation time of **VOPc**, instead, is well reproduced by considering only one vibrational mode at 110 cm^{-1}, which is beyond the available experimental THz range. Interestingly, the inclusion of the experimental vibrational mode at 52 cm^{-1} does not provide any significant improvement to the fit, suggesting that this vibrational mode could be considered not strongly involved in the relaxation. Similarly, the spin-lattice relaxation for **5%-VOTCPP** can be reproduced by considering only one very energetic phonon at 184 cm^{-1}, again beyond the available experimental THz range.

Despite the approximative model here used, the role of the vibrational modes in determining the spin relaxation strongly emerges. This has been done by considering two features: the energy of the vibrational modes and the Raman coefficient. The latter can be associated to the degrees of coupling of the specific mode with the spin, *i.e.* the spin-phonon coupling, which accounts for the efficiency of the phonon to cause relaxation. A more accurate model should consist in the inclusion of the vibrational Density of States (DOS) weighted for the spin-phonon coupling coefficients. This approach, however, can be performed only by theoretical calculations, and it is in progress.

It should be noted that, though the spin-phonon coupling is temperature independent, the efficiency of a specific phonon depends on its population according to the Bose-Einstein distribution. The relaxation of **5%-VOdmit** is determined by very low energetic modes but with a small efficiency, whereas higher energetic phonons are important for the relaxation of **6%-Vdmit**, but with stronger spin-phonon coupling. For **5%-**

VOTCPP the small efficiency is due to the lack of low energy modes, and this produces the very weak temperature dependence of T_1. The latter considerations can be used also to describe the relaxation of **0.1%-VOPc** that has a low-energy vibrational mode at 52 cm^{-1} apparently not effective for the spin relaxation.

4.5.3 Magnetic field dependence of τ

The magnetic field dependence of the relaxation time extracted by ac susceptibility measurements for the investigated molecules can be reproduced by the Brons-van Vleck model (§3.3.7 and eq. 3.48). It is recalled that this model takes into account the competition between the sum of intra- and intermolecular effects, *i.e.* the sum of spin-spin dipolar magnetic interactions and spin-nuclei hyperfine interactions, that are predominant at low fields (ca. $B < 1$ T), and the direct process at high fields (ca. $B > 1$ T). The expression used for the analysis is

$$\tau = \left(cB^4 + d\frac{1+eB^2}{1+fB^2} \right)^{-1} \tag{4.10}$$

where it is recalled that c is the coefficient of the direct process, d is the coefficient related to the strength of the internal active processes, f corresponds to the ability of the external magnetic field to suppress the internal relaxation mechanisms, and e is the attitude of the internal magnetic moments of the molecule to induce relaxation.

However, in some cases this model is not sufficient to reproduce the data and an extended version of the Brons-van Vleck model has been adopted in the analysis

$$\tau = \left(cB^4 + d\frac{1+eB^2}{1+fB^2} + g\frac{1+eB^2}{1+hB^2} \right)^{-1}. \tag{4.11}$$

in which two distinguishable contributions of the internal fields are considered.

The best-fit parameters obtained by applying the Brons-van Vleck models for the relaxation times measured at 5, 10 and 15 K are reported in Table 4.14, Table 4.15 and Table 4.16, respectively. The outcomes of the fits can be found in in Figure 4.7c, Figure 4.8 and Figure 4.9.

Table 4.14. Best-fit parameters obtained using either the model (4.10) or (4.11) to reproduce the magnetic field dependence of τ at 5 K. Asterisks indicate whether that specific curve is shown or not in Figure 4.7c or Figure 4.8 or Figure 4.9.

$T = 5$ K	c (T^{-4} ms^{-1})	d (ms^{-1})	e (T^{-2})	f (T^{-2})	g (ms^{-1})	h (T^{-2})
VOdpm-pwd	$9.6(4) \cdot 10^{-4}$	2.1(2)	7.6(7)	240(30)	-	-
VOdtc*	$6.7(2) \cdot 10^{-4}$	1.5(1)	0.2(5)	110(13)	0.3(1)	0.4(1)
VOTCPP	$6.5(5) \cdot 10^{-4}$	10(2)	21(2)	221(74)	-	-
VOPc*	$3.0(1) \cdot 10^{-3}$	23(3)	0.4(1)	31(11)	5.5(9)	1.0(4)
10%VOPc*	$3.0(2) \cdot 10^{-3}$	37(11)	6.0(1)	74(30)	-	-
VOTPP*	$1.8(1) \cdot 10^{-3}$	47(40)	6.1(6)	$987(10^3)$	9(4)	36(13)
30%VOTPP*	$1.5(1) \cdot 10^{-3}$	14(4)	11(1)	780(600)	3(1)	53(27)
VOdmit	$1.8(1) \cdot 10^{-3}$	10(1)	40(4)	306(60)	-	-
Vdmit*	$8.0(6) \cdot 10^{-3}$	41(1)	5.0(6)	13(2)	-	-
Vcat*	$3.5(1) \cdot 10^{-3}$	1.9(2)	0.13(2)	219(24)	0.24(8)	0.061(3)
Vnaphcat*	$9.4(1) \cdot 10^{-3}$	2.3(2)	0.8(3)	322(45)	0.14(1)	0.3(1)

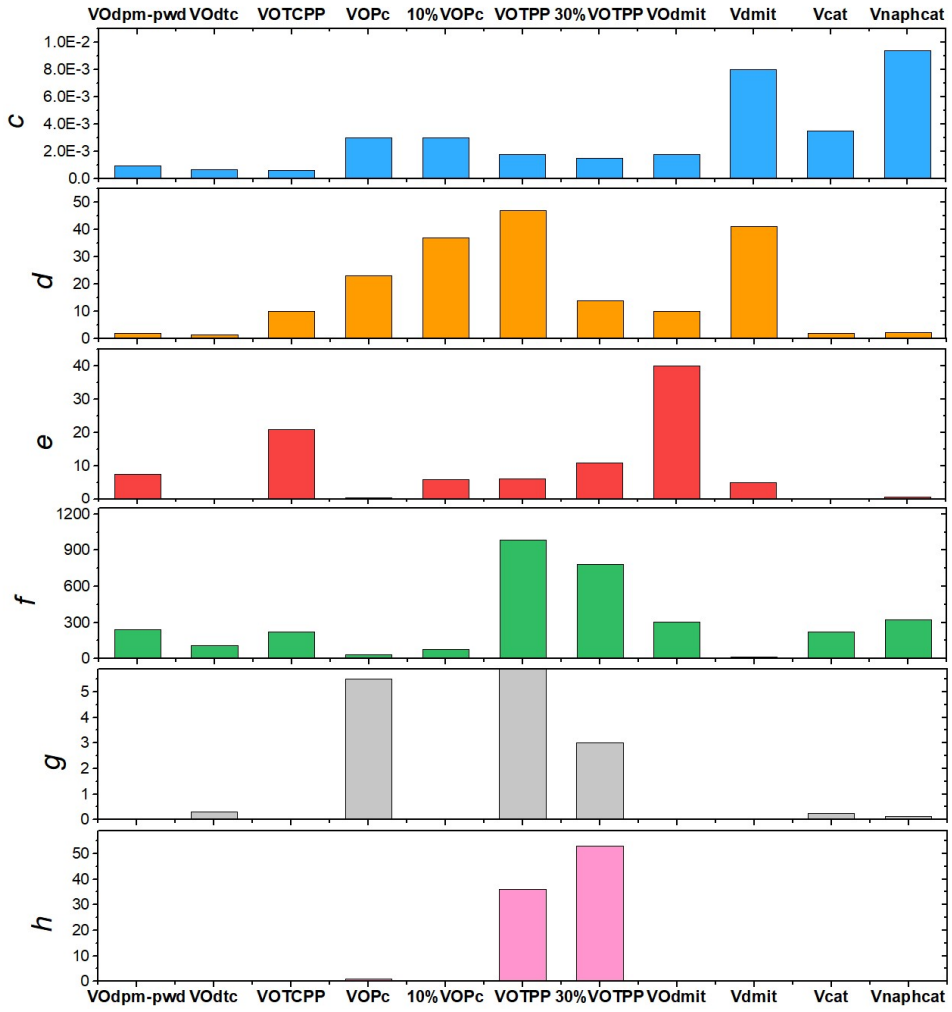

Before commenting the results contained in Table 4.14, it should be noted that the fits performed for **VOTCPP**, **VOPc** and **VOTPP** are non-trivial because of the irregular behaviour presents around 2 T, whose causes are still unclear. Consequently, the parameters obtained for these molecules, and in particular the parameter f, have a noticeable uncertainty. A few points are worth being underlined:

- The coefficients of the direct process, c, are lower for the vanadyl-based molecules, and in particular for **VOdpm**, **VOdtc** and **VOTCPP**. This parameter determines the onset of the abrupt decrease of the relaxation times at high magnetic fields. This result is consistent with the coefficients of the direct process reported, for example, in Table 4.10. Instead, the higher values of c are relative to the relaxation time of the tris-chelate molecules.
- The parameter d is related to the efficiency of the relaxation. It can be evaluated by the slope of the curve at very low fields, as well as by the absolute value of τ. For example, the highest value of d for **VOTPP** reflects the combination between the small values of its relaxation time and the pronounced magnetic field dependence at low magnetic fields. **VOPc** has also a high value of d because of the short τ, but thanks to the weaker magnetic field dependence at low fields, this value is reduced.
- The parameter e is inversely proportional to the density of spins and the strength of the internal fields, *i.e.* dipolar and hyperfine interactions. This is clearly observed by comparing the values of e for **VOPc** and **VOTPP** and those relative to **10%-VOPc** and **30%-VOTPP**. By looking at the spin density values in Table 4.5, it can be noted that **VOdmit** has a density higher than that of **VOTCPP**. These values, at first sight, do not agree with their e parameters. However, this can be explained by considering that the ligands of **VOdmit** are completely nuclear spin free, for which its hyperfine fields are greatly reduced.
- The parameter f is related to the efficiency of the external magnetic field in suppressing the internal fields. When this parameter is small, the maximum of τ is reached for higher applied magnetic fields, with the consequent reduction of the intermediate plateau of τ. This is visible either by comparing the curves of **VOPc** and **10%-VOPc**, or by looking at the behaviour of **VOdtc**, whose limited plateau agrees with its small value of f.
- An additional contribution to the internal fields is required to reproduce the data of **VOdtc**, **VOPc**, **VOTPP**, **Vcat** and **Vnaphcat**. This term contains the parameters g and h that, in analogy to d and f, are related to the efficiency of the relaxation and the efficiency of the magnetic field to suppress the internal contributions. Instead, the parameter e is common for the two internal fields terms. The necessity of a second term into the Brons-van Vleck model can be explained by considering that each term

can be produced by mechanisms affecting the spin relaxation that derive from different sources. If two different mechanisms are strong enough, their individual contributions can appear, and they can be distinguished by the fit.

Table 4.15. Best-fit parameters obtained using either the model (4.10) or (4.11) to reproduce the magnetic field dependence of τ at 10 K. Asterisks indicate whether that specific curve is shown or not in Figure 4.7c or Figure 4.8 or Figure 4.9.

$T = 10$ K	c (T^{-4} ms^{-1})	d (ms^{-1})	e (T^{-2})	f (T^{-2})	g (ms^{-1})	h (T^{-2})
VOdpm*-pwd	$7.3(1) \cdot 10^{-4}$	3.5(1)	7.6(4)	179(12)	-	-
VOdpm-crys	$5.4(1) \cdot 10^{-4}$	0.15(1)	106(8)	300(31)	-	-
VOdtc*	$4.2(1) \cdot 10^{-4}$	7.5(4)	0.2(2)	93(10)	1.19(5)	0.9(1)
VOTCPP*	$9.5(6) \cdot 10^{-4}$	27(8)	27(3)	316(120)	-	-
VOPc*	$1.8(1) \cdot 10^{-3}$	80(22)	0.5(1)	61(30)	11.7(2)	0.9(4)
VOTPP*	$1.5(2) \cdot 10^{-3}$	62(37)	50(11)	430(340)	-	-
VOdmit*	$2.1(1) \cdot 10^{-3}$	19(3)	38(5)	231(60)	-	-
Vcat	$3.5(1) \cdot 10^{-3}$	4.1(1)	0.13(2)	247(15)	0.89(3)	0.063(3)
Vnaphcat	$1.2(1) \cdot 10^{-2}$	4.2(3)	0.3(1)	353(34)	0.61(1)	0.09(2)

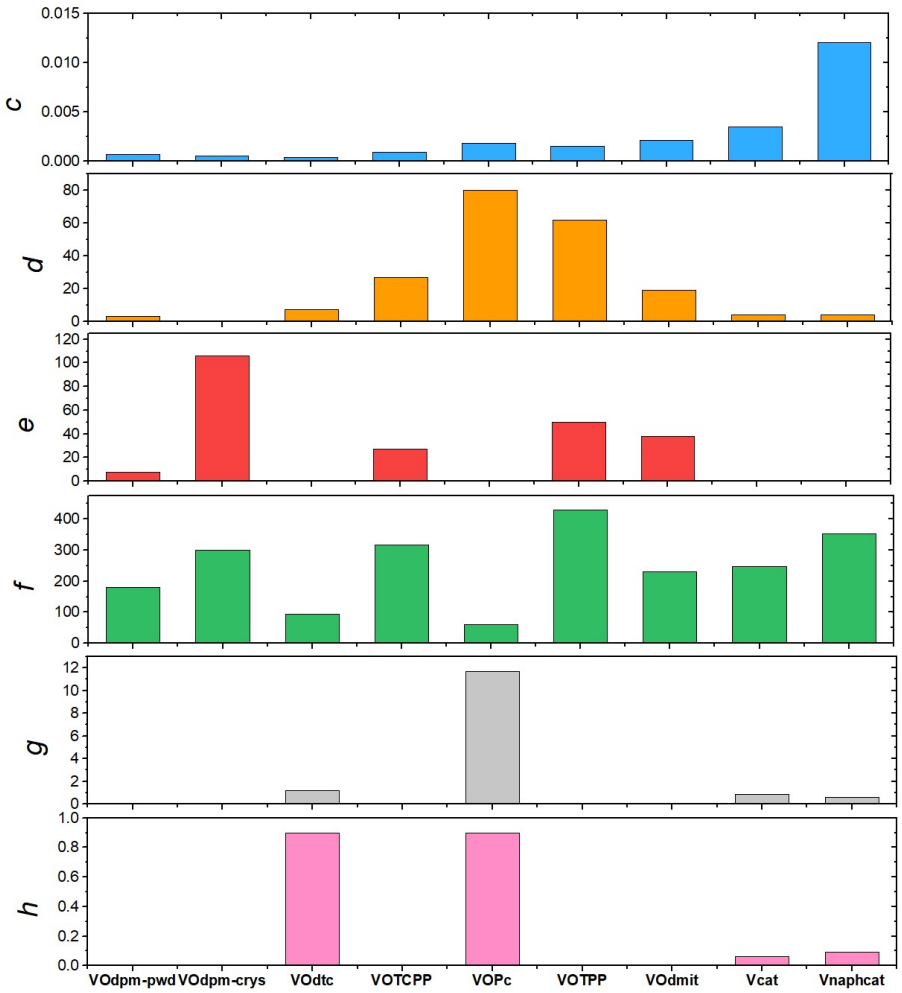

The same care pointed out before in discussing the parameters obtained for **VOTCPP**, **VOPc** and **VOTPP** is required also when looking at Table 4.15.

The coefficients e relative to data at 10 K (Table 4.15) are close to those observed at 5 K (Table 4.14). This result underlines the robustness of the model since a variation either of the internal fields strength or the spin density increasing the temperatures is not expected. The only exception is represented by **VOTPP**, whose parameter exhibits an increase of a factor ten; however, this may be accounted to the uncertainty above mentioned. The coefficients c of the direct process slightly decrease on increasing the temperature. This agrees with the rising of the strength of the Raman process and the simultaneous weakening of the direct process, on increasing the temperature from 5 to 10 K. Accordingly, as the Raman process becomes more important, the parameters d and f also growth. The same argument is valid for the parameters g and h.

It is also interesting to compare the results obtained by the two compounds of **VOdpm**, *i.e.* the crystal and microcrystalline powders samples. The phonon bottleneck effects are stronger in the former sample, and they weaken reducing the crystalline sizes. As it is visible in Table 4.15, the direct process coefficient c is higher for **VOdpm-pwd**, corresponding to an earlier decreasing of τ in the high magnetic field region. The parameter d is also higher for the powder-like compound. This reflects the lower efficiency of the various processes in inducing spin relaxation in **VOdpm-crys**. Accordingly, the efficiency of the external magnetic field in suppressing the internal contributions, accounted for by f, is greater for the macro-crystalline sample. This happens because, in addition to the internal fields, the rising of the magnetic field reduces the phonon bottleneck strength, since increasing the Zeeman splitting more phonons can participate to the relaxation. By looking at the parameter e, there is an unexpected difference between its values for **VOdpm-pwd** and **VOdpm-crys**. Indeed, they should not change since the spin density does not vary as the sample is milled. The cause should be, however, accounted for by the variation of strength of the internal fields. Specifically, such a strength is reduced for the system affected by bottleneck effects and a possible explanation can be that, since the lattice is not able to dissipate the excitation, the continuous re-excitation of the spin system masks the internal field contributions. This is also in agreement with the values of the parameter d.

Table 4.16. Best-fit parameters obtained using either the model (4.10) or (4.11) to reproduce the magnetic field dependence of τ at 15 K. Asterisks indicate whether that specific curve is shown or not in Figure 4.7c or Figure 4.8 or Figure 4.9.

T = 15 K	c (T^{-4} ms^{-1})	d (ms^{-1})	e (T^{-2})	f (T^{-2})	g (ms^{-1})	h (T^{-2})
VOdpm*-pwd	$9.7(3) \cdot 10^{-4}$	5.7(3)	15.1(9)	190(16)	-	-
VOdpm*-crys	$9.2(6) \cdot 10^{-4}$	0.6(2)	329(140)	800(560)	-	-
VOdtc*	$5.1(1) \cdot 10^{-4}$	24(1)	0.31(5)	83(10)	2.9(2)	1.4(3)
VOcat*	$5.1(1) \cdot 10^{-4}$	13.2(8)	9.9(2)	580(42)	-	-
VOnaphcat*	$1.6(1) \cdot 10^{-3}$	2.1(4)	40(5)	365(58)	-	-
Vcat	$3.4(1) \cdot 10^{-3}$	5.7(4)	0.15(2)	279(33)	1.9(1)	0.068(5)
Vnaphcat	$1.1(1) \cdot 10^{-2}$	6.8(2)	0.2(5)	415(30)	1.63(8)	0.08(2)

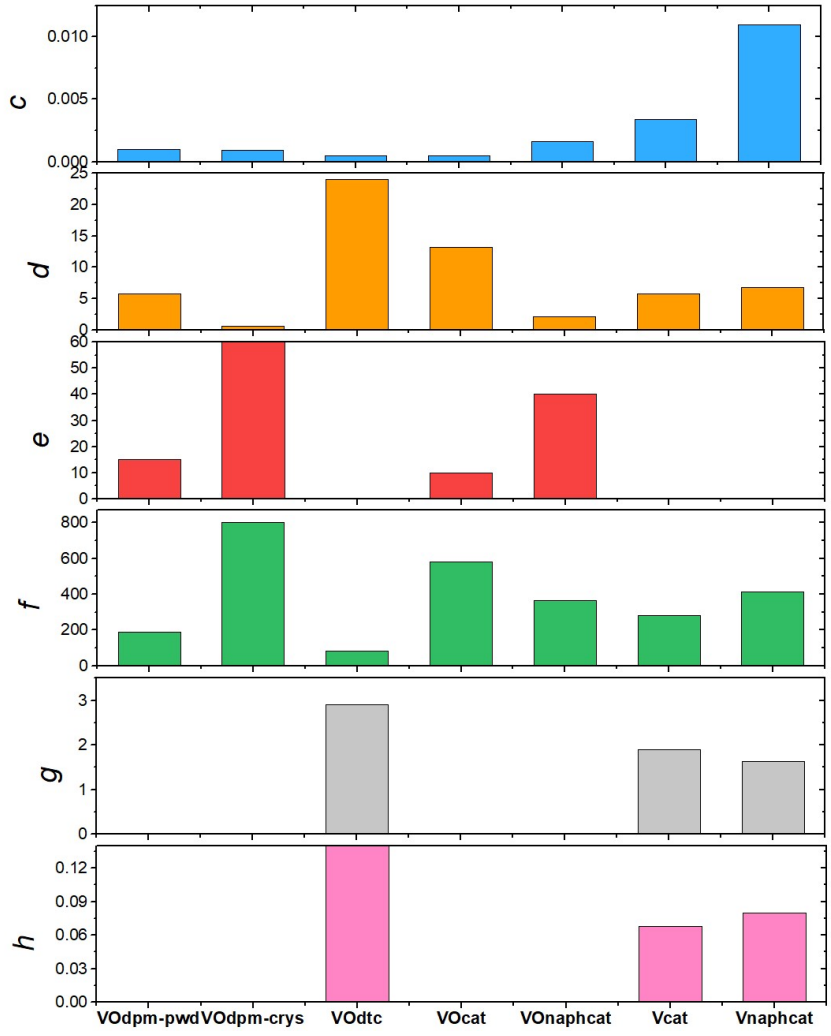

Interestingly, by analysing the temperature dependence of the parameters obtained by fitting the magnetic field dependence of τ with the Brons-van Vleck model, it has been found that, even if the overall temperature dependence of τ does not follow an Arrhenius law, the individual single processes described by d and g parameters are

proportional to exp $\left(\frac{A_{eff}}{kT}\right)$. From this dependence it is possible to extract an effective activation energy value A_{eff} for each contribution. However, since each value of either d or g is obtained from the fit of the entire magnetic field dependence of τ, the fit of the temperature dependence of such parameters requires to measure the magnetic field dependence of τ at several temperatures. This analysis is thus very demanding, and, for this reason, it has been possible to perform this type of investigation only for **VOdtc**, **VOcat**, **VOnaphcat**, **Vcat** and **Vnaphcat**. The extracted effective activation energy values are reported in Table 4.17, while an example of how the various terms of the Brons-van Vleck model contribute to the magnetic field dependence of τ is shown for **VOdtc** in Figure 4.15.

Table 4.17. Effective activation energy, $\boldsymbol{A_{eff}}$, extracted by fitting the temperature dependences of the Brons-van Vleck parameter $\boldsymbol{d}$ and, when used, $\boldsymbol{g}$ with the Arrhenius law. As comparison, the energy value of the closest vibrational mode measured by THz spectroscopy is also reported.

	$U_{eff\ d}$ (cm^{-1})	$\hbar\omega_1$ (cm^{-1})	$U_{eff\ g}$ (cm^{-1})	$\hbar\omega_2$ (cm^{-1})
VOdtc	20(2) → 40	41 (10 K)	15(2) → 30	28 or 33 (10 K)
VOcat	24(2) → 48	46 (10 K)	-	-
VOnaphcat	17(2) → 34	35 (RT)	-	-
Vcat	6(1) → 12	-	10(1) → 20	25 (10 K)
Vnaphcat	9(1) → 18	21 (RT)	16(1) → 32	32 (RT)

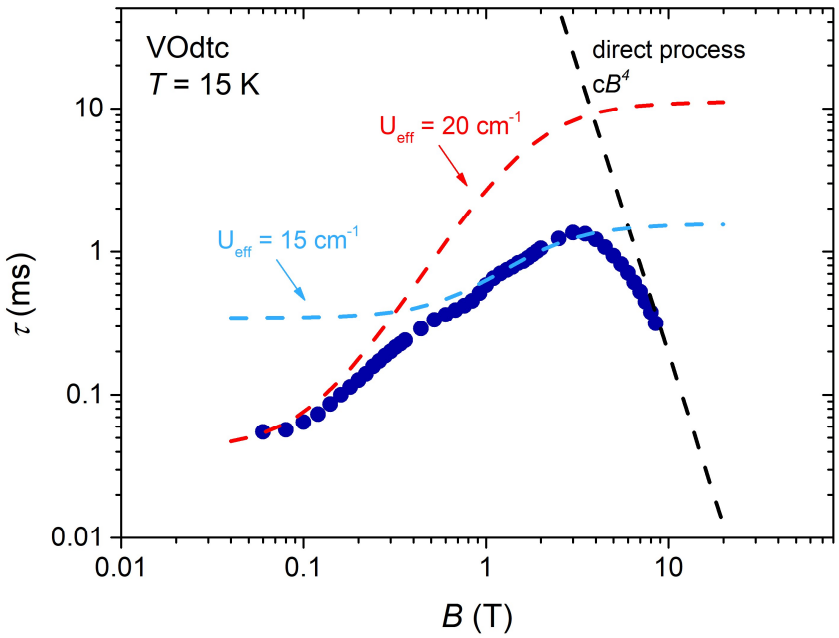

Figure 4.15. Decoupling of the extended Brons-van Vleck contributions for the magnetization relaxation time of **VOdtc** at 15 K.

It is interesting to note that the obtained effective activation energies can be related to the experimental low-energy vibrational modes through the expression

$$A_{eff} = \hbar\omega/2. \tag{4.12}$$

This relation was predicted for the relaxation time of SMMs characterized by excited magnetic states at high energy when the anharmonicity, or finite-line width, of vibrational modes is taken into account.[34] The obtained A_{eff} values are reported in Table 4.17 and compared to the frequency value of the vibrational modes observed by THz spectroscopy. As evidenced by the results contained in Table 4.17, each effective activation energy, extracted by the magnetic analysis, agrees with the experimental vibrational modes present in the THz spectrum, except for the phonons of **Vcat** that are within the sensitivity limit of the set-up. The striking matching between those values suggests that through this type of investigation it is possible to extract the contribution of specific low-energy vibrational modes to the spin-lattice relaxation. The vibrational mode extracted here for **VOcat** is the same found by fitting the temperature dependence of τ by the local modes model. Once more, this value can be attributed to the low-intensity vibrational mode at 46 cm^{-1}, remembering that for some reason its spin-phonon coupling may be particularly effective, or it can be considered as a mixing between the 30-40 cm^{-1} and 60 cm^{-1} groups. However, it is interesting to note that for **VOcat** and **VOnaphcat** the magnetically active vibrational modes seem not to be the lowest in energy. According to a recently reported study on the role of intramolecular vibrations as mediators of spin-lattice relaxation, each vibrational mode should couple with the spin to a different extent, as a function of the type of vibration and electron occupancy in the metal *d*-orbitals.[35] It is thus not surprising that the lowest energy vibrational modes observed herein for **VOcat** and **VOnaphcat** can be not strongly coupled with the spin to promote efficient relaxation, and consequently does not contribute substantially to the fine structure of the τ *vs* B behaviour. From Table 4.17 it should be also noted that the active vibrational modes of **Vcat** and **Vnaphcat** are shifted toward lower energies, with respect to the vanadyl molecules, in agreement with the experimental vibrational spectrum. Moreover, their active modes seem to coincide with the lowest experimental vibrational modes.

From these evidences it can be concluded that the magnetic field dependence of the relaxation time extracted by susceptibility data contains information about the phonons active in the spin-lattice relaxation. Since their contribution can be outlined from the parameters d and g of the Brons-van Vleck model, the relaxation here considered is that relative to the low magnetic fields. Apparently, the magnetic active low-energy optical phonons are too energetic to cause a direct process type of relaxation (for $B = 1$ T the

energy separation between the Kramers doublet is ca. 1 cm^{-1}), suggesting that they should be involved in the relaxation through the Raman process. However, the relation $A_{eff} = \hbar\omega/2$ applies for SMMs when the relaxation occurs through the direct process by involving the phonon distribution linewidth, *i.e.* when the phonons description is not limited to the harmonic approximation. In this frame, it is thus complicate to make a well-defined separation between the direct and Raman process.

One might wonder why in this case the low-energy vibrational modes were found through eq. (4.12), whereas by using the local modes model the values of the active phonons can be directly extracted. This is probably because the former analysis is performed on low temperature data where, according to (A. Lunghi et al., 2017)[34] for SMMs, it is expected to find a relation such as eq. (4.12). Instead, as the temperature increases this relation is not valid anymore and another type of relaxation, involving also the excited spin state, will occur. However, for the investigated vanadium-based molecules there are not excited Kramers doublet before tens of thousands cm^{-1}. Thus, since the local modes model is applied in a wide temperature range, up to 300 K, it can be reasonable to find directly the frequency value of the phonon involved in the relaxation.

4.5.4 Schematic summary of the analysis

The great amount of data analysed in this section can be particularly heavy for a generic reader. For this reason, the main results extracted by the analysis are schematically summarized in this paragraph.

τ *vs* T ac susceptibility	
Simple model	➢ Most of the molecules investigated can be reproduced by considering the combination of the direct and Raman processes, as expected on the basis of literature. However, in some cases deviations from theory have been found because of spin-phonon bottleneck effects. This phenomenon is particularly strong in the β-diketonate derivative, VOdpm, and in the macrocyclic-based molecules, but it is still not well understood. Moreover, the macrocyclic-based molecules exhibit an uncommon weak temperature dependence of τ in an extended temperature range (up to 30 K). According to

theory, this behaviour can be attributed to the lack of low-energy phonons and it agrees with the experimental THz spectra.

- The Raman process for all the investigated molecules depends on temperature as T^3 instead of T^9, which is what theory suggests for an $S = 1/2$ spin system. However, according to literature, other exponents can be found depending on the vibrational structure of the system.

Local modes model

- The use of this model for VOcat and VOnaphcat provides reasonable values of the low-energy vibrational modes that should be involved in the spin relaxation. The estimation of vibrational modes at higher frequencies is limited by the temperature range at which the measurements are performed.

T_1 *vs* T pulsed EPR

Simple model

- The temperature dependence of T_1 is well reproduced by considering the combination of the direct and Raman process. Indeed, in this case the investigated compounds are diluted and no spin-phonon bottleneck effects are present. It is confirmed that the weak temperature dependence of T_1 for the macrocyclic-based molecules can be still attributed to the direct process instead of cross-relaxation processes.
- The temperature dependence T^3 induced by the Raman process is confirmed.

Debye model

- This is a more rigorous model for the Raman process. Since it is able to well reproduce the experimental data, it is a further confirmation about the presence of the Raman process instead of another type of relaxation process.
- The parameters extracted are useful for comparing the different nature of spin relaxation among the various investigated molecules. Moreover, their trend agrees with the results obtained by the simple model. However, the model does not allow to correlate the extracted parameters with the findings of the optical measurements.

Local modes model

- The model well reproduces the data, and the extracted parameters are in agreement with the other models.
- This is particularly interesting when applied at the macrocyclic-based molecules that have distinct low-energy vibrational modes. Instead, for the other cases where more vibrational modes are present, the output parameter is an average frequency value.
- By comparing the results of the model with the experimental THz spectrum, it provides useful clues to identify the vibrational modes that are more relevant for spin relaxation. Indeed, different phonons have different spin-phonon coupling coefficients, so that the more efficient phonon for the spin relaxation is not necessarily the lowest in frequency.

τ *vs* B
ac susceptibility

Brons-van Vleck model

- This model is able to reproduce most of the magnetic field dependence of τ for the investigated molecules. However, in some cases the use of an extended version is necessary. This requires the use of an additional Brons-van Vleck term that accounts for the low magnetic field region.
- The model is a useful tool to separate the various contributions that produce the non-monotonous trend of the magnetic field dependence. In particular, it allows to extract the contribution of the internal fields, produced by spin-spin and spin-nuclei interactions.
- The consequences of spin-phonon bottleneck effects have been investigated in detail since they provoke a strong variation in the spin relaxation. However, this analysis is still qualitative, and more information is required to understand this phenomenon.
- Apparently, by using this model it is possible to distinguish the contribution of the vibrational modes affecting the low temperature spin relaxation. Indeed, the values extracted agrees with the experimental THz spectrum.

4.6 Conclusions

A series of vanadyl- and vanadium-based molecules has been investigated here through a multi-technique approach constituted of cw-EPR, ac susceptometry, THz spectroscopy and pulsed EPR. This investigation has been firstly focused on the structural and static properties of these systems, whose magnetic properties are accounted for by an electronic spin $S = 1/2$ coupled with a nuclear spin $I = 7/2$ for weak magnetic fields. Indeed, at high magnetic fields the spin system can be described simply as a two-levels system. These features are common to all the investigated molecules.

Vanadyl and tris-chelate molecules can be differentiated on the basis of their ground electronic state that is a well-isolated d_{xy} orbital for the former and a more mixed d_{z^2} orbital for the latter. This is reflected in the magnetization dynamics that shows longer relaxation times, τ, for the vanadyl species, both as a function of temperature and magnetic field. Such relaxation times were extracted by ac susceptibility measurements performed on pure microcrystalline compounds within 2 and 70 K, and they are of the order of milliseconds. The behaviour of the thermal variation of τ can be explained by taking into account two relaxation processes: the direct at low temperatures and the Raman at higher temperature. The analysis of magnetic data evidences a typical linear temperature dependence of the direct process for the molecules with bidentate ligands, whereas this dependence weakens for the molecules coordinated by macrocyclic ligands. The Raman process causes a stronger temperature dependent relaxation, which varies roughly as T^3. Interestingly, this dependence is much lower than what expected from the theory, for which a dependence of the type T^9 would occur. This has been observed for all the investigated molecules and in particular for the vanadyl-based systems. This probably results from the interplay of the weak spin-orbit coupling of vanadium and the well-isolated electronic ground state characteristic of the square-pyramidal geometry, both resulting in a weaker spin-phonon coupling. In addition, such a dependence can result from the higher frequencies of the vibrational modes observed by THz spectroscopy. Moreover, effects related to the sample concentration have been observed for several of these systems and were attributed to the spin-phonon bottleneck. This phenomenon is still not-well understood and its presence in the investigated molecules should be attributed to the very small number of low-energy vibrational modes in their vibrational spectra, as evidence experimentally by THz spectroscopy.

The spin dynamics investigation has been extended up to room temperature for the molecules for which it was possible to prepare crystalline solid-state dilutions. For such systems both the spin-lattice relaxation time, T_1, and coherence time, T_m, were measured through pulsed EPR. The obtained results were then analysed through three different models: the simple power-law, the Debye Transport Integral and the local modes model.

The measurements remarkably evidence that T_1 limits T_m, as it was expected. The temperature dependence of the spin-lattice relaxation time can be described considering the combination of direct and Raman processes, according to the ac susceptibility analysis. The coherence time T_m is temperature independent, but as the temperature is increased T_1 shortens and starts to affect T_m. Because of the influence of T_1 on T_m, the latter becomes temperature dependent and it decreases rapidly. This remarks the importance to lengthen T_1 in order to achieve longer T_ms. Indeed, the rapid shortening of T_1 for the tris-chelate vanadium-based molecules is responsible of the decreasing of T_m, which is not detectable above 150 K. The vanadyl molecules, instead, exhibit a relaxation time T_1 that decreases more slowly. Consequently, for these molecules, T_m is detectable even at room temperature where can reaches also values around 1 μs.

A more detailed analysis focused on the temperature dependence of T_1 allowed to relate the spin dynamics features with the experimental low-energy vibrational modes (the term 'low-energy' indicates the vibrational modes between 10-150 cm^{-1}). Indeed, it has been found that molecules with few vibrational modes at high frequencies exhibit relaxation times with weaker temperature dependence. In addition, from this analysis it has emerged that the efficiency of the vibrational modes is not related to its energy, but it is not surprising that the phonon active in inducing spin relaxation does not correspond to the lowest one. This efficiency is a combination of the thermal population of the vibrational mode and the spin-phonon coupling. In this frame, a more accurate model should not be limited to the vibrational modes at the Γ-point of the Brillouin zone, and it should consider the spin-phonon coupling of each vibrational mode. This type of investigation can be done only by using an ab initio approach and, notwithstanding its complexity, it is now in progress.

Nevertheless, the phenomenological analysis here performed succeed in separating and obtaining hints about the various contributions that affect the spin-lattice relaxation.

Additional evidences about the role of the low-energy vibrational modes in the spin-lattice relaxation can be achieved by comparing the results obtained by the magnetic analysis of the magnetic field dependence of τ, extracted by ac susceptometry, with the THz spectroscopy evidences. It should be remarked that the possibility to perform measurements of the relaxation time as a function of the magnetic field is one of the great advantages of ac susceptometry. From these measurements it has been evidenced a non-monotonous behaviour shared by all the V^{IV}-based molecules investigated. This originates from the competition between the internal contributions, such as dipolar fields produced by spin-spin and spin-nuclei interactions, and the direct process. Moreover, though the entire temperature dependence of τ does not vary following an Arrhenius-like behaviour, this type of dependence applies for some parameters extracted by fitting the

magnetic field dependence of τ with the Brons-van Vleck model. From the analysis of their temperature dependence, indeed, it is possible to extract an effective activation energy, A_{eff}. Interestingly, the A_{eff} values extracted seem to well correlate with some of the low-energy vibrational modes experimentally observed, when the relation $A_{eff} = \hbar\omega/2$ is taken into account. This relation has been theoretically derived to explain the spin-lattice relaxation for SMMs when the anharmonicity of phonons is not neglected. Once more, these results evidence the involvement of phonons in determining the behaviour of the spin-lattice relaxation time. Further studies are, however, necessary to clarify whether such phonons are involved through the direct or Raman process.

4.7 Bibliography

1. L. Tesi, A. Lunghi, M. Atzori, E. Lucaccini, L. Sorace, F. Totti and R. Sessoli, *Dalton Trans.*, 2016, **45**, 16635-16643.
2. P. M. Barron, H. T. Son, C. H. Hu and W. Choe, *Cryst. Growth Des.*, 2009, **9**, 1960-1965.
3. D. W. Feng, Z. Y. Gu, J. R. Li, H. L. Jiang, Z. W. Wei and H. C. Zhou, *Angew. Chem. Int. Ed.*, 2012, **51**, 10307-10310.
4. I. Goldberg, *Chem. Commun.*, 2005, **0**, 1243-1254.
5. D. Riou, O. Roubeau and G. Ferey, *Microporous Mesoporous Mater.*, 1998, **23**, 23-31.
6. K. Eguchi, T. Nakagawa, Y. Takagi and T. Yokoyama, *The Journal of Physical Chemistry C*, 2015, **119**, 9805-9815.
7. L. Malavolti, M. Briganti, M. Hänze, G. Serrano, I. Cimatti, G. McMurtrie, E. Otero, P. Ohresser, F. Totti, M. Mannini, R. Sessoli and S. Loth, *Nano Lett.*, 2018, **18**, 7955-7961.
8. K. Henrick, C. L. Raston and A. H. J. White, *Chem. Soc., Dalton Trans.*, 1976, **26**, 26.
9. A. Abragam and B. Bleaney, *Electron Paramagnetic Resonance of Transition Ions*, Dover, New York, 1986.
10. G. E. Matsubayashi, T. Nojo and T. Tanaka, *Inorg. Chim. Acta*, 1988, **154**, 133-135.
11. J. M. Zadrozny, J. Niklas, O. G. Poluektov and D. E. Freedman, *ACS Central Science*, 2015, **1**, 488-492.
12. S. Lenz, K. Bader, H. Bamberger and J. van Slageren, *Chem. Commun.*, 2017, **53**, 4477-4480.
13. S. Stoll and A. Schweiger, *J. Magn. Reson.*, 2006, **178**, 42-55.
14. K. Bader, M. Winkler and J. van Slageren, *Chem. Commun.*, 2016, **52**, 3623-3626.
15. J. R. Pilbrow, ed., *Transition Ion Electron Paramagnetic Resonance*, Oxford University Press, Oxford, 1990.
16. S. Sproules, T. Weyhermuller, S. DeBeer and K. Wieghardt, *Inorg. Chem.*, 2010, **49**, 5241-5261.
17. A. Albino, Master thesis, University of Florence, 2018.

18. J. H. van Vleck, *Physical Review*, 1940, **57**, 426-447.

19. S. Gomez-Coca, A. Urtizberea, E. Cremades, P. J. Alonso, A. Camon, E. Ruiz and F. Luis, *Nature Communications*, 2014, **5**, 4300.

20. D. Gatteschi, R. Sessoli and J. Villain, *Molecular nanomagnets*, Oxford University Press, Oxford, UK, 2006.

21. M. Le Bellac, *A Short Introduction to Quantum Information and Quantum Computation*, Cambridge University Press, Cambridge, 2006.

22. J. A. Weil and J. R. Bolton, in *Electron Paramagnetic Resonance*, John Wiley & Sons, Inc., 2006.

23. S. Eaton and G. Eaton, in *Distance Measurements in Biological Systems by EPR*, eds. L. Berliner, G. Eaton and S. Eaton, Springer US, 2002, vol. 19, ch. 2, pp. 29-154.

24. H. Sato, S. E. Bottle, J. P. Blinco, A. S. Micallef, G. R. Eaton and S. S. Eaton, *J. Magn. Reson.*, 2008, **191**, 66-77.

25. R. Owenius, G. E. Terry, M. J. Williams, S. S. Eaton and G. R. Eaton, *J. Phys. Chem. B*, 2004, **108**, 9475-9481.

26. S. S. Eaton and G. R. Eaton, in *eMagRes*, 2016, DOI: doi:10.1002/9780470034590.emrstm1507.

27. M. Atzori, E. Morra, L. Tesi, A. Albino, M. Chiesa, L. Sorace and R. Sessoli, *J. Am. Chem. Soc.*, 2016, **138**, 11234-11244.

28. T. Yamabayashi, M. Atzori, L. Tesi, G. Cosquer, F. Santanni, M.-E. Boulon, E. Morra, S. Benci, R. Torre, M. Chiesa, L. Sorace, R. Sessoli and M. Yamashita, *J. Am. Chem. Soc.*, 2018, **140**, 12090-12101.

29. J. Tasseva, A. Taschin, P. Bartolini, J. Striova, R. Fontana and R. Torre, *Analyst*, 2017, **142**, 42-47.

30. A. Taschin, P. Bartolini and R. Torre, *Meas. Sci. Technol.*, 2017, **28**.

31. G. Allodi, 1996-2010, copyright CERN.

32. K. J. Standley and R. A. Vaughan, *Electron Spin Relaxation Phenomena in Solids*, Plenum Press, New York, 1969.

33. L. Escalera-Moreno, J. J. Baldov, A. Gaita-Arino and E. Coronado, *Chem. Sci.*, 2018, **9**, 3265-3275.

34. A. Lunghi, F. Totti, R. Sessoli and S. Sanvito, *Nature Communications*, 2017, **8**, 14620.

35. L. Escalera-Moreno, N. Suaud, A. Gaita-Arino and E. Coronado, *J Phys Chem Lett*, 2017, **8**, 1695-1700.

Chapter 5

$VO(acac)_2$: The Vanadyl Showpiece

This chapter is dedicated exclusively to the investigation of the vanadyl acetylacetonate molecule, whose formula is $[VO(acac)_2]$ and hereafter simply labelled as **VOacac**. The β-diketonate ligand here used, composed of 2 oxygen, 5 carbon and 7 hydrogen atoms, is the simplest that could have been chosen, making it particularly suitable for theoretical *ab initio* calculations. Moreover, for this molecule it is possible to grow crystals with dimensions up to several millimetres whereby perform single-crystal measurements. A wide variety of techniques were employed to study the properties of such a molecule, which has become a prototype system for the other vanadyl-based molecules. In addition to the standard magnetic characterization based on cw-EPR and ac susceptometry, which is useful to obtain information on the electronic structure and the relaxation processes affecting the magnetization dynamics, magnetization decays and hysteresis were recorded through a μ-Hall device at the liquid ^{3}He temperatures, evidencing an inherent anisotropy of the spin dynamics. At the same low temperatures, calorimetric measurements were also employed to investigate in more detail the spin-phonon bottleneck effects, that are particularly relevant for $S = 1/2$ spins, as explained in (§3.3.8) and already evidenced in Chapter 4. In addition, given the key role of the vibrational modes for the spin-lattice relaxation, a detailed optical investigation has been done through THz spectroscopy in a wide temperature range on microcrystalline powder samples. Such measurements were flanked by DFT theoretical calculations from which vibrational spectra and density of states were obtained. This analysis is, however, limited to the Γ-point of the Brillouin zone. To explore the vibrational spectrum in all the reciprocal space, acoustic and optical phonons dispersions were measured by 4D-Inelastic Neutron Scattering (INS) on a 'virtual' big single-crystal, composed of ca. 1 g of smaller iso-oriented single crystals of highly deuterated **VOacac**. Once more, the analysis has been supported by DFT-based theoretical calculations that allowed to go deeper inside the composition of the vibrational spectrum.

Despite the many advantages of this simple molecule, which has allowed a detailed characterization of magnetic and optical properties of **VOacac**, it shows some drawbacks

concerning the possibility to perform an accurate characterization of the relaxation times T_1 and T_m. Indeed, to carry out pulsed EPR measurements diluted crystalline samples are the best choice, but the synthesis of an isostructural diamagnetic molecule of **VOacac** has not been achieved. The alternative of using frozen solutions is useless since it does not permit to connect the spin dynamics results with the vibrational properties obtained by the experimental and theoretical studies. Anyway, this does not diminish the value of the detailed investigation. Indeed, the information about the nature of the processes affecting the spin relaxation here studied remain valid for the other vanadyl-based molecular systems.

5.1 Introduction to the molecule

In **VOacac** the vanadyl moiety is coordinated to the oxygen atoms of two β-diketonate ligands providing a distorted square pyramidal geometry; the molecular structure is reported in Figure 5.1. The metal ion is slightly above the basal plane (0.545 Å), the average V-O bond length is 1.969 Å and the V=O bond distance is 1.585 Å. The strong axial distortion imposed by the vanadyl moiety reduces the energy of the d_{xy} electronic orbital, which turns out to be a well-isolated ground level. This feature, together with the weak spin-orbit coupling of vanadium, provides for these $S = 1/2$ vanadyl-based systems long relaxation times as shown in Chapter 4.

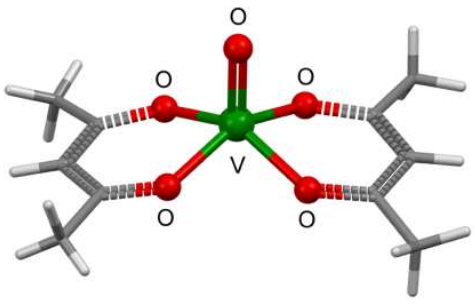

Figure 5.1. Molecular structure of **VOacac**. Colour code: V=green, O=red, C=grey, H=light grey.

The compound crystallizes in the triclinic centrosymmetric space group $P\bar{1}$ (Z=2), thus with only one crystallographically independent molecule in the asymmetric unit, for which the resulting point group is C_1. The V···V shortest distance is 5.61 Å, and the spin density for the pure compound is 3.47 spin/nm^3, which is the highest value among the investigated vanadium-based molecules.

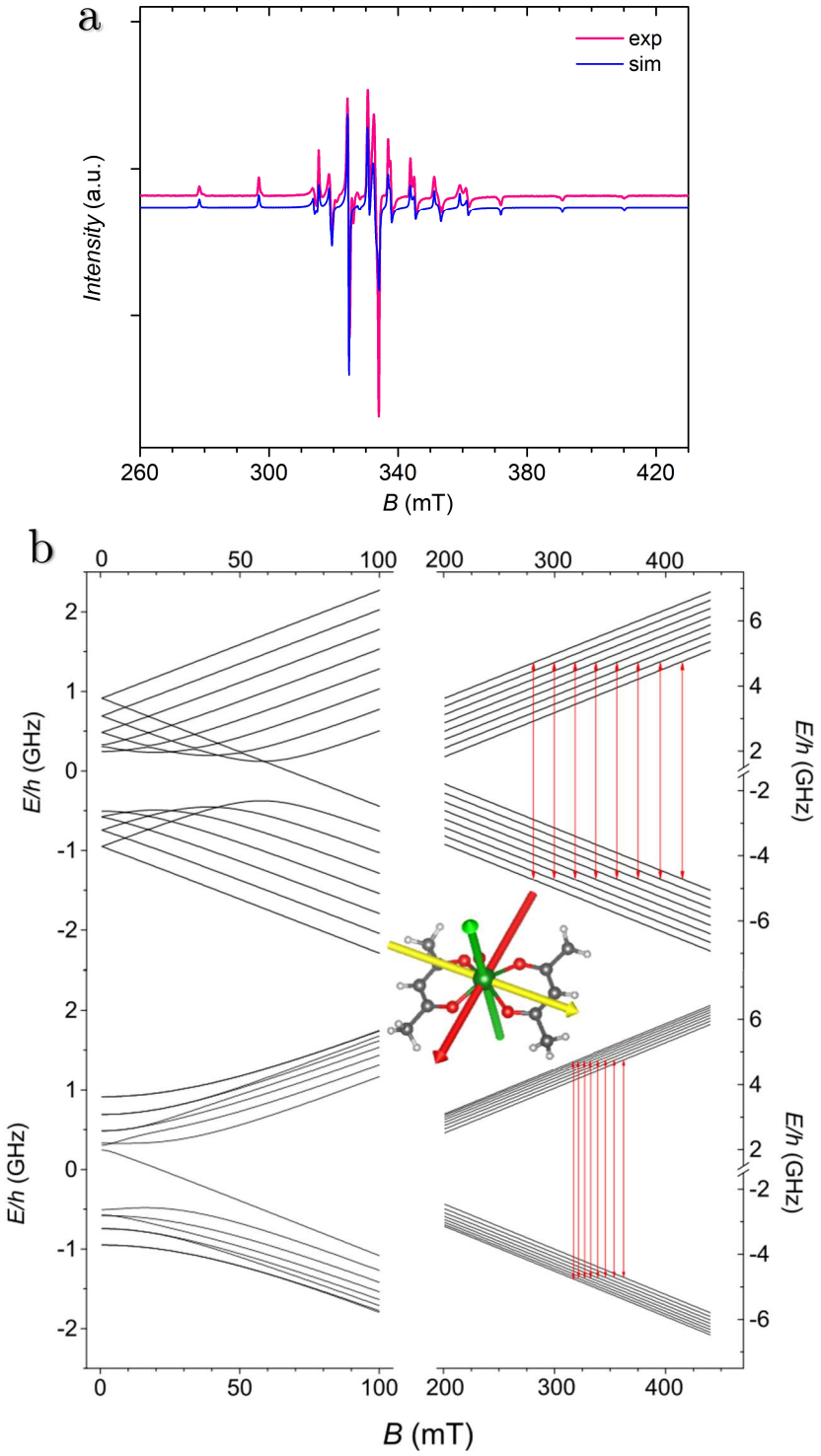

Figure 5.2. (a) Experimental and simulated X-band ($\nu = 9.39$ GHz) cw-EPR spectrum of a frozen solution (1 mM, 2:3 of toluene/CH_2Cl_2) of **VOacac** recorded at $T = 50$ K. The parameters of the simulation are reported in Table 5.1. (b) Energy levels diagrams of **VOacac** when a magnetic field is applied along the largest hyperfine interaction component (upper) and along the smallest (lower). Red arrows indicate the permitted transitions. The diagrams were obtained with EasySpin[1] on the basis of the experimental spin Hamiltonian parameters. At the centre of the image, the molecular magnetic anisotropy axes of the g tensor are reported: g_z=green axis that is along the vanadyl moiety, g_x=red axis that is between the ligands, and g_y=yellow axis that is through the ligands. This has been calculated through CAS-SCF by A. Albino.

The frozen solution cw-EPR spectrum (Figure 5.2) shows the typical features of an anisotropic Kramers doublet $S = 1/2$ interacting with an $I = 7/2$ nuclear spin (^{51}V, abundance 99.76%), with the characteristic 8-fold splitting. The spectrum has been simulated[1] on the basis of the spin Hamiltonian $\mathcal{H} = \mu_B \hat{\boldsymbol{S}} \cdot \boldsymbol{g} \cdot \boldsymbol{B} + \hat{\boldsymbol{I}} \cdot \boldsymbol{A} \cdot \hat{\boldsymbol{S}}$ and the parameters obtained are reported in Table 5.1.

Table 5.1. Best-simulation parameters used to reproduce the cw-EPR spectrum for **VOacac**.

Molecule/ Parameters	g_x	g_y	g_z	A_x **(MHz)**	A_y **(MHz)**	A_z **(MHz)**
VOacac	1.984(1)	1.981(1)	1.9477(1)	173.9(1)	188.0(1)	513.2(1)

Such parameters, characterized by partially rhombic $\boldsymbol{g}$ and $\boldsymbol{A}$ tensors, are very close to those of the other investigated β-diketonate molecule, *i.e.* **VOdpm** (Table 4.2). The parameters obtained by the simulation of the cw-EPR spectrum have been used to calculate the evolution of the energy levels on increasing the magnetic field, as shown in Figure 5.2. From this, it is evident that the degeneracy between the Kramers doublets is already removed in zero magnetic field, since the doublet is split by the hyperfine interaction into two groups of levels, a septet ($F = I - S = 3$) and a nonet ($F = I + S = 4$). Indeed, the anisotropy of the hyperfine interaction removes the degeneracy within the two groups of levels even in zero field, and results in eigenfunctions that are linear combinations of different $|m_S, m_I\rangle$ values.[2] As the external magnetic field is increased, the eigenfunctions of the system can be again regarded as composed by pure $|m_S, m_I\rangle$ states.

5.2 Magnetic properties and phonon bottleneck

The magnetization dynamics of **VOacac** has been investigated by ac susceptometry on microcrystalline powder samples revealing peculiar features caused by spin-phonon bottleneck effects. Such a phenomenon has been already discussed theoretically in Chapter 3 and experimentally in Chapter 4. As expected for $S = 1/2$ paramagnetic systems, the thermal variation of the complex magnetic susceptibility in zero static magnetic field reveals no imaginary component of the susceptibility (χ'') in the whole investigated temperature range. When a small static magnetic field (>20 mT) is applied, slow magnetic relaxation is observed for all samples with the appearance of a peak in the imaginary part of the susceptibility and a concomitant decrease of the real component (χ'). Examples of frequency dependence of χ' and χ'' on varying the magnetic field and temperature were reported in Figure 4.6. The relaxation time (τ) was obtained by fitting the imaginary component χ'' with the Debye equations (eq. 4.2).[3] In the previous chapter,

such a relaxation time has been considered to coincide with the spin-lattice relaxation time T_1. This is true if, considering the global de-excitation transfer process from the spin system to the bath, the transfer of excitation from the spin system to the lattice one is the determining step. In this situation, indeed, the dissipation of the excitation from the lattice to the thermal bath can be assumed instantaneous. An inefficient dissipation within the crystal produces the so-called 'spin-phonon bottleneck effects' that may significantly modify the thermal and magnetic field behaviour of τ (Chapter 3). In this situation, τ is not equivalent anymore to the spin-lattice relaxation time T_1. It is here recalled that the presence of phonon bottleneck is evident when *i)* at low temperature the thermal variation of the direct process varies as T^{-2} rather than linearly, and *ii)* when τ changes consequently to a variation of the crystallite sizes. For **VOacac**, variations of the crystallite sizes cause dramatic changes in τ so that it is fair to talk of 'giant' spin-phonon bottleneck effects. Such changes are evident both varying the temperature and magnetic field, as shown in Figure 5.3.

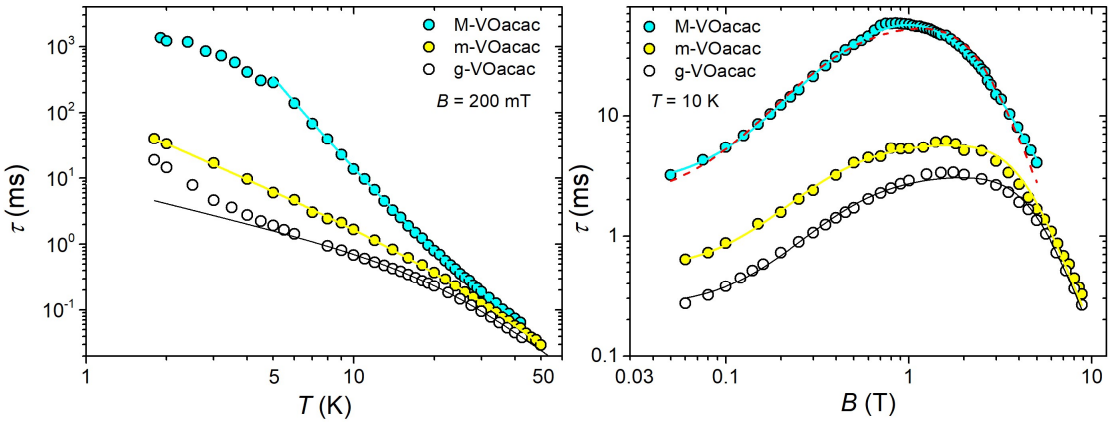

Figure 5.3. Temperature (a) and magnetic field dependence (b) of the magnetization relaxation time extracted by ac susceptibility for the same sample of **VOacac** but with different crystallite sizes: macro-, mid-ground and well-ground crystallites. The solid lines represent the best-fits using eq. (5.2) and (5.3) to reproduce the temperature dependence, and eq. (5.4) for the magnetic field dependence. The dash line results from fitting with the Brons-van Vleck model.

The magnetization dynamics was investigated by ac susceptometry for three polycrystalline samples of **VOacac** with different crystallite dimensions (d): *i)* macroscopic crystals as obtained from crystallization (d ca. 1-5 mm), hereafter **M-VOacac**; *ii)* moderately ground crystals (d ca. 500 μm), hereafter **m-VOacac**; *iii)* well-ground and pressed microcrystalline powders (d ca. 10 μm), hereafter **g-VOacac**. The smaller dimensions were evaluated using X-ray microtomography. It is evident from Figure 5.3 that the three morphologically different samples show distinct τs. At high temperature, around 40 K, the three relaxation times have similar values, but as the

temperature is decreased their temperature dependence follows different power laws: $n > 2$, $n \sim 2$ and $n < 2$ for **M-VOacac**, **m-VOacac** and **g-VOacac**, respectively. This leads to differences in τ of more than one order of magnitude at low temperature. The macro-crystalline sample exhibits a striking pronounced temperature dependence between 5 and 30 K, which weakens below 5 K becoming more similar to that of the smaller sizes samples. Remarkably, at 2 K τ for the macro-crystalline sample reaches few seconds. These comparative measurements between samples with different crystallite sizes were performed by applying 200 mT of external magnetic field. In addition, the temperature dependence of τ for **M-VOacac** has been recorded also at 1 T, as discussed in (§5.4.2).

Focusing on the magnetic field dependence of τ (Figure 5.3b), it is evident that at 1 T and below there is at least one order of magnitude of difference between **M-VOacac** and **g-VOacac** samples. Instead, they become closer for high magnetic field values, until above 4 T the relaxation times of the two ground samples are equivalent. Thus, it is possible to conclude that phonon bottleneck effects are stronger in an intermedium temperature range, between 5 and 20 K, and for magnetic fields below 4 T.

The observed differences between the three samples could be in principle due to a non-statistical random orientation of the crystals, in particular for the pristine macro-crystallites. The anisotropy of the spin Hamiltonian parameters could indeed result in different relaxation times for the magnetic field applied along different crystallographic directions, due to the different energy pattern and wavefunction compositions obtained in the three principal directions for the same magnitude of applied field (Figure 5.2). To exclude this possibility, a 5.4 mg single crystal was investigated by applying the static magnetic field first parallel and then perpendicular to the V=O bond. It should be noted that the triclinic space group means that all the molecules in the crystal structure have the same orientation of the $\boldsymbol{g}$ and $\boldsymbol{A}$ tensors (which are assumed to be collinear), thus providing the same energy pattern for all the molecules in a given applied field. The results, shown in Figure 5.4, revealed no significant differences between the two orientations, corroborating the hypothesis of a giant spin-phonon bottleneck.

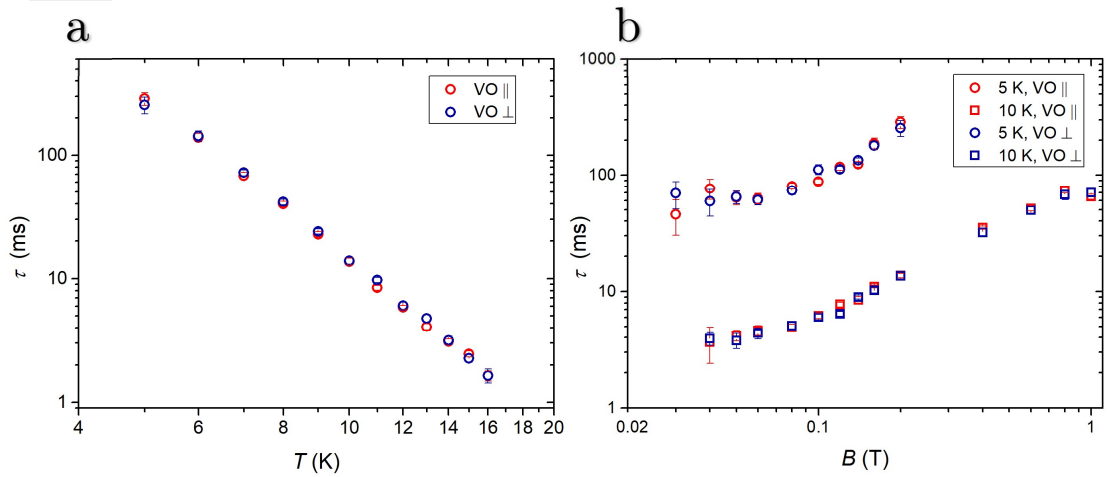

Figure 5.4. Magnetization relaxation time for a single crystal of **VOacac** as a function of the temperature at $B = 200$ mT (a) and the static magnetic field at $T = 5$ and 10 K (b) for two different orientations of the applied magnetic field with respect to the vanadyl moiety.

These results exclude the anisotropy of the hyperfine interaction, as well as that of the g matrix induced by the spin-orbit coupling, as sources for the differences detected by ac susceptometry in the investigated field and temperature ranges. This points out that for the investigated temperatures the sixteen spin states are equally populated. Differences among the relaxation times, for different field orientations, arising from the anisotropy of the electronic structure are however to be expected at lower temperatures.

The magnetic field dependence of τ has been also investigated at several temperatures for both **M-VOacac** and **g-VOacac** samples, and the results are shown in Figure 5.5. Once more, these results remark the differences between macro- and microcrystalline samples.

At 5 K, τ for **M-VOacac** reaches the maximum at 600 mT, and it is worth ca. 460 ms. At the same temperature, τ for **g-VOacac** reaches the maximum at 1 T, corresponding to 9 ms. It can be noted that the magnetic field dependence of **M-VOacac** is globally less pronounced with respect to what seen previously for **VOdpm** (Chapter 4). Although the phonon bottleneck is reduced on increasing the temperature, at 20 K and 1 T there is still almost an order of magnitude of difference between the τ observed for the two samples.

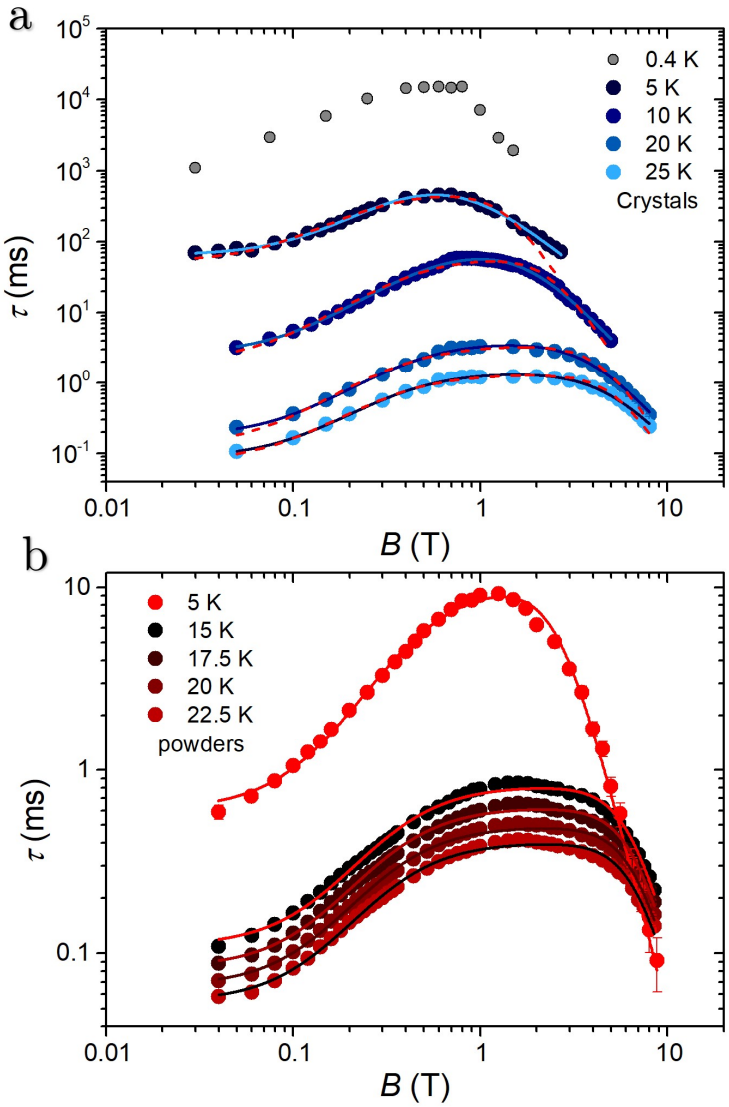

Figure 5.5. Magnetic field dependence of τ extracted by ac susceptibility for **M-VOacac** (a) and **g-VOacac** (b) at different temperatures (see legends). The relaxation time at 0.4 K has been extracted by magnetization decay measurements. The solid lines are the best-fits using eq. (5.4), whereas the dashed lines are obtained using the Brons-van Vleck model.

To investigate more in detail the spin dynamics and how this is related with the magnetic anisotropy, magnetization decays for a single crystal of **VOacac** were recorded between 400 mK and 1 K for three different orientations of the external magnetic field with respect to the crystal: one parallel to the vanadyl moiety and the two others in the plane perpendicular to it. The experiments were carried out in the laboratories of University of Zaragoza (Spain), in collaboration with Prof. F. Luis. The measurements were performed placing a single-crystal with dimensions around 1x0.5x0.5 mm^3 on a μ-Hall device inserted in a ^{3}He-PPMS instrument. By considering the laboratory reference frame *xyz*, in the adopted convention the μ-Hall chip identifies the *xz* plane, while the magnetic field is oriented along *z*. The measurements with the magnetic field quasi-parallel to the V=O direction (labelled as *parallel*) is obtained by placing the crystal with

its crystalline face [011] on the μ-Hall chip, and with the normal to the face [101] lying in the *yz* plane, as shown in Figure 5.6c. In the two other cases, the crystal is placed with the crystalline [101] face on the chip. In the first perpendicular direction (*perp1*) the normal to the face [001] lies in the *yz* plane, whereas the second perpendicular direction (*perp2*) is identified by rotating the crystal on the chip of 90° when this is oriented according to perp1 (Figure 5.6). It should be noted that in perp1 the magnetic field points towards the centre of the oxygen atoms of the same *β*-diketonate ligand, whereas in perp2 it points towards the centre of the oxygen atoms of the two different ligands.

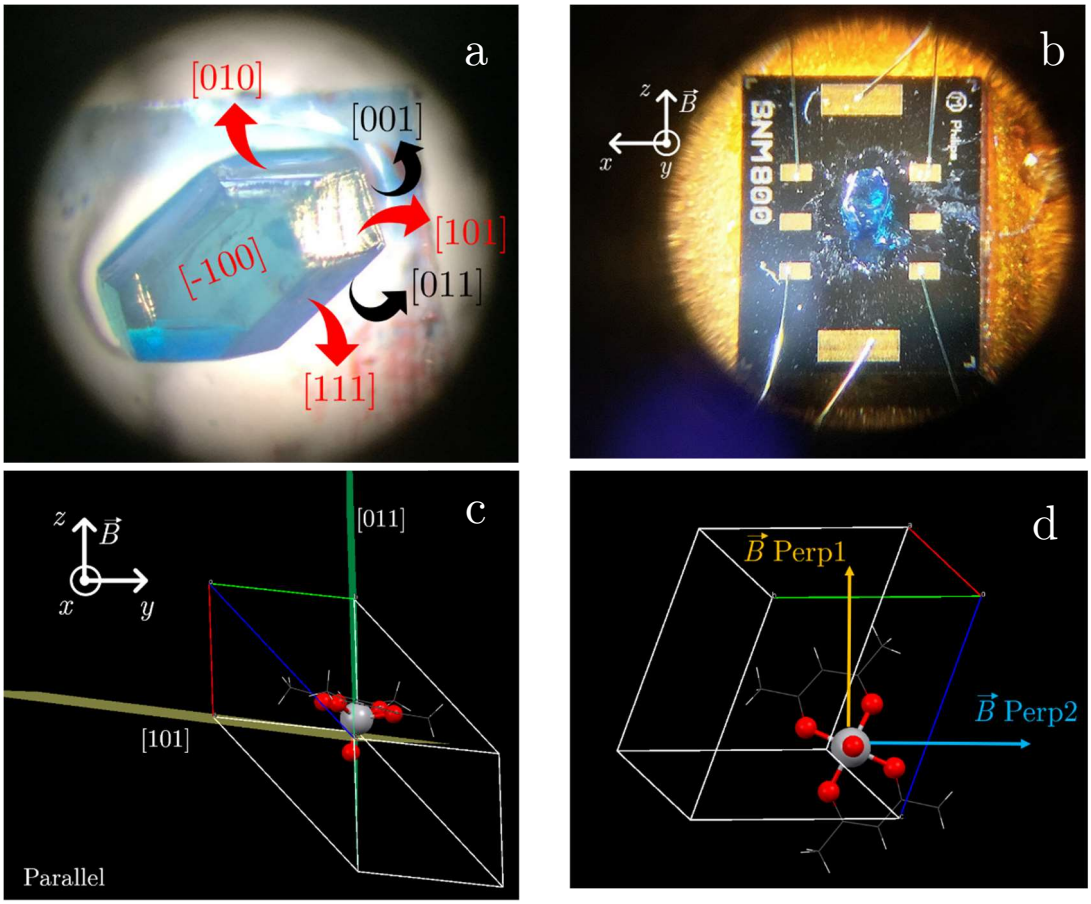

Figure 5.6. (a) Image of the single-crystal of **VOacac** with the labelling of the crystallographic faces used to align the crystal for the experiments; the visible faces are indicated in red, while the hidden faces are indicated in black. (b) Picture of the μ-Hall device with the sample on top, and the reference frame indicated on the right. (c) Crystal alignment used for the μ-Hall and calorimetric measurements. The faces used to align the crystal are highlighted; the reference frame is indicated on the left. (d) Directions of the magnetic field in the perp1 and perp2 crystalline orientation.

Hysteresis curves were recorded by varying the magnetic field with a rate of about 17.6 mT/s at the temperature of 0.4, 0.6 and 1 K. This was repeated for the three different crystalline orientations. The hysteresis curves are reported in Figure 5.7, where the different temperatures and orientations measured are compared. Remarkably, the

relaxation times of **VOacac** are long enough to clearly see a hysteretic behaviour with butterfly-like shape for all the investigated temperatures. Moreover, it should be noted that at zero magnetic field the hysteresis is not completely closed, probably because of the hyperfine interaction that acts as a zero-field splitting term.[2] Differences between the three orientations are evident: the parallel configuration has the largest opening, while the opening of perp1 is slightly larger than that of perp2. This agrees with the rhombic model obtained by the cw-EPR simulation (Table 5.1), though the identification of the origin of the magnetization dynamics anisotropy (whether the *g*-anisotropy or hyperfine interaction) is still not confirmed.

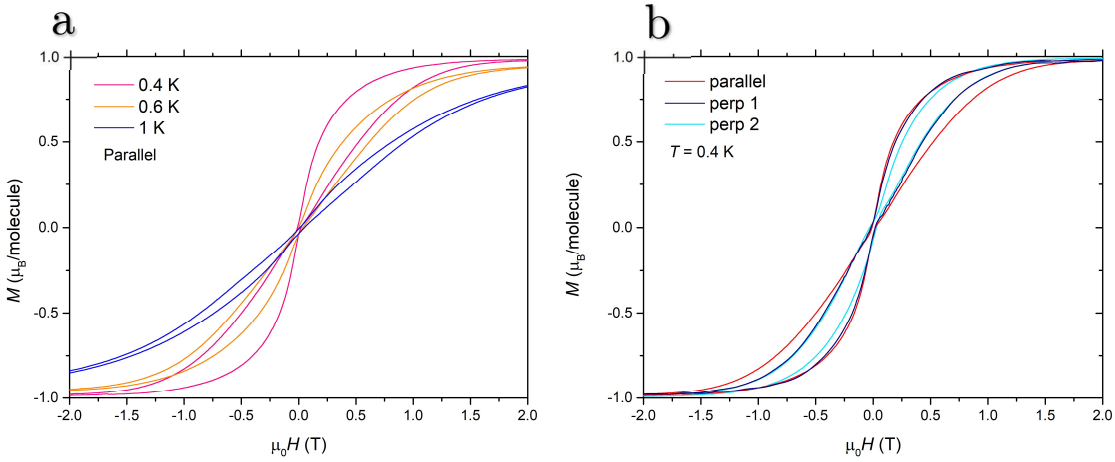

Figure 5.7. Magnetic hysteresis of a single-crystal of **VOacac** (a) at the different temperature values of 0.4, 0.6 and 1 K and (b) for different orientations (V=O parallel to the magnetic field, and perpendicular to it) at the lowest temperature.

The same three orientations used for the hysteresis experiments were used for performing magnetization decays measurements for several temperatures. These were carried out by applying saturating field of 3 T that was then rapidly swept to 8 mT. Instead, the magnetic field dependence of τ was measured by decreasing stepwise the magnetic field (Figure 5.8a). All the decays were fitted by a simple exponential law from which the magnetization relaxation time τ was extracted. Unfortunately, only the results obtained from the parallel orientation are reliable because the other systems have relaxation times too short to allow a proper fit. An example of measurement and fit of the magnetization decay is reported in Figure 5.8b. The temperature dependences of τ extracted by measuring the magnetization decays for each temperature between 0.4 and 1.5 K are reported in Figure 5.8c. It exhibits a linear temperature dependence above 1 K, and a further increase as the temperature is decreased. The magnetic field dependence of τ obtained in such a way is shown in Figure 5.5a, together with the magnetic dependence of τ extracted by ac susceptometry at higher temperatures, and in Figure

5.8d together with the relaxation times extracted by the magnetic hysteresis for the three orientations (parallel, perp1 and perp2) through the expression

$$\tau = -\frac{t}{\ln\left[1 - \frac{|\Delta B|\left(\frac{dM_{up}}{dB} + \frac{dM_{down}}{dB}\right)}{M_{up} - M_{down}}\right]} \tag{5.1}$$

where t is the time of the measurement, $|\Delta B|$ the difference between the final and initial values of the applied magnetic field, $M_{up} - M_{down}$ the difference between the branches of the hysteresis loop characterised by the sweeping direction of the magnetic field, and $\left(\frac{dM_{up}}{dB} + \frac{dM_{down}}{dB}\right)$ the sum between their derivatives. The relaxation times for the parallel orientation obtained from the two experiments agree up to ca. 1 T, as shown in Figure 5.8d; furthermore, it is possible to note that the three orientations are very similar at low magnetic fields and they differentiate only above 0.1 T.

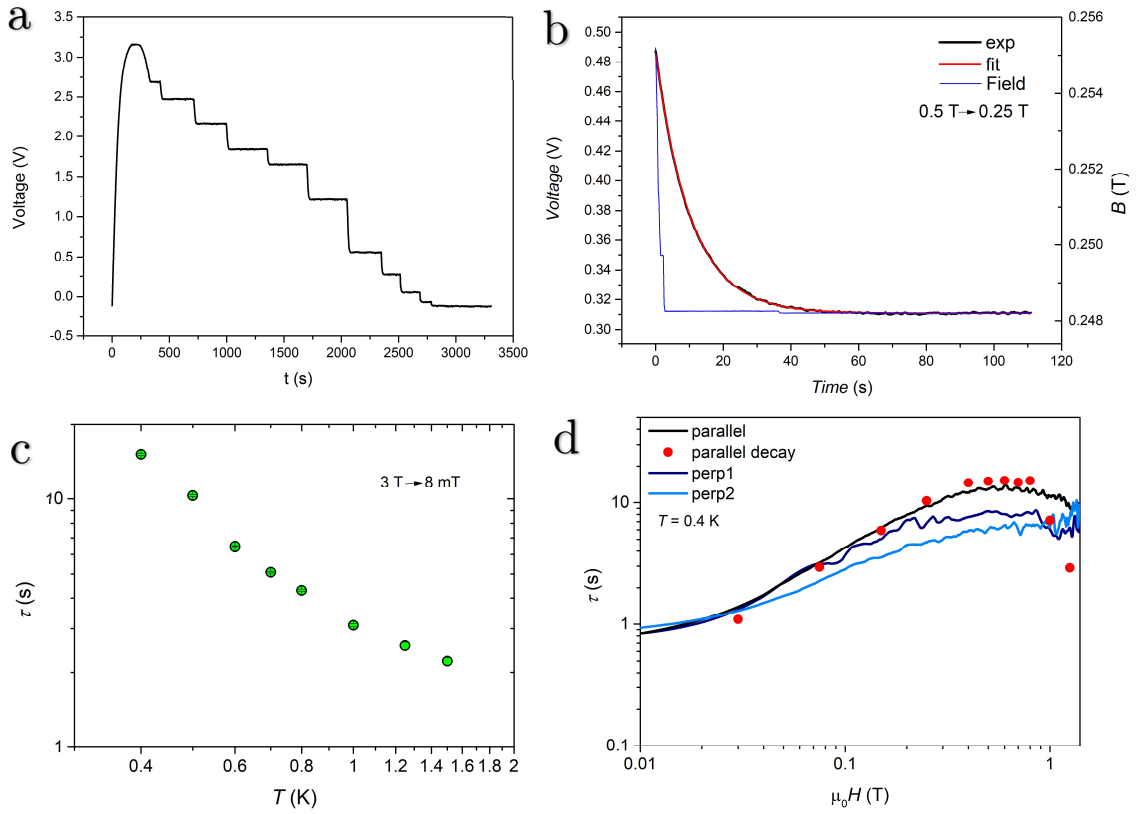

Figure 5.8. (a) Example of stepwise magnetic field variation to measure the field dependence of the magnetization decay and (b) example of a magnetization decay fitted by a simple exponential law. (c) Thermal variation of τ extracted by magnetization decay experiments by saturating the sample with a 3 T field and measuring at 8 mT. (d) Comparison of the relaxation times extracted by the hysteresis for the three different crystal orientations at 0.4 K and of the relaxation time extracted by the magnetization decay experiment for the parallel orientation. All these measurements were performed on a single crystal of **VOacac**.

Since the spin-phonon bottleneck is a phenomenon produced by the inability of the system to dissipate the thermal excitation, calorimetric measurements were performed on a single crystal of **VOacac**, in collaboration with Prof. F. Luis, to get more insights into this phenomenon. A crystal of size around 1x0.8x0.8 mm^3 was placed in the calorimeter chamber in a precise orientation, *i.e.* with the vanadyl moiety oriented parallel to the applied magnetic field, in the same way of the parallel orientation achieved for the μ-Hall measurements (Figure 5.6). The heat capacity has been measured as a function of temperature, between 0.35-100 K, and by applying several magnetic field values, between 0-7 T. The special calorimeter here employed is designed to measure using the relaxation method and high magnetic fields.[4] In this method, the power P to heat the sample is applied in the form of rectangular pulses with typical time periods of the order of seconds. The calorimeter is thermally connected with the mixing chamber through a weak, adjustable heat-link R. When the heater is switched on and off, the calorimeter relaxes to the new thermal equilibrium situation. The heat capacity is obtained by fitting the temperature evolution of the calorimeter to a single exponent. After determining the characteristic relaxation time (τ_e) and the thermal resistance of the heat-link ($R = \Delta T/P$) for each temperature, the heat capacity is easily calculated according to $C = \tau_e/R$. The characteristic time of the experiment, τ_e, can be varied by changing the heat-link resistance. The obtained heat capacity, corrected for the contribution of the grease, is reported in Figure 5.9. In the same figure are reported also the simulations of the experimental data between 0 and 1 T (see §5.4.2).

The heat capacity reported in Figure 5.9 is given by the sum between the magnetic and lattice heat capacity of the crystal. At low temperature it is possible to note a maximum that shifts increasing the magnetic field. Such a feature is called Schottky anomaly and is commonly observed for paramagnetic species with discrete energy levels. This feature occurs when the thermal energy approaches the difference between the spin levels: in this range, small changes in temperature correspond to a strong variation of the spin population of the levels and thus of the spin system heat capacity. As the magnetic field is increased, the energy separation between the two spin level states grows, and consequently the maximum of the Schottky anomaly shifts to higher temperatures.

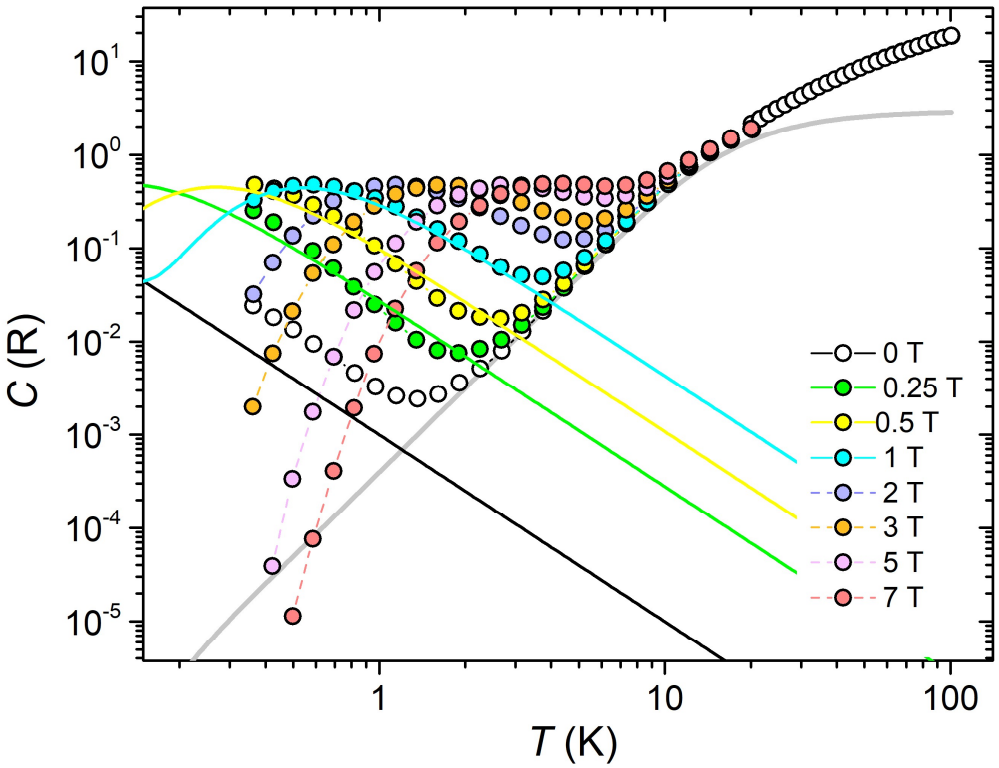

Figure 5.9. Heat capacity measurements of a single crystal of **VOacac** as a function of temperature between 0.35 and 100 K and for several different values of magnetic field between 0 and 7 T. The solid lines are the simulation of the magnetic heat capacity for the curves within 0 and 1 T by using the model of eq. (5.9). The grey solid line is the simulation of the lattice heat capacity by using the Debye model of eq. (5.8). Dashed lines are guide for the eyes.

5.3 Spectroscopic investigation

Given the main role of the vibrational modes and, in this case, of the spin-phonon bottleneck for the spin-lattice relaxation, the low-energy vibrational spectrum of **VOacac** was measured. The experiments were performed for a microcrystalline powders sample embedded in polyethylene using a home-built Terahertz set-up (THz-TD), as also described in (§4.4). All measurements were performed in collaboration with S. Benci of LENS laboratories in Florence. It is recalled that this instrument has a spectral window within 0.3 and 4.0 THz, that is 10-133 cm^{-1}, and a temperature range between 10 and 300 K.[5, 6] The spectra of **VOacac** at the various temperatures are reported in Figure 5.10.

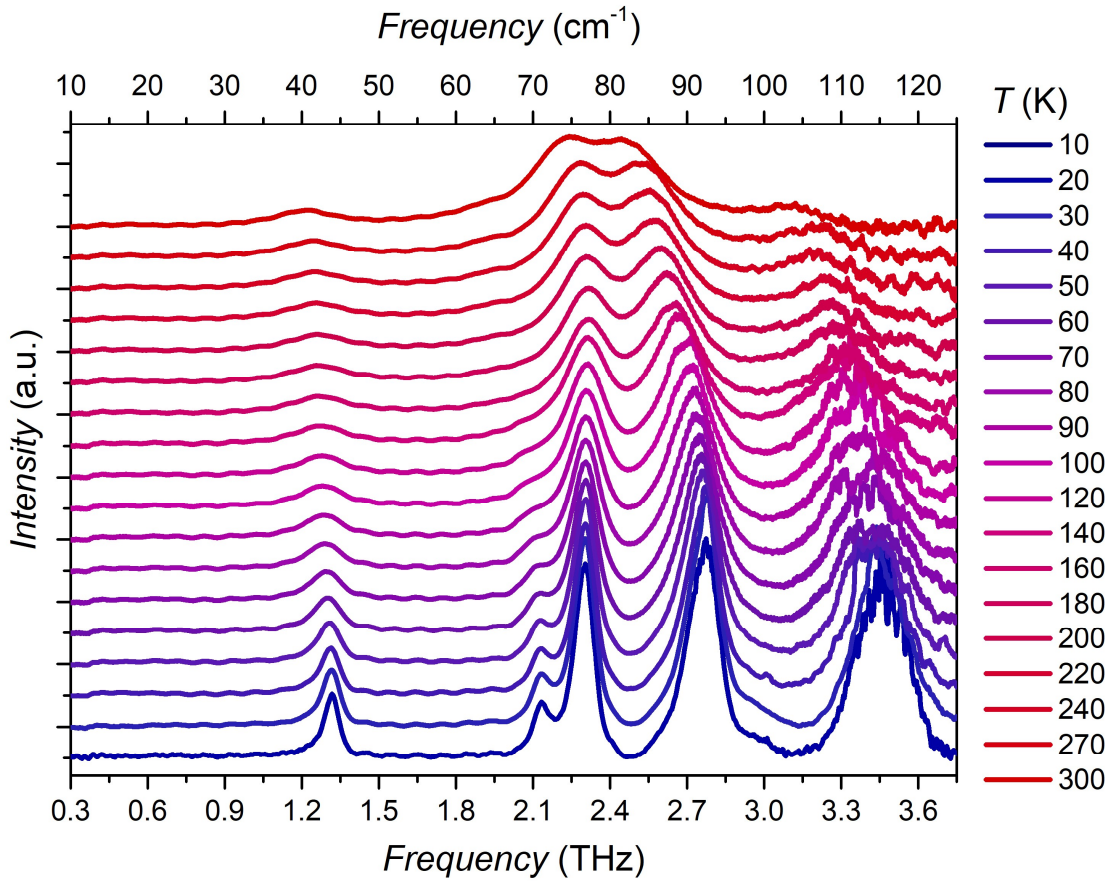

Figure 5.10. Temperature evolution of the vibrational spectra of a microcrystalline powders sample of **VOacac**, embedded in a polyethylene pellet, measured by THz spectroscopy. The spectra are arbitrarily scaled for graphical clarity.

The frequency values of the vibrational modes of **VOacac** observed in the spectra at the lowest and highest temperature are reported in Table 5.2.

Table 5.2. Frequencies of the vibrational modes of **VOacac** obtained by measuring the THz spectrum at the lowest and highest achievable temperatures. The frequency values of the modes simulated by theoretical calculations are also reported.

Temperature /modes	$\hbar\omega_1$ (cm^{-1})	$\hbar\omega_2$ (cm^{-1})	$\hbar\omega_3$ (cm^{-1})	$\hbar\omega_4$ (cm^{-1})	$\hbar\omega_5$ (cm^{-1})	$\hbar\omega_6$ (cm^{-1})	$\hbar\omega_7$ (cm^{-1})
10 K	44	71	77	87	92	99	115
300 K	41	-	75	-	82	-	104
Simulated (0 K)	58	82	91	105	118	123	135

Moving from high temperature (300 K) to low temperature (10 K) significant changes in the terahertz spectrum occur, as shown both from Figure 5.10 and Table 5.2. Indeed, on decreasing the temperature the bands narrow and shift at higher frequencies due to the stiffening of the molecular structure. Such effects could be expected to be more relevant for those vibrational modes with stronger reticular character; however, this is certainly not the only reason for the shifts, and a more detailed model is still in development. At 10 K, the first vibrational mode is at 44 cm^{-1}, the next is at 71 cm^{-1} with lower intensity and there are at least three others with the highest intensities between 77 and 115 cm^{-1}. However, it should be noted that the unit cell of **VOacac** is centrosymmetric, for which only the vibrational modes antisymmetric to the inversion centre are IR-active; the others are thus visible only by using Raman spectroscopy. A modification of the set-up to record Raman spectra in the sub-terahertz regime is in progress.

Additional information about the nature of the observed vibrational modes can be obtained by comparing the THz experimental results with DFT theoretical calculations. The latter were performed by A. Albino of the University of Florence, during his master thesis at the Trinity College of Dublin, in collaboration with Dr. A. Lunghi. The calculations were implemented in CP2K[7, 8] with a PBE functional and a non-local van der Waals correction[9], in order to simulate the **VOacac** low-energy vibrational spectrum. Such a simulation has been made projecting the Cartesian displacements on the basis set constituted by the single molecule degrees of freedom. Consequently, it is possible to decouple the internal and external (rotational and translational) contributions to the motion, as shown in Figure 5.11.

The vibrational spectrum is simulated at 0 K and for this reason it should be compared to the spectrum at 10 K, which is the lowest temperature achievable. As evidenced from the data reported in Table 5.2, there is a non-systematic disagreement within 10-25 cm^{-1}, which is probably due to the inaccurate modelling of the van der Waals interactions for such low energies. Moreover, the vibrational modes appear to have almost

the same composition of internal and external contributions, thus not providing an easy explanation about the different thermal shifts experimentally observed.

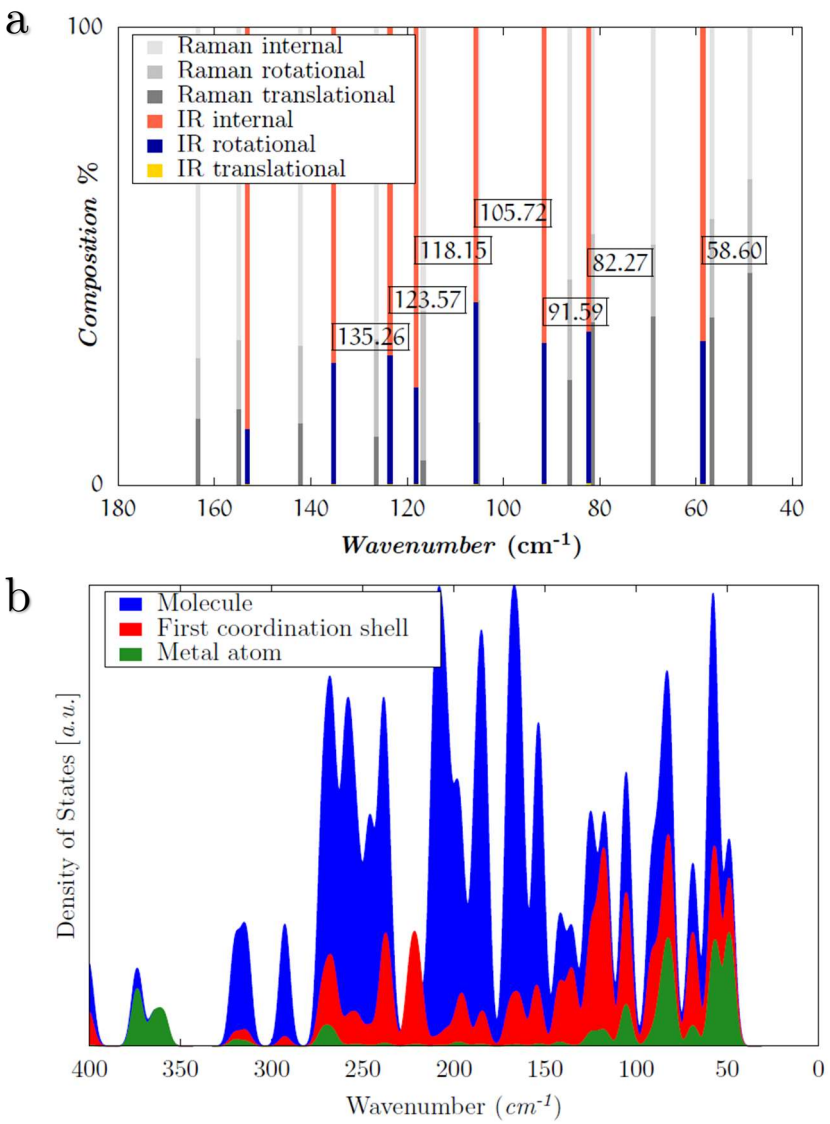

Figure 5.11. (a) Simulation of the vibrational modes for the single-molecule of **VOacac** and their decomposition in internal and external contributions. The IR-active modes are highlighted, whereas the Raman-active are in grey colour scale. (b) Density of states for the molecule, the first coordination shell and the metal atom. The images were taken from ref[10].

The density of states for the molecule, the first coordination shell and metal ion were also obtained by the theoretical investigation and are reported in Figure 5.11b. From this analysis an important feature emerges, that is, the metal ion displacements not only contribute to the typical modes in the 300-400 cm^{-1} range, but they are strongly involved also in the lowest energy vibrations. This points out to the key role of the low-energy vibrational modes in affecting the spin-lattice relaxation.

5.4 Analysis and discussion of the results

The models here used are variations of those described in Chapter 3. All the fits were performed by using the Matlab's script FMinuit[11] and the results of the analysis are reported and discussed in the following section.

5.4.1 Analysis of ac susceptibility data

The temperature and magnetic field dependences of the relaxation time extracted by ac susceptibility measurements have been analysed adopting an approach similar to the one used in Chapter 4. However, in this case, the presence of the giant spin-phonon bottleneck complicates the analysis and comparison of the results. To accounts for this, the relaxation time as a function of temperature for the macro-crystalline sample, **M-VOacac** has been analysed through an expression that contains a direct process strongly affected by phonon bottleneck, in addition to the Raman process

$$\tau = 1/(a_{pb}T^{x}) + 1/(a_{Ram}T^{n}) \tag{5.2}$$

where a_{pb} is the coefficient of the direct process affected by phonon bottleneck, whose temperature dependence is described by the parameter x, and a_{Ram} is the coefficient for the Raman process with exponent n. It should be remarked that this expression is purely phenomenological, and it is not derived by theoretical basis. The best-fit parameters are reported in Table 5.3, while the fit is shown in Figure 5.3. On the other side, the temperature dependence of τ for the mid-ground, **m-VOacac**, and well-ground, **g-VOacac**, microcrystalline samples have been analysed with an expression containing a direct process mildly affected by phonon bottleneck, and thus with a power-law, x, between $x = 1$ and $x = 2$, together with a term related to the Raman process

$$\tau = (a_{dir-pb}T^{x} + a_{ram}T^{n})^{-1} \tag{5.3}$$

where a_{dir-pb} is the coefficient of the hybrid direct-bottleneck process. A similar expression, though with different inherent meaning, has been already met in eq. (4.6). Moreover, the difference between eq. (5.2) and eq. (5.3) can be again explained in analogy with the resistance of a circuit either in series or in parallel, as done in (§4.5.1). The best-fit parameters are reported in Table 5.3, while the fits are shown in Figure 5.3.

Table 5.3. Best-fit parameters obtained using the model in eq. (5.2) for the pristine macro-crystalline **M-VOacac** sample and that in eq. (5.3) for the mid-ground and well-ground microcrystalline samples, **m-VOacac** and **g-VOacac**, respectively. These models reproduce the temperature dependence of τ obtained by ac susceptometry measurements.

Eq. (5.2)	a_{pb} (ms^{-1} K^{-x})	x	a_{ram} (ms^{-1} K^{-n})	n
M-VOacac	$1.3(4) \cdot 10^{-3}$	4.8(2)	0.5(4)	2.8(2)
Eq. (5.3)	a_{dir-pb} (ms^{-1} K^{-x})	x	a_{ram} (ms^{-1} K^{-n})	n
m-VOacac	8.7(3)	1.8(1)	$3(1) \cdot 10^{-2}$	3.5(1)
g-VOacac	0.15(2)	1.0(fixed)	121(2)	3.2(1)

The comparison between the results obtained from the three samples, reported in Table 5.3, is complicated by the fact that different models were used, and for this reason they should be discussed separately. The word 'giant' for the spin phonon bottleneck affecting the pristine macro-crystalline sample of **VOacac** arises from the value of the temperature exponent of the direct process that is close to $x = 5$, instead of the usual maximum value $x = 2$. At higher temperature this slope reduces because of the weakening of the phonon bottleneck and the simultaneous strengthening of the Raman process, whose exponent is close to $n = 3$, in agreement to what found for the other vanadyl systems. A solid proof of the phonon bottleneck as origin of this anomaly in the spin-lattice relaxation comes from the dramatic changes in τ with crystallites dimensions (§3.3.8). Moreover, the Raman process at higher temperatures does not appear much disturbed by the changing of crystallite sizes. This agrees with the fact that phonon bottleneck effects can only influence the direct (and Orbach) process (§3.3.8). It is also remarkable that the huge temperature dependence promoted by phonon bottleneck strongly reduces below 5 K. Indeed, after this temperature the slope becomes ca. $x = 1.4$, which corresponds to a 'normal' case of phonon bottleneck affecting the direct process.

The mid-ground (**m-VOacac**) and well-ground (**g-VOacac**) samples, obtained by grinding the macro-crystallites, show milder phonon bottleneck effects: the former temperature dependence varies with $T^{1.8}$ at low temperature, whereas the latter behaves, above 5 K, following the typical linear-like direct process. This points out to an important reduction of the phonon bottleneck strength for the ground crystal samples. It should be stressed that spin-phonon bottleneck is still a not well-understood phenomenon, for which it is impossible to predict when and how they occur.

The magnetic field dependences of τ for both macro- and micro-crystalline samples of **VOacac** have been reproduced using the Brons-van Vleck model as previously expressed in eq. (4.10). However, in this case it is considered the possibility to have a reduced magnetic field dependence of the direct process when this is strongly affected by bottleneck ($\tau^{-1} \propto cB^n$, with $n = 4$), for which

$$\tau = \left(cB^n + d\frac{1+eB^2}{1+fB^2} \right)^{-1}. \tag{5.4}$$

The best-fit parameters obtained for **M-VOacac**, **m-VOacac** and **g-VOacac** measured at 10 K are reported in Table 5.4, while the results of the fits are shown in Figure 5.3b.

Table 5.4. Best-fit parameters obtained using the model in eq. (5.4) to reproduce the magnetic field dependence of τ at 10 K for three compounds of **VOacac**: a macro-crystalline, a mid-ground and a well-ground sample.

$T = 10\ K$	c ($T^{-n}\ ms^{-1}$)	n	d (ms^{-1})	e (T^{-2})	f (T^{-2})
M-VOacac	$2.4(1) \cdot 10^{-3}$	2.82(4)	0.38(2)	3.4(2)	109(8)
	$5.5(3) \cdot 10^{-4}$	4(fixed)	0.5(1)	5.7(5)	178(53)
m-VOacac	$6.0(2) \cdot 10^{-4}$	4(fixed)	1.9(1)	6.2(6)	72(10)
g-VOacac	$6.4(1) \cdot 10^{-4}$	4(fixed)	3.9(3)	4.1(3)	53(6)

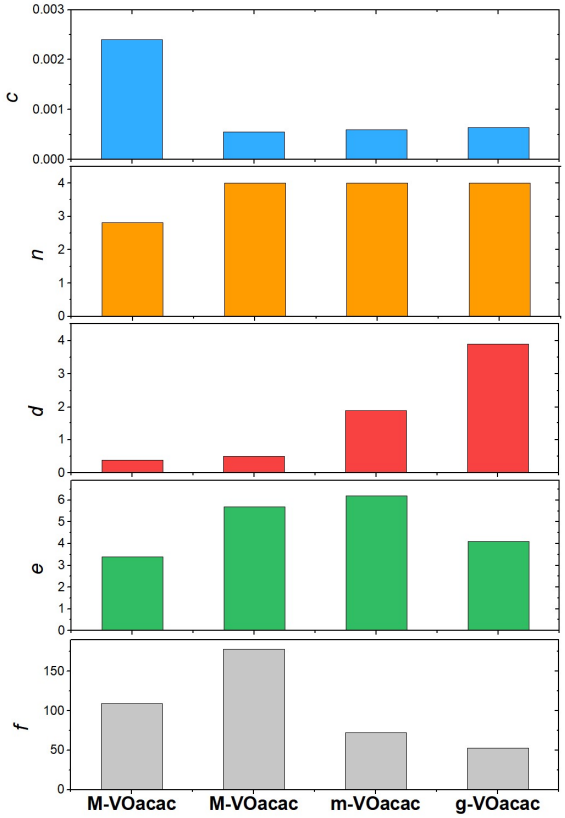

By looking at the results of Table 5.4 it is remarkable the change of magnetic dependence for the direct process from $\tau \propto B^4$ to $\tau \propto B^n$, with n within 2 and 3, for **M-VOacac** due to phonon bottleneck. Since the fit with B^4 scarcely reproduce the experimental data, only the parameters obtained by considering the term $B^{2.8}$ should be used to compare the results of **M-VOacac** with those of **m-VOacac** and **g-VOacac**.

Focusing on the various parameters, it is possible to see that the values of d grow as the crystallite dimensions are reduced, evidencing less efficient relaxation processes when phonon bottleneck occurs. On the contrary, the values of f decrease reducing the phonon bottleneck. This indicates that the external field is more effective in reducing the internal contributions when phonon bottleneck effects occur. Instead, a non-monotonous behaviour is observed for the parameter e.

The trend of the parameters above described, relative to **VOacac**, agrees with those of **VOdpm** (Table 4.15), though the phonon bottleneck affects differently the magnetic field dependence of such systems. Indeed, the magnetic field dependence of τ for **VOdpm-crys** (Figure 4.7c) seems strongly modified by the presence of bottleneck, whereas such a strong modification is less pronounced for τ of **M-VOacac** (Figure 5.5). However, the temperature dependence of τ indicates that phonon bottleneck effects are definitely more effective in **M-VOacac** rather than in **VOdpm**. From this comparison it emerges that the efficiency of phonon bottleneck may affect differently the temperature and magnetic field dependence of τ.

In Table 5.5 the best-fit parameters obtained for the macro-crystalline sample **M-VOacac** at the temperatures of 5, 10, 20 and 25 K are reported; the results of the fits are visible in Figure 5.5.

Table 5.5. Best-fit parameters obtained using the model in eq. (5.4) to reproduce the magnetic field dependence of τ at several temperatures for a macro-crystalline sample **M-VOacac**.

Crystals	c (T^{-n} ms^{-1})	n	d (ms^{-1})	e (T^{-2})	f (T^{-2})
5.0 K	$1.58(7) \cdot 10^{-3}$	2.19(7)	$1.54(6) \cdot 10^{-2}$	6.2(6)	80(6)
10.0 K	$2.4(1) \cdot 10^{-3}$	2.82(4)	0.38(2)	3.4(2)	109(8)
20.0 K	$5.2(1) \cdot 10^{-3}$	2.9(1)	5.6(9)	5.1(5)	115(26)
25.0 K	$9.2(2) \cdot 10^{-3}$	2.8(1)	11.4(9)	6.2(3)	103(12)

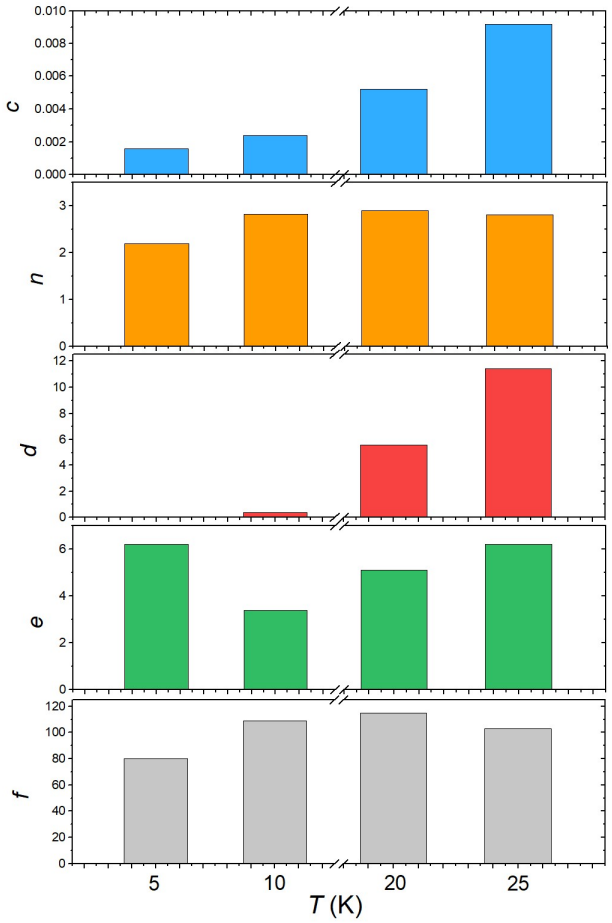

At 5 K and high magnetic field values, the rate of the direct process varies as $B^{2.2}$, that is the lowest magnetic field dependence found in the analysis for the direct process; for the other investigated temperatures, n, which is however different from its normal value $n = 4$, is close to 3. Moreover, the efficiency of the direct process, related to the parameter c, grows increasing the temperature and it is due to a gradual reduction of the phonon bottleneck. The more significant variation is found for the parameter d that increases with temperature, as also observed for the other vanadyl molecules. This can be attributed to an enhancement of the efficiency of the relaxation as the temperature is increased. Finally, the non-monotonous behaviour observed for the parameter e, which should be constant for the same sample, can be attributed to the presence of phonon bottleneck effects that somehow alter the contribution of the internal fields to the spin dynamics.

By recalling the analysis performed in the previous chapter about the temperature dependence of the Brons-van Vleck parameter d, from which it was possible to get insights on the vibrational modes involved in the spin-lattice relaxation, a similar approach has been attempted here. Indeed, also in this case the values of d exhibit an Arrhenius-like temperature dependence ($\tau \propto e^{A_{eff}/kT}$), and the linear fit of $ln(d)$ vs $1/T$

between 10-25 K provides an effective activation energy $A_{eff} = 38.7(9)$ cm^{-1}. By considering the relation $A_{eff} = \hbar\omega/2$ previously introduced (§4.5.3, eq. 4.12),[12] the vibrational mode $\hbar\omega = 77(2)$ cm^{-1} is obtained. This value agrees with the maximum of the vibrational mode at 77 cm^{-1} in the low temperature THz spectrum (Table 5.2). Thus, by following this analysis it appears that already between 10-25 K 'high' energy vibrational modes, such as that at 77 cm^{-1}, can play an active role in the spin-lattice relaxation.

The same analysis has been performed for the magnetic dependence of τ for **g-VOacac** relative to the temperatures 15, 17.5, 20 and 22.5 K; the best-fit parameters are reported in Table 5.6, while the fits are shown in Figure 5.5.

Table 5.6. Best-fit parameters obtained using the model in eq. (5.4) to reproduce the magnetic field dependence of τ at several temperatures for **g-VOacac**.

Powders	c (T^{-n} ms^{-1})	n	d (ms^{-1})	e (T^{-2})	f (T^{-2})
15.0 K	$6.8(2) \cdot 10^{-4}$	4(fixed)	9.0(3)	8.1(4)	60(4)
17.5 K	$7.5(2) \cdot 10^{-4}$	4(fixed)	11.9(3)	8.6(3)	64(3)
20.0 K	$8.7(2) \cdot 10^{-4}$	4(fixed)	15.0(4)	8.8(3)	65(3)
22.5 K	$1.02(5) \cdot 10^{-3}$	4(fixed)	18.3(5)	8.5(3)	63(3)

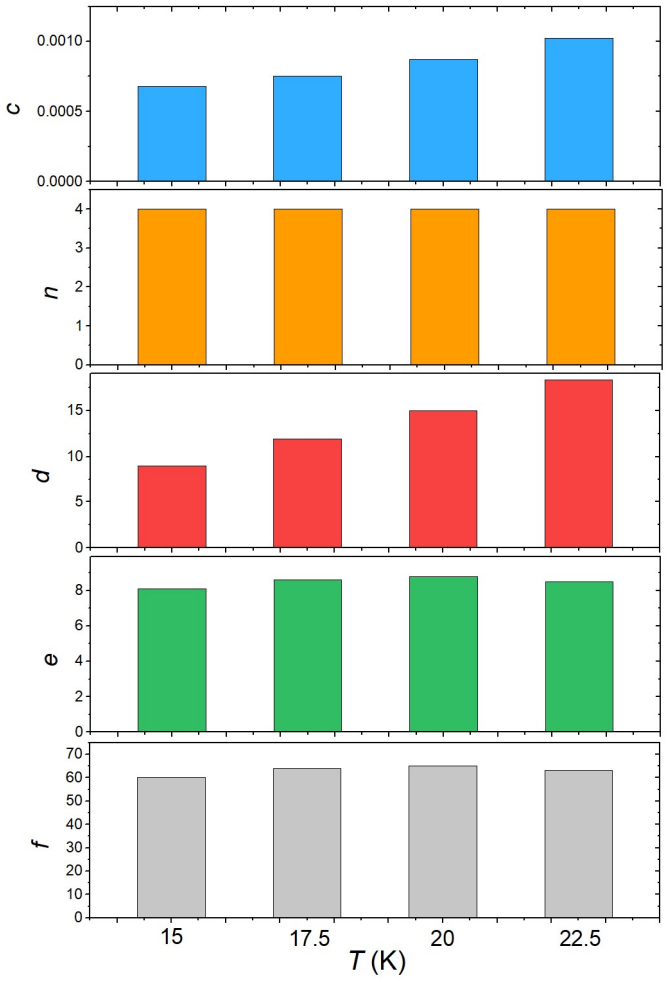

The standard Brons-van Vleck model (eq. 3.48) well-reproduces the magnetic field dependence of τ for the micro-crystalline powder sample of **VOacac**, pointing out that the change of the direct process dependence, parametrized in n, originates from phonon bottleneck effects. According to the previous findings, the parameters c and d grows as the temperature is increased. Instead, the parameters e and f remains constant, as evidenced also by the regular and unchanged shapes of τ in Figure 5.5. From the analysis of the temperature dependence of d, it emerges the contribution of one phonon (A_{eff} = 22(1) cm^{-1}), which well corresponds to the experimentally observed vibrational mode at $\hbar\omega = 44(2)$ cm^{-1} (Table 5.2).

5.4.2 More insights into the phonon bottleneck

Paper in Appendix

Giant spin-phonon bottleneck effects in evaporable vanadyl-based molecules with long spin coherence.

L. Tesi[+], A. Lunghi[+], M. Atzori, E. Lucaccini, L. Sorace, F. Totti and R. Sessoli. In: *Dalton Transactions* **45** (2016), pp. 16635-16643.

A qualitative analysis of the spin-phonon bottleneck has been performed through simple thermodynamic considerations and with the support of the calculated phonon dispersions and density of states. The analysis has been carried out by comparing the results achieved for **VOacac**, **VOdpm** and a third β-diketonate molecule, that is [VO(dbm)$_2$] (*dbm=dibenzoylmethanate*) and hereafter simply named **VOdbm** (Figure 5.12a).

These three molecules share the same vanadyl moiety and have β-diketonate ligands, for which similar coordination geometry and electronic structure are expected. The main difference lies in the terminal part of the ligands: hydrogen atoms for **VOacac**, methyl groups for **VOdpm** and phenyl groups for **VOdbm**. Thus, moving from the first to the last, the number of atoms in the molecule, the mass and the volume grow; these values, together with the spin density are reported in Table 5.7. It is worth noting that **VOacac** and **VOdbm** crystallize in almost isometric crystals with average dimensions around 1 mm; instead, **VOdpm** forms thin plates, few hundreds of μm thick, with an area of the largest face that can reach 2 mm^2.

Table 5.7. Comparison of the structural features of **VOacac**, **VOdpm** and **VOdbm**, useful to compare the influence of spin-phonon bottleneck effects on their spin relaxation.

Molecule/feature	Formula	Molecular weight (g/mol)	Cell volume (Å³)	Spin density (spin/nm³)
VOacac	$C_{10}H_{14}O_5V$	265.16	575.9	3.47
VOdpm	$C_{22}H_{38}O_5V$	433.47	1230.3	1.62
VOdbm	$C_{30}H_{22}O_5V$	513.4	2490.1	1.61

The temperature dependence of τ for macro- or micro-crystalline samples is different, as shown in Figure 5.3 for **VOacac** and in Figure 5.12b for **VOdpm** and **VOdbm**. This is a consequence of spin-phonon bottleneck effects. From their comparison it is possible to note that **VOacac** has the strongest phonon bottleneck effects, whereas **VOdbm** seems the less affected by this phenomenon.

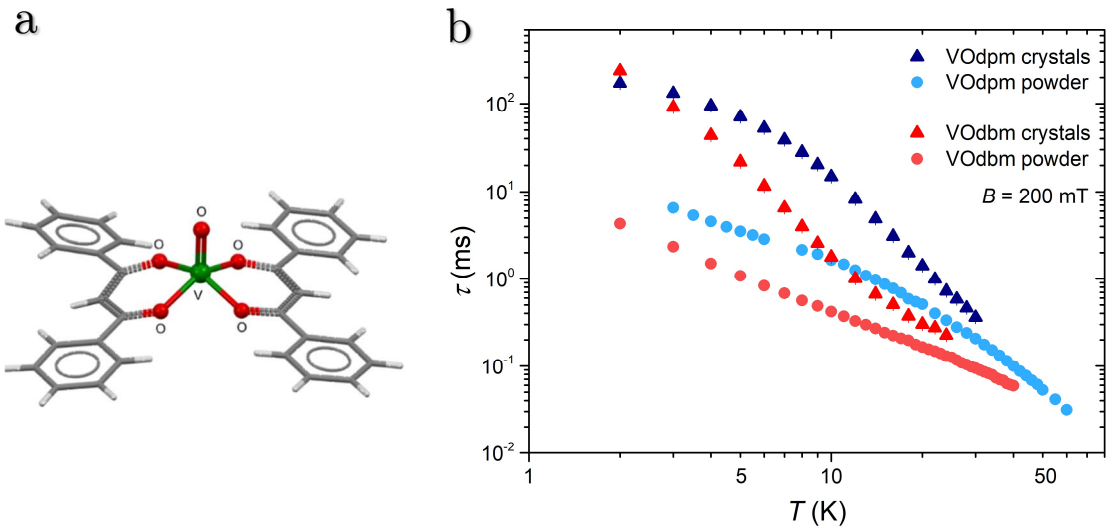

Figure 5.12. (a) Molecular structure of **VOdbm**; colour code: V=green, O=red, C=grey, H=light grey. (b) Temperature dependence of τ measured by ac susceptometry under a static magnetic field of 200 mT, for macro- and micro-crystalline samples of **VOdpm** and **VOdbm**. The relaxation times of **VOdpm** were already shown in Chapter 4 (Figure 4.7), but they are shown again for comparison.

To directly compare the effect of the crystallite size on τ, and thus the strength of bottleneck effects in the three investigated molecules, the ratio between the relaxation time τ measured on macroscopic and well-ground crystallites was calculated; this is reported in Figure 5.13.

The figure highlights a clear trend for the three compounds: the smaller the mass of the molecule, the higher is the temperature at which size effects become visible. Moreover, **VOacac** and **VOdbm** show a constant increase of the ratio $\tau(crystal)/\tau(powder)$ on lowering the temperature, whereas **VOdpm** reaches a plateau around 5 K. This is probably due to the different morphologies of the crystals: **VOacac** and **VOdbm** form

almost isometric crystals, while **VOdpm** forms thin plates from which phonons can more easily 'escape' toward the thermal bath.

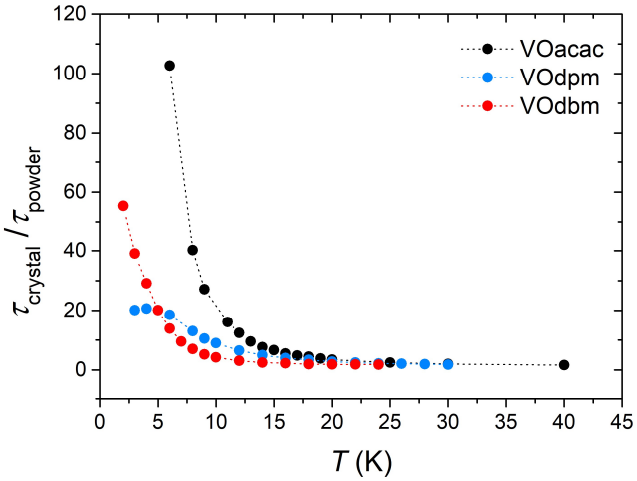

Figure 5.13. Ratio between the relaxation time measured by ac susceptometry of the macro- and micro-crystalline samples for **VOacac**, **VOdpm** and **VOdbm** as a function of temperature at 200 mT.

To provide a description of the paramagnetic relaxation in presence of spin-phonon bottleneck effects, Stoneham[13] decomposed the contributions of the relaxation time measured by ac susceptometry in two steps: *i)* the spin excitation is transferred to the phonons and *ii)* such an excitation is transferred from phonons to the thermal bath surrounding the crystalline sample. This is summarized in the expression

$$\tau = \tau_{SL} + \left(\frac{c_S}{c_L}\right)\tau_{LB} \qquad (5.5)$$

where τ is the spin-bath relaxation time, which is the physical quantity extracted by the ac susceptibility, τ_{SL} is the spin-lattice relaxation time, c_S is the specific heat of the spin system, c_L the lattice specific heat and τ_{LB} the lattice-bath relaxation time.

Following eq. (5.5), if τ_{LB} is sufficiently long, a variation of the magnetic ion concentration (equivalent to a variation of c_S/c_L) or of the crystallite sizes (equivalent to a change of τ_{LB}) results in a modification of the measured relaxation times. The rate-determining step for the phonon-bath exchange can involve either the transfer of energy in space (spatial bottleneck) or in frequency (spectral bottleneck). Stoneham observed that when a spatial bottleneck occurs, then $\tau \propto \tau_{LB}T^{-2}$ and $\tau_{LB} \propto D$, where D is the shortest dimension of the crystallite. The exponent $x = 2$ in $\tau \propto T^{-x}$, which originates from the specific heat ratio of eq. (5.5), is indeed the most commonly found for systems where phonon bottleneck is present.[14] However, van Vleck suggested that taking into

account the finite lifetime of phonons, τ_{LB} could also depend on temperature, in which case an exponent up to $x = 6$ can be expected.[15] This seems to be the case of **VOacac**.

In order to provide a microscopic link between the observed experimental behaviour of τ and the crystal structural features, simulations of the lattice dynamics were performed for **VOacac**, **VOdpm** and **VOdbm**. The phonons dispersions, shown in Figure 5.14, have been calculated along the symmetry directions X-Γ-Y-Γ-Z of the reciprocal space. The theoretical work has been performed by Dr. A. Lunghi at the Trinity College of Dublin; for more detail about the calculations, see ref[16].

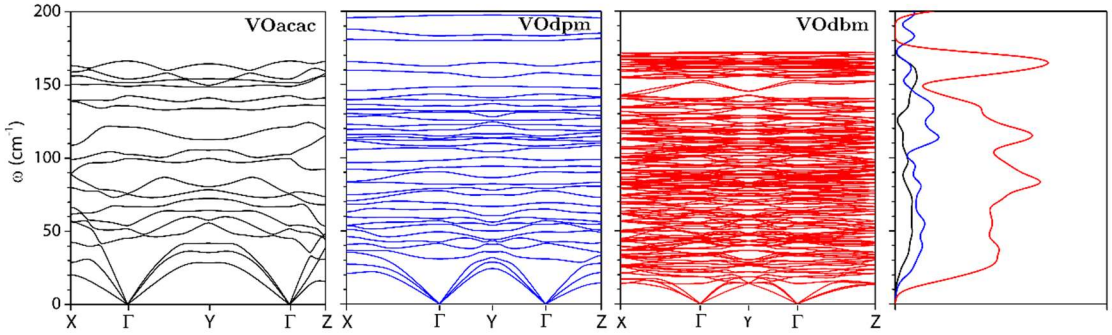

Figure 5.14. Dispersions of the vibrational modes of **VOacac**, **VOdpm** and **VOdbm** along the symmetric directions $X-\Gamma, Y-\Gamma$ and $Z-\Gamma$ (left), and their normalized vibrational DOS (right).

The most significant difference among the dispersions of the three molecules is the increased number of vibrational modes in the low energy region passing from **VOacac** to **VOdbm**. This is due to the increasing size of the unit cell and it is highlighted by the vibrational density of states (DOS) in Figure 5.14; indeed, the smallest density of states is computed for **VOacac**, whereas a much higher phonon density of states is computed for **VOdbm**.

As already mentioned, spin-phonon bottleneck effects are related to the inefficiency of the crystal lattice to dissipate the phonons created during the spin relaxation processes. Therefore, the possibility to have such effects can be related to the thermal conductivity (K) of the material where the spin is embedded in. According to the formula obtained from the Boltzmann transport equation (BTE)[17] and reported in eq. (5.6), each phonon, iq, in the system contributes to this property with three factors: the lifetime τ_{iq}, the group velocity v and the specific heat C_v:

$$K_{\alpha\beta} = \sum_{iq} C_{viq}\, v_{iq}^{\alpha}\, v_{iq}^{\beta}\, \tau_{iq}. \qquad (5.6)$$

At low temperature, the limiting factor of the thermal conductivity is expected to be the lack of heat carriers, *i.e.* the phonons, and this feature is accounted by the specific

heat. This assumption is also in agreement with the Stoneham model, eq. (5.5), where the ratio c_S/c_L gauges the effects on τ by the phonon relaxation time, suppressing them completely for high lattice specific heat. When the latter condition does not apply, non-equilibrium features, such as the phonon lifetime τ_{iq}, become relevant also for the spin dynamics. The specific heat of a given mode with energy $\hbar\omega_{iq}$ vanishes at 0 K and increases with temperature according to the expression

$$C_{viq} = k\left(\frac{\hbar\omega_{iq}}{2kT}\right)^2 cosech^2\left(\frac{\hbar\omega_{iq}}{2kT}\right). \tag{5.7}$$

The higher the phonon density of states near or below a certain kT, the higher is the value of C_v, according to eq. (5.7), and of K at that temperature, according to eq. (5.6), and therefore, the lower is the chance to observe spin-phonon bottleneck effects. By recalling the dispersion curves and DOS of the three investigated molecules (Figure 5.14), **VOacac** is expected to show spin-phonon bottleneck effects up to higher temperatures, with respect to **VOdpm** and **VOdbm**, because of its dramatic drop in the amount of accessible phonons at frequencies lower than 30 cm^{-1} (40 K). It should however be remarked that this is only a qualitative analysis based on simple thermodynamics considerations and a more detailed model should involve the coupling between the vibrational and spin degrees of freedom, which is in development.

It is interesting at this point to recall the experimental heat capacity (Figure 5.9). The contribution to the heat capacity below 20 K is attributed only to the acoustic phonons, according to the Debye temperature model

$$\frac{C_{Debye}}{R} = \frac{12\pi^4}{5}\left(\frac{T}{\theta_D}\right)^3 \tag{5.8}$$

where θ_D is the Debye temperature (§3.3.3). Above 20 K, the contribution of optical phonons cannot be neglected and the temperature dependence of the heat capacity departs from the Debye model. The Debye temperature extracted by fitting the heat capacity at zero field is $\theta_D = 84$ K. It should be noted that the use of a model is necessary since the heat capacity of the lattice cannot be estimated experimentally due to the lack of an isostructural diamagnetic analogue of **VOacac**.

Below 10 K, the magnetic heat capacity grows. As mentioned previously, this effect is caused by the Schottky anomaly and the specific onset of this growth depends on the value of the applied magnetic field. The magnetic heat capacity is given by the analytical expression

$$C_m = \frac{\partial}{\partial T}\langle \mathcal{H}_{mag} \rangle \tag{5.9}$$

where $\mathcal{H}_{mag}$ is the Hamiltonian of the magnetic system. The magnetic heat capacity between 0.25 and 1 T is well-reproduced by considering the spin Hamiltonian $\mathcal{H} = \mu_B \hat{\boldsymbol{S}} \cdot \boldsymbol{g} \cdot \boldsymbol{B} + \hat{\boldsymbol{I}} \cdot \boldsymbol{A} \cdot \hat{\boldsymbol{S}}$, and using the spin Hamiltonian parameters reported in Table 5.1. Instead, a mismatching between experimental and simulation occurs for the zero magnetic field data, which can be explained by considering the lack of dipolar interactions in the model used. The magnitude of the internal dipolar field can be estimated from this simulation and it is worth around 100 G.

The maximum of the Schottky anomaly corresponds to the point in which the difference between the heat capacity of spins and lattice is greatest. Indeed, the lattice heat capacity for that temperature is almost negligible, and thus, according to eq. (5.5), c_S/c_L is maximum. Given these conditions, the phonons are not able to dissipate the high heat capacity of the spin system and one could expect to find an increase of the spin-phonon bottleneck effects. To corroborate this hypothesis, the **VOacac** experimental heat capacity measured at 1 T (the same already reported in Figure 5.9), and the relaxation time τ, extracted by ac susceptibility from 1.9 to 40 K, and by the magnetization decays from 0.4 to 1.6 K for the same external magnetic field value, are compared in Figure 5.15.

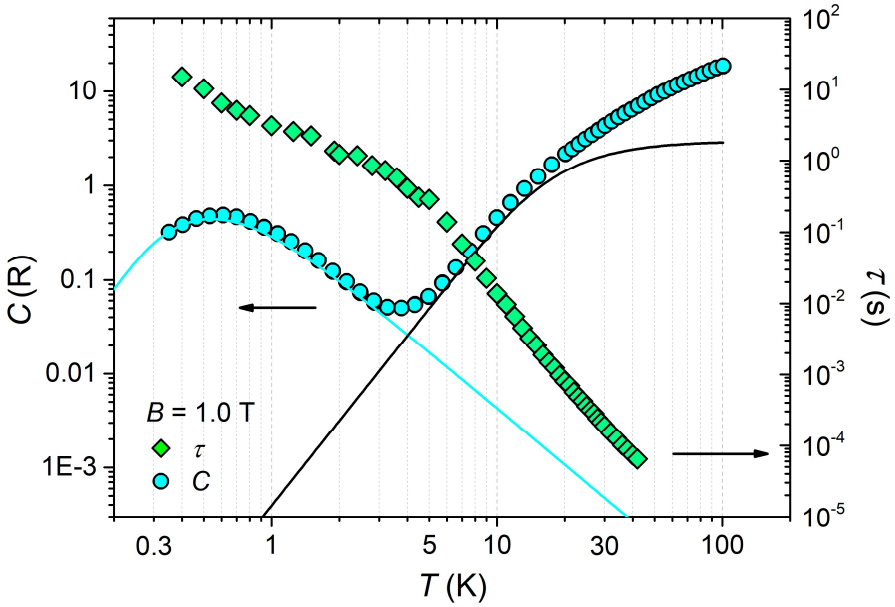

Figure 5.15. Temperature dependence of the heat capacity of a single crystal of **VOacac** under a static magnetic field of 1 T; and relaxation time τ extracted by ac susceptometry, between 1.9 and 40 K, and by magnetization decays, between 0.4 and 1.6 K, for **M-VOacac** under a static magnetic field of 1 T. The cyan solid line is the best-simulation for the magnetic heat capacity, while the black solid line is the best-fit for the lattice heat capacity.

The temperature dependence of the heat capacity of the whole crystal below 5 K is dominated by the Schottky anomaly relative to the electronic spin $S = 1/2$. For the magnetic field value of 1 T, the maximum of the magnetic heat capacity due to the Schottky anomaly is observed between 500 and 700 mK. Above this temperature, the heat capacity decreases again reaching a minimum at 3-4 K, and then it grows because of the increasing contribution of the lattice vibrations. Focusing now on the relaxation time τ, it is possible to identify four different regions. On increasing the temperature, τ varies as T^{-2} (below 1 K), $T^{-1.2}$ (between 1 and 5 K), T^{-4} (between 5 and 30 K) and T^{-3} (between 30 and 40 K). In principle, these different regimes may be attributed to the variation of the spin-phonon bottleneck efficiency (or, alternatively, to the inefficiency of the lattice in dissipating the excitation). Interestingly, the comparison shown in Figure 5.15 evidences a counterintuitive behaviour. According to eq. (5.5), the temperature dependence derives from (c_S/c_L), that is, the ratio between the spins and lattice heat capacity; the growth of this term corresponds to an increasing strength of the phonon bottleneck. As shown in Figure 5.15, at high temperature such a term is minimised, whereas it is maximum in correspondence of the maximum of the Schottky anomaly. However, the slopes of the temperature dependence of τ go in the opposite direction: the major contribution of this effect can be found between 5 and 30 K, whereas the minor one is between 1 and 5 K. On the other hand, though it seems that simple models such as eq. (5.5) are not able to explain the varied temperature dependences of τ introduced by the phonon bottleneck, it is worth to remember that the strength of phonon bottleneck effects continuously grows as temperature is decreased. Indeed, by recalling Figure 5.3, the relaxation times between the macro-crystalline and micro-crystalline samples have the greatest difference at low temperature. This is, thus, in agreement with eq. (5.5).

Concerning the different slopes highlighted in Figure 5.15, it is not clear if the presence of different types of vibrational modes, whether acoustic or optical, may produce changes in the phonon bottleneck influence. The first low-energy vibrational mode is observed at 44 cm^{-1}, and it could be expected that it affects the spin relaxation already around 5-10 K (the magnetic analysis between 10 and 25 K for **M-VOacac** evidenced the contribution of the vibrational mode at 77 cm^{-1}). However, below 5 K only the acoustic modes (within the entire Brillouin zone) should be sufficiently populated to participate in the relaxation. This leads to two relevant questions:

1. May the rapid change of temperature dependence of τ be due to the transition from a situation in which both the acoustic and optical modes contribute to the relaxation to another in which only the acoustic modes contribute?
2. Are the theoretical calculations of the vibrational dispersions of **VOacac** sufficiently accurate and reliable?

While the answer to the former question is unknown, to reply to the latter question, 4D-Inelastic Neutron Scattering (4D-INS) measurements were performed.

5.5 4D Inelastic neutron scattering

Article in preparation

Unveiling phonons in a prototype molecular quantum bit with four-dimensional inelastic neutron scattering.

E. Garlatti, L. Tesi, T. Guidi, M. Atzori, A. Lunghi, D. Voneshen, R. Sessoli and S. Carretta

Neutron Scattering (NS) is a powerful technique that allows to obtain information on the static properties, such as the atomic structure, and dynamics features, such as the collective atomic motions of condensed matter. Indeed, neutron wavelengths are comparable to the interatomic spacings, while their kinetic energy is comparable with that of atoms in condensed matter. In addition, they are highly penetrating, making them suitable to investigate bulk materials. Neutrons not only interact with nuclei via strong nuclear force but, thanks to their non-zero magnetic moment, they can also interact with unpaired electrons of atoms (magnetic scattering). In the scattering process the neutron energy can be either unchanged (elastic scattering) or transferred to the sample (inelastic scattering). Moreover, unlike photons, neutrons have non-zero mass for which they can transfer momentum $\hbar\boldsymbol{Q}$ to the sample, where $\boldsymbol{Q}$ is the scattering vector.

In this work, Inelastic Neutron Scattering (INS) technique has been used to directly investigate the lattice dynamics of **VOacac** by measuring the phonons energies and dispersions in a wide portion of the reciprocal space and for several different neutron incident energies. Such an investigation has been performed in collaboration with Dr. E. Garlatti of the group of Prof. S. Carretta at the University of Parma. It should also be highlighted that this was the first time that such an investigation was performed on molecular magnets.

In general, INS is one of the most employed technique to investigate both phonon density of states and lattice dispersion relations. The investigation of single crystals provides information on the phonon energy through $\hbar\omega$, whereas the information on their dispersions and polarizations is contained in the $\boldsymbol{Q}$ dependence. Instead, if the measurements are performed on a microcrystalline powder sample, the information on $\boldsymbol{Q}$ is lost, so that it is still possible to obtain information such as the density of states, but nothing can be known about their dispersions. The capability of INS to give access to the vibrational dispersions is the main advantage of this technique, and it represents also the main difference with optical spectroscopic techniques such as IR or Raman. Indeed,

coherent INS enables to measure the correlation between the atom i-th at time zero and the atom i'-th at time t, thus giving access to the collective normal modes of vibration of the atoms within the crystal, *i.e.* the phonons.[18, 19] The inelastic one-phonon scattering is described by the 4-dimensional function $S(\boldsymbol{Q},\omega)$, which is called *scattering function.*[20] This function is related to the inelastic scattering cross-section $d\sigma^2/d\Omega dE$, which is what is effectively measured

$$\begin{aligned}&\frac{d\sigma^2}{d\Omega dE} \propto \\ &S(\boldsymbol{Q},\omega) = \sum_{j,q} \delta(\boldsymbol{Q}+\boldsymbol{q}-\boldsymbol{G})\left|F_q^j(\boldsymbol{Q})\right|^2 \frac{1}{2\omega_j(\boldsymbol{q})}[n_j(\boldsymbol{q})\delta(\omega \\ &\qquad + \omega_j(\boldsymbol{q})) + (n_j(\boldsymbol{q})+1)\delta(\omega-\omega_j(\boldsymbol{q}))]\end{aligned} \tag{5.10}$$

where $\hbar\omega_j$ are the energies of phonons. The index j runs over the $3N$ modes, where N is the number of atoms in the unitary cell, of which 3 are the acoustic phonons and $3N-3$ are the optical phonons. The phonon wavevector $\boldsymbol{q}$ is selected by the momentum conservation $\boldsymbol{Q} = \boldsymbol{k'} - \boldsymbol{k} = \boldsymbol{G} \pm \boldsymbol{q}$, where k and k' are the initial and final neutron wavevectors, respectively, and $\boldsymbol{G}$ is the reciprocal lattice vector of the sample. Moreover, n_j is the phonon Bose factor, which is related to the number of phonons available at the temperature of the sample, and $F_q^j(\boldsymbol{Q})$ is the *pair correlation function* expressed as

$$F_q^j(\boldsymbol{Q}) = \sum_d \frac{b_d}{\sqrt{m_d}} e^{iQ\cdot d}(\boldsymbol{Q}\cdot\sigma_{j,d}(\boldsymbol{q})) \tag{5.11}$$

where d are the atoms in the unitary cell; b are their coherent neutron scattering lengths and m_d their masses,[21] and $\sigma_{j,d}$ is the polarisation vector of the phonon from branch j and wavevector $\boldsymbol{q}$.[20] Longitudinal and transverse phonons can be distinguished by properly choosing the relative direction between $\boldsymbol{q}$ and $\sigma_j(q)$. For example, the longitudinal mode is observed when $\boldsymbol{q}$ and $\sigma_j(q)$ are parallel, whereas the transverse modes are visible for specific configurations of these two variables.

The measurements on **VOacac** were performed at the ISIS Neutron and Muon Source on LET. This is a multi-chopper direct geometry cold neutron time-of-flight spectrometer combining a wide dynamic range, 0.6-80 meV (4.8-645 cm^{-1}), with a series of position sensitive detectors covering a wide scattering angle, from 5 to 140 degrees horizontally and ±30° vertically. Data are collected as a function of the crystal orientation (θ) in a series of small angular steps to cover wide portions of the reciprocal space in every direction. The obtained data are then combined to produce a four-dimensional volume, $Q_x \times Q_y \times Q_z \times E$, where Q_i are the three components of the momentum transfer vector $\boldsymbol{Q}$ and E is the energy transferred to the sample. The multi-chopper system of LET

works in repetition rate multiplication mode, which allows to measure simultaneously with different incident energies. The incident energies used in this study were: 4.7 (37.9), 7.3 (58.9), 13 (104.8) and 27 (217.8) meV (cm^{-1}), but the most informative energies are 7.3 and 13 meV, since by increasing the incident energy the experimentally accessible energy range of the phonon spectrum increases, but at the same time the resolution worsens. Further information about the LET@ISIS instrument can be found in (R. I. Bewley et al., 2011).[22]

The investigated sample was composed by 40 co-aligned crystals of highly deuterated **VOacac** in order to reproduce an effective single crystal of about 1 g of weight. Every crystal has been indexed using a single-crystal X-ray diffractometer, from which four crystalline families were selected. These were identified by considering their most developed faces: [011], [0-1-1], [101] and [-10-1]. The crystalline face [100] was present in all the considered crystalline families and, moreover, it was large enough to be used as base of the crystals once these were placed on the sample-holder. Depending on the crystalline family, different sample-holder plates were designed. The 40 crystals were aligned by using the elastic neutron scattering beamline ALF at ISIS, and then fixed over the plates with a hydrogen-free grease. The crystals were aligned so that the reciprocal axis vector b_1 ($\Gamma - \mathrm{X}$) is perpendicular to the plane of the plate, whereas b_2 ($\Gamma - Y$) and b_3 ($\Gamma - Z$) lie in that plane. The plates were then assembled on a custom-designed sample-holder that is shown in Figure 5.16a. The accuracy of the alignment has been confirmed by the Bragg peaks, and the final crystalline mosaicity has been estimated at $\pm 5°$. All the INS measurements at LET have been performed at 5 K. As a final stage, the empty sample-holder was measured for the background subtraction. The four-dimensional data have been analysed using the software Horace;[23] the integration over a certain interval of two out of the four dimensions allows to obtain a three-dimensional image as shown for example in Figure 5.16b, where the integration has been made around $Q_x = 0$ and around $E = 0$.

Looking at the elastic scattering ($E = 0$), it is possible to observe the Bragg peaks in the accessible portion of the reciprocal space (Figure 5.16b); it should be underline that the neutron wavelength for 13 meV is of the order of few Å. By choosing a specific Bragg peak and varying the energy it is possible to follow the dynamics of the phonon in a defined symmetry direction. It is important to note that **VOacac** has a triclinic space group; the critical points and symmetry directions are reported in Figure 5.16c.

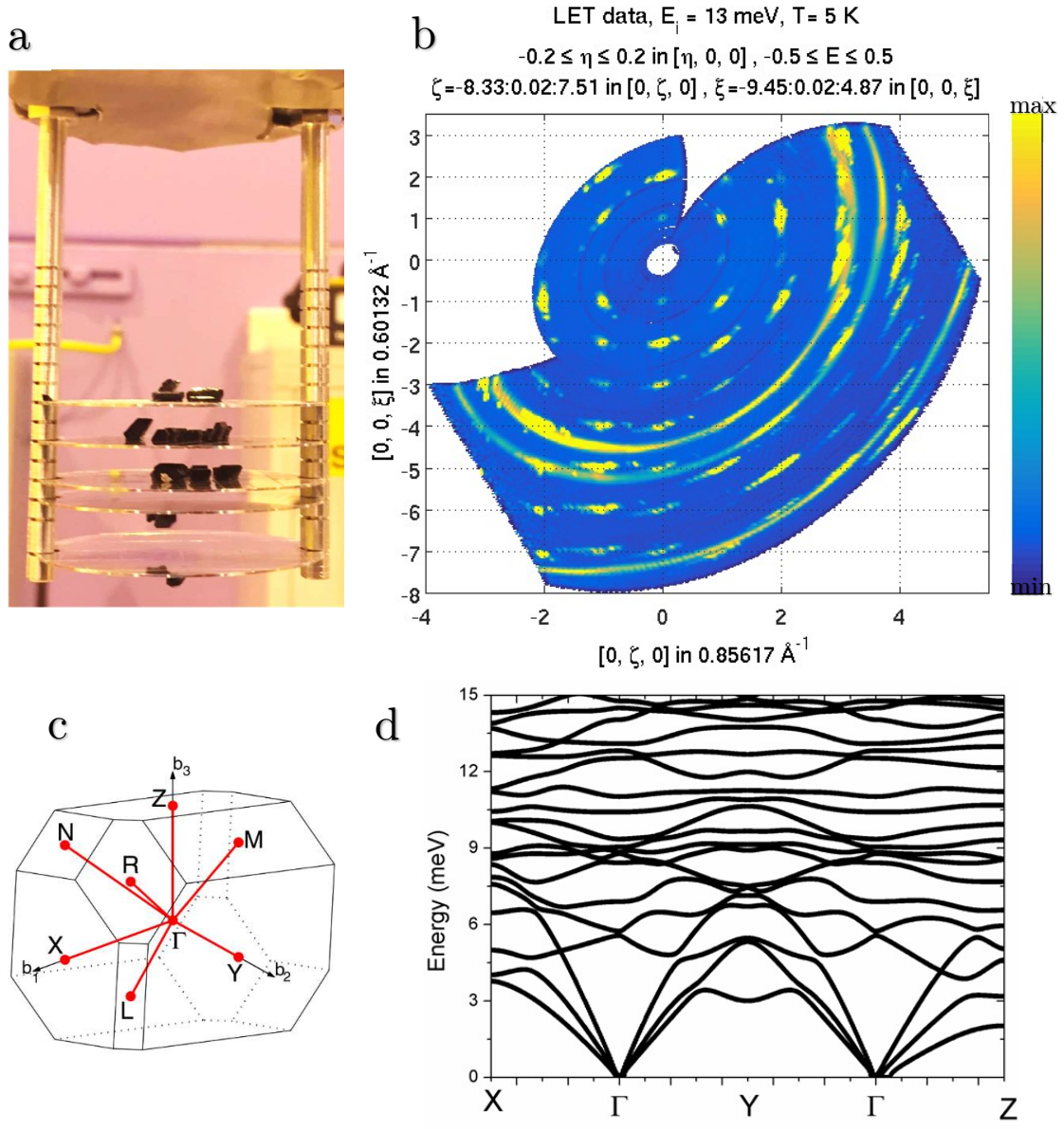

Figure 5.16. (a) Image of the custom-designed sample-holder containing the effective single-crystal of **VOacac** composed by 40 smaller single-crystals. (b) Example of the elastic scattering plane as a function of Q_z (indicated as [0,0,ξ]) and Q_y (indicated as [0,ζ,0]) and integrating Q_x (indicated as [η,0,0]) around zero. The colour scale evidences the intensity of the signal. The values reported above indicate the range of integration. The rings visible in the plane are due to the sample-holder contributions, which have been subtracted during the data analysis. (c) Scheme of the principal directions in the reciprocal space for a triclinic lattice (from Ref.[24]). (d) Phonons dispersions calculated by *ab initio* methods. The image has been taken by Figure 5.14.

In our experiments only the principal directions b_1, b_2 and b_3 were analysed (Figure 5.16c and Figure 5.16d). The dispersions of the longitudinal and transverse phonons for the direction b_3 are shown in Figure 5.17 and Figure 5.18 for the 7.3 and 13 meV energies, respectively. All the experimental spectra have been corrected by subtracting the empty

sample-holder contributions and a flat background due to multiple-scattering, which is constant in all the explored regions of the reciprocal space at low Q values. To compare the experimental spectra obtained by INS, the vibrational dispersions of **VOacac** were simulated by using the phonon energies $\hbar\omega_j$ and eigenvectors σ_j obtained through DFT calculations to evaluate the scattering function of eq. (5.10). The theoretical outcomes are reported in Figure 5.17(b,d) and Figure 5.18(b,d).

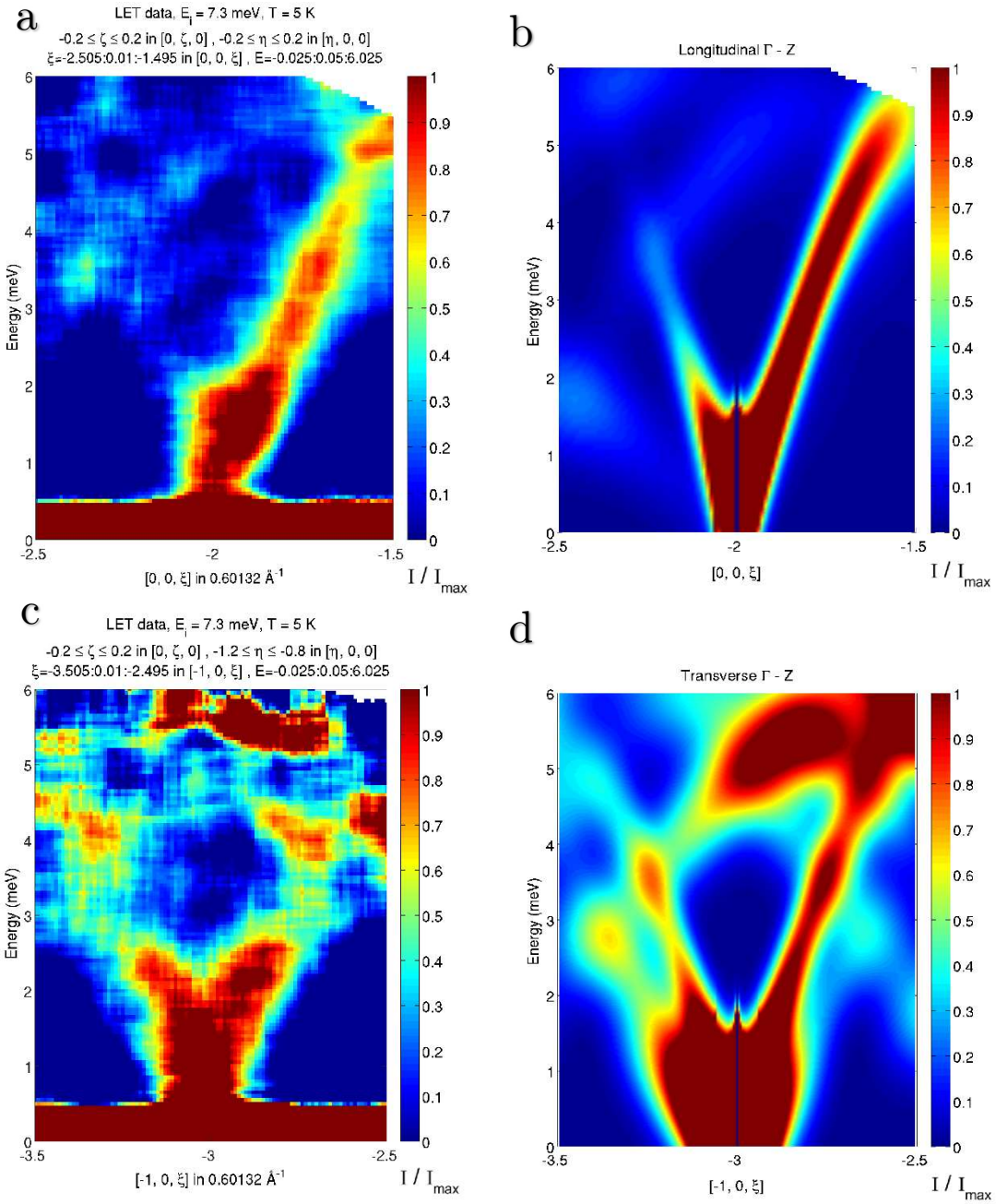

Figure 5.17. Experimental dispersion curves of the longitudinal (a) and transverse (c) modes in the symmetry direction $\Gamma - Z$ measured by 4D-INS, using an incident neutron energy of 7.3 meV. The simulation of the dispersion curves (b) and (d) were also obtained, by calculating the scattering function of eq. (5.10) starting from the DFT outputs.

The spectra obtained using an incident neutron energy of 7.3 meV for $\Gamma - Z$ show the dispersion of longitudinal (Figure 5.17a) and transverse (Figure 5.17c) acoustic modes between 0 and 6 meV. The former has been obtained integrating both Q_x and Q_y around zero and plotting the energy as a function of the direction Q_z. Instead, the transverse mode has been obtained integrating Q_x around -1 and Q_y around zero, and then plotting the energy as a function of Q_z. The agreement between experimental and simulated spectra is remarkable, highlighting the robustness of the analysis. However, it should be noted that the simulated modes were corrected of about 13% in energy. This discrepancy is probably due to the limitation of DFT for reproducing correctly the van der Waals interactions. From the collected data it is, indeed, evident that the three acoustic modes are inherently mixed together, for which features of transverse modes are present also in the experimental and simulated spectra of the longitudinal one. This mixing is due to the very low symmetry of the crystal.

By comparing the experimental and simulated spectra it is possible to note that not only the phonon energies and dispersions, but also the intensities of the modes are in very good agreement. This means that DFT calculations are well-reproducing both the phonon energies and their eigenvectors.

As mentioned previously, by increasing the neutron incident energy the dynamic range expands. In this case the use of the 13 meV energy allows to extend the spectrum up to 11 meV (88.7 cm^{-1}), where optical modes are also clearly evident for the direction $\Gamma - Z$, and in particular for the longitudinal direction (Figure 5.18a). On the other hand, on increasing the energy the resolution decreases and the comparison seems of slightly lower quality with respect to the spectra at 7.3 meV. Even in this case, however, the experimental data are well-reproduced by the simulations, which, remarkably, are also able to reproduce the optical modes, *e.g.* the left corner of Figure 5.18(a,b).

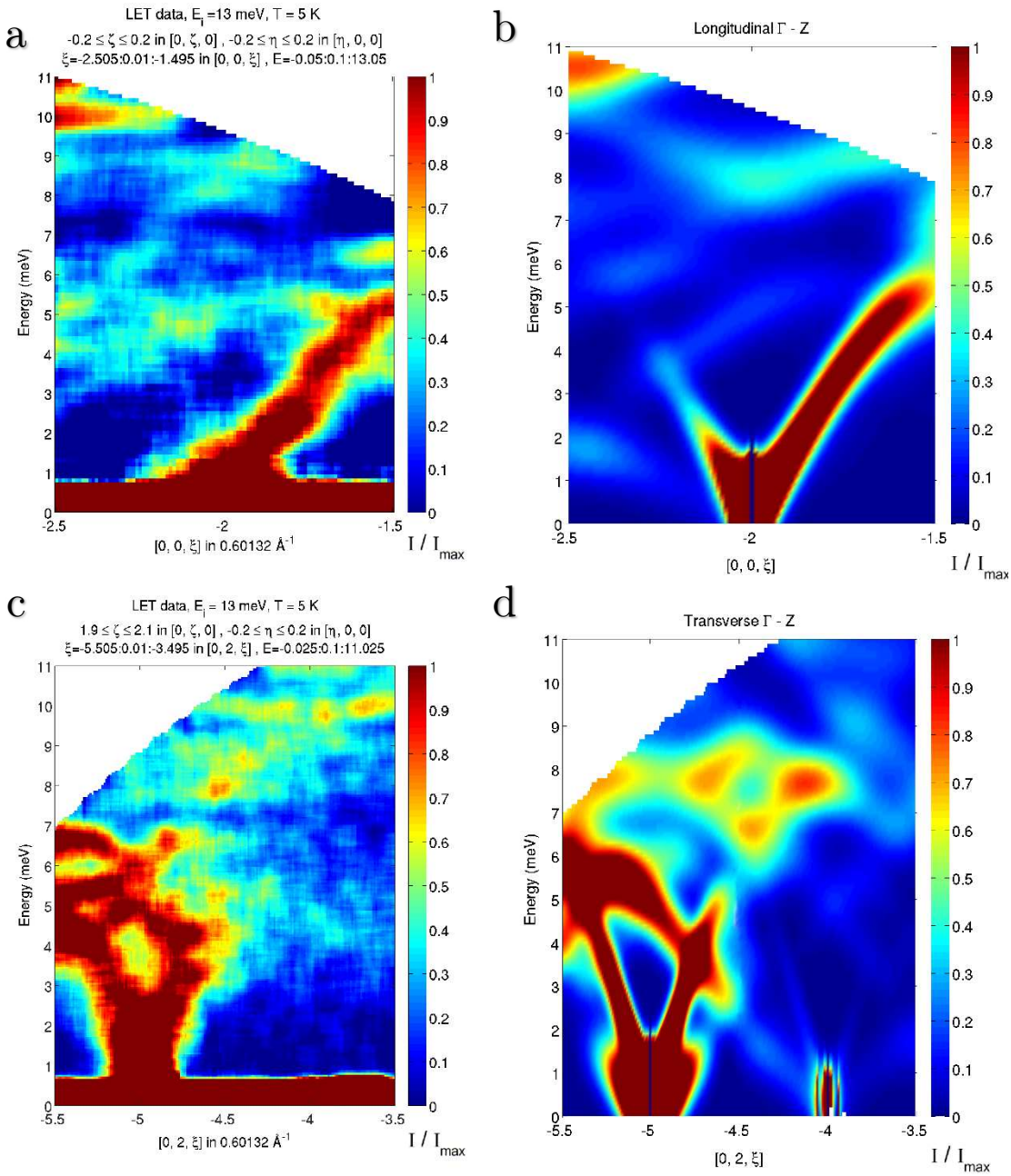

Figure 5.18. Dispersion curves of the longitudinal (a) and transverse (c) modes in the symmetry direction $\Gamma - Z$ measured by 4D-INS, using an incident neutron energy of 13 meV. The simulation of the dispersion curves (b) and (d) were also obtained, by calculating the scattering function of eq. (5.10) starting from the DFT outputs.

An example of vibrational dispersion in the direction $\Gamma - X$ and corresponding to the 13 meV incident energy is reported in Figure 5.19.

The phonon dynamics for the $\Gamma - X$ direction shown in Figure 5.19 originates from the same Bragg peak whose dynamics has been explored in the $\Gamma - Z$ direction and reported in Figure 5.17c. Once more, the agreement between the experimental and theoretical data is very high, for which both the energies and dispersions of the acoustic and optical modes are very well reproduced.

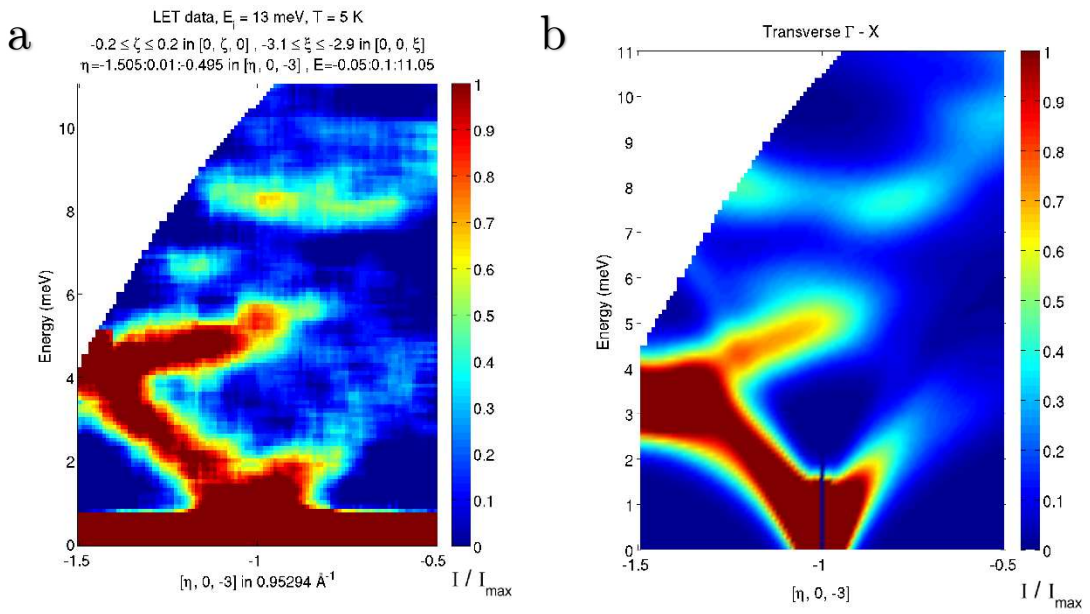

Figure 5.19. Dispersion curve of the transverse modes in the symmetry direction $\Gamma - X$ measured by 4D-INS, using an incident neutron energy of 13 meV (a). The simulation of the dispersion curve (b) was also obtained by calculating the scattering function of eq. (5.10) starting from the DFT outputs.

Other directions as well as other spectra recorded for higher neutron incident energies are still under analysis. It should be stressed that this was the first time that phonon dispersions were measured for molecular magnets, and this has been possible thanks to a combination of factors: the optimal characteristics of LET beamline and the possibility to obtain very large and deuterated single crystals for **VOacac**, together with the possibility to perform DFT calculations of its phonon dispersions. Moreover, because of the high number of aligned crystals and the very low symmetry of the crystal, this experiment has been very challenging. This investigation has confirmed the right track of the theoretical vibrational dispersion calculations and it represents an important step toward the comprehension of the mechanisms behind the spin-lattice relaxation.

5.6 Conclusions

The chapter focused on the investigation of $[VO(acac)_2]$, or **VOacac**, that is a vanadyl-based molecule with the simplest possible β-diketonate ligand. This molecule, like the vanadyl-based molecules previously investigated, presents the same main features that make these systems potential spin qubits; however, the relaxation times T_1 and T_m previously investigated by pulsed EPR were not studied here. **VOacac** has been instead chosen as model to improve our understanding about the mechanisms behind the spin-lattice relaxation. This has been possible thanks to a multitechnique approach flanked by theoretical calculations.

The magnetic field and temperature dependence of the relaxation time τ, as well as the crystallite size dependence, evidenced the presence of a giant spin-phonon bottleneck whose effect is to lengthen the relaxation times up to few seconds. Butterfly-shape hysteresis were even recorded at 0.4, 0.6 and 1 K for three different orientations of a single crystal: one with the external magnetic field applied parallel to the vanadyl moiety and the other two perpendicular to it. From these measurements two main aspects emerge: a small but evident opening at zero field, probably due to the hyperfine interaction, and three different openings of the hysteresis depending on the orientation. This inherent anisotropy in the magnetization dynamics of **VOacac** can be attributed either to the hyperfine or g anisotropy, and a theoretical model is in development to solve this ambiguity.

In order to improve the comprehension about the outcomes of the magnetic measurements, a detailed spectroscopic investigation has been made through THz spectroscopy, by recording the evolution of the vibrational spectrum of a microcrystalline sample of **VOacac** from 300 to 10 K. At low temperature the vibrational spectrum is composed by few vibrational modes, with the first at 44 cm^{-1}. Compared with other systems, this value is quite high in energy. Furthermore, the magnetic analysis suggests the involvement of this vibrational mode on the spin relaxation for the microcrystalline sample measured between 5 and 22.5 K. Instead, the same analysis for the macro-crystalline sample affected by phonon bottleneck and measured up to 25 K shows that, in this case, the vibrational mode at 77 cm^{-1} influences the spin relaxation. Both these vibrational modes values obtained by analysing the magnetic data, result present in the experimental THz spectrum of low temperature. The importance of such low-energy vibrational modes is remarked by the theoretical density of states, for which a strong effect on the displacement of the metal ion occurs because of these.

The complex behaviour of spin-phonon bottleneck effects has been evidenced from the temperature dependence of τ obtained between 0.4 and 40 K through magnetization decays and ac susceptometry. Attempts to explain this behaviour were made by

comparing the ac susceptibility outcomes with the measured temperature dependence of the heat capacity for a single crystal of **VOacac**. By considering a simple thermodynamic approach, for which the thermal conductivity is mainly provided by the heat capacity of the lattice, which in turn depends on the vibrational density of states, it is possible to explain the different onset of phonon bottleneck effects for **VOacac** and two others β-diketonate coordinated molecules. This model, also supported by heat capacity measurements, agrees with a stronger presence of spin-phonon bottleneck at low temperature. However, no explanations were found for the varied temperature dependences of the relaxation time of **VOacac** when affected by phonon bottleneck. It should be remarked that a better comprehension of this phenomenon, which is still missing, could lead to predict when the phonon bottleneck occurs, and hopefully also to control it. Some question remains open, for example if differences in the influence of the spin-phonon bottleneck observed on lowering the temperature can be attributed to the passage from a regime where both acoustic and optical vibrational modes are involved, to another in which only acoustic phonons are effective.

To obtain more insights into the acoustic and optical vibrational modes, the investigation of the vibrational spectrum of **VOacac** has been extended also beyond the Γ-point of the Brillouin zone, by measuring the phonon dispersions through 4D-INS. The experiment was performed on a virtual single crystal, composed by 40 highly deuterated **VOacac** single-crystals, by using the beamline LET at ISIS. This instrument has a very wide detection angle and it allows to measure the neutron scattering at several different incident energies simultaneously. Despite the challenging investigation, the acoustic and low-energy optical phonons dispersions were successfully measured. The comparison with DFT theoretical calculations evidenced a very good agreement between experiment and theory.

Many efforts have been made to understand in detail the mechanisms behind the spin-lattice relaxation, but this work cannot be considered concluded. The understanding of the role of the acoustic and optical vibrational modes outside the Γ-point in inducing spin relaxation, as well as the measurement and analysis of the Raman-active vibrational modes are still open projects. Moreover, the complete theoretical modellization of the spin-lattice relaxation of **VOacac** through the analysis of the phonon dispersions and the calculations of the spin-phonon couplings is also in progress.

5.7 Bibliography

1. S. Stoll and A. Schweiger, *J. Magn. Reson.*, 2006, **178**, 42-55.
2. A. Abragam and B. Bleaney, *Electron Paramagnetic Resonance of Transition Ions*, Dover, New York, 1986.
3. D. Gatteschi, R. Sessoli and J. Villain, *Molecular nanomagnets*, Oxford University Press, Oxford, UK, 2006.
4. F. L. Mettes, F. Luis and L. J. de Jongh, *Physical Review B*, 2001, **64**, 174411.
5. A. Taschin, P. Bartolini and R. Torre, *Meas. Sci. Technol.*, 2017, **28**.
6. J. Tasseva, A. Taschin, P. Bartolini, J. Striova, R. Fontana and R. Torre, *Analyst*, 2017, **142**, 42-47.
7. J. Hutter, M. Iannuzzi, F. Schiffmann and J. VandeVondele, *Wiley Interdisciplinary Reviews: Computational Molecular Science*, 2014, **4**, 15-25.
8. J. VandeVondele, M. Krack, F. Mohamed, M. Parrinello, T. Chassaing and J. Hutter, *Comput. Phys. Commun.*, 2005, **167**, 103-128.
9. R. Sabatini, T. Gorni and S. de Gironcoli, *Physical Review B*, 2013, **87**, 041108.
10. A. Albino, Master thesis, University of Florence, 2018.
11. G. Allodi, 1996-2010, copyright CERN.
12. A. Lunghi, F. Totti, R. Sessoli and S. Sanvito, *Nature Communications*, 2017, **8**, 14620.
13. A. M. Stoneham, *Proceedings of the Physical Society*, 1965, **86**, 1163.
14. B. W. Faughnan and M. W. Strandberg, *J. Phys. Chem. Solids*, 1961, **19**, 155-166.
15. J. H. van Vleck, *Phys. Rev.*, 1941, **59**, 730-736.
16. L. Tesi, A. Lunghi, M. Atzori, E. Lucaccini, L. Sorace, F. Totti and R. Sessoli, *Dalton Trans.*, 2016, **45**, 16635-16643.
17. A. J. H. McGaughey and M. Kaviany, *Physical Review B*, 2004, **69**, 094303.
18. N. W. Ashcroft and N. D. Mermin, *Solid state physics*, Saunders, Philadelphia, 1976.
19. C. Kittel, *Introduction to Solid State Physics*, John Wiley & Sons, Inc., New York, 1986.
20. S. W. Lovesey, *Theory of neutron scattering from condensed matter.*
21. A.-J. Dianoux and G. Lander, *Neutron Scattering Lengths in ILL Neutron Data Booklet*, Philidelphia, PA., second edition edn., 2003.
22. R. I. Bewley, J. W. Taylor and S. M. Bennington, *Nucl Instrum Meth A*, 2011, **637**, 128.
23. R. A. Ewings, A. Buts, M. D. Le, J. van Duijn, I. Bustinduy and T. G. Perring, *Nuclear Instruments and Methods in Physics Research Section A: Accelerators, Spectrometers, Detectors and Associated Equipment*, 2016, **834**, 132-142.
24. W. Setyawan and S. Curtarolo, *Computational Materials Science*, 2010, **49**, 299-312.

Chapter 6

Exploring New Techniques for Spin Dynamics Investigation

The spin dynamics of potential molecular spin qubits has been characterized in the previous chapters by using 'traditional' techniques, *i.e.* ac susceptometry and pulsed EPR. An emergent powerful technique for the investigation of spin dynamics in molecular magnets is Muon Spin Relaxation spectroscopy (μSR). The peculiarity of this technique is indeed the capability to probe the local spin dynamics in condensed matter, both with or without the application of an external magnetic field. Moreover, this technique can be used to investigate bulk systems, as well as thin films of molecular magnets on surface.[1] The first section briefly introduces the μSR technique and it has been written by following the books (P. Carretta and A. Lascialfari, 2007)[2] and (A. Yaouanc and P. Dalmas de Réotier, 2011)[3], and the article (S. J. Blundell, 2002)[4].

So far, μSR has never been exploited to investigate potential molecular spin qubits, and the closer application can be found in the study of SMMs.[5-9] For this reason, before applying μSR on systems such as the vanadyl-based molecules examined in this work, it is important to perform preparatory studies concerning the capability of this technique in providing information on subtle effects on the spin dynamics. The investigation shown in the second section has been performed on a Dy-based SMM, chosen for its large magnetic momentum and because static and dynamics magnetic properties for this type of systems are already well characterized. More specifically, in this work μSR has been used to investigate the effect of nuclear moments on the molecular spin dynamics of two isotopically enriched molecules based on ^{161}Dy (nuclear spin $I = 5/2$) and ^{164}Dy ($I = 0$). It should be note that the relaxation processes that affect the spin dynamics in SMMs may be different from those related to the molecular spin qubits. In particular, quantum tunneling of the magnetization may open a direct pathway between the multi-levels spin structure of SMMs. In addition, the presence of excited Kramers doublets energetically close to the ground doublet provides a further relaxation channel through the Orbach process (§3.3.4).

As anticipated, thanks to the possibility of controlling the muon implantation energy, μSR can be used to investigate depth resolved magnetic properties of thin films of molecular magnets. This capability has been exploited in several cases for molecular films ∽200 nm thick, for example on studying the SMMs $[Dy(hfac)_3(PyNO)]_2$ or TbPc.[10, 11] However, an attempt to investigate a (sub)monolayer molecular film has been performed only once.[12] Bearing in mind the results obtained by the μSR bulk investigation on the two Dy-based SMMs, a monolayer of the same molecule has been studied by LE-μSR (Low Energy Muon Spin Relaxation spectroscopy)[13, 14] in order to explore the sensitivity of μSR. The results are discussed in the third section.

6.1 Basic concepts of μSR

Muon Spin Relaxation is an emergent and versatile technique, whose applications range from chemistry and semiconductor physics to hydrogen storage and muon catalysed nuclear fusion.[15-17] The main research field remains however magnetism and superconductivity, which fully take advantage of the sensitivity of muons in detecting small magnetic fields. This technique has also been employed to characterize the magnetic behaviour of SMMs, since it allows a direct investigation of the magnetization dynamics as local probe and on a time scale faster than what is currently accessible by the ordinary magnetic techniques. However, since muon beams imply the presence of particle accelerators, μSR is available only in large scale facilities. In Europe there are two main centres, ISIS at the Rutherford Appleton Laboratory in England and Paul Scherrer Institute (PSI) in Switzerland. The measurements reported in this dissertation were collected at PSI on GPS (General Purpose Surface-Muon Instrument) and LE-μSR (or simply LEM), in collaboration with Dr. Z. Salman.

Muons (indicated with the symbol μ) are light elementary particles, about nine times lighter than protons and with finite lifetime of 2.2 μs. Muons with either positive or negative charge can be (almost) equally used; for the investigation here performed positive muons were exploited. The process of formation of muons starts with the collision of a high energy proton beam on a carbon (or beryllium) target that produces positive pions π^+ (Figure 6.1). The positive pion then decays (mean life time $\tau_\pi = 26.0$ ns) in a positive muon μ^+ and in a muon neutrino ν_μ according to

$$\pi^+ \rightarrow \bar{\mu}^+ + \nu_\mu. \qquad (6.1)$$

The outgoing muon and neutrino produced by this process have opposite linear momentum equal to 29.79 MeV/c and the kinetic energy of the muon is 4.1 MeV. Since

the pion is a spinless particle and all neutrinos have negative helicity (*i.e.* spin antiparallel to linear momentum), muon and neutrino spins must be opposite to fulfil the angular momentum conservation, as shown in Figure 6.1.

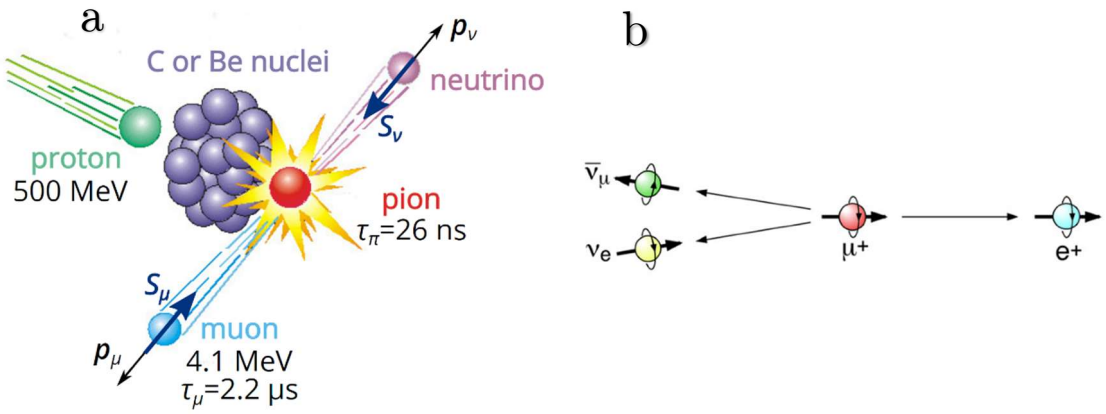

Figure 6.1. (a) Pion production from highly accelerated protons, and its decay in a muon and a neutrino. The muon and neutrino must have the same helicity because of the parity violation. (b) Three-body decay for a positive muon. The conservation of linear and angular momentum, together with the parity violation, produces a correlation between the muon spin direction and the positron linear momentum.

A fundamental feature in this frame is that only neutrinos (antineutrinos) of negative (positive) helicity exist. This is a consequence of the *parity violation* of weak interaction, whose discovery was awarded with the Nobel Prize to Lee and Young (1957), which can be simplified by saying that, although in the macroscopic world the mirror image of any possible event is also a possible event, this symmetry is broken in the microscopic realm of elementary particles. The role of parity violation is crucial for μSR experiments, since it imposes that only muons with negative helicity can be produced by the pion decay of eq. (6.1), for which 100% spin polarized muons can be obtained.

Once produced, muons are directed to the sample where they stop. Being positive charged, μ^+ stops in an electrostatically favourable site of the unit cell, that is in proximity of atoms negatively charged. Muons have spin value $S = 1/2$ and, most interestingly for the study of magnetic properties, they bear a large magnetic moment that is about three times the proton one ($\gamma_\mu/2\pi = 135.5$ MHz/T). The latter is the reason of their high sensitivity to magnetic fields. Indeed, during their lifetime in the sample, the muon spin loses its initial polarization because of the presence of static or dynamical internal fields, and it precesses according to these. The evolution of muon spin polarization reflects thus the static or dynamic internal fields present at their stopping site. The muon decays, as shown in Figure 6.1, into a positron, an electron neutrino and a muon antineutrino, according to

$$\bar{\mu}^+ \rightarrow \bar{e}^+ + \bar{\nu}_\mu + \nu_e \tag{6.2}$$

where, thanks to the parity violation, each particle has a well-defined helicity. In particular, the positron, which among the particles of eq. (6.2) is the only detectable one, has positive helicity and is produced in the same direction of the muon spin in order to conserve angular momentum. However, the situation for the three-body decay is complicated by the fact that there is a continuum of possible geometries and correspondingly a range of possible energies for the emitted positron. More precisely, the probability distribution function for the positron emission is correlated to the instantaneous direction of the muon spin by

$$W(E,\theta) \propto 1 + a_0(E)\cos\theta \tag{6.3}$$

where θ is the angle between the positron direction and muon spin, while the factor a_0 is called initial asymmetry and depends on the positron energy, for example $a_0(E_{max}) = 1$. Since the positron detectors used in μSR are not sensitive to the energy of the particle detected, the average over all angle of the function $a_0(E)$ gives $a_0 = 1/3$. However, a smaller value of a_0, around 0.2, is usually found due to the experimental conditions.

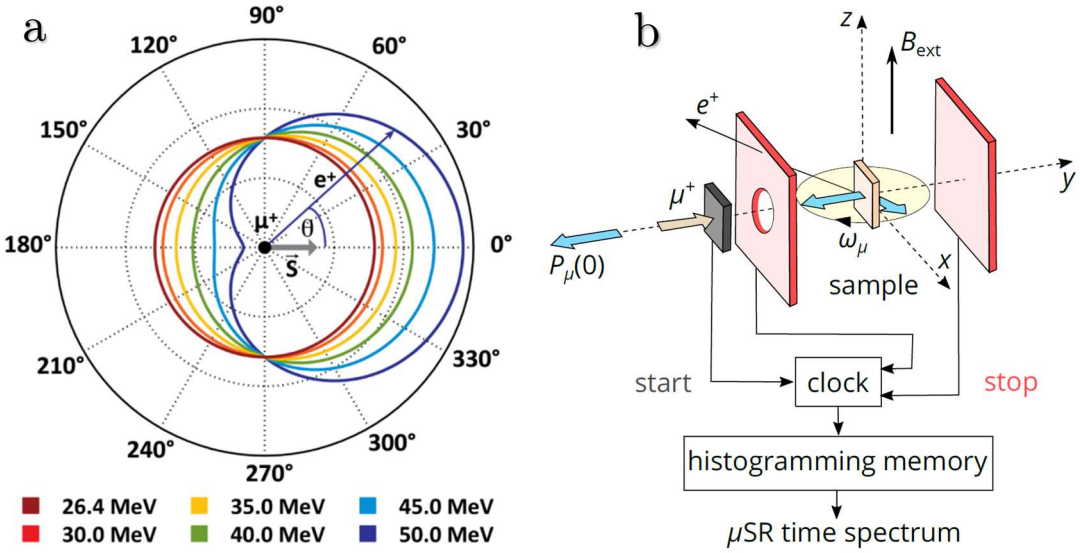

Figure 6.2. (a) Spatial distribution of the positron directions for different energies. (b) Schematic view of a μSR spectrometer. In the example, the experimental configuration is in transverse field mode. These images are taken by ref[18].

In Figure 6.2 the basic set-up of a μSR spectrometer is shown. When a muon trigger passes through a scintillation detector (dark grey in figure) the detector delivers a signal that establishes the zero time (t_0) and starts the digital clock. When the forward or the

backward detector (red in figure) registers a decay event, that is a positron hit, a stop signal is sent to the clock, which stores the elapsed time span $(t - t_0)$ as a digital number. Muons are implanted either one by one, when working with continuous sources such as in PSI, or in branches of hundreds, when pulsed sources such as ISIS are used. Individual lifetimes are thus recorded for millions of muon events, each contributing with one count in one-time bin. All these events are accumulated independently, over long times spanning from minutes to hours. It is important to remark that coherence is guaranteed by the fact that all muons when implanted in the sample have the same spin polarization.

The data collected by the forward detector should be least-square fitted by using

$$N_F(t) = N_F(0)e^{-t/\tau_\mu}(1 - a_0 G(t)) \tag{6.4}$$

where N_F is the counting number of the forward detector and $G(t)$ denotes the spin relaxation function and considers the possible loss of degree of polarization with time. For the backward detector the equation is analogue but, because of the shift of 180°, it is $\propto (1 + a_0 G(t))$. However, usually it is the backward-forward ratio, called asymmetry $A(t)$, which is fitted. Ideally it is defined as

$$A(t) = \frac{N_B(t) - N_F(t)}{N_B(t) + N_F(t)} \tag{6.5}$$

but, since from the experimental point of view the forward and backward detector have different counting efficiencies, it is more useful to define the parameter α

$$\alpha = \frac{N_F(0)}{N_B(0)} \tag{6.6}$$

for which the asymmetry can be rewritten as

$$A(t) = \frac{(1 - \alpha) + (1 + \alpha)a_0 G(t)}{(1 + \alpha) + (1 - \alpha)a_0 G(t)} \tag{6.7}$$

where, if $\alpha = 1$ eq. (6.5) is recovered and $A(t) = a_0 G(t)$. From a practical point of view, the α parameter must be determined at the beginning of a new experiment by performing low transverse field measurements (*see infra*).

It should also be considered that the implantation site of the muon inside the sample is often not unique. The multiple sites are effectively accounted for by considering that

the total asymmetry A of the full implanted muon ensemble is divided into the partial asymmetries of the n distinct muon sites according to

$$A(t) = \sum_{j=1}^{N} A_j(t) \tag{6.8}$$

where the initial partial asymmetry, $A_j(0)$ may be written as $A_j(0) = Ap_i$, where p_i is the stopping probability at the ith site and in general can be calculated through *ab initio* methods.

The spin relaxation function $G(t)$ depends on the type of experiment that is performed and, more specifically, it depends on whether the magnetic field is applied or not, as well as the geometry of the experiment. By considering the xyz frame, as shown in Figure 6.2b, in *zero field* (ZF) and *longitudinal field* (LF) the configuration $G_z(t)$ is measured. Instead, in *transverse field* (TF) the configuration $G_x(t)$ is measured.

For the latter case, the applied magnetic field is oriented perpendicular to the initial muon spin polarization. When sensing a transverse field, the muon spin precesses in the plane perpendicular to the field axis (*i.e.* the z axis) and the probability distribution lobe of the positron emissions precesses with it. The resulting asymmetry has the form

$$A(t) = a_0 G_x(t) \cos(2\pi f_\mu t) \tag{6.9}$$

where f_μ is the spin precession frequency and is related to the magnitude of the field B_μ by $f_\mu = \gamma_\mu B_\mu / 2\pi$. This field corresponds to the overall field experienced by the muon, *i.e.* the sum of the applied field and the average of internal fields of the sample. Depending on the internal fields distribution, $G_x(t)$ will be described by a specific relaxation model.

In ZF and LF mode, the initial muon spin polarization is oriented along the propagation direction, y, and the magnetic field (for LF only) is applied parallel to this. For a true paramagnetic system, such as SMMs or molecular qubits, the local fields are randomly oriented. This means that when measuring in ZF mode, the average value of the experienced magnetic field, $\langle B_\mu \rangle$, vanishes and no precession is observable. However, the second central moment of the field distribution, $\langle B_\mu^2 \rangle$, will result in general different from zero. Once more, the description of $G_z(t)$ depends on the type of system studied. For example, if the distribution of the internal field is stationary and with a Gaussian profile, the muon spin relaxation can be described by the Gaussian Kubo-Toyabe function

$$G_z = \frac{1}{3} + \frac{2}{3}(1 - \Delta_G^2 t^2) \exp\left(-\frac{1}{2}\Delta_G^2 t^2\right) \tag{6.10}$$

that accounts for a dense set of random magnetic moments. Instead, if the internal fields are more diluted, the Lorentzian distribution is more appropriate, and the relaxation can be described by the Lorentzian Kubo-Toyabe function

$$G_z = \frac{1}{3} + \frac{2}{3}(1 - \Delta t) \exp(-\Delta t). \tag{6.11}$$

The long-range order is the only case for which all muons, stopping at the same crystallographic site, experience the same local field. Thus, they all have their polarization evolving according to eq. (6.9) and so does the measured macroscopic asymmetry.

Besides the static random fields, muons can probe also a dynamic component produced by magnetic moment fluctuations of molecular spins (either electronic or nuclear). In general, by considering the average fluctuation rate τ_f and the width of the internal field distribution Δ/γ_μ, if $\tau_f \Delta > 1$ we have the slow-fluctuation limit and the main effect is the 1/3 tail (Figure 6.3). In this case, only 1/3 of muons, those residing in sites where the local magnetic field is parallel or antiparallel to their initial spin direction, will precess. Consequently, the average asymmetry is reduced to 1/3 of its initial value and it does not evolve in time. The application of a longitudinal field B_{LF} may produce the suppression of the spin depolarization (longitudinal field decoupling), for which the 1/3 tail is increased in B_{LF} according to Figure 6.3. This leads to a partial decoupling between the static and dynamic component of the muon relaxation.

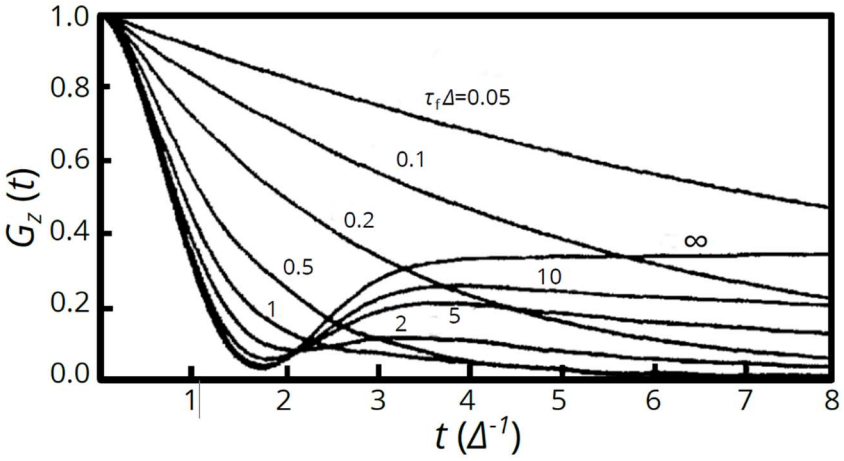

Figure 6.3. Zero field dynamic Gaussian Kubo-Toyabe function for different field fluctuations. The $\tau_f \Delta$ term takes into account the ratio between the static and dynamic contributions to the muon relaxation.

On the other hand, if $\tau_f \Delta < 1$ the minimum vanishes, and the spin relaxation function tends to

$$G_z(t) = e^{-\lambda t} \tag{6.12}$$

where $\lambda = \tau_f \Delta^2$ and it contains information both on the fluctuation rate and on the width of the field distribution. These contributions cannot be separate in ZF. Instead, the application of a B_{LF} can be useful, but only if the corresponding Larmor frequency f_μ is comparable to the fluctuation rate.

6.2 Bulk isotopically enriched Dytta

Paper in Appendix

Isotope effects on the spin dynamics of single-molecule magnets probed using muon spin spectroscopy.

L. Tesi, Z. Salman, I. Cimatti, F. Pointillart, K. Bernot, M. Mannini and R. Sessoli. In: *Chemical Communications* **54** (2018), pp. 7826-7829.

In this work, the effects of nuclear moments on the molecular spin dynamics were studied for two different isotopically enriched compounds of a Dy-based SMM of formula $[Dy(tta)_3(L)] \cdot C_6H_{14}$, where *tta⁻=2-thenoyltrifluoroacetonate* and *L=4,5-bis(propylthio)-tetrathiafulvalene-2-(2-pyridyl)-benzimidazole methyl-2-pyridine*, and hereafter indicated as **Dytta**.[19] The molecular structure is shown in Figure 6.4. The two isotopes investigated in this comparative study are ^{161}Dy and ^{164}Dy, with nuclear spin $I = 5/2$ and $I = 0$, respectively. The Dy^{III} ion is connected to three tta^- ions and one bidentate L ligand. In this configuration the metal results at the centre of a N_2O_6 square antiprism environment leading to an approximate D_{4d} local symmetry in its surrounding; the compounds are isostructural and crystallize in the triclinic *P-1* space group.

The magnetic characterization of **Dytta** was made in a previous study by (T. T. da Cunha et al., 2013)[19] evidencing a robust SMM-like behaviour. The temperature dependence of the magnetization relaxation time, τ_{ac}, extracted from ac susceptibility measurements, were analysed by considering two different relaxation processes: a thermally activated process at high temperatures and a temperature-independent one, which has been attributed to fast quantum tunneling in zero-field. Furthermore, the slow relaxation of the SMM enabled the measurement of butterfly-shape hysteresis curves at 2 K. The findings of the magnetic analysis agreed with an easy axis magnetic anisotropy found by *ab initio* calculations: the anisotropic distribution of the electrostatic potential

around the Dy^{III} ion stabilizes the Kramers doublet $M_J = \pm 15/2$, which results separated from the first-excited state for 126 cm^{-1}.[19] In a subsequent work, (F. Pointillart et al., 2015)[20] synthetized the two isotopically enriched samples **^{161}Dytta** and **^{164}Dytta**, and investigated them by ac susceptometry to study the effects of the hyperfine interaction on the spin dynamics. Remarkably, the quantum-tunneling process has been identified as the only process affected by the isotope effect, exhibiting an increase in the relaxation time of about one order of magnitude when passing from **^{161}Dytta** to **^{164}Dytta**. The reduction of the quantum-tunneling process produced consequently the opening of the hysteresis at zero field, which is a key feature for the potential application of SMMs as data storage.

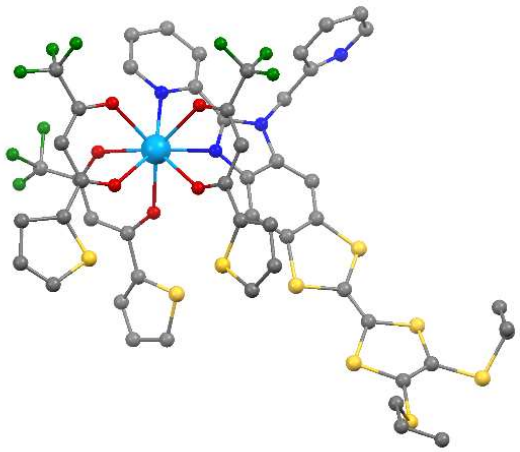

Figure 6.4. Molecular structure of **Dytta**; colour code: Dy=azure, O=red, N=blue, F=green, S=yellow and C=grey. Hydrogen atoms are omitted for clarity.

The μSR investigation has been performed on two bulk compounds constituted by microcrystalline powders of **^{161}Dytta** and **^{164}Dytta** through the GPS spectrometer of the Paul Scherrer Institute (PSI). The measurements were performed at zero magnetic field and using an implantation energy of ∽4 MeV, corresponding to a few 100 μm stopping depth. Moreover, since muons are positively charged, they are expected to stop within the molecule close to the fluorine atoms.

The time dependence of the muon spin polarization, $P_Z(t)$, was recorded for several temperatures between 1.6 and 300 K. Examples of spectra are shown in Figure 6.5. At high temperature, the internal fields of the molecule fluctuate and $P_Z(t)$ decays with a single exponential-like behaviour from its initial value to zero. On decreasing the temperature, the damping rate of the polarization increases gradually and, below 30 K, $P_Z(t)$ exhibits a shallow dip at short times and then a recovery to ∽1/3 for longer times (see for example Figure 6.3).

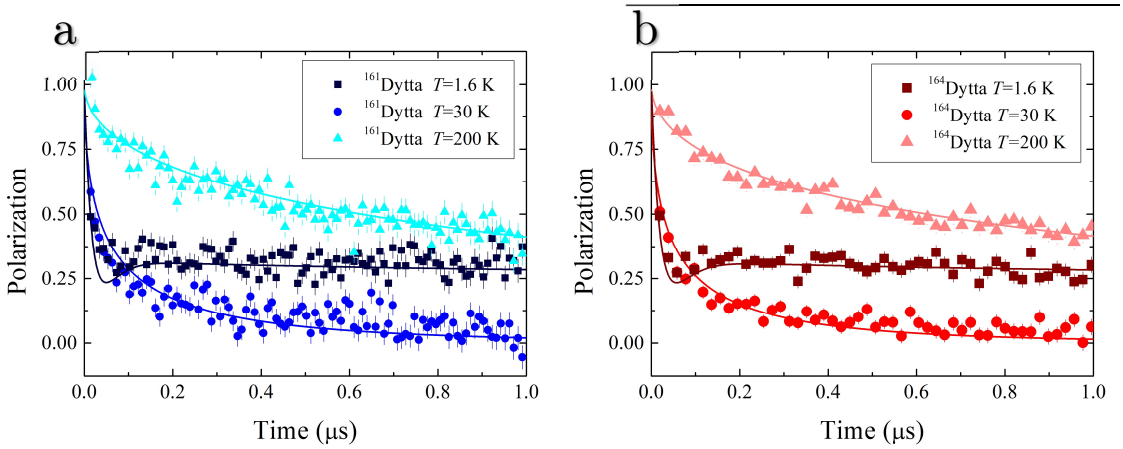

Figure 6.5. Examples of time dependences of the muon spin polarization in zero field, $P_Z(t)$, in the three different temperature regimes for (a) **^{161}Dytta** and (b) **^{164}Dytta**. Solid lines are the best-fits using eq. (6.13).

The time dependence of $P_Z(t)$ can be reproduced by considering the phenomenological Lorentzian Kubo-Toyabe model[21] of eq. (6.11), for the static contribution, multiplied by a square root exponential relaxation function,[10, 11] for the dynamic contribution, which provides

$$P_Z(t) = \left[\frac{1}{3} + \frac{2}{3}(1-\Delta t)e^{-\Delta t}\right] e^{-\sqrt{\lambda t}}. \qquad (6.13)$$

It is here recalled that Δ is the width of the Lorentzian distribution of local static magnetic fields, whereas λ originates from the fluctuations of the Dy^{III} magnetic moments. The square root in the dynamic component originates from averaging many inequivalent sites of the molecule where muons can stop.[22-24] The fits are shown in Figure 6.5, while the outcomes of λ and Δ are reported as a function of temperature in Figure 6.6a. Such parameters are representative of the magnetic properties and spin dynamics of the single-molecule, and their temperature dependence reflects the gradual evolution of Dy^{III} spin dynamics.

Three different regimes can be distinguished: *i)* at high temperatures fast thermally activated Dy^{III} spin fluctuations dominate over the static fields, consequently muons probe a relatively small λ and no local static magnetic fields ($\Delta = 0$). On decreasing the temperature λ increases, because of the slowing down of the fluctuations of the Dy^{III} magnetic moments on a time scale comparable with the muon spin Larmor precession frequency f_μ (see eq. (6.9)), up to ca. 30 K. *ii)* At this temperature value, λ exhibits a narrow peak coinciding with an abrupt increase in Δ, which corresponds to the appearance of static magnetic fields. *iii)* Finally, at low temperature, muons experience mainly the quasi-static fields, for which Δ is large and λ strongly decreases.

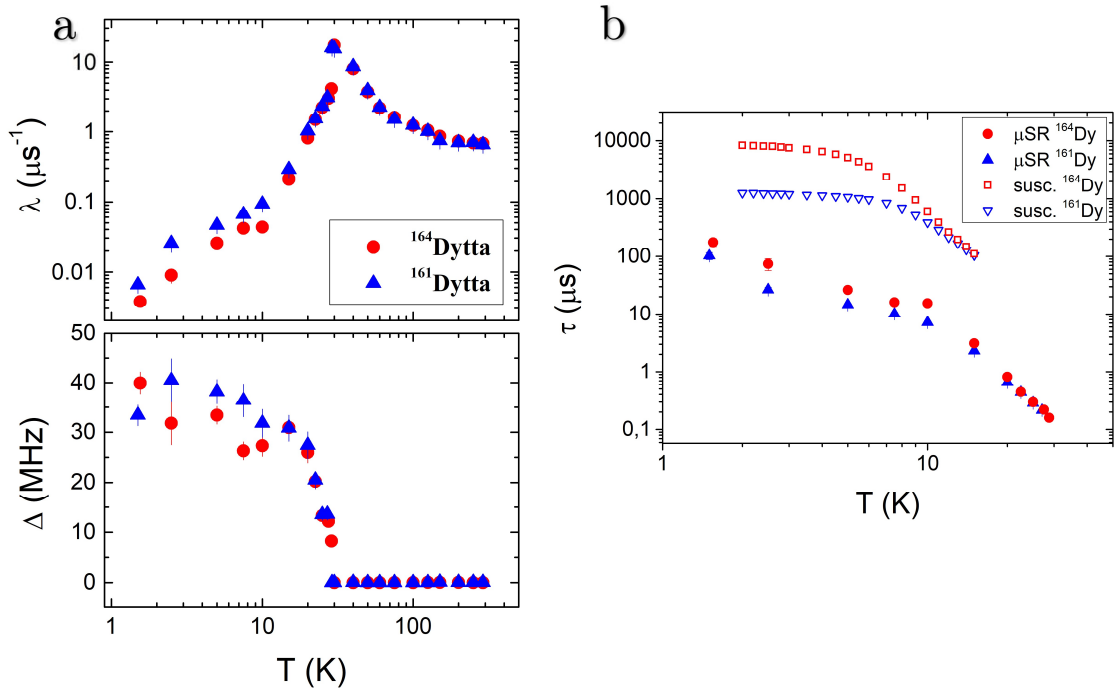

Figure 6.6. (a) Temperature dependence of the relaxation rate λ (top) and width of local static magnetic field distribution Δ (bottom) for **^{164}Dytta** and **^{161}Dytta** measured by μSR in zero field. (b) Correlation times extracted from μSR and magnetization relaxation times extracted by ac susceptibility measurements as a function of temperature for **^{161}Dytta** and **^{164}Dytta**.

Differences between the spin dynamics of the two isotopically enriched compounds emerge below 15 K, revealing a larger dynamic relaxation parameter λ for **^{161}Dytta**. This isotope effect is also evident below 15 K when looking at the correlation time, τ, of the local magnetic field experienced by muons, shown in Figure 6.6b. Such a parameter is extracted from the μSR spectra in different way depending whether fluctuations or quasi-static fields dominate the relaxation. In the former case, $\tau = \lambda/2\Delta_0^2$, in which Δ_0 is the size of the fluctuating field and can be estimated from the saturation value of Δ extrapolated at low temperature. This is worth ∽35 MHz (ca. 41 mT) for both compounds. On the other side, when quasi-static magnetic fields dominate, the correlation time is given by $\tau = 2/3\lambda$.

It is interesting to compare the relaxation time τ obtained by μSR with the relaxation time of the magnetization, τ_{ac}, extracted by ac susceptibility measurements at zero field.[20] These two are shown together in Figure 6.6b. Although one could have expected similar values and temperature dependences, the correlation times are about 1-2 order of magnitude shorter than τ_{ac}s. This can be explained considering that while ac susceptibility is sensitive to excitations with wave-vector $q = 0$, μSR as local probe is sensitive to excitations integrated over all q values of the Brillouin zone.[25, 26] In this frame, ac susceptibility can probe only those processes that reverse the magnetization, *i.e.* inter-well transitions changing the sign of the spin projection along the anisotropy axis. In

contrast, μSR, beyond probing faster dynamics, is sensitive to all types of fluctuations that affect the lifetime of the spin states, including intra-well transitions and decoherence effects. Accordingly, hyperfine fields are crucial to establish the resonant condition for the reversal of magnetization by quantum tunnelling, but they are expected to have less influence on the lifetime of the states. This inherent difference between the dynamics probed by the two techniques also explains the less pronounced isotope effect observed by μSR compared to ac susceptibility, as well as the more pronounced temperature dependence shown by the correlation times below 10 K.

To summarize these findings, μSR is able to capture fine details of the spin dynamics of molecular systems, down to the isotopic effects in a different way with respect to ac susceptometry, thus providing a complementary perspective to that of traditional magnetometry techniques. Indeed, the local probe character and the consequent sensitivity of muons in obtaining information on the lifetime of spin states, together with the possibility to investigate the spin dynamics of molecules addressed on surface, makes μSR a unique and powerful technique.

6.3 Dytta Monolayer on gold

Article in preparation

Spin dynamics of a monolayer of Dy-based Single-Molecule-Magnet probed by Muon spin relaxation.

I. Cimatti, G. Fernandez Garcia, L. Tesi, K. Bernot, G. Serrano, L. Malavolti, E. Otero, M.-A. Arrio, P. Sainctavit, B. Le Guennic, F. Pointillart, F. Totti, R. Sessoli, Z. Salman, and M. Mannini.

Thanks to the possibility of implanting muons at different depths, they can be used to probe the dynamics of molecules close to a surface or an interface. This capability is limited only to synchrotron-based techniques because of the small quantity of magnetic material contained in a (sub)monolayer that prevents the use of standard techniques such as SQUID magnetometry.[27, 28] The investigation of SMMs grafted on surface is mandatory to understand whether, and in certain cases how, the magnetic properties of SMMs are affected by.[29] In this sense, μSR has been applied for several thin films of SMMs. In these cases, muons stop into the molecular film and probe differences in the spin dynamics, sometime evidencing unchanged magnetic properties and other times the loss of such properties.[10, 11] However, so far, the contribution of a (sub)monolayer of molecular magnets on surface investigated by μSR has been reported only once.[12] The following work is, indeed, an explorative study to determine whether muons can be used

to investigate the spin dynamics of monolayers of molecular magnets. For this reason, the experiment has been carried out on the well characterized system **Dytta**.

The preparation of the sample and its characterization have been carried out by Dr. I. Cimatti and co-workers at the CeTeCS laboratory in the University of Florence. The molecular self-assembled monolayer (SAM) of **^{161}Dytta** has been prepared on a gold surface in order to get a monolayer coverage. The preparation is performed in three steps: *i)* an ordered Au(111) surface is obtained by evaporating a ∽130 nm thick Au film on mica, annealed by a hydrogen flame and then rinsed in CH_2Cl_2; *ii)* the annealed Au substrate is incubated in a solution of 2 mM of **^{161}Dytta** in CH_2Cl_2 for 20 hours to ensure a complete molecular coverage of the Au surface; *iii)* the sample is washed several times with CH_2Cl_2 to remove the excess of physiosorbed molecules and then dried under nitrogen flow.[30] After the preparation, the sample has been characterized by X-ray Photoelectron Spectroscopy (XPS) to confirm the grafting of molecules on surface. The same preparation procedure has been performed at the Deimos beamline at the Soleil synchrotron (France), where the magnetic properties of the sample have been characterized by X-ray Absorption Spectroscopy (XAS), X-ray Natural Linear Dichroism (XNLD) and X-ray Circular Magnetic Dichroism (XMCD). The experimental outcomes have been then flanked by *ab initio* calculations based on a combined state-of-art pDFT and post-HF characterization, performed by Dr. G. Fernandez Garcia at the University of Rennes. However, only the main aspects of the characterization will be briefly presented here.

The XPS analysis has been performed on the **^{161}Dytta** monolayer on gold and the results have been compared with those obtained for a reference sample, in order to assess the chemical grafting of the molecule after the SAM preparation process. The reference sample consists in a molecular thick film obtained by dropcasting. The spectra are shown in Figure 6.7. The XPS technique provides information on the binding energy of the electrons of the molecule's atoms. This energy depends on the chemical environment of the atom, *i.e.* the oxidation state and functional groups present. The XPS spectra of the two samples are mostly comparable, showing differences only in the S*2p* region. Indeed, in the thick film the S*2p* component presents only one contribution and the relative spin-orbit splitting contribution, whereas an additional contribution at slightly lower binding energies appears for the monolayer, confirming the presence of a chemical bonding of the molecule with the gold substrate through the sulphur atoms, as expected.[31-33] Moreover, the binding energy of the latter component is in good agreement with that corresponding to self-assembled thioethers on gold surfaces.[31-33] The semi-quantitative analysis of the Dy*4d*, C*1s*, N*1s*, O*1s*, F*1s* and S*2p* regions is in agreement with the expected molecular stoichiometry, confirming the presence of intact molecules after the SAM preparation.

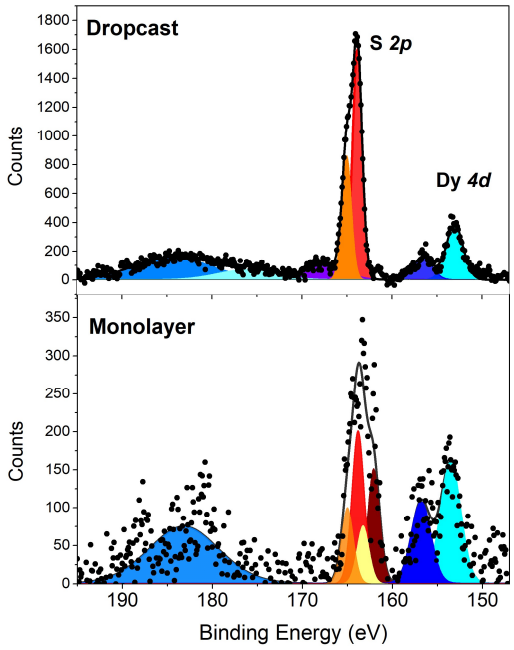

Figure 6.7. Core level XPS spectra of the ^{161}**Dytta** deposited on gold by dropcasting (top panel) and SAM (bottom panel) showing the Dy*4d* and S*2p* region.

Similar findings were also obtained by using synchrotron-based techniques. It should be highlighted that X-ray Absorption Spectroscopy is a fundamental tool for the magnetic and structural investigation of thin films. This provides information on: (*i*) the elements constituting the molecule, (*ii*) the oxidation states of the investigated atomic species, (*iii*) the magnetic properties of the absorber (by measuring the XMCD spectrum) and (*iv*) the anisotropy of the charge distribution around the absorbing atom (by measuring the XNLD spectrum). The XAS and XMCD spectra are shown in Figure 6.8, whereas no signal has been detected by using XNLD. The presence of the molecule on surface is confirmed by comparing the results of XAS and XMCD measurements of the monolayer and reference sample. On the other hand, the absence of a dichroic signal in the XNLD spectrum suggests that there is no preferential orientation of the molecule in the monolayer.

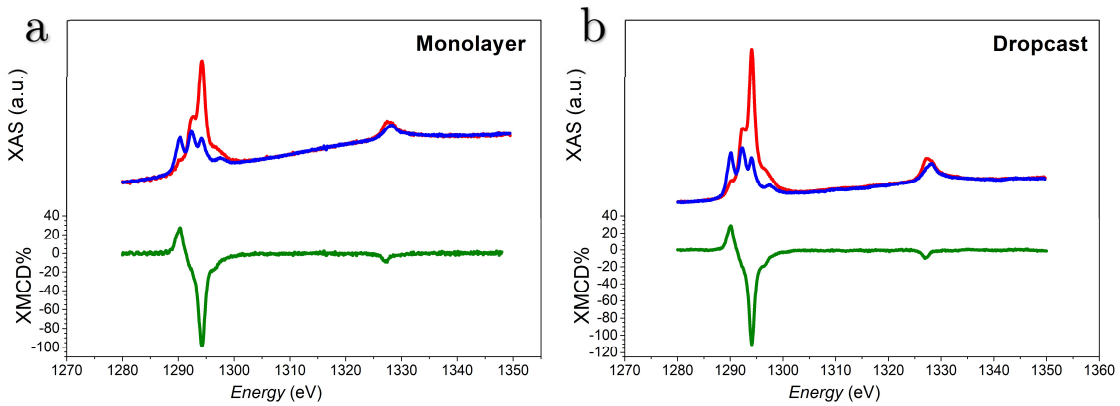

Figure 6.8. XAS and XMCD spectra of **^{161}Dytta** deposited on gold by SAM (a) and dropcasting (b). The spectra are measured at the Dy $M_{4,5}$ edges with a magnetic field of 3 T and 2 K.

Accordingly, the theoretical analysis evidenced a high variability of adsorption of the molecules on surface, for which there is not a unique highly probable conformer on surface, but a series of conformers with different structure but similar energy. This can be explained by considering the complex geometrical shape of the compound. For this reason, a series of structural optimization has been performed starting from eight possible conformers on surface. These structures were designed taking into account the elimination of the two propyl terminations and several possible interactions among the Au surface, the *tta* ligands and the *tetrathiafulvalene* (ttf) moiety. In fact, the elimination of the propyl terminations, in favour of a stronger S-Au bonding, is generally considered the most stable state for such systems.[34, 35] These calculations were performed with the periodic Density Functional Theory (pDFT) using a mixed Gaussian and plane waves approach (GPW), as implemented in the CP2K code.[36] Afterwards a CAS-SCF (Complete Active Space-Self Consistent Field) calculation has been performed on the optimized structures, erasing the gold surface from the simulation cell and using the MOLCAS code.[37] The latter calculations were conducted to understand the structural effect of the surface on the electronic structure of the molecule. However, from a structural point of view and for each conformation, the adsorption process results in a distortion of the ttf moiety, with an almost negligible involvement of the Dy^{III} ion; two examples of possible conformation are reported in Figure 6.9.

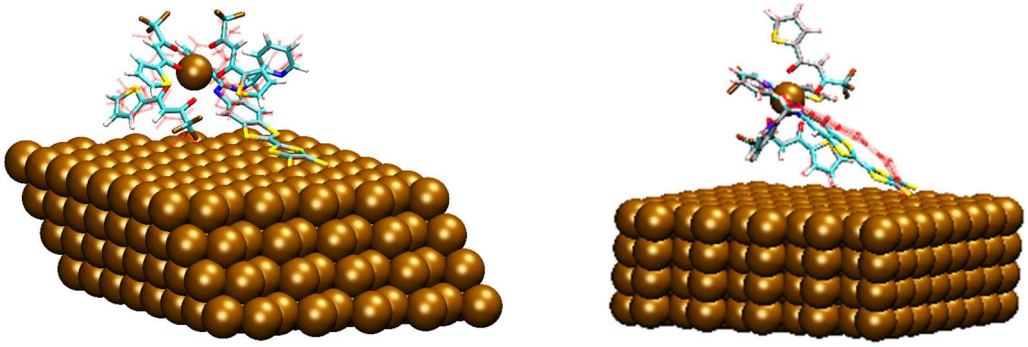

Figure 6.9. Examples of possible conformations of **Dytta** on gold surface. The two graphical representations are obtained by pDFT geometry optimization. Colour code: Dy=Au=brown, O=red, C=light blue, S=yellow, N=blue, F=brown). The starting conformer is represented in transparent red wireframe.

Focusing on the μSR investigation, which I carried out in collaboration with Dr. Z. Salman, the **^{161}Dytta** monolayer on gold has been studied at the Low Energy μSR (LE-μSR or LEM) beamline of the Paul Scherrer Institute.[38] The sample was mounted on a metal plate in an ultra-high-vacuum environment in contact with a cold finger cryostat; the temperature can be varied between 3.5 and 300 K, while the muons implantation energy can be changed between 1 and 12 keV, corresponding to an average implantation depth of 2-80 nm. The stopping depth profile of the implanted muons in gold (density $\rho \approx 19.3$ g/cm^3) can be accurately simulated using the Trim.SP code[39] as shown in Figure 6.10. Muons at 12 keV stop deeply inside the gold, whereas muons at 1 keV, and thus less energetic, will be nearby the surface/molecule interface. It is worth to note that in any case muons stop below the monolayer, into the gold. This is a non-magnetic medium, for which the entire magnetic contribution probed by muons originates from dipolar fields produced by the electronic spin of the Dy^{III} ion of **^{161}Dytta**. It should also be noted that the dipolar fields of nuclear moments (such as those deriving from the magnetic nuclei of ^{1}H and ^{19}F) are too small to be detected by muons stopping a few nanometres away, and only the electronic moments, which are orders of magnitude larger, contribute to the magnetic fields sensed by muons.

The experiments were performed in TF configuration by applying a constant external magnetic field of 10 mT perpendicular to the muon polarization. In this configuration the muon precesses according to B_μ, which is given by the sum of the applied magnetic field and internal contributions. This type of measurement, combined with the possibility to implant the muon at different depths, is a powerful tool to investigate the presence (and eventually the intensity) of the static magnetic fields produced by the paramagnetic ions.

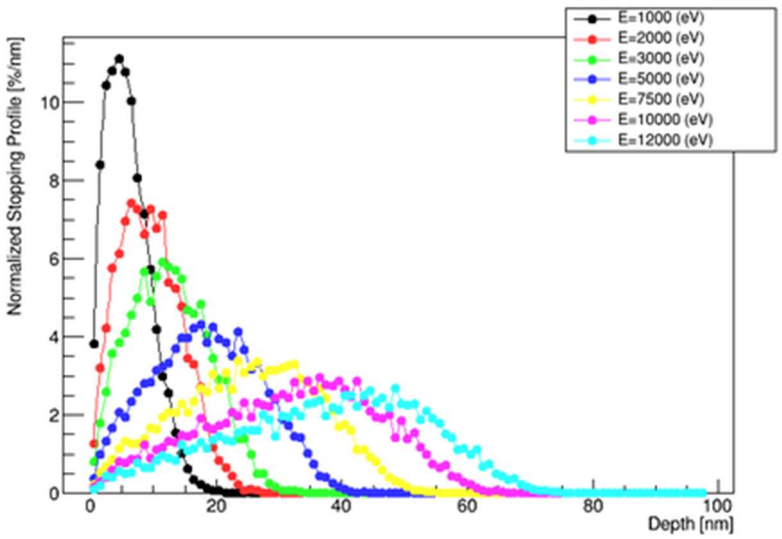

Figure 6.10. Simulation of the stopping muons implantation depth profile into a gold film varying the incident energy of the muon. The simulation has been obtained by using the Trim.SP code.[39]

Typical LE-μSR precession signals recorded at 3.7 K for two different implantation energies are shown in Figure 6.11a, while those recorded at 250 K at the same energies are shown in Figure 6.11b.

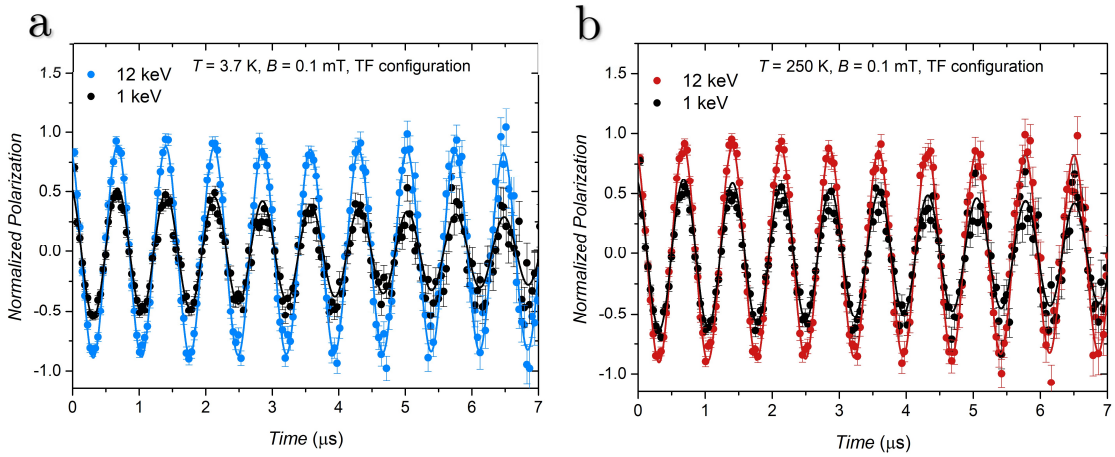

Figure 6.11. Examples of muon spin precession spectra in the rotating reference frame measured for ^{161}**Dytta** at 3.7 K (a) and 250 K (b) under an applied magnetic field of 10 mT and for the two implantation energies 12 and 1 keV. The solid lines correspond to the best-fits.

The time evolution of the muon polarization can be reproduced by using eq. (6.9) multiplied for the relaxation function in eq. (6.12) that provides

$$P_{TF}(t) = a_0 \cos(2\pi f_\mu t)\, e^{-\lambda t} \tag{6.14}$$

where a_0 is the asymmetry and corresponds to the initial polarization, f_μ is the precession frequency and λ is the relaxation rate of the oscillations. It should be recalled that the

precession frequency is $f_\mu = \gamma_\mu B_\mu$, where $\gamma_\mu/2\pi = 135.5$ MHz/T is the muon gyromagnetic ratio and B_μ is the average local magnetic field experienced by the muon, *i.e.* the applied one and those generated by the Dy^{III} magnetic moments. The relaxation rate λ in this case provides a measure of the width of the distribution of local magnetic fields. Thus, a wider field distribution results in a larger λ. Examples of the best-fits resulting from eq. (6.14) are shown in Figure 6.11, while the energy and temperature dependence of the extracted relaxation rate λ are reported in Figure 6.12.

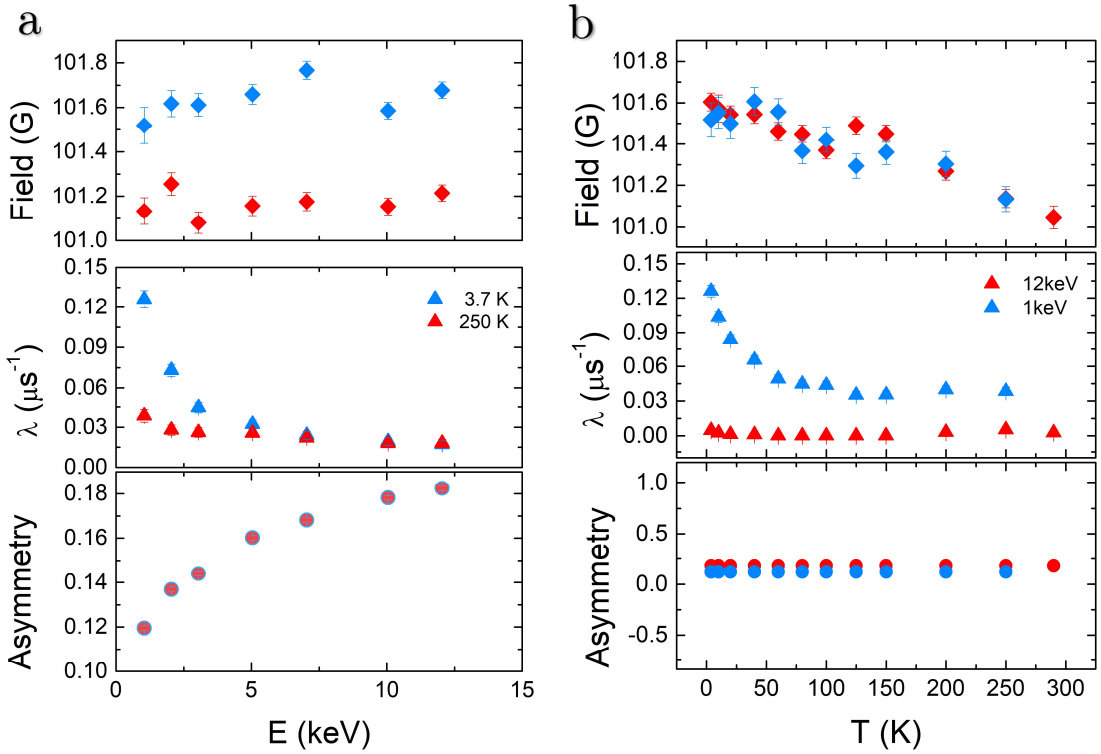

Figure 6.12. Energy (a) and temperature (b) dependence of the main parameters extracted from the time evolution of the muon polarization measured in Transverse Field mode ($B = 10$ mT) through the model of eq. (6.14).

The depth dependence of λ (Figure 6.12a), which is almost flat in the high energy region, shows a remarkable increasing as the energy is decreased, *i.e.* when muons are approaching the molecular interface. Moreover, the variation occurring at low energy is more pronounced at 3.7 K than at 250 K, in agreement with the temperature dependence of λ. Indeed, by observing the temperature dependence of λ (Figure 6.12b), it is possible to note a different behaviour in the dynamics when muons are in proximity of the molecular interface (1 keV), with respect to the case in which muons are implanted deeply into the gold. These findings point out that μSR is able to probe the magnetic contribution of the monolayer of ^{161}**Dytta** on surface.

The performing of ZF measurements would shed light on the magnetic behaviour of the monolayer of ^{161}**Dytta**, and, more specifically, whether its magnetic properties change

or not with respect to those of the bulk sample described in the previous chapter. However, experiments in ZF configuration are even more challenging than in TF configuration. In the latter case, indeed, the application of a magnetic field produces a coherent response of the paramagnetic ions. In zero field, instead, the magnetic fields of molecular spins are randomly oriented with a consequent reduction of the signal, which is already lowered by the distance between the stopping site of the muon and the monolayer of magnetic centres.

6.4 Conclusions

In this chapter, the investigation of the spin dynamics of a Dy-based SMM through μSR spectroscopy is discussed. Following a brief introduction about μSR, exposed in the first section, two studies are described: in the second section focusing on μSR experiments on a bulk sample, whereas in the third section concerning the LE-μSR experiment on a monolayer of the same Dy-based SMM grafted on gold. Both the investigations are preliminary studies to get more insights into the capabilities of μSR. In the former case with the detection of subtle effects such as those provided by nuclear spins on the spin dynamics. In the latter, with the measure of the spin dynamics of a (sub)monolayer deposition of molecules.

The bulk experiment has been carried out on two isotopically enriched samples of ^{161}Dy ($I = 5/2$) and ^{164}Dy ($I = 0$). This study has evidenced the capability of μSR to capture fine details of the spin dynamics of molecular systems, down to the isotopic effects in the tunneling of the magnetization. Moreover, from this study emerges the advantage of using muons as local probes. Indeed, unlike traditional techniques such as ac susceptometry, muons can probe all sources of spin fluctuations affecting the spin state lifetime.

The LE-μSR investigation, reported in the third section, has been performed on a single monolayer of the ^{161}Dy-based SMM by applying a transverse magnetic field (TF configuration). The findings have evidenced that muons can probe also small quantities of sample. In future, ZF measurements will be performed to obtain information about possible changes of the spin dynamics of **Dytta** when passing from bulk to surface.

These preliminary studies are important from a forward-looking perspective in which μSR is employed to investigate molecular spin qubits.

6.5 Bibliography

1. A. Yaouanc and P. D. de Réotier, *Muon Spin Rotation, Relaxation, and Resonance: Applications to Condensed Matter*, OUP: Oxford, 2010.
2. P. Carretta and A. Lascialfari, *NMR-MRI, SR and Mössbauer Spectroscopies in Molecular Magnets*, Springer Science & Business Media, 2007.
3. A. Yaouanc and P. Dalmas de Réotier, *Muon Spin Rotation, Relaxation, and Resonance, Applications to Condensed Matter*, Oxford, 2011.
4. S. J. Blundell, *arXiv:cond-mat/0207699*, 2002.
5. S. J. Blundell, F. L. Pratt, I. M. Marshall, C. A. Steer, W. Hayes, J. F. Letard, S. L. Heath, A. Caneschi and D. Gatteschi, *Synth. Met.*, 2003, **133**, 531-533.
6. T. Lancaster, S. J. Blundell, F. L. Pratt, I. Franke, A. J. Steele, P. J. Baker, Z. Salman, C. Baines, I. Watanabe, S. Carretta, G. A. Timco and R. E. P. Winpenny, *Physical Review B*, 2010, **81**.
7. Z. Salman, S. R. Giblin, Y. Lan, A. K. Powell, R. Scheuermann, R. Tingle and R. Sessoli, *Physical Review B*, 2010, **82**.
8. F. Branzoli, M. Filibian, P. Carretta, S. Klyatskaya and M. Ruben, *Physical Review B*, 2009, **79**.
9. F. Branzoli, P. Carretta, M. Filibian, M. J. Graf, S. Klyatskaya, M. Ruben, F. Coneri and P. Dhakal, *Physical Review B*, 2010, **82**, 134401.
10. A. Hofmann, Z. Salman, M. Mannini, A. Amato, L. Malavolti, E. Morenzoni, T. Prokscha, R. Sessoli and A. Suter, *ACS Nano*, 2012, **6**, 8390-8396.
11. E. Kiefl, M. Mannini, K. Bernot, X. Yi, A. Amato, T. Leviant, A. Magnani, T. Prokscha, A. Suter, R. Sessoli and Z. Salman, *ACS Nano*, 2016, **10**, 5663-5669.
12. Z. Salman, S.J. Blundell, S.R. Giblin, M. Mannini, L. Margheriti, E. Morenzoni, T. Prokscha, A. Suter, A. Cornia and R. Sessoli, *arXiv:0909.4634*, 2009.
13. T. Prokscha, E. Morenzoni, K. Deiters, F. Foroughi, D. George, R. Kobler, A. Suter and V. Vrankovic, *Nucl Instrum Meth A*, 2008, **595**, 317-331.
14. E. Morenzoni, T. Prokscha, A. Suter, H. Luetkens and R. Khasanov, *J. Phys.: Condens. Matter*, 2004, **16**, S4583-S4601.
15. F. Bert, *Collection SFN*, 2014, **13**, 03001.
16. S. J. Blundell, in *Magnetism: Molecules to Materials*, eds. J. S. Miller and M. Drillon, Wiley-VCH, Weinheim, 2001, pp. 235-256.
17. P. Dalmas de Réotier and A. Yaouanc, *J. Phys.: Condens. Matter*, 1997, **9**, 9113.
18. E. Lucaccini, PhD Thesis, University of Florence, 2016.

19. T. T. da Cunha, J. Jung, M.-E. Boulon, G. Campo, F. Pointillart, C. L. M. Pereira, B. Le Guennic, O. Cador, K. Bernot, F. Pineider, S. Golhen and L. Ouahab, *J. Am. Chem. Soc.*, 2013, **135**, 16332-16335.

20. F. Pointillart, K. Bernot, S. Golhen, B. Le Guennic, T. Guizouarn, L. Ouahab and O. Cador, *Angew. Chem. Int. Ed.*, 2015, **54**, 1504-1507.

21. R. Kubo, *Hyperfine Interact.*, 1981, **8**, 731-738.

22. A. Keren, *Physical Review B*, 1994, **50**, 10039-10042.

23. Y. J. Uemura, T. Yamazaki, D. R. Harshman, M. Senba and E. J. Ansaldo, *Physical Review B*, 1985, **31**, 546-563.

24. Z. Salman, A. Keren, P. Mendels, V. Marvaud, A. Scuiller, M. Verdaguer, J. S. Lord and C. Baines, *Physical Review B*, 2002, **65**, 132403.

25. T. Moriya, *J. Phys. Soc. Jpn.*, 1963, **18**, 516-520.

26. Y. J. Uemura, *Hyperfine Interact.*, 1984, **18**, 447-451.

27. A. Cini, M. Mannini, F. Totti, M. Fittipaldi, G. Spina, A. Chumakov, R. Rüffer, A. Cornia and R. Sessoli, *Nature Communications*, 2018, **9**, 480.

28. M. Mannini, F. Pineider, C. Danieli, F. Totti, L. Sorace, P. Sainctavit, M. A. Arrio, E. Otero, L. Joly, J. C. Cezar, A. Cornia and R. Sessoli, *Nature*, 2010, **468**, 417-421.

29. A. Cornia and M. Mannini, in *Struct Bond*, ed. S. Gao, Springer Berlin Heidelberg, Berlin, Heidelberg, 2015, DOI: 10.1007/430_2014_150, pp. 293-330.

30. M. Mannini, F. Pineider, P. Sainctavit, C. Danieli, E. Otero, C. Sciancalepore, A. M. Talarico, M. A. Arrio, A. Cornia, D. Gatteschi and R. Sessoli, *Nat. Mater.*, 2009, **8**, 194-197.

31. P. Angelova, E. Solel, G. Parvari, A. Turchanin, M. Botoshansky, A. Golzhauser and E. Keinan, *Langmuir*, 2013, **29**, 2217-2223.

32. F. Pineider, M. Mannini, C. Danieli, L. Armelao, F. M. Piras, A. Magnani, A. Cornia and R. Sessoli, *J. Mater. Chem.*, 2010, **20**, 187-194.

33. H. Takiguchi, K. Sato, T. Ishida, K. Abe, K. Yase and K. Tamada, *Langmuir*, 2000, **16**, 1703-1710.

34. H. Hakkinen, *Nat. Chem.*, 2012, **4**, 443-455.

35. G. Rajaraman, A. Caneschi, D. Gatteschi and F. Totti, *Phys. Chem. Chem. Phys.*, 2011, **13**, 3886-3895.

36. J. Hutter, M. Iannuzzi, F. Schiffmann and J. VandeVondele, *Wiley Interdisciplinary Reviews: Computational Molecular Science*, 2014, **4**, 15-25.

37. F. Aquilante, J. Autschbach, R. K. Carlson, L. F. Chibotaru, M. G. Delcey, L. De Vico, I. Fdez Galvan, N. Ferre, L. M. Frutos, L. Gagliardi, M. Garavelli, A. Giussani, C. E. Hoyer, G. Li Manni, H. Lischka, D. Ma, P. A. Malmqvist, T. Muller, A. Nenov, M.

Olivucci, T. B. Pedersen, D. Peng, F. Plasser, B. Pritchard, M. Reiher, I. Rivalta, I. Schapiro, J. Segarra-Marti, M. Stenrup, D. G. Truhlar, L. Ungur, A. Valentini, S. Vancoillie, V. Veryazov, V. P. Vysotskiy, O. Weingart, F. Zapata and R. Lindh, *J. Comput. Chem.*, 2016, **37**, 506-541.

38. E. Morenzoni, F. Kottmann, D. Maden, B. Matthias, M. Meyberg, T. Prokscha, T. Wutzke and U. Zimmermann, *Phys. Rev. Lett.*, 1994, **72**, 2793-2796.

39. E. Morenzoni, H. Glückler, T. Prokscha, R. Khasanov, H. Luetkens, M. Birke, E. M. Forgan, C. Niedermayer and M. Pleines, *Nuclear Instruments and Methods in Physics Research Section B: Beam Interactions with Materials and Atoms* 2002, **192**, 254.

Chapter 7

Beyond the Vanadyl-based Molecules

Additional side works carried out during my PhD concern the investigation of SMMs by using Cantilever Torque Magnetometry (CTM) to characterize their magnetic anisotropies. In particular, here is presented the study performed on a cobalt(II)-based SMM, since this investigation provides some hints valid also for the research in molecular spin qubits. It is interesting to show how the behaviour changes when considering systems with $S > 1/2$, such as Co^{II} that has $S = 3/2$ and $I = 7/2$. Such a problem also requires to modify the multi-technique approach previously used to characterize the properties of the vanadium(IV)-based molecules. In particular, the determination of the static anisotropic magnetic properties becomes here mandatory to obtain a clear picture of the electronic structure of the system. Moreover, the relaxation processes affecting the spin dynamics are different from those found for the vanadium-based molecules: now quantum tunneling effects may occur, as well as the Orbach relaxation process (§3.3.4).[1] The use of the spin Hamiltonian model, which has been used so far for describing the spin structure of V^{IV}, also requires caution. Indeed, it may not be valid anymore, with the result that more accurate models must be employed. Thus, despite my contribution in this investigation was principally devoted to the CTM experiment and analysis, it is interesting to expose the obtained results in order to provide an example of the spin dynamics behaviour in such systems. All these aspects are briefly discussed in the first section for a pseudo-octahedral Co^{II}-based single molecule magnet.

The chapter briefly reviews also the goals achieved by investigating a series of Ln-based systems. This second section concerns the investigation of 1D chiral chains through CTM, providing an example of its capability in disentangling the single-ion magnetic anisotropy also when complex non-collinear spin structures are studied.

7.1 Characterization of a Co(II)-based SMM

Paper in Appendix

A pseudo-octahedral cobalt(II) complex with bispyrazolylpyridine ligands acting as a zero-field single-molecule magnet with easy axis anisotropy.

L. Rigamonti, N. Bridonneau, G. Poneti, L. Tesi, L. Sorace, D. Pinkowicz, J. Jover, E. Ruiz, R. Sessoli and A. Cornia. In: *Chemistry-A European Journal* **24** (2018), pp. 8857-8868.

The use of the $S = 1/2$ ground Kramers doublet of Co^{II} as potential molecular spin qubit has been proposed by (Zadrozny et al., 2017)[2]. However, when working with metal ions with multiple excited Kramers doublets relatively close to the ground doublet, it should be stressed that the spin dynamics may significantly differ with respect to what previously shown for real $S = 1/2$ systems.

The here investigated Co^{II}-based molecule is $[Co(bpp\text{-}COOMe)_2](ClO_4)_2$, where *bpp-COOMe = methyl-2,6-di(pyrazol-1-yl)pyridine-4-carboxylate*, and hereafter indicated as **Cobpyr**; the molecular structure is shown in Figure 7.1. The Co^{II} metal ion has three unpaired electrons and nuclear spin $I = 7/2$ (^{59}Co, abundance 100%).

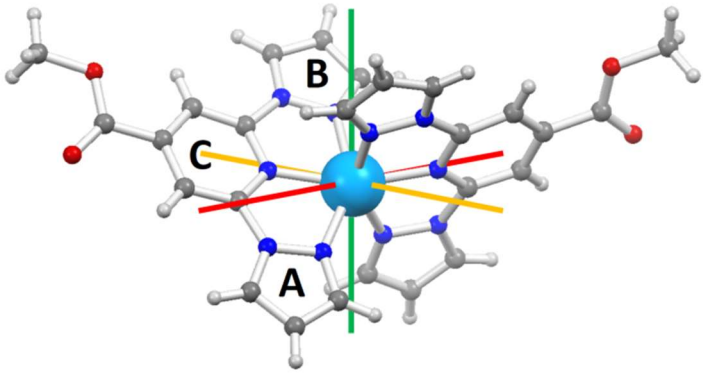

Figure 7.1. Molecular structure of **Cobpyr**. The colour code is: Co=azure, O=red, N=blue, C=light grey, H=white. The magnetic anisotropy axes found experimentally by CTM and EPR measurements are also reported: easy axis=red, intermediate axis=green and hard axis=yellow.

It can be anticipated that the pseudo-octahedral coordination environment produced by the inherent shape of the bpp ligands leads to a stabilization of the d_{xy} orbital relative to d_{xz} and d_{yz} that results in a magnetic easy-axis anisotropy for Co^{II}.[3, 4] The magnetic field dependence of the isothermal molar magnetization (M_M) measured for several values of temperature, as well as the temperature dependence of the product between the molar magnetic susceptibility (χ_M) and the temperature itself, can be well-reproduced by using the following spin Hamiltonian

$$\mathcal{H} = \mathcal{H}_{Zeeman} + \mathcal{H}_{ZFS} = \mu_B \hat{S} \cdot \boldsymbol{g} \cdot \hat{B} + \hat{S} \cdot \boldsymbol{D} \cdot \hat{S}$$
$$= g_x \mu_B B_x S_x + g_y \mu_B B_y S_y + g_z \mu_B B_z S_z + \tag{7.1}$$
$$D[S_z^2 - \frac{1}{3} S(S+1) + E(S_x^2 - S_y^2)]$$

where D and E are the axial and transverse second-order anisotropy parameters, and g_x, g_y and g_z the principal components of the $\boldsymbol{g}$ matrix for the $S = 3/2$ state. The best-fit parameters are $D = -57.5(7)$ and $|E| = 15.7(3)$ cm^{-1}; $g_x = g_y = 2.332(4)$ and $g_z = 2.6687(15)$, thus indicating an easy-axis magnetic anisotropy with a relevant rhombic distortion, $|E/D| = 0.273$. From these values, the splitting of the $S = 3/2$ manifold can be estimated to be ca. 127 cm^{-1}, with the doublet $M_S = \pm 3/2$ forming the ground doublet.

The cantilever torque measurements were performed on a single-crystal in order to characterize the magnetic anisotropy of **Cobpyr**, and in particular to obtain information about the directions of the principal magnetic anisotropy axes (see Figure 7.1). Cantilever torque magnetometry is a very sensitive technique that requires a face-indexed single crystal of few μg depending on the intensity of the magnetic anisotropy. The crystal is placed on the upper plate of a capacitor that can be rotated in a static magnetic field $\boldsymbol{B}$. Depending on the rotation angle with respect to the direction of the magnetic field, the magnetic sample bends the upper plate of the cantilever trying to align its magnetic easy direction with the magnetic field. This bending changes the distance between the capacitor's plates, for which it is possible to detect the torque, $\boldsymbol{\tau}$, acting on the sample as a change in the capacitance. By considering the laboratory frame XYZ, the rotation axis of the cantilever, Y, and the magnetic field applied normal to Y, in the XZ plane at an angle θ from Z, then the device measures the torque component τ_Y. This is described by

$$\tau_Y = m_Z B_X - m_X B_Z \tag{7.2}$$

where $\boldsymbol{m} = (m_X, m_Y, m_Z)$ is the magnetic moment of the sample. In the low-field limit $g\mu_B \boldsymbol{B} \ll kT$, the magnetization can be assumed to be linear with magnetic field, and the measured torque is connected to the susceptibility tensor χ by the expression

$$\tau_Y = B^2(\chi_{ZZ} - \chi_{XX}) \sin\phi \cos\phi \tag{7.3}$$

where ϕ is the angle between the projection of the z principal axis of the molecular anisotropy in the XZ plane and $\boldsymbol{B}$. It should be noted that this angle differs from the

rotation angle of the cantilever. An additional term dependent on χ_{XZ} can be set at zero by arbitrarily choosing the zero in the rotation. When the B/T ratio is increased beyond the low-field regime, the torque curves deform such that the angular dependence becomes very different depending whether the easy axis is almost parallel or perpendicular to the field. It will be shown later that this is a key feature to disentangle individual contributions to the crystal magnetic anisotropy. Besides the advantage of being extreme sensitivity to the presence of anisotropic sources inside a sample, if high magnetic fields are available this technique enable us to investigate the magnetic anisotropy up to room temperature. This last feature makes possible to characterize not only the ground state, but also the S (or J for lanthanides) manifold.[5]

In this case, data were collected for two different rotations of the **Cobpyr** crystal and by applying various magnetic field and temperature values. For example, in Figure 7.2 the measurements and simulations for the rotation in the frame $X = a^*, Y = b,\ Z = c$ are reported, where a^*bc is the orthogonalized crystallographic frame. In this configuration the rotation axis Y corresponds to the binary axis b of the monoclinic $C2/c$ space group, thus coinciding with one of the principal directions of the magnetic anisotropy tensor. The other two anisotropy principal directions are thus in the plane perpendicular to it. The simulation of the low temperature measurements (10 K) confirmed the spin Hamiltonian parameters extracted from the static magnetic measurements. On the other hand, the agreement between experimental and simulated data at 100 K is less satisfactory, suggesting that on increasing the temperature the magnetic properties are affected by spin-orbit coupled states at higher energies, for which the description of the metal ion as a simple $S = 3/2$ spin may be no longer valid.[6]

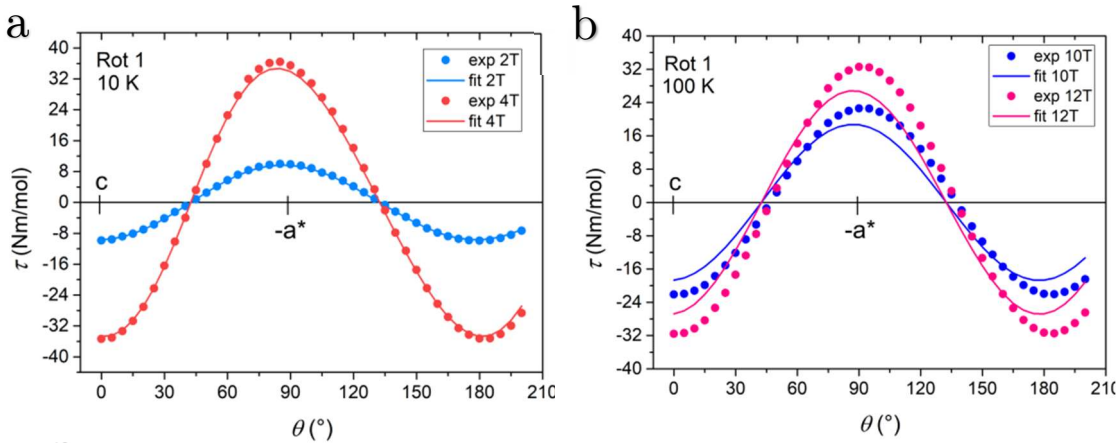

Figure 7.2. Experimental (dots) and simulated (solid lines) curves obtained by CTM for the rotation around the binary axis b at 10 (a) and 100 K (b) under different static magnetic fields.

Complementarily to CTM, EPR spectroscopy can easily provide detailed information on the $\boldsymbol{g}$ matrix relative to the fundamental Kramers doublet.[7] Low temperatures X-band

cw-EPR spectra were recorded for single-crystal and powders samples of **Cobpyr** diluted in its Zn^{II}-based isostructural diamagnetic analogue: $[Zn_{0.95}Co_{0.05}(bpp\text{-}COOMe)_2](ClO_4)_2$, hereafter indicated as **Cobpyr/Zn**. The analysis performed on the single crystal confirmed unambiguously the principal magnetic anisotropy directions of the ground doublet already identified by CTM measurements. The orientation of these directions with respect to the molecule are shown in Figure 7.1. Furthermore, the parameters obtained by dc magnetic analysis well reproduced the cw-EPR spectrum of the powder sample: by fixing the previously obtained anisotropy, $E/D = -0.273$, then $g_x = 2.125$, $g_y = 1.935$ and $g_z = 2.825$ (or alternatively, $E/D = +0.273$, then $g_x = 1.935$, $g_y = 2.125$ and $g_z = 2.825$).[8] These results evidence that $\boldsymbol{g}$ has a non-negligible rhombicity, which cannot be detected by the other magnetic characterization techniques (SQUID magnetometry and CTM) as they are mainly sensitive to the main component of the $\boldsymbol{D}$ anisotropy. Moreover, the only way to reconcile the data obtained by the various techniques is by assuming that the $\boldsymbol{g}$ and $\boldsymbol{D}$ matrices for the $S = 3/2$ state have opposite rhombicity: the smallest $\boldsymbol{g}$ principal value is collinear with the intermediate direction of the $\boldsymbol{D}$ tensor, whereas the intermediate $\boldsymbol{g}$ component is along the hard direction of the $\boldsymbol{D}$ tensor. Such a behaviour has never been reported in literature previously and it is a counterintuitive feature since both anisotropy terms arise from the spin-orbit coupling.

Collecting the obtained results, the spin Hamiltonian approach successfully reproduces the low temperature magnetic and EPR data. However, it still cannot reproduce satisfactorily the high temperature results of CTM, probably because of the contribution of the unquenched orbital momentum.[6] An alternative description of the electronic structure of distorted octahedral Co^{II}, which explicitly takes into account the unquenched orbital angular momentum, can be obtained by using the Griffith Hamiltonian[9] that operates on the ground $^4T_{1g}$ term of the octahedral Co^{II} ion

$$\mathcal{H} = -\frac{3}{2}\kappa\lambda\hat{L}\cdot\hat{S} \;+\; \Delta_{ax}\left[\hat{L}_z^2 - \frac{1}{3}L(L+1)\right] \;+\; \Delta_{rh}\left[\hat{L}_x^2 - \hat{L}_y^2\right] + \\ + \mu_B\boldsymbol{B}\cdot\left(g_e\hat{S} - \frac{3}{2}\kappa\hat{L}\right) \tag{7.4}$$

where the orbital $L = 1$ interacts through the spin-orbit coupling with the spin $S = 3/2$ as described by the first term of the Hamiltonian; here λ is the spin-orbit coupling constant and the orbital-reduction parameter κ accounts for the covalence effects and the mixing between $^4T_{1g}(^4F)$ and $^4T_{1g}(^4P)$. The second term of the Hamiltonian eq. (7.4) represents the effect of an axial crystal field, which results in the splitting of the orbital triplet $^4T_{1g}$ in octahedral symmetry into the states $^4A_{2g}$ ($M_L = 0$) and ^4E_g ($M_L = \pm 1$) in tetragonal symmetry. The third term models the rhombic component of the crystal field,

which removes the degeneracy of the orbital doublet further lowering the symmetry to C_2. In this framework, a negative (positive) value of Δ_{ax} results in a ground $^4E_g(^4A_{2g})$ term and corresponds to easy-axis (easy-plane) anisotropy (Figure 7.3).[6, 10, 11] Finally, the fourth term is the Zeeman interaction, which includes spin and orbital contributions.

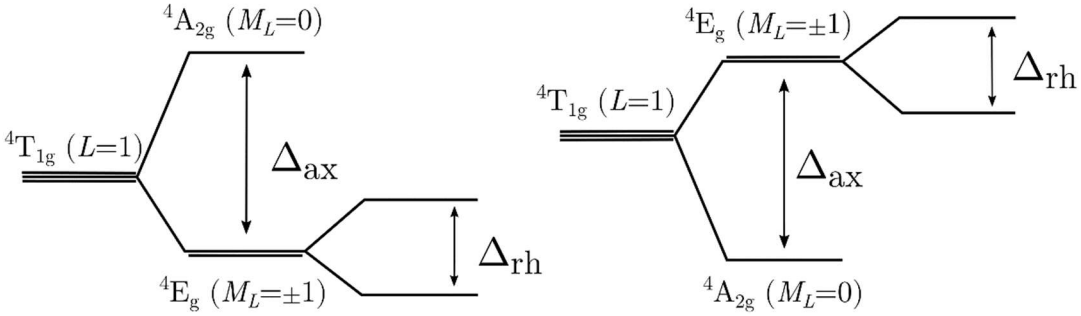

Figure 7.3. The two possible splittings of the $^4T_{1g}$ (L=1) term by axial and rhombic crystal fields.

Without entering into the detail, the best agreement, with respect to the cw-EPR spectrum and dc magnetic data, is found for $\Delta_{ax} = -1850$ cm^{-1}, $\Delta_{rh} = 130$ cm^{-1}, $\kappa = 0.9$ and by fixing λ to the tabulated free-ion value -180 cm^{-1}. This set of parameters corresponds to a first-, second- and third-excited spin-orbit doublets lying at 210, 558 and 820 cm^{-1} from the ground state, respectively. This outcome confirms that the spin Hamiltonian might not be entirely appropriate for modelling the magnetic behaviour at high temperatures, such as 100 K, because of the influence of the second-excited doublet on the first-excited one.[6]

The easy-axis magnetic anisotropy has also been rationalised by theoretical calculations performed by using ORCA[12] and MOLCAS[13-15] software that provided the electronic structure diagram reported in Figure 7.4a.[16, 17] According to this, the d_{xy} orbital is the lowest in energy, and thus the first excitation occurs within the d_{xz}/d_{yz} orbital pair. Since these transitions do not cause a change of $|m_l|$ value, the $M_s = \pm 3/2$ components become more stable and, consequently, a negative contribution of the D value is obtained.[16, 18]

The electronic spin levels are also computed and are in good agreement with the energies of the first-, second- and third-excited Kramers doublets obtained by using the Griffith Hamiltonian: ca. 191, 648 and 929 cm^{-1}. The robustness of the calculations is underlined because the use of a larger basis set does not significantly change the results. The calculated $|D|$ values are approximately 50% larger than those obtained from fitting the experimental magnetic data, whereas the computed values of E are in good agreement. Once more, this confirms the low reliability of the spin Hamiltonian formalism

for this particular case. Moreover, the directions of the principal magnetic anisotropy axes, as well as the $\boldsymbol{g}$ values obtained by cw-EPR, are well reproduced by the theoretical calculations. The non-collinearity of the anisotropy tensors, for which the hard axis of $\boldsymbol{g}$ corresponds to the intermediate $\boldsymbol{D}$ principal direction, is also reproduced by the calculations.

Ac susceptibility measurements were performed to study the spin dynamics of a microcrystalline powder sample of **Cobpyr**. Similarly to the vanadyl systems, no peaks of the imaginary component of the susceptibility χ'' appear without the application of an external magnetic field. However, as the external magnetic field is applied, slow relaxation occurs. The frequency dependence of χ'' can be fitted by using the Debye model (eq. 4.2), from which a relaxation time τ is obtained. The temperature dependence of the extracted relaxation time τ under a dc field of 100 mT is reported in Figure 7.4c as $\ln\tau$ *vs* $(1/T)$. The investigated temperature range is between 1.9 and 9.5 K, with τ that goes from 6 ms to 10 μs, respectively. In addition to the relaxation processes that were accounted for the V^{IV}-based $S = 1/2$ systems previously studied, the presence of Kramers doublets close to the ground doublet requires to consider other relaxation processes. Indeed, the Orbach process (§3.3.4) is one of the principal processes often found to play a key role in the spin-lattice relaxation of SMMs. Another common process, which one should consider when working with SMMs, is the quantum tunneling (QT). This process may be active in systems with spin states close in energy for which an overlap of their wavefunctions occurs.[1] By combining these terms with the direct and Raman processes described in the previous chapters, the following general expression for τ is obtained

$$\tau^{-1} = \tau_0 \exp(-U_{eff}/kT) + A + BT + CT^n \qquad (7.5)$$

where τ_0 and U_{eff} are the parameters of the Arrhenius law, A is the quantum tunneling (temperature independent) rate, B is the coefficient of the direct process, while C is the coefficient of the Raman process and n its exponent.

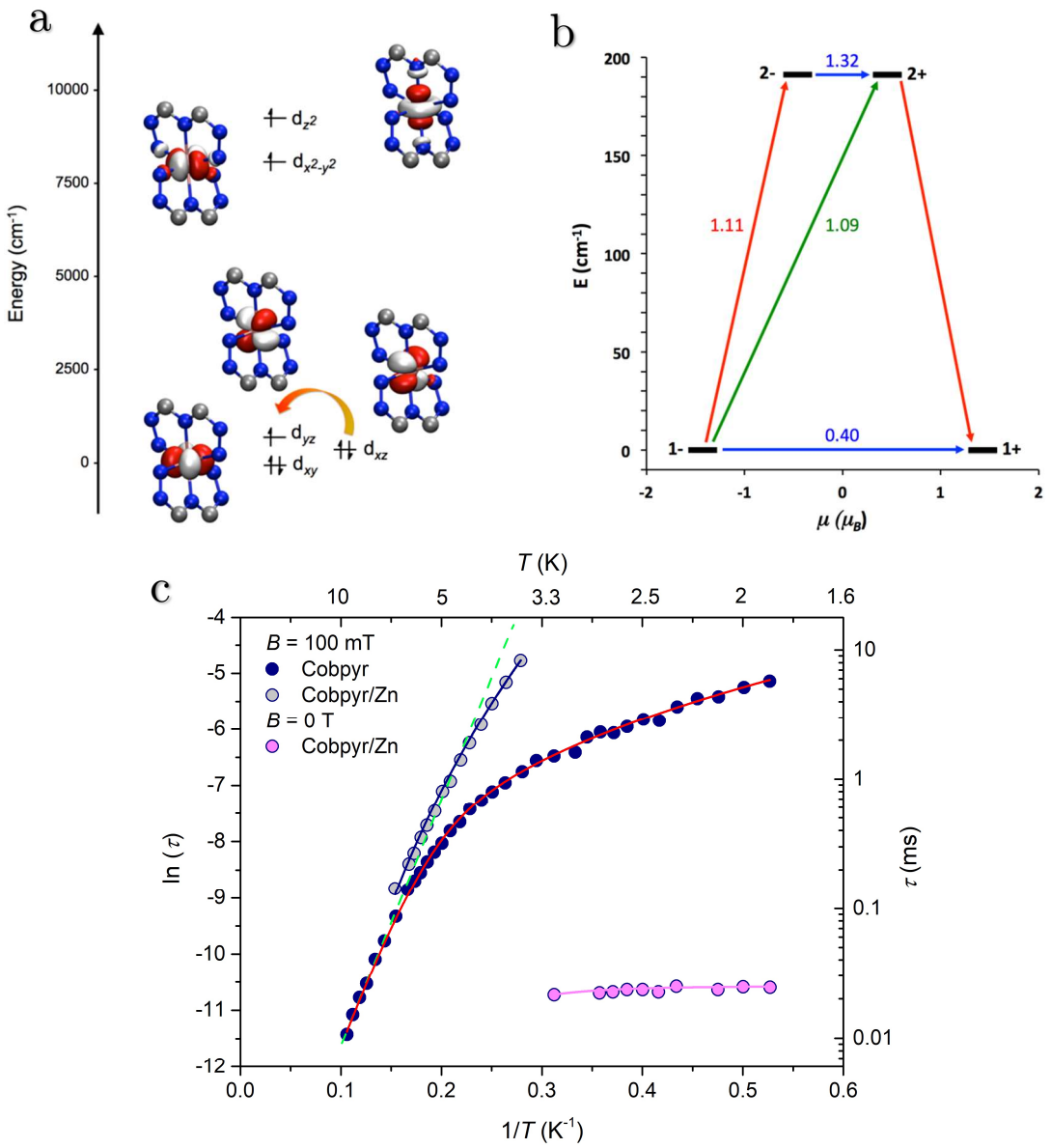

Figure 7.4. (a) Theoretically computed *d*-orbital splitting for **Cobpyr** (orbital energies: d_{xy}=0.0, d_{xz}=444.6, d_{yz}=697.9, $d_{x^2-y^2}$=8121.0, d_{z^2}=9257.3 cm^{-1}). Colour code: Co=red/white, C=gray, N=blue; hydrogen atoms and part of the ligands have been omitted for clarity. The orange arrow indicates the lowest-energy transition. (b) Lowest two Kramers doublets and *ab initio* relaxation processes computed for **Cobpyr**. The thick black lines are the doublets as a function of their magnetic moment along the main anisotropy axis. Red lines indicate the magnetization reversal mechanism. Blue lines correspond to ground state QT and thermally assisted QT through the first-excited doublet. Green lines show the hypothetical Orbach relaxation processes. The values reported indicate the matrix elements of the transition magnetic moments. (c) Arrhenius plot for **Cobpyr** at an applied static field of 100 mT and for **Cobpyr/Zn** in zero field and under a static field of 100 mT. The dashed green line derives by the Arrhenius fit on the **Cobpyr** high temperature data. The red and blue lines result from the fit made by combining the direct and Raman processes. The magenta line results from the fit made by combining the QT and Raman processes.

It should be stressed that the U_{eff} energy barrier, which is extracted by considering the Orbach process, must correspond to a real excited state (§3.3.4). For lanthanides-

based systems the values obtained by the analysis of spin dynamics can be confirmed by spectroscopic techniques.[19, 20] Instead, for transition metals as Co^{II}, a cross-investigation such as the one here performed is required to clarify whether the excited state plays a role in the spin-lattice relaxation or not. This is of particular importance in the present case, where the competition between the Orbach and Raman processes makes difficult to identify, starting from the ac susceptibility data, which process dominates the relaxation. Indeed, the high temperature range can be satisfactorily fitted with the Arrhenius law by using the following best-fit parameters: $U_{eff} = 30.3(2)$ cm^{-1} and $\tau_0 = 1.2(2) \cdot 10^{-7}$ s (green line in Figure 7.4c). This analysis would thus suggest the main role of an excited state at ca. 30 cm^{-1} in the relaxation. On the other hand, the entire curve can also be reproduced considering the direct and Raman processes terms, for which the best-fit parameters are $C = 0.45(8)$ s^{-1}K^{-n}, $n = 5.38(9)$ and $B = 103(4)$ K^{-1} (red line in Figure 7.4c). The exponent n of the Raman process for a Kramers ion should be equal to 9, but values close to $n = 5$ can occur when low-lying excited electronic states are present (§3.3.3).[21-23]

The hindered detection of zero-field relaxation may be due to a strong quantum tunneling relaxation induced by hyperfine interactions or intermolecular dipolar couplings that accelerate the relaxation of the magnetization. Dilution of SMMs in a diamagnetic matrix has been identified as a key tool for reducing such long-range couplings, thus affording a measurable zero-field relaxation.[24-29] The effects of dipolar interactions for **Cobpyr** were then ascertained by measuring the ac response of **Cobpyr/Zn**. This was done both at zero-field and under a static magnetic field of 100 mT. As expected, the diluted sample exhibits an out-of-phase magnetic susceptibility response also at zero field, which indicates the onset of slow relaxation. The corresponding temperature dependence of the relaxation rate can be reproduced by considering a combination of the Raman relaxation process and QT. A best-fit procedure yields $C =$ 11(2) s^{-1} K^{-n} and a tunneling frequency of $A = 40.3(5)$ kHz, with the n exponent fixed at 5.38 as for the concentrated **Cobpyr** sample, to avoid over-parametrization. Upon application of a static field of 100 mT, the magnetization dynamics of **Cobpyr/Zn** slows down significantly due to the further suppression of the relaxation pathways induced by QT. The effective barrier value obtained this time by fitting the high temperature region with the Arrhenius law is $U_{eff} = 24$ cm^{-1}, thus differing with respect to the value extracted for **Cobpyr** (for which $U_{eff} = 30$ cm^{-1}). Since the separation between the ground and first-excited doublets does not change by diluting the sample, the relaxation process prevailing at high temperature must be the Raman process. This is also consistent with the absence of real excited states at energy close to U_{eff}. The data measured for the diluted sample with an applied magnetic field are thus reproduced by the combination

of the direct and Raman processes; the best-fit parameters obtained are $C = 0.015(5)$ s^{-1} K^{-n}, $n = 7.0(2)$ and $B = 0(4)$ K^{-1}. These values indicate that the application of a static magnetic field of 100 mT is sufficient to suppress the quantum tunneling pathway and leads to an increased n exponent, in line with a previous report on trigonal distorted octahedron Co^{II} complexes with easy-axis anisotropy.[30]

The spin-relaxation pathways can be obtained directly through the theoretical calculations performed within the MOLCAS software (Figure 7.4b).[16, 31-33] Such calculations confirm a plausible relaxation pathway through quantum tunneling in the ground doublet. Indeed, the matrix element of the transition within the 1-/1+ ground doublet takes a value of 0.40, which is higher than the required threshold of 0.1 for an efficient relaxation process. In addition, an Orbach process could be also plausible. For example, the first-excited doublet is quite low in energy (191 cm^{-1}) and the matrix elements related to the vertical and diagonal (Orbach) excitations (1.09 and 1.11, respectively) are sufficient to cause spin relaxation through these pathways. However, as discussed above, the experimental effective barrier for the Orbach process is significantly smaller than the calculated one (U_{eff}~30 cm^{-1} vs $\Delta E = 191$ cm^{-1}) making it implausible in the investigated temperature range. The experimental outcomes indeed confirmed the key role of the spin-phonon Raman relaxation process as opposed to the Orbach one.[34] This underlines a strong limitation of *ab initio* methods, since the Raman process is still not routinely and appropriately evaluated by theoretical calculations. This lack limits the understanding of the spin-lattice relaxation and points out to the need of a multitechnique approach for appropriate determining the electronic structure of the investigated systems.

7.2 Exploring the non-collinearity of spin helices

Paper in Appendix

Spin helicity in chiral lanthanide chains.

I. Mihalcea, M. Perfetti, F. Pineider, L. Tesi, V. Mereacre, F. Wilhelm, A. Rogalev, C. E. Anson, A. K. Powell and R. Sessoli. In: *Inorganic Chemistry* **55** (2016), pp. 10068-10074.

The non-collinearity of spins is a desirable feature for multi-qubits systems as it allows to address individually qubits for manipulating the superposition state. However, the interest concerning the resolution of the spin structure when spins are non-collinear is very broad and touch several different topics. In this work, for example, the helical spin structure of three Ln-based chiral chains has been determined by means of CTM. This study, besides trying to gain insights into mixed effects that emerges from the

combination of chirality and magnetism, such as the magneto-chiral dichroism,[35-37] demonstrates the efficiency of CTM to solve the spin structure of these three helical spin chains.

The investigated chiral 1D chains have formula $[Ln(Hnic)\text{-}(nic)_2(NO_3)]_n$, where *Hnic= nicotinic acid* and Ln=Tb, Dy and Er, and hereafter simply indicated as **Tb**, **Dy** and **Er**, respectively.[38] The metal ions are coordinated by 8 oxygen atoms (2 from the nitrate anion and 6 from the nic^- ligands) forming a triangular dodecahedral geometry with quasi-D_{2d} symmetry. The bridge between the metal centres is provided by the *1,3-carboxylic* moiety of the nic^- ligand that fixes the distance between the metal ions to ∽4.8 Å. Pure enantiomeric compounds with space groups $P6_1$ and $P6_5$ are spontaneously obtained from their crystallization, even without chiral ligands; furthermore, they crystallize isotopically to each other. Among the possible Ln ions, the work focused on the highly anisotropic ions Tb^{III} (ground state $J = 6$), Dy^{III} (ground state $J = 15/2$)[39] and Er^{III} (ground state $J = 15/2$).

Cantilever torque magnetometry measurements were performed on single crystals of **Tb**, **Dy** and **Er** at 5 K and in relatively strong magnetic fields. In this case, since the response τ_Y is no more tensorial in character and does not follow eq. (7.3), their symmetry-related contributions do not cancel out completely. This allows to disentangle the signals of the non-collinear centres. More information on this peculiar feature of CTM can be found in the review (M. Perfetti, 2017).[5] The three investigated systems have a C_6 axis parallel coincident with the crystallographic c axis, for which the orientation of the anisotropy tensors, assumed to be axial, of the six crystallographically equivalent ions can be determined just using two Euler angles. In this work were chose the angle between the z molecular axis and c axis, ξ, equal for all spins, and the angle between the a axis and the projection of the z molecular axis on the ab plane, ρ. In doing so, once the principal directions of the first anisotropy tensor are found, the others can be easily determined by adding a factor $(60i)°$ to ρ, with $i = 1$ to 5.

The most efficient way to determine the magnetic anisotropy is by measuring the magnetic torque when performing rotations along two orthogonal axes. The first rotation (Rot1) was performed using the c axis as rotation axis, while for the second one (Rot2) the rotation axis laid in the ab' plane. Consequently, by recalling how ξ and ρ are defined, Rot1 is more sensitive to the latter, whereas Rot2 is extremely dependent on ξ. The measured torque curves for **Tb**, **Dy** and **Er** are reported in Figure 7.5b.

As visible from the reported data (Figure 7.5b), all samples exhibit the 6-fold symmetry imposed by the structure. Six zero-torque points are visible in Rot1, corresponding to the three independent projections on the ab' plane of the six anisotropy tensors arising from the Ln ions, and all the maxima have similar intensities as expected

when c is the rotation axis (see also Figure 7.5a). Rot2 shows instead more complicated features that differ for the three compounds, but the signal always vanishes near 0° and 90°, corresponding to $c \parallel \boldsymbol{B}$ and $c \perp \boldsymbol{B}$, respectively, as expected.

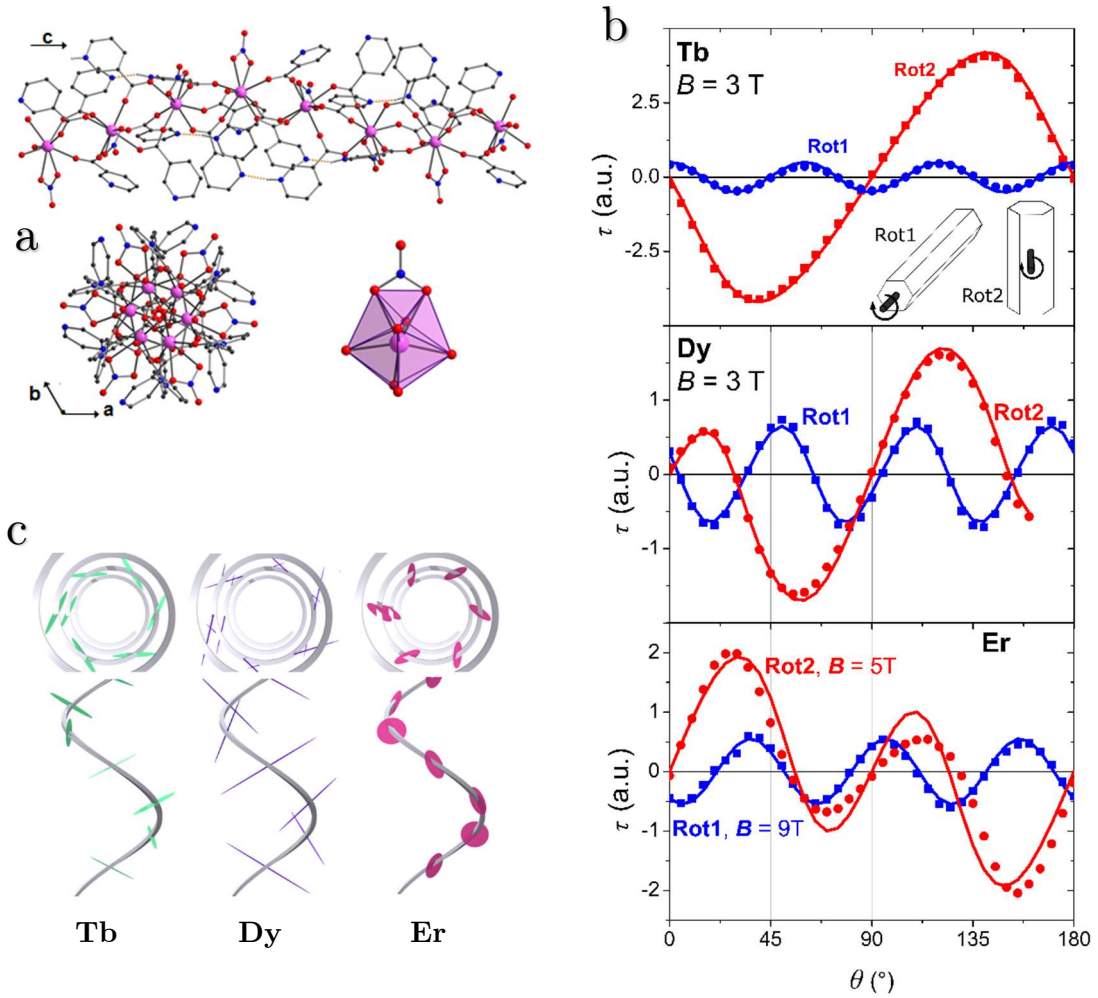

Figure 7.5. (a) Structure of the **Er** helical chain viewed from the side (top) and down the 6_5 axes (bottom left), and coordination polyhedron of the Er^{III} ion showing its idealized dodecahedral C_{2v} symmetry (bottom right). Colour code: Er=pink, O=red, N=blue, C=gray. The hydrogen atoms are omitted for clarity. The other complexes are isostructural. (b) Experimental (dots or squares) and fitted (solid lines) results obtained for **Tb**, **Dy** and **Er**. (c) Schematic representation of the spin helicity obtained by plotting the susceptibility tensors calculated from the CTM experiments at $T = 5$ K (top, view along the $\boldsymbol{c}$ axis; bottom, view along the ab' plane). The susceptibility of the hard directions (x and y) of **Dy** has been multiplied by a factor of 5 to give more solid aspect to the ellipsoids.

The single-ion magnetic anisotropy of lanthanide ions can be obtained by modelling the system with the following spin Hamiltonian:

$$\mathcal{H} = g_J \mu_B \boldsymbol{B} \cdot \hat{\boldsymbol{J}} + \sum_{k=2,4,6} \sum_{q=-k}^{k} b_k^q \hat{O}_k^q \qquad (7.6)$$

in which the first term accounts for the Zeeman splitting, while the second refers to the magnetic anisotropy and corresponds to the crystal field (CF) potential acting on the metal centre; $\hat{\boldsymbol{J}}$ is the total angular momentum operator and b_k^q are the coefficients of the O_k^q Stevens operators,[21] which act on the $|J, m_J\rangle$ space, where m_J is the projection of J in the z direction. In principle, given the low symmetry of the metal site, all terms up to sixths order should be taken into account. However, since the interest in this case concerns the determination of the nature and direction of individual low temperature magnetic anisotropies, the model has been limited to the second order terms. Furthermore, satisfactory fits were obtained for **Dy** and **Er** using only second-order axial (*i.e.* $q = 0$) terms, whereas the inclusion of a rhombic term (O_2^2) was necessary for **Tb**. This simple model works only for the low-temperature regime, and a more accurate model is required to describe the low-symmetry coordination environment for higher temperatures. The best-fit parameters are reported in Table 7.1.

Table 7.1. Best-fit parameters obtained by reproducing the CTM data of **Tb**, **Dy** and **Er** with eq. (7.6).

System /parameter	$\boldsymbol{b_2^0}$ **(cm^{-1})**	$\boldsymbol{b_2^2}$ **(cm^{-1})**	$\boldsymbol{\rho}$ **(°)**	$\boldsymbol{\xi}$ **(°)**	$\boldsymbol{\psi}$ **(°)**
Tb	-1.54	-3.8	31(1)	76(1)	23(1)
Dy	-1.91	-	41(1)	61(1)	-
Er	+2.33	-	21(1)	56(1)	-

The inclusion of a transverse term in the Hamiltonian of **Tb** requires the use of a third Euler angle, as shown in Table 7.1. From the analysis it emerges that **Dy** is characterized by single-ion easy axis magnetic anisotropy, whereas the **Er** anisotropy is of easy-plane type. Instead, **Tb** has rhombic single-ion anisotropy and, for the convention here used, the easiest direction lies along the z molecular axis. The observation of a different anisotropy for Er^{III} agrees with the expected 4f-shell electron density, which can be approximated as an oblate spheroid for Tb^{III} and Dy^{III} and a prolate spheroid for Er^{III} (see Figure 7.6).

From Table 7.1 it is possible to note that the ξ values for all systems are slightly larger than 54.7° (magic angle), indicating that the c crystallographic axis is closer to the hard direction in **Tb** and **Dy**, and the easy direction in **Er**. The largest difference between the intensity of the signal for the two rotations is observed for **Tb**, which has, indeed, the largest value of ξ. Instead, the overall crystal anisotropy of **Dy** and **Er** is very weak because the angle ξ is close to the magic angle. The parameters obtained can be used to graphically represent the spin helicity of the three investigated chains, shown

in Figure 7.5c, in which the anisotropy susceptibility tensors generated by the 6-fold screw axis are depicted.

It is interesting to notice that the overall crystal anisotropy of the three compounds has the opposite nature of the single-ion anisotropy. In particular, **Tb** and **Dy** have larger magnetization in the *ab'* plane, while the *c* axis is the easy axis of magnetization for **Er**.

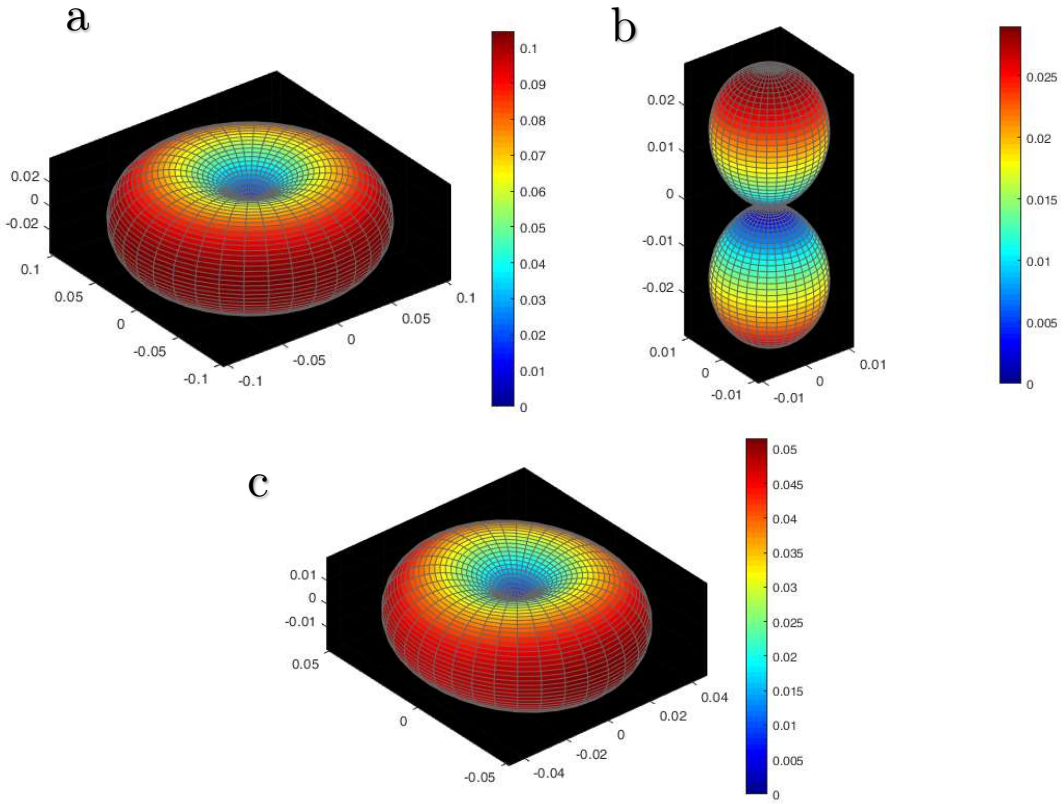

Figure 7.6. Simulations of the magnetic free energy for (a) **Dy**, (b) **Er** and (c) **Tb**, obtained by using the parameters in Table 7.1. The simulations and images have been made by M. Perfetti.

This work is an example of the capability of CTM in disentangling the single-ion magnetic anisotropy also for exotic and complicated non-collinear spin structures, such as the spin helices of the three 1D spin chains here shown. Further information about the spin dynamics, as well as the magnetochiral effect, for the three investigated systems, which are not described here, can be found in the original work[40].

7.3 Conclusions

Although the chapter does not deal directly with molecular spin qubits, the studies here exposed can provide some useful hint for the improvement and investigation of molecular spin qubits.

The first section exposes the features that originate from investigating a molecular magnet with $S > 1/2$ and the importance of a complete characterization of the static magnetic properties. In this case, this has been done by using a multi-technique approach based on magnetometry measurements, cw-EPR and torque magnetometry, together with the support of *ab initio* theoretical models, in order to characterize a pseudo-octahedral Co^{II}-based SMM. The study points out that in certain conditions the spin Hamiltonian may fail in describing the magnetic properties of such systems, and in particular when the orbital contribution is non-completely quenched. In such cases, more accurate (and thus complex) models should be considered. The spin dynamics measured by ac susceptometry reveals in principle the contribution of quantum tunneling, Orbach and Raman processes, though the competition between the last two processes complicates the analysis. It is shown here that the achievement of a reliable frame can be done only thanks to the multi-technique approach. Indeed, though the theoretical analysis would suggest an efficient Orbach process, this is not the dominant one, which is, instead, the Raman process. The QT process is present in the concentrated sample and it hinders the relaxation in zero field. However, this can be suppressed through a crystalline solid dilution of the SMM and by applying a dc magnetic field. This aspect is crucial when dealing with SMMs since the bistability in zero field is one of the main requisites for their potential application as information storage. This work is, thus, a nice example about which types of problems should be tackled when dealing with systems whose spin value is $S > 1/2$.

The second section exposes the capability of cantilever torque magnetometry in disentangling the single-spin anisotropy contribution also for complex structures such as 1D chains composed of non-collinear spins. Indeed, the spin structure of three spin chains based on Tb^{III}, Dy^{III} and Er^{III} has been resolved by using CTM. This is a fundamental aspect in the light of an individual addressing of coupled molecular spin qubits, by using microwave pulses of different frequencies, which could be achieved by synthetizing non-collinear spin systems.

7.4 Bibliography

1. D. Gatteschi, R. Sessoli and J. Villain, *Molecular nanomagnets*, Oxford University Press, Oxford, UK, 2006.
2. J. M. Zadrozny, A. T. Gallagher, T. D. Harris and D. E. Freedman, *J. Am. Chem. Soc.*, 2017, **139**, 7089-7094.
3. S. Gomez-Coca, A. Urtizberea, E. Cremades, P. J. Alonso, A. Camon, E. Ruiz and F. Luis, *Nature Communications*, 2014, **5**, 4300.
4. N. Bridonneau, L. Rigamonti, G. Poneti, D. Pinkowicz, A. Forni and A. Cornia, *Dalton Trans.*, 2017, **46**, 4075-4085.
5. M. Perfetti, *Coord. Chem. Rev.*, 2017, **348**, 171-186.
6. E. A. Buvaylo, V. N. Kokozay, O. Y. Vassilyeva, B. W. Skelton, A. Ozarowski, J. Titis, B. Vranovicova and R. Boca, *Inorg. Chem.*, 2017, **56**, 6999-7009.
7. J. A. Weil and J. R. Bolton, in *Electron Paramagnetic Resonance*, John Wiley & Sons, Inc., 2006.
8. J. R. Pilbrow, ed., *Transition Ion Electron Paramagnetic Resonance*, Oxford University Press, Oxford, 1990.
9. J. S. Griffith, *The theory of transition metal ions*, University Press, Cambridge, UK, 1961.
10. A. V. Palii, D. V. Korchagin, E. A. Yureva, A. V. Akimov, E. Y. Misochko, G. V. Shilov, A. D. Talantsev, R. B. Morgunov, S. M. Aldoshin and B. S. Tsukerblat, *Inorg. Chem.*, 2016, **55**, 9696-9706.
11. A. Abragram and M. H. L. Pryce, *Proc. R. Soc. Lond. A*, 1951, **206**, 173-191.
12. F. Neese, *WIREs Comput. Mol. Sci.*, 2012, **2**, 73-78.
13. F. Aquilante, L. De Vico, N. Ferré, G. Ghigo, P.-å. Malmqvist, P. Neogrády, T. B. Pedersen, M. Pitoňák, M. Reiher, B. O. Roos, L. Serrano-Andrés, M. Urban, V. Veryazov and R. Lindh, *J. Comput. Chem.*, 2010, **31**, 224-247.
14. G. Karlström, R. Lindh, P.-Å. Malmqvist, B. O. Roos, U. Ryde, V. Veryazov, P.-O. Widmark, M. Cossi, B. Schimmelpfennig, P. Neogrady and L. Seijo, *Computational Materials Science*, 2003, **28**, 222-239.
15. V. Veryazov, P.-O. Widmark, L. Serrano-Andrés, R. Lindh and B. O. Roos, *Int. J. Quantum Chem.*, 2004, **100**, 626-635.
16. S. Gomez-Coca, D. Aravena, R. Morales and E. Ruiz, *Coord. Chem. Rev.*, 2015, **289**, 379-392.
17. M. Atanasov, D. Ganyushin, K. Sivalingam and F. Neese, in *Struct. Bond.*, eds. D. M. P. Mingos, P. Day and J. Peder, Springer, Berlin, 2012, pp. 149-220.

18. S. Gomez-Coca, E. Cremades, N. Aliaga-Alcalde and E. Ruiz, *J. Am. Chem. Soc.*, 2013, **135**, 7010-7018.

19. T. T. da Cunha, J. Jung, M.-E. Boulon, G. Campo, F. Pointillart, C. L. M. Pereira, B. Le Guennic, O. Cador, K. Bernot, F. Pineider, S. Golhen and L. Ouahab, *J. Am. Chem. Soc.*, 2013, **135**, 16332-16335.

20. R. Marx, F. Moro, M. Dorfel, L. Ungur, M. Waters, S. D. Jiang, M. Orlita, J. Taylor, W. Frey, L. F. Chibotaru and J. van Slageren, *Chem. Sci.*, 2014, **5**, 3287-3293.

21. A. Abragam and B. Bleaney, *Electron Paramagnetic Resonance of Transition Ions*, Dover, New York, 1986.

22. Y. Rechkemmer, F. D. Breitgoff, M. van der Meer, M. Atanasov, M. Hakl, M. Orlita, P. Neugebauer, F. Neese, B. Sarkar and J. van Slageren, *Nature Communications*, 2016, **7**.

23. K. N. Shrivastava, *physica status solidi (b)*, 1983, **117**, 437-458.

24. R. Ruamps, L. J. Batchelor, R. Guillot, G. Zakhia, A.-L. Barra, W. Wernsdorfer, N. Guihéry and T. Mallah, *Chem. Sci.*, 2014, **5**, 3418-3424.

25. S. Sottini, G. Poneti, S. Ciattini, N. Levesanos, E. Ferentinos, J. Krzystek, L. Sorace and P. Kyritsis, *Inorg. Chem.*, 2016, **55**, 9537-9548.

26. J. M. Zadrozny and J. R. Long, *J. Am. Chem. Soc.*, 2011, **133**, 20732-20734.

27. J. M. Zadrozny, J. Telser and J. R. Long, *Polyhedron*, 2013, **64**, 209-217.

28. M. A. Palacios, J. Nehrkorn, E. A. Suturina, E. Ruiz, S. Gómez-Coca, K. Holldack, A. Schnegg, J. Krzystek, J. M. Moreno and E. Colacio, *Chemistry – A European Journal*, 2017, **23**, 11649-11661.

29. F. Pointillart, K. Bernot, S. Golhen, B. Le Guennic, T. Guizouarn, L. Ouahab and O. Cador, *Angew. Chem. Int. Ed.*, 2015, **54**, 1504-1507.

30. Y.-Z. Zhang, S. Gómez-Coca, A. J. Brown, M. R. Saber, X. Zhang and K. R. Dunbar, *Chem. Sci.*, 2016, **7**, 6519-6527.

31. L. F. Chibotaru, L. Ungur, C. Aronica, H. Elmoll, G. Pilet and D. Luneau, *J. Am. Chem. Soc.*, 2008, **130**, 12445-12455.

32. L. F. Chibotaru, L. Ungur and A. Soncini, *Angew. Chem. Int. Ed.*, 2008, **47**, 4126-4129.

33. L. F. Chibotaru, L. Ungur and A. Soncini, *Angew. Chem.*, 2008, **120**, 4194-4197.

34. A. Lunghi, F. Totti, R. Sessoli and S. Sanvito, *Nature Communications*, 2017, **8**, 14620.

35. G. Rikken and E. Raupach, *Nature*, 1997, **390**, 493-494.

36. R. Sessoli, M.-E. Boulon, A. Caneschi, M. Mannini, L. Poggini, F. Wilhelm and A. Rogalev, *Nat. Phys.*, 2014, **11**, 69.

37. L. D. Barron and J. Vrbancich, *Mol. Phys.*, 1984, **51**, 715-730.

38. I. Mihalcea, N. Zill, V. Mereacre, C. E. Anson and A. K. Powell, *Cryst. Growth Des.*, 2014, **14**, 4729-4734.

39. S. Liu, L. L. Li, H. Li, H. L. Gao, J. Z. Cui and P. Cheng, *Dalton Trans.*, 2015, **44**, 6169-6174.

40. I. Mihalcea, M. Perfetti, F. Pineider, L. Tesi, V. Mereacre, F. Wilhelm, A. Rogalev, C. E. Anson, A. K. Powell and R. Sessoli, *Inorg. Chem.*, 2016, **55**, 10068-10074.

Conclusions

The scientific work described in this dissertation has been devoted to the identification of the main ingredients that allow to increase the relaxation times of molecular spin qubits. More specifically, the investigation has focused on the improvement of the spin-lattice relaxation time T_1 as a means to increase the quantum coherence time, in particular at higher temperature. Such an investigation has been performed on several different homoleptic mononuclear magnetic molecules based on vanadium(IV), which has electronic spin value $S = 1/2$ and nuclear spin $I = 7/2$, in different coordination environments. The disclosure of the relaxation processes, including the mechanisms whereby they influence the spin relaxation, has been possible by combining the results of many different investigation techniques. Indeed, besides the standard techniques, such as pulsed EPR spectroscopy and ac susceptometry, more exotic ones have been employed, *i.e.* THz spectroscopy and 4D-Inelastic Neutron Scattering. Moreover, Muon Spin Relaxation (μSR) spectroscopy has been proposed in order to investigate the spin dynamics of potential molecular qubits. In view of this, preliminary studies have been performed on a well characterized Dy-based SMM. The combination of the magnetic (ac susceptometry and pulsed EPR) and optical (THz spectroscopy) investigations has been particularly relevant to identify the key role of low-energy vibrational modes for the spin-lattice relaxation. Indeed, such vibrations have been recognised as the main parameter in determining the temperature dependence of T_1 when affected by the direct and Raman relaxation processes. Accordingly, the lack of low-energy vibrational modes provides very weak temperature dependences of T_1s. This may represent a key aspect in realizing molecular-based quantum systems with manipulable quantum properties even at room temperature. Moreover, the extensive experimental investigation performed on the vanadyl-based molecular spin qubit of formula $[VO(acac)_2]$, together with the virtuous interplay of accurate theoretical calculations, is expected to provide in the near future an exhaustive model of the spin-lattice relaxation for systems with spin value $S = 1/2$. On the other hand, spin-phonon bottleneck effects have been found to strongly affect the spin-lattice relaxation of such $S = 1/2$ systems. First attempts in explaining this phenomenon by starting from simple thermodynamic considerations have succeeded. In this frame, the presence of spin-phonon bottleneck can

be attributed to the combination of voluminous crystals, high spin density and lack of low energy phonons. However, a model able to completely rationalize this phenomenon is still missing.

To conclude, the rational design used in this work for realizing molecular spin qubits has led to relaxation times long enough to make them appealing for applications toward the quantum technologies. For instance, one of the vanadyl-based molecules here investigated, namely VOPc, has been used in superconductive resonance cavities, demonstrating promising performances for realizing hybrid quantum circuit architectures. However, despite the great developments achieved in these years toward the use of molecular spins for quantum technology applications, this research field is still lagging behind other types of more advanced potential platforms. On the other hand, we have just begun to explore the potentialities of the quantistic properties of molecules, which have their great advantage of being macroscopic systems with extraordinary tunability (metal, ligand, environment). Moreover, in this work molecules have proved to preserve quantum coherence also at room temperature, thus paving the way for exploring new types of quantum applications.

Certainly, the control of the spin carrier's environment represents a main future perspective. One strategy could be the embedding of the spin centre in a rigid lattice like the diamond lattice of Nitrogen-Vacancies centres. Alternatively, the effect of vibrations on the spin could be further mitigated by reducing the orbital contribution to the spin state or by exploiting the symmetry. For example, cycloalkenyl-anionic ligands form a particular coordination with the metal ion through the π-electrons in the p-orbitals, for which the displacements of ligand atoms are expected to have a weaker effect on the spin state. Recently, these types of ligand have been found particularly effective in obtaining SMMs with magnetic hysteresis up to 80 K. On the other hand, these approaches appear difficult to reconcile with the requirement of realizing molecular systems containing two or more interacting qubits, which is mandatory to build up logic quantum gates. Actually, this is one of the most challenging requirements that still remains an open issue for many qubit platforms. In this respect, molecules seem to be very promising candidates for realizing multi-qubits architectures and many efforts are going toward this direction. A first step in the use of vanadyl molecules to realize two-qubits gates has been already achieved, demonstrating also the possibility to implement hybrid electron-nuclear spin schemes by exploiting the hyperfine interaction of the vanadium atom. Indeed, the metal's nuclear spin could represent a significant key source for exploiting approaches that involve the mixing between the electronic and nuclear spin, whose potentialities are still little explored. For example, the hyperfine levels could be used to encode qubits into the nuclear spins, which are more shielded from the environment and exhibit longer

coherence times, while the interaction with other qubits is mediated by the exchange interaction involving the electronic spin. Another example of this hybrid approach concerns the realization of *qudits*, *i.e.* multi-levels qubits, within a single molecule. The availability of multiple spin levels within the same spin carrier, indeed, could indeed be used for performing quantum error correction, which at the moment is one of the main limitations of the other investigated qubit platforms.

Finally, another important aspect to bear in mind is that most of the investigated vanadyl-based molecules can be addressed on surface. This has been successfully done, for example, in depositing molecular monolayers of VOdpm and VOPc on several substrates. On the other hand, the technology nowadays available is still not able to detect relaxation times for the single molecule. Hopefully all the advancements that have been made in these years for measuring EPR spin dynamics of atoms on surface will be extended also to molecules. This is expected to accelerate the realization of real devices in the context of quantum technologies, as well as spintronics.

Appendix

Published Papers

1) L. Tesi, E. Lucaccini, I. Cimatti, M. Perfetti, M. Mannini, M. Atzori, E. Morra, M. Chiesa, A. Caneschi, L. Sorace and R. Sessoli. "Quantum coherence in a processable vanadyl complex: new tools for the search of molecular spin qubits". In: *Chemical Science* **7** (2016), pp. 2074–2083;

2) M. Atzori, L. Tesi, E. Morra, M. Chiesa, L. Sorace and R. Sessoli. "Room-temperature quantum coherence and Rabi oscillations in vanadyl phthalocyanine: toward multifunctional molecular spin qubits". In: *Journal of the American Chemical Society* **138** (2016), pp. 2154-2157;

3) M. Atzori, E. Morra, L. Tesi, A. Albino, M. Chiesa, L. Sorace and R. Sessoli. "Quantum coherence times enhancement in vanadium(IV)-based potential molecular qubits: the key role of the vanadyl moiety". In: *Journal of the American Chemical Society* **138** (2016), pp. 11234-11244;

4) I. Mihalcea, M. Perfetti, F. Pineider, L. Tesi, V. Mereacre, F. Wilhelm, A. Rogalev, C. E. Anson, A. K. Powell and R. Sessoli. "Spin helicity in chiral lanthanide chains". In: *Inorganic Chemistry* **55** (2016), pp. 10068-10074;

5) L. Tesi, A. Lunghi, M. Atzori, E. Lucaccini, L. Sorace, F. Totti and R. Sessoli. "Giant spin-phonon bottleneck effects in evaporable vanadyl-based molecules with long spin coherence". In: *Dalton Transactions* **45** (2016), pp. 16635-16643;

6) M. Atzori, L. Tesi, S. Benci, A. Lunghi, R. Righini, A. Taschin, R. Torre, L. Sorace and R. Sessoli. "Spin dynamics and low energy vibrations: insights from vanadyl-based potential molecular qubits". In: *Journal of the American Chemical Society* **139** (2017), pp. 4338-4341;

7) M. Atzori, S. Benci, E. Morra, L. Tesi, M. Chiesa, R. Torre, L. Sorace and R. Sessoli. "Structural effects on the spin dynamics of potential molecular qubits". In: *Inorganic Chemistry* **57** (2018), pp. 731-740;

8) L. Rigamonti, N. Bridonneau, G. Poneti, L. Tesi, L. Sorace, D. Pinkowicz, J. Jover, E. Ruiz, R. Sessoli and A. Cornia. "A pseudo-octahedral cobalt(II) complex with bispyrazolylpyridine ligands acting as a zero-field single-molecule magnet with easy axis anisotropy". In: *Chemistry-A European Journal* **24** (2018), pp. 8857-8868;

9) L. Tesi, Z. Salman, I. Cimatti, F. Pointillart, K. Bernot, M. Mannini and R. Sessoli. "Isotope effects on the spin dynamics of single-molecule magnets probed using muon spin spectroscopy". In: *Chemical Communications* **54** (2018), pp. 7826-7829;

10) T. Yamabayashi, M. Atzori, L. Tesi, G. Cosquer, F. Santanni, M.-E. Boulon, E. Morra, S. Benci, R. Torre, M. Chiesa, L. Sorace, R. Sessoli and M. Yamashita. "Scaling up electronic spin qubits into a three-dimensional metal-organic framework". In: *Journal of the American Chemical Society* **140** (2018), pp. 12090-12101.

Chemical Science

EDGE ARTICLE

View Article Online
View Journal | View Issue

Cite this: *Chem. Sci.*, 2016, **7**, 2074

Quantum coherence in a processable vanadyl complex: new tools for the search of molecular spin qubits†

Lorenzo Tesi,[a] Eva Lucaccini,[a] Irene Cimatti,[a] Mauro Perfetti,[a] Matteo Mannini,[a] Matteo Atzori,[a] Elena Morra,[b] Mario Chiesa,[b] Andrea Caneschi,[a] Lorenzo Sorace*[a] and Roberta Sessoli*[a]

Electronic spins in different environments are currently investigated as potential qubits, *i.e.* the logic units of quantum computers. These have to retain memory of their quantum state for a sufficiently long time (phase memory time, T_m) allowing quantum operations to be performed. For molecular based spin qubits, strategies to increase phase coherence by removing nuclear spins are rather well developed, but it is now crucial to address the problem of the rapid increase of the spin–lattice relaxation rate, T_1^{-1}, with increasing temperature that hampers their use at room-temperature. Herein, thanks to the combination of pulsed EPR spectroscopy and AC susceptometry we evidence that an evaporable vanadyl complex of formula $VO(dpm)_2$, where dpm^- is the anion of dipivaloylmethane, presents a combination of very promising features for potential application as molecular spin-qubit. The spin–lattice relaxation time, T_1, studied in detail through AC susceptometry, decreases slowly with increasing temperature and, more surprisingly, it is not accelerated by the application of an external field up to several Teslas. State-of-the art phase memory times for molecular spin systems in protiated environment are detected by pulsed EPR also in moderate dilution, with values of 2.7 μs at 5 K and 2.1 μs at 80 K. Low temperature scanning tunnel microscopy and X-ray photoelectron spectroscopy *in situ* investigations reveal that intact molecules sublimated in ultra-high vacuum spontaneously form an ordered monolayer on Au(111), opening the perspective of electric access to the quantum memory of ensembles of spin qubits that can be scaled down to the single molecule.

Received 10th November 2015
Accepted 11th December 2015

DOI: 10.1039/c5sc04295j

www.rsc.org/chemicalscience

Introduction

The realization of a quantum computer is expected to trigger a second revolution in information and communication technology,[1–4] allowing for unequalled computation capabilities in disparate fields, ranging from structural biology[5] to quantum physics.[3] Quantum bits, or qubits, are at the basis of quantum computation, and different strategies to realize them are currently explored,[6] including ionic traps,[7] quantum dots in semiconductors,[8,9] photons,[10] and superconducting nanostructures.[11] Spins, either nuclear[12–14] or electronic,[15–19] are among the most efficiently addressable targets to build these logical units, as their initialization and read-out can be performed by well-established magnetic resonance techniques. The parameters to be optimized in the design of these qubits are: i) the longitudinal relaxation time, T_1, which corresponds to the lifetime of a classical bit that can assume either the |0> or the |1> value; ii) the characteristic time in which the spin loses the memory of the phase of the superposition state in which it has been prepared. A lower estimation of this decoherence time, T_2, can be extracted by the memory time, T_m, which is commonly measured with pulsed EPR or NMR: the ratio of T_m over the time necessary for an individual quantum operation has to be larger than 10^4 to allow for fault tolerant quantum computing.

In the field of electron spin-based qubits nitrogen vacancies in diamond[20,21] and impurities in silicon and silicon carbide[22] exhibit long-lived quantum coherence but present major challenges in the control of their organization and coupling to perform quantum logic operations. Molecular spin based qubits, on the contrary, can be organized on surfaces and the interaction between them tuned at will through a rational synthetic design. After an extensive research on polynuclear transition metal complexes[16,23,24] optimized to exhibit a long T_m, the research in this field has recently focused back on the

[a]*Department of Chemistry "Ugo Schiff", University of Florence & INSTM RU of Florence, Via della Lastruccia 3-13, 50019 Sesto Fiorentino, Italy*

[b]*Department of Chemistry, University of Turin & NIS Centre, via P. Giuria 7, 10125, Torino, Italy. E-mail: roberta.sessoli@unifi.it; lorenzo.sorace@unifi.it*

† Electronic supplementary information (ESI) available: Full experimental section and methods. Additional characterization including: AC susceptibility data (Fig. S1–S5); CW- and pulsed EPR results (Fig. S6–S11); STM and XPS of the UHV deposition (Fig. S12–S14); calculated field dependence of the eigenvectors composition (Fig. S15). See DOI: 10.1039/c5sc04295j

simplest spin $S = 1/2$ systems constituted either by organic radicals[25] or by 3d transition metal ions.[26–28] These have relatively long T_m, in particular at high temperature, because there are no excited spin levels that can foster the magnetic relaxation when thermally populated. In these systems the interaction of the electronic spin with the nuclear spins is the most relevant source of decoherence. Outstanding results have very recently been obtained with vanadium(IV) ions assembled with nuclear spin-free ligands.[27] When magnetic dilution is made in a nuclear spin-free solvent, such as CS_2, T_m approaches one millisecond at low temperature,[29] showing that molecular spin systems can be as performant as extended inorganic structures. Unfortunately this remarkable long coherence is rapidly lost on increasing temperature because the spin–lattice relaxation acts as a limiting factor for T_2.[30] A recent investigation has clearly evidenced that solid crystalline solutions can enhance T_1, thus resulting in enhanced coherence time at high temperature[26] but the mechanisms of relaxation, as well as strategies to enhance T_1, are still poorly investigated.

In this study we have investigated the magnetic relaxation of a simple mononuclear complex of vanadium(IV) by the combination of AC magnetic susceptometry to study spin–lattice relaxation with pulsed EPR spectroscopy to characterize the spin coherence. The two techniques can in fact shed light on different contributions to the relaxation but their association is unprecedented in the search for potential spin-based qubits.

The vanadyl complex $VO(dpm)_2$, where dpm^- is the anion of dipivaloylmethane, has been selected because the strong V=O bond is expected to increase the rigidity of the coordination sphere with a reduction of spin–lattice relaxation efficiency. The presence of β-diketonate ligands in a neutral complex imparts a high volatility that can be exploited to deposit the molecule on surfaces. An unexpected long T_1 over wide field and temperature ranges has been found to accompany T_m values that are among the longest ones observed in molecular species surrounded by spin active nuclei. The *in situ* morphological and spectroscopic characterization of a monolayer deposit of $VO_2(dpm)_2$ on Au(111) suggest that the molecules are intact on the surface, making these simple units potential candidates as molecular qubit individually addressable by scanning probe techniques.

Results and discussion

The synthesis of crystalline $VO(dpm)_2$ was achieved according to an earlier reported procedure,[31] operating under inert atmosphere to avoid oxidation. $VO(dpm)_2$, prepared in the crystalline form and characterized by X-ray diffractometry (see ESI†), presents a typical square pyramidal coordination (Fig. 1) with a short V=O double bond (1.59 Å *vs.* an average of 1.964 Å for the V–O single bonds). Deviations from tetragonal symmetry are already visible in the first coordination sphere in both bond lengths and bond angles. Given that the system crystallizes in the monoclinic $P2_1$ space group, two sets of molecules with the V=O directions forming an angle of 64.1° are present in the crystal lattice. The strongly axial ligand field produced by the short V=O bond removes orbital degeneracy with the d_{xy} orbital being the lowest in energy and the only one to be half occupied.

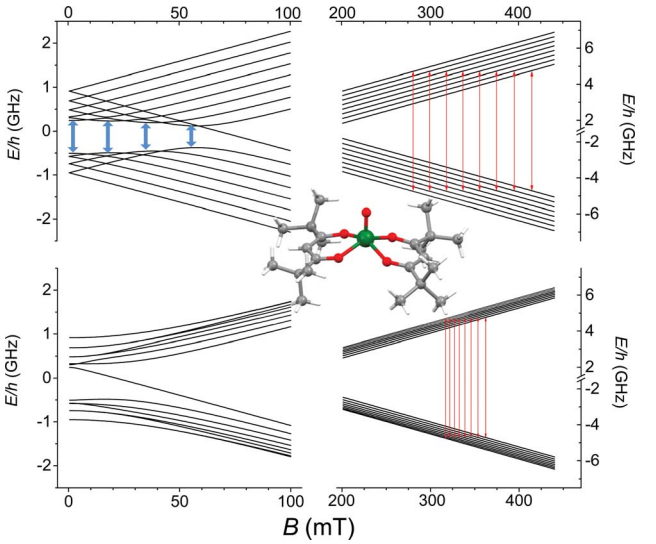

Fig. 1 Zeeman splitting of the $S = 1/2$, $I = 7/2$ manifold calculated with the field applied along the largest hyperfine coupling component (upper) and along the smallest (lower) (parameters in the text). Red lines correspond to the observed X-band (ν = 9.62 GHz) EPR transitions while in pale blue are drawn the potential low frequency transitions at the avoided level crossings. In the inset the molecular structure of $VO(dpm)_2$.

Vanadyl systems are therefore well described by a spin $S = 1/2$ with slightly anisotropic $\boldsymbol{g}$ tensor close to the free electron value. The most abundant isotope of vanadium, ^{51}V (99.75%), is characterized by $I = 7/2$ thus the $S = 1/2$ doublet is further split in 16 states by hyperfine interaction as schematized in Fig. 1.

Magnetization dynamics

The magnetization dynamics, investigated by AC-susceptometry (see ESI†), of a polycrystalline sample of $VO(dpm)_2$, hereafter **1**bulk, revealed no imaginary component of the susceptibility in zero static field down to the lowest investigated temperature (1.9 K). The application of a weak field induced however slow relaxation of the magnetization with the concomitant decrease of the real component χ' and the appearance of a peak in χ'' component (ESI Fig. S1†). In a field of 0.2 T the entire magnetization of the system relaxed slowly and this field was selected to investigate the temperature dependence of the relaxation time.

Maxima in χ'' were observed up to 80 K for frequencies lower than 10 kHz, as shown in Fig. 2a (ESI Fig. S2† for χ'), evidencing also a gradual increase in the width of the distribution on lowering the temperature (see ESI and Fig. S3†). Such a high temperature slow relaxation is usually observed in molecules exhibiting strong magnetic anisotropy known as Single-Molecule Magnet (SMMs), for instance in double-decker $TbPc_2$ complexes,[32] but clearly it has a different origin here. The data, reproduced with the Debye model,[33] allowed to extract the relaxation time of the susceptibility, τ, reported in Fig. 2b. It is evident that τ does not follow the Arrhenius behaviour, in agreement with the lack of electronic/magnetic states that can be thermally populated providing a path for the multiphonon

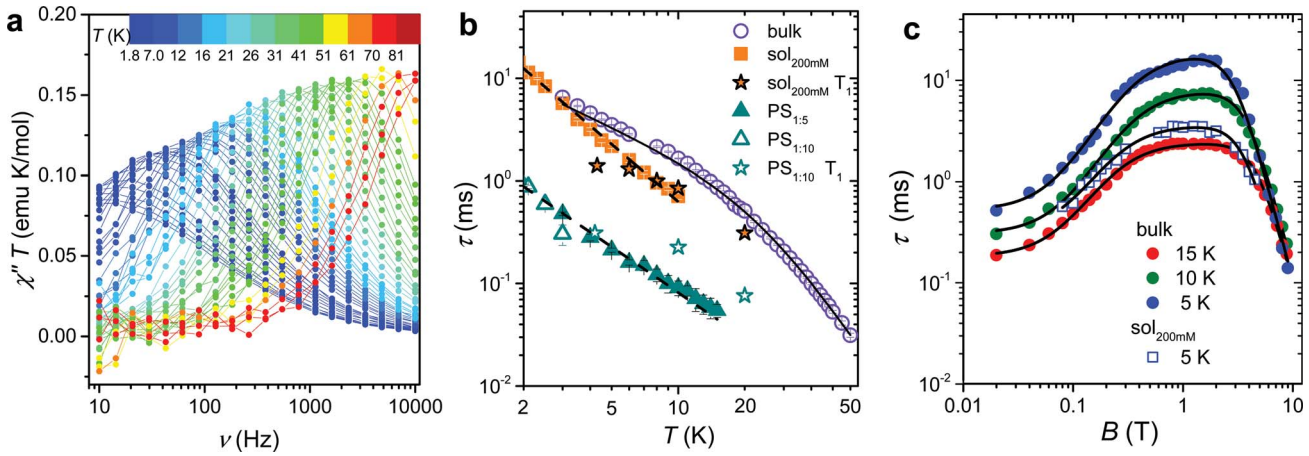

Fig. 2 (a) Frequency dependence of the imaginary component of the AC susceptibility of **1**bulk in $B_{dc} = 0.2$ T multiplied by temperature to be readable in the whole 2–80 K temperature range. (b) Temperature dependence of the relaxation time of the magnetic susceptibility measured in $B_{dc} = 0.2$ T for the pure and the diluted samples of **1**: two dispersions in polystyrene with 1 : 5 and 1 : 10 mass ratio and a 200 mM CH_2Cl_2 : toluene frozen solution (see legend). The black solid line corresponds to the best-fit of **1**bulk data using eqn (1), while the broken lines correspond to simulation with T^{-n} law. T_1 for the diluted sample, extracted from pulsed EPR spectra, are shown for comparison. (c) Field dependence of the relaxation time of the magnetic susceptibility of **1**bulk and **1**$sol_{200\ mM}$ frozen solution sample (see legend). The solid lines represent the best fit obtained with eqn (3). Best fit parameters are reported in Table 1.

Orbach mechanism of relaxation.[34,35] On the contrary the temperature dependence of τ can be reproduced by considering different contributions to the relaxation rate:

$$\tau^{-1} = aT + bT^n \quad (1)$$

where the first term ($a = 59 \pm 2\ s^{-1}\ K^{-1}$) corresponds to the direct mechanism, dominating at low temperature, and the second one ($b = 0.052\ s^{-1}\ K^{-n}$) to a Raman-like, *i.e.* a multi-phonon process involving virtual excited states.[34] Interestingly the exponent $n = 3.22 \pm 0.02$ is much smaller than the value of 9 or higher expected for the Raman process,[35] but approaches the value of 3 predicted in the case that both acoustic (lattice) and optical (molecular) vibrations are involved in the process.[34]

To shed light on the mechanisms of magnetic relaxation the AC susceptibility was investigated in a wide field range, *i.e.* up to 8.8 T, for three different temperatures, 5, 10, and 15 K. Notice that in this temperature range the direct process dominates as indicated by the almost linear dependence of τ^{-1} on T. The corresponding relaxation times are reported in Fig. 2c. The initial increase of τ for weak applied field is followed by an almost flat region that extends up to *ca.* 4 T, followed by a rapid decrease at higher fields. Data of Fig. 2c were reproduced considering different relaxation mechanisms that can be active in $S = 1/2$ systems. According to the seminal work done by de Vroomen *et al.* on the Cu^{2+} Tutton salt,[36] two contributions to the relaxation rate can be considered:

$$\tau^{-1} = {\tau_Z}^{-1} + {\tau_{int}}^{-1} \quad (2)$$

The first term represents the direct mechanism between the two states split by the Zeeman energy, which is expected to vanish in zero field as a result of the Kramers theorem.[37] In fact, a pure and isolated $S = 1/2$ should not be able to relax in zero field. The second term takes into account a sort of internal field whose origin can be either intramolecular (*i.e.* hyperfine interactions) or intermolecular (*i.e.* due to dipolar or exchange interactions). The latter is responsible for the efficient relaxation in zero field and presents, for the direct mechanism,[38] a field dependence that is similar to the Brons-van Vleck formula developed to describe the Raman process in concentrated systems.[39] Summing up the two contributions to the field dependence in eqn (2) the data of Fig. 2c have been reproduced according to:

$$\tau^{-1} = cB^4 + d\frac{1 + eB^2}{1 + fB^2} \quad (3)$$

The first term is the typical field dependence of the direct process for a $S = 1/2$ spin and reflects the fact that the larger is the Zeeman splitting between the states the higher is the density of phonons matching it. In the second one the d term represent the zero field relaxation rate, similar to the tunnelling rate in SMMs,[33] the f parameter takes into account the ability of the external field to suppress these mechanisms, while the e parameter, strongly dependent on the concentration of the spin centres, takes into account the field effects on the relaxation of interacting spins.[39] The best-fit values obtained with eqn (3) are summarized in Table 1. The c parameter for $T = 5$ K should be considered with caution because only a small fraction of the susceptibility is detected at such high fields. The field range where the relaxation remains slow is really remarkable, suggesting that the direct mechanism of relaxation is not very efficient.

In ESI Fig. S3 and S4† we also report the temperature and field dependence of the width of the distribution of relaxation rate, respectively. The width is correlated to the parameter α of the extended Debye formula (see ESI†). In general the

Table 1 Best-fit parameters of eqn (3) used to reproduce the field dependence of the magnetization relaxation rate of **1**bulk measured at the three investigated temperatures and of **1**sol$_{200\ mM}$ at 5 K (last row)

T (K)	c (T^{-4} s^{-1})	d (s^{-1})	e (T^{-2})	f (T^{-2})
5	0.96 ± 0.04	2060 ± 180	7.6 ± 0.7	240 ± 30
10	0.73 ± 0.01	3460 ± 150	7.6 ± 0.4	179 ± 12
15	0.97 ± 0.03	5740 ± 270	15.1 ± 0.9	190 ± 16
5	2.00 ± 0.11	3600 ± 550	13.7 ± 1.4	160 ± 40

distribution is quite narrow increasing up to 0.3 at the lowest temperature (ESI Fig. S3†). The decrease of α with increasing fields, see ESI Fig. S4,† is indicative that τ_{int}^{-1} is more sensitive to the local environment, as indeed expected. The non-monotonous trend at low temperature suggests the presence also in this powdered sample of a moderate phonon-bottleneck effect.[40]

The long spin–lattice relaxation time of $VO(dpm)_2$, above 10 ms at low temperatures, suggests that also decoherence times can be comparatively long. The latter are however accessible only by pulsed EPR techniques and require narrow lines that can be achieved in diluted systems. Unfortunately, extensive efforts to prepare the titanyl-based diamagnetic analogue failed due to the instability of the mononuclear species $TiO(dpm)_2$ in favour of the dimeric one $[TiO(dpm)_2]_2$,[41] thus precluding the preparation of isomorphous crystalline solid solutions. As an alternative, two dispersions of **1** in polystyrene with mass ratio 1 : 5, **1**PS$_{1:5}$, and 1 : 10, **1**PS$_{1:10}$, as well as a frozen 200 mM solution of **1** in a 2 : 3 CH_2Cl_2 : toluene mixture (**1**sol$_{200\ mM}$), were prepared and investigated by AC susceptometry (Fig. S5†). This was aimed at getting information on the relaxation time of the magnetic susceptibility to be compared to T_1 extracted from pulsed EPR data. Even if a reduced range of temperature and fields are accessible on the diluted samples for instrumental reasons, it is well evident that also diluted samples show slow relaxation of the magnetization (Fig. 2b): polymeric dispersions are characterized by a relaxation rate which is *ca.* 20 times faster than bulk sample, with minor difference between the two concentrations, suggesting that matrix effects to the relaxation dominate over those induced by dilutions. On the other hand, the low temperature relaxation rate of the frozen solution is comparable to the bulk phase but increases much faster on increasing temperatures. The almost linear temperature dependence in the log(τ) *vs.* log(T) plot of Fig. 2b allowed to analyse the data as $\tau^{-1} \propto T^n$, with $n = 1.49 \pm 0.04$ for **1**PS$_{1:5}$ and $n = 1.86 \pm 0.04$ for **1**sol$_{200\ mM}$. Exponents larger than one for the direct mechanism are generally attributed to spin–phonon bottleneck effects,[34] which are expected to be more relevant for these samples that have a small contact-surface with the helium bath than the ground microcrystalline powder of the bulk sample.[40] The field dependence of τ of **1**sol$_{200\ mM}$ was also investigated at $T = 5$ K (see Fig. 2c) and revealed the same wide plateau observed in the bulk phase, thus indicating that, despite some matrix effects, this interesting feature is an intrinsic property of the structure of the molecule. Unfortunately, a more direct comparison between the parameters reported in Table 1 for bulk and diluted samples would only be possible for a solid crystalline solution.

Continuous wave and pulsed EPR spectroscopy

The low temperature CW-EPR X-band spectrum of a frozen 1 mM solution of **1** (**1**sol$_{1\ mM}$) is shown in Fig. 3a. Similar features are observed for the other investigated samples (**1**bulk, **1**PS$_{1:5}$, **1**PS$_{1:10}$, and **1**sol$_{200\ mM}$ spectra available in ESI Fig. S6†), the effect of concentration being mirrored by the narrowing of the EPR lines when going from pure sample to dispersions and frozen solutions. On the other hand, the position of the lines is not varying, indicating that the spin Hamiltonian parameters, and then the electronic structure, are maintained in different environments.

The spectra clearly show the features due to the anisotropic hyperfine coupling of the electron spin to the $I = 7/2$ nuclear spin of ^{51}V: at the high and low field extreme region, peaks due to the parallel components of the hyperfine structure are observed, whereas in the centre the closely spaced perpendicular ones are evident, as schematized by the resonant fields in Fig. 1.

Spectral simulations were performed[42] on the basis of the following spin Hamiltonian:

$$\mathscr{H} = \hat{I}\cdot\boldsymbol{A}\cdot\hat{S} + \mu_B\hat{S}\cdot\boldsymbol{g}\cdot B \qquad (4)$$

providing as best-fit parameters: $g_x = 1.9880(2)$; $g_y = 1.9815(3)$; $g_z = 1.9490(2)$ and $A_x = 0.0056(1)$ cm^{-1} (167.9 MHz); $A_y =$

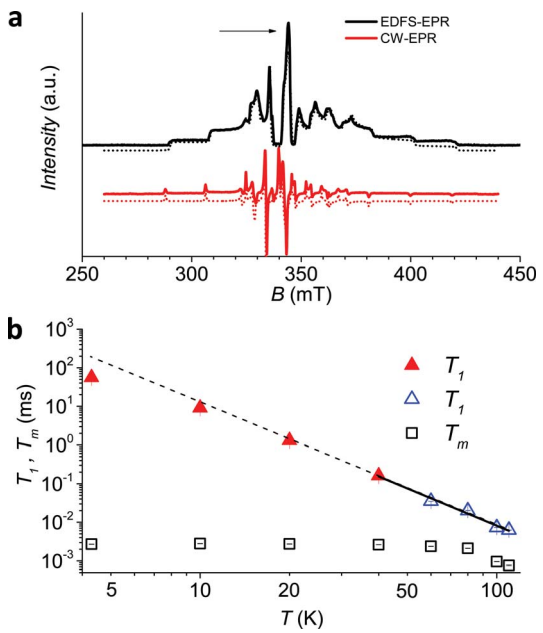

Fig. 3 (a) Echo detected (black trace) and CW (red trace) experimental EPR spectra of **1**sol$_{1\ mM}$, measured at 5 K, and best simulations (dotted traces). The arrow marks the field position of T_1 and T_m determination. (b) Temperature dependence of T_1 and T_m for **1**sol$_{1\ mM}$ sample. Full symbols refer to experiments of echo saturation by fast repetition, empty ones to inversion recovery experiments (see ESI† for details). The solid line corresponds to the best-fit of the high temperature data with $T_1 \propto T^{-n}$.

0.0063(3) cm^{-1} (190.4 MHz); $A_z = 0.0170(2)$ cm^{-1} (509.6 MHz). These parameters are in the range previously reported for VO^{2+} β-diketonate-type derivatives[43,44] and are consistent with the slight structural rhombicity observed by X-ray diffractometry. These spin Hamiltonian parameters have been employed to draw the Zeeman diagrams reported in Fig. 1.

An echo-detected field-swept EPR spectrum (EDFS) was recorded using the standard Hahn sequence (see ESI†) for **1**$sol_{200\ mM}$, **1**$sol_{1\ mM}$, and **1**$PS_{1:10}$ diluted samples (Fig. 3a and ESI Fig. S7†). The observation of a spin-echo is a first indication that quantum coherence is observed in these samples. Further, the same spin Hamiltonian parameters used for the simulation of the CW spectrum yielded good simulations of the EDFS spectrum, confirming that the entire $VO(dpm)_2$ sample is experiencing the detected coherence.

Determination of the potential applicability of diluted samples of **1** as molecular qubit was performed by measuring the coherence time, T_m, as a function of temperature and field position for **1**$sol_{1\ mM}$ to reduce spin–spin interactions. To maximize the observed echo the temperature dependence of T_m has been investigated on the so-called powder like line evidenced by an arrow in Fig. 3a.

The echo decay traces (Fig. 4a) were then fitted using a stretched-exponential equation:

$$y = y_0 + k_m \exp[-(2t/T_m)^{\beta_m}] \quad (5)$$

It is evident that between 4 K and 80 K the resulting T_m values (Fig. 3b) are almost temperature independent (varying from 2.7 μs to 2.1 μs). Above 80 K the softening of the solvent glassy matrix, and consequently of the *tert*-butyl groups of the ligands, opens new relaxation pathways leading to the loss of echo above 110 K. The temperature dependence of β_m parameter essentially follows the same pattern, being slightly larger than 1 at 5 K and approaching a mono-exponential decay above 80 K (Fig. S8†). This behaviour suggests that decoherence is essentially dominated by physical motions of the magnetic nuclei.[45]

In agreement with the long coherence time observed at low temperature, Rabi-like oscillations of the echo intensity were observed for **1**$sol_{1\ mM}$ in nutation experiments performed at different microwave powers as shown in Fig. 4b, where the observed linear dependence of the Rabi oscillation on the intensity of the oscillating field is reported in the inset. This indicates the possibility of creating any arbitrary superposition of states, thus fulfilling one of the two main requirements for creating universal quantum gates.[46]

Since earlier studies revealed strong correlation between the spin–lattice relaxation time T_1 and T_m for some molecular species candidate for quantum information processing (QIP),[26,30] we determined the temperature dependence of T_1 between 5 K and 110 K in **1**$sol_{1\ mM}$, for which the AC susceptibility technique does not have the necessary sensitivity.

Given the large range of relaxation times two different experimental procedures were applied: at low temperature (5–60 K) the echo saturation by fast repetition, suitable for long relaxation times[47] was used, whereas at higher temperature the standard inversion recovery procedure was applied (see ESI† for details). Saturation recovery traces have been fitted using the following equation:

$$y = y_0 + k_1 \exp(-t/T_1)^{\beta_1} \quad (6)$$

with best-fit stretched parameter β_1 being in the range 0.6–0.9 in the investigated temperature range (ESI Fig. S9†). The results (Fig. 3b), consistent with those previously reported by Eaton *et al.* for $VO(acac)_2$ in H_2O:glycerol solution,[43] indicate that quite long values of T_1 are observed at low temperature (50 ms at 4 K) and on heating T_1 tends toward T_m (6 μs at 110 K). Interestingly, a T^{-n} dependence with $n = 3.2 \pm 0.2$ is observed above 40 K, with a gradual decrease of n at lower temperatures, in agreement with AC susceptibility results.

To have a more quantitative comparison we also measured the temperature dependence of the spin–lattice relaxation time for **1**$sol_{200\ mM}$ by pulsed EPR: the obtained results are consistent with those obtained by AC susceptibility (Fig. 2b), confirming that the two techniques are actually probing the same process.

As a final test to establish whether this molecule maintains its long decoherence time in a solid matrix not affected by the melting of the frozen solution we measured the temperature dependence of relaxation times for **1**$PS_{1:10}$. Remarkably, for

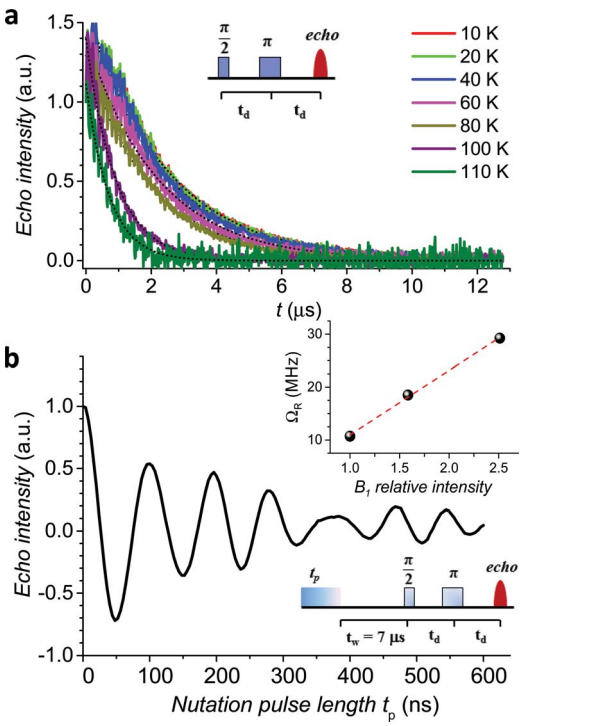

Fig. 4 (a) Pulsed EPR Hahn echo decay traces for **1**$sol_{1\ mM}$ at different temperatures recorded at 343 mT. In the inset the employed pulse sequence. (b) Rabi oscillations for **1**$sol_{1\ mM}$ recorded at 4.3 K at 10 dB microwave attenuation. The change in oscillations observed at t_p > 400 ns is due to the interaction between the electron spin and surrounding protons.[48] In the inset the Rabi frequency (Ω_R) *vs.* oscillating field intensity superimposed to the linear best-fit.

this relatively concentrated sample it is possible to observe an echo and measure T_m up to 220 K (Fig. S10†). In particular while T_m is 0.36 μs at 4.3 K, *i.e.* about one order of magnitude faster than for **1**sol$_{1\ mM}$, at the highest measured temperature a T_m value of 0.1 μs could be determined.

Deposition on Au(111) and *in situ* characterization

The high volatility of VO(dpm)$_2$ was here exploited to obtain thick films as well as sub-monolayer (ML) deposit assembled on the Au(111) surface. A complete *in situ* X-ray photoelectron spectroscopy (XPS) and low temperature scanning tunnelling microscopy (STM) characterization was carried out, while the stability of the sample toward oxidation was investigated by exposing a thick film to air. Fig. 5 reports the STM topography obtained at $T = 30$ K for sub-ML coverage. As observed for other complexes with dpm$^-$ ligands,[49,50] the molecules weakly interact with the substrate and form patches of variable size constituted by regularly packed molecules. The islands present regular boundaries maintaining the herringbone modulation of the gold substrate. Sub-molecular resolution was hard to achieve inside the patches, though isolated features were visible at the kinks of the herringbone structure.

The height of the molecular layer is 0.27 ± 0.02 nm (ESI Fig. S12†), in good agreement with similar deposits obtained with iron β-diketonate complex,[49] though no reports are available on VO(dpm)$_2$. By increasing the deposition time full coverage was achieved: regularly packed molecules still revealing the herringbone structure underneath were found (ESI Fig. S13†). Interestingly, as in the case of Fe(dpm)$_3$,[49] no additional molecular layer can be deposited at the employed low deposition rates (see ESI†).

In order to check if the complex is intact on the surface, the full monolayer deposit was investigated by XPS, revealing the presence of the expected elements (see Fig. 6).

The observed broad O 1s peak around 532 eV was reproduced by considering two components. The smaller one at 531.3 eV was attributed to the oxygen of the vanadyl group ($O_{V=O}$), in good agreement with what observed for vanadyl phthalocyanine, VOPc, on Ag(111),[51,52] while the larger one at 532.1 eV, was

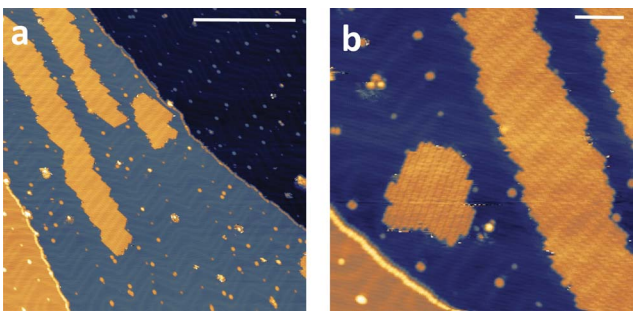

Fig. 5 STM images of a sub-monolayer deposition of VO(dpm)$_2$ measured at 30 K. Bias voltage = −2 V (empty states), tunnelling current = 5 pA. The scanned regions are 150 × 150 nm^2 in (a) and 60 × 60 nm^2 in (b) and the bars correspond to 50 nm and 10 nm, respectively.

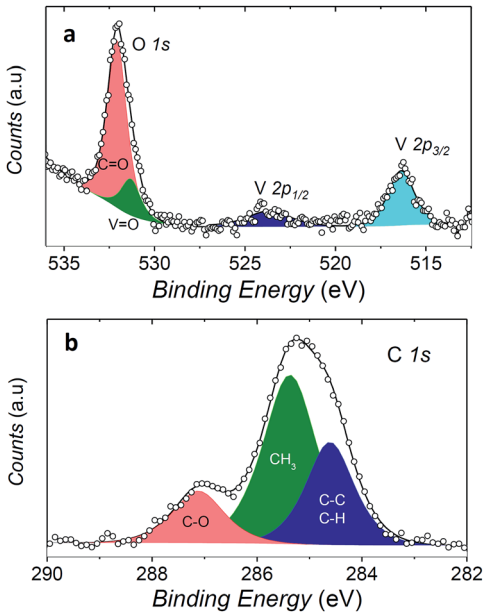

Fig. 6 XPS spectra of a monolayer coverage of **1** on Au(111). The O 1s and V 2p regions are shown in (a) while the C 1s region in (b). Filled area and lines represent the best fit components and resulting spectra, respectively.

associated to the oxygen atoms of the two dpm$^-$ ligands ($O_{C=O}$). The ratio of the area of the two peaks is close to 1 : 4, as expected for the stoichiometry of the molecule, thus confirming the integrity of the complex on surface. An analogous analysis allows to distinguish three components contributing to the C 1s region: the carbonylic carbon (287.2 eV), methyl carbon (285.4 eV) and the third one regrouping the remaining carbons (CH, CC, at 284.6 eV).

Even more interestingly the vanadium photoelectron peaks allowed to provide specific hints on the oxidation state of this element and thus on possible interaction with the metal surface. The V 2p$_{3/2}$ was observed at 516.4 eV, showing a distance to the oxygen peak $\Delta E(O_{V=O}\ 1s - V\ 2p_{3/2})$ of 14.9 eV which well compares with that observed in VOPc monolayer and multilayers ($\Delta E(O_{V=O}\ 1s - V\ 2p_{3/2}) = 14.6$ eV).[51] A semi-quantitative analysis of the composition according to the integrated peak signals gave for the three investigated elements the molar composition C = 81 ± 4%, O = 16 ± 1%, V = 2.6 ± 0.6% that well compares with the theoretical one (C = 78.6%, O = 17.9%, V = 3.6%).

These observations indicate that the VO(dpm)$_2$ molecules can be deposited intact on the surface and features a weak interaction with the gold substrate as the only occupied d orbital, d_{xy}, is expected to lie flat with limited overlap with the substrate orbitals. A similar scenario was observed for copper(II) phthalocyanine molecules that are known to retain their unpaired electron in the $d_{x^2-y^2}$ orbital.[53] In the vanadyl derivative VOPc the metal atom is slightly above the plane of the equatorial oxygen atoms; the distance of the metal ion from the surface is therefore further increased thus reducing the interaction with the substrate. It is thus not surprising that

synchrotron-based experiments on monolayers of VOPc on Ag(111)[51] detected a substantially unchanged magnetism of the $S = 1/2$ of V^{IV} compared to thicker films. It is therefore reasonable to envisage that $VO(dpm)_2$ molecules retain their paramagnetic nature when in contact with the gold substrate. This system represents therefore an appealing alternative to the use of N-donors phthalocyanine- and porphyrin-based systems for deposition on surfaces, though $VO(dpm)_2$ films resulted somehow instable in air: *ex situ* prepared thick films of about 150 nm showed a partial surface oxidation as suggested by the decrease in the ($\Delta E(O_{V=O}\ 1s - V\ 2p_{3/2})$) value accompanied by a progressive shift of the V 2p peak (ESI Fig. S14†).

Comparison with other molecular spin qubits

AC-susceptometry is currently widely employed to evidence slow relaxation in SMMs characterized by easy axis anisotropy and large magnetic moments; however, Luis *et al.*[54] have recently used this technique to characterize in detail the dynamics of a pseudo spin-doublet resulting from the large easy plane anisotropy of the $S = 3/2$ of Co^{II} in $Co(acac)_2(H_2O)_2$.[54] The role of hyperfine interaction and of the coupling of the nuclear spins with the phonon bath has been found to contribute to the opening of relaxation pathways otherwise forbidden in zero field for a pure $S = 1/2$ due to time reversal symmetry. $VO(dpm)_2$ corresponds exactly to the hyperfine-split $S = 1/2$ model recently developed[54] and indeed analogies in the magnetic behaviour of the two molecular systems are observed. In zero static field the hyperfine interaction with the $I = 7/2$ gives origin to two sets of states characterized by $F = |S \pm I|$ with multiplicity 9 and 7, respectively, as can be observed in Fig. 1. The isotropic hyperfine coupling is responsible for the gap between $F = 4$ and $F = 3$ states, which are however further split by the anisotropic components of the hyperfine tensor (see eqn (4)). The application of a weak static field has a different effect when applied along the molecular z direction, the one of largest hyperfine interaction corresponding to the V=O bond direction, or perpendicular to it, as also indicated in the eigenvectors composition (ESI Fig. S15†).

If similar features were already observed in the $Co(acac)_2(H_2O)_2$ *pseudo*-spin $S = 1/2$ system, some striking quantitative differences are evident. The first one is that the relaxation time remains long over a wide field range, *ca.* 30 times larger in $VO(dpm)_2$ compared to the Co^{II} derivative. At 5 K, where the relaxation is still governed by the direct mechanism, the relaxation rate starts to grow above 3 T, to be compared to the drastic 0.1 T upturn observed for Co^{II} at 1.8 K.[54] The comparison with early works on the dynamics of Cu^{II} spins[36] confirms that the field stability of slow relaxation of $VO(dpm)_2$ is unprecedented. This is extremely appealing for technological applications as it allows to exploit higher frequencies to coherently manipulate the spins, *e.g.* at W-band, corresponding to 95 GHz, with significant improvement of sensitivity. Moreover, working at W-band was also shown to increase T_m in samples of Yb^{3+} diluted in $CaWO_4$, though at the same time the larger field was found to reduce T_1. This serious drawback of the use of high frequencies is not expected for $VO(dpm)_2$.[55]

The origin of the striking difference between the two compounds can be associated to the reduced efficiency of the direct mechanism of relaxation, which relies on the spin–phonon coupling. The latter is mediated by the spin–orbit coupling, which is significantly lower for such a light transition metal as vanadium. As a result, T_1 of $VO(dpm)_2$ remains long over a wide temperature range. For instance, a relaxation time of 2 ms is observed at 6 K for diluted $Co(acac)_2(H_2O)_2$ but at temperatures as high as 40 K in concentrated $VO(dpm)_2$. The anomaly arises from the small exponent of the T^n dependence of the Raman-like mechanism of relaxation. Such low exponents are relatively common for $S = 1/2$ states with small orbital contributions comprising light elements and have been associated to the soft character of the molecular lattices.[35,56]

It is also interesting to compare the measured decoherence times with those of other molecules proposed as potential molecular qubits. Among similarly investigated electron spin-qubits of vanadium, we note that the T_m values observed for a frozen solution of $VO(dpm)_2$ are slightly longer – in the whole investigated temperature range – than those reported for a dispersion in protiated solvents at the same concentration of a vanadium complex with nuclear-spin free ligands:[27] this is of particular interest, since in our case an evaporable system containing a large number of protons has been chosen without optimizing the ligand to reduce the number of nuclear spins. We have in fact confirmed that the ligand hydrogen magnetic nuclei play the dominant role in the relaxation by investigating the coherence time of $VO(dpm)_2$ diluted in deuterated solvents. A substantially unchanged T_m was detected (Fig. S11†), in contrast to the improvement of at least an order of magnitude of T_m[45,47] expected upon solvent deuteration when nuclei flip-flops of the latter dominate the decoherence process.

The observed decoherence times for $VO(dpm)_2$ are also comparable, despite the higher concentration of our samples, to those reported by Warner *et al.*[28] for a 0.1% diluted film of CuPc (2.1 *vs.* 1 μs at 80 K, if one consider the frozen solution $\mathbf{1}sol_{1\ mM}$, 0.16 *vs.* 1 μs if one consider the $\mathbf{1}PS_{1:10}$). We must stress that the processability and the surface stability of this β-diketonate complex are comparable to those of metal porphyrins, without the drawback of introducing ^{14}N magnetic nuclei. This is not only relevant for reducing the efficiency of decoherence; as suggested by Freedman *et al.*,[27] the well-defined hyperfine states of vanadium ions coordinated by non-magnetic nuclei can be used to investigate multiple quantum coherence. It is interesting to notice that in the Zeeman diagram of Fig. 1 pronounced level anti-crossings with gaps of the order of 0.5–1 GHz are observed at low longitudinal magnetic field. These transitions (in pale blue in Fig. 1), also known as clock transitions, are inherently robust to external perturbations because their effective g is practically zero and therefore are weakly affected by changes in the local field. Enhanced coherence time for these clock transitions have been recently observed in Bi doped silicon enriched in ^{29}Si nuclei.[57] Similar effects should be observable at the molecular level in $VO(dpm)_2$ for which clock transitions are expected at fields where the magnetization dynamics is already rather slow.

On the other hand, when T_m of $VO(dpm)_2$ is compared with relaxation times for a copper dithiolate complex with deuterated PPh_4^+ cation reported by van Slageren *et al.*[26] it is found to be an order of magnitude shorter: this might be attributed both to the larger concentration of the electronic spins in our system as well as to the large number of mobile protons present on the ligand. Further, the use of Q-band frequency, as done by van Slageren *et al.*, is expected to increase T_m of $VO(dpm)_2$ as well as its T_1.

Conclusions

We have shown here that a more rational search for potential qubits can significantly benefit from the combination of AC susceptometry with pulsed EPR techniques. This multi-technique approach is of particular relevance to define synthetic strategies because the optimization of T_1, in terms of both temperature and field dependence, is mandatory for the realization of molecular spin qubits that can be operated at room temperature. AC susceptibility gives easily access to the field dependence of T_1, in contrast to EPR, which relies on the resonance condition. Though T_1 extracted with the two techniques are exactly the same only in the case of a $S = 1/2$ with no hyperfine splitting, a close relation exists also for systems with more than two levels. The simple molecule we have picked up with this approach, though not yet optimized for coherent manipulation of the spin state, presents state-of-the-art phase memory times combined with additional interesting features. The spin–lattice relaxation remains slow even in strong fields, allowing the use of higher frequencies for coherent spin manipulation without losses in performances.

A particularly low efficient spin–phonon coupling appears to be at the basis of this behaviour and the potentially positive role played by the strong V=O bond needs to be further investigated by extending the approach developed here to other and more promising systems.[27,29] *Ab initio* modellization of the spin relaxation could also help to identify which structural features can favour long T_1, and consequently long T_m, at high temperature.

Even if the crucial aspect of qubits entanglement has not been addressed in this work it can be easily achieved through connection of β-diketonate pockets in more complex architectures.[58,59] This approach has already been successfully employed to couple different spin centers[60] and to address them individually in resonance experiments in particular in lanthanide polynuclear complexes thanks to their significantly different ***g***-factors.[61]

Of great relevance is the possibility to obtain monolayers of ordered arrays of intact $VO(dpm)_2$ molecules, retaining their paramagnetic nature thanks to the reduced interaction of the orbital carrying the unpaired electron with the substrate. Metallic nanostructures can be easily decorated with a monolayer of ordered $VO(dpm)_2$ molecules, allowing to investigate the response of an ensemble of identical molecular qubits, whose size can be easily controlled by lithographic exposure of the metallic substrate. Thin films of $VO(dpm)_2$ could be evaporated directly on a μ-SQUID to detect by AC susceptometry the effects of surface confinement on the dynamics of the magnetization, as already done on SMMs.[62] Our low temperature STM investigation suggests that $VO(dpm)_2$ could be also a good candidate to investigate quantum coherence at the single molecule level thanks to the recently developed approach based on spin-polarized scanning tunnelling microscopy, employed at very low temperature on single Fe atoms deposited on a MgO surface.[63]

Combining the optimization of T_2 in nuclear spin free environments with the possibility to control the spin–lattice relaxation through a rational synthetic design is foreseen to boost the interest for molecular spin systems as potential qubits.

Acknowledgements

The support of ERC through AdG MolNanoMaS (267746), of Italian MIUR through the project Futuro in Ricerca 2012 (RBFR12RPD1) and of Fondazione Ente Cassa di Risparmio di Firenze is acknowledged. Brunetto Cortigiani and Dr Shengwei Shi are acknowledged for the assistance in the XPS characterization. This paper is dedicated to Prof. Dante Gatteschi on the occasion of his retirement.

Notes and references

1 R. P. Feynman, *Found. Phys.*, 1986, **16**, 507–531.
2 P. W. Shor, *35th Annual Symposium on Foundations of Computer Science*, 1994.
3 A. M. Steane, *Rep. Prog. Phys.*, 1998, **61**, 117–173.
4 D. Deutsch, *Proc. R. Soc. London, Ser. A*, 1985, **400**, 97–117.
5 P. Ball, *Nature*, 2011, **474**, 272–274.
6 T. D. Ladd, F. Jelezko, R. Laflamme, Y. Nakamura, C. Monroe and J. L. O'Brien, *Nature*, 2010, **464**, 45–53.
7 R. Blatt and D. Wineland, *Nature*, 2008, **453**, 1008–1015.
8 R. Hanson and D. D. Awschalom, *Nature*, 2008, **453**, 1043–1049.
9 J. T. Muhonen, J. P. Dehollain, A. Laucht, F. E. Hudson, R. Kalra, T. Sekiguchi, K. M. Itoh, D. N. Jamieson, J. C. McCallum, A. S. Dzurak and A. Morello, *Nat. Nanotechnol.*, 2014, **9**, 986–991.
10 E. Knill, R. Laflamme and G. J. Milburn, *Nature*, 2001, **409**, 46–52.
11 J. Clarke and F. K. Wilhelm, *Nature*, 2008, **453**, 1031–1042.
12 I. L. Chuang, L. M. K. Vandersypen, X. Zhou, D. W. Leung and S. Lloyd, *Nature*, 1998, **393**, 143–146.
13 S. Thiele, F. Balestro, R. Ballou, S. Klyatskaya, M. Ruben and W. Wernsdorfer, *Science*, 2014, **344**, 1135–1138.
14 J. J. Pla, K. Y. Tan, J. P. Dehollain, W. H. Lim, J. J. L. Morton, F. A. Zwanenburg, D. N. Jamieson, A. S. Dzurak and A. Morello, *Nature*, 2013, **496**, 334–338.
15 F. Troiani and M. Affronte, *Chem. Soc. Rev.*, 2011, **40**, 3119–3129.
16 G. Aromi, D. Aguila, P. Gamez, F. Luis and O. Roubeau, *Chem. Soc. Rev.*, 2012, **41**, 537–546.
17 A. Morello, J. J. Pla, F. A. Zwanenburg, K. W. Chan, K. Y. Tan, H. Huebl, M. Mottonen, C. D. Nugroho, C. Yang, J. A. van

Donkelaar, A. D. C. Alves, D. N. Jamieson, C. C. Escott, L. C. L. Hollenberg, R. G. Clark and A. S. Dzurak, *Nature*, 2010, **467**, 687–691.
18 J. J. Pla, K. Y. Tan, J. P. Dehollain, W. H. Lim, J. J. L. Morton, D. N. Jamieson, A. S. Dzurak and A. Morello, *Nature*, 2012, **489**, 541–545.
19 K. Sato, S. Nakazawa, R. Rahimi, T. Ise, S. Nishida, T. Yoshino, N. Mori, K. Toyota, D. Shiomi, Y. Yakiyama, Y. Morita, M. Kitagawa, K. Nakasuji, M. Nakahara, H. Hara, P. Carl, P. Hofer and T. Takui, *J. Mater. Chem.*, 2009, **19**, 3739–3754.
20 S. Takahashi, R. Hanson, J. van Tol, M. S. Sherwin and D. D. Awschalom, *Phys. Rev. Lett.*, 2008, **101**, 047601.
21 G. Balasubramanian, P. Neumann, D. Twitchen, M. Markham, R. Kolesov, N. Mizuochi, J. Isoya, J. Achard, J. Beck, J. Tissler, V. Jacques, P. R. Hemmer, F. Jelezko and J. Wrachtrup, *Nat. Mater.*, 2009, **8**, 383–387.
22 A. M. Tyryshkin, S. Tojo, J. J. L. Morton, H. Riemann, N. V. Abrosimov, P. Becker, H.-J. Pohl, T. Schenkel, M. L. W. Thewalt, K. M. Itoh and S. A. Lyon, *Nat. Mater.*, 2011, **11**, 143–147.
23 A. Ardavan, O. Rival, J. J. L. Morton, S. J. Blundell, A. M. Tyryshkin, G. A. Timco and R. E. P. Winpenny, *Phys. Rev. Lett.*, 2007, **98**, 057201.
24 C. J. Wedge, G. A. Timco, E. T. Spielberg, R. E. George, F. Tuna, S. Rigby, E. J. L. McInnes, R. E. P. Winpenny, S. J. Blundell and A. Ardavan, *Phys. Rev. Lett.*, 2012, **108**, 107204.
25 A. Collauto, M. Mannini, L. Sorace, A. Barbon, M. Brustolon and D. Gatteschi, *J. Mater. Chem.*, 2012, **22**, 22272–22281.
26 K. Bader, D. Dengler, S. Lenz, B. Endeward, S.-D. Jiang, P. Neugebauer and J. van Slageren, *Nat. Commun.*, 2014, **5**, 5304.
27 J. M. Zadrozny, J. Niklas, O. G. Poluektov and D. E. Freedman, *J. Am. Chem. Soc.*, 2014, **136**, 15841–15844.
28 M. Warner, S. Din, I. S. Tupitsyn, G. W. Morley, A. M. Stoneham, J. A. Gardener, Z. Wu, A. J. Fisher, S. Heutz, C. W. M. Kay and G. Aeppli, *Nature*, 2013, **503**, 504–508.
29 J. M. Zadrozny, J. Niklas, O. G. Poluektov and D. E. Freedman, *ACS Cent. Sci.*, 2015, **1**, 488.
30 C. Schlegel, J. van Slageren, M. Manoli, E. K. Brechin and M. Dressel, *Phys. Rev. Lett.*, 2008, **101**, 147203.
31 M. A. K. Ahmed, H. Fjellvåg, A. Kjekshus and B. Klewe, *Z. Anorg. Allg. Chem.*, 2004, **630**, 2311–2318.
32 N. Ishikawa, M. Sugita, T. Ishikawa, S. Koshihara and Y. Kaizu, *J. Am. Chem. Soc.*, 2003, **125**, 8694–8695.
33 D. Gatteschi, R. Sessoli and J. Villain, *Molecular nanomagnets*, Oxford University Press, Oxford, UK, 2006.
34 K. N. Shrivastava, *Phys. Status Solidi B*, 1983, **117**, 437–458.
35 A. Abragam and B. Bleaney, *Electron Paramagnetic Resonance of Transition Ions*, Dover, New York, 1986.
36 A. C. de Vroomen, E. E. Lijphart and N. J. Poulis, *Physica*, 1970, **47**, 458–484.
37 H. A. Kramers, *Proc. Acad. Sci. Amsterdam*, 1930, **33**, 959.
38 J. Soeteman, L. Bevaart and A. J. van Duyneveldt, *Physica*, 1974, **74**, 126–134.
39 J. H. van Vleck, *Phys. Rev.*, 1940, **57**, 426–447.
40 J. Soeteman, A. J. van Duyneveldt, C. L. M. Pouw and W. Breur, *Physica*, 1973, **66**, 63–69.
41 N. B. Morozova, A. E. Turgambaeva, I. A. Baidina, V. V. Krysyuk and I. K. Igumenov, *J. Struct. Chem.*, 2005, **46**, 1047–1051.
42 S. Stoll and A. Schweiger, *J. Magn. Reson.*, 2006, **178**, 42–55.
43 A. J. Fielding, D. B. Back, M. Engler, B. Baruah, D. C. Crans, G. R. Eaton and S. S. Eaton, *ACS Symp. Ser.*, 2007, **974**, 364–375.
44 J. P. Fackler, J. D. Levy and J. A. Smith, *J. Am. Chem. Soc.*, 1972, **94**, 2436–2445.
45 G. R. Eaton and S. S. Eaton, *J. Magn. Reson.*, 1999, **136**, 63–68.
46 M. A. Nielsen and I. L. Chuang, *Quantum Computation and Quantum Information: 10th Anniversary Edition*, Cambridge University Press, 2011.
47 A. Schweiger and G. Jeschke, *Principles of Pulse Electron Paramagnetic Resonance*, Oxford University Press, 2001.
48 S. R. Hartmann and E. L. Hahn, *Phys. Rev.*, 1962, **128**, 2042–2053.
49 I. Cimatti, S. Ninova, V. Lanzilotto, L. Malavolti, L. Rigamonti, B. Cortigiani, M. Mannini, E. Magnano, F. Bondino, F. Totti, A. Cornia and R. Sessoli, *Beilstein J. Nanotechnol.*, 2014, **5**, 2139–2148.
50 L. Malavolti, V. Lanzilotto, S. Ninova, L. Poggini, I. Cimatti, B. Cortigiani, L. Margheriti, D. Chiappe, E. Otero, P. Sainctavit, F. Totti, A. Cornia, M. Mannini and R. Sessoli, *Nano Lett.*, 2015, **15**, 535–541.
51 K. Eguchi, Y. Takagi, T. Nakagawa and T. Yokoyama, *J. Phys. Chem. C*, 2013, **117**, 22843–22851.
52 K. Eguchi, T. Nakagawa, Y. Takagi and T. Yokoyama, *J. Phys. Chem. C*, 2015, **119**, 9805–9815.
53 S. Stepanow, A. Mugarza, G. Ceballos, P. Moras, J. C. Cezar, C. Carbone and P. Gambardella, *Phys. Rev. B: Condens. Matter Mater. Phys.*, 2010, **82**, 014405.
54 S. Gómez-Coca, A. Urtizberea, E. Cremades, P. J. Alonso, A. Camón, E. Ruiz and F. Luis, *Nat. Commun.*, 2014, **5**, 4300.
55 R. M. Rakhmatullin, I. N. Kurkin, G. V. Mamin, S. B. Orlinskii, M. R. Gafurov, E. I. Baibekov, B. Z. Malkin, S. Gambarelli, S. Bertaina and B. Barbara, *Phys. Rev. B: Condens. Matter Mater. Phys.*, 2009, **79**, 172408.
56 J.-L. Du, G. R. Eaton and S. S. Eaton, *J. Magn. Reson., Ser. A*, 1996, **119**, 240–246.
57 G. Wolfowicz, A. M. Tyryshkin, R. E. George, H. Riemann, N. V. Abrosimov, P. Becker, H.-J. Pohl, M. L. W. Thewalt, S. A. Lyon and J. J. L. Morton, *Nat. Nanotechnol.*, 2013, **8**, 561–564.
58 C. Pariya, C. R. Sparrow, C.-K. Back, G. Sandí, F. R. Fronczek and A. W. Maverick, *Angew. Chem.,Int. Ed.*, 2007, **46**, 6305–6308.
59 J. K. Clegg, F. Li, K. A. Jolliffe, L. F. Lindoy, G. V. Meehan, S. Parsons, P. A. Tasker and F. J. White, *Dalton Trans.*, 2013, **42**, 14315–14323.
60 L. A. Barrios, D. Aguilà, O. Roubeau, P. Gamez, J. Ribas-Ariño, S. J. Teat and G. Aromí, *Chem.–Eur. J.*, 2009, **15**, 11235–11243.

61 D. Aguila, L. A. Barrios, V. Velasco, O. Roubeau, A. Repolles, P. J. Alonso, J. Sese, S. J. Teat, F. Luis and G. Aromi, *J. Am. Chem. Soc.*, 2014, **136**, 14215–14222.
62 E. Bellido, P. Gonzalez-Monje, A. Repollés, M. Jenkins, J. Sesé, D. Drung, T. Schurig, K. Awaga, F. Luis and D. Ruiz-Molina, *Nanoscale*, 2013, **5**, 12565–12573.
63 S. Baumann, W. Paul, T. Choi, C. P. Lutz, A. Ardavan and A. J. Heinrich, *Science*, 2015, **350**, 417–420.

JACS
JOURNAL OF THE AMERICAN CHEMICAL SOCIETY

Communication

pubs.acs.org/JACS

Room-Temperature Quantum Coherence and Rabi Oscillations in Vanadyl Phthalocyanine: Toward Multifunctional Molecular Spin Qubits

Matteo Atzori,[†] Lorenzo Tesi,[†] Elena Morra,[‡] Mario Chiesa,[‡] Lorenzo Sorace,[†] and Roberta Sessoli*[,†]

[†]Dipartimento di Chimica "Ugo Schiff" & INSTM RU, Università degli Studi di Firenze, Via della Lastruccia 3, I50019 Sesto Fiorentino (Firenze), Italy

[‡]Dipartimento di Chimica & NIS Centre, Università di Torino, Via P. Giuria 7, I10125 Torino, Italy

Supporting Information

ABSTRACT: Here we report the investigation of the magnetic relaxation and the quantum coherence of vanadyl phthalocyanine, VOPc, a multifunctional and easy-processable potential molecular spin qubit. VOPc in its pure form (**1**) and its crystalline dispersions in the isostructural diamagnetic host TiOPc in different stoichiometric ratios, namely VOPc:TiOPc 1:10 (**2**) and 1:1000 (**3**), were investigated via a multitechnique approach based on the combination of alternate current (AC) susceptometry, continuous wave, and pulsed electron paramagnetic resonance (EPR) spectroscopy. AC susceptibility measurements revealed a linear increase of the relaxation rate with temperature up to 20 K, as expected for a direct mechanism, but τ remains slow over a very wide range of applied static field values (up to ∼5 T). Pulsed EPR spectroscopy experiments on **3** revealed quantum coherence up to room temperature with T_m ∼1 μs at 300 K, representing the highest value obtained to date for molecular electronic spin qubits. Rabi oscillations are observed in this nuclear spin-active environment (^{1}H and ^{14}N nuclei) at room temperature also for **2**, indicating an outstanding robustness of the quantum coherence in this molecular semiconductor exploitable in spintronic devices.

In the development of spin-based information technology, magnetic molecules represent particularly versatile building blocks as they can serve for the realization of both "static" and "dynamic" components of a potential quantum computer.[1] While single-molecule magnets (SMMs) show magnetic bistability resulting from magnetic anisotropy and large spin,[2] molecules with lower spin values can be exploited in quantum computation as quantum bits, or qubits.[3] A qubit is a two state quantum mechanical system able to be placed in a state of coherent superposition of these levels. Physical realizations of qubits can be found in superconductive circuits, trapped ions, photons, etc.[1,4] Nuclear and electronic spins are also interesting because their superposition of spin states can be realized by pulsed magnetic resonance techniques. The most investigated electronic spin systems are nitrogen-vacancy pairs in diamonds[5] or defects in silicon[6] or silicon carbide.[7] Polynuclear metal complexes,[3,8] in particular ferrimagnetic rings,[9] have been also investigated for the possibility to use synthetic chemistry to obtain multibit systems. Only recently, molecular spin systems have become really competitive. The realization of a qubit requires, in fact, the accomplishment of stringent and antithetic requirements known as Di Vincenzo criteria.[10] If molecules are better suited to satisfy some of them, like addressing and control of qubits entanglement, the short lifetime of the quantum superposition of states, T_m, has up to now posed some limitations in their use as qubits. Recently promising results have been obtained on simple $S = 1/2$ complexes.[11,12] Remarkably, mononuclear V^{IV} complexes with nuclear spin-free ligands like dithiolenes,[13] when dispersed in nuclear spin-free solvents like CS_2, can attain, at low temperature, T_m of the order of the millisecond,[14] a value comparable to those observed for vacancies in extended lattices. Their use at room temperature is however hampered by the rapid decrease, on increasing the temperature, of the spin-lattice relaxation time, T_1, which acts as a limiting factor for T_m.

In a recent investigation, we have shown that alternate current (AC) susceptibility can flank pulsed electron paramagnetic resonance (EPR) techniques to identify species that show slow spin-lattice relaxation as potential spin qubits.[15] A vanadyl complex with β-diketonate ligands has revealed remarkable T_m despite the proton-rich ligands and, more interestingly, a long T_1 over a wide range of temperature and applied magnetic fields.

Keeping in mind the growing interest to address single molecules on surfaces exploiting their electric conductance, we focused our attention on vanadyl phthalocyanine, VOPc. This system exhibits the expected electronic and structural features to behave as a molecular spin qubit combined with other technologically relevant physical properties, such as extrinsic and photoinduced semiconductivity[16] and the ability of being deposited on different surfaces in oriented dispositions,[17] fundamental requisites for a suitable processability and incorporation of these materials in real devices. The high stability of the diamagnetic analogue, titanyl phthalocyanine, TiOPc, allows the preparation of crystalline materials with different percentage of paramagnetic component diluted in the diamagnetic host leading to two important advantages: (i) reduce the interactions between electronic magnetic moments, that significantly increase the T_2 relaxation time,[18] and (ii) extend the investigation up to room temperature, avoiding the melting

Received: December 23, 2015
Published: February 7, 2016

DOI: 10.1021/jacs.5b13408
J. Am. Chem. Soc. 2016, 138, 2154−2157

of frozen solutions. We have thus investigated the magnetic relaxation and the quantum coherence of VOPc in its pure form (**1**) and its crystalline dispersions in the isostructural diamagnetic host TiOPc in different molar ratios, 1:10 (**2**) and 1:1000 (**3**), through a multitechnique approach based on the combination of AC susceptometry and continuous wave (CW) and pulsed EPR spectroscopies.

VOPc is a nonplanar metal-phthalocyanine in which the vanadyl ion VO^{2+}, coordinated by four nitrogen donor atoms of the dianionic phthalocyaninato ligand, points out of the plane of the ligand. The coordination geometry around the pentacoordinated V^{IV} ion is a distorted square pyramid with the metal slightly above the basal plane (0.575(1) Å).[19] The apical position is occupied by an oxo ligand which forms a double bond with the V^{IV} ion having a V═O distance of 1.580(3) Å, whereas the V−N bond lengths are in the 2.008(7)−2.034(7) Å range (Figure 1).

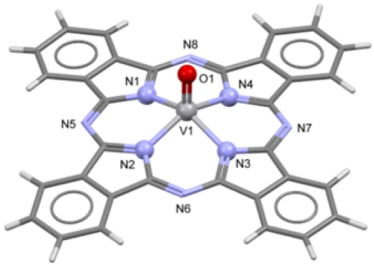

Figure 1. Molecular structure of VOPc with principal atoms labeling scheme and coordination geometry of the V^{IV} ion highlighted.

The presence of such short V═O bond distance is responsible for a d-orbital splitting that leaves the d_{xy} orbital lowest in energy and well separated from the other orbitals. This, together with the single unpaired electron of d^1 configuration makes this molecule a perfect two levels potential molecular qubit. VOPc and its diamagnetic analogue TiOPc exhibit a rich polymorphism and crystallize in at least four different structural phases showing slightly different crystal packings (Type I−IV polymorphs).[20] Type II was selected because π-stacked supramolecular dimers are absent in the crystal structure and is the preferred one for VOPc (Figure S1). Moreover, TiOPc can be conveniently converted in this structural phase by dissolution in a 1:4 mixture of CF_3COOH:CH_2Cl_2 and successive precipitation in isopropanol (see SI).[20] Powder X-ray diffraction analyses performed on polycrystalline samples show structural phase homogeneity for all the investigated samples and a good agreement between experimental and simulated patterns (Figure S2).

Compounds **1** and **2** were investigated by AC susceptometry in order to get deeper insights on their magnetization dynamics. The thermal variation of the magnetic susceptibility in zero static magnetic field reveals no imaginary component of the susceptibility (χ'') in the whole investigated T range (1.9−40 K). When a small static magnetic field (>40 mT) is applied, slow magnetic relaxation is observed with appearance of a peak in the imaginary component of the susceptibility and a concomitant decrease of the real part (χ') (Figures S3−S10). Both **1** and **2** under a static magnetic field (B) of 0.2 T show slow relaxation of the entire magnetization, so that this field and a higher one (1 T) were selected to investigate the T dependence of the relaxation time (τ). The frequency dependence of χ'' is well reproduced with the Debye model (Figures S3−S10), and the extracted values of τ as a function of T for the two selected fields are reported in Figure 2a.

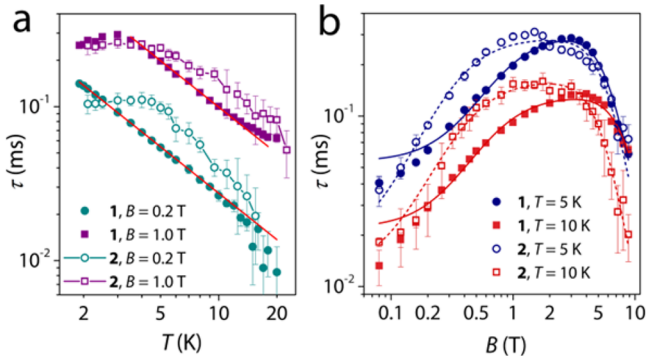

Figure 2. (a) T and (b) B dependence of τ extracted from AC susceptibility measurements on **1** and **2** at different applied static magnetic-field values and temperatures (see legends). Solid and dashed lines are the best-fits of the models.

Figure 2a shows that **1** exhibits up to 20 K a τ dependence typical of the direct mechanism of relaxation in absence of phonon-bottleneck effects.[21] The field dependence of τ in this T range (Figure 2b) shows an increase up to ∼3 T, while the rapid decrease expected for the direct mechanism is only visible above 5 T. The nonmonotonous behavior is due to two antagonist effects of the magnetic field. An isolated $S = 1/2$ spin in zero field should not be able to relax due to time-reversal symmetry, but spin−spin and spin−nuclei interactions promote a rapid relaxation, as recently discussed for a Co^{II} pseudo $S = 1/2$ spin system.[22] The latter mechanisms are suppressed when the magnetic field splits the energy of the doublet, similarly to the phenomenon of resonant quantum tunneling in SMMs.[2] On the other hand, the larger is the energy separation of the doublet the more efficient is the spin-phonon direct mechanism providing $\tau^{-1} \propto B^4$. In general, fields weaker than 1 T are sufficient to accelerate the relaxation.[23] The two mechanisms can be taken into account in a phenomenological model described by the following equation:[24]

$$\tau^{-1} = cB^4 + d\frac{e(f + B^2)}{ef + B^2} \quad (1)$$

where the first term considers the typical field dependence of a direct process while in the second term, d represents the zero-field relaxation rate, e is a parameter related to the concentration, and f is a parameter proportional to the square of the internal field generated by neighboring spins. The best-fit parameters are reported in Table S1. It is interesting to notice that f decreases significantly passing from **1** to **2**, in agreement with the reduction of the internal field upon dilution. The increase of the zero-field relaxation rate, which is not expected, appears however as an artifact of the poor reproduction of the low field data, as testified by the large errors. As a result, τ increases much faster in moderate field in **2**, indicating that both spin−spin and hyperfine interactions are active in promoting relaxation in weak applied fields. A comparison with a recent report on the compound $VO(dpm)_2$ (dpm^- is the anion of dipivaloylmethane)[15] shows, in both cases, a remarkable wide field range where τ remains long, suggesting that the V═O double bond increases the energy of vibrational modes relevant for the magnetic relaxation. We can notice that τ is in general shorter for VOPc than $VO(dpm)_2$ and that the maximum τ is observed at higher fields, in agreement with the additional contributions to the spin relaxation of the nitrogen nuclear spins directly coordinated to the V^{IV} ion. This

DOI: 10.1021/jacs.5b13408
J. Am. Chem. Soc. 2016, 138, 2154−2157

could also justify the low-temperature saturation of τ, not detected in $VO(dpm)_2$.

The CW-EPR X-band spectra of compounds **1**−**3** at 300 and 5 K are reported in Figure S11. **1** shows a broad spectrum very likely due to the presence of an extensive network of intermolecular interactions between paramagnetic molecules.[19] The 1:10 crystalline dispersion of VOPc in TiOPc (**2**) dramatically changes the EPR spectrum, which reveals already at room temperature the expected hyperfine splitting due to the coupling with the nuclear spin of ^{51}V (I = 7/2, natural abundance: 99.75%). By lowering the concentration of the paramagnetic component to 1:1000 (**3**), the superhyperfine spectral features due to the further coupling with the nuclear spins (I = 1) of the chelating ^{14}N nuclei become visible (Figure 3a).[25] As far as the position of the resonance lines are concerned,

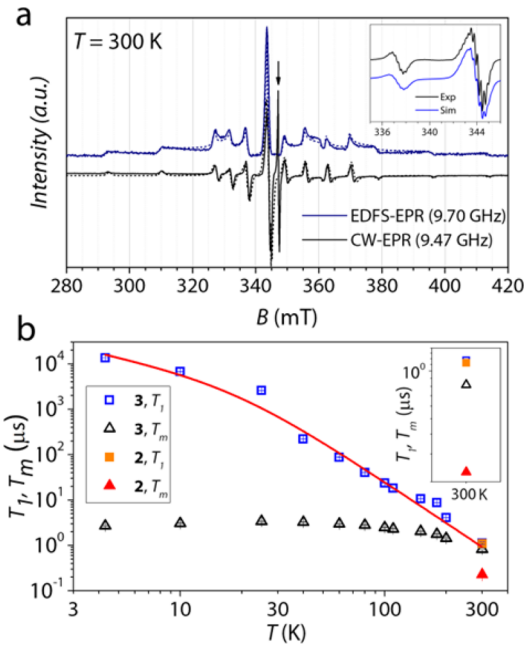

Figure 3. (a) EDFS- and CW-EPR X-band spectra for **3**. CW data were translated for ease of comparison with EDFS data. Short-dashed lines are the best simulations. Inset shows the CW superhyperfine spectral feature of **3**. The arrow indicates the signal of the organic radical. (b) T dependence of T_1 and T_m relaxation times for **3**. The solid line is the best fit of the model. Inset shows the room-temperature data for **2** and **3**.

no significant variations are observed between **2** and **3**, thus confirming that VOPc retains the same molecular geometry and environment (Figure S11).

Good spectral simulations[26] (Figures 3a and S12) were performed on the basis of the spin Hamiltonian:

$$\mathcal{H} = \hat{\mathbf{I}}_V \cdot {}^V\mathbf{A} \cdot \hat{\mathbf{S}} + {}^N A \sum_{i=1}^{4} \hat{\mathbf{I}}_{N_i} \cdot \hat{\mathbf{S}} + \mu_B \hat{\mathbf{S}} \cdot \mathbf{g} \cdot \mathbf{B} \quad (2)$$

which provides as best-fit parameters the values reported in Table S2. In the EPR spectrum of **3** an additional exchange narrowed signal[27] of an organic radical is present (Figures 3a and S12). This signal, also observed in the TiOPc matrix before and after purification (Figure S13), was assigned to the reduced species, $TiOPc^{\cdot-}$.[28] Double integration of the spectrum allowed to estimate the amount of this species as 1 order of magnitude less concentrate than VOPc, viz. 0.01% of the entire diamagnetic TiOPc. The quantities of $TiOPc^{\cdot-}$ observed in **3** and in the TiOPc diamagnetic matrix were of the same order of magnitude, thus confirming that this species is not generated as a result of the doping process.

X-band echo-detected field-swept (EDFS) EPR spectra for **3** were recorded by using a standard Hahn echo sequence (Figures 3a and S14). As evidenced by the presence of a spin-echo, we can anticipate that quantum coherence is expected for this compound. Moreover the spin Hamiltonian parameters obtained through the CW spectrum simulation provide good simulations of the EDFS spectra as well, thus indicating that the entire VOPc is experiencing the detected coherence. Inversion recovery experiments were performed in the 4.3−300 K T range to investigate the T dependence of T_1 for **3** since the amount of paramagnetic component was too low for an investigation through AC susceptometry. The resulting saturation recovery traces were fitted with a standard stretched monoexponential equation (see SI), and the extracted T_1 values are reported in Figure 3b. T_1 decreases very slowly from the maximum value of ∼14 ms at 4.3 K to 0.22 ms at 40 K in a way that is qualitatively similar to what observed for **1** and **2** through AC susceptometry. At higher temperature, a higher slope is observed, and T_1 reaches the value of 1.1 μs at room temperature. The entire curve has been simulated assuming the contribution of a direct and a Raman-like process (see SI), dominating at low and high T, respectively. Best-fit values give a very low Raman-like exponent n of ∼3 as already observed in closely related systems[12,15,29] and attributed to the involvement of both optical and acoustic phonons in the relaxation.

To investigate the quantum coherence in details and to quantify the phase memory time, T_m, of VOPc in the doped material **3** as a function of T, echo decay experiments were performed at the so-called powder-like line field (345 mT) and at a lower field line (338 mT, Figure S15). Remarkably, echo decay traces (Figure 4a) were detected up to room temperature.

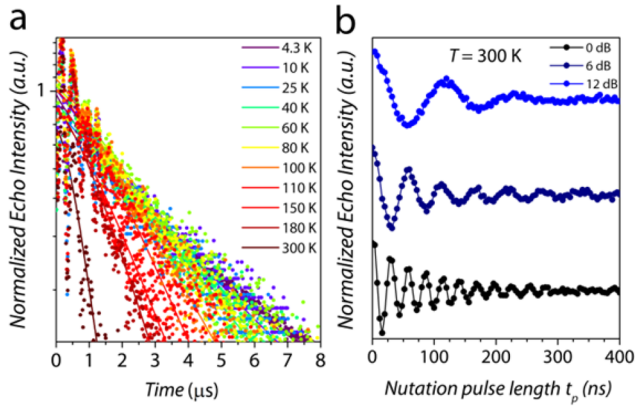

Figure 4. (a) Echo decay traces for **3** at different T (see legend). Solid lines are the best fits (see SI). (b) Rabi oscillations recorded for **3** at 300 K for different microwave attenuations. Both experiments were performed at 345 mT.

The thermal variation of T_m shows an almost temperature-independent behavior in the 4.3−150 K range, with values within the 2.04−3.41 μs range, then it slowly decreases as the temperature increases reaching a still remarkable value of 0.83 μs at room temperature (Figure 3b). Interestingly, CuPc exhibits similar low temperature T_m but no room-temperature coherence because of the rapid decrease of its T_1 on increasing T.[11] To date, a slightly shorter T_m at room temperature in a solid-phase

DOI: 10.1021/jacs.5b13408
J. Am. Chem. Soc. 2016, 138, 2154−2157

molecular system was obtained for $[(Ph)_4P]_2[Cu(mnt)_2]$ (mnt = maleonitriledithiolate, H-free ligand) highly diluted (0.001%) in the Ni^{II} isostructural diamagnetic host.[12] Preliminary results obtained on **2** revealed that T_1 and T_m are not suppressed by the high concentration of VOPc, assuming really remarkable values of 1.1 μs (T_1) and 0.23 μs (T_m) at room temperature (Figures 3b and S16). The observation of coherence times comparable to T_1 in concentrated and nuclear spin-rich environments points out the need for strategies to decrease spin-lattice relaxation in the quest for molecular-based spin qubits.

To prove that such coherence times allow to perform coherent spin manipulations, i.e., place the spins in any arbitrary superposition of states, nutation experiments were performed at different microwave powers at 4.3 and 300 K. Remarkably, Rabi oscillations were clearly observed at room temperature for both **2** and **3**, with the expected linear dependence of the Rabi frequency, Ω_R, as a function of the B_1 relative intensity (Figures 4b and S17−S20). To the best of our knowledge, this is the first report of Rabi oscillations detected at room temperature in a molecular spin system in the solid state. Even more remarkable is their observation in a concentrated sample, indicating a particular robustness of quantum coherence in this vanadyl-based systems.

In conclusion, VOPc in its crystalline dispersion in TiOPc represents one of the few examples of potential molecular qubit showing room-temperature quantum coherence. The combination of these features with its high thermal stability and high processability makes these materials extremely appealing, as they can be used as paramagnetic semiconductors in spintronics devices. It is also known that VOPc molecules retain their paramagnetism when in direct contact with metallic surfaces thanks to the protected nature of the d_{xy} magnetic orbital.[17] The recent observation of EPR resonance by scanning tunneling microscopy[30] and the possibility to measure T_1 and T_m of individual atoms on surfaces further widen the interest in this vanadyl system.

■ ASSOCIATED CONTENT

Supporting Information

The Supporting Information is available free of charge on the ACS Publications website at DOI: 10.1021/jacs.5b13408.

Experimental details and data (PDF)

■ AUTHOR INFORMATION

Corresponding Author

*roberta.sessoli@unifi.it

Notes

The authors declare no competing financial interest.

■ ACKNOWLEDGMENTS

European Research Council (ERC) through AdG MolNanoMaS (267746), Italian MIUR through the project Futuro in Ricerca 2012 (RBFR12RPD1), and Fondazione Ente Cassa di Risparmio di Firenze are acknowledged for financial support.

■ REFERENCES

(1) Nielsen, M. A.; Chuang, I. L. *Quantum Computation and Quantum Information*; Cambridge University Press: Cambridge, 2000.

(2) Gatteschi, D.; Sessoli, R.; Villain, J. *Molecular nanomagnets*; Oxford University Press: Oxford, U.K., 2006.

(3) (a) Troiani, F.; Affronte, M. *Chem. Soc. Rev.* **2011**, *40*, 3119. (b) Aromi, G.; Aguila, D.; Gamez, P.; Luis, F.; Roubeau, O. *Chem. Soc. Rev.* **2012**, *41*, 537.

(4) Ladd, T. D.; Jelezko, F.; Laflamme, R.; Nakamura, Y.; Monroe, C.; O'Brien, J. L. *Nature* **2010**, *464*, 45.

(5) (a) Kennedy, T. A.; Colton, J. S.; Butler, J. E.; Linares, R. C.; Doering, P. J. *Appl. Phys. Lett.* **2003**, *83*, 4190. (b) Balasubramanian, G.; Neumann, P.; Twitchen, D.; Markham, M.; Kolesov, R.; Mizuochi, N.; Isoya, J.; Achard, J.; Beck, J.; Tissler, J.; Jacques, V.; Hemmer, P. R.; Jelezko, F.; Wrachtrup, J. *Nat. Mater.* **2009**, *8*, 383.

(6) Pla, J. J.; Tan, K. Y.; Dehollain, J. P.; Lim, W. H.; Morton, J. J. L.; Jamieson, D. N.; Dzurak, A. S.; Morello, A. *Nature* **2012**, *489*, 541.

(7) Tyryshkin, A. M.; Tojo, S.; Morton, J. J. L.; Riemann, H.; Abrosimov, N. V.; Becker, P.; Pohl, H.-J.; Schenkel, T.; Thewalt, M. L. W.; Itoh, K. M.; Lyon, S. A. *Nat. Mater.* **2011**, *11*, 143.

(8) Takahashi, S.; Tupitsyn, I. S.; van Tol, J.; Beedle, C. C.; Hendrickson, D. N.; Stamp, P. C. E. *Nature* **2011**, *476*, 76.

(9) (a) Ardavan, A.; Rival, O.; Morton, J. J. L.; Blundell, S. J.; Tyryshkin, A. M.; Timco, G. A.; Winpenny, R. E. P. *Phys. Rev. Lett.* **2007**, *98*, 057201. (b) Ardavan, A.; Bowen, A. M.; Fernandez, A.; Fielding, A. J.; Kaminski, D.; Moro, F.; Muryn, C. A.; Wise, M. D.; Ruggi, A.; McInnes, E. J. L.; Severin, K.; Timco, G. A.; Timmel, C. R.; Tuna, F.; Whitehead, G. F. S.; Winpenny, R. E. P. *Npj Quantum Information* **2015**, *1*, 15012.

(10) DiVincenzo, D. P. *Fortschr. Phys.* **2000**, *48*, 771.

(11) Warner, M.; Din, S.; Tupitsyn, I. S.; Morley, G. W.; Stoneham, A. M.; Gardener, J. A.; Wu, Z.; Fisher, A. J.; Heutz, S.; Kay, C. W. M.; Aeppli, G. *Nature* **2013**, *503*, 504.

(12) Bader, K.; Dengler, D.; Lenz, S.; Endeward, B.; Jiang, S.-D.; Neugebauer, P.; van Slageren, J. *Nat. Commun.* **2014**, *5*, 5304.

(13) Zadrozny, J. M.; Niklas, J.; Poluektov, O. G.; Freedman, D. E. *J. Am. Chem. Soc.* **2014**, *136*, 15841.

(14) Zadrozny, J. M.; Niklas, J.; Poluektov, O. G.; Freedman, D. E. *ACS Cent. Sci.* **2015**, *1*, 488.

(15) Tesi, L.; Lucaccini, E.; Cimatti, I.; Perfetti, M.; Mannini, M.; Atzori, M.; Morra, E.; Chiesa, M.; Caneschi, A.; Sorace, L.; Sessoli, R. *Chem. Sci.* **2016**, DOI: 10.1039/C5SC04295J.

(16) Zhang, Y.; Learmonth, T.; Wang, S.; Matsuura, A. Y.; Downes, J.; Plucinski, L.; Bernardis, S.; O'Donnell, C.; Smith, K. E. *J. Mater. Chem.* **2007**, *17*, 1276.

(17) Eguchi, K.; Takagi, Y.; Nakagawa, T.; Yokoyama, T. *J. Phys. Chem. C* **2013**, *117*, 22843.

(18) Abragam, A.; Bleaney, B. *Electron Paramagnetic Resonance of Transition Ions*; Dover: New York, 1986.

(19) Ziolo, R. F.; Griffiths, C. H.; Troup, J. M. *J. Chem. Soc., Dalton Trans.* **1980**, 2300.

(20) Duff, J. M.; Mayo, J. D.; Hsiao, C.-K.; Hor, A.-M.; Bluhm, T. L.; Hamer, G. K.; Kazmaier, P. M Processes for the preparation of titanium phthalocyanines. Patent 5166339, November 24, 1992.

(21) Shrivastava, K. N. *Phys. Status Solidi B* **1983**, *117*, 437.

(22) Gómez-Coca, S.; Urtizberea, A.; Cremades, E.; Alonso, P. J.; Camón, A.; Ruiz, E.; Luis, F. *Nat. Commun.* **2014**, *5*, 4300.

(23) Soeteman, J.; van Duyneveldt, A. J.; Pouw, C. L. M.; Breur, W. *Physica* **1973**, *66*, 63.

(24) De Vroomen, A. C.; Lijphart, E. E.; Prins, D. Y. H.; Marks, J.; Poulis, N. J. *Physica* **1972**, *61*, 241.

(25) Sato, M.; Kwan, T. *J. Chem. Phys.* **1969**, *50*, 558.

(26) Stoll, S.; Schweiger, A. *J. Magn. Reson.* **2006**, *178*, 42.

(27) Konarev, D. V.; Kuzmin, A. V.; Faraonov, M. A.; Ishikawa, M.; Khasanov, S. S.; Nakano, Y.; Otsuka, A.; Yamochi, H.; Saito, G.; Lyubovskaya, R. N. *Chem. - Eur. J.* **2015**, *21*, 1014.

(28) Guzy, C. M.; Raynor, J. B.; Stodulski, L. P.; Symons, M. C. R. *J. Chem. Soc. A* **1969**, 997.

(29) Du, J.-L.; Eaton, G. R.; Eaton, S. S. *J. Magn. Reson., Ser. A* **1996**, *119*, 240.

(30) Baumann, S.; Paul, W.; Choi, T.; Lutz, C. P.; Ardavan, A.; Heinrich, A. J. *Science* **2015**, *350*, 417.

DOI: 10.1021/jacs.5b13408
J. Am. Chem. Soc. 2016, 138, 2154−2157

JACS
JOURNAL OF THE AMERICAN CHEMICAL SOCIETY

Article

pubs.acs.org/JACS

Quantum Coherence Times Enhancement in Vanadium(IV)-based Potential Molecular Qubits: the Key Role of the Vanadyl Moiety

Matteo Atzori,*[,†] Elena Morra,[‡] Lorenzo Tesi,[†] Andrea Albino,[†] Mario Chiesa,[‡] Lorenzo Sorace,[†] and Roberta Sessoli*[,†]

[†]Dipartimento di Chimica "Ugo Schiff" e INSTM, Università degli Studi di Firenze, Via della Lastruccia 3, I50019 Sesto Fiorentino (Firenze), Italy

[‡]Dipartimento di Chimica e NIS Centre, Università di Torino, Via P. Giuria 7, I10125 Torino, Italy

Supporting Information

ABSTRACT: In the search for long-lived quantum coherence in spin systems, vanadium(IV) complexes have shown record phase memory times among molecular systems. When nuclear spin-free ligands are employed, vanadium(IV) complexes can show at low temperature sufficiently long quantum coherence times, T_m, to perform quantum operations, but their use in real devices operating at room temperature is still hampered by the rapid decrease of T_1 caused by the efficient spin−phonon coupling. In this work we have investigated the effect of different coordination environments on the magnetization dynamics and the quantum coherence of two vanadium(IV)-based potential molecular spin qubits in the solid state by introducing a unique structural difference, i.e., an oxovanadium(IV) in a square pyramidal versus a vanadium(IV) in an octahedral environment featuring the same coordinating ligand, namely, the 1,3-dithiole-2-thione-4,5-dithiolate. This investigation, performed by a combined approach of alternate current (ac) susceptibility measurements and continuous wave (CW) and pulsed electron paramagnetic resonance (EPR) spectroscopies revealed that the effectiveness of the vanadyl moiety in enhancing quantum coherence up to room temperature is related to a less effective mechanism of spin−lattice relaxation that can be quantitatively evaluated by the exponent n (ca. 3) of the temperature dependence of the relaxation rate. A more rapid collapse is observed for the non-oxo counterpart (n = 4) hampering the observation of quantum coherence at room temperature. Record coherence time at room temperature (1.04 μs) and Rabi oscillations are also observed for the vanadyl derivative in a very high concentrated material (5 ± 1%) as a result of the additional benefit provided by the use of a nuclear spin-free ligand.

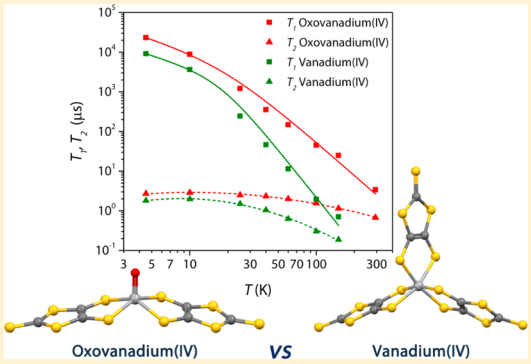

INTRODUCTION

Quantum computation, one of the pillars of the technological revolution that is foreseen for the next decades, has its core in the quantum bit, or qubit,[1,2] i.e., a two states quantum−mechanical system able to be placed in a state of coherent superposition of these two states.[3] Physical realizations of qubits can be found in superconductive circuits and trapped ions and can be based on photons, spins, and so on.[3,4] Among them, spins, both nuclear and electronic, are particularly interesting because the superposition of spin states can be realized by accessible pulsed magnetic resonance techniques. The most investigated electronic spin systems are nitrogen-vacancy pairs in diamond[5,6] or defects in silicon[7] or silicon carbide.[8] In this context, magnetic molecules can play a key role due to the wide range of physical properties they exhibit and the intrinsic quantum nature of some of them. Both "static" and "dynamic" components of a quantum computer can be in principle realized by exploiting, for the former, the magnetic bistability due to the magnetic anisotropy and the large spin of single-molecule magnets (SMMs)[9] and, for quantum logic operations, the long coherence that characterizes molecules with an isotropic small spin. Recently, the interest has been extended to forbidden spin transitions in molecules with $S > 1/2$,[10] as well as to lanthanide complexes in highly symmetric coordination environments.[11,12] The realization of a qubit requires, however, the accomplishment of stringent and somehow conflicting prerequisites known as Di Vincenzo criteria,[13] and their preparation and investigation represent a current and very challenging research field. Molecule-based systems such as polynuclear metal complexes[1,2,14] are currently investigated for the possibility offered by synthetic chemistry to obtain multibit systems with controlled exchange interaction between them.[15] Despite the advantage of chemical tunability of molecular systems with respect to classical inorganic materials, the short lifetime of the quantum superposition of states, represented by the spin−spin relaxation time T_2 or the phase memory time T_m, has up to now posed important limitations in their perspective use as qubits. Even if coherence can be significantly enhanced by exploiting atomic clock

Received: May 31, 2016
Published: August 12, 2016

DOI: 10.1021/jacs.6b05574
J. Am. Chem. Soc. 2016, 138, 11234−11244

Scheme 1. Reaction Schemes for the Synthesis of Compounds 1 and 3 (a), 4 (b), and 2 (c)

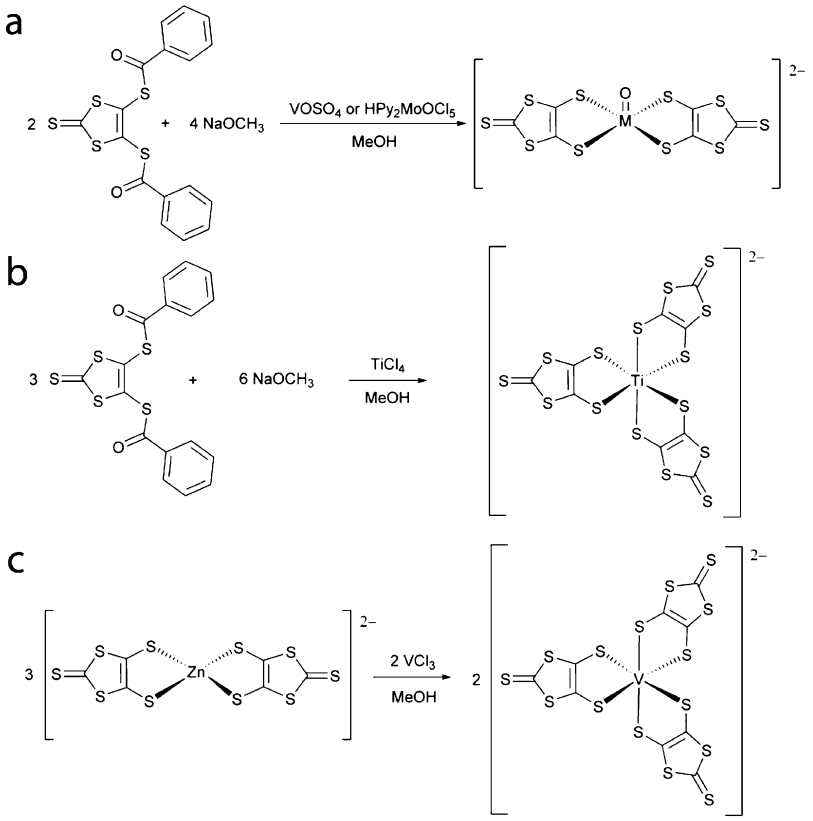

transitions between hyperfine states, as recently reported for a Ho(III) polyoxometallate,[12] the most promising systems remain $S = 1/2$ complexes.[16,17] Remarkably, mononuclear V^{IV} complexes with nuclear spin-free ligands such as dithiolenes[18] when dispersed in a nuclear spin-free solvent, CS_2, can attain at low temperature T_m on the order of a millisecond,[19] a value comparable to those observed for vacancies in extended lattices. Their use at room temperature is however hampered by the rapid decrease on increasing the temperature of the spin−lattice relaxation time, T_1, which acts as a limiting factor for T_m, as well as by the loss of a rigid structure provided by the frozen solution.

In a recent investigation we have shown that alternate current (ac) susceptometry can flank pulsed electron paramagnetic resonance (EPR) techniques to identify species that show slow spin−lattice relaxation.[20] A vanadyl complex with a β-diketonate ligand has revealed remarkable T_m despite the proton-rich ligands and, more interestingly, a long T_1 over a wide range of temperature and applied magnetic fields.[20] We have then extended these studies to a multifunctional and processable potential molecular spin system, vanadyl phthalocyanine, by preparing crystalline materials with different percentages of paramagnetic component diluted in the diamagnetic host titanyl phthalocyanine.[21] This allowed us to extend the investigation of the quantum coherence up to room temperature leading to a remarkable T_m of ca. 1 μs at 300 K, representing the highest value obtained to date for molecular electronic spin qubits.[21] Rabi oscillations were also observed in this nuclear spin-active environment (^{1}H and ^{14}N nuclei) at room temperature, indicating an outstanding robustness of the quantum coherence in these vanadyl-based systems.

Both the robustness of the quantum coherence of V^{IV} in an oxovanadium(IV) environment[20,21] and the benefit provided by employing nuclear spin-free ligand[18,19] are then tangible clues for coherence time optimization. We have combined these features to prepare a novel optimized molecular system as a potential spin qubit and to prove the effectiveness of the vanadyl moiety in the enhancement of the quantum coherence times by comparing its properties with those of a non-oxo V^{IV} complex with the same ligand. We have thus investigated the magnetic relaxation and the quantum coherence in solid crystalline phase of two potential molecular spin qubits, $[(Ph)_4P]_2[VO(dmit)_2]$ (**1**) and $[(Ph)_4P]_2[V(dmit)_3]$ (**2**) (dmit = 1,3-dithiole-2-thione-4,5-dithiolate), by means of a multitechnique approach based on ac susceptibility measurements and pulsed electron paramagnetic resonance spectroscopy. Experiments performed on 5 ± 1% crystalline dispersions of **1** and **2** in their isostructural diamagnetic hosts $[(Ph)_4P]_2[MoO(dmit)_2]$ (**3**) and $[(Ph)_4P]_2[Ti(dmit)_3]$ (**4**), respectively, namely, $[(Ph)_4P]_2[VO_{0.05}MoO_{0.95}(dmit)_2]$ (**5**) and $[(Ph)_4P]_2[V_{0.06}Ti_{0.94}(dmit)_3]$ (**6**), allowed to investigate the magnitude and the temperature dependence of the relaxation times. To evaluate the contribution to the decoherence provided by ^{1}H nuclei, we have also prepared a 5 ± 1% VO/MoO crystalline dispersion, an analogue to compound **5**, where the $(Ph)_4P^+$ counterion has been replaced with the deuterated cation d_{20}-$(Ph)_4P^+$, $[(d_{20}$-$Ph)_4P]_2[VO_{0.05}MoO_{0.95}(dmit)_2]$ (**5′**). The difference in the observed relaxation times for **1** and **2** and those of their crystalline dispersions **5** and **6** are discussed on the basis of the unique structural difference introduced in the two selected systems, i.e., oxovanadium(IV) versus vanadium(IV) moieties, and the resultant coordination geometry change, i.e., square

DOI: 10.1021/jacs.6b05574
J. Am. Chem. Soc. 2016, 138, 11234−11244

pyramidal versus octahedral, representing a fundamental step in the identification of key design criteria for the enhancement of the quantum coherence time in molecule-based systems.

RESULTS AND DISCUSSION

Synthesis of Pure Compounds and Doped Materials Preparation. Compounds **1** and **3** were obtained through a common synthetic strategy by slightly changing that already reported in the literature for the preparation of **3**.[22] The reaction between the $dmit^{2-}$ ligand, obtained in situ by deprotecting 4,5-bis(benzoylthio)-1,3-dithiole-2-thione with sodium methoxide and vanadyl(IV) sulfate or pyridinium molybdenyl(V)pentachloride, allowed us to obtain compounds **1** and **3**, respectively, in good yields (Scheme 1a).

While compound **4** was obtained through a similar procedure with respect to that adopted for **1** and **3** by reacting the deprotected $dmit^{2-}$ ligand with $TiCl_4$ (Scheme 1b), compound **2** was more conveniently obtained by a metal ion substitution operated by reacting VCl_3 with $[(Ph)_4P]_2[Zn(dmit)_2]$, in accordance with that already reported (Scheme 1c).[23] It should be mentioned that an alternative synthesis based on the reaction of VCl_3 with the uncoordinated $dmit^{2-}$ ligand under inert atmosphere, similar to that more recently reported,[19] resulted in the formation of a mixture of the desired product **2** and the diamagnetic monoanionic oxidized species $[(Ph)_4P][V(dmit)_3]$ (**7**) that has been structurally characterized (see the Supporting Information).

The preparation of the crystalline dispersions **5**, **5′**, and **6** were performed following two different approaches as a consequence of the different solubility features exhibited by the bis- and tris-chelated derivatives. To overcome the reduced solubility of **1** and **3**, the crystalline dispersions **5** and **5′** were obtained through a direct synthesis between weighted amounts of VO^{2+} (5% molar) and MoO^{2+} (95% molar) metal ions sources (vide supra) and the $dmit^{2-}$ ligand, as done for the preparation of the pure compounds. **6** was otherwise obtained by dissolution of weighted amounts of pure compounds **2** (5% molar) and **4** (95% molar) in acetone and subsequent precipitation by solvent evaporation under reduced pressure.

While the choice of using a Ti^{IV} complex as diamagnetic host for a V^{IV} paramagnetic system appears quite expectable, the choice of using a molybdenyl(IV)-based system as diamagnetic host for a vanadyl one deserves some comments. This choice was dictated by the lack of stable titanyl-based heteroleptic coordination compounds, especially with coligands having oxygen or sulfur as donor atoms. An elegant way to overcome this drawback is to exploit the ability of dithiolene ligands, such as $dmit^{2-}$ ligand selected for this study, to promote the stabilization of a square pyramidal coordination geometry of the Mo^{IV} ion featuring a single Mo═O double bond.[22] This provides the same coordination environment usually exhibited by vanadyl-based mononuclear compounds, thus allowing us to realize crystalline dispersions of a vanadyl complex in an isostructural matrix based on an apparently dissimilar metal ion.

Crystal Structures. Although the preparation of a coordination compound containing the dianionic complex $[VO(dmit)_2]^{2-}$ was already claimed in the past,[23] no structural data were reported so far. Single crystals suitable for X-ray diffraction analysis of compounds **1** and **3** were obtained by slow evaporation of acetone solutions. Compounds **1** and **3** are isostructural and crystallize in the monoclinic $C2/c$ space group with half of the anionic complex and one tetraphenylphosphonium counterion in the asymmetric unit. Their crystal structure consists of $[MO(dmit)_2]^{2-}$ (M = V^{IV}, Mo^{IV}) anions alternated in M═O up and M═O down configurations separated by tetraphenylphosphonium cations (Figure S1). The shortest M···M distances are in the 10.50−15.79 Å and 10.69−15.51 Å ranges for **1** and **3**, respectively. Very few intramolecular contacts shorter than the sum of the van der Waals radii are observed between metal complexes, most of them involving the cations.

The molecular structures of the dianionic complex of **1** and **3** are shown in Figure 1. Both systems present a distorted square

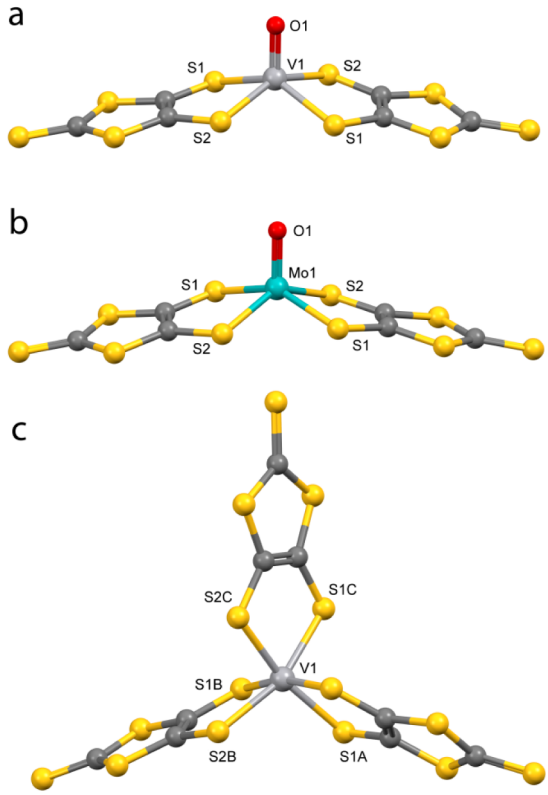

Figure 1. Molecular structures of the dianionic complexes of compounds **1** (a), **2** (c), and **3** (b) with principal atom labeling scheme.

pyramidal coordination geometry with the metal ions slightly above the basal plane (0.68 Å (**1**) and 0.72 Å (**3**)). The apical position is occupied by an oxo ligand which forms a double bond with the M^{IV} ions with a M═O bond distance of 1.594 and 1.689 Å, for **1** and **3**, respectively, whereas the M−S single bond lengths are 2.386 and 2.387 Å for **1** and 2.394 and 2.402 Å for **3**.

The presence of a short M═O bond is responsible for a d-orbital splitting of the metal centers that leaves the d_{xy} orbital lowest in energy and well-separated from the other orbitals. This, together with a single unpaired electron of the $S = 1/2$ V^{IV} ion, makes **1** a perfect two-level-state potential molecular qubit. On the contrary, the two d-electrons of the Mo^{IV} occupy the same d-orbital and are paired in a low spin configuration, making **3** a useful diamagnetic matrix (vide supra).

Single crystals suitable for X-ray diffraction analysis of compound **2** were obtained by slow diffusion of diethyl ether in an acetone solution. Compound **2** crystallizes in the monoclinic $P2_1/c$ with one anionic complex and two tetraphenylphosphonium counterions in the asymmetric unit. The crystal structure

DOI: 10.1021/jacs.6b05574
J. Am. Chem. Soc. 2016, 138, 11234−11244

consists of homoleptic tris-chelated $[V(dmit)_3]^{2-}$ anions showing Λ and Δ chirality and tetraphenylphosphonium cations (Figure S2). The shortest M···M distances are in the 9.75−15.98 Å range and are comparable to those observed for **1** and **3**. Also in this case, few S···S contacts shorter than the sum of the van der Waals radii between metal complexes are observed, whereas the interactions with the counterions dominate.

The molecular structure of the complex anion of **2** is reported in Figure 1. The coordination geometry around the V^{IV} ion is a distorted octahedron with an average V−S distance of 2.386 Å, an average twist angle of 41.0°, and an average chelate fold angle of 7.2°.[24] All these structural parameters are in good agreement with those observed in the already reported crystal structures of compounds containing this complex anion with a different counterion[23] and with that of a recently reported structure of an acetone solvate of **2**.[19] These structural parameters match well with those reported for similar dianionic tris-chelated V^{IV} complexes with dithiolenes ligands and confirm their effectiveness to evaluate the oxidation states of both the metal centers and the dithiolenes ligands in these redox-active systems.[24] In this case, the ligand field symmetry is responsible for a d-orbital splitting that leaves the d_{z^2} orbital (where z is the trigonal axis of the distorted octahedron) lowest in energy with respect to the other orbitals, as evidenced by EPR spectroscopy (vide infra) and by density functional theory calculations (DFT) on analogous vanadium(IV)-based tris-chelated complexes.[24]

In all structurally characterized compounds (**1**−**3**) the intraligand bond distances are in the usual range for the coordinated dianionic unoxidized $dmit^{2-}$ ligand (Table S1). All attempts to crystallize **4** were unsuccessful; however, powder X-ray diffraction (PXRD) measurements performed on a polycrystalline sample of **4** clearly show that this compound is isostructural with its V^{IV} analogue **2** (Figure S3).

PXRD analyses were performed on polycrystalline samples of all investigated systems, both pure compounds (**1**−**4**) and crystalline dispersions (**5**, **5′**, and **6**), to ascertain their structural phase homogeneity. This is clearly evidenced by the good agreement between experimental and simulated patterns (Figures S4−S7).

Magnetization Dynamics. Compounds **1** and **2** have been investigated by ac susceptometry in order to get deeper insights on their magnetization dynamics. The thermal variation of the magnetic susceptibility in a zero static magnetic field reveals no imaginary component of the susceptibility (χ'') in the whole investigated temperature range (2.0−40 K for **1**, and 2.0−10 K for **2**). When a small static magnetic field (>40 mT) is applied, slow magnetic relaxation is observed with appearance of a peak in the imaginary component of the susceptibility and a concomitant decrease of the real part (χ') (Figures S8−S14). Both compounds **1** and **2** under a static magnetic field of 0.2 T show slow relaxation of the entire magnetization, so this field was selected to investigate the temperature dependence of the relaxation time τ that is representative of the spin−lattice relaxation (indicated as T_1 in pulsed resonance spectroscopies). To investigate the temperature dependence of τ under a static magnetic field where τ is maximized, the studies were also performed at 1.0 T (vide infra). The frequency dependence of χ'' is well-reproduced with the Debye model (Figures S8−S14), and the extracted values of τ as a function of the temperature for the two selected field values for **1** and **2** are reported in Figure 2a.

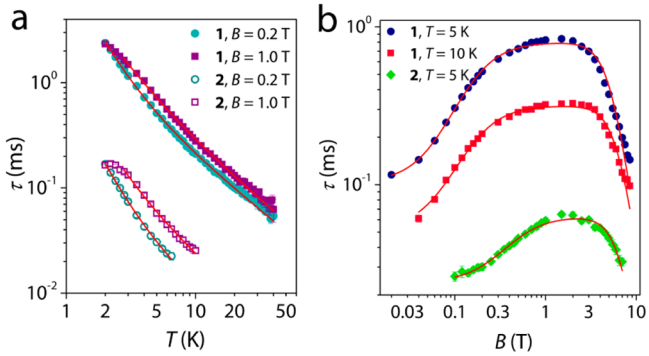

Figure 2. (a) Temperature and (b) field dependence of τ extracted from ac susceptibility measurements for compounds **1** and **2** at different applied static magnetic field values and temperatures (see legends). Solid lines are the best-fits of the models.

1 shows slow magnetic relaxation in the temperature range between 2.0 and 40 K with quite long relaxation times ranging from ca. 2.3 ms at 2.0 K to ca. 0.05 ms at 40 K. **2** exhibits relaxation times in the 0.17−0.025 ms range that are substantially lower with respect to those of **1**. This results in a reduced temperature range where slow magnetic relaxation is detectable (2.0−10 K). Minor differences in the magnitude of τ are observed between 0.2 and 1.0 T, especially for **1** because τ is almost maximum at 0.2 T (vide infra and Figure 2b). The temperature dependence of τ, reported in Figure 2a in a $\log(\tau)$ vs $\log(T)$ plot, reveals an increase in the slope at low temperature indicative of a phonon-bottleneck effect affecting the direct mechanism of relaxation in concentrated samples.[25] To account for these contributions to the relaxation, the τ decay was fitted (solid lines in Figure 2a) assuming two sequential steps in the relaxation process: the energy transfer from the spin to the phonon lattice and then its release to the thermostatic bath, according to the Scott and Jefferies model[26]

$$\tau = \frac{1}{aT} + \frac{1}{bT^n} \quad (1)$$

where a is the coefficient of the direct mechanism and b and n the coefficient and the exponent of the phonon-bottleneck, respectively. This model satisfactorily reproduces the T dependence of τ with the best-fit parameter reported in Table 1.

Table 1. Best-Fit Parameters of the Model Used (Equation 1) to Reproduce the Temperature Dependence of the Relaxation Time for 1 and 2 at B = 0.2 and 1.0 T

compound	B (T)	a (ms^{-1} K^{-1})	b (ms^{-1} K^{-n})	n
1	0.2	0.52(1)	0.11(1)	2.6(1)
	1.0	0.44(2)	0.14(1)	2.1(1)
2	0.2	9.6(6)	1.31(9)	2.7(1)
	1.0	4.9(5)	1.14(3)	2.4(3)

From the values of the extracted coefficients, it can be noted that both direct and phonon-bottleneck terms are higher for **2** than for **1**, in agreement with the more effective relaxation observed for **2** (Figure 2a). It should be also noted that the extracted values of the T exponent for the phonon-bottleneck effect, within the 2−3 range, are slightly higher than those usually observed (ca. 2) for classical atom-based inorganic systems.[27]

DOI: 10.1021/jacs.6b05574
J. Am. Chem. Soc. 2016, 138, 11234−11244

To get better insights on the relaxation mechanisms involved in such compounds, the relaxation time was also investigated as a function of the static magnetic field in a wide field range (0.0−8.5 T) at different temperatures, 5 and 10 K for **1** and 5 K for **2** due to instrumental limitations. The relaxation times extracted with the Debye model (Figures S12−S14) for **1** and **2** are reported in Figure 2b. The field dependence of the relaxation time for **1** shows already at low fields a rapid increase of τ. It reaches the maximum value at ca. 0.4 T, then remains almost unchanged up to ca. 3.5 T, and finally starts to decrease at higher fields reaching a minimum at the highest applied field (8.5 T). **2** shows a similar behavior with respect to that of **1** but with a less abrupt increase of τ as the strength of the field increases, thus resulting in a narrower range where τ is maximized (1.0−3.5 T). This nonmonotonous behavior is similar to that already reported for closely related systems[20,21] and reflects two antagonist effects of the magnetic field. Spin−spin and spin−nuclei interactions promote rapid relaxation at low fields. These interactions are suppressed by increasing the field due to the lower influence of the hyperfine and spin−spin coupling (vide infra). However, the larger the energy separation of the two levels, the higher the phonon density with an energy corresponding to this difference, leading to a more efficient spin−phonon direct mechanism of relaxation ($\tau \propto B^4$). To account for these two contributions to the relaxation, the B dependence of the relaxation rate (τ^{-1}) for **1** and **2** was reproduced (solid lines in Figure 2b) with the Brons−van Vleck model[28,29]

$$\tau^{-1} = cB^4 + d\frac{1 + eB^2}{1 + fB^2} \tag{2}$$

This model well reproduces the B dependence of τ with the best-fit parameter reported in Table 2.

Table 2. Best-Fit Parameters of the Model Used to Reproduce the Field Dependence of the Magnetization Relaxation Rate (Equation 2) for 1 at T = 5 and 10 K and 2 at T = 5 K

compound	T (K)	c ($T^{-4}ms^{-1}$)	d (ms^{-1})	e (T^{-2})	f (T^{-2})
1	5	$1.8(1) \times 10^{-3}$	10(1)	40(4)	306(60)
	10	$2.1(1) \times 10^{-3}$	19(3)	38(5)	231(60)
2	10	$8.0(6) \times 10^{-3}$	41(1)	5.0(6)	13(2)

The coefficients reported in Table 2 indicate that (i) the direct mechanism of relaxation (c coefficient) is more efficient for **2** with respect to **1**, in accordance with the thermal dependence of τ, and (ii) the ability of the field to suppress the effect of spin−spin and spin−nuclei interactions to the relaxation (f coefficient) is lower for **2** than for **1**, in accordance with the less abrupt increase of τ as the field increase and the narrower range where τ is maximized.

CW and Pulsed Electron Paramagnetic Resonance Spectroscopy. While ac susceptometry provides useful information about T_1 as a function of the temperature and the magnetic field in quite concentrated samples (**1** and **2** in this study), pulsed EPR spectroscopy allows us to characterize both T_1 and T_m in diluted systems characterized by narrow resonance lines. A common way to achieve this condition is the dispersion of the paramagnetic component in a diamagnetic matrix. With this scope, crystalline dispersions of **1** and **2** in **3** and **4** have been prepared with an amount of paramagnetic component dispersed in the diamagnetic host of ca. 5 ± 1% (**5**, **5′**, and **6**) (vide supra).

The room temperature CW-EPR X-band spectra (9.43 GHz) of compounds **1** and **5**, as well as those of **2** and **6**, are reported in Figure S15. Compound **1** shows an EPR spectrum where the expected 8-fold hyperfine splitting of all anisotropic components typical of V^{IV} (^{51}V I = 7/2, abundance 99.76%) is poorly resolved due to line broadening induced by dipolar interactions between the magnetic moments of the paramagnetic V^{IV} ions (Figure S15a). A lower resolution is observed for compound **2**, where only a broad unresolved absorption is observed (Figure S15b). The crystalline dispersions of **1** in **3** (**5**) and **2** in **4** (**6**) dramatically change the EPR spectra. In fact, even if **5** and **6** contain a relatively high concentration of paramagnetic species (ca. 5 ± 1%), they exhibit the expected hyperfine splitting with well-defined narrow lines also at room temperature. Notably, **5** shows very narrow resonance lines that are further narrowed in deuterated analogue **5′** (Figure S16). Peaks due to the parallel components of the hyperfine coupling are observed at low and high field values, whereas those due to the perpendicular components are observed in the central region.

Spectral simulations[30] were performed at X- and Q-band frequencies on the basis of the following spin Hamiltonian

$$\mathcal{H} = \hat{I}\cdot\boldsymbol{A}\cdot\hat{S} + \mu_B\hat{S}\cdot\boldsymbol{g}\cdot\boldsymbol{B} \tag{3}$$

The spectrum of **5** can be satisfactorily simulated at both frequencies (Figures 3a and S17a) assuming a collinear rhombic model, i.e., $x \neq y \neq z$, with the parameters reported in Table 3. Attempts to simulate the EPR spectra of **6** using a similar rhombic model were unsuccessful. Indeed, although it gave reasonable fits at X-band frequency, notable discrepancies in the positions of the hyperfine transitions and line shapes were observed at Q-band frequency (Figure S18). Therefore, the possibility of a noncollinearity between $\boldsymbol{A}$ and $\boldsymbol{g}$ tensors, consistent with the triclinic point symmetry of the complex anion,[31] was investigated. A process of trial and error gave spectral simulations in good agreement with the experimental results (Figures 3b and S17b) using the parameters reported in Table 3.

We note that such phenomenon was not previously recognized for tris-dithiolene V^{IV} complexes; the possibility to detect it here is clearly due to the improved resolution of the solid crystalline spectra, together with the multifrequency EPR approach, compared to the frozen solution ones.[19,24] Further confirmation of the goodness of the obtained parameters was provided by the simulation of the room temperature solution spectrum of **6** in the fast motion regime (Figure S19), which allowed us to confirm the value of the A_z component, to which the solid-state spectra are not very sensitive.

The two compounds are thus characterized by distinctly different spin Hamiltonian parameters, which reflect the different chemical structure of the V^{IV} ions in **5** and **6**. An empirical correlation between the g_{iso} ($g_{iso} = (g_1 + g_2 + g_3)/3$) and ^{51}V a_{iso} ($a_{iso} = (A_1 + A_2 + A_3)/3$) has been proposed to discriminate between $V^{IV}O^{2+}$ and V^{IV} centers.[32] Indeed the spin Hamiltonian parameters of **5** fit well within known values for vanadyl ions, while the values of **6** are representative for V^{IV} centers.

In the EPR spectra of **5** and **5′**, an additional signal exhibiting the typical features of an organic radical (g = 2.00) is present. This signal can be ascribed to an impurity of monooxidized uncoordinated $dmit^{\cdot-}$ ligand as tetraphenylphosphonium salt,

DOI: 10.1021/jacs.6b05574
J. Am. Chem. Soc. 2016, 138, 11234−11244

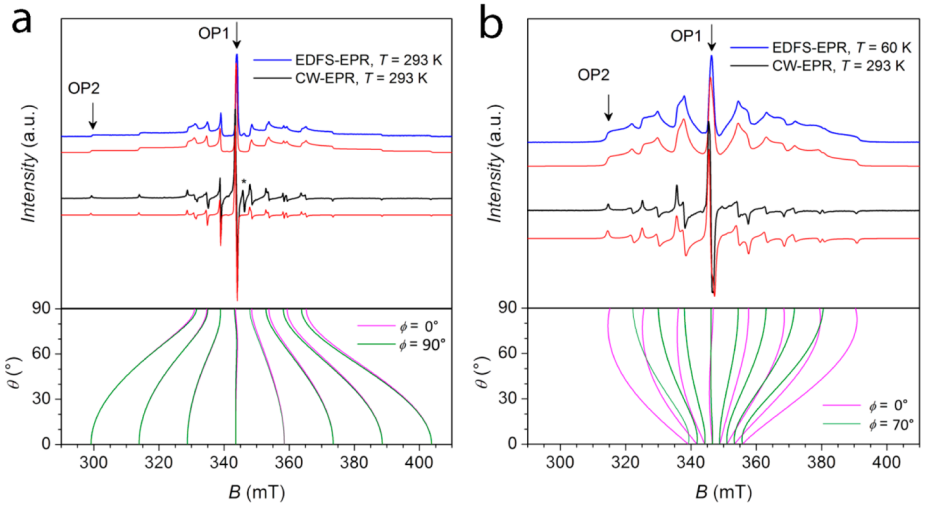

Figure 3. Experimental EDFS (blue line) and CW (black line) EPR spectra for **5** (a) and **6** (b) at X-band frequency (9.7 GHz). The spectral simulations corresponding to the spin Hamiltonian parameters reported in Table 3 are shown in red. The arrows indicate the two magnetic field settings at which pulse EPR experiments were performed. The asterisk indicates the signal of an organic radical impurity. The angular dependency profile (θ vs magnetic field) is shown for two values of ϕ.

Table 3. Spin Hamiltonian Parameters Extracted from Simulation of the Experimental Spectra of 5 and 6[a]

compound	g_x	g_y	g_z	$\lvert A_x \rvert$ (MHz)	$\lvert A_y \rvert$ (MHz)	$\lvert A_z \rvert$ (MHz)	α, β, and γ (°)
5	1.986(1)	1.988(1)	1.970(1)	138(2)	128(2)	413(2)	0, 0, 0
6	1.961(1)	1.971(1)	1.985(1)	299(2)	230(2)	40(5)	−20, − 10, 0

[a]The Euler angles α, β, and γ define the passive rotation of the hyperfine principal axes system into the $\boldsymbol{g}$-matrix principal axes system, $\boldsymbol{A} = R(\alpha, \beta, \gamma)\, A_{\text{diagonal}}\, R^{+}(\alpha, \beta, \gamma)$. It must be noted that the reference system for the two compounds is different. For **5**, the z axis can be considered collinear to the V═O bond, while for **6** it is close to the octahedron pseudo-C_3 symmetry axis, i.e., perpendicular to its trigonal faces.

being a redox active ligand susceptible of one-electron oxidation.[24] This signal is not observed in **6** most likely as a result of the different synthetic approaches followed for the crystalline dispersion preparation (vide supra).

The X- and Q-band echo-detected field-swept (EDFS) EPR spectra for **5** and **6** were recorded at different temperatures by using a standard Hahn echo sequence. Figure 3 reports the highest temperature data at the X-band, whereas those recorded at the Q-band are reported in Figure S17.

As evidenced by the presence of an intense spin−echo, we can anticipate that quantum coherence is expected for **5** up to room temperature. Moreover, the spin Hamiltonian parameters obtained through the simulation of the CW spectrum allow us to provide good simulations of the EDFS spectra as well, thus indicating that the entire paramagnetic component of **5** is experiencing the detected coherence. Analogous results are observed for deuterated analogue **5′**. Interestingly, while **5** shows an intense spin−echo at room temperature, **6** does not show an EDFS spectrum working at the X-band at the same temperature. A spin−echo is only hardly detected working at Q-band (Figure S18). Nonetheless, by lowering the temperature, **6** shows the expected coherence, as could be anticipated on the basis of recent studies performed on **2** in frozen solutions.[19]

Inversion recovery experiments were performed in the 4.5−293 K temperature range for **5**, **5′**, and **6** at X- and Q-band frequencies to investigate the temperature dependence of the spin−lattice relaxation time T_1. Experiments at X-band were performed at two magnetic field settings: (i) the so-called powder-like position, $m_I = -1/2$ (OP1), where all molecules are excited due to the negligible angular dependency of the resonance field, and (ii) the single-crystal-like position, $m_I = -7/2$ (OP2), where only molecules with their z axis within 10° from the field direction are selected (Figure 3). Q-band experiments were instead performed only at the $m_I = -7/2$ position. The reason for this is that the angular dependency of the EPR spectra for **5** and **6** show that (i) this position corresponds to a pure transition for both systems allowing for a direct comparison with X-band and (ii) a powder-like position is not present at Q-band frequency for both **5** and **6** (Figure S17). The resulting saturation recovery traces were fitted with a stretched monoexponential equation

$$I = I_0 + k_1 \exp^{[-(\tau_p/T_1)^{\beta_1}]} \quad (4)$$

and the extracted T_1 values are reported in Figure 4. Only the values obtained at the $m_I = -7/2$ are reported for clarity because no major differences are observed working at the $m_I = -1/2$ observer position (Figure S20).

5 and **5′** show similar T_1 values in almost the whole investigated temperature range. Deuteration of the cation increases T_1 only at low temperature (Figure 4) and more significantly at X-band than at Q-band (Tables S2−S7). A moderate increase of T_1 upon deuteration is not unprecedented and can be related either to the different dipolar coupling[33] or to the isotope mass effect.[34] T_1 values for **5** and **5′** are higher than those of **6** in the entire investigated T range, in agreement with that observed with the field dependence of τ from ac susceptibility data on pure compounds **1** and **2**. This suggests that hyperfine interactions are responsible for the fast relaxation observed in weak or zero applied fields.[35] The thermal variation of T_1 for **5** and **5′** shows a slow decrease from the maximum values of ca. 23 ms (**5**) and ca. 58 ms (**5′**) at 4.5 K to the lowest but still remarkable values of 3.37 μs (**5**) and 4.03 μs (**5′**) at

DOI: 10.1021/jacs.6b05574
J. Am. Chem. Soc. 2016, 138, 11234−11244

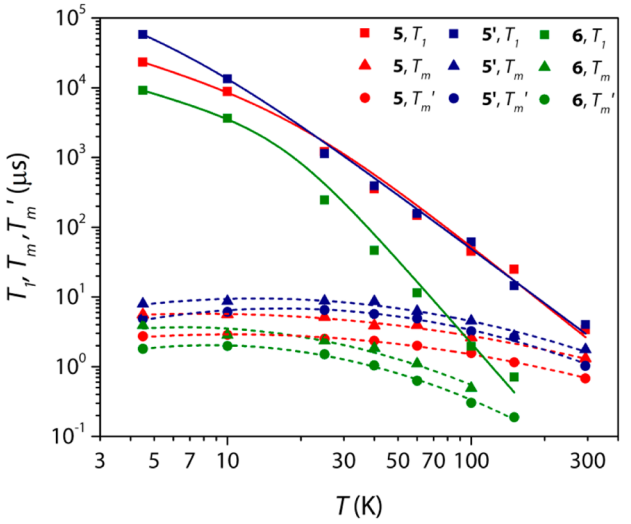

Figure 4. Temperature dependence of T_1, T_m, and T_m' for **5**, **5′**, and **6** (see legend) obtained at OP2. Solid lines are the best-fit of the model (see text). Dashed lines represent a guide for the eyes. Error bars are within the size of the symbols.

293 K. Moving from X- to Q-band (Figure S21), a slight increase of T_1 is observed at the lowest temperatures, which is in agreement with the weak field dependence of the relaxation time observed in that range (Figure 2b). The extracted relaxation times from pulsed EPR are, however, almost 1 order of magnitude longer than those of **1** and **2** from ac susceptibility, as expected for magnetically diluted compounds, and do not show the upturn at low temperature typical of the spin−phonon bottleneck effect observed in concentrated samples. The temperature dependence of T_1 has been modeled assuming two contributions to the relaxation. A direct mechanism dominating at low temperature, as suggested from ac susceptometry, and a Raman-like mechanism dominating at high temperature.

$$T_1^{-1} = aT + bT^n \quad (5)$$

The best-fit values for **5** and **5′** give a very low value of the Raman-like exponent $n < 3$, 2.8(4), and 2.6(2). Values of ca. 3 were already observed in closely related vanadyl-based systems[20,21,36] and are attributed to the involvement of both optical and acoustic phonons to the relaxation.[37] The thermal variation of T_1 for **6** shows a slow decrease from the maximum value of ca. 9 ms up to ca. 15 K, then a more abrupt decrease is observed as the temperature increases, resulting in the lowest detectable value of T_1 of 0.71 μs at 150 K (Figure 4). The temperature dependence of T_1 has been simulated with the same model used for **5** and **5′**. The best-fit values give a Raman-like exponent n of 4.0(5), in agreement with the more abrupt decrease of T_1 that acts as a limiting factor for T_2 (vide infra).

To investigate the quantum coherence in details and to quantify the phase memory time, T_m, of **1** and **2** in the doped materials **5**/**5′** and **6** as a function of the temperature, echo decay experiments were also performed (Figure 5). Remarkably, echo decay traces were detected up to room temperature for **5** and **5′**, with an increased value of T_m for the deuterated analogue (Figure 4). On the contrary, **6** shows echo decay traces up to 150 K with T_m values shorter than those of **5** and **5′** as evidenced by the restricted time scale of the echo decay (Figure 5).

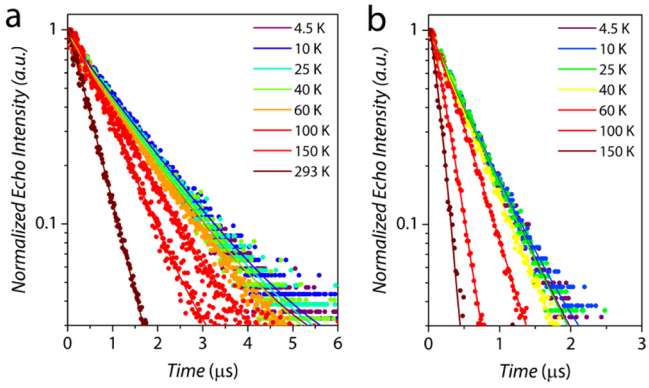

Figure 5. Echo decay traces recorded at the OP1 (X-band) for **5** (a) and **6** (b) at different temperatures (see legend).

The decay traces were fitted using the stretched exponential equation

$$I = I_0 + k_m \exp^{[-(2\tau_p/T_m)^{\beta_m}]} \quad (6)$$

as usually done for transition metal systems,[38] where I indicates the echo intensity, $2\tau_p$ is the delay between the initial pulse and the echo detection, and β_m is the stretch factor. For the sake of comparison, transverse relaxation times were also measured by using the Car−Purcell−Meiboom−Gill (CPMG) sequence.[39,40] Phase memory times (T_m') only weakly longer were obtained by CPMG than by two-pulse spin echo (Tables S2). This is in agreement with the expectations, given the relatively high concentration of electron spins in our system[41−43] and the broad EPR spectrum.[44] The temperature dependences of both T_m and T_m' for **5**, **5′**, and **6** are reported in Figure 4.

The thermal variation of T_m for **5** and **5′** shows an almost temperature-independent behavior in the 4.5−100 K range, with values of T_m and T_m' within the 2.9−1.6 μs and 5.6−2.6 μs ranges for **5** and within the 6.5−3.2 μs and 8.7−4.5 ranges for **5′**. Then, they slowly decrease as the temperature increases reaching remarkable values of 0.68 and 1.0 μs (T_m) at room temperature (Figure 4). It should be highlighted that the values of T_m at room temperature for the concentrated dispersions of **5** and **5′** (ca. 5 ± 1%) are slightly higher than values observed to date for transition-metal-based molecular qubits in more diluted environment, e.g., the 0.001% crystalline dispersion of $[P(Ph)_4]_2[Cu(mnt)_2]$ in $[P(Ph)_4]_2[Ni(mnt)_2]$ (0.60 μs)[17] and the 0.1% crystalline dispersion of VOPc in TiOPc (0.83 μs).[21] T_m' values are even higher, being T_m' a better estimation of T_2, but we cannot compare these values with that already reported because most literature reports provide only T_m estimations by Hahn echo experiments.

The thermal variation of T_m and T_m' for **6** shows an almost temperature-independent behavior in a limited temperature range (4.3−25 K) with values of T_m and T_m' within the 2.0−1.5 μs and 3.9−2.4 μs ranges; then, they slowly decrease as the temperature increases reaching a value of T_m of 0.19 μs at 150 K. The quantum coherence times T_m for **6** are in general lower than those of **5** and **5′**, but the most important result is that they are strongly limited in temperature by the more abrupt decrease of T_1.

To prove that the observed coherence times for **5** and **5′** allow us to perform coherent spin manipulations at room temperature, i.e., place the spins in any arbitrary superposition of states, nutation experiments were performed at different microwave powers at both X- and Q-bands. Remarkably, Rabi

DOI: 10.1021/jacs.6b05574
J. Am. Chem. Soc. 2016, 138, 11234−11244

oscillations were clearly observed at room temperature with the expected linear dependence of the Rabi frequency, Ω_R, as a function of the microwave attenuation (Figure 6). Rabi oscillations were instead observed for **6** only at low temperature (Figure S22).

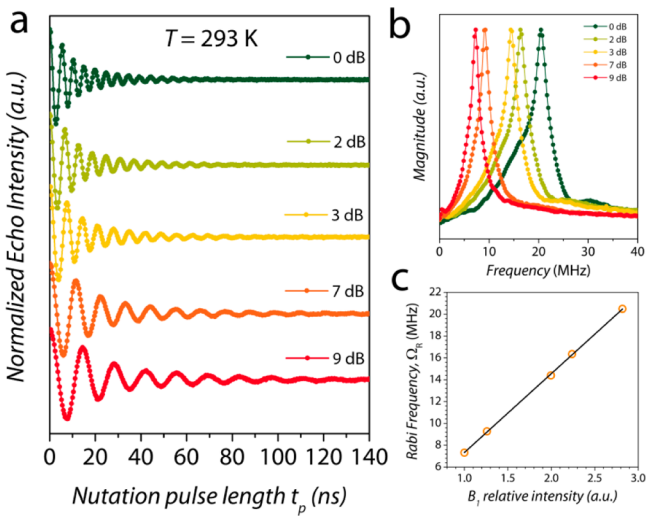

Figure 6. (a) Rabi oscillations recorded for **5** at 293 K for different microwave attenuations (Q-band). (b) Fourier transform of the Rabi oscillations. (c) Linear dependence of the Rabi frequency (Ω_R) as a function of the relative intensity of the oscillating field B_1.

To fully characterize the local environment of the V^{IV} ions in the two compounds, Q-band Mims ENDOR spectra were recorded (Figure S23). The spectra show that in both cases the V^{IV} ions have a similar proton rich environment with maximum couplings of 3.5(1) MHz for compound **5** and 3.0(1) MHz for compound **6**. On the basis of a point−dipole approximation and assuming a pure dipolar interaction, these couplings correspond to shortest V···H distances of the order of 3.6(1) and 3.8(1) Å, respectively. These values are in excellent agreement with the structural findings, which reveal shortest V···H distances of 3.6(1) Å and 3.8(1) Å for **5** and **6**, respectively. This excludes the possibility that the better performances of the vanadyl species are due to a more favorable nuclear spin environment generated by the counterions and highlights the key role of the coordination mode.

This comparative detailed investigation has evidenced significant differences in the dynamic properties of two closely related vanadium(IV) complexes. **2** shows, in general, a faster relaxation with respect to **1**, and this behavior can be tentatively ascribed to a more pronounced contribution to the SOMO by different orbitals, i.e., the ground state is not a pure d_z^2 one. This is demonstrated by the observed noncollinearity of the ***A*** and ***g*** tensors as well as by the significant deviation of g_z from the value of 2.00 expected for this geometry. The larger the deviations from the free electron values, the more efficient the spin−orbit coupling in promoting magnetic relaxation. In this respect, the EPR-derived spin Hamiltonian parameters can also explain the stronger static magnetic field required to slow down the relaxation for **2**. Indeed, the analysis of the eigenvector composition for an applied field of 0.1 T clearly evidences that **2** is characterized by a larger mixing of the states compared to **1** which is further enhanced by the noncollinearity of the ***g*** and ***A*** tensors (Figure S24). However, the most relevant difference between the two compounds is the temperature dependence of the spin−lattice relaxation time. Excitation of vibrational modes that can couple to the spin are responsible of the acceleration of the relaxation with increasing temperature. The phonon spectrum of the two compounds seems to significantly deviate from the Debye model as both systems do not show T^n with n = 9 dependence of the spin−lattice relaxation rate expected for S = 1/2 systems at high temperature.[45,46] However, there are significant differences in n between the two compounds that cannot be attributed to the different spectrum of acoustic phonons. The latter are in fact strongly dependent on cell size and content,[47] which are however rather similar for **1** and **2**. The coordination mode seems instead the key parameter in determining n because n of ca. 3 has been already observed for other vanadyl complexes,[20,21,34] despite the very different unit cell content.

Localized vibrations involving the metal ion coordination sphere, which are known to contribute to the relaxation in two-phonons processes,[48] are on the contrary dramatically different for the two compounds. The V=O double bond resonates at much higher frequencies (ca. 980 cm^{-1}) with respect to the V−S single bonds (in the 400 cm^{-1} range). It is therefore not surprising to observe a faster relaxation for the less rigid coordination environment, though other factors beyond the frequency of the vibrational modes, such as their lifetime and their coupling to the spin, are also relevant.[49] We can safely suppose that V−S vibrations, though similar in energy for the two compounds, have a reduced effect on the vanadyl system because the ***g*** and ***A*** tensors of the latter are dominated by the short V=O bond whose vibrational modes are populated at much higher temperatures.

CONCLUDING REMARKS

The parallel multitechnique investigation of two V^{IV} complexes with nuclear-spin-free ligands both in pure phases and diluted in diamagnetic crystalline hosts has revealed significant differences in the spin−lattice relaxation times, which are much longer for the vanadyl complex compared to those of the tris-chelated one. A poorly efficient mechanism of relaxation seems most often encountered on oxovanadium(IV)-based systems,[20,21,34,50] making this moiety a very useful building block for the preparation of performing potential molecular qubits. On the contrary, the same metal ion in a different coordination environment as in the distorted octahedral coordination geometry herein investigated is not capable to retain quantum coherence up to room temperature, as a result of a slightly different Raman-like relaxation mechanism.

Our results represent the first experimental evidence of the proposed importance of the rigidity of the molecular structure in the enhancement of quantum coherence.[17] If the general rule is now rather clear, then to develop more performing molecular spin qubits it is crucial to understand in detail which vibrational modes are the most effective in promoting spin relaxation. In this regard, state-of-the art ab initio calculations combining density functional theory (DFT) and post Hartree−Fock approaches have been recently employed to evaluate the spin−vibration coupling in a square planar copper(II)-based complex in a simplified environment.[51] However, the rationalization of the magnetic relaxation in molecular systems requires an accurate description of the lattice dynamics, which is beyond current computation capabilities for the compounds herein investigated that contain bulky counterions. Vanadyl-based neutral complexes of β-diketonate ligands, whose phonon spectrum has been recently evaluated and correlated to a giant

DOI: 10.1021/jacs.6b05574
J. Am. Chem. Soc. 2016, 138, 11234−11244

spin−phonon bottleneck effect at low temperature,[47] appear more suitable candidates for this scope. A deeper understanding of the relaxation mechanisms which takes into account both hyperfine interactions and vibrational modes seems then the winning strategy to enhance quantum coherence in molecular systems.

EXPERIMENTAL SECTION

General Remarks. 4,5-Bis(benzoylthio)-1,3-dithiole-2-thione,[52] d_{20}-tetraphenylphosphonium bromide,[17] and pyridinium molybdenyl(V) pentachloride[53] were synthesized accordingly to the literature procedures. Tetraphenylphosphonium bis(1,3-dithiole-2-thione-4,5-dithiolate)zincate(II) was obtained according to the literature procedure[48] by replacing tetraethylammonium bromide with tetraphenylphosphonium bromide. All others reagents were purchased and used as received.

Synthesis. *[(Ph)$_4$P]$_2$[VO(dmit)$_2$] (**1**).* An aqueous solution (5 mL) of $VOSO_4{\cdot}xH_2O$ (0.245 g, 1.5 mmol) was added dropwise to a methanol solution (35 mL) of sodium 1,3-dithiole-2-thione-4,5-dithiolate (Na_2dmit) obtained in situ by reacting 4,5-bis(benzoylthio)-1,3-dithiole-2-thione (1.22 g, 3.0 mmol) and sodium (0.150 g, 6.5 mmol). A methanol solution (5 mL) of tetraphenylphosphonium bromide (1.70 g, 4.0 mmol) was added dropwise to the resulting solution with precipitation of **1** as a red-brown microcrystalline solid. The precipitate was separated from the mother liquor by vacuum filtration and washed several times with methanol, then with diethyl ether. Yield 74%. Compound **1** was crystallized in acetone to give red-orange shiny crystals suitable for X-ray analysis. Elemental anal. calcd for $C_{54}H_{40}OP_2S_{10}V$: C, 56.97; H, 3.54. Found: C, 56.75; H, 3.38. FT-IR ($\overline{\nu}_{max}$/cm^{-1}, KBr pellet): 3166 vw, 3087vw, 3074vw, 3053w, 3035vw, 3016vw, 3004vw, 2987vw, 1583w, 1570vw, 1558vw, 1541vw, 1481w, 1440s, 1434s, 1338w, 1315w, 1186w, 1163w, 1107s, 1043m, 1023s, 995m, 956m (ν V═O), 902w, 892w, 854vw, 852vw, 758m, 752m, 723s, 689s, 526vs, 464m.

*[(Ph)$_4$P]$_2$[V(dmit)$_3$] (**2**).* VCl_3 (0.069 g, 0.44 mmol) was added to a stirred methanol solution (50 mL) of $[(Ph)_4P]_2[Zn(dmit)_2]$ (0.500 g, 0.44 mmol). After few minutes, a brown microcrystalline solid of **2** starts to precipitate. The mixture was stirred for 1 h at room temperature; then, the precipitate was separated from the mother liquor by vacuum filtration and washed several times with methanol, then with diethyl ether. Yield 60%. Compound **2** was crystallized by diffusion of diethyl ether in acetone to give black shiny crystals suitable for X-ray analysis. Elemental anal. calcd for $C_{57}H_{40}P_2S_{10}V$: C, 51.91; H, 3.06. Found: C, 52.07; H, 2.57. FT-IR ($\overline{\nu}_{max}$/cm^{-1}, KBr pellet): 3163 vw, 3076vw, 3053w, 3016vw, 3006vw, 2987vw, 1583w, 1570vw, 1558vw, 1541vw, 1481w, 1435s, 1396w, 1338w, 1315w, 1186w, 1163w, 1109s, 1049vs, 1028s, 995m, 891w, 845vw, 752m, 723s, 689s, 615w, 526s, 469m, 445w.

*[(Ph)$_4$P]$_2$[MoO(dmit)$_2$] (**3**).* A methanol solution (10 mL) of HPy_2MoOCl_5 (1.125 g, 2.5 mmol) was added dropwise to a methanol solution (50 mL) of sodium 1,3-dithiole-2-thione-4,5-dithiolate (Na_2dmit) obtained in situ by reacting 4,5-bis(benzoylthio)-1,3-dithiole-2-thione (2.04 g, 5.0 mmol) and sodium (0.280 g, 12.0 mmol). A methanol solution (10 mL) of tetraphenylphosphonium bromide (2.50 g, 6.0 mmol) was added dropwise to the resulting solution with precipitation of **3** as a brown microcrystalline solid. The precipitate was separated from the mother liquor by vacuum filtration and washed several times with methanol, then with diethyl ether. Yield 63%. Compound **3** was crystallized in acetone to give orange-brown shiny crystals suitable for X-ray analysis. Elemental anal. calcd for $C_{54}H_{40}OP_2S_{10}Mo$: C, 54.80; H, 3.41. Found: C, 53.96; H, 3.14. FT-IR ($\overline{\nu}_{max}$/cm^{-1}, KBr pellet): 3166 vw, 3087vw, 3074vw, 3053w, 3035vw, 3016vw, 3004vw, 2987vw, 1583w, 1570vw, 1558vw, 1541vw, 1481w, 1448m, 1440m, 1435s, 1338w, 1315w, 1186w, 1163w, 1107s, 1043m, 1024m, 995m, 922m (ν Mo═O), 889w, 883w, 854vw, 852vw, 758m, 752m, 723s, 689s, 526vs, 464m.

*[(Ph)$_4$P]$_2$[Ti(dmit)$_3$] (**4**).* An aqueous solution (10 mL) of $TiCl_4$ (0.302 g, 1.6 mmol) was added dropwise to a methanol solution (50 mL) of sodium 1,3-dithiole-2-thione-4,5-dithiolate (Na_2dmit) obtained in situ by reacting 4,5-bis(benzoylthio)-1,3-dithiole-2-thione (2.04 g, 5.0 mmol) and sodium (0.280 g, 12.0 mmol). A methanol solution (10 mL) of tetraphenylphosphonium bromide (1.70 g, 4.0 mmol) was added dropwise to the resulting solution with precipitation of **4** as a black-purple microcrystalline solid. The precipitate was separated from the mother liquor by vacuum filtration and washed few times with methanol, then with diethyl ether. Yield 42%. Elemental anal. calcd for $C_{57}H_{40}OP_2S_{15}Ti$: C, 52.03; H, 3.06. Found: C, 51.78; H, 2.94. FT-IR ($\overline{\nu}_{max}$/cm^{-1}, KBr pellet): 3163 vw, 3076vw, 3053w, 3016vw, 3006vw, 2987vw, 1583w, 1570vw, 1558vw, 1541vw, 1481w, 1435s, 1396w, 1338w, 1315w, 1186w, 1163w, 1107s, 1049vs, 1028s, 995m, 904w, 891w, 845vw, 752m, 723s, 689s, 615w, 526s, 467m, 445w.

*[(Ph)$_4$P]$_2$[VO$_{0.05}$MoO$_{0.95}$(dmit)$_2$] (**5**).* A methanol solution (10 mL) of $VOSO_4{\cdot}xH_2O$ (0.041 g, 0.25 mmol) and HPy_2MoOCl_5 (0.450 g, 2.25 mmol) was added dropwise to a methanol solution (50 mL) of sodium 1,3-dithiole-2-thione-4,5-dithiolate (Na_2dmit) obtained in situ by reacting 4,5-bis(benzoylthio)-1,3-dithiole-2-thione (2.04 g, 5.0 mmol) and sodium (0.280 g, 12.0 mmol). A methanol solution (10 mL) of tetraphenylphosphonium bromide (2.50 g, 6.0 mmol) was added dropwise to the resulting solution with precipitation of **5** as a brown microcrystalline solid. The precipitate was separated from the mother liquor by vacuum filtration and washed few times with methanol, then with diethyl ether. Yield 52%. Elemental anal. calcd for $C_{57}H_{40}OP_2S_{15}Ti$: C, 52.03; H, 3.06. Found: C, 51.78; H, 2.94. FT-IR ($\overline{\nu}_{max}$/cm^{-1}, KBr pellet): 3166 vw, 3087vw, 3074vw, 3053w, 3035vw, 3016vw, 3004vw, 2987vw, 1583w, 1570vw, 1558vw, 1541vw, 1481w, 1448m, 1440m, 1435s, 1338w, 1315w, 1186w, 1163w, 1107s, 1043m, 1024m, 995m, 956m (ν V═O), 922m (ν Mo═O), 889w, 883w, 854vw, 852vw, 758m, 752m, 723s, 689s, 526vs, 464m. X-ray fluorescence (XRF) analysis was used to estimate the effective percentage of doping by comparing the intensity of the XRF intensity of vanadium Kα emission of compound **5** to a calibration curve obtained by mixing weighted amounts of the pure compounds (**1** and **3**) in the 1−20% concentration range. This was found to be 5(1)% VO^{2+} and 95(1)% MoO^{2+}.

*[d_{20}-(Ph)$_4$P]$_2$[VO$_{0.05}$MoO$_{0.95}$(dmit)$_2$] (**5′**).* Compound **5′** was obtained by following the same procedure reported for **5** by using perdeutereted tetraphenylphosphonium bromide instead of tetraphenylphosphonium bromide. Yield 49%. FT-IR ($\overline{\nu}_{max}$/cm^{-1}, KBr pellet): 2289 vw, 2282vw, 2265vw, 2255vw, 1545w, 1533vw, 1448m, 1308m, 1061m, 1043s, 1024m, 962vw, 954w (ν V═O), 927m (ν Mo═O), 889vw, 883vw, 872vw, 837m, 829w, 694w, 548w, 542w, 500vs, 463w, 445vw. X-ray fluorescence (XRF) analysis was used to estimate the effective percentage of doping by comparing the intensity of the XRF intensity of vanadium Kα emission of compound **5′** to a calibration curve obtained by mixing weighted amounts of the pure compounds (**1** and **3**) in the 1−20% concentration range. This was found to be 5(1)% VO^{2+} and 95(1)% MoO^{2+}.

*[(Ph)$_4$P]$_2$[V$_{0.05}$Ti$_{0.95}$(dmit)$_2$] (**6**).* **2** (0.075 g, 0.0057 mmol) and **4** (0.1425 g, 0.108 mmol) were dissolved in 120 mL of acetone. The solution was filtrated to remove few undissolved particles and the solvent evaporated under reduced pressure. **6** precipitates as a black-purple microcrystalline solid. Yield: quantitative. Elemental anal. calcd for $C_{57}H_{40}OP_2S_{15}Ti_{0.95}V_{0.05}$: C, 52.02; H, 3.06. Found: C, 52.10; H, 2.91. FT-IR ($\overline{\nu}_{max}$/cm^{-1}, KBr pellet): 3163 vw, 3076vw, 3053w, 3016vw, 3006vw, 2987vw, 1583w, 1570vw, 1558vw, 1541vw, 1481w, 1435s, 1396w, 1338w, 1315w, 1186w, 1163w, 1107s, 1049vs, 1028s, 995m, 904w, 891w, 845vw, 752m, 723s, 689s, 615w, 526s, 467m, 445w. X-ray fluorescence (XRF) analysis was used to estimate the effective percentage of doping by comparing the intensity of the XRF intensity of vanadium Kβ emission of **6** to a calibration curve obtained by mixing weighted amounts of the pure compounds (**2** and **4**) in the 1−10% concentration range. This was found to be 6(1)% V^{IV} and 94(1)% Ti^{IV}.

Characterization. C, H, and N analyses were performed with a CHN-S Flash E1112 Thermofinnigan analyzer. FT-IR spectra were performed on KBr pellets and collected with a Shimadzu-8400S spectrophotometer. X-ray fluorescence analyses were performed with a WD-XRF Rigaku PrimusII spectrophotometer.

DOI: 10.1021/jacs.6b05574
J. Am. Chem. Soc. 2016, 138, 11234−11244

Table 4. Summary of X-ray Crystallographic Data for 1−3

	1	2	3
empirical formula	$C_{54}H_{40}OP_2S_{10}V$	$C_{57}H_{40}P_2S_{15}V$	$C_{54}H_{40}OP_2S_{10}Mo$
formula weight	1138.34	1318.67	1183.34
crystal size (mm)	0.60 × 0.40 × 0.40	0.50 × 0.40 × 0.10	0.20 × 0.20 × 0.10
crystal system	monoclinic	monoclinic	monoclinic
space group	$C2/c$	$P2_1/c$	$C2/c$
a (Å)	20.4747(5)	24.5669(3)	19.9651(3)
b (Å)	12.7283(4)	13.8150(1)	12.5335(1)
c (Å)	20.6032(5)	18.1309(2)	20.8994(2)
α (°)	90	90	90
β (°)	95.297(2)	111.014(1)	94.260(1)
γ (°)	90	90	90
V (Å^3)	5346.4(2)	5744.2(1)	5215.3(1)
Z	4	4	4
T (K)	293(2)	100(2)	100(2)
ρ (calcd) (Mg/m^3)	1.414	1.525	1.507
μ (mm^{-1})	6.071	7.379	6.691
θ range (°)	4.31−61.86	4.14−72.42	4.24−70.56
GooF	1.024	1.050	1.106
R_1[a]	0.0587	0.0372	0.0280
wR_2[a]	0.0678	0.0910	0.0624

[a] $R_1 = \Sigma||F_o|-|F_c||/\Sigma|F_o|$; $wR_2 = [\Sigma[w(F_o^2-F_c^2)^2]/\Sigma[w(F_o^2)^2]]^{1/2}$, $w = 1/[\sigma^2(F_o^2) + (aP)^2 + bP]$, where $P = [\max(F_o^2, 0) + 2F_c^2]/3$.

Single-Crystal X-ray Crystallography. Single-crystal X-ray diffraction measurements were performed on an Oxford Xcalibur PX Ultra - Onyx CCD diffractometer, using an Enhance Ultra X-ray graphite-monochromated Cu Kα radiation (λ = 1.540 Å). The structures were solved by direct methods (SHELXS-97) and refined on F^2 with full-matrix least-squares (SHELXL-97),[54] using the Wingx software package.[55] All non-H atoms were refined with anisotropic displacement parameters. Graphical material was prepared using Mercury CSD 3.5.[56] A summary of the crystallographic data and the structure refinement for compounds **1**−**3** is reported in Table 4.

Full crystallographic data for the solved structures have been deposited in the Cambridge Crystallographic Data Centre with CCDC numbers 1482025 (**1**), 1482026 (**2**), 1482027 (**3**), 1482028 (**7**), respectively.

Powder X-ray Crystallography. Wide-angle powder X-ray diffraction (PXRD) patterns on polycrystalline samples were recorded on a Bruker New D8 Advance DAVINCI diffractometer in a theta−theta configuration equipped with a linear detector. The scans were collected within the range 5−40° (2θ) using Cu Kα radiation (λ = 1.540 Å). Simulated patterns were generated from the atomic coordinates of the single-crystal structure solutions using the Mercury CSD 3.5 software[56] (copyright CCDC, http://www.ccdc.cam.ac.uk/mercury/) using a fwhm (full width at half-maximum) of 0.10 and a 2θ step of 0.025.

Electron Paramagnetic Resonance. CW X-band EPR spectra of all samples were recorded on a Bruker Elexsys E500 spectrometer equipped with a SHQ cavity (ν = 9.43 GHz). Low-temperature measurements were obtained using an Oxford Instruments ESR900 continuous flow helium cryostat. Pulsed EPR measurements were carried out with a Bruker Elexsys E580 at X-band ($\nu \cong$ 9.70 GHz) equipped with a flexline dielectric ring ENDOR resonator (Bruker EN 4118X-MD4). Temperatures between 4.5 and 250 K were obtained with an Oxford Instruments CF935 continuous flow helium cryostat. Echo-detected field-swept EPR spectra were recorded by using the Hahn Echo pulse sequence ($\pi/2-\tau-\pi-\tau-$echo) with fixed interpulse delay time τ = 200 ns, $t_{\pi/2}$ = 16 ns and t_π = 32 ns. Phase memory times were measured both by the Hahn Echo sequence upon increasing the interpulse delay τ starting from τ = 98 ns and by a CPMG sequence with a fixed interpulse delay 2τ in the echo train and τ = 800 ns. Typical pulse lengths were $t_{\pi/2}$ = 40 ns and t_π= 80 ns. Spin−lattice relaxation times were measured using the standard inversion recovery sequence ($\pi-t_d-\pi/2-\tau-\pi-\tau-$echo), with $\pi/2$ = 16 ns. The uncertainty in T_1 estimated from replicate measurements was 5−10% depending upon the signal-to-noise ratio at a given temperature-field combination. Nutation measurements were performed with a nutation pulse (t_p) of variable length followed by a Hahn echo sequence ($t_p-t_d-\pi/2-\tau-\pi-\tau-$echo) with $t_d \gg T_m$, i.e., t_d = 7 μs for 4 K and 2 μs for room temperature measurements. The interpulse delay τ was 200 ns, and the pulse length of the detection sequence was adjusted depending on the attenuation level of B_1.

Magnetic Measurements. The ac susceptibility measurements were performed in the temperature range of 2.0−40 K with applied magnetic fields up to 8.5 T on polycrystalline samples of compounds **1** (55.71 mg) and **2** (53.10 mg), by using a Quantum Design Physical Property Measurement System (PPMS) equipped with an ac susceptometer operating in the 10 Hz to 10 kHz frequency range. Susceptibility data were corrected for the sample holder previously measured using the same conditions and for the diamagnetic contributions as deduced by using Pascal's constant tables.[57]

■ ASSOCIATED CONTENT

Supporting Information

The Supporting Information is available free of charge on the ACS Publications website at DOI: 10.1021/jacs.6b05574.

Crystal structures, bond distances, powder X-ray crysallography data, ac susceptometry results, CW-EPR, pulsed EPR, EDFS-EPR, and ^{1}H Mims ENDOR spectra, temperature dependence data, Rabi oscillations, eigenvector composition analysis, and relaxation times (PDF)

Crystallographic information file for **1** (CIF)

Crystallographic information file for **2** (CIF)

Crystallographic information file for **3** (CIF)

Crystallographic information file for **7** (CIF)

■ AUTHOR INFORMATION

Corresponding Authors

*E-mail: matteo.atzori@unifi.it

*E-mail: roberta.sessoli@unifi.it

Notes

The authors declare no competing financial interest.

DOI: 10.1021/jacs.6b05574
J. Am. Chem. Soc. 2016, 138, 11234−11244

■ ACKNOWLEDGMENTS

European Research Council (ERC) through AdG MolNanoMaS (267746), Italian MIUR through the project Futuro in Ricerca 2012 (RBFR12RPD1), and Fondazione Ente Cassa di Risparmio di Firenze are acknowledged for financial support. We thank A. Lunghi for fruitful discussion.

■ REFERENCES

(1) Troiani, F.; Affronte, M. *Chem. Soc. Rev.* **2011**, *40*, 3119−3129.
(2) Aromì, G.; Aguila, D.; Gamez, P.; Luis, F.; Roubeau, O. *Chem. Soc. Rev.* **2012**, *41*, 537−546.
(3) Nielsen, M. A.; Chuang, I. L. *Quantum Computation and Quantum Information*; Cambridge University Press: Cambridge, 2000.
(4) Ladd, T. D.; Jelezko, F.; Laflamme, R.; Nakamura, Y.; Monroe, C.; O'Brien, J. L. *Nature* **2010**, *464*, 45−53.
(5) Kennedy, T. A.; Colton, J. S.; Butler, J. E.; Linares, R. C.; Doering, P. J. *Appl. Phys. Lett.* **2003**, *83*, 4190−4192.
(6) Balasubramanian, G.; Neumann, P.; Twitchen, D.; Markham, M.; Kolesov, R.; Mizuochi, N.; Isoya, J.; Achard, J.; Beck, J.; Tissler, J.; Jacques, V.; Hemmer, P. R.; Jelezko, F.; Wrachtrup, J. *Nat. Mater.* **2009**, *8*, 383−387.
(7) Pla, J. J.; Tan, K. Y.; Dehollain, J. P.; Lim, W. H.; Morton, J. J. L.; Jamieson, D. N.; Dzurak, A. S.; Morello, A. *Nature* **2012**, *489*, 541−545.
(8) Tyryshkin, A. M.; Tojo, S.; Morton, J. J. L.; Riemann, H.; Abrosimov, N. V.; Becker, P.; Pohl, H.-J.; Schenkel, T.; Thewalt, M. L. W.; Itoh, K. M.; Lyon, S. A. *Nat. Mater.* **2011**, *11*, 143−147.
(9) Gatteschi, D.; Sessoli, R.; Villain, J. *Molecular nanomagnets*; Oxford University Press: Oxford, UK, 2006.
(10) Fataftah, M. S.; Zadrozny, J. M.; Coste, S. C.; Graham, M. J.; Rogers, D. M.; Freedman, D. E. *J. Am. Chem. Soc.* **2016**, *138*, 1344−1348.
(11) Pedersen, K. S.; Ariciu, A.-M.; McAdams, S.; Weihe, H.; Bendix, J.; Tuna, F.; Piligkos, S. *J. Am. Chem. Soc.* **2016**, *138*, 5801−5804.
(12) Shiddiq, M.; Komijani, D.; Duan, Y.; Gaita-Ariño, A.; Coronado, E.; Hill, S. *Nature* **2016**, *531*, 348−351.
(13) DiVincenzo, D. P. *Fortschr. Phys.* **2000**, *48*, 771−783.
(14) Takahashi, S.; Tupitsyn, I. S.; van Tol, J.; Beedle, C. C.; Hendrickson, D. N.; Stamp, P. C. E. *Nature* **2011**, *476*, 76−79.
(15) Ferrando-Soria, J.; Moreno Pineda, E.; Chiesa, A.; Fernandez, A.; Magee, S. A.; Carretta, S.; Santini, P.; Vitorica-Yrezabal, I. J.; Tuna, F.; Timco, G. A.; McInnes, E. J. L.; Winpenny, R. E. P. *Nat. Commun.* **2016**, *7*, 11377.
(16) Warner, M.; Din, S.; Tupitsyn, I. S.; Morley, G. W.; Stoneham, A. M.; Gardener, J. A.; Wu, Z.; Fisher, A. J.; Heutz, S.; Kay, C. W. M.; Aeppli, G. *Nature* **2013**, *503*, 504−508.
(17) Bader, K.; Dengler, D.; Lenz, S.; Endeward, B.; Jiang, S.-D.; Neugebauer, P.; van Slageren, J. *Nat. Commun.* **2014**, *5*, 5304.
(18) Zadrozny, J. M.; Niklas, J.; Poluektov, O. G.; Freedman, D. E. *J. Am. Chem. Soc.* **2014**, *136*, 15841−15844.
(19) Zadrozny, J. M.; Niklas, J.; Poluektov, O. G.; Freedman, D. E. *ACS Cent. Sci.* **2015**, *1*, 488.
(20) Tesi, L.; Lucaccini, E.; Cimatti, I.; Perfetti, M.; Mannini, M.; Atzori, M.; Morra, E.; Chiesa, M.; Caneschi, A.; Sorace, L.; Sessoli, R. *Chem. Sci.* **2016**, *7*, 2074−2083.
(21) Atzori, M.; Tesi, L.; Morra, E.; Chiesa, M.; Sorace, L.; Sessoli, R. *J. Am. Chem. Soc.* **2016**, *138*, 2154−2157.
(22) Matsubayashi, G.-E.; Nojo, T.; Tanaka, T. *Inorg. Chim. Acta* **1988**, *154*, 133−135.
(23) Matsubayashi, G.; Akiba, K.; Tanaka, T. *Inorg. Chem.* **1988**, *27*, 4744−4749.
(24) Sproules, S.; Weyhermüller, T.; DeBeer, S.; Wieghardt, K. *Inorg. Chem.* **2010**, *49*, 5241−5261.
(25) van Vleck, J. H. *Phys. Rev.* **1941**, *59*, 724−729.
(26) Scott, P. L.; Jeffries, C. D. *Phys. Rev.* **1962**, *127*, 32−51.
(27) Standeley, K. J.; Vaughan, R. A. *Electron spin relaxation phenomena in solids*; Plenum Press: New York, 1969; pp 199−236.
(28) van Vleck, J. H. *Phys. Rev.* **1940**, *57*, 426−447.
(29) De Vroomen, A. C.; Lijphart, E. E.; Prins, D. Y. H.; Marks, J.; Poulis, N. J. *Physica* **1972**, *61*, 241−249.
(30) Stoll, S.; Schweiger, A. *J. Magn. Reson.* **2006**, *178*, 42−55.
(31) Pilbrow, J. R.; Lowrey, M. R. *Rep. Prog. Phys.* **1980**, *43*, 433.
(32) Jakes, P.; Eichel, R.-A. *Mol. Phys.* **2012**, *110*, 277−282.
(33) Sato, H.; Bottle, S. E.; Blinco, J. P.; Micallef, A. S.; Eaton, G. R.; Eaton, S. S. *J. Magn. Reson.* **2008**, *191*, 66−77.
(34) Owenius, R.; Terry, G. E.; Williams, M. J.; Eaton, S. S.; Eaton, G. R. *J. Phys. Chem. B* **2004**, *108*, 9475−9481.
(35) Gómez-Coca, S.; Urtizberea, A.; Cremades, E.; Alonso, P. J.; Camón, A.; Ruiz, E.; Luis, F. *Nat. Commun.* **2014**, *5*, 4300.
(36) Du, J.-L.; Eaton, G. R.; Eaton, S. S. *J. Magn. Reson., Ser. A* **1996**, *119*, 240−246.
(37) Shrivastava, K. N. *Phys. Status Solidi B* **1983**, *117*, 437−458.
(38) Eaton, S. S.; Eaton, G. R. In *Distance Measurements in Biological Systems by EPR*; Berliner, L. J., Eaton, G. R., Eaton, S. S., Eds.; Springer: Boston, MA, 2002; pp 29−154.
(39) Carr, H. Y.; Purcell, E. M. *Phys. Rev.* **1954**, *94*, 630−638.
(40) Meiboom, S.; Gill, D. *Rev. Sci. Instrum.* **1958**, *29*, 688−691.
(41) Harbridge, J. R.; Eaton, S. S.; Eaton, G. R. *J. Magn. Reson.* **2003**, *164*, 44−53.
(42) de Lange, G.; Wang, Z. H.; Ristè, D.; Dobrovitski, V. V.; Hanson, R. *Science* **2010**, *330*, 60−63.
(43) Zaripov, R.; Vavilova, E.; Miluykov, V.; Bezkishko, I.; Sinyashin, O.; Salikhov, K.; Kataev, V.; Büchner, B. *Phys. Rev. B: Condens. Matter Mater. Phys.* **2013**, *88*, 094418.
(44) Kurshev, V. V.; Raitsimring, A. M. *J. Magn. Reson.* **1990**, *88*, 126−129.
(45) Abragam, A.; Bleaney, B. *Electron Paramagnetic Resonance of Transition Ions*; Dover: New York, 1986.
(46) Hoffmann, S. K.; Lijewski, S. *J. Magn. Reson.* **2013**, *227*, 51−56.
(47) Tesi, L.; Lunghi, A.; Atzori, M.; Lucaccini, E.; Sorace, L.; Totti, F.; Sessoli, R. *Dalton Trans.* **2016**, DOI: 10.1039/C6DT02559E.
(48) Huang, C.-Y. *Phys. Rev.* **1967**, *154*, 215−219.
(49) Rechkemmer, Y.; Breitgoff, F. D.; van der Meer, M.; Atanasov, M.; Hakl, M.; Orlita, M.; Neugebauer, P.; Neese, F.; Sarkar, B.; van Slageren, J. *Nat. Commun.* **2016**, *7*, 10467.
(50) Bader, K.; Winkler, M.; van Slageren, J. *Chem. Commun.* **2016**, *52*, 3623−3626.
(51) Escalera-Moreno, L.; Suaud, N.; Gaita-Ariño, A. Theoretical determination of the spin-vibration coupling in the highly coherent molecular spin qubit [Cu(mnt)2]2-. 2015. http://arxiv.org/abs/1512.05690 (accessed on December 17, 2015).
(52) Hansen, T. K.; Becher, J.; Jørgensen, T.; Varma, K. S.; Khedekar, R.; Cava, M. P. *Org. Synth.* **1996**, *73*, 270.
(53) Hanson, G. R.; Brunette, A. A.; McDonell, A. C.; Murray, K. S.; Wedd, A. G. *J. Am. Chem. Soc.* **1981**, *103*, 1953−1959.
(54) Sheldrick, G. M. *Programs for the Refinement of Crystal Structures*; University of Göttingen, Göttingen, Germany, 1996.
(55) Farrugia, L. *J. Appl. Crystallogr.* **1999**, *32*, 837−838.
(56) Macrae, C. F.; Bruno, I. J.; Chisholm, J. A.; Edgington, P. R.; McCabe, P.; Pidcock, E.; Rodriguez-Monge, L.; Taylor, R.; van de Streek, J.; Wood, P. A. *J. Appl. Crystallogr.* **2008**, *41*, 466−470.
(57) Bain, G. A.; Berry, J. F. *J. Chem. Educ.* **2008**, *85*, 532.

DOI: 10.1021/jacs.6b05574
J. Am. Chem. Soc. 2016, 138, 11234−11244

Inorganic Chemistry

Forum Article

pubs.acs.org/IC

Spin Helicity in Chiral Lanthanide Chains

Ionut Mihalcea,[#] Mauro Perfetti,[*,‡,§] Francesco Pineider,[‡,⊥] Lorenzo Tesi,[‡] Valeriu Mereacre,[†] Fabrice Wilhelm,[∥] Andrei Rogalev,[∥] Christopher E. Anson,[†] Annie K. Powell,[*,†,#] and Roberta Sessoli[*,‡]

[#]Institute of Nanotechnology, Karlsruhe Institute of Technology, Hermann-von-Helmholtz-Platz 1, D-76344 Eggenstein-Leopoldshafen, Germany

[‡]Department of Chemistry, "U. Schiff" Università di Firenze and INSTM RU Firenze via della Lastruccia 3-13, 50019 Sesto Fiorentino, Italy

[⊥]Department of Chemistry and Industrial Chemistry, University of Pisa, via Moruzzi 3, 56124 Pisa, Italy

[†]Institute of Inorganic Chemistry, Karlsruhe Institute of Technology, Engesserstrasse 15, D-76131 Karlsruhe, Germany

[∥]European Synchrotron Radiation Facility (ESRF), 38043 Grenoble, France

Supporting Information

ABSTRACT: We report here the determination of the helical spin structure of three Ln-based chiral chains of the formula $[Ln(Hnic)(nic)_2(NO_3)]_n$ (Hnic = nicotinic acid; Ln = Tb, Dy, and Er) by means of cantilever torque magnetometry. While the Dy and Er derivatives are strongly axial (easy-axis and easy-plane anisotropy, respectively), the Tb derivative is characterized by a remarkable rhombicity. In agreement with these findings, alternating-current susceptibility reveals slow magnetic relaxation only in the Dy derivative. Dilution of Dy^{III} ions in the diamagnetic Y-based analogue shows that the weak ferromagnetic intrachain interactions do not contribute significantly to the energy barrier for the reversal of magnetization, which is better described as a single-ion process. Single crystals of the two enantiomers of the Dy derivative have also been investigated using hard X-ray synchrotron radiation at the L-edge of the metal revealing optical activity although with negligible involvement of the 4f electrons of the Dy^{III} ion.

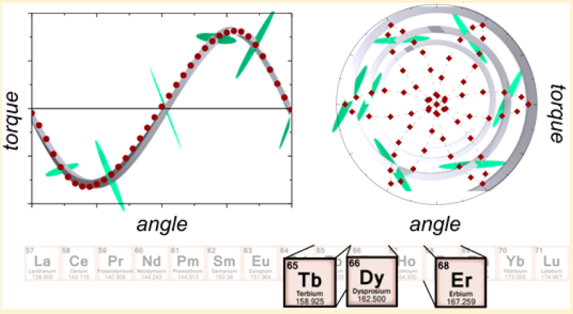

INTRODUCTION

The interplay between the chirality and magnetism is a fascinating but still scarcely explored topic in solid-state physics. Even if the correlation between these two properties of matter was first sensed in the 19th century,[1] the magnetochiral effect (MChE),[2,3] was observed only recently,[4] and a full rationalization of this effect is still missing. The arising of MChE is possible in magnetoelectrical media and multiferroics[5,6] but also in magnetic systems when an external magnetic field is applied. Indeed, the observation of this effect, which is, in general, very challenging because of its intrinsic weakness, is possible only when the parity reversal and time-reversal symmetry are simultaneously broken. This is due to the fact that magnetic moments are generated by a circulation of electrons that is ruled by time-reversal symmetry while the chirality is obviously parity odd. The literature reports on this effect are quite scarce in 2D and 3D architectures,[7,8] and to the best of our knowledge, only one 1D system has been reported.[9] This last paper, published by some of us, testifies that chiral chains based on transition-metal (TM) ions can be good candidates to observe this effect using synchrotron hard X-rays. What emerged from the study of these metal−nitronyl nitroxide chains[9] is that the main ingredients to have a strong MChE are high mixing between orbitals of different parity, allowed in noncentrosymmetric structures, and a strong magnetic anisotropy. In fact, while the Co^{II} derivative provided a giant magnetochiral dichroism, the signal was practically absent in the isotropic Mn^{II} derivative. What still remained unclear was whether the spin helicity played a significant role. Indeed, only the Co^{II} derivative exhibited a nonzero angle between the chain direction and easy axis of the magnetization of the metal centers.

As we shift from TM to lanthanides (Ln ions), an increase of the orbital contribution to the magnetization and thus of the magnetic anisotropy is expected. Moreover, Ln^{III} ions exhibit a magnetic anisotropy that can vary significantly in nature and orientation also along an isostructural series. This variation is often explained by simple electrostatic considerations about the electronic density generated by the partially filled 4f orbitals around the metal center.[10]

Among the few reports of chiral 1D systems comprising Ln^{III} ions,[11−14] some of us recently reported the synthesis and structural and magnetic characterization of a series of chiral chains of the formula $[Ln(Hnic)(nic)_2(NO_3)]_n$, where Hnic is

Special Issue: New Trends and Applications for Lanthanides

Received: April 22, 2016
Published: July 13, 2016

DOI: 10.1021/acs.inorgchem.6b01010
Inorg. Chem. 2016, 55, 10068−10074

nicotinic acid and Ln = Eu, Gd, and Tb.[15] Magnetic studies on the Gd derivative revealed a weak ferromagnetic exchange between metallic centers. Despite the absence of chiral ligands, spontaneous resolution of the two helicities occurs through crystallization in the enantiomeric $P6_1$ and $P6_5$ space groups; Flack parameters χ_F of zero from the structure refinements demonstrate that any one crystal is enantiomerically pure. While this work was in progress, Liu et al. published the structure and magnetic data of the isotypic Dy analogue, which showed slow relaxation of its magnetization.[16] With the purpose of investigating the correlation between the electronic structure and the presence/absence of MChE, we have now analyzed the spin structure of the Tb, Dy, and Er members of this series, hereafter labeled with the respective lanthanide atomic symbol in bold (**Tb**, **Dy**, and **Er**). Figure 1 shows the structure of the Er derivative, which crystallizes isotypically to the other analogues.

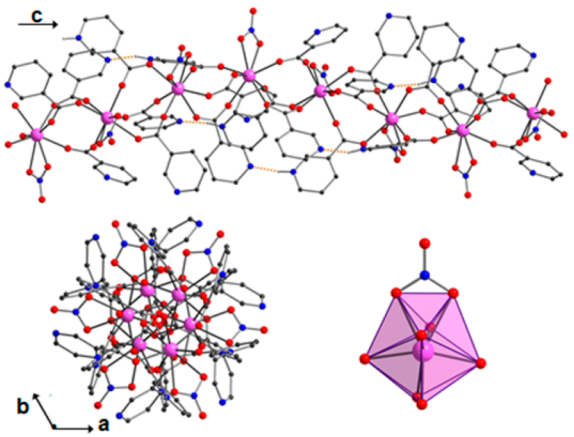

Figure 1. Structure of the helical chain in **Er** viewed from the side (top) and down the 6_5 axis (bottom left) and the coordination polyhedron of the Er^{III} ion showing its idealized dodecahedral C_{2v} symmetry (bottom right). Color code: Er, pink; O, red; N, blue; C, gray. Organic H omitted for clarity. Hydrogen bonds are presented as dashed orange lines. The other complexes are isostructural.

Among the Ln ions, we focused on the highly anisotropic ions Tb^{III}, Dy^{III}, and Er^{III} (J = 6, $^{15}/_2$, and $^{15}/_2$ ground states, respectively). In order to disentangle the single-ion contributions to the magnetic anisotropy and to gain insight into the spin helicity, we exploited the high sensitivity of cantilever torque magnetometry (CTM).[17,18] Moreover, we investigated natural circular dichroism by irradiating single crystals with hard X-ray synchrotron radiation at the Ln metal L-edge.[19]

EXPERIMENTAL SECTION

Crystals of $[Ln(Hnic)(nic)_2(NO_3)]_n$ (**Tb**, **Dy**, and **Er**) as well as the derivative where Dy is diluted in the diamagnetic Y analogue (**DyY**) were prepared according to the reported method. For **DyY**, a 1:5 molar ratio of $Dy(NO_3)_3{\cdot}6H_2O$ and $Y(NO_3)_3{\cdot}6H_2O$ was used. A 14.7(5):85.3(5) molar ratio between Dy and Y was determined by wavelength-dispersive X-ray fluorescence spectrometry (Rigaku Primus II) using a 1 mm spot on a 3-mm-diameter pellet of crushed crystals.

The crystal structures of **Er** and **DyY** were determined using Cu Kα (Oxford Diffraction SuperNova E) and Mo Kα (Bruker SMART Apex) radiation, respectively, and found to crystallize isotypically with the Eu, Gd, Tb, and Dy analogues.[15,16] The metal ion in **DyY** was refined as a mixture of Y and Dy. With rigid bond restraints to the thermal parameters of the metal and surrounding O atoms, the proportion of Dy refined to11.9(3)% (in good agreement with the X-ray fluorescence results and with the value of 15% from the magnetic data) and the composition was fixed at 88% Y and 12% Dy in final refinements. As before, both the presence of merohedral twinning by 180° rotation about $a + b$ (which does not change the chirality) and of twinning by inversion (which does) was checked. For **Er** and **DyY**, the merohedral twinning amounted to 0.248(1) and 0.0205(4) and the Flack parameters χ_F (both from 100% Friedel coverage) were −0.016(6) and −0.012(3), respectively, showing that the crystals were, once again, enantiomerically pure.

Er: $C_{18}H_{13}ErN_4O_9$, 596.58 g mol^{-1}, hexagonal, $P6_5$, a = 11.1520(2) Å, c = 26.4830(4) Å, Z = 6, V = 2852.35(13) Å^3, T = 100(2) K, ρ_{calc} = 2.084 g cm^{-3}, $F(000)$ = 1734, μ(Cu Kα) = 8.763 mm^{-1}; 15510 data, 3717 unique (R_{int} = 0.0384), 294 parameters, final wR2 = 0.0435, S = 1.062 (all data), R1 [3699 data with $I > 2\sigma(I)$] = 0.0179, Flack χ_F = −0.016(6), max peak/hole in the final difference map = +0.32/−0.33 e Å^{-3}.

DyY: $C_{18}H_{13}Dy_{0.12}N_4O_9Y_{0.88}$, 527.06 g mol^{-1}, hexagonal, $P6_5$, a = 11.1664(3) Å, c = 26.5948(18) Å, Z = 6, V = 2871.8(2) Å^3, T = 100(2) K, ρ_{calc} = 1.829 g cm^{-3}, $F(000)$ = 1579, μ(Mo Kα) = 3.213 mm^{-1}; 24095 data, 4421 unique (R_{int} = 0.0299), 294 parameters, final wR2 = 0.0486, S = 1.039 (all data), R1 [4315 data with $I > 2\sigma(I)$] = 0.0207, Flack χ_F = −0.012(3), max peak/hole in the final difference map = +0.64/−0.33 e Å^{-3}.

Crystallographic data for the structures of **Er** and **DyY** have been deposited with the Cambridge Crystallographic Data Center as supplementary publications CCDC 1473784 and 1473785. Copies of the data can be obtained from https://summary.ccdc.cam.ac.uk/structure-summary-form.

CTM measurements were performed using a homemade two-legged CuBe cantilever separated by 0.1 mm from a gold plate. The cantilever was inserted in an Oxford Instruments MAGLAB2000 platform with automated rotation of the cantilever chip in a vertical magnet. The capacitance of the cantilever was detected with a Andeen-Hegerling 2500A Ultra Precision Capacitance Bridge. A more detailed sketch of the experimental setup is reported in Figure S1.

The static and dynamic magnetic properties were measured on polycrystalline powders restrained with eicosane grease using a Quantum Design MPMS SQUID magnetometer.

X-ray absorption near-edge fine structure (XANES) and X-ray natural circular dichroism (XNCD) experiments at the L_3-edge of Dy were carried out at the ID12 beamline of the European Synchrotron Radiation Facility (Grenoble, France), dedicated to polarization-dependent X-ray spectroscopy in the 2−15 keV energy range.[20] A high flux of circularly polarized photons was provided by an APPLE-II helical undulator. X-rays were monochromatized by a Si ⟨111⟩ double-crystal monochromator. Samples were mounted on an aluminum sample holder and oriented so that the crystal's c axis and the photons' wave vector formed an angle of approximately 18°. All spectra were recorded in total X-ray fluorescence mode in backscattering geometry. Each set of XNCD spectra was acquired by alternating the photon helicity 18 times, for a total of 36 XANES spectra.

RESULTS AND DISCUSSION

Torque Magnetometry. Determination of the principal directions of anisotropy in crystals with noncollinear anisotropy tensors can be achieved using CTM, as was already reported in the literature for mononuclear lanthanide compounds[21−23] and TM clusters.[24] The technique requires indexed single crystals fixed on the upper plate of a capacitor that can be rotated in a static magnetic field ($\mathbf{B}$). When the temperature (T) is lowered enough, it is possible to detect the torque ($\boldsymbol{\tau}$) acting on the sample as a change in the capacitance. In the low-field limit ($g\mu_B\mathbf{B} \ll k_BT$), the torque along a fixed direction (e.g., the Y axis in the laboratory XYZ frame) is connected to the susceptibility tensor ($\boldsymbol{\chi}$) by the following relationship:

$$\tau_Y = M_Z B_X - M_X B_Z = B^2(\chi_{ZZ} - \chi_{XX}) \sin\varphi \cos\varphi \qquad (1)$$

DOI: 10.1021/acs.inorgchem.6b01010
Inorg. Chem. 2016, 55, 10068−10074

where φ is the angle between the projection of the z molecular axis in the XZ plane and **B**. Note that this angle is, in general, not coincident with the angle of rotation of the cantilever, θ. An additional term dependent on χ_{XZ} was omitted because it is always possible to rotate the reference frame and set it to zero. When the field is increased, the torque curves deform such that the angular dependence becomes very different if the easy axis is almost parallel or perpendicular to the field. Because the response is no more tensorial in character, deconvolution of the signals of the noncollinear centers becomes possible because their symmetry-related contributions do not cancel out completely.

This approach has been used to extract information on the single-ion anisotropy in the chiral coordination polymers investigated here. Because the $P6_1/P6_5$ enantiomeric space groups possess a C_6 axis parallel to the crystallographic c axis, assuming uniaxial anisotropy of the individual metal ions, this exotic structure imposes that the orientation of the anisotropy tensors of the six crystallographically equivalent ions can be determined using two relevant Euler angles, e.g., the angle between the z molecular axis and the c axis (ξ), which is equal for all spins, and the angle between the a axis and the projection of the z molecular axis on the ab plane (ρ). When the principal directions of the first anisotropy tensor are fixed, the others can be easily determined by adding a factor $(60i)°$ (where $i = 1-5$) to ρ. It is important to notice here that the helicity of the spin chain is only dependent on the value of the angle ξ; in particular, it is present for any value of this angle different from 0°.

All data were recorded with variation of the angle between **B** and the upper plate of the cantilever (θ) at fixed temperature (see Figure S1). For each derivative, two rotations were performed. During the first one (Rot1), the rotation axis was the c axis, while in the second one (Rot2), the rotation axis laid in the ab' plane (see Figure S2 for detailed positions of all of the crystals). This set of rotations is particularly useful to determine the Euler angles because Rot1 is particularly sensitive to ρ while Rot2 is extremely dependent on ξ (see Figure S3 for sample calculations evidencing the dependence of the crystal torque signal on the ξ and ρ angles).

In Figure 2, we report the torque curves for **Tb**, **Dy**, and **Er** in the relevant (0−180°) angular range. Other curves recorded at different temperatures and fields are reported in Figures S4−S6. We also investigated a crystal of the **DyY** sample. The obtained torque curves, reported in Figure S7, are very similar to those of the pure **Dy**. This is not surprising because the very weak ferromagnetic interaction (vide infra) is not affecting the magnetic behavior of the system in the relatively strong magnetic field employed in the torque measurements.

Looking at Figure 2, it is evident at first glance that all samples exhibit the 6-fold symmetry imposed by the structure. Rot1 has, in fact, six zero-torque points that correspond to the three independent projections on the ab plane of the six anisotropy tensors (we recall here that a 180° rotation does not affect the anisotropy) arising from the Ln ions, and all of the maxima have similar intensities, as expected when the rotation axis coincides with c. Rot2 has more complicated features that differ for the three compounds, but the signal always vanishes near 0° and 90°, corresponding to $c\|\mathbf{B}$ and $c\perp\mathbf{B}$, respectively.

To extract the single-ion magnetic anisotropy, modeling including both the Zeeman and anisotropy terms is necessary. The latter at the simplest level can be described by a crystal-field (CF) potential acting on the metal center. We thus used the following Hamiltonian:

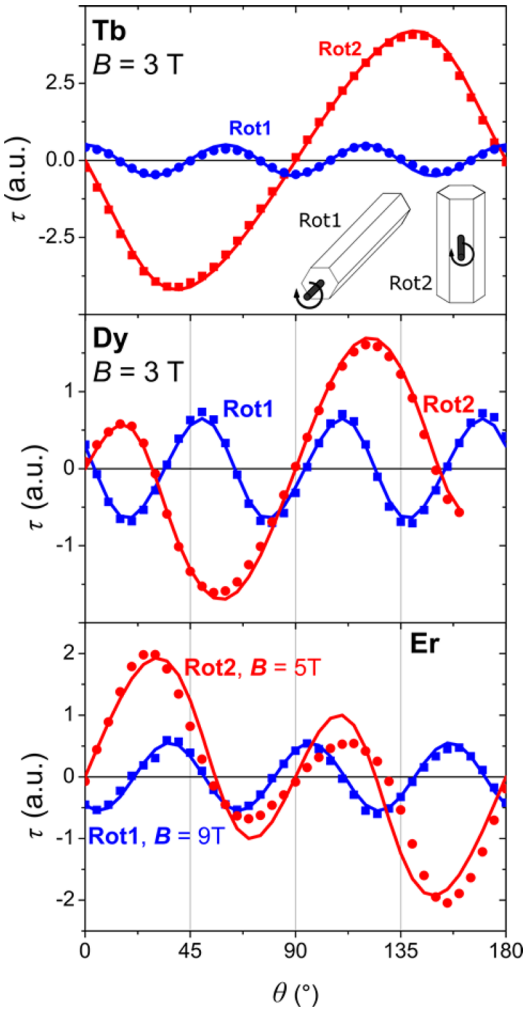

Figure 2. Experimental (dots or squares) and fitted (solid lines) curves obtained for **Tb** (top), **Dy** (middle), and **Er** (bottom).

$$\mathcal{H} = g_L \mu_B \mathbf{B}\cdot\hat{\mathbf{J}} + \sum_{k=2,4,6}\sum_{q=-k}^{k} b_k^q \hat{O}_k^q \qquad (2)$$

where g_L is the Landé factor of the Ln ion, μ_B is the Bohr magneton, $\hat{\mathbf{J}}$ is the total angular momentum operator, and $b^q{}_k$ are the coefficients of the $O^q{}_k$ Stevens operators,[25] which act on the $|J,m_J\rangle$ space, where m_J is the projection of J in the z direction.

The experimental points were reproduced by adjusting the $b^0{}_2$ parameter and letting the two Euler angles vary freely (Figure 2). Also, a scale factor was included in the fit to take into account the inaccuracy in the mass determination of such small crystals (according to that, the torque is given in atomic units, a.u.). The inclusion of a single CF operator gave satisfactory fits for **Dy** and **Er**, while for **Tb**, the inclusion of a $\mathbf{O}_2^2$ operator was necessary. It is clear that using only a few CF parameters is not sufficient to fully describe the magnetic anisotropy of these complexes, which are characterized by a low-symmetry coordination environment. Moreover, the low-temperature regime of all measurements does not allow us to extract information on the energy of m_J excited states, so the values of the CF parameters given here are only accurate in

DOI: 10.1021/acs.inorgchem.6b01010
Inorg. Chem. 2016, 55, 10068−10074

providing information on the low-temperature magnetic anisotropy. The simulation of the experimental torque data provided, however, the sign of the b_2^0 parameter, thus determining the easy axis or easy plane nature of the magnetic anisotropy of the metal ions. The best fit was achieved by fixing negative b_2^0 values for **Tb** (b_2^0 = −1.54 cm^{-1}) and **Dy** (b_2^0 = −1.91 cm^{-1}); therefore, they were both characterized by single-ion easy-axis anisotropy, while easy-plane anisotropy was detected for **Er** (b_2^0 = +2.33 cm^{-1}).[26] In the case of **Tb**, the inclusion of a transverse term O_2^2 (b_2^2 = −3.8 cm^{-1}) in the Hamiltonian makes, in principle, the use of a third Euler angle ψ = 23(1)° mandatory.[27] A similar sign of the magnetic anisotropy for **Tb** and **Dy**, and an opposite one for **Er**, is not unexpected because the electronic density of the 4f shell can be approximated as an oblate spheroid in the case of Tb^{III} and Dy^{III} and a prolate spheroid for Er^{III}.[10] The obtained energy splitting of the ground-state J multiplet is reported for all derivatives in Figure S8.

The best-fit values of Euler angles were ρ = 31(1)° and ξ = 76(1)° for **Tb**, ρ = 41(1)° and ξ = 61(1)° for **Dy**, and ρ = 21(1)° and ξ = 56(1)° for **Er**. The values of ξ deserve some comments. All of the values are larger than 54.7° (magic angle), indicating that the c crystallographic axis is closer to the hard direction in **Tb** and **Dy** and the easy direction in **Er**. The largest difference between the signals of the two rotations is observed for **Tb**, which has, in fact, the largest value of ξ.

Interestingly, for the three helices, the observed spin arrangement reflects an overall magnetic anisotropy of the crystals, which is reversed compared to that of the single ions: easy ab plane of magnetization for **Tb** and **Dy** and easy c axis for **Er**, as shown by the single-crystal M versus H curves reported in Figure S9. Moreover, the overall crystal anisotropy of **Dy** and **Er** is very weak because the angle ξ is close to the magic angle.

In Figure 3, we provide a graphic representation of the spin helicity of the three investigated chains, where the anisotropy susceptibility tensors generated by the 6-fold screw axis are depicted. The CF parameters determined by CTM were employed to calculate the low-field susceptibility tensors at T = 5 K. To make the strongly axial tensor of **Dy** visible, the hard directions of the tensor reported in Figure 3 were multiplied by a factor of 5.

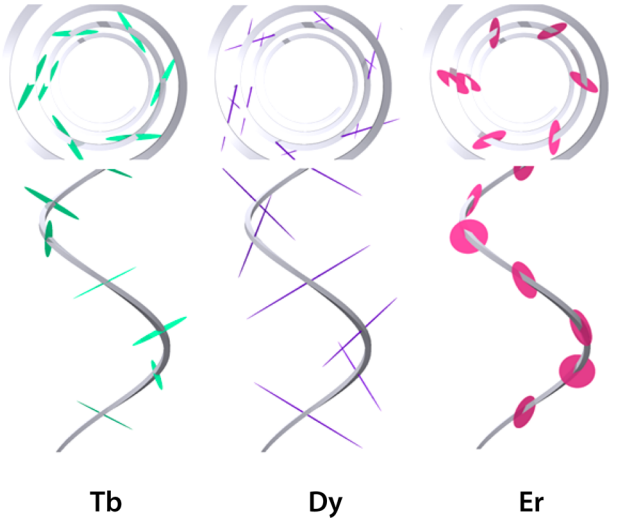

Figure 3. Schematic representation of the spin helicity obtained by plotting the susceptibility tensors calculated from the CTM experiments at T = 5 K and H = 1 Oe (top, view along the c axis; bottom, view along the ab plane). The susceptibility of the hard directions (x and y) of **Dy** has been multiplied by a factor of 5 to give a more solid aspect to the ellipsoids.

Although CTM is very powerful in disentangling the single-ion contributions, additional information is necessary to associate the extracted Euler's angles to a specific site, and a 6-fold ambiguity remains on the ρ value. A simple electrostatic modeling of the Dy^{III} ion coordination environment with *Magellan* software[28] provides a theoretical ξ value close to 81°, significantly different from the experimental one (61°).

Static and Dynamic Magnetic Properties. Having successfully extracted the single-ion anisotropy from the almost isotropic crystals, it is interesting to investigate whether the detected large single-ion magnetic anisotropy correlates with the dynamic properties of the three helices. In agreement with the Kramers nature of the ion and its easy-axis anisotropy stabilizing the $m_J = \pm^{15}/_2$ doublet, **Dy** exhibits slow relaxation of the magnetization in zero field, which further slows down in an applied field, as was already reported by Liu et al.[16] We investigated here the alternating-current (ac) susceptibility of the other two lanthanide helices in zero and static applied fields. Interestingly, neither **Tb**, which shows a significant rhombic anisotropy with the ground-state singlet separated by 2.4 cm^{-1} from the first excited state (see Figure S8 for energy and compositions of the lower states), nor **Er**, with easy-plane single-ion anisotropy (ground-state $m_J = \pm^1/_2$), presents single-molecule-magnet behavior.

Static magnetic data have evidenced an upturn at low temperature of the χT product for the **Gd**[15] and **Dy**[16] derivatives indicative of weak ferromagnetic interactions. In contrast, **Tb**[15] only showed a steady decrease of χT upon decreasing temperature. A similar steady decrease of χT is also observed for **Er** (see Figure S10), suggesting that interactions between paramagnetic centers are practically negligible in this derivative.

Magnetically coupled centers with strong easy-axis magnetic anisotropy are characterized by slow dynamics of the magnetization, known as single-chain-magnet (SCM) behavior.[29] In general, the effective barrier for the reversal of magnetization is higher in SCMs because the exchange interaction contributes significantly to the energy cost of the relaxation process.[30,31] Most reported SCMs, including the archetypal CoPhOMe,[32] are based on TM ions. There are a few reports of slow magnetization dynamics in 1D structures comprising 4f ions,[33−36] but an assessment of the role played in the slow dynamics of the magnetization by the weak exchange interactions that characterize these magnetic centers is not straightforward.[37−40] For this purpose, we investigated the diluted **DyY**, where the dilution percentage (15%) assures that most Dy ions are connected to two diamagnetic neighbors. Figure 4 reports the temperature dependence in a 1 kOe field of χT per mole of Dy^{III} ion for pure and diluted samples. The upturn is not observable for the **DyY** sample, as expected.

To quantify the interaction active in the pure chain, the low-temperature χT data in a logarithmic scale were reported versus $1/T$. Linearity is observed with a slope of 0.33(1) K (see Figure S11). In the Ising limit, the slope of the semilogarithmic plot corresponds to the interaction energy, E_{exch}, i.e., the difference in energy for parallel and antiparallel alignment of neighboring spins. Interestingly, this value is not too dissimilar to that found for the Gd derivative, where $E_{exch} = 2jS^2$ = 0.46 K for a coupling

DOI: 10.1021/acs.inorgchem.6b01010
Inorg. Chem. 2016, 55, 10068−10074

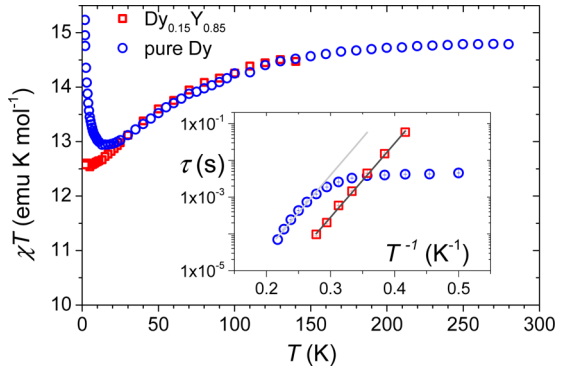

Figure 4. Temperature dependence of the χT product for the pure and diluted **Dy** helices measured by applying H = 1000 Oe. In the inset, the relaxation times for the two samples in the same static field. Gray and black lines correspond to the best fit with Arrhenius law of the data in the linear regime (see the text).

constant j = 0.013 cm^{-1} with the interaction Hamiltonian written as $\mathcal{H}_{int} = jS_a \cdot S_b$.[15] As expected for pure 4f systems, the estimated interactions are very weak and, in the present case, comparable to dipolar contributions, as encountered in other pure lanthanide chain systems.[36] Suppression of ferromagnetic interactions in Tb and Er derivatives, in contrast to Gd and Dy ones, could actually originate from a different contribution of dipolar interactions, given the different orientations of the magnetic moments in the chains.

The dynamic behavior of the pure and diluted Dy helices was also investigated by ac susceptometry. A static field of 1000 Oe was employed to slow down the magnetization. Maxima in the imaginary component susceptibility versus frequency were observed below 4.5 K for **Dy** and 3.8 K for **YDy** (Figures S12–S14). Data analyzed with the Debye model provided the temperature dependence of the relaxation times reported as an Arrhenius plot in the inset of Figure 4. The width of the distribution of the relaxation time, described by the phenomenological parameter α, is found to be rather large for both samples (see the Supporting Information and Figure S15).

Both samples exhibit a linear high-temperature region, with leveling of the relaxation time at low temperature. This effect is far more pronounced in the pure sample, indicating that spin–spin interactions are promoting fast relaxation. This observation is in contrast with what is expected for SCMs, suggesting that the magnetization dynamics is still dominated by single-ion anisotropy. Similar conclusions were reached by Bartolomé et al. in investigating the dynamic behavior of a Dy^{III} coordination polymer based on the furoate ligand.[37] Interestingly, in the case of furoate chains, the Tb derivative also exhibits slow magnetization dynamics, in agreement with the axial magnetic anisotropy and the small energy splitting of the two lowest levels that was estimated for the Tb ion.[41]

Fitting of the linear regime provided the parameters of the Arrhenius law $\tau = \tau_0 \exp(\Delta E/k_B T)$: ΔE = 47(2) K and τ_0 = 3(1) × 10^{-9} s for **Dy** and ΔE = 46.2(8) K and τ_0 = 2.7(7) × 10^{-10} s for **YDy**. The difference in the effective barrier is within the experimental error, which is, however, comparable to the expected contribution derived from the intrachain interaction (note also the similar width of the relaxation time distribution reported in Figure S15). Significant is, however, the difference of almost an order of magnitude in the preexponential factor, with the longer τ_0 observed for the pure sample. The decrease of τ_0 with diamagnetic doping was already observed in SCM[42] and attributed to the increase of the number of defective sites (i.e., those with a diamagnetic neighbor), where the domain walls preferentially nucleate because of the reduced exchange energy cost. However, this picture cannot be reconciled to our finding because of the almost negligible contribution to the spin dynamics arising from magnetic interaction along the chain. An alternative explanation could be that by magnetic dilution more phonons become available to promote magnetic relaxation. Acceleration of the relaxation is, in fact, observed in diluted samples when spin-phonon bottleneck effects are present,[43] but further experiments at different dilutions of the Dy magnetic moments are necessary to elucidate this point.

XNCD. Our investigation gives evidence for a spin helicity in the Dy coordination polymer very similar to that detected in the cobalt(II) nitronyl–nitroxide chain exhibiting strong X-ray natural and magnetic circular dichroisms as well as giant X-ray magnetochiral dichroism at the K-edge of Co. With the optical activity of the Dy crystals already assessed,[16] we decided to investigate the Ln contribution to it by exploiting the element sensitivity of X-ray spectroscopy.

XANES and XNCD measurements have been attempted on Dy crystals at the L_3-edge of Dy, i.e., where optical transitions from the $2p_{3/2}$ core orbitals to the unoccupied states are involved. This is not the edge usually employed to access the magnetic properties of the 4f states of Ln ions because, at the L_3-edge absorption of a rare-earth atom, the dominant electric dipolar (E1) transitions are toward unoccupied 5d orbitals and the electric quadrupolar (E2) transitions toward partially filled 4f orbitals and empty 6p orbitals are much weaker. It should be recalled that the term of the matter–radiation interaction leading to optical activity, i.e., XNCD, in the X-ray range is an interference dipole–quadrupole term (E1E2) which averages to zero in randomly oriented samples and could only be detected on systems featuring an orientational order, e.g., single crystals.

Two relatively large (ca. 2.5 × 0.2 × 0.2 mm) enantiopure single crystals of opposite chirality [$P6_1$, Flack χ_F = −0.016(8); $P6_5$, Flack χ_F = −0.017(6)] were selected for X-ray absorption experiments. The Dy L_3-edge XANES and XNCD spectra were measured at room temperature and shown in Figure 5. The isotropic contribution to XANES is dominated by the characteristic intense peak due to transitions into 5d empty

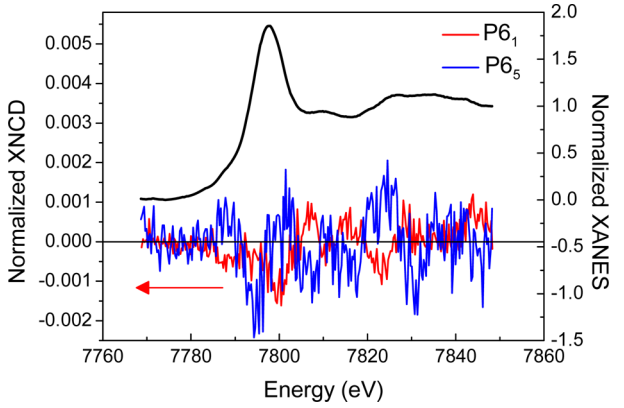

Figure 5. XANES spectrum at the L_3-edge of Dy measured at room temperature in zero field (black line) obtained as $1/2(\sigma^r + \sigma^l)$ and XNCD spectra given by $(\sigma^r - \sigma^l)$ for two enantiomeric crystals. σ^r and σ^l denote X-ray absorption cross sections for right and left circularly polarized X-rays, respectively.

DOI: 10.1021/acs.inorgchem.6b01010
Inorg. Chem. 2016, 55, 10068–10074

orbitals, the so-called "white line" with a maximum at 7795 eV. Quadrupolar transitions into unoccupied 4f orbitals occur at about 5−10 eV lower energy because of a strong interaction of the $2p_{3/2}$ hole and 4f electrons, which, however, can hardly be seen in isotropic XANES spectra dominated by the white line. On the other hand, these transitions are nicely observable in the corresponding X-ray magnetic circular dichroism spectra.[44] A rather weak XNCD signal is observed at the Dy L_3-edge, with opposite signs for the $P6_1$ and $P6_5$ enantiomeric crystals. The magnitude of the normalized XNCD signal is in the low 10^{-3} range, similar to previous reports on XNCD at the L-edge of Ln chiral complexes.[45] The relatively weak dichroism can reasonably be ascribed to the fact that f orbitals are strongly localized on the Ln ion and thus are scarcely influenced by a supramolecular chiral arrangement such as that of the nicotinate helix studied in this work. This is also confirmed by the very weak XNCD intensities at photon energies, where electronic transitions to states with strong 4f character is expected (ca. 7787 eV). On the other hand, quadrupolar transitions at the L_3-edge to extended 6p states of rare-earth ions are also allowed by the selection rules, thus giving rise to a finite XNCD signal in a wide energy range up to 30 eV above the edge. These extended states are indeed strongly affected by the chiral arrangement of the ligands. In this respect, the X-ray optical activity at the L_3-edge of rare-earth ions in Dy helices strongly differs from those of the previously investigated Co^{II} and Mn^{II}, which revealed a large XNCD signal due to interference of 1s → 3d quadrupolar and 1s → 4p dipolar transitions. These findings suggest that, despite the fact that strong spin noncollinearity of Ln-based helices makes them strong candidates for the observation of MChEs, using hard X-rays does not appear to be straightforward for such investigations.

CONCLUSIONS

In conclusion, we have exploited the power of CTM to investigate the spin helicity of a series of isomorphous coordination polymers, extracting precious information on single-ion magnetic anisotropy. All derivatives exhibit spin noncollinearity, and thus a marked spin helicity, although only the Dy derivative has the correct anisotropy to promote slow relaxation of the magnetization. The synchrotron investigation of the element selective optical activity also suggested a weak admixing of the 4f orbitals with orbitals of opposite parity, thus making detection with this technique of a significant MChE rather problematic. This, however, does not preclude the observation of MChD in the near-IR−visible region, although the necessity to use single crystals poses additional experimental difficulties.

ASSOCIATED CONTENT

Supporting Information

The Supporting Information is available free of charge on the ACS Publications website at DOI: 10.1021/acs.inorgchem.6b01010.

Details about the torque magnetometry experiments, additional data and simulations, and additional ac and dc magnetometry data (PDF)

X-ray crystallographic data in CIF format (CIF)

X-ray crystallographic data in CIF format (CIF)

AUTHOR INFORMATION

Corresponding Authors

*E-mail: mauro.perfetti@ipc.uni-stuttgart.de.
*E-mail: annie.powell@kit.edu.
*E-mail: roberta.sessoli@unifi.it.

Present Address

§Institut für Physikalische Chemie, Pfaffenwaldring 55, 70569 Stuttgart, Germany.

Notes

The authors declare no competing financial interest.

ACKNOWLEDGMENTS

We thank Lena Friedrich for assistance with the synthesis and Drs. Samuele Ciattini and Laura Chelazzi for X-ray fluorescence analysis. ESRF is acknowledged for providing access to the ID12 beamline through the beamtime proposal HC-1810. Dr. Lorenzo Sorace and Eva Lucaccini are acknowledged for scientific discussion. Funding was provided by the ERC AdG MolNanoMaS (Project 267746), Italian MIUR through FIRB Project RBAP117RWN, DFG-funded transregional collaborative research center SFB/TRR 88 "3MET", and HGF-funded program STN.

REFERENCES

(1) Pasteur, L. *Rev. Sci.* **1884**, *7*.
(2) Wagnière, G.; Meier, A. *Chem. Phys. Lett.* **1982**, *93*, 78−81.
(3) Barron, L. D.; Vrbancich, J. *Mol. Phys.* **1984**, *51*, 715−730.
(4) Rikken, G.; Raupach, E. *Nature* **1997**, *390*, 493−494.
(5) Cheong, S.-W.; Mostovoy, M. *Nat. Mater.* **2007**, *6*, 13−20.
(6) Khomskii, D. *Physics* **2009**, *2*, 20.
(7) Train, C.; Gheorghe, R.; Krstic, V.; Chamoreau, L.-M.; Ovanesyan, N. S.; Rikken, G. L. J. A.; Gruselle, M.; Verdaguer, M. *Nat. Mater.* **2008**, *7*, 729−734.
(8) Kubota, M.; Arima, T.; Kaneko, Y.; He, J.; Yu, X.; Tokura, Y. *Phys. Rev. Lett.* **2004**, *92*, 137401.
(9) Sessoli, R.; Boulon, M.-E.; Caneschi, A.; Mannini, M.; Poggini, L.; Wilhelm, F.; Rogalev, A. *Nat. Phys.* **2014**, *11*, 69−74.
(10) Rinehart, J. D.; Long, J. R. *Chem. Sci.* **2011**, *2*, 2078−2085.
(11) Luo, Y.-D.; Sun, G.-M.; Li, D.-M.; Luo, F. *Inorg. Chem. Commun.* **2011**, *14*, 778−780.
(12) Han, T.; Leng, J.-D.; Ding, Y.-S.; Wang, Y.; Zheng, Z.; Zheng, Y.-Z. *Dalton Trans.* **2015**, *44*, 13480−13484.
(13) Zaleski, C. M.; Depperman, E. C.; Kampf, J. W.; Kirk, M. L.; Pecoraro, V. L. *Inorg. Chem.* **2006**, *45*, 10022−10024.
(14) Chen, K.; Hu, Y.-F.; Xiao, X.; Xue, S.-F.; Tao, Z.; Zhang, Y.-Q.; Zhu, Q.-J.; Liu, J.-X. *RSC Adv.* **2012**, *2*, 3217−3220.
(15) Mihalcea, I.; Zill, N.; Mereacre, V.; Anson, C. E.; Powell, A. K. *Cryst. Growth Des.* **2014**, *14*, 4729−4734.
(16) Liu, S.; Li, L.-L.; Li, H.; Gao, H.-L.; Cui, J.-Z.; Cheng, P. *Dalton Trans.* **2015**, *44*, 6169−6174.
(17) Cornia, A.; Gatteschi, D.; Sessoli, R. *Coord. Chem. Rev.* **2001**, *219*, 573−604.
(18) Mitra, S. *Prog. Inorg. Chem.* **1977**, *22*, 309−408.
(19) Beaurepaire, E.; Bulou, H.; Scheurer, F.; Kappler, J.-P. *Magnetism and Synchrotron Radiation*; Springer: Berlin, 2010; Vol. *133*.
(20) Rogalev, A.; Goulon, J.; Goulon-Ginet, C.; Malgrange, C., Instrumentation developments for polarization dependent x-ray spectroscopies. *Magnetism and Synchrotron Radiation*; Springer: Berlin, 2001; pp 60−86.
(21) Perfetti, M.; Cucinotta, G.; Boulon, M. E.; El Hallak, F.; Gao, S.; Sessoli, R. *Chem. - Eur. J.* **2014**, *20*, 14051−14056.
(22) Perfetti, M.; Lucaccini, E.; Sorace, L.; Costes, J. P.; Sessoli, R. *Inorg. Chem.* **2015**, *54*, 3090−3092.
(23) Lucaccini, E.; Briganti, M.; Perfetti, M.; Vendier, L.; Costes, J. P.; Totti, F.; Sessoli, R.; Sorace, L. *Chem. - Eur. J.* **2016**, *22*, 5552−5562.

DOI: 10.1021/acs.inorgchem.6b01010
Inorg. Chem. 2016, 55, 10068−10074

(24) Rigamonti, L.; Cornia, A.; Nava, A.; Perfetti, M.; Boulon, M.-E.; Barra, A.-L.; Zhong, X.; Park, K.; Sessoli, R. *Phys. Chem. Chem. Phys.* **2014**, *16*, 17220−17230.
(25) Abragam, A.; Bleaney, B. *Electron Paramagnetic Resonance of Transition Ions*; Dover: New York, 1986.
(26) The coefficients b^k_q contain the appropriate reduced matrix elements ($\alpha_{Tb} = -1/99$, $\alpha_{Dy} = -2/315$, and $\alpha_{Er} = 4/1575$).
(27) The parameters so expressed do not satisfy the condition $|b_2^0| > |b_2^2|$, commonly used to define the *xyz* molecular reference frame. We decided to express the parameters using the easiest direction as the quantization axis to emphasize the similarity with Dy.
(28) Chilton, N. F.; Collison, D.; McInnes, E. J.; Winpenny, R. E.; Soncini, A. *Nat. Commun.* **2013**, *4*, 2551.
(29) Clerac, R.; Miyasaka, H.; Yamashita, M.; Coulon, C. *J. Am. Chem. Soc.* **2002**, *124*, 12837−12844.
(30) Coulon, C.; Miyasaka, H.; Clérac, R. Single-chain magnets: theoretical approach and experimental systems. *Single-molecule magnets and related phenomena*; Springer: Berlin, 2006; pp 163−206.
(31) Bartolomé, J.; Luis, F.; Fernández, J. F. *Molecular Magnets*; Springer: Berlin, 2014.
(32) Caneschi, A.; Gatteschi, D.; Lalioti, N.; Sangregorio, C.; Sessoli, R.; Venturi, G.; Vindigni, A.; Rettori, A.; Pini, M. G.; Novak, M. A. *Angew. Chem., Int. Ed.* **2001**, *40*, 1760−1763.
(33) Chen, Q.; Meng, Y.-S.; Zhang, Y.-Q.; Jiang, S.-D.; Sun, H.-L.; Gao, S. *Chem. Commun.* **2014**, *50*, 10434−10437.
(34) Brunet, G.; Habib, F.; Korobkov, I.; Murugesu, M. *Inorg. Chem.* **2015**, *54*, 6195−6202.
(35) Novitchi, G.; Pilet, G.; Ungur, L.; Moshchalkov, V. V.; Wernsdorfer, W.; Chibotaru, L. F.; Luneau, D.; Powell, A. K. *Chem. Sci.* **2012**, *3*, 1169−1176.
(36) Jung, J.; Le Natur, F.; Cador, O.; Pointillart, F.; Calvez, G.; Daiguebonne, C.; Guillou, O.; Guizouarn, T.; Le Guennic, B.; Bernot, K. *Chem. Commun.* **2014**, *50*, 13346−13348.
(37) Bartolomé, E.; Bartolomé, J.; Melnic, S.; Prodius, D.; Shova, S.; Arauzo, A.; Luzón, J.; Luis, F.; Turta, C. *Dalton Trans.* **2013**, *42*, 10153−10171.
(38) Wang, Y.; Li, X.-L.; Wang, T.-W.; Song, Y.; You, X.-Z. *Inorg. Chem.* **2010**, *49*, 969−976.
(39) Zheng, Y. Z.; Lan, Y. H.; Wernsdorfer, W.; Anson, C. E.; Powell, A. K. *Chem. - Eur. J.* **2009**, *15*, 12566−12570.
(40) Zhu, Y.; Luo, F.; Song, Y.-M.; Huang, H.-X.; Sun, G.-M.; Tian, X.-Z.; Yuan, Z.-Z.; Liao, Z.-W.; Luo, M.-B.; Liu, S.-J.; Xu, W.-Y.; Feng, X.-F. *Dalton Trans.* **2012**, *41*, 6749−6755.
(41) Bartolomé, E.; Bartolomé, J.; Arauzo, A.; Luzon, J.; Badia, L.; Cases, R.; Luis, F.; Melnic, S.; Prodius, D.; Shova, S.; Turta, C. I. *J. Mater. Chem. C* **2016**, *4*, 5038−5050.
(42) Bogani, L.; Caneschi, A.; Fedi, M.; Gatteschi, D.; Massi, M.; Novak, M. A.; Pini, M. G.; Rettori, A.; Sessoli, R.; Vindigni, A. *Phys. Rev. Lett.* **2004**, *92*, 207204.
(43) Shrivastava, K. *Phys. Status Solidi B* **1983**, *117*, 437−458.
(44) Giorgetti, C.; Dartyge, E.; Brouder, C.; Baudelet, F.; Meyer, C.; Pizzini, S.; Fontaine, A.; Galéra, R.-M. *Phys. Rev. Lett.* **1995**, *75*, 3186−3189.
(45) Alagna, L.; Prosperi, T.; Turchini, S.; Goulon, J.; Rogalev, A.; Goulon-Ginet, C.; Natoli, C. R.; Peacock, R. D.; Stewart, B. *Phys. Rev. Lett.* **1998**, *80*, 4799−4802.

DOI: 10.1021/acs.inorgchem.6b01010
Inorg. Chem. 2016, 55, 10068−10074

Dalton Transactions

PAPER

View Article Online
View Journal | View Issue

Cite this: *Dalton Trans.*, 2016, **45**, 16635

Giant spin–phonon bottleneck effects in evaporable vanadyl-based molecules with long spin coherence†

L. Tesi,‡[a] A. Lunghi,‡[a,b] M. Atzori,[a] E. Lucaccini,[a] L. Sorace,[a] F. Totti[a] and R. Sessoli*[a]

Received 26th June 2016,
Accepted 19th July 2016

DOI: 10.1039/c6dt02559e

www.rsc.org/dalton

Vanadium(IV) complexes have recently shown record quantum spin coherence times that in several circumstances are limited by spin–lattice relaxation. The role of the environment and vibronic properties in the low temperature dynamics is here investigated by a comparative study of the magnetization dynamics as a function of crystallite size and the steric hindrance of the β-diketonate ligands in $VO(acac)_2$ (**1**), $VO(dpm)_2$ (**2**) and $VO(dbm)_2$ (**3**) evaporable complexes ($acac^-$ = acetylacetonate, dpm^- = dipivaloylmethanate, and dbm^- = dibenzoylmethanate). A pronounced crystallite size dependence of the relaxation time is observed at unusually high temperatures (up to 40 K), which is associated with a giant spin–phonon bottleneck effect. We model this behaviour by an *ad hoc* force field approach derived from density functional theory calculations, which evidences a correlation of the intensity of the phenomenon with ligand dimensions and the unit cell size.

Introduction

Magnetic molecules characterized by a large spin and easy axis magnetic anisotropy have been the focus of significant interest for two decades.[1] The interest in their properties is dual: from one side, their long relaxation time of magnetization makes them appealing to build miniaturized memory units, while, from a fundamental point of view, they are studied as model systems to investigate quantum effects in the magnetization dynamics. Molecular magnets are nowadays investigated also at the single molecule level mainly by depositing them on surfaces[2,3] or inside nanojunctions[4] to realize single molecule spintronics devices.[5,6] More recently another class of magnetic molecules, characterized by a small (S = 1/2) and essentially isotropic spin state, has gained much attention thanks to their relatively long spin–spin or spin coherence time, T_2.[7–14] The latter is one of the key features if magnetic molecules have to be used as quantum bits, or qubits, *i.e.* the fundamental unit of a quantum computer.[15] Though many different physical realizations of qubits are available, magnetic molecules present some advantages. First, the electronic spin is the most intuitive and simple choice to reproduce the sought-after quantum behaviour of qubits.[15] Moreover, molecules can be processed to obtain ordered nanostructures, which is a prerequisite if a real device is to be developed,[10] and synthetic chemistry techniques allow in principle the tuning of the interaction to couple two or more qubits.[16,17] On the other hand, their spin coherence time (*i.e.* the lifetime of any quantum superposition of states), is, in general, significantly shorter than that observed for other qubit candidates based on electronic spins, such as defects in inorganic semiconductors.[18,19] However, remarkably long quantum coherence times have been recently achieved in molecular systems by a rational design of the nuclear spin environment. Freedman *et al.*[14] reported a value of the phase memory time T_m (a lower estimation of T_2), for a vanadium(IV) complex dissolved in CS_2 of *ca.* 0.7 ms at 10 K. Furthermore, dilution in crystalline matrices provided detectable quantum coherence at room temperature in $[(Ph)_4P]_2[Cu(mnt)_2]$ (mnt = maleonitriledithiolate)[8] and, more recently, for the processable VOPc (Pc = phthalocyanine) complex, where Rabi oscillations were also observed at room temperature.[9] Although the optimization of quantum coherence times is fundamental to perform coherent quantum logic operations, another step toward the integration of these molecular systems in real devices is their controlled deposition on solid surfaces and the investigation of their quantum coherence in the hybrid architecture. In this respect, still very little is known about the role that an unusual environment, such as that of an isolated molecule on a surface, can have on the spin–lattice relaxation time, T_1, as well as on T_2. Indeed, a recent report

[a]*Dipartimento di Chimica "U. Schiff" and INSTM UdR Firenze, Università degli Studi di Firenze, Via della Lastruccia 3, I50019 Sesto Fiorentino, Firenze, Italy. E-mail: roberta.sessoli@unifi.it*

[b]*School of Physics, CRANN and AMBER Trinity College Dublin 2, Ireland*

†Electronic supplementary information (ESI) available: X-ray powder diffraction data, EPR spectra and analysis, AC susceptibility data, and details of the force field and DFT calculations. See DOI: 10.1039/c6dt02559e

‡These authors equally contributed to the paper.

highlighted the environment role played by a substrate made of a thin layer of MgO deposited on Ag in the magnetic bistability of a Ho atom, which reaches a very long relaxation time of magnetization, 1500 s at 10 K.[20]

We have recently shown that the combination of alternating current (AC) susceptometry and pulsed electron paramagnetic resonance (EPR) spectroscopy can help in identifying molecular systems with long-lived coherence at high temperatures, where the coherence time is limited by the spin–lattice relaxation.[9] In our previous studies,[10] we observed a relatively long T_m for frozen solutions of $VO(dpm)_2$ (dpm^- = dipivaloylmethanate), 2 μs at 80 K, and an anomalous coefficient for the direct mechanism of spin–lattice relaxation at low temperatures. The latter behaviour was attributed to the spin–phonon bottleneck effect, a phenomenon due to the lack of an efficient exchange between the spins and the thermal bath mediated by low-frequency phonons, with the resulting slowing down of the relaxation process.[21] This environmental effect, which depends on the crystallite size and on the concentration of paramagnetic ions, is particularly relevant for $S = 1/2$ systems at low temperatures, when the relaxation occurs through the direct process, which involves low energy resonant phonons.[22–25] On the contrary, few observations[26–28] on spin–phonon bottleneck effects were reported for molecules with spin higher than 1/2, *e.g.* Single Molecule Magnets (SMMs), because multi-phonon processes like the Orbach mechanism, which involves higher energy phonons, dominate.[1]

The interaction of the magnetic systems with the environment presents several crucial aspects, which involve structural, electronic, and vibrational properties. In this framework, the spin–phonon bottleneck effect in molecular systems is an intriguing issue that can evidence the key role of the environment on the magnetic relaxation and consequently also on the quantum coherence time. Indeed, it is clear that a deeper understanding of this effect and its control by tiny chemical modifications could in principle allow a further enhancement of the quantum coherence time.

To evaluate the spin–phonon bottleneck effect in potential molecular spin qubits, we have performed an experimental investigation of the spin dynamics for three crystalline vanadyl β-diketonate complexes, namely $VO(acac)_2$ (**1**), $VO(dpm)_2$ (**2**) and $VO(dbm)_2$ (**3**)($acac^-$ = acetylacetonate, and dbm^- = dibenzoylmethanate), which feature the same vanadyl ion and ligand moiety with substituents of different steric hindrance. The spin dynamics of compounds **1–3** have been investigated by AC susceptometry on macro and microcrystalline samples over a wide range of temperatures and static magnetic fields. A giant spin–phonon bottleneck effect, detectable up to 40 K, with the magnetization relaxation time, τ, spanning two orders of magnitude depending on the crystallite sizes, has been observed. Theoretical modelling has been used to gain insights into the origin of this effect. For this purpose, an *ad hoc* force field for the three systems has been derived from density functional theory (DFT) calculations and exploited to rationalize lattice properties such as phonon dispersion curves and vibrational density of states (DOS) for the three complexes. A strong correlation of the intensity of the phenomenon with the ligand dimensions and the unit cell size has been evidenced.

Results and discussion

Synthesis and crystal structure description

1, **2** and **3** were prepared according to a general synthetic procedure already reported in the literature.[29] The reaction between an aqueous solution of $VOSO_4{\cdot}xH_2O$ and the β-diketonate ligand (1 : 2 molar ratio) partially deprotonated with Na_2CO_3 in $EtOH/H_2O$ (1 : 1) solution affords the desired products in good yields. The polycrystalline samples of compounds **1–3** were characterized through powder X-ray diffraction (PXRD) analyses by comparing the experimental patterns with those calculated from the atomic coordinates of the reported single crystal X-ray structures.[30–32] The good agreement between the experimental and simulated patterns (see the ESI, Fig. S1–S3†) demonstrates the phase purity of the investigated samples.

All the investigated compounds show a vanadyl ion VO^{2+} coordinated by two chelating bidentate β-diketonate ligands. The coordination geometry around the penta-coordinated V^{IV} metal centre is a distorted square pyramid with the metal ion slightly above the basal plane (0.545(1) Å (**1**), 0.573(1) Å (**2**), 0.559(1) Å (**3**)) (Fig. 1). The V═O bond distances are 1.585(1) Å, 1.574(1) Å, and 1.578(1) Å for **1**, **2** and **3**, respectively, whereas the average V–O bond lengths are 1.969(2) Å for **1**, 1.964(2) Å for **2**, and 1.946(2) Å for **3**. The V═O double bond, being *ca.* 0.4 Å shorter than the V–O single bonds, induces a strong axial distortion of the ligand field acting on the d-orbitals of the metal ion; this, together with the out-of-plane position of the metal atom, results in the d_{xy} orbital lying the lowest and being singly occupied. The large energy difference between the magnetic orbital and the unoccupied orbitals makes these $S = 1/2$ systems ideal candidates as molecular spin qubits.[33]

The substituents on the common β-diketonate ligand moiety have a steric hindrance that increase in the order **1** < **2** < **3**. Accordingly, the unit cell parameters increase in the same order, although they are further increased by the higher symmetry of the space groups of **3**. Indeed, even if all compounds crystallize with only one crystallographically independent molecule in the asymmetric unit, **1** crystallizes in the triclinic centrosymmetric space group $P\bar{1}$ ($Z = 2$), whereas **2** and **3** crystallize in the $P2_1$ and *Pbca* monoclinic space groups with $Z = 2$ and $Z = 8$, respectively. Such crystallographic differences have important implications on the theoretical calculations of the lattice properties (*vide infra*).

The very similar coordination environment along the series is reflected in practically identical frozen solution EPR spectra (Fig. S4†), which show the typical features of an anisotropic doublet interacting with an $I = 7/2$ nuclear spin (^{51}V, n. ab. 99.75%). The spectra have been simulated[34] on the basis of the Spin Hamiltonian $H = \mu_B \boldsymbol{B}{\cdot}\boldsymbol{g}{\cdot}\boldsymbol{S} + \boldsymbol{I}{\cdot}\boldsymbol{A}{\cdot}\boldsymbol{S}$, providing almost identical parameters for the three derivatives (Table S1†) indicating only negligible differences in the electronic structure of

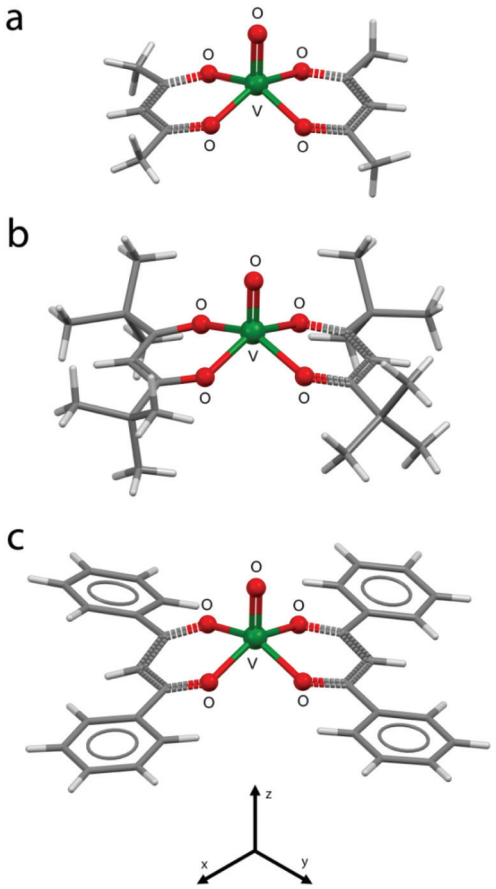

Fig. 1 Molecular structures of **1** (a), **2** (b), and **3** (c), with the principal atom labelling scheme and coordination geometry of the V^{IV} ions highlighted. The reference system used throughout the paper is shown at the bottom.

the complexes. The obtained parameters are in the range previously reported for VO^{2+} β-diketonate-type derivatives[35,36] and are characterized, as expected, by partially rhombic g and A tensors. Larger deviations from the free electron values for g and larger hyperfine coupling are observed along the z direction, which is directed along the V═O bond.[36] The corresponding field/energy levels obtained for the field applied along the z and along the x-axis are shown in Fig. S5.†

Magnetization dynamics

The investigation of the spin–phonon bottleneck effect was based on the comparison of the AC susceptibility data measured for several samples of **1–3** made up of crystallites of different sizes. We began our investigation by measuring AC magnetic susceptibility as a function of the applied static magnetic field (Fig. 2) and temperature (Fig. 3a) on three polycrystalline samples of **1** with different crystallite dimensions (d): macroscopic crystals as obtained from crystallization (d *ca.* 1–5 mm) (**1a**), moderately crushed crystals (d *ca.* 500 μm) (**1b**), and well crushed and pressed microcrystalline powders (d *ca.* 10 μm) (**1c**). The dimensions of the crystallites were qualitatively estimated by X-ray microtomography (Fig. S6†). As

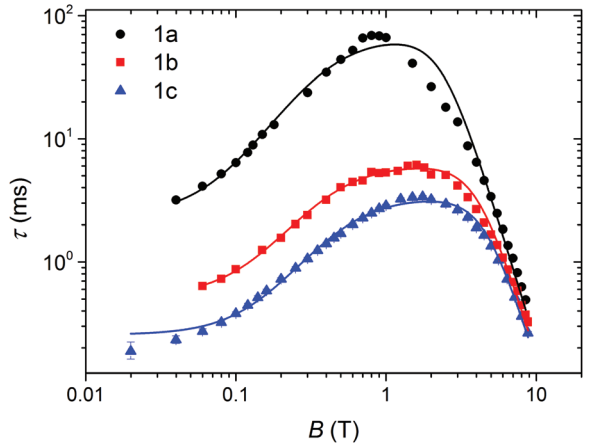

Fig. 2 Magnetization relaxation time for samples **1a**, **1b**, **1c** as a function of the static magnetic field at T = 10 K, reported as a log–log plot. Solid lines are the best fit curves obtained by using eqn (1) with the parameters reported in Table 1.

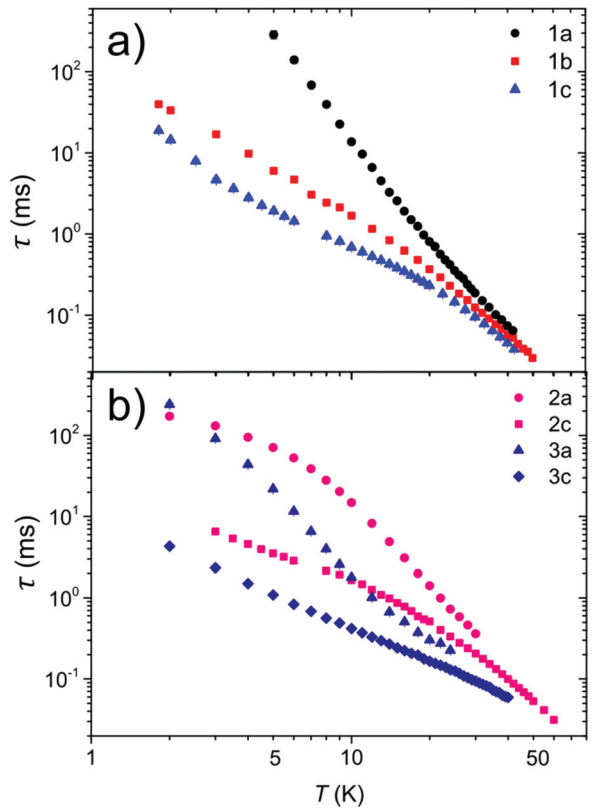

Fig. 3 Temperature dependence of the magnetization relaxation time for **1a**, **1b** and **1c** (a) and for **2a**, **2c** and **3a**, **3c** (b), at B = 0.2 T.

expected, the imaginary component of magnetic susceptibility, χ'', is zero for all the compounds in zero static magnetic field; on application of a moderate static magnetic field (20 mT) a maximum in the $\chi''(\nu)$ plot is observed accompanied by a concomitant decrease of the real part, χ' (Fig. S7–S9†). The Debye model[1] has been used to reproduce the frequency dependence

of χ'', thus allowing the extrapolation of the values of the relaxation time, τ, the width of the relaxation time distribution, α, and the difference between the isothermal and the adiabatic susceptibility, $\chi_T - \chi_S$ as a function of temperature and applied field.

It is evident from Fig. 2 that the three morphologically different samples show very different absolute values of the relaxation time τ, which is *ca.* one order of magnitude higher for **1a** with respect to **1c** at T = 10 K and B up to 1 T. Remarkably the sample dependence of τ remains constant up to 1–2 T but almost disappears at the highest investigated field of 8.8 T. On the other hand, it increases dramatically on lowering the temperature, being as high as two orders of magnitude at T = 5 K and B = 0.2 T (Fig. 3a).

The field dependence of the relaxation time follows for all three samples, a behaviour observed for other vanadyl-based compounds,[9,10] which can be simulated using eqn (1), derived from the Brons-van Vleck model.[37,38]

$$\tau^{-1} = cB^4 + d\frac{1 + eB^2}{1 + fB^2} \quad (1)$$

The first term accounts for the field dependence of the direct mechanism of relaxation between the two states split by the Zeeman energy, while the second term takes into account several mechanisms of mixing between the levels depending on the inter and intramolecular interactions. The best-fit parameters are reported in Table 1.

The observed differences between **1a**, **1b** and **1c** could be in principle due to a non-statistical random orientation of the crystals, especially for non-crushed crystallites, as in sample **1a**: the anisotropic spin Hamiltonian parameters might indeed result in different relaxation times for the field applied along different directions. To test this hypothesis, a 5.4 mg single crystal of **1** was investigated, following the same protocol used for polycrystalline samples, by applying the static and AC magnetic fields parallel and perpendicular to the V=O bond. The triclinic space group of this derivative further ensures that all the molecules in the crystal structure have the same orientation of the $\boldsymbol{g}$ and $\boldsymbol{A}$ tensors, thus providing the same energy pattern for all the molecules in a given applied field. The results, given in the ESI, Fig. S10,† revealed no significant differences between the two orientations, clearly demonstrating the key role of the crystallite dimensions in determining the spin dynamics. Indeed, these results evidence that the strong anisotropy in the hyperfine interaction does not play a role in the investigated field and temperature range, despite that both energy and composition of the eigenstates are strongly affected by the orientation of the field (Fig. S5†). The reason is that at the investigated temperatures all the 16 states of the hyperfine split doublet are essentially equi-populated: temperatures below 100 mK will be necessary to evidence nuclear spin effects on the dynamics of the magnetization.[39]

Having established that the observed differences in τ are due to the different crystallite sizes in the three samples and then to spin-phonon bottleneck effect, the smaller differences observed at higher field values (Fig. 2) can be easily explained. Indeed, the splitting of the S = 1/2 doublet increases with the field and phonons of a higher frequency are involved in the resonance mechanism of relaxation, thus reducing the efficiency of the spin–phonon bottleneck effect.

A pronounced dependence of τ for **1** on the crystallite size is also evident by analysing its temperature dependence (Fig. 3a). These differences become more evident on lowering the temperature, but are still present at the highest investigated temperature, 42 K. The slopes in the log–log plot of τ for the three samples and their trends are quite different: they tend toward the same value at high temperatures, but from *ca.* 20 K to lower temperatures, the slope for **1b** and **1c** decreases, while for **1a** increases. This behaviour can be qualitatively interpreted to be due to two different regimes: a low temperature one, where a direct process dominates, and a higher temperature one, where a Raman-like process drives the relaxation.[40] According to this interpretation, we obtained the slope coefficients below and above 20 K for **1a**, **1b** and **1c** by two distinct linear fits (Table 2) of the thermal dependence of τ.

The results given in Table 2 are unusual because the direct mechanism, which is dominant at low temperatures, should depend linearly on temperature, while deviations from this behaviour are observed for all the samples, especially for **1a**. Above 20 K the Raman-like mechanism dominates and a T^{-3} dependence on temperature, typical of vanadyl-based systems,[9,10,41,42] is observed.

To describe the paramagnetic relaxation in the presence of the spin–phonon bottleneck effect Stoneham[23] derived, from thermodynamic bases, an equation to take into account the contributions involved in the relaxation (eqn (2)), independently from the mechanisms of the relaxation process:

$$\tau = \tau_{SL} + \left(\frac{c_S}{c_L}\right)\tau_{LB} \quad (2)$$

where τ is the spin–bath relaxation time, actually the one measured by AC susceptibility, τ_{SL} is the spin–lattice relaxation

Table 1 The best-fit parameters of the model (eqn (1)) used to reproduce the field dependence of the magnetization relaxation rate τ^{-1} for **1a**, **1b** and **1c**

Sample	$c \times 10^{-4}$ (T^{-4} ms^{-1})	d (ms^{-1})	e (T^{-2})	f (T^{-2})
1a	4.8 ± 0.2	0.5 ± 0.2	11 ± 3	248 ± 163
1b	6.0 ± 0.2	1.9 ± 0.1	6.1 ± 0.6	72 ± 10
1c	6.3 ± 0.1	4.0 ± 0.3	4.2 ± 0.3	56 ± 6

Table 2 Slopes of the temperature dependence of τ in the log–log plot for **1a**, **1b**, and **1c**, given as the n parameter of $\tau \propto T^{-n}$

Sample\temperature	<20 K	>20 K
1a	4.2	3.4
1b	1.9	2.7
1c	1.5	2.4

time, c_S is the specific heat of the spin system, c_L the lattice specific heat, and τ_{LB} the lattice–bath relaxation time. Eqn (2) suggests that, if τ_{LB} is high enough, a variation of the magnetic ion concentration (equal to a change in c_S/c_L) or on the crystallite size (equal to a change of τ_{LB}) results in a modification of the observed relaxation time.

The rate-determining step for the phonon–bath exchange process could involve the transfer of energy in space (spatial bottleneck) or in frequency (spectral bottleneck). Stoneham observed that when a spatial bottleneck dominates then $\tau \rightarrow \tau_{LB} \cdot T^{-2}$ and $\tau_{LB} \propto d$, where d is the size of the crystallites. The exponent $n = 2$ in $\tau \propto T^{-n}$, originated from the specific heat ratio in eqn (2), is indeed the most commonly found in $S = 1/2$ systems affected by the spin–phonon bottleneck,[24] including the pseudo-spin $S = 1/2$ of an Yb^{III} complex.[22] However, van Vleck suggested that, taking into account the finite life-time of phonons, τ_{LB} could also depend on temperature and an exponent up to $n = 6$ can be expected.[21] The latter seems to be the case of **1a**, which, thanks to the rapid divergence at low temperatures, reaches remarkably large values of τ, *e.g.* 400 ms at 5 K, and shows butterfly-like magnetic hysteresis around 2 K (Fig. S11†). This occurs at a much higher temperature than previously observed in other vanadium(IV) containing systems.[25]

To confirm that our observation can be associated with a poorly efficient energy transfer to the thermal bath and not with the changes induced by the mechanical stress on the crystallites, we have investigated the magnetization dynamics of **1a** covered by activated carbon (**1a′**). This is expected to favour the thermal exchange between the helium gas (acting as the bath) and the crystallites, resulting in a faster relaxation process. The extracted spin–lattice relaxation times, (Fig. S12†) evidence a small but significant reduction of τ for **1a′**, and that this effect is more pronounced at low temperatures. These results confirm that the heat exchange between the crystallites and the bath plays a key role in determining the relaxation time.

Finally, to evaluate the contribution of the crystal and the molecular structures on spin–phonon bottleneck, we analysed the magnetization dynamics of **2** and **3**. AC susceptibility was measured only for macroscopic crystallites as obtained from crystallization (*d ca.* 1 mm) (**2a** and **3a**) and for the same crystallites subsequently crushed into microcrystalline powders (*d ca.* 10 μm) (**2c** and **3c**), in the same field and temperature range of **1**. The data for the real, χ', and the imaginary, χ'', component of the susceptibility for **2** and **3** are given in the ESI (Fig. S13–S16†). Fig. 3b shows the temperature dependence of the extrapolated relaxation times τ, evidencing that, as observed for **1**, also **2** and **3** exhibit a significant dependence of τ on the crystallite size.

To directly compare the effect of the crystallite size on τ, and thus the relative importance of the bottleneck effect in the three investigated complexes, we also show in Fig. 4 the ratio between the relaxation time τ of the macroscopic crystallites (**a**) and that of the crushed crystallites (**c**). Indeed, according to eqn (2), in the macroscopic crystallites the effect should be maximum, whereas it should be negligible in the other ones.

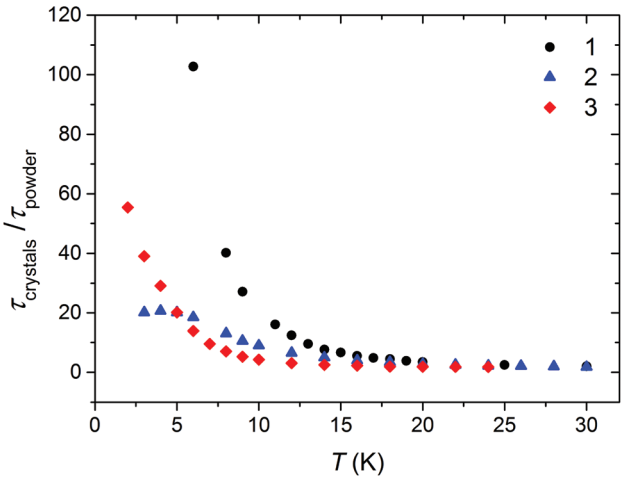

Fig. 4 Ratio between the relaxation time of the magnetization of the macroscopic crystallites (crystals) and the crushed crystallites (powders) for **1**, **2** and **3** as a function of the temperature at $B = 0.2$ T.

This approach allows one to highlight a clear trend for the three compounds: the smaller the mass of the molecule, the higher is the temperature at which size effects become visible. We further note that while **1** and **3** show a constant increase of this ratio on lowering the temperature, **2** reaches a plateau around 5 K. This is probably due to the different morphologies of the crystals: **1** and **3** form almost isometric crystals, while **2** forms thin plates, thus hampering the realization of the infinite size regime for this compound.

We can conclude that this experimental investigation surprisingly proved a neat and remarkable relationship between the dynamic magnetic properties of vanadyl β-diketonate and their organic ligand moieties, suggesting a strong correlation between the spin relaxation and vibrational degrees of freedom.

Theoretical calculations

In order to provide a microscopic link between the observed experimental behaviour for the relaxation time in **1**, **2** and **3** and their structural features, lattice dynamics simulations were performed for all of them.

The phonon dispersion curves for **1–3**, shown in Fig. 5, have been calculated along the arbitrary path X(0.5,0,0)-Γ(0,0,0)-Y(0,0.5,0)-Γ(0,0,0)-Z(0,0,0.5), where the coordinates are expressed in the reciprocal lattice basis units. They show optical modes lying at extremely low energy. This hints at a possible important role of these modes in the lattice dynamics even in the low temperature regime, where usually only acoustic phonons are expected to be populated. Furthermore, the mixing between the latter and the low lying optical modes is present for all the compounds.

The most striking difference between the three compounds is the increased number of bands in the low energy region of the vibrational spectra, passing from **1** to **3**. This effect is due to the increasing size of their unit cells, which in turn makes

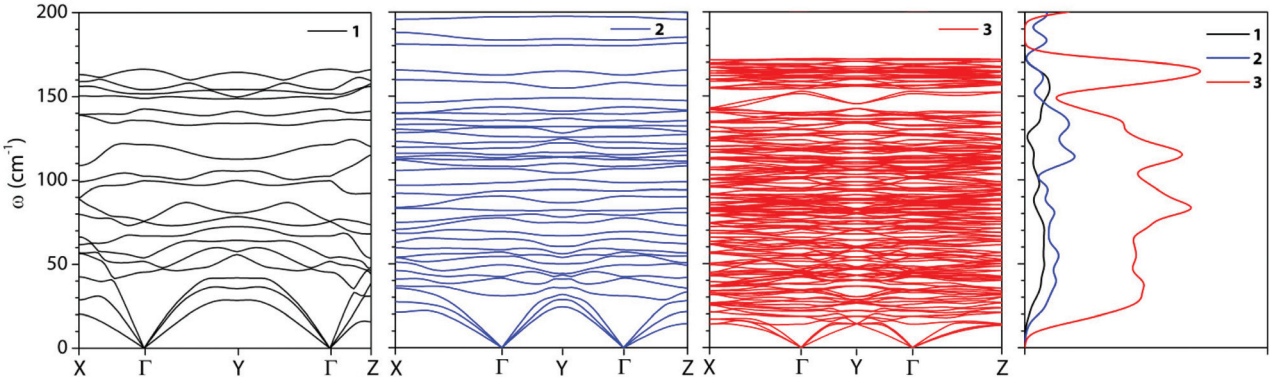

Fig. 5 Dispersion curves for **1**, **2** and **3** (left) and normalized vibrational DOS (right).

possible the formation of more low-energy delocalized vibrations, involving, for instance, local molecular rotations and internal torsions. This feature is also highlighted by the vibrational density of states (DOS), shown on the right hand side of Fig. 5. Indeed, the smallest density of states is computed for **1** while a much higher phonon density of states is computed for **3**. An intermediate result is computed for **2**.

A similar trend is also observed for the temperatures at which the three systems access the non-zero density of states: the lowest and the highest were found for **3** and **1**, respectively.

Along the same progression of the unit cell dimensions (*vide supra*), it is also possible to observe the reduction of the acoustic bands slope. This is in agreement with the dependence of this property on the inverse square root of the mass of the unit cell. Indeed, proceeding from **1** to **3**, the slope of the acoustic branch, which correlates with the speed of sound in the crystal, decreases and an increased efficiency in promoting relaxation is thus expected.

As already discussed, the spin–phonon bottleneck effect is related to the inefficiency of the crystal lattice to dissipate the phonons created during the spin relaxation process. Therefore, the possibility to observe a deviation of the spin dynamics as a side effect of the spin–phonon bottleneck is directly related to the conductivity of the material where the spin is embedded in. According to the thermal conductivity (k) formula obtained from the Boltzmann transport equation (BTE), eqn (3),[43] each phonon (iq) in the system contributes to this property with three factors: its life-time τ_{iq}, its group velocity v and its specific heat C_v:

$$k_{\alpha\beta} = \sum_{iq} C_{viq} v_{iq}^{\alpha} v_{iq}^{\beta} \tau_{iq} \qquad (3)$$

At low temperatures, the k limiting factor is expected to be the lack of heat carriers (phonons) and this feature is accounted by the specific heat. This assumption is also in agreement with the Stoneham model (eqn (2)), where the ratio of the spin and lattice specific heats gauges the effects on τ by the phonon relaxation time, suppressing them completely for high lattice specific heat. When the latter condition does not apply, the crystal non-equilibrium features, such as the phonon life-time, become relevant also for the spin dynamics. It should also be noted that τ_{iq} itself would in principle contribute to reduce the lattice thermal conductivity. However, its effects in this respect are expected to become notable only at high temperatures, where the anharmonic phonon–phonon scattering processes take place. The specific heat of a given mode, with energy $\hbar\omega_{iq}$, vanishes at 0 K and starts increasing with T according to:

$$C_{viq} = k_B \left(\frac{\hbar\omega_{iq}}{2k_B T}\right)^2 \mathrm{cosech}^2\left(\frac{\hbar\omega_{iq}}{2k_B T}\right) \qquad (4)$$

According to eqn (3) and (4), the higher the phonon density of states near or below a certain $k_B T$, the higher would be the value of C_v and k at that temperature and, therefore, the lower would be the chance to observe the spin–phonon bottleneck. For what concerns the three samples under study, **1** is expected to show a spin–phonon bottleneck effect up to higher temperatures with respect to **2** and **3**, due to the dramatic drop in the amount of accessible phonons at frequencies lower than 30 cm^{-1} (40 K), corresponding to the highest temperature at which the spin–phonon bottleneck has been observed for this compound. The same argument holds for the comparison between **2** and **3**, where the latter would be expected to show a spin–phonon bottleneck to a lesser extent, as it indeed does. The presented analysis is, of course, mainly based on simple statistic considerations since it does not take into account the coupling of the vibrational and the spin degrees of freedom, but only a larger or minor density of states accessible at low temperatures. A preliminary attempt to face this problem was reported by Moreno *et al.*[44]

Conclusions

In the last couple of years, the investigation of the spin dynamics of simple molecules by AC susceptometry has allowed the identification of the vanadyl unit as of the most promising candidates for potential application as molecule based quantum bits.[9,10,33] However, the present study points out that these slow relaxing systems exhibit a giant spin–

phonon bottleneck and the relaxation times can vary over several orders of magnitude depending on the crystallite size. This evidences the need to carry out comparison of relaxation times obtained by different samples with special care. In particular, it is of absolute importance to separate the effects coming from the electronic structure and those related to the exchange of energy with the thermal bath.

The investigation of a series of compounds exhibiting the same electronic properties but different peripheral groups on the ligands has evidenced the key role played by the phonon spectrum on the magnetization dynamics, highlighting that smaller molecules exhibit a more pronounced spin–phonon bottleneck effect and in general a slower relaxation due to a higher velocity of acoustic phonons, as estimated from a combination of DFT and molecular dynamics approaches. Interestingly, similar comparative studies performed in frozen solution have not highlighted any significant trend.[14]

Though the concentrated samples investigated here are not expected to exhibit long coherence times, the possibility to evaporate them on surfaces makes this family of complexes extremely appealing to further investigate the spin dynamics, once these molecules are deposited on a substrate. Indeed the latter can influence not only electronic but also vibrational degrees of freedom of the molecular system, as evidenced in this work. The reduced efficiency of energy exchange from the spin system to the thermal bath could actually contribute to enhance the magnetic bistability, as observed for Ho atoms[20] or $TbPc_2$ SMMs[45] on MgO thin films, which constitute a very rigid lattice. In these experiments, performed under ultra-high vacuum conditions, the thermalisation of the spin systems occurs, in fact, through the substrate, whose rational choice could be an additional tool to control the molecular spin dynamics.

Experimental

General remarks

Acetylacetone (acac), dipivaloylmethane (dpm) and dibenzoylmethane (dbm) were purchased from Sigma-Aldrich.

Powder X-ray crystallography

Wide-Angle Powder X-ray Diffraction (PXRD) patterns on polycrystalline samples were recorded on a Bruker New D8 Advance DAVINCI diffractometer in a θ–θ configuration equipped with a linear detector. The scans were collected within the range of 5–40° (2θ) using CuK_α radiation (λ = 1.540 Å). The simulated patterns were generated from the atomic coordinates of the single crystal structure solutions using the Mercury CSD 3.3 program[46] (copyright CCDC, http://www.ccdc.cam.ac.uk/mercury/) using a FWHM (full width at half maximum) of 0.15 and a 2θ step of 0.025.

Electron paramagnetic resonance (EPR) analysis

X-Band EPR spectra were recorded on a Bruker Elexsys E500 spectrometer equipped with a SHQ cavity (ν = 9.392 GHz). The low temperature (50 K) needed to freeze the measured solutions (1 mM, 2 : 3 toluene : CH_2Cl_2) was obtained using an Oxford Instruments ESR900 continuous flow helium cryostat.

Magnetic measurements

Alternate current (AC) susceptibility measurements were performed in the temperature range of 1.8–40 K with applied magnetic fields up to 8.8 T on polycrystalline samples of compounds **1–3**, by using a Quantum Design Physical Property Measurement System (PPMS) equipped with an AC susceptometer operating in the 10 Hz–10 kHz frequency range and a Quantum Design Magnetic Property Measurement System (MPMS) equipped with a Superconducting Quantum Interference Device (SQUID) AC susceptometer operating in the 0.1 Hz–1 kHz frequency range at the same gas exchange pressure (*ca.* 10 Torr) for all measurements. All samples were measured by wrapping in Teflon. The well crushed (c) samples were also pressed into a pellet. Susceptibility and magnetic data were corrected for the sample holder previously measured under the same conditions and for the diamagnetic contributions as deduced by using Pascal's constant tables (Fig. S7–S16†).[47]

Force field parameterization

Force field parameters for the three molecules have been derived following the procedure outlined by Ryde[48] and using the software Hess2FF.[49] This approach requires the calculation of the Hessian matrix for the three isolated molecules in order to map their eigenvalues and eigenvectors on the chosen intramolecular force field energy representation. In this work, the energy has been chosen according to the GAFF procedure,[50] except for the choice of completely screening the non-bonded 1–4 interactions (they have been set to zero) in order to minimize the known shortcomings of the parameterization method.[48] In this framework, all the parameters related to the internal degrees of freedom have been optimized and no use of the GAFF library has been made for the intra-molecular interactions. On the other hand, the non-bonded part of the force field, composed of vdW and coulomb interactions, has been set up with the original GAFF's Lennard Jones parameters and with RESP charges. The assessment of the FF quality has been made on the basis of its ability to reproduce the structural features of both isolated molecules and their crystalline cells. While the isolated DFT calculations used as a basis for the FF mapping offer a straightforward way to rationalize the quality of the mapping itself, another set of *ab initio* reference calculations for the periodic crystals must be provided. This second reference has been produced through the optimization of the unit cells for **1**, **2** and **3** with a periodic boundary condition based DFT software (pDFT). A good overall agreement has been obtained between FF, DFT, pDFT and experimental parameters. The details of these tests are listed and further discussed in the ESI.†

All the aforementioned optimization, Hessian and RESP charge calculations on the isolated molecules have been carried out with the software Gaussian 09[51] at the DFT level of theory. All the elements have been described with a 6-31G*

basis set and the PBE[52] functional. pDFT calculations have been executed on the molecular unit cell with the CP2K software,[53] employing the PBE functional with the DZVP-MOLOPT basis set and a plane wave cut-off of 500 Ry, for all the elements. In all DFT simulation protocols the Grimme's D3 vdW correction scheme has been employed.[54]

Lattice dynamics

Crystal property calculations have been carried out with in-house software for the lattice dynamics part and with the LAMMPS molecular dynamics package[55] for what concerns crystal cell optimization and force calculations. Forces have been calculated employing Ewald summations on the reciprocal space with an accuracy of 1.0×10^{-8} for the long-range part of both electrostatic and dispersion interactions.

The dynamical matrices of the three molecule supercells have been computed by force fields through LAMMPS. The supercell of **1** and **2** has been modelled as $3 \times 3 \times 3$ times the primitive cell (two molecules each), while the supercell of **3**, due to the larger amount of molecules contained, has been modelled as $2 \times 2 \times 2$ times the primitive cell (eight molecules). The three supercells have been optimized with LAMMPS through a thermal annealing procedure with a final optimization at 0 K of both atomic positions and cell parameters. The optimized supercells were then used to evaluate the lattice properties by perturbation theory.[56] The real space dynamical matrix elements are defined as

$$f_{st}(ki,k'j) = \frac{\partial^2 E}{\partial x_{kis} \partial x_{k'jt}} \quad (5)$$

The indexes k and k' run over the cells inside the supercell, i and j run over the atoms inside the specific cell while s and t run over the three Cartesian spatial coordinates. The calculation of $f_{st}(ki, k'j)$ has been done by numerical differentiation, displacing each atom in the primitive cell by +/−0.01 Å along the three spatial directions. Convergence of the results with respect to the differentiation step has been checked. The real space force constants have then been used to build the dynamical matrix

$$D_{st}(ij,q) = \frac{1}{\sqrt{m_i m_j}} \sum_{k'} f_{st}(ki,k'j) \exp[iq \cdot (r(k') - r(k))] \quad (6)$$

where m are the masses of the atoms in the $k\backslash k'$ cell inside the considered supercell and q represents a vector in the reciprocal primitive lattice. Finally, $r(k) - r(k')$ represents the distance between the primitive cell k and the considered cell k' in the supercell.

The vibrational density of states (DOS) is defined as

$$\mathrm{DOS}(\omega) = \frac{1}{N_q} \sum_{\alpha q} \delta(\omega - \omega_{\alpha q}) \quad (7)$$

where N_q is the number of q-points in the reciprocal space and $\omega_{\alpha q}$ is the α eigenvalue obtained through diagonalization of the dynamical matrix $D(q)$.

The DOS values have been obtained integrating the Brillouin zone with an $8 \times 8 \times 8$ regular mesh of points in the crystal reciprocal space. A normalized Gaussian broadening, with a σ of 5 cm^{-1}, has also been applied to all frequencies.

Acknowledgements

Dr S. Ciattini (CRIST, Univ. of Florence) is acknowledged for assistance in microtomography experiments and Dr M. Perfetti for useful discussion. We acknowledge the financial support of the European Research Council (ERC) through AdG MolNanoMaS (267746), the Italian MIUR through the project Futuro in Ricerca 2012 (RBFR12RPD1), and Fondazione Ente Cassa di Risparmio di Firenze.

Notes and references

1 D. Gatteschi, R. Sessoli and J. Villain, *Molecular nanomagnets*, Oxford University Press, Oxford, UK, 2006.
2 J. Dreiser, *J. Phys.: Condens. Matter*, 2015, **27**, 183203.
3 A. Cornia and M. Mannini, *Struct. Bonding*, 2014, **150**, 1–38.
4 M. L. Perrin, E. Burzurí and H. S. J. van der Zant, *Chem. Soc. Rev.*, 2015, **44**, 902–919.
5 M. Urdampilleta, S. Klyatskaya, J. P. Cleuziou, M. Ruben and W. Wernsdorfer, *Nat. Mater.*, 2011, **10**, 502–506.
6 E. Burzurí, Y. Yamamoto, M. Warnock, X. Zhong, K. Park, A. Cornia and H. S. J. van der Zant, *Nano Lett.*, 2014, **14**, 3191–3196.
7 A. Ardavan, O. Rival, J. J. L. Morton, S. J. Blundell, A. M. Tyryshkin, G. A. Timco and R. E. P. Winpenny, *Phys. Rev. Lett.*, 2007, **98**, 057201.
8 K. Bader, D. Dengler, S. Lenz, B. Endeward, S.-D. Jiang, P. Neugebauer and J. van Slageren, *Nat. Commun.*, 2014, **5**, 5304.
9 M. Atzori, L. Tesi, E. Morra, M. Chiesa, L. Sorace and R. Sessoli, *J. Am. Chem. Soc.*, 2016, **138**, 2154–2157.
10 L. Tesi, E. Lucaccini, I. Cimatti, M. Perfetti, M. Mannini, M. Atzori, E. Morra, M. Chiesa, A. Caneschi, L. Sorace and R. Sessoli, *Chem. Sci.*, 2016, **7**, 2074–2083.
11 M. Warner, S. Din, I. S. Tupitsyn, G. W. Morley, A. M. Stoneham, J. A. Gardener, Z. Wu, A. J. Fisher, S. Heutz, C. W. M. Kay and G. Aeppli, *Nature*, 2013, **503**, 504–508.
12 C. J. Wedge, G. A. Timco, E. T. Spielberg, R. E. George, F. Tuna, S. Rigby, E. J. L. McInnes, R. E. P. Winpenny, S. J. Blundell and A. Ardavan, *Phys. Rev. Lett.*, 2012, **108**, 107204.
13 J. M. Zadrozny, J. Niklas, O. G. Poluektov and D. E. Freedman, *J. Am. Chem. Soc.*, 2014, **136**, 15841–15844.
14 J. M. Zadrozny, J. Niklas, O. G. Poluektov and D. E. Freedman, *ACS Cent. Sci.*, 2015, **1**, 488–492.
15 M. A. Nielsen and I. L. Chuang, *Quantum Computation and Quantum Information*, Cambridge University Press, Cambridge, 2000.

16 J. Ferrando-Soria, E. M. Pineda, A. Chiesa, A. Fernandez, S. A. Magee, S. Carretta, P. Santini, I. J. Vitorica-Yrezabal, F. Tuna, G. A. Timco, E. J. L. McInnes and R. E. P. Winpenny, *Nat. Commun.*, 2016, **7**, 11377.
17 K. Bader, M. Winkler and J. van Slageren, *Chem. Commun.*, 2016, **52**, 3623–3626.
18 A. Morello, *Nat. Mater.*, 2015, **14**, 135–136.
19 A. Morello, *Nanotechnology*, 2015, **26**, 502501.
20 F. Donati, S. Rusponi, S. Stepanow, C. Wäckerlin, A. Singha, L. Persichetti, R. Baltic, K. Diller, F. Patthey, E. Fernandes, J. Dreiser, Ž. Šljivančanin, K. Kummer, C. Nistor, P. Gambardella and H. Brune, *Science*, 2016, **352**, 318–321.
21 J. H. van Vleck, *Phys. Rev.*, 1941, **59**, 724–729.
22 K. S. Pedersen, J. Dreiser, H. Weihe, R. Sibille, H. V. Johannesen, M. A. Sørensen, B. E. Nielsen, M. Sigrist, H. Mutka, S. Rols, J. Bendix and A. S. Piligkos, *Inorg. Chem.*, 2015, **54**, 7600–7606.
23 A. M. Stoneham, *Proc. Phys. Soc.*, 1965, **86**, 1163.
24 K. J. Standley and R. A. Vaughan, *Electron Spin Relaxation Phenomena in Solids*, Plenum Press, New York, 1969.
25 I. Chiorescu, W. Wernsdorfer, A. Muller, H. Bogge and B. Barbara, *Phys. Rev. Lett.*, 2000, **84**, 3454–3457.
26 K. Petukhov, S. Bahr, W. Wernsdorfer, A.-L. Barra and V. Mosser, *Phys. Rev. B: Condens. Matter*, 2007, **75**, 064408.
27 G. de Loubens, D. A. Garanin, C. C. Beedle, D. N. Hendrickson and A. D. Kent, *Europhys. Lett.*, 2008, **83**, 37006.
28 O. Waldmann, R. Koch, S. Schromm, P. Müller, I. Bernt and R. W. Saalfrank, *Phys. Rev. Lett.*, 2002, **89**, 246401.
29 D. M. Murphy, I. A. Fallis, R. D. Farley, R. J. Tucker, K. L. Avery and D. J. Willock, *Phys. Chem. Chem. Phys.*, 2002, **4**, 4937–4943.
30 E. Shuter, S. J. Rettig and C. Orvig, *Acta Crystallogr., Sect. C: Cryst. Struct. Commun.*, 1995, **51**, 12.
31 M. Mohamadi, S. Y. Ebrahimipour, M. Torkzadeh-Mahani, S. Foro and A. Akbari, *RSC Adv.*, 2015, **5**, 101063.
32 M. A. K. Ahmed, H. Fjellvåg, A. Kjekshus and B. Klewe, *Z. Anorg. Allg. Chem.*, 2004, **630**, 2311–2318.
33 M. Atzori, E. Morra, L. Tesi, A. Albino, M. Chiesa, L. Sorace and R. Sessoli, *J. Am. Chem. Soc.*, submitted for publication.
34 S. Stoll and A. Schweiger, *J. Magn. Reson.*, 2006, **178**, 42–55.
35 A. J. Fielding, D. B. Back, M. Engler, B. Baruah, D. C. Crans, G. R. Eaton and S. S. Eaton, *ACS Symp. Ser.*, 2007, **974**, 364–375.
36 J. P. Fackler, J. D. Levy and J. A. Smith, *J. Am. Chem. Soc.*, 1972, **94**, 2436–2445.
37 A. C. De Vroomen, E. E. Lijphart, D. Y. H. Prins, J. Marks and N. J. Poulis, *Physica*, 1972, **61**, 241–249.
38 J. H. van Vleck, *Phys. Rev.*, 1940, **57**, 426–447.
39 S. Gómez-Coca, A. Urtizberea, E. Cremades, P. J. Alonso, A. Camón, E. Ruiz and F. Luis, *Nat. Commun.*, 2014, **5**, 4300.
40 A. Abragam and B. Bleaney, *Electron Paramagnetic Resonance of Transition Ions*, Dover, New York, 1986.
41 K. N. Shrivastava, *Phys. Status Solidi B*, 1983, **117**, 437–458.
42 J.-L. Du, G. R. Eaton and S. S. Eaton, *J. Magn. Reson., Ser. A*, 1996, **119**, 240–246.
43 A. J. H. McGaughey and M. Kaviany, *Phys. Rev. B: Condens. Matter*, 2004, **69**, 094303.
44 L. E. Moreno, N. Suaud and A. Gaita-Ariño, arXiv:1512.05690, 2015.
45 C. Wäckerlin, F. Donati, A. Singha, R. Baltic, S. Rusponi, K. Diller, F. Patthey, M. Pivetta, Y. Lan, S. Klyatskaya, M. Ruben, H. Brune and J. Dreiser, *Adv. Mater.*, 2016, **28**, 5195–5199.
46 C. F. Macrae, P. R. Edgington, P. McCabe, E. Pidcock, G. P. Shields, R. Taylor, M. Towler and J. van de Streek, *J. Appl. Crystallogr.*, 2006, **39**, 453–457.
47 G. A. Bain and J. F. Berry, *J. Chem. Educ.*, 2008, **85**, 532.
48 L. H. Hu and U. Ryde, *J. Chem. Theory Comput.*, 2011, **7**, 2452–2463.
49 P. Rydberg, L. Olsen, P.-O. Norrby and U. Ryde, *J. Chem. Theory Comput.*, 2007, **3**, 1765–1773.
50 J. M. Wang, R. M. Wolf, J. W. Caldwell and P. A. Kollman, *J. Comput. Chem.*, 2004, **25**, 1157–1174.
51 M. J. Frisch, G. W. Trucks, H. B. Schlegel, G. E. Scuseria, M. A. Robb, J. R. Cheeseman, G. Scalmani, V. Barone, B. Mennucci, G. A. Petersson, H. Nakatsuji, M. Caricato, X. Li, H. P. Hratchian, A. F. Izmaylov, J. Bloino, G. Zheng, J. L. Sonnenberg, M. Hada, M. Ehara, K. Toyota, R. Fukuda, J. Hasegawa, M. Ishida, T. Nakajima, Y. Honda, O. Kitao, H. Nakai, T. Vreven, J. A. Montgomery Jr., J. E. Peralta, F. Ogliaro, M. Bearpark, J. J. Heyd, E. Brothers, K. N. Kudin, V. N. Staroverov, R. Kobayashi, J. Normand, K. Raghavachari, A. Rendell, J. C. Burant, S. S. Iyengar, J. Tomasi, M. Cossi, N. Rega, J. M. Millam, M. Klene, J. E. Knox, J. B. Cross, V. Bakken, C. Adamo, J. Jaramillo, R. Gomperts, R. E. Stratmann, O. Yazyev, A. J. Austin, R. Cammi, C. Pomelli, J. W. Ochterski, R. L. Martin, K. Morokuma, V. G. Zakrzewski, G. A. Voth, P. Salvador, J. J. Dannenberg, S. Dapprich, A. D. Daniels, Ö. Farkas, J. B. Foresman, J. V. Ortiz, J. Cioslowski and D. J. Fox, *Gaussian 09, Revision E.01*, 2009.
52 A. Becke, *J. Chem. Phys.*, 1993, **98**, 5648–5652.
53 J. Hutter, M. Iannuzzi, F. Schiffmann and J. VandeVondele, *Wiley Interdiscip. Rev.: Comput. Mol. Sci.*, 2014, **4**, 15–25.
54 S. Grimme, J. Antony, S. Ehrlich and H. Krieg, *J. Chem. Phys.*, 2010, **132**, 154104.
55 S. Plimpton, *J. Comput. Phys.*, 1995, **117**, 1–19.
56 S. Califano, V. Schettino and N. Neto, *Lattice Dynamics of Molecular Crystals*, Springer, Berlin, 1981.

JACS
JOURNAL OF THE AMERICAN CHEMICAL SOCIETY

Communication

pubs.acs.org/JACS

Spin Dynamics and Low Energy Vibrations: Insights from Vanadyl-Based Potential Molecular Qubits

Matteo Atzori,*[,†] Lorenzo Tesi,[†] Stefano Benci,[†,‡] Alessandro Lunghi,[§] Roberto Righini,[†,‡] Andrea Taschin,[‡] Renato Torre,[‡,∥] Lorenzo Sorace,[†] and Roberta Sessoli*[,†]

[†]Dipartimento di Chimica "Ugo Schiff" & INSTM RU, Università degli Studi di Firenze, I50019 Sesto Fiorentino, Italy
[‡]European Laboratory for Nonlinear Spectroscopy, Università degli Studi di Firenze, I50019 Sesto Fiorentino, Italy
[§]School of Physics, AMBER and CRANN, Trinity College, Dublin 2, Ireland
[∥]Dipartimento di Fisica ed Astronomia, Università degli Studi di Firenze, I50019 Sesto Fiorentino, Italy

Supporting Information

ABSTRACT: Here we report the investigation of the magnetization dynamics of a vanadyl complex with diethyldithiocarbamate (Et_2dtc^-) ligands, namely $[VO(Et_2dtc)_2]$ (**1**), in both solid-state and frozen solution. This showed an anomalous and unprecedentedly observed field dependence of the relaxation time, which was modeled with three contributions to the relaxation mechanism. The temperature dependence of the weight of the two processes dominating at low fields was found to well correlate with the low energy vibrations as determined by THz spectroscopy. This detailed experimental comparative study represents a fundamental step to understand the spin dynamics of potential molecular quantum bits, and enriches the guidelines to design molecule-based systems with enhanced quantum coherence.

Quantum properties of matter such as entanglement, superposition and tunneling can be fruitfully employed to develop quantum computation, a novel computational paradigm based on the quantum bit, or qubit.[1] A qubit, with respect to the bit, has the property to be placed in a coherent superposition state other than the two classical 0 and 1 states. Various physical systems can be regarded as viable qubits, and among them electronic spins are seen as promising candidates.[2] Mainly, this is due to their easy manipulation through pulsed microwave radiations and electric fields.[2b,3] Electronic defects on silicon,[4] silicon carbide,[5] or diamond[6] are the best qubits candidates in the realm of purely inorganic materials. Although they satisfy some of the requirements to behave as viable qubits, they lack chemical tunability of their electronic/magnetic properties. Such a tunability can be instead achieved through chemical design of transition metal complexes.[7] Indeed, coordination compounds, mostly based on V^{IV} and Cu^{II},[8] have been demonstrated as effective as electronic defects in inorganic materials potential qubits, as far as the lifetime of the superposition state is concerned.[8c] Furthermore, the ability of coherently manipulate this superposition state up to room temperature was also proven.[8d]

The lifetime of the superposition state is denoted by T_2 or T_m, which are the spin−spin relaxation time, and the phase memory or quantum coherence time, respectively. Several efforts have been done in the last years to understand the factors affecting the absolute values and the temperature dependence of T_m. These studies provide specific design criteria to develop potential qubits with improved performances.[8e,9]

Another key parameter to evaluate the performances of a spin qubit is the spin−lattice relaxation time, T_1, which defines the time required to an excited spin to relax back to its ground state. Control of T_1 is of paramount importance; if too long it limits the speed of initialization of the qubit, while if too short it can limit T_2.[8e] This means that to enhance both the absolute value of T_m and its operational temperature range, a judicious control of T_1 is required. By introducing a unique structural difference, i.e., an oxovanadium(IV) in a square pyramidal versus a vanadium(IV) in an octahedral environment featuring the same coordinating ligand, we have recently demonstrated the effect of the vanadyl moiety in enhancing quantum coherence up to room temperature.[8e] This has been related to a less effective mechanism of spin−lattice relaxation, which can be evaluated by the exponent n (ca. 3) of the T dependence of the relaxation rate, T_1^{-1}, when compared to the nonoxo counterpart (n = 4). Indeed, the latter shows a more rapid collapse which hampers the observation of quantum coherence at room temperature, while the former reaches record T_m. Despite the relevance of the n exponent and its general relation to the stiffness of the lattice, i.e., to the Debye temperature θ_D,[10] clear correlations with the structural and electronic parameters of the spin center have not been established yet.

Moved from the interest to better understand the relation between relaxation mechanisms and vibrational energies in potential molecular qubits, we have selected as a promising candidate the diethyldithiocarbamate complex $[VO(Et_2dtc)_2]$ (**1**). Its magnetization dynamics, studied by alternate current (AC) susceptometry, showed an anomalous and unprecedentedly observed field dependence of the relaxation time. A detailed analysis revealed important insights on the role of low energy vibrations, experimentally detected by THz spectroscopy, on this behavior.

Compound **1** can be obtained by reaction of vanadyl sulfate with sodium diethyldithiocarbamate in a disareated water solution, similarly to what was already reported.[11] The

Received: February 6, 2017
Published: March 6, 2017

DOI: 10.1021/jacs.7b01266
J. Am. Chem. Soc. 2017, 139, 4338−4341

molecular structure of **1** shows a square pyramidal coordination geometry with the V^{IV} ion above the basal plane (0.75 Å). The apical position is occupied by an oxo ligand that forms a double bond with the V^{IV} ion. The V═O bond distance is 1.591 Å long and it is in the usual range for vanadyl complexes.[8d,e,9b,c,12] On the other coordination sites the metal is chelated by two Et_2dtc^- anions (Figure 1).

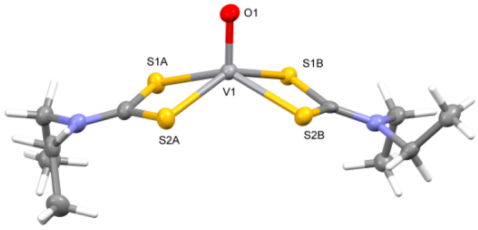

Figure 1. Molecular structure of **1** with principal atoms labeling scheme. A and B refer to two crystallographically independent ligands.

The V—S single bond lengths are in the 2.395−2.414 Å range and are slightly longer than those observed for vanadyl−dithiolenes complexes.[8e,9b,c] The presence of such a short V═O bond is responsible for a *d*-orbitals splitting of the metal centers in which the d_{xy} orbital lies lowest in energy and well separated from the other orbitals. This quenches the orbital contribution to the ground state when compared to other coordination geometries, as the pseudo-octahedral one, and makes **1** a potential qubit with expected enhanced performances. Interestingly, the terminal methyl groups of one Et_2dtc^- ligand are oriented, as expected, above and below the S_2CN plane of the ligand, whereas in the other one they are both oriented in the same direction (Figure 1). This sterically unfavorable orientation may be driven from the presence of short-contacts involving the terminal methyl groups (Figure S1).[11] Powder X-ray diffraction analysis performed on **1** allowed to ascertain structural phase homogeneity (Figure S2).

Continuous-wave EPR spectra on frozen solution were recorded to have a full description of the electronic properties of **1** (Figure S3). The spectrum shows the 8-fold hyperfine splitting due to the coupling between the $S = 1/2$ electronic spin of V^{IV} and the $I = 7/2$ nuclear spin of ^{51}V (natural abundance 99.76%). The signal is further split by the anisotropic components of the Landé factor and the hyperfine coupling. Spectral simulations[13] performed on the basis of the following spin Hamiltonian

$$\mathcal{H} = \hat{I}\cdot\mathbf{A}\cdot\hat{S} + \mu_B\hat{S}\cdot\mathbf{g}\cdot\mathbf{B} \quad (1)$$

allow one to simulate the spectrum of **1** with the following parameters: $g_x = 1.985(1)$, $g_y = 1.989(1)$, $g_z = 1.969(1)$; $A_x = 153(2)$ MHz, $A_y = 135(2)$ MHz, $A_z = 440(2)$ MHz (Figure S3).

The relaxation time τ, which is representative of the spin−lattice relaxation, was investigated by AC susceptometry as a function of the temperature at four selected static magnetic field values. When a small static magnetic field (>40 mT) is applied, **1** shows slow relaxation of the magnetization. The frequency dependence of the imaginary component of the susceptibility (χ'') are well reproduced with the Debye model (Figures S4−S7) and the extracted values of τ as a function of T are reported in Figure 2a. Slow magnetic relaxation is observed in the entire studied T range (4.0−50 K) with quite long relaxation times. They range from ca. 5.0 ms at 4.0 K to ca. 0.03 ms at 50 K. As the strength of the magnetic field increases, longer relaxation times are observed. The T dependence of τ, reveals, independently from the strength of the applied field, a change in the slope at low temperature (Figure 2a), which is indicative of a change in the nature of the main relaxation mechanism involved. Thus, the T dependence of the relaxation rate (τ^{-1}) has been modeled assuming two contributions to the relaxation. A direct mechanism dominating at low temperature and a Raman mechanism dominating at high temperature

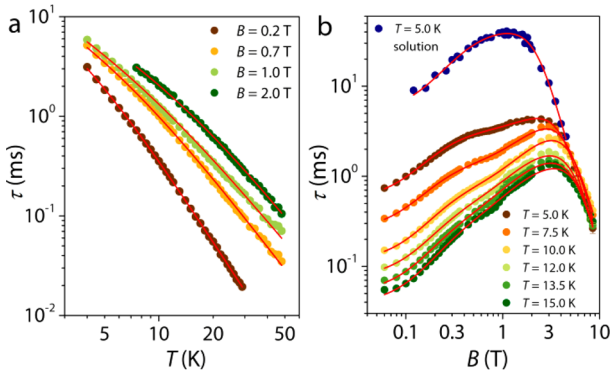

Figure 2. Temperature (a) and field (b) dependence of τ for **1** at different static magnetic fields and temperatures (see legends). Solid lines are the best-fits of the models (see text).

$$\tau^{-1} = aT + bT^n \quad (2)$$

where a is the coefficient of the direct mechanism, and b and n the coefficient and the exponent of the Raman mechanism, respectively. This model satisfactorily reproduces the T dependence of τ with the best-fit parameters reported in Table S1. The fit furnishes very low values of the Raman exponent $n < 3$, which are not unusual for vanadyl systems, as recently found.[8d,e] Attempts to reproduce the data either assuming an Orbach process or expanding the Raman term according to the Debye model[10] (Figure S8) were unsuccessful, the latter providing a field dependent θ_D.

To get deeper insights on the relaxation mechanisms involved, the dynamics was studied as a function of the static magnetic field in a wide field range (0.0−8.5 T) at different temperatures (Figures S9−S14). The extracted relaxation times are reported in Figure 2b. The field dependence of τ for **1** shows (i) very long relaxation times, and (ii) an anomalous and unprecedentedly observed behavior. The relaxation time shows a rapid increase at low fields, reaches an apparent maximum value at ca. 0.5 T, stays almost constant up to ca. 1.0 T, and then suddenly increases further up to ca. 3.0 T. If the field is increased further, τ quickly collapses to ca. 0.3 ms. Previously investigated vanadyl systems have shown a more regular behavior: τ rapidly reaches a maximum value and then remains almost unchanged up to ca. 3.5−4 T.[8d,e,12] The behavior at high fields ($B > 3.0$ T) is related to the more efficient spin-phonon direct mechanism of relaxation ($\tau^{-1} \propto B^4$). Indeed, the larger is the energy separation of the two m_S states, the higher is the phonon density with an energy corresponding to this difference. At low fields ($B < 0.3$ T), the relaxation is instead promoted by spin−spin and spin−nuclei interactions. These interactions are suppressed by increasing the field due to the lower influence of the hyperfine and spin−spin coupling, so that τ usually shows maximum values at intermediate fields.

What it is unusual here is the presence of a pronounced shoulder at ca. 0.5 T, suggesting that more than two

DOI: 10.1021/jacs.7b01266
J. Am. Chem. Soc. 2017, 139, 4338−4341

contributions to the relaxation are involved in determining the B dependence of τ^{-1} for **1**. To exclude that this effect is related to inhomogeneous crystallite sizes, and, consequently, to spin-phonon bottleneck effects,[12] the measurements were also repeated on a finely milled sample. No appreciable differences were observed in the two morphological states, and only a small discrepancy in the absolute values of τ is evidenced (Figure S15).

Prior to this work, the magnetic field dependence of the relaxation rate was reproduced with the Brons–van Vleck model, which takes into account the two above-mentioned contributions to the relaxation through the following expression[14]

$$\tau^{-1} = cB^4 + d\frac{1 + eB^2}{1 + fB^2} \quad (3)$$

where the first term is related to the direct mechanism, and the second term takes into account the effect of the internal magnetic field in promoting relaxation. This can be viewed as the sum of intra- and intermolecular effects, i.e., the sum of spin–nuclei hyperfine interactions and spin–spin dipolar magnetic interactions. More specifically, d represents the relaxation at zero field, f the ability of the external magnetic field to suppress the internal relaxation mechanisms, and e the attitude of the internal magnetic moments to induce relaxation. This last may be considered proportional to the number and strength of the internal spins. This model does not reproduce the B dependence of τ shown by **1** due to the anomalous behavior at intermediate fields. An analysis of the various magnetic field regions suggests that for $B > 3.0$ T the relaxation rate decay is well reproduced through a B^4 dependence for all temperatures, as expected for the direct mechanism, while at intermediate fields the dependence of the relaxation rate suggests the presence of two distinguishable contributions of the internal-field-type. Accordingly, the expression of the Brons–van Vleck model (eq 3) has been extended as follows

$$\tau^{-1} = cB^4 + d\frac{1 + eB^2}{1 + fB^2} + g\frac{1 + eB^2}{1 + hB^2} \quad (4)$$

This model well reproduces the B dependence of τ^{-1} (red lines in Figure 2b) with the best-fit parameters reported in Table S2. It must be stressed here that at any field and temperature only one relaxation time with a narrow distribution is observed. Thus, eq 4 refers to three intrinsic relaxation mechanisms of the same molecular species.

It emerges from this analysis that (i) the efficiency of the direct mechanism to promote relaxation at high fields is almost temperature independent in the investigated T range, (ii) the attitude of the internal spins to promote relaxation does not significantly change and allows to fit well all the $B < 3.0$ T region, (iii) the T dependences of both d and g parameters follow an exponential growth, thus suggesting that some well-defined energy levels are involved in the relaxation mechanism. Even if the overall T dependence of τ^{-1} does not follow an Arrhenius law, the individual single processes described by the d and g parameters actually seem to be proportional to $\exp(U_{eff}/k_BT)$. The plots of $\ln(d)$ and $\ln(g)$ vs T^{-1} (Figure 3a,b) are in fact almost linear over a relatively wide T range and the corresponding linear fit provides U_{eff} values of ca. 20(2) cm^{-1} and 15(2) cm^{-1} for d and g respectively, which well match with the typical energies of low energy vibration modes.[12] An analogous analysis has been thus performed on a microcrystal-

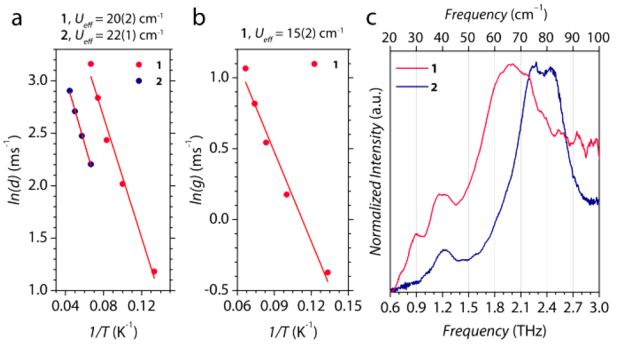

Figure 3. Arrhenius plots of d (a) and g (b) parameters, and vibrational spectra in the 0.6–3.0 THz range (c) for **1** and **2**.

line sample of a previously investigated vanadyl-complex, $[VO(acac)_2]$ (acac = acetylacetonate) (**2**),[12] which has been taken as reference. **2** shows a B dependence of τ^{-1} that can be described through the simpler Brons–van Vleck model (eq 3), with only one direct and one Raman mechanism (Figure S16 and Table S3). The T dependence of the d parameter furnishes for **2** an U_{eff} of ca. 22(1) cm^{-1}.

To validate the hypothesis that vibrational modes are involved in the relaxation, room temperature time-domain THz spectroscopy (0.1–3.0 THz range) was employed to record high signal-to-noise spectra (see Supporting Information)[15] on **1** and **2** (Figure 3c). THz spectroscopy has already been used in the field of molecular magnetism to characterize the zero field splitting of 3d and 4f based complexes,[16] but, to the best of our knowledge, its use to correlate spin dynamics and low energy vibrations is unprecedented, although the latter are attracting increasing interest.[17] The spectra (Figure 3c) reveal significant differences for the two compounds. In particular, the lowest energy vibration is observed at ca. 40 cm^{-1} for **2**, whereas two well separated peaks at ca. 30 and 40 cm^{-1} are observed for **1**. Both exhibit a stronger absorption at ca. 65 and 80 cm^{-1}, respectively. The energy values of the vibrational modes well correlates with the extracted activation energies of the relaxation mechanism in competition with the direct process. A relation of the type $U_{eff} = h\omega_v/2$ seems to hold. Interestingly, this dependence was recently theoretically predicted for the relaxation of $S > 1/2$ systems characterized by easy-axis magnetic anisotropy, i.e., single molecule magnets (SMM), when excited spin levels with lower $|m_S|$ are much higher in energy than the low energy optical phonons.[18] It thus appears that $S = 1/2$ spin systems can be seen as a limiting case of this model.

Thus, although the field dependence of the spin dynamics of $S = 1/2$ systems at high fields is clearly described through the direct mechanism of relaxation, at low and intermediate fields a relaxation mechanism dependent on the frequency of the low energy vibrational modes seems involved. Interestingly, the detailed analysis of the field dependence on **1** has allowed to disentangle the two contributions coming from the two low energy vibrational modes. As these modes, most likely, involve vibrations distributed on the molecular periphery and strongly admixed with lattice vibrations, a less discontinuous behavior should be observed in frozen solution where the asymmetry of the ethyl groups, induced by the intermolecular contacts, is lost. To corroborate this hypothesis, the magnetization dynamics of **1** was investigated as a function of the magnetic field at $T = 5$ K in a CH_2Cl_2/toluene frozen solution. The relaxation times extracted with the Debye model (Figure S17) are reported in

DOI: 10.1021/jacs.7b01266
J. Am. Chem. Soc. 2017, 139, 4338–4341

Figure 2b. A striking change in the B dependence of τ is observed when passing from the solid-state to the solution. Whereas at high fields the relaxation time decay is that typical of the direct process, at low fields the pronounced shoulder of the crystalline phase is not observed, and the data can thus be well reproduced with eq 3 (Table S2). This suggests that the asymmetry of the ethyl groups on the ligand, most likely lost in solution, plays a key role. A detailed theoretical analysis is necessary to confirm this hypothesis, as well as to elucidate why the two processes in **1** exhibit different field dependences. We can only anticipate that distinct vibrations can affect different parameters of the spin Hamiltonian, resulting in eigenstates composition which might then be differently affected by the applied field.

In conclusion, this study represents a first attempt to correlate experimentally the spin relaxation parameters to the vibrational spectrum of molecular systems of interest as potential qubits. Low energy vibrations, whose role has been recently highlighted for anisotropic magnetic molecules, seems to govern the spin dynamics in a wide field and temperature range of these vanadyl $S = 1/2$ systems. In contrast to SMMs, where an Arrhenius law with an effective barrier not matching the spin levels is encountered, a less informative power law temperature dependence is usually observed for molecular spin qubits. A detailed analysis of the magnetization dynamics through a bidimensional AC susceptometry investigation, scanning both field and temperature, has allowed to isolate the T dependence of the single processes contributing to the magnetic relaxation, and to retrieve for the first time physical parameters that seem to correlate directly with the very low energy vibration modes. The combination with THz spectroscopy studies contributed to shed light on the relaxation mechanism involved. If widely employed, such a multitechnique approach will allow one to establish rational synthetic strategies to protect spin quantum coherence from vibrations.

■ ASSOCIATED CONTENT

Supporting Information

The Supporting Information is available free of charge on the ACS Publications website at DOI: 10.1021/jacs.7b01266.

Additional figures and tables, and experimental section (PDF)

Crystallographic data for **1** (CIF)

■ AUTHOR INFORMATION

Corresponding Authors

*matteo.atzori@unifi.it

*roberta.sessoli@unifi.it

ORCID

Matteo Atzori: 0000-0003-1357-6159

Lorenzo Tesi: 0000-0003-4001-8363

Stefano Benci: 0000-0001-6492-1616

Alessandro Lunghi: 0000-0002-1948-4434

Roberto Righini: 0000-0003-0260-0248

Lorenzo Sorace: 0000-0003-4785-1331

Roberta Sessoli: 0000-0003-3783-2700

Notes

The authors declare no competing financial interest.

■ ACKNOWLEDGMENTS

The financial support of Italian MIUR (PRIN Project 2015 HYFSRT), Fondazione Ente Cassa di Risparmio di Firenze, and European COST (CA15128 MOLSPIN) is acknowledged.

■ REFERENCES

(1) Nielsen, M.; Chuang, I. *Quantum Computation and Quantum Information*; Cambridge University Press: Oxford, 2004.

(2) (a) Leuenberger, M. N.; Loss, D. *Nature* **2001**, *410*, 789. (b) Ardavan, A.; Rival, O.; Morton, J. J. L.; Blundell, S. J.; Tyryshkin, A. M.; Timco, G. A.; Winpenny, R. E. P. *Phys. Rev. Lett.* **2007**, *98*, 057201.

(3) Laucht, A.; Muhonen, J. T.; Mohiyaddin, F. A.; Kalra, R.; Dehollain, J. P.; Freer, S.; Hudson, F. E.; Veldhorst, M.; Rahman, R.; Klimeck, G.; Itoh, K. M.; Jamieson, D. N.; McCallum, J. C.; Dzurak, A. S.; Morello, A. *Sci. Adv.* **2015**, *1*, e1500022.

(4) Pla, J. J.; Tan, K. Y.; Dehollain, J. P.; Lim, W. H.; Morton, J. J. L.; Jamieson, D. N.; Dzurak, A. S.; Morello, A. *Nature* **2012**, *489*, 541.

(5) Tyryshkin, A. M.; Tojo, S.; Morton, J. J. L.; Riemann, H.; Abrosimov, N. V.; Becker, P.; Pohl, H.-J.; Schenkel, T.; Thewalt, M. L. W.; Itoh, K. M.; Lyon, S. A. *Nat. Mater.* **2012**, *11*, 143.

(6) Balasubramanian, G.; Neumann, P.; Twitchen, D.; Markham, M.; Kolesov, R.; Mizuochi, N.; Isoya, J.; Achard, J.; Beck, J.; Tissler, J.; Jacques, V.; Hemmer, P. R.; Jelezko, F.; Wrachtrup, J. *Nat. Mater.* **2009**, *8*, 383.

(7) (a) Troiani, F.; Affronte, M. *Chem. Soc. Rev.* **2011**, *40*, 3119. (b) Aromi, G.; Aguila, D.; Gamez, P.; Luis, F.; Roubeau, O. *Chem. Soc. Rev.* **2012**, *41*, 537. (c) Ferrando-Soria, J.; Moreno Pineda, E.; Chiesa, A.; Fernandez, A.; Magee, S. A.; Carretta, S.; Santini, P.; Vitorica-Yrezabal, I. J.; Tuna, F.; Timco, G. A.; McInnes, E. J. L.; Winpenny, R. E. P. *Nat. Commun.* **2016**, *7*, 11377.

(8) (a) Warner, M.; Din, S.; Tupitsyn, I. S.; Morley, G. W.; Stoneham, A. M.; Gardener, J. A.; Wu, Z.; Fisher, A. J.; Heutz, S.; Kay, C. W. M.; Aeppli, G. *Nature* **2013**, *503*, 504. (b) Bader, K.; Dengler, D.; Lenz, S.; Endeward, B.; Jiang, S.-D.; Neugebauer, P.; van Slageren, J. *Nat. Commun.* **2014**, *5*, 5304. (c) Zadrozny, J. M.; Niklas, J.; Poluektov, O. G.; Freedman, D. E. *ACS Cent. Sci.* **2015**, *1*, 488. (d) Atzori, M.; Tesi, L.; Morra, E.; Chiesa, M.; Sorace, L.; Sessoli, R. J. *J. Am. Chem. Soc.* **2016**, *138*, 2154. (e) Atzori, M.; Morra, E.; Tesi, L.; Albino, A.; Chiesa, M.; Sorace, L.; Sessoli, R. *J. Am. Chem. Soc.* **2016**, *138*, 11234.

(9) (a) Bader, K.; Winkler, M.; van Slageren, J. *Chem. Commun.* **2016**, *52*, 3623. (b) Yu, C.-J.; Graham, M. J.; Zadrozny, J. M.; Niklas, J.; Krzyaniak, M. D.; Wasielewski, M. R.; Poluektov, O. G.; Freedman, D. E. J. *J. Am. Chem. Soc.* **2016**, *138*, 14678. (c) Graham, M. J.; Yu, C.-J.; Krzyaniak, M. D.; Wasielewski, M. R.; Freedman, D. E. J. *J. Am. Chem. Soc.* **2017**, *139*, 3196.

(10) Fielding, A. J.; Fox, S.; Millhauser, G. L.; Chattopadhyay, M.; Kroneck, P. M. H.; Fritz, G.; Eaton, G. R.; Eaton, S. S. *J. Magn. Reson.* **2006**, *179*, 92.

(11) Henrick, K.; Raston, C. L.; White, A. H. *J. Chem. Soc., Dalton Trans.* **1976**, *26*, 26.

(12) Tesi, L.; Lunghi, A.; Atzori, M.; Lucaccini, E.; Sorace, L.; Totti, F.; Sessoli, R. *Dalton Trans.* **2016**, *45*, 16635.

(13) Stoll, S.; Schweiger, A. *J. Magn. Reson.* **2006**, *178*, 42.

(14) (a) Van Vleck, J. H. *Phys. Rev.* **1940**, *57*, 426. (b) De Vroomen, A. C.; Lijphart, E. E.; Prins, D. Y. H.; Marks, J.; Poulis, N. J. *Physica* **1972**, *61*, 241.

(15) Tasseva, J.; Taschin, A.; Bartolini, P.; Striova, J.; Fontana, R.; Torre, R. *Analyst* **2017**, *142*, 42.

(16) Rechkemmer, Y.; Fischer, J. E.; Marx, R.; Dörfel, M.; Neugebauer, P.; Horvath, S.; Gysler, M.; Brock-Nannestad, T.; Frey, W.; Reid, M. F.; van Slageren, J. *J. Am. Chem. Soc.* **2015**, *137*, 13114.

(17) Escalera-Moreno, L.; Suaud, N.; Gaita-Ariño, A. http://arxiv.org/abs/1512.05690v2 (accessed December 5, 2016).

(18) Lunghi, A.; Totti, F.; Sessoli, R.; Sanvito, S. *Nat. Commun.* **2017**, *8*, 14620.

DOI: 10.1021/jacs.7b01266
J. Am. Chem. Soc. 2017, 139, 4338−4341

Inorganic Chemistry
Cite This: Inorg. Chem. 2018, 57, 731−740
Article
pubs.acs.org/IC

Structural Effects on the Spin Dynamics of Potential Molecular Qubits

Matteo Atzori,*[,†] Stefano Benci,[‡] Elena Morra,[▽] Lorenzo Tesi,[†] Mario Chiesa,[▽] Renato Torre,[‡,§] Lorenzo Sorace,[†] and Roberta Sessoli*[,†]

[†]Dipartimento di Chimica "Ugo Schiff" & INSTM RU, Università degli Studi di Firenze, Via della Lastruccia 3, I50019 Sesto Fiorentino (Firenze), Italy

[‡]European Lab. for Non-Linear Spectroscopy, Università degli Studi di Firenze, I50019 Sesto Fiorentino (Firenze), Italy

[§]Dipartimento di Fisica ed Astronomia, Università degli Studi di Firenze, I50019 Sesto Fiorentino (Firenze), Italy

[▽]Dipartimento di Chimica e NIS Centre, Università di Torino, Via P. Giuria 7, I10125 Torino, Italy

Supporting Information

ABSTRACT: Control of spin−lattice magnetic relaxation is crucial to observe long quantum coherence in spin systems at reasonable temperatures. Such a control is most often extremely difficult to achieve, because of the coexistence of several relaxation mechanisms, that is *direct, Raman,* and *Orbach*. These are not always easy to relate to the energy states of the investigated system, because of the contribution to the relaxation of additional spin-phonon coupling phenomena mediated by intramolecular vibrations. In this work, we have investigated the effect of slight changes on the molecular structure of four vanadium(IV)-based potential spin qubits on their spin dynamics, studied by alternate current (AC) susceptometry. The analysis of the magnetic field dependence of the relaxation time correlates well with the low-energy vibrational modes experimentally detected by time-domain THz spectroscopy. This confirms and extends our preliminary observations on the role played by spin-vibration coupling in determining the fine structure of the spin−lattice relaxation time as a function of the magnetic field, for $S = {}^1/_2$ potential spin qubits. This study represents a step forward in the use of low-energy vibrational spectroscopy as a prediction tool for the design of molecular spin qubits with long-lived quantum coherence. Indeed, quantum coherence times of ca. 4.0−6.0 μs in the 4−100 K range are observed for the best performing vanadyl derivatives identified through this multitechnique approach.

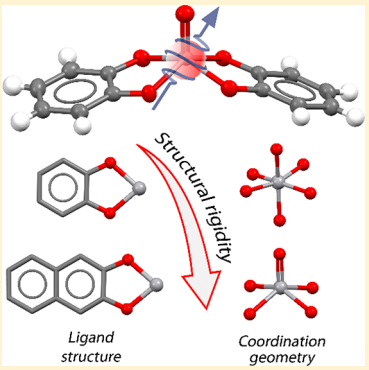

INTRODUCTION

In the past few years, great interest has been devoted to the experimental implementation of quantum information, one of the pillars of the technological revolution that is foreseen for the next decades. Quantum information has its core in the quantum bit, or qubit, i.e., a two-level quantum-mechanical system able to be placed in a state of coherent superposition.[1] Qubits implementation requires the accomplishment of stringent and somehow conflicting prerequisites known as DiVincenzo criteria,[2] and the preparation and investigation of viable qubits represents a current challenging research task. Several systems have been proposed as qubits, such as photons,[3] ionic traps,[4] superconducting circuits,[5] and spins.[6,7] Spin systems are particularly advantageous, from an application point of view, because they can be easily manipulated through external magnetic[8] and electric fields,[9] such as in electron paramagnetic resonance (EPR) techniques.

Spin qubits can be either nuclear or electronic, and nowadays, the most investigated ones are nitrogen-vacancy pairs in diamond[10,11] or defects in silicon.[6,12] In contrast, electronic spin systems based on paramagnetic metal ions in coordination complexes[13,14] are, to date, less investigated, even if they show higher tunability than purely inorganic systems. Indeed, the electronic spin in molecular systems can be finely controlled by playing with the coordination geometries and the bonded ligands.[7,15−18]

Despite the advantages related to their chemical tunability, molecular systems still show shorter lifetimes of the quantum superposition of states, which is a key parameter to evaluate their potential application for quantum logic operations.[1] The lifetime of the superposition state is determined by the spin−spin relaxation time T_2, and it is usually quantified by the phase memory time (T_m), which is a measurable lower limit of T_2. Remarkably, mononuclear vanadium(IV) complexes with nuclear spin-free ligands can attain, at low temperature, a T_m value on the order of a millisecond when dispersed in a nuclear spin-free solvent such as CS_2;[19] this value is comparable to those observed for electronic defects in extended lattices. Another fundamental parameter to evaluate the spin qubit performances is the spin−lattice relaxation time T_1, which represents the time required for an excited spin to relax back

Received: October 12, 2017
Published: December 27, 2017

DOI: 10.1021/acs.inorgchem.7b02616
Inorg. Chem. 2018, 57, 731−740

to its ground state. Control of T_1 is of crucial importance; if it is too long, it limits the speed of initialization of the qubit, whereas if it is too short, it induces a collapse of T_2, especially as the temperature increases.[20]

Control of spin−lattice relaxation in molecular systems, either spin qubits or single-molecule magnets (SMMs),[21] is very difficult to achieve as a consequence of different types of relaxation mechanisms that can be potentially involved, that is *direct*, *Raman*, and *Orbach*, all of which are related to different and specific energy states of the system and its surrounding lattice. Restricting the discussion to the class of molecular spin qubits based on $S = {}^1/_2$ spin states, where the Orbach mechanism of relaxation cannot be observed, because of the lack of available magnetic states besides the $m_S = \pm{}^1/_2$ doublet, the temperature dependence of the spin−lattice relaxation is mainly determined by the direct and the Raman mechanisms.

In a recent investigation, we have however suggested that the magnetic field dependence of the spin−lattice relaxation time in potential qubits based on the $S = {}^1/_2$ spin of the V^{IV} ion, is not simply determined by the combination of direct and Raman mechanisms of relaxation, but is also affected by relaxation mechanisms that involve low-energy vibrational modes.[22] Intramolecular vibrational modes were identified as one of the means by which the magnetization can relax back to the ground state, but the study concerning the correlation between the energy of the involved phonons and the spin−lattice relaxation time is still in its infancy. Indeed, a recent theoretical study has highlighted the key role of specific local vibration in determining the magnetic relaxation of molecular spin qubits by analyzing the modulation of the spin energy levels operated by molecular vibrations,[23] while another one has highlighted the role of phonons anharmonicity in determining the experimentally observed spin−lattice relaxation time in SMMs.[24,25] Both studies have stressed that control of local vibrations can be a winning strategy to design functional spin qubits or SMMs that can operate at higher temperatures.

Herein, we report the investigation of the magnetization dynamics of four vanadium(IV)-based complexes performed to understand the role played by the molecular structure of highly coherent spin qubits on their spin dynamics via spin-vibration coupling. More specifically, the rigidity of the coordination sphere was modified by synthesizing tris-chelated octahedral and vanadyl square-pyramidal complexes of the same ligand, while the ligand rigidity was modified by increasing the number of condensed aromatic rings. We have then identified and prepared two vanadyl complexes with catecholate (cat) and naphthalene-catecholate (naph-cat) ligands, namely $[(Ph)_4P]_2[VO(cat)_2]$ (**1**) and $[(Ph)_4P]_2[VO(naph\text{-}cat)_2]$ (**3**), and their respective tris-chelated octahedral complexes of the bare V^{IV} ion, namely, $[(Ph)_4P]_2[V(cat)_3]$ (**2**) and $[(Ph)_4P]_2[V(naph\text{-}cat)_3]$ (**4**). We have thus investigated (i) the magnetic relaxation as a function of the temperature and the applied magnetic field by alternate current (AC) susceptibility measurements, (ii) the low-energy vibrational modes for the four systems by time-domain THz spectroscopy, and (iii) the quantum coherence time of the best performing systems, identified by the combination of the above-mentioned techniques, as a function of the temperature, through pulsed EPR spectroscopy experiments.

The differences on the spin dynamics of the four selected systems are discussed with respect to the two main structural modifications introduced, revealing important insights on the role of chemical design to improve the performances of potential molecular spin qubits or SMMs.

RESULTS AND DISCUSSION

Synthesis. Catechol has exceptional chelating ability. In aqueous media, it is able to displace the oxygen of the vanadyl ion to generate the tris-chelated octahedral coordination complexes of the bare V^{IV} ion.[26] Consequently, reaction of catecholate or naphthalene-catecholate with vanadyl(IV) sulfate easily provides the octahedral coordination complexes **2** and **4** (see Scheme 1b). The preparation of the square pyramidal

Scheme 1. Reaction Schemes for the Synthesis of (a) 1 and 3 and (b) 2 and 4

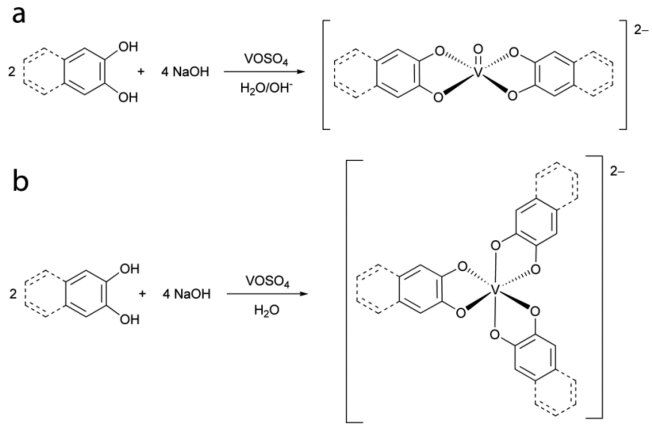

complexes of the vanadyl ion can instead be achieved by working in strongly basic solution. Indeed, the presence of an extra content of base forces the $[VO(L)_2]^{2-} + HL^- \rightleftarrows [V(L)_3]^{2-} + OH^-$ (L = cat or naph-cat) equilibrium toward the formation of the $[VO(L)_2]^{2-}$ species[26], **1** and **3** in this work (see Scheme 1a).

Crystal Structures. Single crystals suitable for X-ray diffraction (XRD) analysis of compound **1** were obtained by recrystallization from acetone of the crude product obtained from aqueous media. Compound **1** crystallizes in the monoclinic $P2_1/c$ space group with one anionic complex and two tetraphenylphosphonium counterions in the asymmetric unit. Its crystal structure consists of symmetry-related $[VO(cat)_2]^{2-}$ anions separated by tetraphenylphosphonium counterions (Figures S1 and S2 in the Supporting Information) that preclude intramolecular contacts shorter than the sum of the van der Waals radii between metal complexes. As a result, the shortest M···M distance in the crystal structure of **1** is 11.95 Å.

The molecular structure of the dianionic complex of **1** is shown in Figure 1a. It presents a slightly distorted square pyramidal coordination geometry due to the chelating ligand, with the metal ion slightly above the basal plane (ca. 0.62 Å) formed by the four oxygen donor atoms. The apical position is occupied by an oxo ligand, which forms a double bond with the V^{IV} ion, with a resulting V═O bond distance of 1.614 Å, whereas the V−O single bond lengths in the basal plane are in the 1.960−1.980 Å range. These structural findings match well with those previously reported for the same anionic complex having K^+ as a counterion.[26]

Single crystals suitable for XRD analysis of compounds **2** and **4** were obtained by slow evaporation of CH_2Cl_2 solutions. Compound **2** crystallizes in the monoclinic $C2/c$ space group with half anionic complex and one tetraphenylphosphonium in the asymmetric unit, while compound **4** crystallizes in the monoclinic $P2_1/n$ space group with one anionic complex and two tetraphenylphosphonium counterions in the asymmetric unit.

DOI: 10.1021/acs.inorgchem.7b02616
Inorg. Chem. 2018, 57, 731−740

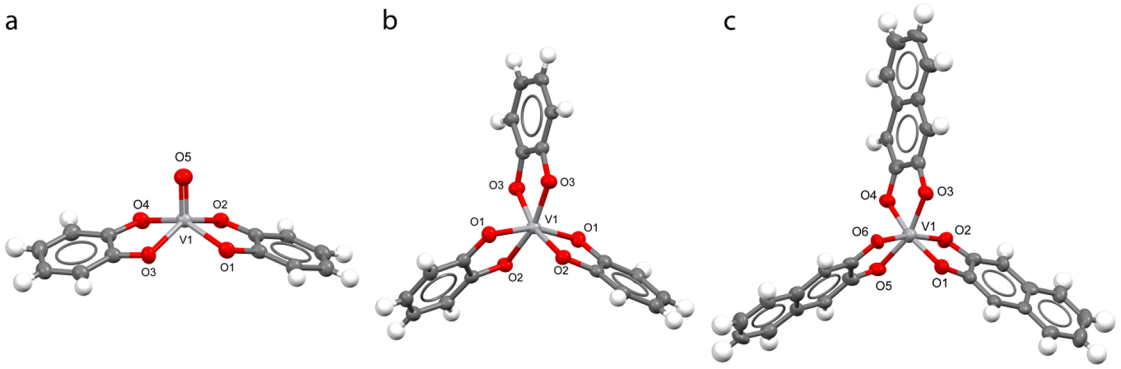

Figure 1. Molecular structure of the dianionic complexes of compounds (a) **1**, (b) **2**, and (c) **4**, using the principal atoms labeling scheme.

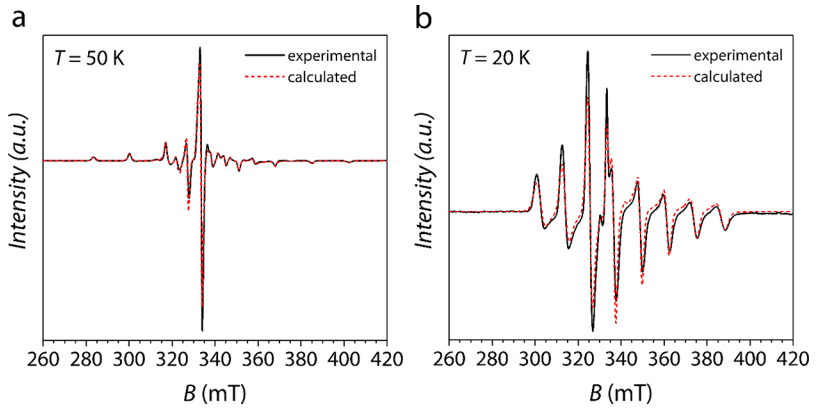

Figure 2. Experimental and simulated (see legend) CW EPR on frozen solution (1.0 mM in 3:1 CH_2Cl_2:C_6H_6) spectra for (a) **1** and (b) **2** at X-band frequency (9.39 GHz).

The crystal structures of **2** and **4** consist of homoleptic tris-chelated $[V(cat)_3]^{2-}$ or $[V(naph\text{-}cat)_3]^{2-}$ anions showing Λ and Δ chirality and tetraphenylphosphonium cations (Figure S3 in the Supporting Information). The shortest M···M distance is 10.12 Å for **2** and 14.30 Å for **4**. The longer distance observed for the latter is clearly due to the presence of a bulkier coordinating ligand.

The molecular structures of the complex anions of **2** and **4** are reported in Figures 1b and 1c. The coordination geometry around the V^{IV} ion is a distorted octahedron with an average V−O distance of 1.946 and 1.941 Å for **2** and **4**, respectively. These structural findings are in agreement with those previously reported for the tris-chelated complex of V(IV) with catecholate as ligand and triethylammonium as counterion,[26] while no structural data have been reported so far for octahedral complexes of V^{IV} with naph-cat as a ligand.

In all structurally characterized compounds, the intraligand bond distances are in the usual range for the dianionic coordinated catecholate moiety (Table S1 in the Supporting Information), thus excluding any evidence for the quinone or semiquinone forms of the ligand.

All attempts to crystallize **3** were unsuccessful, because of its tendency to slowly convert in solution into the tris-chelated complex **4** during the crystallization process. However, single-crystal structural data already reported in the literature for the same anionic complex, $[VO(naph\text{-}cat)]^{2-}$, with a different counterion, namely, trimetylenediammonium,[27] provides a V═O bond length of 1.604 Å, and V−O single bond lengths in the 1.927−1.975 Å range, that well compare to those observed for **1**.

Continuous Wave Electron Paramagnetic Resonance Spectroscopy. Continuous wave electron paramagnetic resonance (CW EPR) spectra on frozen solution of compounds **1**−**4** were recorded to have a full description of their electronic properties. The spectra recorded at 50 K for **1** and **2** are reported in Figure 2, together with their simulations, while those of **3** and **4** are reported in Figure S4 in the Supporting Information.

As expected, the EPR spectra show the 8-fold hyperfine splitting due to the coupling between the $S = {}^1/_2$ electronic spin of V^{IV} and the $I = {}^7/_2$ nuclear spin of its most abundant isotope (^{51}V, abundance 99.76%). The signals are further split by the anisotropic components of the hyperfine coupling in perpendicular and parallel directions. Spectral simulations[28] were then performed on the basis of the following spin Hamiltonian:

$$\mathcal{H} = \hat{\mathbf{I}}\cdot\mathbf{A}\cdot\hat{\mathbf{S}} + \mu_B\hat{\mathbf{S}}\cdot\mathbf{g}\cdot\mathbf{B} \quad (1)$$

to evaluate the anisotropy of the ***g***-factor as well as that of the hyperfine coupling tensor ***A*** for all complexes. The spectra can be satisfactorily simulated assuming a rhombic model (i.e., $x \neq y \neq z$) for **1**, **3**, and **4**, and an axial model (i.e., $x = y \neq z$) for **2**. In all the cases, the line width was assumed to be a pseudo-Voigtian, and some *A*-strain had to be introduced for a reasonable simulation of the line broadening observed at the extreme of the experimental spectra. The best-fit parameters are reported in Table 1.

The parameters reported in Table 1 indicate that the presence of a short V═O bond in **1** and **3** is responsible for a *d*-orbital splitting of the metal centers that leaves the d_{xy} orbital

DOI: 10.1021/acs.inorgchem.7b02616
Inorg. Chem. 2018, 57, 731−740

Table 1. Best-Fit Parameters Extracted from Simulation of the Experimental Spectra of 1−4

compound	g_x	g_y	g_z	$\|A_x\|$ (MHz)	$\|A_y\|$ (MHz)	$\|A_z\|$ (MHz)	Pseudo-Voigtian line width (Gauss) L:G
1	1.980(1)	1.988(1)	1.956(1)	159(2)	126(2)	465(2)	6:9
2	1.945(1)	1.945(1)	1.989(2)	330(6)	330(6)	65(5)	5:10
3	1.979(1)	1.988(1)	1.955(2)	156(2)	127(2)	465(4)	3.5:6.5
4	1.914(1)	1.927(1)	2.001(2)	394(2)	245(3)	30(7)	13:13

lowest in energy, as expected. In contrast, the octahedral coordination geometry of **2** and **4** is responsible for a *d*-orbital splitting that leaves the d_z^2 orbital lowest in energy. This feature, together with a single unpaired electron of the $S = {}^1/_2$ V^{IV} ion, makes such compounds suitable two-level states potential molecular qubits.

It is worth noting that the structural modification introduced by extending the ligand structure induces only minor modification on the Spin Hamiltonian parameters of the metal center for **1** and **3**, suggesting that the key structural feature for these systems is the constrain imposed by the V═O bond. In contrast, higher variability in the ***g*** and ***A*** constants is encountered for the more flexible coordination geometry of **2** and **4**.

Magnetization Dynamics. The magnetization dynamics of compounds **1**−**4** have been investigated by AC susceptometry on polycrystalline samples. The thermal variation of the magnetic susceptibility in zero static magnetic field reveals no imaginary component of the susceptibility (χ'') in the entire investigated temperature range. When a small static magnetic field (>40 mT) is applied, slow magnetic relaxation is observed with appearance of a peak in the imaginary component of the susceptibility and a concomitant decrease of the real part (χ') (see Figures S5−S12 in the Supporting Information).

Under a static magnetic field of 1.0 T, all compounds show slow relaxation of the entire magnetization, so that this field was selected to investigate the temperature dependence of the relaxation time τ, which is representative of spin−lattice relaxation. The frequency dependences of χ'' are well-reproduced with the Debye model (Figures S5−S8) and the extracted values of τ as a function of the temperature are reported in Figure 3.

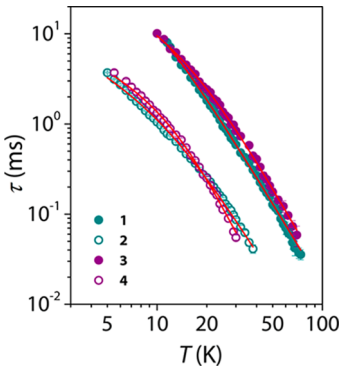

Figure 3. Temperature dependence of τ extracted from AC susceptibility measurements for microcrystalline powders of compounds **1**−**4**

The oxovanadium(IV) complexes **1** and **3** show slow magnetic relaxation up to ca. 70−80 K (Figures S5 and S7) with exceptionally long relaxation times. They range from ca. 10 ms at 10 K to ca. 0.040−0.060 ms at 75 K. The vanadium(IV) complexes **2** and **4** also show slow relaxation of the magnetization, but with relaxation times that are an order of magnitude shorter than the oxovanadium(IV) counterparts. More specifically, they range from ca. 4.0 ms at 5 K to ca. 0.050−0.072 ms at 30 K, above which they are not measurable.

The temperature dependence of τ, reported in Figure 3 in a $\log(\tau)$ vs $\log(T)$ plot, shows, for all compounds, a change in the slope of the curve as the temperature increases. This is almost unperceivable for **1** and more pronounced for **4**. This behavior is indicative of the competition between the direct and the Raman mechanisms of relaxation, the former dominating at lower temperature, with respect to the latter. To account for these two contributions to the relaxation, the spin−lattice relaxation rate (τ^{-1}) was fitted (solid lines in Figure 3) with the following model:

$$\tau^{-1} = aT + bT^n \quad (2)$$

where a is the coefficient of the direct mechanism, while b and n are the coefficient and the exponent of the Raman mechanism, respectively.[17,18,20] This model satisfactorily reproduces the T dependence of τ with the best-fit parameters reported in Table 2.

Table 2. Best-Fit Parameters of the Model Used (eq 2) to Reproduce the Temperature Dependence of the Spin−Lattice Relaxation Rate for 1−4

compound	a (μs^{-1} K^{-1})	b (μs^{-1} K^{-n})	n
1	4.0(5)	0.051(7)	3.0(1)
2	51(1)	0.38(1)	3.0(1)
3	7.8(4)	0.016(3)	3.2(1)
4	49(2)	0.049(2)	3.7(1)

The values of the Raman exponent n (ca. 3) are particularly low with respect to what is expected for paramagnetic centers in inorganic solids,[29] but they are commonly observed for vanadium(IV)-based molecular systems investigated through both AC susceptometry and pulsed EPR spectroscopy.[17,18,20]

Remarkably, the relaxation times observed for the oxovanadium(IV) derivatives **1** and **3** are the highest among the vanadyl-based molecular spin qubits studied up to date,[17,18,20,22] excluding the case in which τ is further increased at low temperatures as a result of spin-phonon bottleneck effects, because of the crystallite size.[30] Here, we can exclude the latter effect, because of the finely ground nature of the sample. Moreover, the poor efficiency of the spin relaxation mechanisms herein involved allows one to observe quite long relaxation times in a relatively wide temperature range also for the octahedral complexes **2** and **4** (see Figure 3).

It is worth noting that the square pyramidal oxovanadium(IV) complexes **1** and **3** show similar absolute values of the relaxation times and similar temperature dependences independently from the structural modification introduced by the different ligand. Analogous consideration holds for the octahedral complexes **2** and **4**. This confirms our previous observations on the role played by the different orbital contribution to the ground state in determining the enhancement of the absolute values of τ when passing from the square pyramidal to the octahedral coordination.[20] Interestingly, a factor of ca. 10 between the values of τ for square pyramidal versus octahedral

DOI: 10.1021/acs.inorgchem.7b02616
Inorg. Chem. 2018, 57, 731−740

complexes was also observed for the $[VO(dmit)_2]^{2-}/[V(dmit)_3]^{2-}$ (dmit = 1,3-dithiole-2-thione-4,5-dithiolate) pair of complexes.[20]

In order to get better insights on the relaxation mechanisms involved in such compounds, the relaxation time was also investigated as a function of the static magnetic field in a wide field range (0.0−8.5 T) at different temperatures. The relaxation times extracted with the Debye model (Figures S9−S12) for **1**−**4** are reported in Figure 4.

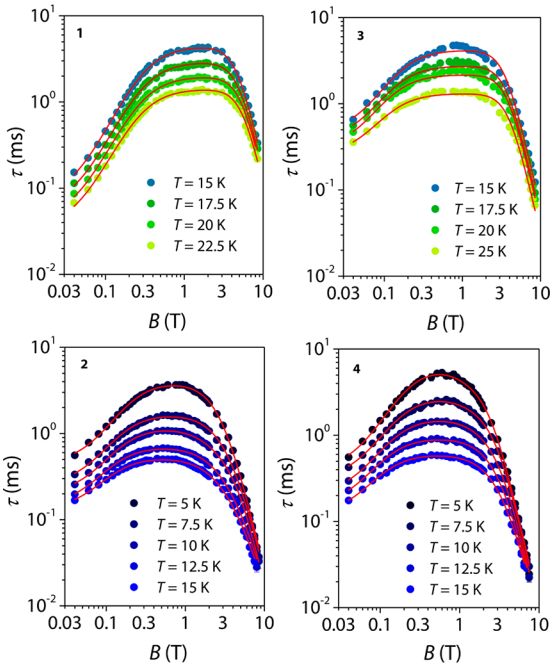

Figure 4. Magnetic field dependence of τ extracted from AC susceptibility measurements for compounds **1**−**4** at different temperatures (see legends). Solid lines are the best-fits of the models (see text).

The field dependences of the relaxation time for **1**−**4** show a nonmonotonous behavior with an extended plateau similarly to what already reported for closely related systems.[17,18,20,22] Passing from **1** to **3**, the width of the plateau is slightly reduced, while it is strongly reduced when passing to **2** and **4**, both showing very similar behaviors.

The nonmonotonous behavior reflects two antagonist effects of the magnetic field: (i) a suppression of the rapid relaxation promoted by spin−spin and spin-nuclei interactions, and (ii) a more efficient spin-phonon direct mechanism of relaxation at high fields ($\tau \propto B^4$). The mixing of the energy levels due to spin−spin and spin-nuclei interactions is indeed reduced by increasing the field strength, while the more efficient direct mechanism of relaxation at high field is due to the higher phonon-density at energies matching the separation between the $m_S = \pm^1/_2$ levels. To account for these two contributions, the B dependence of the relaxation rate is usually reproduced with the Brons−van Vleck model:[31,32]

$$\tau^{-1} = cB^4 + d\left(\frac{1 + eB^2}{1 + fB^2}\right) \quad (3)$$

where the first term corresponds to the direct mechanism of relaxation, while the second term takes into account the effect of an internal magnetic field in promoting relaxation, considered as a sum of spin-nuclei hyperfine and spin−spin dipolar interactions.

The B dependence of τ for the oxovanadium(IV) compounds **1** and **3** herein investigated is well reproduced through the Brons−van Vleck phenomenological model (eq 3), whereas the vanadium(IV) compounds **2** and **4** require an extended Brons−van Vleck law (eq 4),[22] to provide an adequate fit of the experimental data (Figure S13 in the Supporting Information), suggesting a more-complex relaxation process.

$$\tau^{-1} = cB^4 + d\left(\frac{1 + eB^2}{1 + fB^2}\right) + g\left(\frac{1 + eB^2}{1 + hB^2}\right) \quad (4)$$

The best-fit parameters are reported in Table S2 in the Supporting Information.

We have recently found that the d parameters, extracted from the fit of the magnetic field dependence, follow an exponential temperature dependence.[22] The resulting Arrhenius behavior allowed us to extract effective energy values (U_{eff}), which also correlate well with the experimental low-energy vibrational modes detected by time-domain THz spectroscopy (vide infra). Interestingly, a complex behavior of the magnetic field dependence of τ has been found to be accompanied by the presence of more than one predominant low-energy vibration, suggesting a correlation between the observed activation energy and the frequency (ω_α) of the involved phonon of the type $U_{eff} = h\omega_\alpha/2$. The same relation has been theoretically proposed for the relaxation time of SMMs characterized by excited magnetic states at high energy, when the anharmonicity, or finite line width, of vibrational modes is taken into account.[24]

In this case, the analysis of the T dependence of the d parameter extracted by the field dependence measurements performed at various temperatures provides a unique value of U_{eff} for **1** (U_{eff} = 24(2) cm^{-1}) and for **3** (U_{eff} = 17(2) cm^{-1}) (see Figure S14 in the Supporting Information). On the other hand, the linear fit of $\ln(d)$ and $\ln(g)$ vs T^{-1} provides U_{eff} = 6(1) cm^{-1} and 10(1) cm^{-1} for **2**, and U_{eff} = 9(1) cm^{-1} and 16(1) cm^{-1} for **4**, respectively (Figure S14). Note that the e and f parameters show, in some cases, a weak temperature dependence that was not foreseen by the Brons−van Vleck model. This evidence some limitations for the application of this phenomenological model to the dynamics of these complexes, and makes the comparison between the field-dependent behavior of different systems still qualitative.

The long spin−lattice relaxation times observed for **1** are in agreement with the predicted higher activation energy of the vibrational mode (detected by THz spectroscopy, vide infra) involved in the relaxation (ca. 48(4) cm^{-1}) with respect to the one (40 cm^{-1}) of the best performing system identified to date, namely, $[VO(acac)_2]$ (acac = acetylacetonate), which shows slightly lower values of τ (Figure S15 in the Supporting Information).[30] This suggests that the lowest energy vibrational modes are expected to be higher in energy for **1**, with respect to $[VO(acac)_2]$.

FT-IR and THz Vibrational Spectroscopy. An accurate determination of the energy of the vibrational modes active in these compounds is crucial for a better understanding of the correlation between vibrational modes and the spin dynamics. We have thus collected room-temperature infrared (4000−400 cm^{-1}) and THz (100−20 cm^{-1}) spectra (the latter through time-domain THz spectroscopy) of the protonated ligands H_2cat and H_2naph-cat. The comparison between the spectra indicates that the structural modification herein introduced by expanding

DOI: 10.1021/acs.inorgchem.7b02616
Inorg. Chem. 2018, 57, 731−740

the ligand from one to two condensed aromatic rings has important implications on the overall molecular rigidity. Indeed, in the middle-infrared region, most of the absorption peaks related to the aromatic skeleton vibrations of H_2naph-cat are shifted toward higher energies, when compared to H_2cat (Figure S16 in the Supporting Information).[33] The low-energy vibrations are also affected by the skeleton rigidity. Indeed, the predominant lowest energy absorption occurs at a frequency ca. 15 cm^{-1} higher for the H_2naph-cat ligand, with respect to the H_2cat one (Figure 5).

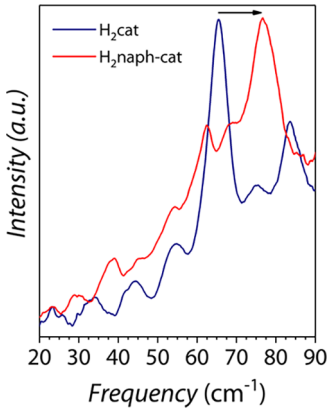

Figure 5. Comparison between experimental THz (20−90 cm^{-1}) spectra of H_2cat and H_2naph-cat ligands. Arrow indicate the shift toward higher frequencies of the lowest energy vibrational mode.

These findings are in agreement with what was previously reported for the 1,4-dihydroxy isomers of the 1,2-dihydroxy compounds herein investigated.[34,35]

When passing to the vibrational spectra of the complexes, the middle-infrared region of **1** and **2** do not show substantial differences between the two compounds, except for the presence of an extra absorption peak at ca. 942 cm^{-1} for **1**, which is clearly attributable to the V═O stretching normal mode (Figure S17 in the Supporting Information). These results are not surprising, because of the strictly local nature of the molecular vibrational modes falling in this spectral region, and are in agreement with previous findings.[20] Analogous results are observed comparing the spectra of **3** and **4**. Indeed, they show very similar spectra, except for the extra peak at ca. 958 cm^{-1} (V═O stretching) for **3** (Figure S18 in the Supporting Information).

The comparison between the middle-infrared spectra of **1** and **3** provides instead some insights on the role of the structural rigidity introduced through the ligand. Excluding the vibrational modes related to the PPh_4^+ counterion falling at ca. 1105, 995, 754, 722, 687, 623, and 528 cm^{-1}, the higher rigidity of the two condensed rings in the naph-cat^{2-} ligand with respect to the cat^{2-} results in a slight shift toward higher frequency of some specific vibrational modes centered at ca. 1255, 948, and 535 cm^{-1} (Figure S19a in the Supporting Information), including the V═O stretching vibrational mode. The same considerations are valid for the octahedral complexes **2** and **4** (Figure S19b in the Supporting Information).

Room-temperature time-domain THz spectra were recorded in the 0.3−3.0 THz range (15−100 cm^{-1}) to characterize the low-energy vibration frequencies of compounds **1**−**4** (see Figure 6).

Generally, the THz spectra of compounds **1**−**4** appear more complicated with respect to those of $[VO(acac)_2]$ and $[VO(Et_2dtc)_2]$ already studied.[22] This might be partially related

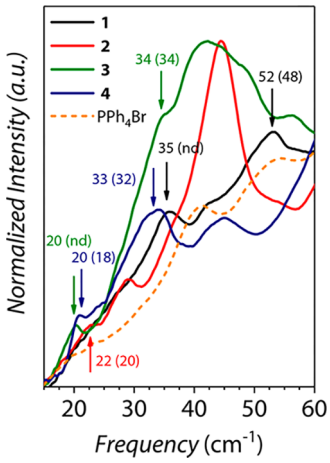

Figure 6. Vibrational spectra in the 0.3−1.8 THz range (15−60 cm^{-1}) of compounds **1**−**4** and $(Ph)_4PBr$ for comparison (orange dashed line). Arrows indicates the lowest energy absorptions for all compounds together with experimental frequencies and those found through magnetic susceptibility analysis (shown in parentheses). (nd = not determined through magnetic analysis.)

to the presence of the PPh_4^+ counterion, which was absent in the previously studied compounds.

The spectra of the oxovanadium(IV) complexes **1** and **3** show lowest energy absorptions at ca. 35 and 52 cm^{-1} for **1**, and 20 and 34 cm^{-1} for **3**, respectively. Interestingly, in this frequency region, the lowest-energy vibrational modes are shifted toward higher frequencies for the complex of the smaller cat^{2-} ligand, with respect to that of the naph-cat^{2-}, in agreement with the magnetic analysis. More specifically, assuming the relation $U_{eff} = h\omega_a/2$ to hold,[22,24] the magnetic analysis suggests that the phonons involved in the relaxation mechanism should have a frequency of 48 and 34 cm^{-1}, for **1** and **3**, respectively, which agree with the spectroscopic findings. Both **1** and **3** show one additional peak at lower frequencies that was not determined through the magnetic analysis. According to a recently reported study on the role of intramolecular vibrations as mediators of spin−lattice relaxation, each vibrational mode should couple with the spin in a different extent, as a function of the type of vibration and electron occupancy in the metal *d*-orbitals.[23] More specifically, it has been observed that, for the compound $[(Ph)_4P]_2[Cu(mnt)_2]$ (mnt = 1,2-dicyanoethilene-1,2-dithiolate), which has been theoretically investigated, only 3 out of 16 calculated vibrational modes in the 0−150 cm^{-1} range were identified as effective in mediating spin−lattice relaxation, with the first active low-energy mode being fourth in energy (at ca. 35 cm^{-1}). Consequently, it is not surprising that the lowest-energy vibrational mode observed herein for **1** and **3** is not strongly coupled with the spin to promote efficient relaxation, and consequently does not contribute substantially to the fine structure of the τ vs B behavior (vide infra). This hypothesis is corroborated by the fact that both **1** and **3**, which share the same coordination geometry, show the same feature. Accordingly, the nature of the lowest-energy detected vibrational mode for **1** and **3** is likely to be the same, with a different resonating frequency, because of the different ligand mass.

The spectra of the vanadium(IV) tris-chelated complexes show, in general, low-energy absorption bands, which are shifted toward lower energies, with respect to the oxovanadium(IV) complexes, again in agreement with the findings of the magnetic analysis. More specifically, **2** and **4** show lowest-energy

DOI: 10.1021/acs.inorgchem.7b02616
Inorg. Chem. 2018, 57, 731−740

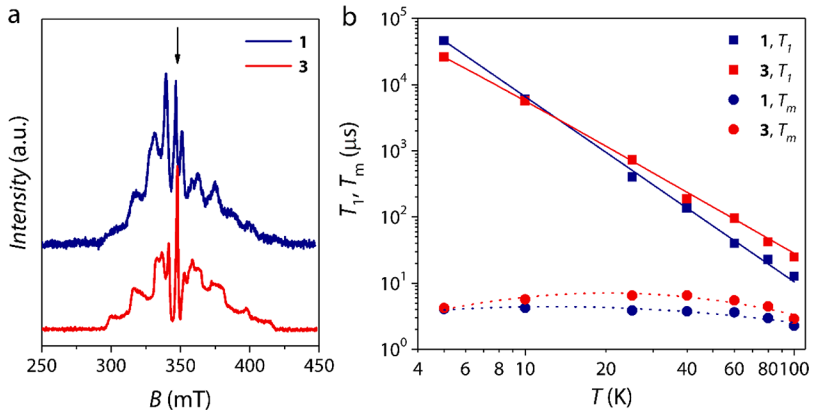

Figure 7. (a)Experimental X-band (9.7 GHz) ED-EPR spectrum of **1** and **3** (1.0 mM in CH_2Cl_2:C_6H_6 3:1) recorded at 5 K. The arrow indicates the magnetic field setting at which pulsed EPR experiments were performed. (b) Temperature dependence of T_1 and T_m for **1** and **3**. The solid line is the best fit of the model (see text). The short-dashed line represents a guide for the eyes. Error bars are within the size of the symbols.

absorptions at 22 cm^{-1} and ca. 28 cm^{-1} for **2**, and 20 and 33 cm^{-1} for **4**. A correlation with the magnetic analysis can be found for **4**, with two phonon modes expected at 18 and 32 cm^{-1}, whereas, for **2**, relevant phonon modes are expected at 12 and 20 cm^{-1}, the former falling out from our detection range.

Finally, it should be remarked that all spectra show an absorption at ∼40 cm^{-1}, where the first vibrational mode of the PPh_4^+ counterion is observed (dotted orange line in Figure 6), but no correspondence to relaxation processes is observed for this vibration.

Pulsed Electron Paramagnetic Resonance Spectroscopy. Coherence times (T_m) and spin−lattice relaxation times (T_1) for compounds **1** and **3** in frozen solution were measured at the X-band in the 4.5−100 K temperature range. The measurements were performed at the so-called "powder line" of the echo-detected field-swept (EDFS) EPR spectrum (see arrow in Figure 7a). The spectral features of the EDFS-EPR spectra reflect those of the corresponding CW-EPR spectra (Figure 2a), although some distortions are present at the high-field end of the spectral pattern of **1**, because of field-dependent nuclear modulation effects.

The thermal variation of T_1 for **1** and **3** were obtained by inversion recovery experiments performed in the 4.5−100 K temperature range. The resulting traces were fitted with a stretched monoexponential equation,

$$I = I_0 + k_1 \exp\left[-\left(\frac{\tau_p}{T_1}\right)^{\beta_1}\right] \quad (5)$$

and the extracted T_1 values are reported in Figure 7b (squares).

The stretched exponential recovery is characteristic of a distribution of relaxation times, which is typical of glassy frozen solutions and polycrystalline systems, where the neighborhood of the paramagnetic species varies slightly from site to site. This is consistent with the pseudo-Voigt line shape function and the *A*-strain used in the simulation of the CW EPR experiments to reproduce the inhomogeneously broadened line widths. The stretching parameter (β_1) is ∼0.3 at 5 K and approaches unity at 100 K, indicating that the local heterogeneity is averaged out at temperatures approaching the melting point. This is consistent with what we observed for other vanadyl complexes in frozen solutions.[17]

The thermal variation of T_1 for the two compounds shows a constant slow decrease from the maximum values of ca. 20−40 ms at 4.5 K, to the lowest, but still remarkable values of ca. 20−30 μs at 100 K. This indicates that measurable values of T_1 were expected at higher temperatures if the temperature range were not limited by the melting point of the frozen solution. As shown in Figure 7b, the T_1 values exhibit linear temperature dependence behaviors, which have been modeled assuming only one predominant contribution of Raman type to the relaxation with n = 2.8(2) and 2.6(2) for **1** and **3**, respectively, in agreement with the AC susceptibility data (vide supra). Interestingly, slightly longer T_1s are observed for **3**, in agreement with AC susceptibility data, whereas at temperatures <10 K, the trend is reversed.

To investigate the quantum coherence in detail and to quantify the phase memory time (T_m) of **1** and **3** as a function of the temperature, echo decay experiments were also performed.

The decay traces were fitted using the stretched-exponential equation,

$$I = I_0 + k_m \exp\left[-\left(\frac{2\tau_p}{T_m}\right)^{\beta_m}\right] \quad (6)$$

as usually done for transition metal-based systems,[36] where I indicates the echo intensity, $2\tau_p$ is the delay between the initial pulse and the echo detection, and β_m is the stretch factor.

The thermal variation of the T_m values for **1** and **3** shows an almost-temperature-independent behavior in the 4.5−80 K range, with T_m values within 4.2−3.6 μs and 4.2−6.5 μs, for **1** and **3**, respectively. Then, at 100 K, T_m decreases slightly, to ca. 2.3 μs for **1** and 2.9 μs for **3**, most likely as a result of the significant decrease of T_1 in that temperature range (Figure 7b).

It should be highlighted that the T_m values observed at low temperature (ca. 4.0−6.0 μs) are generally higher than those already reported so far in the literature for similar compounds measured in analogous protiated solvent matrixes.[37] Moreover, they are slightly higher than those reported for vanadyl complexes containing nuclear spin-free ligands (ca. 3.0−3.5 μs), which are also characterized by a more abrupt decrease of T_m as the temperature increases.[37]

CONCLUSIONS

We have here investigated the spin−lattice relaxation of four V^{IV}-based potential molecular qubits where specific structural modifications have been introduced to study correlations between the spin dynamics and the role played by low-energy

DOI: 10.1021/acs.inorgchem.7b02616
Inorg. Chem. 2018, 57, 731−740

vibrational modes as mediators of spin−lattice relaxation. Both the influence of the different coordination geometries, *square-pyramidal* versus *octahedral*, as well as the increased rigidity of the coordinating ligand, have been correlated to the observed spin−lattice relaxation.

The analysis of the temperature dependence of the relaxation time did not show major differences between catecholate and naphthalene-catecholate complexes, while substantial differences between square pyramidal and octahedral complexes were observed. Indeed, the former provide relaxation times that are ca. 10-fold longer, with respect to the latter. A similar factor was also observed for another independent pair of vanadium(IV) and oxovanadium(IV) complexes with a different ligand, thus indicating that the specific coordination geometry plays a key role on the absolute values of the relaxation time, not simply by generically increasing them, but enhancing the relaxation times by a specific factor, independently from the coordinating ligand structure.

The relaxation times herein reported for the vanadyl species are higher than those observed for β-diketonate derivatives and for complexes where the ligands have sulfur donor atoms, such as the 1,3-dithiole-2-thione-4,5-dithiolate ($dmit^{2-}$) and diethyldithiocarbamate (Et_2dtc^-) ligands (Figure S15). This may be due either to the fine modulation of the electronic parameters of the metal centers, or to the specific force of the vibrational modes related to the *metal−donor atoms* bonds. Moreover, compounds **1** and **3** show quantum coherence times that compare well with the best results obtained so far for molecular spin qubits.

From this comparative multitechnique study, further insights emerge on the factors affecting the spin dynamics. Analysis of the field-dependent data confirms the generality of the Arrhenius-type dependence related to the efficiency of the processes responsible for the nonmonotonic field dependence of the relaxation time. This allowed us to find further correspondence between the activation energy values obtained by this magnetic analysis and the frequency of the low-energy phonons spectroscopically detected by time-domain THz spectroscopy. Unfortunately, clear correlations with the nature of vibrational modes involved cannot be performed with certitude, as a consequence of the spectra complexity, which is further enhanced by the presence of the counterion.

As the temperature dependence of the spin−lattice relaxation time is concerned, it emerges that naphthalene-catecholate, identified by experimental middle-infrared and THz spectroscopy as a more rigid ligand than catecholate, provides minor enhancements of the relaxation times only in the high-temperature range. The slower relaxation of **1**, compared to **3**, at low temperatures correlates with the trend of the lowest-energy vibrational modes. Indeed, they occur at slightly lower energy in **3** than in **1**, independently from the shift toward higher frequencies observed in higher-frequency regions. A possible explanation of such behavior might be found in the mixing between low-energy vibrational modes with rotational components, with the latter being expected to be observed at higher energies for smaller masses.

In conclusion, we have demonstrated that a multitechnique approach based on the combination of AC susceptometry, pulsed-EPR, and THz spectroscopy can shed light on the most effective structural parameters involved in the magnetic relaxation of $S = {}^1/_2$ potential molecular spin qubits.

EXPERIMENTAL SECTION

Synthesis. *[(Ph)$_4$P]$_2$[VO(cat)$_2$] (**1**).* An aqueous solution (15 mL) of $VOSO_4 \cdot xH_2O$ (1.0 g, 6.0 mmol) was refluxed overnight with NaOH (0.32 g, 8.0 mmol) resulting in the formation of a green precipitate. The solid was filtered, washed with cold water, and added in portions to an aqueous solution (15 mL) of catechol (1.1 g, 10.0 mmol) and an excess of NaOH (1.2 g, 30.0 mol). A methanol solution (5 mL) of tetraphenylphosphonium bromide (5.0 g, 12.0 mmol) was added dropwise to the resulting green solution with precipitation of **1** as a green-gray microcrystalline solid. The precipitate was separated from the mother liquor by vacuum filtration, washed several times with water, and dried under vacuum. Yield: 85%. Compound **1** was recrystallized by the addition of acetone to a CH_2Cl_2 solution, which gives green shiny crystals suitable for X-ray analysis. Elemental analysis calcd for $C_{60}H_{48}O_5P_2V$: C, 74.92; H, 5.03; found: C, 73.91; H, 5.05. FT-IR ($\overline{\nu}_{max}/cm^{-1}$, KBr pellet): 3049(w), 2995(w), 1584(w), 1560(vw), 1474(vs), 1435(s), 1409(w), 1340(w), 1322(w), 1249(vs), 1193(w), 1163(w), 1106(s), 1013(w), 995(m), 942(m) (ν V═O), 887(w), 870(m), 791(m), 762(m), 753(m), 738(m), 723(s), 688(s), 623(s), 526(vs), 504(m), 453(w), 412(m).

*[(Ph)$_4$P]$_2$[V(cat)$_3$] (**2**).* An aqueous solution (10 mL) of $VOSO_4 \cdot xH_2O$ (0.550 g, 2.7 mmol) was added dropwise to an aqueous solution (20 mL) of catechol (0.890 g, 8.1 mmol) and NaOH (0.400 g, 10.0 mmol). A methanol solution (5 mL) of tetraphenylphosphonium bromide (2.85 g, 6.8 mmol) was added dropwise to the resulting blue solution with precipitation of **2** as a blue microcrystalline solid. The precipitate was separated from the mother liquor by vacuum filtration, washed several times with water, and dried under vacuum. Yield: 78%. Compound **2** was recrystallized by slow diffusion of Et_2O vapors to a MeOH solution, which gives deep-blue block crystals suitable for X-ray analysis. Elemental analysis calcd for $C_{66}H_{52}O_6P_2V$: C, 75.21; H, 4.97; found: C, 75.62; H, 4.95. FT-IR ($\overline{\nu}_{max}/cm^{-1}$, KBr pellet): 3049(w), 2995(w), 1585(w), 1569(vw), 1513(m), 1483(m), 1467(vs), 1435(s), 1372(w), 1340(w), 1317(w), 1258(vs), 1201(w), 1163(w), 1106(s), 1013(w), 995(m), 870(m), 855(w), 805(m), 754(m), 738(m), 723(s), 688(s), 623(s), 526(vs), 504(m), 463(w), 420(m).

*[(Ph)$_4$P]$_2$[VO(naph-cat)$_2$] (**3**).* An aqueous solution (10 mL) of $VOSO_4 \cdot xH_2O$ (0.330 g, 2.0 mmol) was added dropwise to an aqueous solution (20 mL) of catechol (0.60 g, 3.75 mmol) and NaOH (0.450 g, 11.2 mmol). A methanol solution (5 mL) of tetraphenylphosphonium bromide (2.0 g, 4.70 mmol) was added dropwise to the resulting green solution with precipitation of **3** as a green microcrystalline solid. The precipitate was separated from the mother liquor by vacuum filtration, washed several times with water, and dried under vacuum. Yield: 87%. Compound **3** was recrystallized via the addition of acetone to a freshly prepared CH_2Cl_2 solution, which gives green shiny microcrystals. Elemental analysis calcd for $C_{68}H_{52}O_5P_2V$: C, 76.90; H, 4.94; found: C, 76.15; H, 4.73. FT-IR ($\overline{\nu}_{max}/cm^{-1}$, KBr pellet): 3053(w), 3004(w), 1584(w), 1567(vw), 1459(vs), 1437(s), 1340(w), 1322(w), 1269(vs), 1190(w), 1167(m), 1107(m), 995(w), 958(m) (ν V═O), 857(m), 749(m), 738(m), 723(s), 688(s), 652(w), 624(m), 560(m), 525(s), 476(w), 453(w).

*[(Ph)$_4$P]$_2$[V(naph-cat)$_3$] (**4**).* Compound **4** was obtained by slow conversion of **3** in CH_2Cl_2 solution. Slow evaporation of the solvent provides deep-blue block crystals suitable for X-ray analysis. Elemental analysis calcd for $C_{78}H_{58}O_6P_2V$: C, 77.80; H, 4.85; found: C, 77.67; H, 4.81. FT-IR ($\overline{\nu}_{max}/cm^{-1}$, KBr pellet): 3044(w), 3000(w), 1584(w), 1567(vw), 1482(w), 1450(vs), 1440(s), 1436(s), 1340(w), 1322(w), 1269(vs), 1190(w), 1167(m), 1107(m), 995(w), 864(m), 839(m), 749(m), 738(m), 723(s), 688(s), 642(w), 624(m), 560(m, 525(s), 476(w), 453(w).

Characterization. C, H, N analyses were performed with a CHN-S Flash E1112 Thermofinnigan analyzer. FT-IR spectra were performed on KBr pellets and collected with a spectrophotometer (Shimadzu, Model 8400S).

Single-Crystal X-ray Crystallography. Single-crystal XRD measurements were performed on an Oxford Xcalibur PX Ultra Onyx CCD diffractometer, using an Enhance Ultra X-ray graphite-monochromated Cu Kα (λ = 1.540 Å) or Mo Kα (λ = 0.7107 Å)

DOI: 10.1021/acs.inorgchem.7b02616
Inorg. Chem. 2018, 57, 731−740

Table 3. Summary of X-ray Crystallographic Data for 1, 2, and 4

property	Value/Comment		
	1	2	4
empirical formula	$C_{60}H_{48}O_5P_2V$	$C_{66}H_{52}O_6P_2V$	$C_{78}H_{58}O_6P_2V$
formula weight	961.86	1053.96	1204.12
crystal size, mm	0.50 × 0.30 × 0.30	0.30 × 0.20 × 0.15	0.20 × 0.20 × 0.10
crystal system	monoclinic	monoclinic	monoclinic
space group	$P2_1/c$	$C2/c$	$P2_1/n$
a, Å	13.2529(2)	15.3120(8)	11.1798(5)
b, Å	12.2534(1)	13.2289(7)	27.8301(14)
c, Å	29.1923(3)	25.317(1)	19.4916(13)
α, deg	90	90	90
β, deg	92.804(1)	102.016(6)	103.704(5)
γ, deg	90	90	90
V, Å^3	4734.95(9)	5015.9(5)	5891.9(6)
Z	4	4	4
T, K	100(2)	100(2)	100(2)
ρ(calc), Mg/m^3	1.349	1.396	1.357
μ, mm^{-1}	2.805	0.319	2.385
θ range, deg.	4.40−72.40	4.11−26.32	4.19−68.00
goodness of fit, GooF	1.034	1.038	0.933
$R1$[a]	0.0567	0.0633	0.0882
$wR2$[b]	0.1384	0.1473	0.1528

[a] $R1 = \sum||F_o| - |F_c||/\sum|F_o|$. [b] $wR2 = [\sum[w(F_o^2 - F_c^2)^2]/\sum[w(F_o^2)^2]]^{1/2}$, $w = 1/[\sigma^2(F_o^2) + (aP)^2 + bP]$, where $P = [\max(F_o^2,0) + 2F_c^2]/3$.

radiation source. The structures were solved by direct methods (SHELXS-97) and refined on F^2 using a full-matrix least-squares methodology (SHELXL-97),[38] using the Wingx software package.[39] All non-H atoms were refined with anisotropic displacement parameters. Graphical material was prepared using Mercury CSD 3.9.[40] A summary of the crystallographic data and the structure refinement for compounds **1**, **2**, and **4** is reported in Table 3.

Full crystallographic data for the solved structures have been deposited in the Cambridge Crystallographic Data Centre with CCDC numbers 1572974 (**1**), 1572976 (**2**), and 1572975 (**4**), respectively.

Electron Paramagnetic Resonance. CW X-Band EPR spectra of all samples were recorded on a Bruker Elexsys E500 spectrometer equipped with a SHQ cavity (ν = 9.39 GHz). Low-temperature measurements were obtained using a continuous flow helium cryostat (Oxford Instruments, Model ESR900). Pulsed-EPR measurements were carried out with a Bruker Elexsys E580 at the X-band ($\nu \cong$ 9.70 GHz) equipped with a flexline dielectric ring ENDOR resonator (Bruker, Model EN 4118X-MD4). Temperatures between 4.5 K and 100 K were obtained with a continuous flow helium cryostat (Oxford Instruments, Model CF935). Echo detected field swept EPR spectra were recorded by using the Hahn Echo pulse sequence ($\pi/2$—τ—π—τ—echo) with fixed interpulse delay time τ = 200 ns, $t_{\pi/2}$ = 16 ns, and t_π = 32 ns. Phase memory times were measured by the Hahn Echo sequence upon increasing the interpulse delay τ, starting from τ = 98 ns. Spin−lattice relaxation times were measured using the standard inversion recovery sequence (π—t_d—$\pi/2$—τ—π—τ—echo), with $\pi/2$ = 16 ns. The uncertainty in T_1 estimated from replicate measurements was 5%−10%, depending upon the signal-to-noise ratio at a given temperature-field combination.

Magnetic Measurements. AC susceptibility measurements were performed in the temperature range 5.0−80 K with applied magnetic fields up to 8.5 T on polycrystalline samples of compounds **1** (56.12 mg), **2** (48.10 mg), **3** (54.20 mg), and **4** (45.00 mg) by using a Quantum Design Physical Property Measurement System (PPMS) equipped with a AC susceptometer operating in the frequency range from 10 Hz to 10 kHz. Susceptibility data were corrected for the diamagnetic contributions as deduced by using Pascal's constant tables.[41]

THz Time-Domain Spectroscopy Setup. THz spectra were measured by time-domain transmission spectroscopy, using a table-top experimental setup equipped with optical laser pulses (T-light 780 nm fiber laser, MenloSystems) and low-temperature GaAs photoconductive antennas. The developed acquisition procedure enables one to achieve a very high signal-to-noise ratio, which is higher than what is commonly achieved in standard far-infrared investigations. The accurate analysis of the data enables one to disentangle the signals from spurious contributions coming from multiple reflections. Detailed descriptions of the experimental setup and the data analysis procedure are reported elsewhere.[42] The spectra were measured in pellet samples of 13.2 mm in diameter, with a thickness of ∼0.7 mm. These were made by pressing, under a manual hydraulic press (∼0.8 GPa), a mixture of microcrystals and polyethylene powder (Merck).

■ ASSOCIATED CONTENT

Supporting Information

The Supporting Information is available free of charge on the ACS Publications website at DOI: 10.1021/acs.inorgchem.7b02616.

Additional figures and data as mentioned in the text (PDF)

Accession Codes

CCDC 1572974−1572976 contain the supplementary crystallographic data for this paper. These data can be obtained free of charge via www.ccdc.cam.ac.uk/data_request/cif, or by e-mailing data_request@ccdc.cam.ac.uk, or by contacting The Cambridge Crystallographic Data Centre, 12 Union Road, Cambridge CB2 1EZ, U.K.; fax: +44 1223 336033.

■ AUTHOR INFORMATION

Corresponding Authors

*E-mail: matteo.atzori@unifi.it (M. Atzori).
*E-mail: roberta.sessoli@unifi.it (R. Sessoli).

ORCID

Matteo Atzori: 0000-0003-1357-6159
Stefano Benci: 0000-0001-6492-1616
Lorenzo Tesi: 0000-0003-4001-8363
Mario Chiesa: 0000-0001-8128-8031
Lorenzo Sorace: 0000-0003-4785-1331
Roberta Sessoli: 0000-0003-3783-2700

Notes

The authors declare no competing financial interest.

■ ACKNOWLEDGMENTS

Italian MIUR (through Project No. PRIN 2015-HYFSRT) and Fondazione Ente Cassa di Risparmio di Firenze are acknowledged for financial support. European COST Action (No. CA15128 MOLSPIN) is also acknowledged.

■ REFERENCES

(1) Nielsen, M. A.; Chuang, I. L. *Quantum Computation and Quantum Information*; Cambridge University Press: Cambridge, U.K., 2000.
(2) DiVincenzo, D. P. Quantum Computation. *Science* **1995**, *270*, 255−261.
(3) Knill, E.; Laflamme, R.; Milburn, G. J. A scheme for efficient quantum computation with linear optics. *Nature* **2001**, *409*, 46−52.
(4) Blatt, R.; Wineland, D. Entangled states of trapped atomic ions. *Nature* **2008**, *453*, 1008−1015.
(5) Clarke, J.; Wilhelm, F. K. Superconducting quantum bits. *Nature* **2008**, *453*, 1031−1042.

DOI: 10.1021/acs.inorgchem.7b02616
Inorg. Chem. 2018, 57, 731−740

(6) Pla, J. J.; Tan, K. Y.; Dehollain, J. P.; Lim, W. H.; Morton, J. J. L.; Jamieson, D. N.; Dzurak, A. S.; Morello, A. A single-atom electron spin qubit in silicon. *Nature* **2012**, *489*, 541−545.
(7) Warner, M.; Din, S.; Tupitsyn, I. S.; Morley, G. W.; Stoneham, A. M.; Gardener, J. A.; Wu, Z.; Fisher, A. J.; Heutz, S.; Kay, C. W. M.; Aeppli, G. Potential for spin-based information processing in a thin-film molecular semiconductor. *Nature* **2013**, *503*, 504−508.
(8) Ardavan, A.; Rival, O.; Morton, J. J. L.; Blundell, S. J.; Tyryshkin, A. M.; Timco, G. A.; Winpenny, R. E. P. Will Spin-Relaxation Times in Molecular Magnets Permit Quantum Information Processing? *Phys. Rev. Lett.* **2007**, *98*, 057201.
(9) Laucht, A.; Muhonen, J. T.; Mohiyaddin, F. A.; Kalra, R.; Dehollain, J. P.; Freer, S.; Hudson, F. E.; Veldhorst, M.; Rahman, R.; Klimeck, G.; Itoh, K. M.; Jamieson, D. N.; McCallum, J. C.; Dzurak, A. S.; Morello, A. Electrically controlling single-spin qubits in a continuous microwave field. *Sci. Adv.* **2015**, *1*, e1500022.
(10) Kennedy, T. A.; Colton, J. S.; Butler, J. E.; Linares, R. C.; Doering, P. J. Long coherence times at 300 K for nitrogen-vacancy center spins in diamond grown by chemical vapor deposition. *Appl. Phys. Lett.* **2003**, *83*, 4190−4192.
(11) Balasubramanian, G.; Neumann, P.; Twitchen, D.; Markham, M.; Kolesov, R.; Mizuochi, N.; Isoya, J.; Achard, J.; Beck, J.; Tissler, J.; Jacques, V.; Hemmer, P. R.; Jelezko, F.; Wrachtrup, J. Ultralong spin coherence time in isotopically engineered diamond. *Nat. Mater.* **2009**, *8*, 383−387.
(12) Tyryshkin, A. M.; Tojo, S.; Morton, J. J. L.; Riemann, H.; Abrosimov, N. V.; Becker, P.; Pohl, H.-J.; Schenkel, T.; Thewalt, M. L. W.; Itoh, K. M.; Lyon, S. A. Electron spin coherence exceeding seconds in high-purity silicon. *Nat. Mater.* **2011**, *11*, 143−147.
(13) Troiani, F.; Affronte, M. Molecular spins for quantum information technologies. *Chem. Soc. Rev.* **2011**, *40*, 3119−3129.
(14) Aromi, G.; Aguila, D.; Gamez, P.; Luis, F.; Roubeau, O. Design of magnetic coordination complexes for quantum computing. *Chem. Soc. Rev.* **2012**, *41*, 537−546.
(15) Bader, K.; Dengler, D.; Lenz, S.; Endeward, B.; Jiang, S.-D.; Neugebauer, P.; van Slageren, J. Room temperature quantum coherence in a potential molecular qubit. *Nat. Commun.* **2014**, *5*, 5304.
(16) Zadrozny, J. M.; Niklas, J.; Poluektov, O. G.; Freedman, D. E. Multiple Quantum Coherences from Hyperfine Transitions in a Vanadium(IV) Complex. *J. Am. Chem. Soc.* **2014**, *136*, 15841−15844.
(17) Tesi, L.; Lucaccini, E.; Cimatti, I.; Perfetti, M.; Mannini, M.; Atzori, M.; Morra, E.; Chiesa, M.; Caneschi, A.; Sorace, L.; Sessoli, R. Quantum Coherence in a processable vanadyl complex: new tools for the search of molecular spin qubits. *Chem. Sci.* **2016**, *7*, 2074−2083.
(18) Atzori, M.; Tesi, L.; Morra, E.; Chiesa, M.; Sorace, L.; Sessoli, R. Room-Temperature Quantum Coherence and Rabi Oscillations in Vanadyl Phthalocyanine: Toward Multifunctional Molecular Spin Qubits. *J. Am. Chem. Soc.* **2016**, *138*, 2154−2157.
(19) Zadrozny, J. M.; Niklas, J.; Poluektov, O. G.; Freedman, D. E. Millisecond Coherence Time in a Tunable Molecular Electronic Spin Qubit. *ACS Cent. Sci.* **2015**, *1*, 488.
(20) Atzori, M.; Morra, E.; Tesi, L.; Albino, A.; Chiesa, M.; Sorace, L.; Sessoli, R. Quantum Coherence Times Enhancement in Vanadium(IV)-based Potential Molecular Qubits: the Key Role of the Vanadyl Moiety. *J. Am. Chem. Soc.* **2016**, *138*, 11234−11244.
(21) Gatteschi, D.; Sessoli, R.; Villain, J. *Molecular Nanomagnets*; Oxford University Press: Oxford, U.K., 2006.
(22) Atzori, M.; Tesi, L.; Benci, S.; Lunghi, A.; Righini, R.; Taschin, A.; Torre, R.; Sorace, L.; Sessoli, R. Spin Dynamics and Low Energy Vibrations: Insights from Vanadyl-Based Potential Molecular Qubits. *J. Am. Chem. Soc.* **2017**, *139*, 4338−4341.
(23) Escalera-Moreno, L.; Suaud, N.; Gaita-Ariño, A.; Coronado, E. Determining Key Local Vibrations in the Relaxation of Molecular Spin Qubits and Single-Molecule Magnets. *J. Phys. Chem. Lett.* **2017**, *8*, 1695−1700.
(24) Lunghi, A.; Totti, F.; Sessoli, R.; Sanvito, S. The role of anharmonic phonons in under-barrier spin relaxation of single molecule magnets. *Nat. Commun.* **2017**, *8*, 14620.
(25) Lunghi, A.; Totti, F.; Sanvito, S.; Sessoli, R. Intra-molecular origin of the spin-phonon coupling in slow-relaxing molecular magnets. *Chem. Sci.* **2017**, *8*, 6051−6059.
(26) Cooper, S. R.; Koh, Y. B.; Raymond, K. N. Synthetic, structural, and physical studies of bis(triethylammonium) tris(catecholato)-vanadate(IV), potassium bis(catecholato)oxovanadate(IV), and potassium tris(catecholato)vanadate (III). *J. Am. Chem. Soc.* **1982**, *104*, 5092−5102.
(27) Chi, Z.; Zhu, L.; Lu, X.; Yu, H.; Liu, B. Comparative Study of three Mononuclear Vanadium-Aromatic 1,2-Diol Complexes: Structure, Characterization and Anti-Proliferating Effects Against Cancer Cells. *Z. Anorg. Allg. Chem.* **2012**, *638*, 1523−1530.
(28) Stoll, S.; Schweiger, A. EasySpin, a comprehensive software package for spectral simulation and analysis in EPR. *J. Magn. Reson.* **2006**, *178*, 42−55.
(29) Standeley, K. J.; Vaughan, R. A. *Electron Spin Relaxation Phenomena in Solids*; Plenum Press: New York, 1969; pp 199−236.
(30) Tesi, L.; Lunghi, A.; Atzori, M.; Lucaccini, E.; Sorace, L.; Totti, F.; Sessoli, R. Giant spin-phonon bottleneck effects in evaporable vanadyl-based molecules with long spin coherence. *Dalton Trans.* **2016**, *45*, 16635−16643.
(31) Van Vleck, J. H. Paramagnetic Relaxation Times for Titanium and Chrome Alum. *Phys. Rev.* **1940**, *57*, 426−447.
(32) De Vroomen, A. C.; Lijphart, E. E.; Prins, D. Y. H.; Marks, J.; Poulis, N. J. Electron spin-lattice relaxation of the Zeeman and interaction systems in $CuCs_2(SO_4)_2{\cdot}6H_2O$. *Physica* **1972**, *61*, 241−249.
(33) Butcher, F. K.; Gerrard, W.; Howarth, M.; Mooney, E. F.; Willis, H. A. The infrared spectra of the aryl boronate esters derived from catechol and 2:3 dihydroxynaphthalene. *AcSpe* **1964**, *20*, 79−95.
(34) Ponseca, C. J. S.; Estacio, E.; Murakami, H.; Sarukura, N.; Pobre, R.; Tominaga, K.; Nishizawa, J.; Sasaki, T.; Suto, K. Experimental and calculated terahertz spectra of naphthalene and 1,4-dihydroxynaphthalene in the 0.5 - 6 terahertz region. *J. Phys.: Conf. Ser.* **2008**, *112*, 042073.
(35) Zheng, Z.-P.; Fan, W.-H.; Yan, H. Terahertz absorption spectra of benzene-1,2-diol, benzene-1,3-diol and benzene-1,4-diol. *Chem. Phys. Lett.* **2012**, *525-526*, 140−143.
(36) Eaton, S. S.; Eaton, G. R. In *Distance Measurements in Biological Systems by EPR*; Berliner, L. J., Eaton, G. R., Eaton, S. S., Eds.; Springer: Boston, MA, 2002; pp 29−154.
(37) Yu, C.-J.; Graham, M. J.; Zadrozny, J. M.; Niklas, J.; Krzyaniak, M. D.; Wasielewski, M. R.; Poluektov, O. G.; Freedman, D. E. Long Coherence Times in Nuclear Spin-Free Vanadyl Qubits. *J. Am. Chem. Soc.* **2016**, *138*, 14678−14685.
(38) Sheldrick, G. M. *Programs for the Refinement of Crystal Structures*; University of Göttingen: Göttingen, Germany, 1996.
(39) Farrugia, L. WinGX suite for small-molecule single-crystal crystallography. *J. Appl. Crystallogr.* **1999**, *32*, 837−838.
(40) Macrae, C. F.; Edgington, P. R.; McCabe, P.; Pidcock, E.; Shields, G. P.; Taylor, R.; Towler, M.; van de Streek, J. Mercury: visualization and analysis of crystal structures. *J. Appl. Crystallogr.* **2006**, *39*, 453−457.
(41) Bain, G. A.; Berry, J. F. Diamagnetic Corrections and Pascal's Constants. *J. Chem. Educ.* **2008**, *85*, 532.
(42) Taschin, A.; Bartolini, P.; Tasseva, J.; Torre, R. THz time-domain spectroscopic investigations of thin films. *Measurement* **2017**, DOI: 10.1016/j.measurement.2017.05.074.

DOI: 10.1021/acs.inorgchem.7b02616
Inorg. Chem. 2018, 57, 731−740

CHEMISTRY
A European Journal

www.chemeurj.org

Reprint

A Journal of
ChemPubSoc Europe
ACES
Asian Chemical Editorial Society
WILEY-VCH

ChemPubSoc Europe

DOI: 10.1002/chem.201801026

CHEMISTRY A European Journal Full Paper

Molecular Magnetism

A Pseudo-Octahedral Cobalt(II) Complex with Bispyrazolylpyridine Ligands Acting as a Zero-Field Single-Molecule Magnet with Easy Axis Anisotropy

Luca Rigamonti,*[a] Nathalie Bridonneau,[a, e] Giordano Poneti,[b, f] Lorenzo Tesi,[b] Lorenzo Sorace,[b] Dawid Pinkowicz,[c] Jesus Jover,[d] Eliseo Ruiz,[d] Roberta Sessoli,[b] and Andrea Cornia[a]

Abstract: The homoleptic mononuclear compound [Co(bpp-COOMe)$_2$](ClO$_4$)$_2$ (**1**) (bpp-COOMe = methyl 2,6-di(pyrazol-1-yl)pyridine-4-carboxylate) crystallizes in the monoclinic *C*2/*c* space group, and the cobalt(II) ion possesses a pseudo-octahedral environment given by the two *mer*-coordinated tridentate ligands. Direct-current magnetic data, single-crystal torque magnetometry, and EPR measurements disclosed the easy-axis nature of this cobalt(II) complex, which shows single-molecule magnet behavior when a static field is applied in alternating-current susceptibility measurements. Diamagnetic dilution in the zinc(II) analogue [Zn(bpp-COOMe)$_2$](ClO$_4$)$_2$ (**2**) afforded the derivative [Zn$_{0.95}$Co$_{0.05}$(bpp-COOMe)$_2$](ClO$_4$)$_2$ (**3**), which exhibits slow relaxation of magnetization even in zero field thanks to the reduction of dipolar interactions. Theoretical calculations confirmed the overall electronic structure and the magnetic scenario of the compound as drawn by experimental data, thus confirming the spin-phonon Raman relaxation mechanism, and a direct quantum tunneling in the ground state as the most plausible relaxation pathway in zero field.

Introduction

Single-molecule magnets (SMMs) can in principle be used for encoding binary information and for data processing, thus exploiting their magnetic bistability and inherent quantum behavior.[1] Research in this field moves in different directions, such as finding better performing systems,[2,3] developing reliable methods to deposit molecules on solid substrates,[4,5] and finding ways to control molecular magnetism by external stimuli, including light and pressure.[6–8] Complexes that contain only one metal center may represent the smallest chemically tuneable SMMs for spin-based devices,[9] and significant progress has been made in this regard by using lanthanides[3,10] and, more recently, 3d metal ions.[10,11] In the latter case, relaxation by quantum tunneling is usually very fast in zero field, so that application of a static field is required to observe SMM behavior by alternating-current (ac) susceptibility measurements. However, few examples of zero-field SMMs based on mononuclear complexes of iron(I)[12] iron(III),[13] and cobalt(II) have been reported,[14–25] which all feature half-integer spin states ($S = 3/2$ or 5/2). In particular, individual cobalt(II) ions were found to exhibit zero-field SMM behavior when embedded in tetrahedral,[14–17,20,22,24] trigonal prismatic,[18,19,23] or linear[21] coordination environments or in a solid-state lattice.[25] In all these cases, the metal complexes possess a negative zero field splitting (zfs) parameter (D), thus suggesting the investigation of other coordination environments suitable to enforce an easy-axis magnetic anisotropy on the cobalt(II) ion.

[a] Dr. L. Rigamonti, Dr. N. Bridonneau, Prof. A. Cornia
Dipartimento di Scienze Chimiche e Geologiche
Università degli Studi di Modena e Reggio Emilia
and INSTM RU of Modena and Reggio Emilia
via G. Campi 103, 41125 Modena (Italy)
E-mail: luca.rigamonti@unimore.it
luca.rigamonti@yahoo.com

[b] Dr. G. Poneti, Dr. L. Tesi, Prof. L. Sorace, Prof. R. Sessoli
Laboratory of Molecular Magnetism (LAMM), Dipartimento di Chimica 'Ugo Schiff', Università degli Studi di Firenze, and INSTM RU of Firenze
via della Lastruccia 3–13, 50019 Sesto Fiorentino, FI (Italy)

[c] Dr. D. Pinkowicz
Faculty of Chemistry, Jagiellonian University
Gronostajowa 2, 30-387 Kraków (Poland)

[d] Dr. J. Jover, Prof. E. Ruiz
Departament de Química Inorgànica i Orgànica,
Institut de Química Teòrica i Computacional
Universitat de Barcelona, Diagonal 645, 08028 Barcelona (Spain)

[e] Dr. N. Bridonneau
Current address:
Laboratoire Interfaces Traitements Organisation
et Dynamique des Systèmes (ITODYS), UMR 7086 CNRS
Université Paris 7 Diderot, Paris Bât. Lavoisier
15 rue Jean-Antoine de Baïf, 75205 Paris Cedex 13 (France)

[f] Dr. G. Poneti
Current address:
Instituto de Química, Universidade Federal do Rio de Janeiro
21941-909 Rio de Janeiro (Brazil)

Supporting information and the ORCID numbers for the authors of this article can be found under https://doi.org/10.1002/chem.201801026.

The 2,6-bis(pyrazol-1-yl)pyridine (bpp) class of ligands is well known for the promotion of spin-crossover (SCO) in octahedral iron(II) metal complexes.[26–28] These ligands can host both high-spin (HS) and low-spin (LS) iron(II) centers,[27] thus enabling spin-state modulation by temperature or application of light.[29,30] In some cases, the distortion of the octahedral geometry is so pronounced as to block the metal center in its HS state, as we recently found when using methyl 2,6-di(pyrazol-1-yl)pyridine-4-carboxylate (bpp-COOMe).[26] In particular, in the distorted molecular structure of $[Fe(bpp\text{-}COOMe)_2](ClO_4)_2$, the pseudo-octahedral coordination environment leads to a stabilization of the d_{xy} orbital relative to d_{xz} and d_{yz} (where *z* represents the *trans*-N{pyridyl}-Fe-N{pyridyl} direction and *x* and *y* represent the directions of the coordinated pyrazolyl nitrogen atoms).[26]

Such an orbital pattern is expected to produce an easy-axis anisotropy for cobalt(II), as sought for.[31] We have thus synthesized $[Co(bpp\text{-}COOMe)_2](ClO_4)_2$ (**1**) by reaction of cobalt(II) perchlorate with bpp-COOMe and found this compound to be isostructural to the iron(II) complex.[26] From the study of the magnetic properties of **1**, we discovered that it has an easy-axis anisotropy and shows SMM behavior under an applied external field. Magnetic dilution in the zinc(II) analogue $[Zn(bpp\text{-}COOMe)_2](ClO_4)_2$ (**2**) afforded $[Zn_{0.95}Co_{0.05}(bpp\text{-}COOMe)_2](ClO_4)_2$ (**3**), in which dipolar interactions are reduced and slow relaxation of the magnetization is detectable even in zero field. To the best of our knowledge, this finding discloses the first fully characterized pseudo-octahedral cobalt(II) complex with easy-axis anisotropy that acts as a zero-field SMM.[32] Herein, we present detailed and critical descriptions of the experimental data collected by direct-current (dc) and ac magnetic measurements, X-band electron paramagnetic resonance (EPR) spectroscopy, single-crystal cantilever torque magnetometry (CTM), and ab initio theoretical calculations in support for the magnetic properties of **1**.

Results and Discussion

Synthesis, crystallization, and molecular structures

The reaction of a suspension of bpp-COOMe in acetonitrile with $[M(ClO_4)_2]\cdot 6H_2O$ (M=Co, Zn; either as pure salts or in a mixture) at room temperature produced the immediate dissolution of the ligand and formation of a solution, which gave well-formed X-ray-quality crystals of **1** (light red), **2** (colorless), or **3** (very light orange) in good yield by vapour diffusion with diethyl ether. The crystals of the three compounds are air stable, belong to the monoclinic space group *C*2/*c*, and are isomorphous to the iron(II) derivative recently studied for its SCO properties (see Tables S1 and S2 in the Supporting Information for a comparison of the room-temperature unit-cell parameters).[26] X-ray diffraction data were collected at 295 and 161 K for **1** and at 120 K for **2** to determine the molecular structures, and the main bond lengths and angles obtained are reported in Table 1.

In all cases, the metal coordination environments show a pronounced distortion from a perfect octahedral geometry

Table 1. Main bond lengths [Å] and angles [°] of **1** (Co) and **2** (Zn).

	1 [T = 295 K]	**1** [T = 161 K]	**2** [T = 120 K]
M1–N1	2.142(2)	2.141(2)	2.1428(16)
M1–N14	2.148(2)	2.152(2)	2.2056(16)
M1–N15 (py)	2.082(2)	2.080(2)	2.1216(16)
N1-M1-N15	74.56(9)	74.73(8)	74.43(6)
N15-M1-N14	74.91(9)	74.93(8)	73.49(6)
N1-M1-N14 (ψ)	148.76(9)	148.99(8)	147.72(6)
N15-M1-N15′[a] (ϕ)	161.12(13)	161.45(8)	160.36(6)
θ[b]	81.21	81.59	82.92
Σ[c]	140.1	139.1	145.6
Θ[c]	445	444	457

[a] The N15′ atom is obtained from N15 through a twofold rotation. [b] Dihedral angle between the two ligands (the plane of each ligand was defined as the least-squares plane through its sixteen aromatic C/N atoms). [c] See ref. [28] for the definition. py = pyridine.

(see Figure 1 and Figure S1 in the Supporting Information). This finding is best outlined by the *trans*-N{pyridyl}-M-N{pyridyl} angle (ϕ) and the dihedral angle between the least squares (ls) planes of the two *mer*-coordinated ligands (θ), which lie far from the ideal values of 180 and 90°, respectively.[27] Although

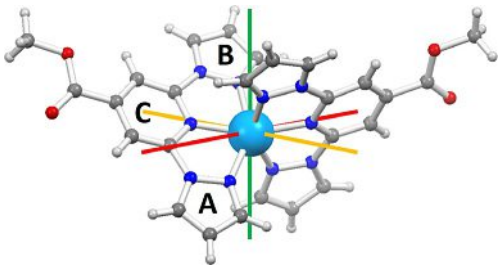

Figure 1. Molecular structure of the $[Co(bpp\text{-}COOMe)_2]^{2+}$ cation of **1** at low temperature in a perspective view with ring labeling (ring A = N1N4C3C2C1, ring B = N14N10C11C12C13, ring C = N15C5C6C7C8C9, where N1, N14, and N15 are the donor atoms to cobalt). The magnetic anisotropy axes were obtained by single-crystal CTM and EPR measurements. Co = azure, O = red, N = blue, C = light gray, H = white; easy axis = red, intermediate axis = green, hard axis = yellow.

the cobalt(II) ion in **1** is Jahn–Teller active,[33] the described distortion is most probably caused by crystal-packing effects because this distortion is present, to almost the same extent, in the zinc(II) derivative **2**. Note that the most regular geometry would still exhibit departures from the perfect octahedral symmetry due to the intrinsic shape of the bpp ligands, which imposes a clamp angle (ψ) of less than 180°. The distortion is also highlighted by the high values of the parameters Σ and Θ (Table 1). The first parameter is a general measure of the deviation of a metal ion from an ideal octahedral geometry, whereas the Θ value more specifically indicates the distortion from an octahedral environment toward a trigonal-prismatic structure.[28] In fact, a perfectly octahedral complex would give $\Sigma = \Theta = 0$.

The Co–N bond lengths in **1** (Table 1) range from 2.08 Å with the pyridyl nitrogen atom (ring C) to about 2.15 Å with

the pyrazolyl moieties (rings A and B), which are partially rotated by about 6–10° with respect to the ls plane of the whole ligand; furthermore, these values remain the same within experimental error upon variation of the temperature. The ester group is coplanar with the pyridyl ring C and is involved in one of the two shortest intermolecular interactions with one pyrazolyl C–H group (C1(H1)···O17 = 3.252/3.291 Å, C1-H1···O17 = 147.6/148.9° at 161/295 K), which leads to a Co···Co distance of 9.642/9.664 Å. The second short intermolecular contact involves another C–H group and the pyrazolyl ring of the adjacent molecule (C12(H12)···centroid(ring A) = 3.47/3.52 Å, C12-H12···centroid(ring A) = 150/149° at 161/295 K) with a shorter intermolecular Co···Co distance of 8.494/8.530 Å. Perchlorate anions are located in the voids between the cations, and all the oxygen atoms are involved in weak C–H···O interactions (see Figure S1 and Tables S3 and S4 in the Supporting Information).

The zinc derivative **2** shows similar structural features relative to **1**, with only slightly longer Zn–N distances with the pyrazolyl rings (Table 1), but fully comparable crystal packing (see Table S5 in the Supporting Information), which allowed us to successfully obtain the diamagnetically diluted crystalline sample **3** containing a Zn/Co ratio of 18:1 (i.e., $Zn_{0.9475}Co_{0.0525}$), as confirmed by inductively coupled plasma optical emission spectrometry (ICP-OES).

Static magnetic properties

Dc magnetic susceptibility data of **1** were recorded in the temperature range 2–300 K in a low-field regime (1 kOe up to 40 K and 10 kOe from 30 to 300 K), together with the field dependence of the isothermal molar magnetization (M_M) at low temperature (Figure 2). The product of the molar magnetic susceptibility (χ_M) and the temperature (T) was about 2.84 emu K mol^{-1} at 300 K, against an expected spin-only value of 1.875 emu K mol^{-1} for an $S = 3/2$ ion with $g = 2.00$. This difference indicates a relevant orbital contribution to the magnetism, which can be parametrized in the first approximation by

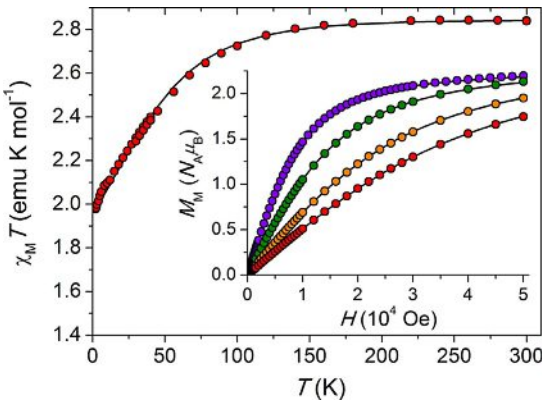

Figure 2. Temperature dependence of the $\chi_M T$ product for **1** (red circles in the main panel; overlapped points in the range 30–40 K refer to measurements at 1 and 10 kOe). Inset: field dependence of the molar magnetization (M_M) at 1.8 (blue), 3.0 (green), 5.0 (yellow), and 7.0 (red) K. Solid lines are given by the best-fit parameters (see the text for details).

assuming $g = 2.46$. The $\chi_M T$ value remains almost unvaried upon cooling down to 90 K, at which point it begins to slowly decrease to 1.98 emu K mol^{-1} at 2.0 K, which is consistent with the depopulation of the spin-orbit and low-symmetry split states of the $^4T_{1g}(O_h)$ electronic term.

Although a spin Hamiltonian formalism might be inadequate to account for the electronic structure of the cobalt(II) ion,[34] we first used the following Hamiltonian to fit the experimental $\chi_M T(T)$ and $M_M(H)$ data simultaneously by using the PHI program [Eq. (1)]:[35]

$$\begin{aligned}\mathcal{H} &= \mathcal{H}_{Zeeman} + \mathcal{H}_{zfs} = \mu_B \hat{B}\cdot\bar{\boldsymbol{g}}\cdot\hat{S} + \hat{S}\cdot\bar{\boldsymbol{D}}\cdot\hat{S} \\ &= g_x\mu_B B_x S_x + g_y\mu_B B_y S_y + g_z\mu_B B_z S_z + \\ &\quad D\left[S_z^2 - \frac{1}{3}S(S+1)\right] + E\left(S_x^2 - S_y^2\right)\end{aligned} \tag{1}$$

in which D and E are the axial and transverse second-order anisotropy parameters (defined from the principal components of the $\bar{\boldsymbol{D}}$ matrix as $D = 3D_{zz}/2$ and $E = (D_{xx} - D_{yy})/2$) and g_x, g_y, and g_z are the principal components of the $\bar{\boldsymbol{g}}$ matrix for the $S = 3/2$ state ($\bar{\boldsymbol{D}}$ and $\bar{\boldsymbol{g}}$ were assumed to be collinear). By taking an axial $\bar{\boldsymbol{g}}$ matrix with $g_x = g_y$ for simplicity, a systematic survey was performed with g_α values ($\alpha = x, y, z$) from 1.8 to 3.2 and diagonal components of $\bar{\boldsymbol{D}}$ from −90 to 90 cm^{-1}. An accurate fit was only possible for negative D values and a unique solution fulfilled the condition expected for easy-axis cobalt(II) ions, namely $g_z > g_x = g_y$: $D = -57.5(7)$, $|E| = 15.7(3)$ cm^{-1}; $g_x = g_y = 2.332(4)$, $g_z = 2.6687(15)$. As can be noted, the cobalt(II) ion has an easy-axis anisotropy, but with a relevant rhombic distortion, as given by $|E/D| = 0.273$ (the sign of E is irrelevant for powder measurements when $g_x = g_y$). The resulting splitting of the $S = 3/2$ manifold is $2(D^2 + 3E^2)^{1/2} = 127$ cm^{-1}.

Torque magnetometry

To gain independent experimental evidence of the magnetic anisotropy, CTM experiments were performed on a face-indexed single crystal of **1** mounted on a rotating capacitive cantilever torquemeter. The device measures the torque component (τ_Y) along the rotation axis (Y), whereas the magnetic field is applied normal to Y in the XZ plane at an angle θ from Z (θ increases going from Z toward $-X$).[36,37] The measured torque is thus given by Equation (2):

$$\tau_Y = m_Z B_X - m_X B_Z \tag{2}$$

in which $\mathbf{m} = (m_X, m_Y, m_Z)$ is the magnetic moment of the sample and $\mathbf{B} = (B_X, 0, B_Z)$ is the applied magnetic field. Two rotations (Rot1 and Rot2) were performed in which the XYZ frame corresponds to the orthogonalized crystallographic frame a^*bc (Rot1) or $-a^*cb$ (Rot2) (see the Supporting Information for further details). Thanks to the fact that the cobalt(II) ion in **1** is located on a binary axis of the monoclinic $C2/c$ space group, only one molecule is magnetically independent. Moreover, one of the principal directions of the magnetic anisotropy tensor (e.g., y) must coincide with this binary axis,

which is parallel to *b*, whereas the others (*x* and *z*) must lie in the *a***c* plane. When scanning this plane, as in Rot1, and working in the low-field limit Equation (2) becomes Equation (3):

$$\tau_y(\phi) = B^2(\chi_{zz}-\chi_{xx})\sin\phi\cos\phi \quad (3)$$

in which $\bar{\chi}$ is the susceptibility tensor and $\phi=\theta_z-\theta$ is the angle between the principal anisotropy axis *z* and **B** (i.e., the magnetic field is applied along *z* at $\theta=\theta_z$). The principal directions of the anisotropy tensor, separated by $\pi/2$ but arbitrarily located in the *a***c* plane, are easily detected as zero-torque points. Furthermore, the easy or hard character becomes evident by increasing the field at low temperature; as a result, when the low-field limit is no longer valid the curves become steeper around the hard-axis zero-torque point.[37] The measurements, performed at 10 K under a static magnetic field of 2 and 4 T and at 100 K with a magnetic field of 10 and 12 T, are reported in Figure 3, whereas the data at intermediate temperatures are available in Figure S2 (see the Supporting Information).

In Rot1 (*XYZ*=*a***bc*) at 10 K, we find the first torque zero point at $\theta=43^\circ$ on going from *c* toward $-a^*$; thus, the first in-plane principal direction (*x*) deviates by only about 10° from the *a* crystallographic axis (see Figure S3 in the Supporting Information). The second torque zero point occurs at $\theta=133^\circ$ and corresponds to the second in-plane principal direction *z* ($\theta_z=133^\circ$). The sign of the measured torque signal directly indicates that *z* (*x*) is the easy (hard) in-plane direction. The same conclusion can be reached looking at the data obtained at 4 T. At this field, the torque curve deviates from the simple angular dependence given by Equation (3), thus showing a steeper angular variation $\theta=43^\circ$, which is identified as the hard direction in the scanned plane.

For Rot2 (*XYZ*=−*a***cb*), the two torque zero points are found at $\theta=0$ and 90°, as expected; that is, when the field is applied along the *b* and *a** crystallographic axes, respectively. Unlike the former, the latter field orientation does not individuate a principal anisotropy axis, but only the projection on the *a***b* plane. Both the sign and shape of the torque signal in this rotation indicate that the crystal is more easily magnetized along *a** than *b*. However, it is not possible to establish whether *b* is the overall intermediate or hard anisotropy axis from a qualitative analysis. To solve this ambiguity, the data obtained at $T=10$ K were numerically simulated with the $S=3/2$ spin Hamiltonian in Equation (1). As a first step, the $\bar{\boldsymbol{g}}$ and $\bar{\boldsymbol{D}}$ matrices were constrained to have principal values determined by means of dc magnetic measurements, but the common principal directions were left free to reorient in space and an overall scale factor was refined to account for the incertitude on the mass of the crystal (ca. 80 μg). In a second step, the principal values were also left free to vary; however, this approach did not provide any improvement in the agreement.

In the end, the fitting procedure indicated that *b* is the overall intermediate axis (i.e., *y* in [Eq. (1)] with $E>0$), whereas the

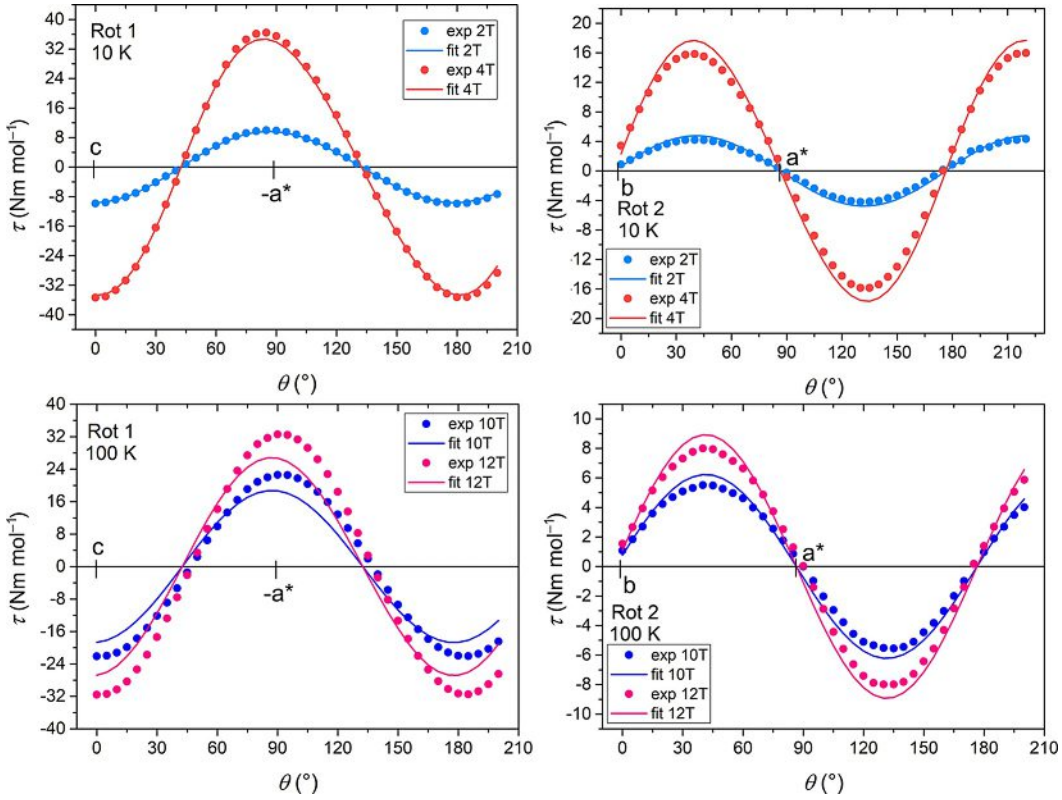

Figure 3. Experimental data (dots) and simulated curves with $S=3/2$ spin Hamiltonian (solid lines; N m mol^{-1}) of **1** obtained with CTM for two rotations at 10 and 100 K under different static magnetic fields. The common orientation of the $\bar{\boldsymbol{g}}$ and $\bar{\boldsymbol{D}}$ matrices was optimized from the 10 K data by using the principal values obtained from magnetization and susceptibility data.

*a***c* plane contains the easy (*z*) and hard (*x*) molecular magnetic axes, with the latter at approximately 10° from *a*. The orientation of the anisotropy axes shown in Figure 1 is superimposed onto the molecular structure, where the principal axes do not point toward, but between, the ligand atoms. The good agreement between the simulated and experimental torque data confirms the spin Hamiltonian parameters extracted from the static magnetic measurements, in particular the negative sign of *D* with a relatively large rhombicity. On the other hand, Figure 3 shows that the agreement is less satisfactory at 100 K. The inclusion of rhombicity in the $\bar{g}$ matrix (see the section on EPR spectroscopy), that is, $g_x \neq g_y$, does not improve the quality of the fit, as indeed expected because the torque measurements are mainly sensitive to the $\bar{D}$ tensor. Keeping in mind that the orbital angular momentum of the cobalt(II) ion may be not completely quenched, the magnetic properties are affected on increasing the temperature by spin-orbit coupled states at higher energies and the description of the metal ion as a simple $S=3/2$ spin may be no longer valid. This outcome would result in a failure of the spin Hamiltonian approach, thus leaving ab initio methods and explicit inclusion of the orbital contribution[34] as the only ways to appropriately describe the system (see below).

EPR spectroscopy

EPR spectroscopy can be regarded as a complementary technique to CTM because EPR spectroscopic analysis can easily provide detailed information on the $\bar{g}$ matrix. Low-temperature continuous-wave X-band EPR spectra were recorded for powder and single-crystal samples. The experimental spectrum of a powder sample of **3** (Figure 4) can be easily interpreted as arising from an effective spin doublet with strongly anisotropic *g* factor and hyperfine coupling with the nuclear spin $I=7/2$ of ^{59}Co (natural abundance = 100%). Similar spectra were obtained for **1**, although dominant dipolar broadening precludes resolution of the hyperfine structure (see Figure S4 in the Supporting Information). In this frame, it is evident that the anisotropy of the ground doublet is of the easy-axis type, with "parallel" transition at low fields, and a non-negligible rhombicity,

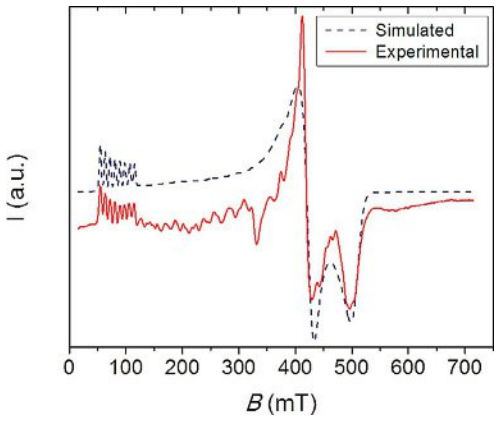

Figure 4. X-band ($\tilde{\nu}=9.43$ GHz) continuous wave EPR spectrum recorded at 5 K on a powder sample of **3** (solid line) and its simulation (dash line).

as evidenced by the separation of the perpendicular transitions in the region 400–500 mT. The experimental spectrum was simulated by using the following spin Hamiltonian [Eq. (4)]:[38]

$$\mathcal{H}' = \mathcal{H}'_{Zeeman} + \mathcal{H}'_{hyperfine} = \mu_B \hat{B} \cdot \bar{g}' \cdot \hat{S}' + \hat{S}' \cdot \bar{A}' \cdot \hat{I}' \qquad (4)$$

in which the primed parameters are associated with the effective spin $S'=1/2$. The best simulation was obtained by assuming an axial hyperfine coupling tensor ($\mathscr{A}'_{1,2}=2\pm1\times10^{-3}$ and $\mathscr{A}'_3=3.20\pm0.05\times10^{-2}$ cm^{-1}) and a moderately rhombic effective $\bar{g}'$ matrix ($g'_1=1.37\pm0.02$, $g'_2=1.62\pm0.02$, and $g'_3=7.930\pm0.002$).

The principal values of the effective $\bar{g}'$ matrix can be related to the spin Hamiltonian parameters of an $S=3/2$ system through the following equations, which are valid only for easy-axis systems (i.e., $D<0$) [Eq. (5)]:[39]

$$g'_1 = g_x\left(1-\frac{1-3\eta}{\sqrt{1+3\eta^2}}\right),\quad g'_2 = g_y\left(1-\frac{1+3\eta}{\sqrt{1+3\eta^2}}\right),\quad g'_3 = g_z\left(\frac{2}{\sqrt{1+3\eta^2}}+1\right) \qquad (5)$$

in which $\eta=E/D$. For purely axial anisotropy ($\eta=0$), Equation (5) affords $g'_1=g'_2=0$ and $g'_3=3g_z$. The non-zero experimental values of g'_1 and g'_2 are then consistent with a significant rhombic anisotropy. It is evident that, depending on the value of η, different solutions for g_x, g_y, and g_z can be found because the problem is over-parametrized. However, sets of solutions in reasonable accordance with those extrapolated from magnetic measurements and confirmed by CTM measurements can be found by assuming the rhombicity to lie in the range $-0.28<\eta<-0.22$. In particular, if one fixes $\eta=-0.273$, as obtained from the magnetic analysis, the application of Equation (5) provides the following estimates of the principal *g* values for the $S=3/2$ system: $g_x=2.125$, $g_y=1.935$, and $g_z=2.825$ (alternatively, assuming $\eta=0.273$, $g_x=1.935$, $g_y=2.125$, and $g_z=2.825$). We note that no reproduction of the effective g' pattern can be obtained for $\eta=0.273$ and $g_x>g_y$ or for $\eta=-0.273$ and $g_y>g_x$. The outcome of this analysis is that the $\bar{g}$ matrix also has a non-negligible rhombicity, which can be clearly detected only by EPR analysis, whereas the magnetic characterization techniques are mainly sensitive to $\bar{D}$ anisotropy. It should also be noted that the only way to reconcile the Hamiltonian description in Equation (4) with that of the Hamiltonian description in Equation (1) is by assuming that the $\bar{g}$ and $\bar{D}$ matrices for the $S=3/2$ state have opposite rhombicities. This means that the smallest $\bar{g}$ principal value is collinear with the intermediate direction of the $\bar{D}$ tensor, whereas the intermediate $\bar{g}$ component is along the hard direction of the $\bar{D}$ tensor. The resulting partial compensation of the two rhombicities is consistent with the relatively small separation of the perpendicular transitions at high field. At first sight, such behavior is counterintuitive because both anisotropies arise from the same phenomenon, that is, spin-orbit coupling (SOC).

Finally, we measured the angular dependence of the X-band EPR spectrum of a single crystal of **1** at low temperature to assign the easy, hard, and intermediate directions of the mag-

netic anisotropy of the ground doublet. The sample was set to rotate around the *b* axis from $\theta = 0^\circ$, where **B** is parallel to the *c* axis, to $\theta = 90^\circ$, where **B** is parallel to the $-a^*$ axis, as in Rot1 of the CTM measurements. The angular dependence of the spectra is shown in Figure 5. The maximum resonant field ($B_{res} = 491.5$ mT, thus corresponding to $g_{eff} = 1.37$) is observed at $\theta = 40^\circ$, whereas the minimum is found at $\theta = 130^\circ$ ($B_{res} = 85.7$ mT, $g_{eff} = 7.93$). Within experimental error ($\pm 5^\circ$), these two extremes occur along the principal directions of the $\bar{D}$ tensor, as determined by CTM (Figure 3). Furthermore, because $g_{eff} = 1.37$ and 7.93 are also the highest and lowest resonance fields observed in the powder spectrum (Figure 4), both the easy and hard directions of g_{eff} lie in the a^*c plane, thus confirming our assignment of *b* as the intermediate anisotropy axis, although it corresponds to the smallest component of the true $\bar{g}$ tensor.

An alternative description of the electronic structure of distorted octahedral cobalt(II), which explicitly takes into account the unquenched orbital angular momentum, should involve the use of the Griffith Hamiltonian [Eq. (6)]:[40]

$$\mathcal{H} = -\frac{3}{2}\kappa\lambda\hat{L}\cdot\hat{S} + \Delta_{ax}\left[\hat{L}_z^2 - \frac{1}{3}L(L+1)\right] + \Delta_{rh}\left[\hat{L}_x^2 - \hat{L}_y^2\right] + \mu_B\mathbf{B}\cdot\left(g_e\hat{S} - \frac{3}{2}\kappa\hat{L}\right) \quad (6)$$

which operates on the ground $^4T_{1g}$ term of the octahedral cobalt(II) ion. By using the T–P isomorphism,[41] the orbital ($L = 1$) and spin ($S = 3/2$) angular momenta interact through SOC, as described by the first term of the Hamiltonian. Here, the orbital-reduction parameter (κ) takes into account the covalence effect and the mixing of $^4T_{1g}(^4F)$ with $^4T_{1g}(^4P)$ due to the crystal field, whereas $-3/2$ is a constant required by T–P isomorphism. The second term of this Hamiltonian represents the effect of an axial crystal field, thus resulting in a splitting of the orbital triplet $^4T_{1g}$ in octahedral symmetry into $^4A_{2g}$ ($M_L = 0$) and ^4E_g ($M_L = \pm 1$) in tetragonal symmetry. The third term models the rhombic component of the crystal field, which removes the degeneracy of the orbital doublet as symmetry is further lowered to C_2. In this framework, a negative (positive) value of Δ_{ax} results in a ground $^4E_g(^4A_{2g})$ term and corresponds to easy-axis (easy-plane) anisotropy.[34,42,43] Finally, the fourth term is the Zeeman interaction, which comprises spin and orbital contributions. Despite the large number of parameters, by fixing the SOC constant to the free-ion value ($\lambda = -180$ cm^{-1}), the pattern of effective *g* factors for the ground doublet could be reproduced[38] by using parameters that lie in a relatively narrow range, that is, $-2100 < \Delta_{ax} < -1650$, $100 < \Delta_{rh} < 160$ cm^{-1}, $0.8 < \kappa < 1.0$ (see Figure S5 in the Supporting Information). The best agreement was found for $\Delta_{ax} = -1850$, $\Delta_{rh} = 130$, $\kappa = 0.9$, $\lambda = -180$ cm^{-1}, which correspond to $|\Delta_{rh}/\Delta_{ax}| \approx 0.07$. With this set of parameters, the first- and second-excited spin-orbit doublets lie at 210 and 558 cm^{-1} from the ground state, respectively (see Table S6 in the Supporting Information). This outcome suggests that a spin Hamiltonian formalism might not be entirely appropriate for modeling the high-temperature magnetic behaviour because the thermal energy is not completely negligible compared to the second-excited doublet. Interestingly, when the same set of parameters is used to simulate the powder dc magnetic data, the resulting curves are in reasonable agreement with the experimental ones (see Figure S6 in the Supporting Information). On the other hand, if applied to torque measurements, the same set of values reproduces the experimental data of Rot1 well, but is less accurate in simulating the data of Rot2 at 100 K (see Figure S7 in the Supporting Information). This outcome indicates that even this approach is too approximate to capture the finest details of the electronic structure of this system and in particular the information related to rhombicity.

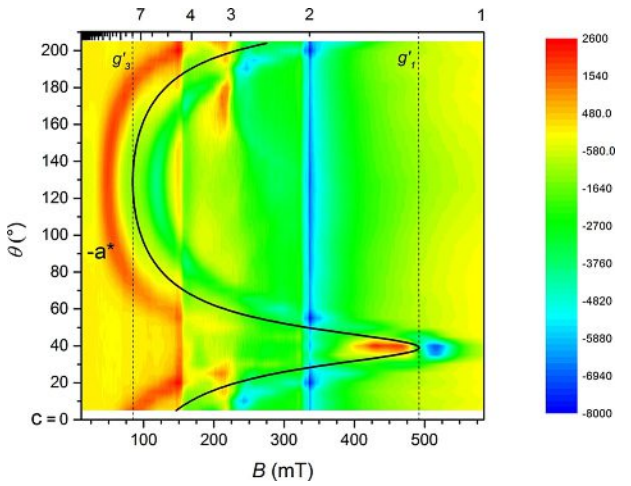

Figure 5. Angular dependence of the resonant fields of the X-band ($\tilde{\nu} = 9.41$ GHz) EPR of a single crystal of **1** at 5 K. The black solid line is the simulated angular dependence of the resonance field by using the parameters reported in the text. The blue line marks a $g = 2.00$ reference impurity in the cavity.

Dynamic magnetic properties

Ac magnetic susceptibility measurements of **1** in zero static field did not display any temperature-dependent peak in out-of-phase susceptibility (χ_M'') measurements. The Kramers nature of the cobalt(II) ion suggests that quantum-tunneling (QT) relaxation paths, induced by hyperfine interactions or intermolecular dipolar couplings, accelerate the relaxation of the magnetization beyond detection. In a static field of 1 kOe, however, clear maxima appeared in the frequency range 10–10000 Hz, the position of which are temperature dependent (see Figure 6a and Figure S8 in the Supporting Information). Treatment of the isothermal $\chi_M''(\nu)$ plots with a generalized Debye model allowed us to extract the relaxation time (τ) at each temperature.[44] These data are shown in Figure 6b as a plot of $\ln\tau(1/T)$. At the highest-temperature interval between 6.5 and 9.5 K, the plot appears to be linear and can be suitably fitted with the Arrhenius law ($\ln\tau = \ln\tau_0 + U_{eff}/k_BT$) with the best-fit parameters $U_{eff}/k_B = 43.6(2)$ K and $\tau_0 = 1.2(2)\times10^{-7}$ s (green line in Figure 6b). These values are in the range previously observed for field-induced pseudo-octahedral mononuclear SMMs.[45] The observed activation barrier to magnetic re-

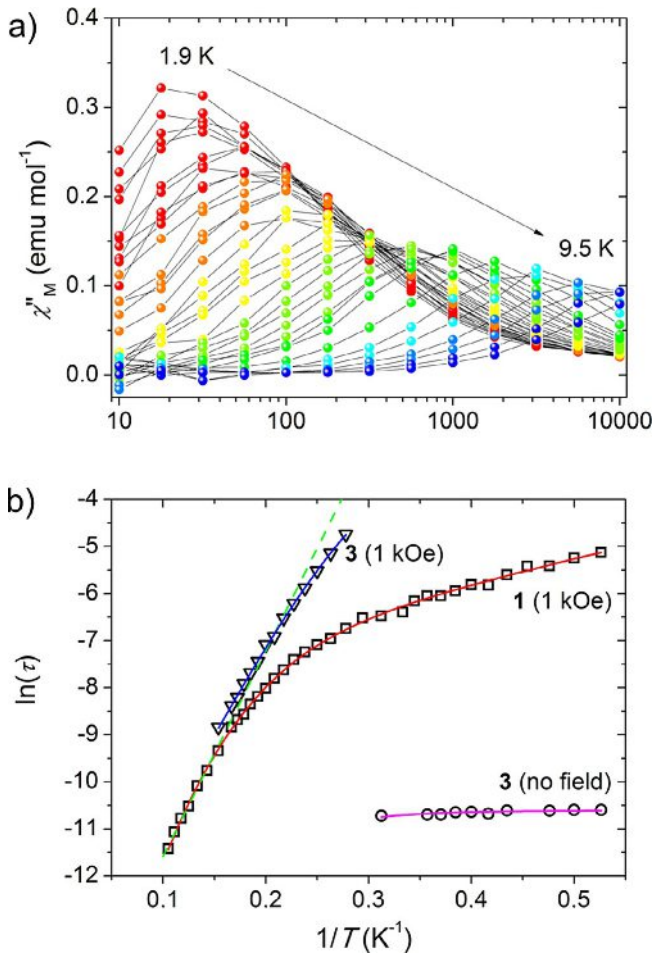

Figure 6. a) Imaginary component of the ac susceptibility (χ_M'') of **1** measured at an applied static field of 1 kOe in the frequency range 10–10 000 Hz and in the temperature range 1.9 (red)–9.5 (blue) K (the gray lines are given as a guide for the eye). b) Arrhenius plot for **1** at an applied static field of 1 kOe (□) and for **3** in a zero field (▽) and a static field of 1 kOe (○). The green dotted line is given by the fitting of **1** in the range 6.5–9.5 K with an Orbach model, whereas the red curve employs a mixed Raman and direct model. The magenta and blue lines display the data fitting of **3** at zero field and an applied field of 1 kOe, respectively (see the text for further discussion).

laxation, however, is well below the splitting between the two lowest-lying doublets (127 cm^{-1} or 165 K, as estimated from dc magnetic data of **1**; see above). On lowering the temperature, a distinct curvature appears in the plot. This deviation from the simple Arrhenius-like behavior can be due to processes induced by either nonresonant spin-phonon interactions in the solid state[46,47] or tunnel mechanisms. To reproduce the temperature dependence of the magnetic relaxation over the whole temperature range, QT (A), direct (BT), and Raman (CT^n) relaxation processes were taken into account in addition to the previous Orbach term, as outlined by Equation (7):

$$\tau^{-1} = \tau_0{}^{-1} \exp(-U_{eff}/k_B T) + A + BT + CT^n \quad (7)$$

To avoid over-parametrization, the number of fitting terms was kept as low as possible and the quantum-tunneling mechanism was considered to be quenched by the applied static field ($A = 0$). Upon either including an Orbach mechanism (with fixed τ_0 and U_{eff} values taken from the high-temperature region) or excluding the Raman term, the model was unable to account for the low-temperature relaxation behavior. A Raman process along with direct phonon-induced relaxation at low temperature ($C = 0.45(8)$ s^{-1}K^{-n}, $n = 5.38(9)$, $B = 103(4)$ K^{-1}) gave the best results (red line in Figure 6b). The exponent n of the Raman relaxation process for a Kramer ion should be equal to 9,[20,48] but several factors can contribute to lower its value,[20] such as the presence of low-lying excited electronic states, for which $n = 5$ is postulated.[48]

Dipolar interactions in the solid state can provide efficient relaxation pathways in zero field and hinder the detection of magnetization dynamics. Dilution of SMMs in a diamagnetic matrix has been identified as a key tool for reducing such long-range couplings, thus affording a measurable zero-field relaxation.[14,49] The effect of dipolar interactions in **1** was then ascertained by analysing the ac response of diamagnetically diluted sample **3**. Unlike in **1**, a set of clearly visible peaks appeared in the $\chi_M''(\nu)$ isothermal profiles of **3** in zero field in the range 1.9–3.2 K (see Figure S9 in the Supporting Information). The maxima of these peaks display a feeble dependence on temperature that could be reproduced considering a Raman relaxation process with QT. A best-fit procedure, the results of which are reported as a magenta line in Figure 6b, yielded $C = 11(2)$ s^{-1}K^{-n} and a tunneling frequency of $A = 40.3(5)$ kHz, with the n exponent fixed at 5.38 as in **1** to avoid over-parametrization. The onset of a QT relaxation path in zero field is in line with the rhombicity of **1** and the unavoidable presence of hyperfine interactions, which are necessary to promote tunneling. These data show for the first time, to the best of our knowledge, that slow magnetic relaxation in zero field can be achieved in a pseudo-octahedral cobalt(II) complex, provided that intermolecular magnetic interactions are efficiently reduced. A similar effect given by magnetic dilution on easy-axis systems was previously reported only in a tetrahedral cobalt(II) compound.[14] It is also most probably the reason for zero-field slow magnetic relaxation in the $Co^{II}Co^{III}_3$ SMM family, in which the magnetically active trigonal prismatic cobalt(II) ion is partly isolated from the neighbouring paramagnetic centers by three diamagnetic cobalt(III) ions.[18]

Upon application of a static field of 1 kOe, the magnetization dynamics of **3** slows down significantly due to the further suppression of relaxation pathways induced by QT (see Figure S10 in the Supporting Information). The high-temperature data almost overlap with the data detected for **1**, thus suggesting that when a linear regime in the Arrhenius plot is observed the effective barrier is much smaller than the separation between the ground and the first-excited doublets. This finding indicates the key role played by nonresonant phonons in the high-temperature range.[46] The data can be phenomenologically reproduced including Raman and direct relaxation processes (blue line in Figure 6b), as for data fitting of **1**. The best-fit parameters ($C = 0.015(5)$ s^{-1}K^{-n}, $n = 7.0(2)$, $B = 0(4)$ K^{-1}) indicate that application of a dc field of 1 kOe suppresses the direct pathway and leads to an increased n exponent, in line

Table 2. *D* values, *E* values, diagonalized $\tilde{g}$ and $\tilde{D}$ matrices, and energy differences between the ground and the first-excited KD (Δ_E).[a]

Method	g_{xx}, g_{yy}, g_{zz}	D_{xx}, D_{yy}, D_{zz} [cm^{-1}]	D [cm^{-1}]	E [cm^{-1}]	Δ_E [cm^{-1}]	δ_E [cm^{-1}]
ORCA/CASSCF	2.156, 1.945, 3.069	48.68, 13.42, −62.11	−93.2	17.6	196.1	364.7
ORCA/NEVPT2	2.152, 1.960, 3.004	43.11, 14.34, −57.45	−86.2	14.4	179.4	467.4
MOLCAS/CASSCF	2.169, 1.963, 3.070	49.22, 12.19, −61.41	−92.1	18.5	195.1	368.9
MOLCAS/CASPT2	2.149, 1.960, 3,058	47.30, 13.25, −60.55	−90.8	17.0	191.0	364.6

[a] Computed by using the structure of **1** at 161 K with different methods and the standard basis set (see the Supporting Information); for comparison, the first-excitation energy (δ_E) in the absence of SOC for the ground state is also reported.

with a previous report on trigonal antiprismatic cobalt(II) complexes with uniaxial anisotropy.[50]

Theoretical calculations

To better understand and quantify the overall electronic structure of the cobalt(II) center and its magnetic anisotropy in **1**, ab initio multireference calculations that used the ORCA[51] and MOLCAS[52] software packages were carried out. The ORCA software produces two sets of results: CASSCF and NEVPT2, both including spin-orbit contributions introduced by the quasidegenerate perturbation theory (QDPT). The MOLCAS software was employed to provide CASSCF and CASPT2 results, including spin-orbit effects that have been introduced with the SO-RASSI method. Tables S7–S10 (see the Supporting Information) report the spin-free (δ_E) and spin-orbit (Δ_E) state energies, and Table 2 and Tables S11 and S12 (see the Supporting Information) gather the second-order anisotropy parameters, as described by Eq. (1), the diagonalized $\tilde{g}$ and $\tilde{D}$ matrices and the energy differences between the ground and the first-excited Kramers doublet (KD) computed with different methods and the standard basis set, starting from the structure of **1** at 161 and 295 K.

Before including the spin-orbit effects, all the calculations agree indicating an orbitally nondegenerate $S=3/2$ ground state. In fact, the crystal-field term of the octahedrally coordinated high-spin cobalt(II) ion ($^4T_{1g}$) splits into three orbital singlets as the symmetry is lowered to C_2. Each of these orbitally nondegenerate spin quartets is further split by SOC into two KDs (see Figure S11 in the Supporting Information). In all the calculations, the ground and first-excited KDs are energetically well separated from the higher KDs, thus suggesting that a spin Hamiltonian formalism may be justified in the present case. Moreover, the energy of the first-, second-, and third-excited doublets (ca. 191, 648, and 929 cm^{-1}, respectively, determined by using MOLCAS/CASPT2) resemble the energies found when the Griffith Hamiltonian is employed to reproduce the EPR data (i.e., 210, 558, and 820 cm^{-1}, respectively; see Table S6 in the Supporting Information).

These calculations also produce similar and negative values of *D*, with a negligible effect due to the use of the molecular structures at the two different temperatures (i.e., 161 and 295 K; see Table S11 in the Supporting Information). However, a small but systematic trend can be observed, which consists of a decrease in the $|D|$ value and an increase in the value of *E* upon cooling. The calculated $|D|$ values are approximately 50% larger than when obtained from the fitting of the experimental magnetic data, whereas the computed values of *E* are in good agreement with the experiments. To evaluate the possible effect of the employed basis set on the computed *zfs* parameters, the calculations were repeated with a larger basis set for the structure of **1** at 161 K (see the Experimental Section and Table S12 in the Supporting Information). The new results show just small differences relative to the standard basis, with slightly larger $|D|$ and *E* values. The effect is more pronounced in MOLCAS than in ORCA.

The sign and value of *D* can be rationalized by using the spin-orbit operator, which is responsible for the coupling between the ground and excited states.[10,53] When the excitation occurs between orbitals with the same $|m_l|$ values, the $M_S=\pm 3/2$ components become more stable, and thus a negative contribution to the *D* value is obtained. On the other hand, an excitation between orbitals that involves a $|\Delta m_l|=1$ change, which produces stabilized $M_S=\pm 1/2$ components, leads to a positive contribution to the *D* value. Compound **1** displays a distorted octahedral core that produces the d-orbital splitting shown in Figure 7, which is obtained from the ORCA/NEVPT2

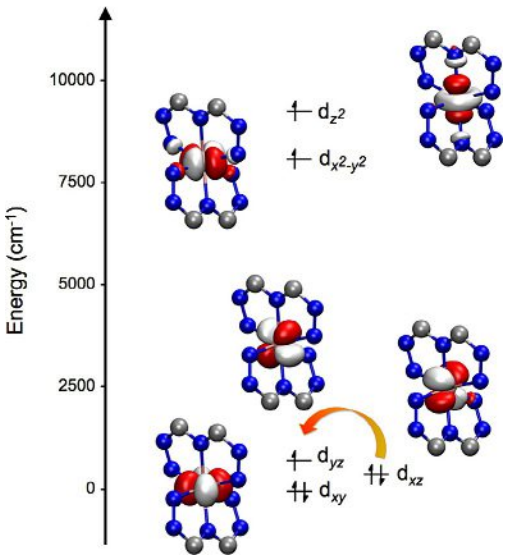

Figure 7. AILF-computed d-orbital splitting for **1** (orbital energies: $d_{xy}=0.0$, $d_{xz}=444.6$, $d_{yz}=697.9$, $d_{x2-y2}=8121.0$, $d_{z2}=9257.3$ cm^{-1}). Co = pink, C = gray, N = blue; hydrogen atoms and part of the ligands have been omitted for clarity. The orange arrow indicates the lowest-energy transition.

calculation by using the ab initio ligand-field theory (AILF).[10,54] As may be observed, the degeneracy of the t_{2g} and e_g orbitals of the regular octahedron is lifted, which indicates that the initial octahedral $^4T_{1g}$ ground state should evolve into a lower-energy term in C_2 symmetry (see Figure S11 in the Supporting Information). The AILF method allows the identification of the d orbitals in **1** after splitting, and the lowest-energy doubly occupied orbital is d_{xy}, which is followed by the doubly occupied orbital d_{xz} (or d_{yz} because these orbitals cannot be distinguished), whereas the first semioccupied orbital is d_{yz} (or d_{xz}; where *z* represents the *trans*-N{pyridyl}-Co-N{pyridyl} direction and *x* and *y* represent the directions of the pyrazolyl nitrogen atoms). The other two orbitals (d_{x2-y2} and d_{z2}) are found at higher energies. Thus, the first excitation should occur within the d_{xz}/d_{yz} orbital pair and, because these orbitals have the same $|m_l|$ value, the larger contribution to the *D* value should be negative; consequently, the magnetic easy-axis nature of **1** is confirmed. This outcome is in opposition with the most common orbital splitting for pseudo-octahedral cobalt(II) complexes, which usually yields the d_{xy} orbital as the first semioccupied orbital,[31] and subsequently resulting in easy-plane systems.

The calculated $\tilde{\boldsymbol{D}}$ matrix has its intermediate axis (i.e., *y* in Eq. (1) with $E>0$) along the twofold crystallographic *b* axis and the hard (*x*) and easy (*z*) directions in the *a***c* plane (see Figure S12 in the Supporting Information), with the hard *x* axis at 10° from *a*. Thus, the computed orientation of the *zfs* tensor compares very well with that obtained by single-crystal CTM measurements and EPR spectroscopic analysis. Turning now to *g* factors, the ab initio values (Table 2) are remarkably close to the values obtained by using Equation (5). For example, the *g* factors that result from ORCA/NEVPT2 calculations are $g_x=2.152$, $g_y=1.960$, and $g_z=3.004$, which can be compared with the *g* factors estimated by analysis of the EPR spectra, that is, $g_x=2.125$, $g_y=1.935$, and $g_z=2.825$. The effective $\tilde{\boldsymbol{g}}'$ factors of the ground KD found in this same calculation, which can be directly compared with the values obtained from the EPR experiments, are slightly more anisotropic, that is, $g'_1=0.999$, $g'_2=1.172$, and $g'_3=8.566$ (from EPR: $g'_1=1.37\pm0.02$, $g'_2=1.62\pm0.02$, and $g'_3=7.930\pm0.002$). The results obtained in the MOLCAS/CASPT2 calculation are also quite similar to both these sets of values, that is, $g'_1=1.108$, $g'_2=1.287$, and $g'_3=8.570$. The principal directions of the $\tilde{\boldsymbol{g}}$ matrix are collinear with those of $\tilde{\boldsymbol{D}}$, in which the largest *g* factor is along the *z* direction. However, the smallest *g* value is computed along the twofold crystallographic axis (*y*) rather than along the hard direction of $\tilde{\boldsymbol{D}}$ (*x*) (see Figure S12 in the Supporting Information). As observed in the single-crystal EPR experiments, the theoretical calculations indicate an inversion of the intermediate and hard axes between $\tilde{\boldsymbol{g}}$ and $\tilde{\boldsymbol{D}}$, that is, opposite rhombicities.

The CTM experiments can be nicely reproduced in the MOLCAS calculations by recomputing the magnetization of the system along the different axes upon application of a rotating magnetic field (see the Experimental Section in the Supporting Information for further details). The agreement between the experimental and theoretical torque values for Rot1 in the temperature range 10–100 K is very satisfactory, whereas some discrepancy is observed in Rot2 when increasing the temperature (see Figures S13 and S14 in the Supporting Information), as observed by applying the Griffith model. It is important to underline that Rot2, which mainly probes the intermediate and hard magnetic directions, is mostly affected by the inversion of the corresponding components of the $\tilde{\boldsymbol{g}}$ and $\tilde{\boldsymbol{D}}$ matrices; the origin of this phenomenon remains unclear.

The spin-relaxation pathways, which can be related to the dynamic magnetic properties of transition-metal complexes, can be obtained directly through the SINGLE ANISO[55] code implemented in the MOLCAS software. The computed relative energies of the lowest-lying KDs and the magnetization reversal pathway for **1**, as obtained by applying the MOLCAS/CASPT2 calculation, are shown in Figure 8. The calculations indicate a plausible relaxation pathway through a direct QT in the ground state; the matrix element of the transition within the $1-/1+$ ground doublet takes a value of 0.40, which is higher than the required threshold of 0.1 for an efficient relaxation mechanism.[10] In addition, an Orbach process could be also plausible; for example, the first-excited KD is quite low in energy (191.0 cm^{-1}) and the matrix elements related to the vertical and diagonal (Orbach) excitations are high enough (1.09 and 1.11, respectively) to allow the spin relaxation through these pathways. However, the experimental effective barrier for the thermally activated process is significantly smaller than the calculated barrier. Obviously, the horizontal transition between the $2-$ and $2+$ states is allowed, thus enabling the possibility of QT between them. The second- and third-excited KDs are much higher in energy and, therefore, are not expected to participate in the relaxation mechanism. These results, combined with the ac magnetic susceptibility measurements of **1**, confirm the spin-phonon Raman relaxation mechanism.

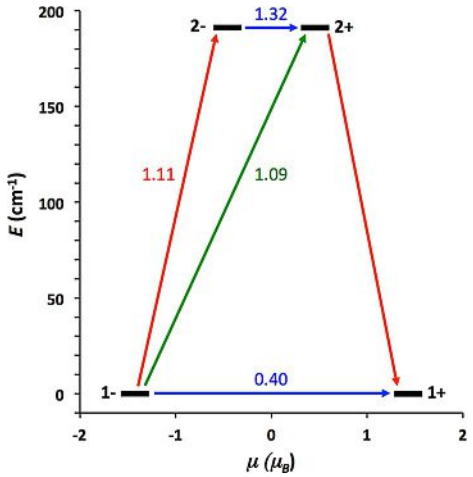

Figure 8. Lowest two KDs and the ab initio MOLCAS/CASPT2 computed relaxation mechanism for **1**. The thick black lines imply KDs as a function of their magnetic moment along the main anisotropy axis. Red lines indicate the magnetization reversal mechanism. Blue lines correspond to ground state QT and thermally assisted QT through the first-excited KD. Green lines show the possible Orbach relaxation processes. The values close to the arrows indicate the matrix elements of the transition magnetic moments (i.e., an efficient spin relaxation mechanism is expected if the matrix elements are greater than 0.1).

If **1** were to follow the Orbach mechanism depicted by the calculations, the U_{eff} value would take a higher value than the value obtained in the fitting (i.e., 43.6(2) K), which is clearly not the case, thus indicating that the spin-relaxation pathway does not proceed by overcoming a thermal activation barrier. This behavior is quite general for systems with large D values, and an explanation can be based on the fact that the Arrhenius law is only expected if the Debye description of the phonons is correct. A much smaller energy barrier and a deviation from the Arrhenius law at low temperature can be ascribed to the anharmonicity of the vibrational modes (a source of Raman-like relaxation).

Conclusion

We have presented detailed magnetic and spectroscopic characterizations, both on powder and single-crystal samples, of a pseudo-octahedral cobalt(II) complex, which we have used as a test bench for different theoretical approaches that ranged from ab initio calculations to the ligand-field model and spin Hamiltonian descriptions. We can conclude that the main features of the magnetic behavior of this system are accounted for by using an $S=3/2$ spin Hamiltonian approach. However, by exploiting the variety of the experimental and theoretical techniques employed, we were also able to evidence the hitherto unreported inversion of the hard and intermediate axes of $\tilde{\boldsymbol{g}}$ and $\tilde{\boldsymbol{D}}$ matrices, a phenomenon that was nicely reproduced by ab initio calculations.

The present results have further highlighted the possibility of obtaining slow magnetic relaxation in a mononuclear pseudo-octahedral HS cobalt(II) complex with dominant easy-axis anisotropy in the absence of an applied dc field. In particular, the distortion of the coordination environment from a perfect octahedral geometry, as created by the two *mer* bpp-COOMe ligands in **1**, induces the easy-axis nature of the compound.

The observed magnetization dynamics is strongly affected by tunnel processes due to the rhombic magnetic anisotropy in zero field. In an applied magnetic field, the behavior deviated from the Arrhenius behavior expected for an ideal SMM as the highest estimation of the energy barrier to be overcome is significantly smaller than the separation between the ground and first doublets. This behavior has been observed in other highly anisotropic complexes[56] and attributed to the efficiency of nonresonant optical phonons,[46,47] which cannot be neglected if anharmonicity is taken into account. Even if the optimization of the magnetization dynamics of SMM requires the control of several factors, such as tunneling mechanisms and vibrational modes, the rational design of the coordination environment remains the first step to be able to generate magnetic bistability through the appropriate sign of the magnetic anisotropy. An octahedral cobalt(II) environment, despite its large orbital contribution, has so far eluded the successful provision of examples of genuine SMM behavior. The combination of a detailed experimental investigation with theoretical modeling at different levels, as described herein, can provide valuable hints for a rational design of cobalt(II)-based SMMs.

Experimental Section

General information

$Co(ClO_4)_2{\cdot}6H_2O$ and $Zn(ClO_4)_2{\cdot}6H_2O$ were of reagent grade and used as received. Diethyl ether was predried over $CaCl_2$ overnight and distilled from sodium/benzophenone under N_2 before use. CH_3CN was treated with CaH_2 and distilled under N_2. Elemental analyses were recorded on a Carlo Erba EA1110 CHNS-O automatic analyser. The Zn and Co content in **3** were evaluated with a PerkinElmer Optima 5300 DV inductively coupled plasma optical emission spectrometer equipped with a concentric nebulizer. ^{1}H NMR spectra were recorded on a 400 MHz Bruker FT-NMR Advance400 spectrometer at room temperature. Proton chemical shifts are given in parts per million (ppm) versus external TMS and were determined by reference to the solvent residual signals ($\delta=1.94$ ppm for CHD_2CN); coupling constants are given in Hz. IR spectra were recorded as KBr discs on a Jasco FTIR-4700LE spectrophotometer with a resolution of 2 cm^{-1}. The bpp-COOMe ligand was synthesized as previously reported.[26] Further details on the X-ray structure determination of **1** and **2** (see Table S1 in the Supporting Information), dc and ac magnetic measurements, CTM and EPR experiments, and the theoretical calculations can be found in the Supporting Information.

Synthesis of bis[methyl 2,6-di(pyrazol-1-yl)pyridine-4-carboxylate]cobalt(II) bis(perchlorate) $[Co(bpp\text{-}COOCH_3)_2](ClO_4)_2$ (1)

Ligand bpp-COOMe (36.0 mg, 0.134 mmol) was suspended in acetonitrile (3 mL). The addition of $Co(ClO_4)_2{\cdot}6H_2O$ (24.3 mg, 0.0664 mmol) to the reaction mixture caused dissolution of the ligand upon formation of the desired complex with an immediate color change to purple/red. After stirring for 30 min, the filtered solution was subjected to vapour diffusion with diethyl ether (5 mL). X-ray-quality light-red crystals appeared within 1 day and were collected after 1 week at complete diffusion (39.4 mg, 74.5 %). IR (KBr): $\tilde{\nu}_{max}=1738$ (s; νC=O ester), 1632 (s), 1580 (s), 1523 (s) and 1405 (s) (νC=N and νC=C), 1460 (s) and 1444 (m) (δC–H), 1095 (s; νClO_4^-), 1056 (s; νC–O) cm^{-1}; elemental analysis (%) calcd for $C_{26}H_{22}Cl_2CoN_{10}O_{12}$ (796.35): C 39.21, H 2.78, N 17.59; found: C 39.90, H 2.88, N 17.99.

Synthesis of bis[methyl 2,6-di(pyrazol-1-yl)pyridine-4-carboxylate]zinc(II) bis(perchlorate) $[Zn(bpp\text{-}COOCH_3)_2](ClO_4)_2$ (2)

The above-described procedure was employed using bpp-COOMe (39.0 mg, 0.145 mmol) and $Zn(ClO_4)_2{\cdot}6H_2O$ (27.6 mg, 0.0741 mmol) to afford colorless crystals suitable for X-ray diffraction studies (40.0 mg, 68.8 %).^{1}H NMR (400 MHz, CD_3CN, 293 K): $\delta=8.73$ (d, $J_1=2.8$ Hz, 2H; H^5-pz), 8.45 (s, 2H; $H^{3/5}$-py), 7.62 (d, $J_2=1.6$ Hz, 2H; H^3-pz), 6.70 (dd, $J_1=2.8$, $J_2=1.6$ Hz, 2H; H^4-pz), 4.11 ppm (s, 3H; OCH_3); IR (KBr): $\tilde{\nu}_{max}=1738$ (s; νC=O ester), 1632 (s), 1584 (s), 1522 (s) and 1405 (s) (νC=N and νC=C), 1458 (s) and 1444 (m) (δC–H), 1095 (s; νClO_4^-), 1058 (s; νC–O) cm^{-1}; elemental analysis (%) calcd for $C_{26}H_{22}Cl_2N_{10}O_{12}Zn$ (802.83): C 38.90, H 2.76, N 17.45; found: C 39.05, H 3.04, N 17.48.

Synthesis of $[Zn_{0.95}Co_{0.05}(bpp\text{-}COOCH_3)_2](ClO_4)_2$ (3)

The above-described procedure was employed using bpp-COOMe (81.2 mg, 0.302 mmol), $Co(ClO_4)_2{\cdot}6H_2O$ (2.9 mg, 0.0079 mmol), and $Zn(ClO_4)_2{\cdot}6H_2O$ (53.9 mg, 0.145 mmol) in acetonitrile (6 mL) and di-

ethyl ether (10 mL) to afford very light-orange crystals suitable for X-ray diffraction studies (91.7 mg, 75.8%). IR (KBr): $\tilde{\nu}_{max} = 1737$ (s; νC=O ester), 1632 (s), 1584 (s), 1522 (s) and 1405 (s) (νC=N and νC=C), 1458 (s) and 1444 (m) (δC–H), 1095 (s; νClO_4^-), 1058 (s; νC–O) cm^{-1}; elemental analysis (%) calcd for $C_{26}H_{22}Cl_2N_{10}O_{12}Zn_{0.95}Co_{0.05}$ (802.51): C 38.91, H 2.76, N 17.45, Co 0.37, Zn 7.74; found: C 39.22, H 2.83, N 17.46, Co 0.40, Zn 8.04.

Acknowledgements

We thank the European Research Council, the Italian Ministero dell'Istruzione, dell'Università e della Ricerca (MIUR), the Polish Ministry of Science and Higher Education, and the Spanish Ministerio de Economía *y* Competitividad for funding through Advanced Grant MolNanoMas no. 267746, FIRB project no. RBAP117RWN, the Iuventus Plus Programme grant agreement no. 0370/IP3/2015/73, and grant CTQ2015-64579-C3-1-P, MINECO/FEDER, UE, respectively. All authors kindly acknowledge COST CA 15128. E.R. thanks the Generalitat de Catalunya for an ICREA Academia award. J.J. and E.R. thankfully acknowledge the computer resources in the Consorci Serveis Universitaris de Catalunya (CSUC). L.S. and L.T. acknowledge the help of Dr. Mauro Perfetti (University of Copenhagen) for helping in preliminary CTM measurements and data analysis.

Conflict of interest

The authors declare no conflict of interest.

Keywords: ab initio calculations · cobalt · EPR spectroscopy · single-molecule magnets · torque magnetometry

[1] D. Gatteschi, R. Sessoli, J. Villain, *Molecular Nanomagnets*, Oxford University Press, Oxford, **2006**.

[2] J. D. Rinehart, M. Fang, W. J. Evans, J. R. Long, *J. Am. Chem. Soc.* **2011**, *133*, 14236 – 14239.

[3] a) F.-S. Guo, B. M. Day, Y.-C. Chen, M.-L. Tong, A. Mansikkamaki, R. A. Layfield, *Angew. Chem. Int. Ed.* **2017**, *56*, 11445 – 11449; *Angew. Chem.* **2017**, *129*, 11603 – 11607; b) C. A. P. Goodwin, F. Ortu, D. Reta, N. F. Chilton, D. P. Mills, *Nat. Lett.* **2017**, *548*, 439 – 442.

[4] a) M. Mannini, F. Pineider, C. Danieli, F. Totti, L. Sorace, Ph. Sainctavit, M.-A. Arrio, E. Otero, L. Joly, J. C. Cezar, A. Cornia, R. Sessoli, *Nature* **2010**, *468*, 417 – 421; b) C. Wäckerlin, F. Donati, A. Singha, R. Baltic, S. Rusponi, K. Diller, F. Patthey, M. Pivetta, Y. Lan, S. Klyatskaya, M. Ruben, H. Brune, J. Dreiser, *Adv. Mater.* **2016**, *28*, 5195 – 5199.

[5] a) L. Rigamonti, M. Piccioli, L. Malavolti, L. Poggini, M. Mannini, F. Totti, B. Cortigiani, A. Magnani, R. Sessoli, A. Cornia, *Inorg. Chem.* **2013**, *52*, 5897 – 5905; b) L. Rigamonti, M. Piccioli, A. Nava, L. Malavolti, B. Cortigiani, R. Sessoli, A. Cornia, *Polyhedron* **2017**, *128*, 9 – 17.

[6] a) O. Sato, *Nat. Chem.* **2016**, *8*, 644 – 656; b) D. Pinkowicz, M. Rams, M. Mišek, K. V. Kamenev, H. Tomkowiak, A. Katrusiak, B. Sieklucka, *J. Am. Chem. Soc.* **2015**, *137*, 8795 – 8801.

[7] a) P. Parois, S. A. Moggach, J. Sanchez-Benitez, K. V. Kamenev, A. R. Lennie, J. E. Warren, E. K. Brechin, S. Parsons, M. Murrie, *Chem. Commun.* **2010**, *46*, 1881 – 1883; b) S. A. Corrales, J. M. Cain, K. A. Uhlig, A. M. Mowson, C. Papatriantafyllopoulou, M. K. Peprah, A. Ozarowski, A. J. Tasiopoulos, G. Christou, M. W. Meisel, C. Lamprapoulos, *Inorg. Chem.* **2016**, *55*, 1367 – 1369.

[8] a) A. Prescimone, C. J. Milios, J. Sanchez-Benitez, K. V. Kamenev, C. Loose, J. Kortus, S. A. Moggach, M. Murrie, J. E. Warren, A. R. Lennie, S. Parsons, E. K. Brechin, *Dalton Trans.* **2009**, 4858 – 4867; b) A. Prescimone, J. Sanchez-Benitez, K. V. Kamenev, S. A. Moggach, A. R. Lennie, J. E. Warren, M. Murrie, S. Parsons, E. K. Brechin, *Dalton Trans.* **2009**, 7390 – 7395; c) C. H. Woodall, G. A. Craig, A. Prescimone, M. Misek, J. Cano, J. Faus, M. R. Probert, S. Parsons, S. Moggach, J. Martinez-Lillo, M. Murrie, K. V. Kamenev, E. K. Brechin, *Nat. Commun.* **2016**, *7*, 13870; d) G. A. Craig, A. Sarkar, C. H. Woodall, M. A. Hay, K. E. R. Marriott, K. V. Kamenev, S. A. Moggach, E. K. Brechin, S. Parsons, G. Rajaraman, M. Murrie, *Chem. Sci.* **2018**, *9*, 1551 – 1559.

[9] F. D. Natterer, K. Yang, W. Paul, P. Willke, T. Choi, T. Greber, A. J. Heinrich, C. P. Lutz, *Nature* **2017**, *543*, 226 – 231.

[10] S. Gómez-Coca, D. Aravena, R. Morales, E. Ruiz, *Coord. Chem. Rev.* **2015**, *289 – 290*, 379 – 392.

[11] a) G. A. Craig, M. Murrie, *Chem. Soc. Rev.* **2015**, *44*, 2135 – 2147; b) J. M. Frost, K. L. M. Harriman, M. Murugesu, *Chem. Sci.* **2016**, *7*, 2470 – 2491.

[12] a) J. M. Zadrozny, D. J. Xiao, M. Atanasov, G. J. Long, F. Grandjean, F. Neese, J. R. Long, *Nat. Chem.* **2013**, *5*, 577 – 581; b) J. M. Zadrozny, D. J. Xiao, J. R. Long, M. Atanasov, F. Neese, F. Grandjean, G. J. Long, *Inorg. Chem.* **2013**, *52*, 13123 – 13131.

[13] S. Mossin, B. L. Tran, D. Adhikari, M. Pink, F. W. Heinemann, J. Sutter, R. K. Szilagyi, K. Meyer, D. J. Mindiola, *J. Am. Chem. Soc.* **2012**, *134*, 13651 – 13661.

[14] a) J. M. Zadrozny, J. R. Long, *J. Am. Chem. Soc.* **2011**, *133*, 20732 – 20734; b) J. M. Zadrozny, J. Telser, J. R. Long, *Polyhedron* **2013**, *64*, 209 – 217.

[15] D.-K. Cao, J.-Q. Feng, M. Ren, Y.-W. Gu, Y. Song, M. D. Ward, *Chem. Commun.* **2013**, *49*, 8863 – 8865.

[16] M. S. Fataftah, J. M. Zadrozny, D. M. Rogers, D. E. Freedman, *Inorg. Chem.* **2014**, *53*, 10716 – 10721.

[17] E. Carl, S. Demeshko, F. Meyer, D. Stalke, *Chem. Eur. J.* **2015**, *21*, 10109 – 10115.

[18] a) Y.-Y. Zhu, C. Cui, Y.-Q. Zhang, J.-H. Jia, X. Guo, C. Gao, K. Qian, S.-D. Jiang, B.-W. Wang, Z.-M. Wang, S. Gao, *Chem. Sci.* **2013**, *4*, 1802 – 1806; b) Y.-Y. Zhu, Y.-Q. Zhang, T.-T. Yin, C. Gao, B.-W. Wang, S. Gao, *Inorg. Chem.* **2015**, *54*, 5475 – 5486.

[19] V. V. Novikov, A. A. Pavlov, Y. V. Nelyubina, M.-E. Boulon, O. A. Varzatskii, Y. Z. Voloshin, R. E. P. Winpenny, *J. Am. Chem. Soc.* **2015**, *137*, 9792 – 9795.

[20] Y. Rechkemmer, F. D. Breitgoff, M. van der Meer, M. Atanasov, M. Hakl, M. Orlita, P. Neugebauer, F. Neese, B. Sarkar, J. van Slageren, *Nat. Commun.* **2016**, *7*, 10467.

[21] X.-N. Yao, J.-Z. Du, Y.-Q. Zhang, X.-B. Leng, M.-W. Yang, S.-D. Jiang, Z.-X. Wang, Z.-W. Ouyang, L. Deng, B.-W. Wang, S. Gao, *J. Am. Chem. Soc.* **2017**, *139*, 373 – 380.

[22] D. Tu, D. Shao, H. Yan, C. Lu, *Chem. Commun.* **2016**, *52*, 14326 – 14329.

[23] A. A. Pavlov, Y. V. Nelyubina, S. V. Kats, L. V. Penkova, N. N. Efimov, A. O. Dmitrienko, A. V. Vologzhanina, A. S. Belov, Y. Z. Voloshin, V. V. Novikov, *J. Phys. Chem. Lett.* **2016**, *7*, 4111 – 4116.

[24] S. Vaidya, S. Tewary, S. K. Singh, S. K. Langley, K. S. Murray, Y. Lan, W. Wernsdorfer, G. Rajaraman, M. Shanmugam, *Inorg. Chem.* **2016**, *55*, 9564 – 9578.

[25] P. E. Kazin, M. A. Zykin, W. Schnelle, Y. V. Zubavichus, K. A. Babeshkin, V. A. Tafeenko, C. Felser, M. Jansen, *Inorg. Chem.* **2017**, *56*, 1232 – 1240.

[26] N. Bridonneau, L. Rigamonti, G. Poneti, D. Pinkowicz, A. Forni, A. Cornia, *Dalton Trans.* **2017**, *46*, 4075 – 4085.

[27] a) M. A. Halcrow, *Coord. Chem. Rev.* **2009**, *253*, 2493 – 2514; b) L. J. Kershaw Cook, R. Mohammed, G. Sherborne, T. D. Roberts, S. Alvarez, M. A. Halcrow, *Coord. Chem. Rev.* **2015**, *289 – 290*, 2 – 12.

[28] M. A. Halcrow, *Chem. Soc. Rev.* **2011**, *40*, 4119 – 4142.

[29] a) Y. Hasegawa, K. Takahashi, S. Kume, H. Nishihara, *Chem. Commun.* **2011**, *47*, 6846 – 6848; b) K. Takahashi, Y. Hasegawa, R. Sakamoto, M. Nishikawa, S. Kume, E. Nishibori, H. Nishihara, *Inorg. Chem.* **2012**, *51*, 5188 – 5198.

[30] L. J. Kershaw Cook, F. L. Thorp-Greenwood, T. P. Comyn, O. Cespedes, G. Chastanet, M. A. Halcrow, *Inorg. Chem.* **2015**, *54*, 6319 – 6330.

[31] S. Gómez-Coca, A. Urtizbarea, E. Cremades, P. J. Alonso, A. Camón, E. Ruiz, F. Luis, *Nat. Commun.* **2014**, *5*, 4300.

[32] Song and co-workers reported the appearance of an out-of-phase ac signal upon diamagnetic dilution of an easy-axis octahedral cobalt(II) derivative, but no maxima were observed in temperature-dependent measurements and no Arrhenius plot was presented; see: J. Li, Y. Han, F. Cao, R.-M. Wei, Y.-Q. Zhang, Y. Song, *Dalton Trans.* **2016**, *45*, 9279 – 9284.

[33] H. A. Jahn, E. Teller, *Proc. R. Soc. London Ser. A* **1937**, *161*, 220 – 235.

[34] E. A. Buvaylo, V. N. Kokozay, O. Yu. Vassilyeva, B. W. Skelton, A. Ozarowski, J. Titiš, B. Vranovičová, R. Boča, *Inorg. Chem.* **2017**, *56*, 6999 – 7009.
[35] N. F. Chilton, R. P. Anderson, L. D. Turner, A. Soncini, K. S. Murray, *J. Comput. Chem.* **2013**, *34*, 1164 – 1175.
[36] L. Rigamonti, A. Cornia, A. Nava, M. Perfetti, M.-E. Boulon, A.-L. Barra, X. Zhong, K. Park, R. Sessoli, *Phys. Chem. Chem. Phys.* **2014**, *16*, 17220 – 17230.
[37] M. Perfetti, *Coord. Chem. Rev.* **2017**, *348*, 171 – 186.
[38] S. Stoll, A. Schweiger, *J. Magn. Reson.* **2006**, *178*, 42 – 55.
[39] J. R. Pilbrow, *Transition Ion Electron Paramagnetic Resonance*, Clarendon Press, Oxford, UK, **1990**.
[40] J. S. Griffith, *The Theory of Transition Metal Ions*, University Press, Cambridge, UK, **1961**.
[41] F. Lloret, M. Julve, J. Cano, R. Ruiz-García, E. Pardo, *Inorg. Chim. Acta* **2008**, *361*, 3432 – 3445.
[42] A. V. Palii, D. V. Korchagin, E. A. Yureva, A. V. Akimov, E. Ya. Misochko, G. V. Shilov, A. D. Talantsev, R. B. Morgunov, S. M. Aldoshin, B. S. Tsukerblat, *Inorg. Chem.* **2016**, *55*, 9696 – 9706.
[43] A. Abragam, M. H. L. Pryce, *Proc. R. Soc. London Ser. A* **1951**, *206*, 173 – 191.
[44] a) K. S. Cole, R. H. Cole, *J. Chem. Phys.* **1941**, *9*, 341 – 352; b) C. Dekker, A. F. M. Arts, H. W. Wijn, A. J. van Duyneveldt, J. A. Mydosh, *Phys Rev. B* **1989**, *40*, 11243 – 11251.
[45] a) C. Plenk, J. Krause, E. Rentschler, *Eur. J. Inorg. Chem.* **2015**, 370 – 374; b) J. Palion-Gazda, T. Klemens, B. Machura, J. Vallejo, F. Lloret, M. Julve, *Dalton Trans.* **2015**, *44*, 2989 – 2992; c) X. Liu, L. Sun, H. Zhou, P. Cen, X. Jin, G. Xie, S. Chen, Q. Hu, *Inorg. Chem.* **2015**, *54*, 8884 – 8886; d) A. Świtlicka-Olszewska, J. Palion-Gazda, T. Klemens, B. Machura, J. Vallejo, J. Cano, F. Lloret, M. Julve, *Dalton Trans.* **2016**, *45*, 10181 – 10193; e) J. P. S. Walsh, G. Bowling, A.-M. Ariciu, N. F. M. Jailani, N. F. Chilton, P. G. Waddell, D. Collison, F. Tuna, L. J. Higham, *Magnetochem.* **2016**, *2*, 23 – 32.
[46] A. Lunghi, F. Totti, R. Sessoli, S. Sanvito, *Nat. Commun.* **2017**, *8*, 14620.
[47] A. Lunghi, F. Totti, S. Sanvito, R. Sessoli, *Chem. Sci.* **2017**, *8*, 6051 – 6059.
[48] A. Abragam, B. Bleaney, *Electron Paramagnetic Resonance of Transition Ions*, Dover Publications, Inc., Mineola, NY, **1986**.
[49] a) R. Ruamps, L. J. Batchelor, R. Guillot, G. Zakhia, A.-L. Barra, W. Wernsdorfer, N. Guihery, T. Mallah, *Chem. Sci.* **2014**, *5*, 3418 – 3426; b) S. Sottini, G. Poneti, S. Ciattini, N. Levesanos, E. Ferentinos, J. Krzystek, L. Sorace, P. Kyritsis, *Inorg. Chem.* **2016**, *55*, 9537 – 9548; c) M. A. Palacios, J. Nehrkorn, E. A. Suturina, E. Ruiz, S. Gomez-Coca, K. Holldack, A. Schnegg, J. Krzystek, J. M. Moreno, E. Colacio, *Chem. Eur. J.* **2017**, *23*, 11649 – 11661.
[50] Y.-Z. Zhang, S. Gómez-Coca, A. J. Brown, M. R. Saber, X. Zhang, K. R. Dunbar, *Chem. Sci.* **2016**, *7*, 6519 – 6527.
[51] F. Neese, *WIREs Comput. Mol. Sci.* **2012**, *2*, 73 – 78.
[52] a) G. Karlström, R. Lindh, P.-Å. Malmqvist, B. O. Roos, U. Ryde, V. Veryazov, P.-O. Widmark, M. Cossi, B. Schimmelpfennig, P. Neogrady, L. Seijo, *Comput. Mater. Sci.* **2003**, *28*, 222 – 239; b) V. Veryazov, P.-O. Widmark, L. Serrano-Andrés, R. Lindh, B. O. Roos, *Int. J. Quantum Chem.* **2004**, *100*, 626 – 635; c) F. Aquilante, L. De Vico, N. Ferré, G. Ghigo, P.-Å. Malmqvist, P. Neogrády, T. B. Pedersen, M. Pitoňák, M. Reiher, B. O. Roos, L. Serrano-Andrés, M. Urban, V. Veryazov, R. Lindh, *J. Comput. Chem.* **2010**, *31*, 224 – 247.
[53] S. Gomez-Coca, E. Cremades, N. Aliaga-Alcalde, E. Ruiz, *J. Am. Chem. Soc.* **2013**, *135*, 7010 – 7018.
[54] M. Atanasov, D. Ganyushin, K. Sivalingam, F. Neese in *Struct. Bond.* (Eds.: D. M. P. Mingos, P. Day, J. Peder), Springer, Berlin, **2012**, pp. 149 – 220.
[55] a) L. F. Chibotaru, L. Ungur, C. Aronica, H. Elmoll, G. Pillet, D. Luneau, *J. Am. Chem. Soc.* **2008**, *130*, 12445 – 12455; b) L. F. Chibotaru, L. Ungur, A. Soncini, *Angew. Chem. Int. Ed.* **2008**, *47*, 4126 – 4129; *Angew. Chem.* **2008**, *120*, 4194 – 4197.
[56] W. H. Harman, T. D. Harris, D. E. Freedman, H. Fong, A. Chang, J. D. Rinehart, A. Ozarowski, M. T. Sougrati, F. Grandjean, G. J. Long, J. R. Long, C. J. Chang, *J. Am. Chem. Soc.* **2010**, *132*, 18115 – 18126.

Manuscript received: February 28, 2018
Accepted manuscript online: April 14, 2018
Version of record online: May 30, 2018

ChemComm

COMMUNICATION

View Article Online
View Journal | View Issue

Cite this: *Chem. Commun.*, 2018, **54**, 7826

Received 12th June 2018,
Accepted 19th June 2018

DOI: 10.1039/c8cc04703k

rsc.li/chemcomm

Isotope effects on the spin dynamics of single-molecule magnets probed using muon spin spectroscopy†

Lorenzo Tesi, [a] Zaher Salman, *[b] Irene Cimatti, [a] Fabrice Pointillart, [c] Kevin Bernot, [c] Matteo Mannini [a] and Roberta Sessoli *[a]

Muon spin relaxation (μSR) experiments on a single-molecule magnet enriched in different Dy isotopes detect unambiguously the slowing down of the zero field spin dynamics for the non-magnetic isotope. This occurs in the low temperature regime dominated by quantum tunnelling, in agreement with previous ac susceptibility investigations. In contrast to the latter, however, μSR is sensitive to all fluctuation modes affecting the lifetime of the spin levels.

Single-Molecule Magnets (SMMs) are transition metal or lanthanide-based systems characterized by a large magnetic moment whose dynamics is governed by magnetic anisotropy which creates a double well energy potential.[1] Through a rational chemical design, anisotropy barriers exceeding a thousand Kelvin have been obtained and blocking of the magnetization observed at a temperature as high as 60 K.[2] The quantum nature of SMMs, however, dominates the low temperature regime revealing themselves in many fascinating effects related to under-barrier mechanisms of relaxation.[3] Among them, quantum tunnelling of electronic magnetization was found to be very sensitive to the environment and in particular to the presence of nuclear spins. The acceleration of the quantum tunnelling in an isotopically enriched Fe_8 SMM using ^{57}Fe (nuclear spin value $I = 1/2$) was for the first time evidenced by measuring the time dependence of magnetization.[4] Following this, the quantum tunnelling between hyperfine levels was also investigated in detail in lanthanide-based SMMs.[5] More recently the spin dynamics of some SMMs comprising either ^{161}Dy ($I = 5/2$) or ^{164}Dy ($I = 0$) tri-positive ions has been investigated by using alternate current (ac) susceptometry. Also in this case quantum tunnelling relaxation was slowed down by reducing the hyperfine field.[6,7] Furthermore, the control of the nuclear magnetic environment is crucial to enhance the quantum coherence in spin systems which can be potentially employed as quantum bits in quantum information technology.[8]

The great appeal of molecular spins to store information or to be operated in quantum gates requires addressing individual or arrays of molecules, for instance by creating monolayer deposits on a surface[9] or embedding a molecule inside an electrical junction.[10] In these cases different tools need to be developed to investigate the spin dynamics. Going beyond the use of XMCD and other synchrotron-based characterization tools, often used to study SMM dynamics on a nanoscale,[11] Muon Spin Relaxation (μSR) emerges as a powerful and versatile technique. In μSR, fully spin-polarized muons, which are positively charged elementary particles with spin value $\frac{1}{2}$, are implanted in the sample. The spin of the implanted muons interacts with the magnetic fields produced by nearby molecules which govern its temporal evolution.[12] The implanted muons decay into positrons (mean lifetime $\sim$2.2 μs), which are emitted preferentially along the muon spin direction at the time of decay. Thus, using appropriately positioned detectors it is possible to reconstruct the time dependence profile of muon spin polarization.

This technique has been extensively employed to characterize the magnetic behaviour of SMMs,[13,14] since it allows a direct investigation of the magnetization dynamics of individual molecules and on a time scale faster than what is currently accessible by magnetic techniques like ac susceptometry. Furthermore, thanks to the possibility of controlling the muon implantation energy, μSR has also been used to investigate depth resolved magnetic properties of thin films of $TbPc_2$ evidencing the critical role of the packing of the molecules.[15] Another Ln-based complex investigated using this technique is $[Dy(hfac)_3(PyNO)]_2$ (DyPyNO), where PyNO = pyridine-*N*-oxide and $hfac^-$ = hexafluoroacetylacetonate. Interestingly, this SMM exhibited the same magnetic behaviour, in the entire temperature range, in bulk and sublimated thin film forms. Moreover, depth resolved experiments provided a homogeneous response from the whole SMM film volume.[16]

[a] *Department of Chemistry "U. Schiff" – Università degli Studi di Firenze and INSTM UdR Firenze, Via della Lastruccia 3, 50019, Sesto Fiorentino, Italy. E-mail: roberta.sessoli@unifi.it*

[b] *Laboratory for Muon Spin Spectroscopy, Paul Scherrer Institute, CH-5232 Villigen PSI, Switzerland. E-mail: zaher.salman@psi.ch*

[c] *Université de Rennes, INSA Rennes, CNRS, ISCR (Institut des Sciences Chimiques de Rennes) – UMR 6226, 35000 Rennes, France*

† Electronic supplementary information (ESI) available. See DOI: 10.1039/c8cc04703k

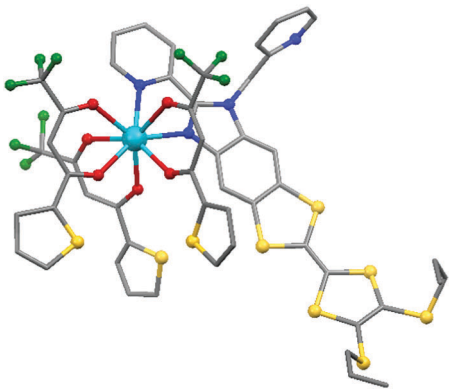

Fig. 1 Molecular structure of Dytta. Turquoise Dy, red O, blue N, green F, yellow S and grey C (for clarity H atoms are omitted).

Although several other SMMs were studied using μSR so far, the effect of nuclear moments on the molecular spin dynamics has not yet been investigated using this technique. In this communication, we show that μSR is able to detect effects of isotopic enrichment on the molecular spin dynamics. Here we report on the μSR investigation of the $[Dy(tta)_3(L)]\cdot C_6H_{14}$ (Dytta) system, where tta^- = 2-thenoyltrifluoroacetonate and L = 4,5-bis(propylthio)-tetrathiafulvalene-2-(2-pyridyl)-benzimidazole methyl-2-pyridine (see Fig. 1).[17] In particular we performed these characterizations on two isotopically enriched variants of this mononuclear complex with ^{161}Dy (I = 5/2) and ^{164}Dy (I = 0), and hereafter referred to as ^{161}Dytta and ^{164}Dytta,[6] respectively. In this system the Dy^{III} ion is connected to three tta^- ions and one bidentate L ligand, as shown in Fig. 1, which could promote the grafting on the gold surface. In this configuration, the metal is at the centre of a N_2O_6 square antiprism environment leading to a D_{4d} local symmetry around the Dy^{III} ion. The J = 15/2 manifold resulting from the spin–orbit coupling of the L = 5 and S = 5/2 of the $4f^9$ configuration is split by the crystalline field. The anisotropic distribution of the electrostatic potential around the Dy^{III} ion stabilizes the Kramers doublet $M_J = \pm 15/2$. This corresponds to an easy axis magnetic anisotropy and effective g values of the ground state $g_x = g_y = 0$ and $g_z \sim 20$. *Ab initio* calculations confirmed this picture and estimated the first excited doublet, $M_J = \pm 13/2$, at ~180 K.[17] Magnetic measurements performed on solid state compounds revealed SMM behaviour, *i.e.* slow relaxation up to 15 K with and without the application of a static magnetic field. Two relaxation mechanisms were evidenced: (i) a thermally activated process, though with an estimated energy barrier much smaller than that estimated from the separation between the ground and first excited doublets, as often observed in highly anisotropic systems,[18] and (ii) a temperature-independent process, attributed to fast quantum tunnelling in zero field.[17] In the latter regime, an increase in the relaxation time of about an order of magnitude was observed when passing from ^{161}Dytta to ^{164}Dytta.[6] In contrast, no isotope effect was evidenced in the thermally activated regime.

Microcrystalline powders of ^{161}Dytta and ^{164}Dytta (see Table S1 for isotope compositions and Fig. S1, ESI† for PXRD spectra) were investigated at the GPS spectrometer of the Paul Scherrer Institute. Conventional bulk μSR measurements (with an implantation energy of ~4 MeV corresponding to a few 100 μm stopping depth) were performed in zero magnetic field (ZF). The time dependence of muon spin polarization, $P_Z(t)$, was recorded as a function of temperature and selected spectra recorded for both samples are presented in Fig. S2 and S3 (ESI†), whereas spectra for all measured temperatures are shown in Fig. S4 and S5 (ESI†). At high temperature $P_Z(t)$ decays exponentially from its initial value to zero, as expected, when the local magnetic field experienced by each muon is fluctuating. As the temperature is decreased, the damping rate of the polarization increases gradually. However, below ~30 K, we find that $P_Z(t)$ exhibits a shallow dip at short times, and then a recovery to ~1/3 followed by slow relaxation at even longer times. As in the case of other SMMs, $P_Z(t)$ can be fitted throughout the full temperature range using a phenomenological Kubo–Toyabe model[19] multiplied by a square root exponential relaxation function[15,16]

$$P_Z(t) = \left[\frac{1}{3} + \frac{2}{3}(1 - \Delta t)e^{-\Delta t}\right]e^{-\sqrt{\lambda t}}. \quad (1)$$

This function accounts for depolarization due to a Lorentzian distribution of local static magnetic fields of width Δ, with an additional relaxation, λ, due to fluctuating magnetic field components from the Dy^{III} magnetic moments. The square root in the dynamic component originates from averaging many inequivalent sites of the molecule where muons can stop.[20,21] Best fits of $P_Z(t)$ (see the ESI† for details) provide the values of Δ and λ as a function of temperature, as shown in Fig. 2, and exhibit similar behaviour to other investigated SMMs.[14–16,21] These parameters are representative of the magnetic properties and spin dynamics of the single-molecule, since each implanted muon is sensitive to the dipolar fields

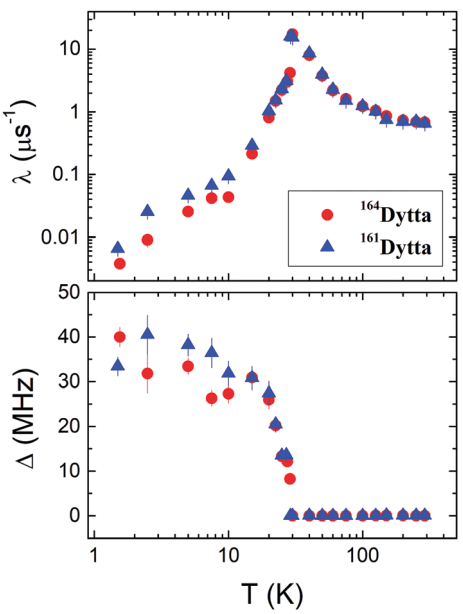

Fig. 2 Temperature dependence of the relaxation rate (top) and width of local static magnetic field distribution (bottom) for ^{164}Dytta and ^{161}Dytta measured using μSR in zero field.

from its nearest neighbour. The temperature dependences of Δ and λ reflect the gradual evolution of Dy^{III} spin dynamics, from fast fluctuating spins at high temperature to a quasi-static (*i.e.* very slow dynamics) at low temperature. We outline three specific regimes: (i) at high temperatures fast thermally activated spin fluctuations dominate, with $\Delta = 0$, *i.e.* no local static magnetic fields probed by muons, and a relatively small λ. The latter increases upon decreasing the temperature due to the slowing down of the fluctuations of the Dy^{III} magnetic moments on a time scale comparable with the muon spin Larmor precession frequency. (ii) Around 30 K, λ exhibits a narrow peak coinciding with an abrupt increase (non-zero value) in Δ, which corresponds to the appearance of static magnetic fields. (iii) Finally, at low temperature, large quasi-static fields (large Δ) are experienced by muons together with a pronounced decrease of λ.

Although no significant dissimilarities are observed in the high temperature region, below $\sim$15 K a clear difference emerges, exceeding the experimental uncertainty and revealing a larger dynamic relaxation parameter λ for ^{161}Dytta. In a similar way to what is observed in ac susceptibility measurements, the isotope effect is visible in the temperature region where under-barrier relaxation dominates. However, when comparing ^{161}Dytta to ^{164}Dytta, only an increase by a factor of $\sim$2 is observed in λ, to be compared with a factor of $\sim$10 for the relaxation time of the bulk magnetization detected by ac susceptometry.[6]

The isotope effect is also evident below 15 K when looking at the correlation time, τ, of the local magnetic field experienced by muons, as shown in Fig. 3 (full temperature range data are reported in Fig. S7, ESI†). This parameter can be extracted from the μSR spectra assuming two different regimes. At low temperature, where quasi-static magnetic fields dominate, the correlation time depends only on λ as $\tau = 2/(3\lambda)$, whereas at high temperature, where thermal fluctuations dominate, $\tau = \lambda/2\Delta_0^2$. Here Δ_0 is the size of the fluctuating field, whose value can be estimated from the saturation value of Δ extrapolated at low temperature. This was taken to be $\sim$35 MHz for both ^{164}Dytta and ^{161}Dytta. Note that there is some scatter in Δ at low temperature since it is on the limit of what is measurable using μSR. However, the exact value of Δ_0 will only affect our estimates of τ at high temperature by up to 10–20%. Moreover, the fact that λ and Δ are the same at high temperature supports our conclusion regarding the lack of the isotope effect at high temperature.

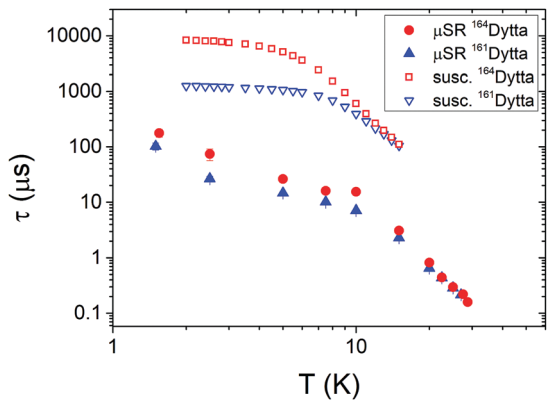

Fig. 3 Correlation time extracted from μSR and relaxation time of magnetization obtained from ac susceptibility as a function of temperature for ^{161}Dytta and ^{164}Dytta. Data are reported on a log–log scale.

It is interesting to note that the extracted τ captures the dynamics of the Dy^{III} magnetic moments but not necessarily in the same way as bulk magnetic measurements do. Indeed, the extracted correlation times are about 1–2 order of magnitude shorter than those extracted from ac susceptibility (Fig. 3). We point out that whereas ac susceptibility is sensitive to excitations with wave-vector $q = 0$, μSR (as a local probe) is sensitive to excitations integrated over all q values of the Brillouin zone.[22] This difference is however not relevant for pure paramagnetic solids, *i.e.* where intermolecular interactions are negligible. In the case of Dytta it has been observed that dipolar interactions, though weak, play a relevant role in the dynamics at low temperature, where quantum tunnelling is dominating. In contrast, the τ extracted from μSR data is shorter over the entire investigated temperature range. To reconcile ac susceptometry and μSR results we should consider that the former is mainly sensitive to relaxation processes that reverse the magnetization, *i.e.* inter-well transitions changing the sign of the spin projection along the anisotropy axis. In fact, in zero field, the equilibrium population of excited spin levels is practically unaffected by the weak oscillating field. In contrast μSR, beyond probing faster dynamics, is sensitive to all types of fluctuations which affect the lifetime of the spin states, including intra-well transitions as well as decoherence. It is therefore not surprising to observe a less pronounced isotope effect by μSR. The hyperfine fields are in fact crucial to establish the resonant condition for the reversal of magnetization by quantum tunnelling, but they are expected to have less influence on the lifetime (or width) of the states. Indeed, it is well known that nuclei, which are not strongly coupled with the electronic spins, provide the largest contribution to decoherence.[23] Finally, it should be remarked that other nuclei, such as ^{1}H and ^{19}F, may affect the electronic spin dynamics of the Dy^{III} ion, but this would not explain the difference between the two samples or the different τ values measured using μSR and ac susceptometry.

As evident from Fig. 3, τ values from μSR show more pronounced temperature dependence than ac susceptibility data below 10 K. This is also in agreement with the sensitivity of muons for intra-well transitions. Similar low temperature behaviour has been observed also for the DyPyNO SMM.[16] The latter has an energy separation between the ground doublet with $M_J = \pm 15/2$ and the first excited doublet with $M_J = \pm 13/2$ of $\sim$170 K, comparable to that calculated for Dytta SMMs. Interestingly, μSR data of $TbPc_2$, which has a much larger separation ($\sim$800 K) between the ground and first excited doublets, show that τ is fully saturated below 50 K.[15] Moreover, the τ value of $TbPc_2$ obtained using μSR is closer to that obtained using ac susceptometry applying a magnetic field of 1 kG.[14]

To summarize, our μSR investigation confirms the capability of the technique to capture fine details of the spin dynamics of molecular systems, down to the isotopic effects in the tunnelling

of magnetization. Moreover, this alternative way to study the spin dynamics provides a different and complementary perspective compared to traditional magnetometry. This arises from its local probe character and the consequent sensitivity not only to processes which lead to magnetization reversal but to all sources of spin fluctuations. This aspect is of particular interest in light of current trends in using molecular spin systems for quantum information to realize quantum gates.[24] In this respect, the final goal is using single-molecules or isolated supramolecular structures to perform quantum operations. This poses the additional challenge of preserving, in isolated molecules on substrates, not only the memory effect but also an acceptable quantum coherence time. Thanks to the possibility of implanting muons at different energies, they can be used to probe the dynamics of molecules close to a surface or an interface. The μSR technique provides therefore an almost unique tool to obtain information on the lifetime of spin states and how this is affected by the proximity to the substrate.

Part of this work was performed at the Swiss Muon Source (SμS), the Paul Scherrer Institute (PSI, Switzerland), and it was financially supported by the Italian MIUR (PRIN Project 2015 HYFSRT), the ERC Consolidator Grant MULTIPROSMM (Proj. no. 725184) and Institut Universitaire de France (IUF). We would like to thank Prof. Robert Kiefl and Prof. Elvezio Morenzoni for reading and commenting on the manuscript.

Conflicts of interest

There are no conflicts to declare.

Notes and references

1 R. Sessoli, D. Gatteschi, A. Caneschi and M. A. Novak, *Nature*, 1993, **365**, 141.
2 (*a*) C. A. P. Goodwin, F. Ortu, D. Reta, N. F. Chilton and D. P. Mills, *Nature*, 2017, **548**, 439; (*b*) F. S. Guo, B. M. Day, Y. C. Chen, M. L. Tong, A. Mansikkamäki and R. A. Layfield, *Angew. Chem., Int. Ed.*, 2017, **56**, 11445.
3 (*a*) L. Thomas, F. Lionti, R. Ballou, D. Gatteschi, R. Sessoli and B. Barbara, *Nature*, 1996, **383**, 145; (*b*) J. R. Friedman, M. P. Sarachik, J. Tejada and R. Ziolo, *Phys. Rev. Lett.*, 1996, **76**, 3830; (*c*) W. Wernsdorfer and R. Sessoli, *Science*, 1999, **284**, 133.
4 W. Wernsdorfer, A. Caneschi, R. Sessoli, D. Gatteschi, A. Cornia, V. Villar and C. Paulsen, *Phys. Rev. Lett.*, 2000, **84**, 2965.
5 (*a*) N. Ishikawa, M. Sugita and W. Wernsdorfer, *J. Am. Chem. Soc.*, 2005, **127**, 3650; (*b*) F. Luis, M. J. Martínez-Pérez, O. Montero, E. Coronado, S. Cardona-Serra, C. Martí-Gastaldo, J. M. Clemente-Juan, J. Sesé, D. Drung and T. Schurig, *Phys. Rev. B: Condens. Matter Mater. Phys.*, 2010, **82**, 060403.
6 F. Pointillart, K. Bernot, S. Golhen, B. Le Guennic, T. Guizouarn, L. Ouahab and O. Cador, *Angew. Chem., Int. Ed.*, 2015, **54**, 1504.
7 (*a*) G. Huang, X. Yi, J. Jung, O. Guillou, O. Cador, F. Pointillart, B. Le Guennic and K. Bernot, *Eur. J. Inorg. Chem.*, 2018, 326; (*b*) Y. Kishi, F. Pointillart, B. Lefeuvre, F. Riobe, B. Le Guennic, S. Golhen, O. Cador, O. Maury, H. Fujiwara and L. Ouahab, *Chem. Commun.*, 2017, **53**, 3575.
8 J. M. Zadrozny, J. Niklas, O. G. Poluektov and D. E. Freedman, *ACS Cent. Sci.*, 2015, **1**, 488.
9 (*a*) A. Cornia and M. Mannini, in *Molecular Nanomagnets and Related Phenomena*, ed. S. Gao, Structure and Bonding, Springer, Berlin, Heidelberg, 2014, vol. 164, pp. 293–330; (*b*) R. J. Holmberg and M. Murugesu, *J. Mater. Chem. C*, 2015, **3**, 11986.
10 (*a*) E. Burzurí, A. S. Zyazin, A. Cornia and H. S. J. van der Zant, *Phys. Rev. Lett.*, 2012, **109**, 147203; (*b*) R. Vincent, S. Klyatskaya, M. Ruben, W. Wernsdorfer and F. Balestro, *Nature*, 2012, **488**, 357.
11 (*a*) A. Cini, M. Mannini, F. Totti, M. Fittipaldi, G. Spina, A. Chumakov, R. Rüffer, A. Cornia and R. Sessoli, *Nat. Commun.*, 2018, **9**, 480; (*b*) M. Mannini, F. Pineider, C. Danieli, F. Totti, L. Sorace, P. Sainctavit, M. A. Arrio, E. Otero, L. Joly, J. C. Cezar, A. Cornia and R. Sessoli, *Nature*, 2010, **468**, 417.
12 S. J. Blundell, in *Magnetism: Molecules to Materials*, ed. J. S. Miller and M. Drillon, Wiley-VCH, Weinheim, 2001, pp. 235–256.
13 (*a*) S. J. Blundell, F. L. Pratt, I. M. Marshall, C. A. Steer, W. Hayes, J. F. Letard, S. L. Heath, A. Caneschi and D. Gatteschi, *Synth. Met.*, 2003, **133**, 531; (*b*) F. Branzoli, M. Filibian, P. Carretta, S. Klyatskaya and M. Ruben, *Phys. Rev. B: Condens. Matter Mater. Phys.*, 2009, **79**, 220404; (*c*) Z. Salman, S. R. Giblin, Y. Lan, A. K. Powell, R. Scheuermann, R. Tingle and R. Sessoli, *Phys. Rev. B: Condens. Matter Mater. Phys.*, 2010, **82**, 174427; (*d*) T. Lancaster, S. J. Blundell, F. L. Pratt, I. Franke, A. J. Steele, P. J. Baker, Z. Salman, C. Baines, I. Watanabe, S. Carretta, G. A. Timco and R. E. P. Winpenny, *Phys. Rev. B: Condens. Matter Mater. Phys.*, 2010, **81**, 140409.
14 F. Branzoli, P. Carretta, M. Filibian, M. J. Graf, S. Klyatskaya, M. Ruben, F. Coneri and P. Dhakal, *Phys. Rev. B: Condens. Matter Mater. Phys.*, 2010, **82**, 134401.
15 A. Hofmann, Z. Salman, M. Mannini, A. Amato, L. Malavolti, E. Morenzoni, T. Prokscha, R. Sessoli and A. Suter, *ACS Nano*, 2012, **6**, 8390.
16 E. Kiefl, M. Mannini, K. Bernot, X. Yi, A. Amato, T. Leviant, A. Magnani, T. Prokscha, A. Suter, R. Sessoli and Z. Salman, *ACS Nano*, 2016, **10**, 5663.
17 T. T. da Cunha, J. Jung, M.-E. Boulon, G. Campo, F. Pointillart, C. L. M. Pereira, B. Le Guennic, O. Cador, K. Bernot, F. Pineider, S. Golhen and L. Ouahab, *J. Am. Chem. Soc.*, 2013, **135**, 16332.
18 A. Lunghi, F. Totti, R. Sessoli and S. Sanvito, *Nat. Commun.*, 2017, **8**, 14620.
19 R. Kubo, *Hyperfine Interact.*, 1981, **8**, 731.
20 (*a*) A. Keren, *Phys. Rev. B: Condens. Matter Mater. Phys.*, 1994, **50**, 10039; (*b*) Y. J. Uemura, T. Yamazaki, D. R. Harshman, M. Senba and E. J. Ansaldo, *Phys. Rev. B: Condens. Matter Mater. Phys.*, 1985, **31**, 546.
21 Z. Salman, A. Keren, P. Mendels, V. Marvaud, A. Scuiller, M. Verdaguer, J. S. Lord and C. Baines, *Phys. Rev. B: Condens. Matter Mater. Phys.*, 2002, **65**, 132403.
22 (*a*) T. Moriya, *J. Phys. Soc. Jpn.*, 1963, **18**, 516; (*b*) Y. J. Uemura, *Hyperfine Interact.*, 1984, **18**, 447.
23 M. J. Graham, C.-J. Yu, M. D. Krzyaniak, M. R. Wasielewski and D. E. Freedman, *J. Am. Chem. Soc.*, 2017, **139**, 3196.
24 (*a*) J. Ferrando-Soria, E. M. Pineda, A. Chiesa, A. Fernandez, S. A. Magee, S. Carretta, P. Santini, I. J. Vitorica-Yrezabal, F. Tuna, G. A. Timco, E. J. L. McInnes and R. E. P. Winpenny, *Nat. Commun.*, 2016, **7**, 11377; (*b*) C. Godfrin, A. Ferhat, R. Ballou, S. Klyatskaya, M. Ruben, W. Wernsdorfer and F. Balestro, *Phys. Rev. Lett.*, 2017, **119**, 187702; (*c*) M. Atzori, A. Chiesa, E. Morra, M. Chiesa, L. Sorace, S. Carretta and R. Sessoli, *Chem. Sci.*, 2018, DOI: 10.1039/C8SC01695J.

JACS
JOURNAL OF THE AMERICAN CHEMICAL SOCIETY
Article
Cite This: J. Am. Chem. Soc. XXXX, XXX, XXX−XXX
pubs.acs.org/JACS

Scaling Up Electronic Spin Qubits into a Three-Dimensional Metal−Organic Framework

Tsutomu Yamabayashi,[†] Matteo Atzori,[‡] Lorenzo Tesi,[‡] Goulven Cosquer,[†] Fabio Santanni,[‡] Marie-Emmanuelle Boulon,[‡] Elena Morra,[§] Stefano Benci,[∥] Renato Torre,[∥,⊥] Mario Chiesa,[§] Lorenzo Sorace,[‡] Roberta Sessoli,*[,‡,#] and Masahiro Yamashita*[,†,∇,○]

[†]Department of Chemistry, Graduate School of Science, Tohoku University, 6-3 Aramaki Aza-Aoba, Aoba-ku, Sendai 980-8578, Japan
[‡]Dipartimento di Chimica "Ugo Schiff" and INSTM RU, Università degli Studi di Firenze, Via della Lastruccia 3, I50019 Sesto Fiorentino, Firenze, Italy
[§]Dipartimento di Chimica e NIS Centre, Università di Torino, Via P. Giuria 7, I10125 Torino, Italy
[∥]European Laboratory for Non-Linear Spectroscopy, Università degli Studi di Firenze, Via Nello Carrara 1, I50019 Sesto Fiorentino, Firenze, Italy
[⊥]Dipartimento di Fisica ed Astronomia, Università degli Studi di Firenze, Via G. Sansone 1, I50019 Sesto Fiorentino, Firenze, Italy
[#]Istituto di Chimica dei Composti Organometallici - ICCOM-CNR, Research Area Firenze, Via Madonna del Piano 10, I50019 Sesto Fiorentino, Firenze, Italy
[∇]WPI, Advanced Institute for Materials Research, Tohoku University, 2-1-1 Katahira, Aoba-Ku, Sendai 980-8577, Japan
[○]School of Materials Science and Engineering, Nankai University, Tianjin 300350, China

Supporting Information

ABSTRACT: Practical implementation of highly coherent molecular spin qubits for challenging technological applications, such as quantum information processing or quantum sensing, requires precise organization of electronic qubit molecular components into extended frameworks. Realization of spatial control over qubit−qubit distances can be achieved by coordination chemistry approaches through an appropriate choice of the molecular building blocks. However, translating single qubit molecular building units into extended arrays does not guarantee a priori retention of long quantum coherence and spin−lattice relaxation times due to the introduced modifications over qubit−qubit reciprocal distances and molecular crystal lattice phonon structure. In this work, we report the preparation of a three-dimensional (3D) metal−organic framework (MOF) based on vanadyl qubits, [VO(TCPP-Zn_2-bpy)] (TCPP = tetracarboxylphenylporphyrinate; bpy = 4,4′-bipyridyl) (**1**), and the investigation of how such structural modifications influence qubits' performances. This has been done through a multitechnique approach where the structure and properties of a representative molecular building block of formula [VO(TPP)] (TPP = tetraphenylporphyrinate) (**2**) have been compared with those of the 3D MOF **1**. Pulsed electron paramagnetic resonance measurements on magnetically diluted samples in titanyl isostructural analogues revealed that coherence times are retained almost unchanged for **1** with respect to **2** up to room temperature, while the temperature dependence of the spin−lattice relaxation time revealed insights into the role of low-energy vibrations, detected through terahertz spectroscopy, on the spin dynamics.

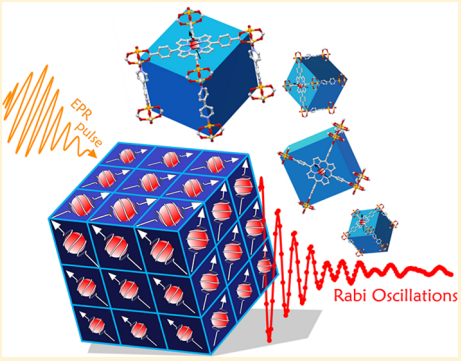

INTRODUCTION

Quantum bits, or qubits, represent the elementary units for the realization of quantum computers[1] as well as the active units of potential quantum sensors.[2−4] For both applications, the quantum superposition of state that characterizes qubits' physical realizations is exploited for specific purposes. In quantum computation, a highly coherent superposition state allows for the retention of the quantum information on the qubits for a time longer than that required to perform a quantum operation (quantum gate), whereas in quantum sensing a loss of coherent superposition is used to probe the presence of environmental perturbations. Nowadays, finding suitable, robust, and scalable systems as potential qubits represents one of the main challenges in chemistry, physics, and materials science for the development of these technological applications.

Many physical systems, such as photons,[5] trapped ions,[6] quantum dots,[7] and coherent coupled systems of superconducting qubits[8] with nitrogen-vacancy centers in diamond,[9−11] are investigated as qubit candidates, each of them showing both merits and demerits. Among these qubit realizations, molecule-based spin qubits have been investigated only recently and have

Received: June 26, 2018
Published: August 26, 2018

DOI: 10.1021/jacs.8b06733
J. Am. Chem. Soc. XXXX, XXX, XXX−XXX

shown remarkable advantages, such as the capacity of facile addressing via pulsed electron paramagnetic resonance (EPR) techniques[12]—although not yet at the single qubit level—a high processability through surface deposition,[13] and a high degree of chemical tunability.[14,15] These features are crucial for their practical development and are not easily satisfied for other classes of potential qubits, such as electronic defects in extended inorganic solids.[9−11] On the other hand, molecular spin qubits often suffer from a relatively short lifetime of the quantum superposition states compared to other potential systems. This loss of information is related to the spin−spin relaxation time (T_2), which is usually estimated by measuring the phase memory time (T_m), which is a lower limit of T_2. Interactions with the environment contribute to the collapse of the already fragile superposition state of electronic spins in a process known as decoherence. In this respect, intense investigations aimed at increasing molecular qubits' performance through chemical design have been reported in recent years.[16−22]

Another feature that places molecule-based spin qubits in a noteworthy position with respect to electronic defects in extended inorganic solids is the potential spatial control over qubit−qubit distances achievable through coordination chemistry approaches. Indeed, extended coordination polymers, or metal−organic frameworks (MOFs), with specific structural features such as overall dimensionality (bidimensional, 2D, or tridimensional, 3D), type of structural backbone (cubic, hexagonal), and controlled internal surface area, can be prepared at will through a wise selection of the molecular building blocks and well-developed coordination chemistry strategies.[23−25] This bottom-up approach can play a key role for quantum computation in increasing the scalability of the system by controlling the number of interconnected qubits within an extended network. This is equally relevant for quantum sensing, since extended porous networks allow analytes to diffuse selectively inside the voids of the solid and to be precisely detected by the qubit sensor units.[4,26−28]

The above-mentioned bottom-up approach has been employed for the preparation of 2D nanosheets embedding copper(II) tetracarboxylphenylporphyrinate units[29] and a porous 3D network obtained by linking cobalt(II) tetracarboxylphenylporphyrinate complexes through $[Zr_6(OH)_8]$ units.[30] For both materials, the coherence times of the corresponding Cu^{II}- and Co^{II}-based electronic spin qubits have been investigated. In the latter, the strong hyperfine coupling induces a mixing of M_S and M_I levels of the $S = 1/2$ and $I = 7/2$ electronic and nuclear spin values of Co^{II}. This generates an avoided level crossing at low magnetic fields (<0.3 T), whose related EPR transition frequencies are characterized by a weak magnetic field dependence, i.e., $\Delta f/\Delta B = 0$. Such a condition is typically observed for isolated atoms and can be used for the realization of a certain class of atomic clocks; thus, these transitions assume the name of clock transitions. Such transitions are particularly insensitive to the magnetic noise, leading to enhanced coherence. However, it is exactly the low sensitivity to magnetic noise that makes them not ideal for quantum sensor applications, as also pointed out by the authors of the study.[30]

It should also be considered that room temperature coherence is highly desirable for sensing purposes. In this temperature regime, spin−lattice relaxation is a limiting factor. Indeed, both local and extended vibrational modes (phonons) can be significantly modified by passing from isolated molecules that weakly interact in the crystal structure, mainly through noncovalent interactions, to extended molecular networks, where the units are covalently linked. This can induce relevant modifications of the spin dynamics.[22,31−33]

For the design of molecular spin qubits with viable coherence times, oxidovanadium(IV) complexes constitute one of the most promising choices thanks to the weak orbital contribution to the magnetism and an inefficient spin−phonon coupling interaction, which provides slow spin−lattice relaxation even at room temperature.[16,34] The characterization of the spin−lattice relaxation time (T_1) is then crucial in the design of highly performing molecular spin qubits since this process provides an upper limit for the coherence time.[13] Moreover, the investigation of spin−lattice and coherence times of vanadyl-based potential qubits embedded into a 3D crystalline material has not been reported yet.

Motivated by the need to acquire additional insights into the role of the crystal lattice properties in determining electronic spin qubits' performance, here we report the preparation of a porous vanadyl-based 3D MOF of formula [VO(TCPP-Zn_2-bpy)] (**1**) (TCPP = tetracarboxylphenylporphyrinate; bpy = 4,4′-bipyridyl). The spin−lattice relaxation times of **1** were studied by alternate current (ac) susceptibility measurements, and the coherence times of an isostructural magnetically diluted sample [$VO_{0.05}TiO_{0.95}$(TCPP-Zn_2-bpy)] (**1′**) were investigated through pulsed EPR spectroscopy. The results have been compared to those obtained on a representative mononuclear molecular building block (0D) of formula [VO(TPP)] (TPP = tetraphenylporphyrinate) (**2**) and its isostructural magnetically diluted sample [$VO_{0.02}TiO_{0.98}$(TCPP)] (**2′**). The analysis of the temperature dependence of the spin−lattice relaxation time, which plays a crucial role in determining the coherence at room temperature for the two materials, is discussed considering the different structural and spectroscopic features in the terahertz regime shown by the 3D network and the 0D mononuclear analogue.

RESULTS

Design and Synthesis. Metalated tetraphenylporphyrins have been largely employed as molecular building blocks for the preparation of regular 3D hetero- and homometallic MOFs.[30,35,36] Unlike other metalloligands, their planar and symmetric structure is ideal to both accommodate a large variety of metal ions inside the porphyrinate macrocycle and to prepare crystal structures with well-defined topologies. In particular, it has been shown that combination of metalated tetracarboxylphenylporphyrinates with bare divalent metal ions such as Zn^{II} or Cu^{II} and a pillar-like molecular ligand such as bpy allows preparation of porphyrinate paddlewheel frameworks for which the 3D stacking is controlled by the coordination geometry of the porphyrin metal center (Figure 1).[35]

As an example, tetracoordinated ions such as Mn^{II} and Fe^{II} ions easily allow further axial coordination with the N-donating pillar ligand, while Pt^{II} and Ni^{II} prefer to maintain the square planar coordination geometry of the porphyrin macrocycle; in the latter case, further axial coordination is limited to the bridged Cu^{II} and Zn^{II} ions within the paddlewheel motif.[35] The case of oxidovanadium(IV) is expected to be peculiar because further coordination with the pillar-like ligand is in this case hampered by the preformed bond between V^{IV} and the oxido ligand, which results in an overall modification of the coordination geometry of the metal center to a square pyramidal one.

Within this general scheme, the reaction between preformed vanadyl and/or titanyl tetracarboxylphenylporphyrinates with

DOI: 10.1021/jacs.8b06733
J. Am. Chem. Soc. XXXX, XXX, XXX−XXX

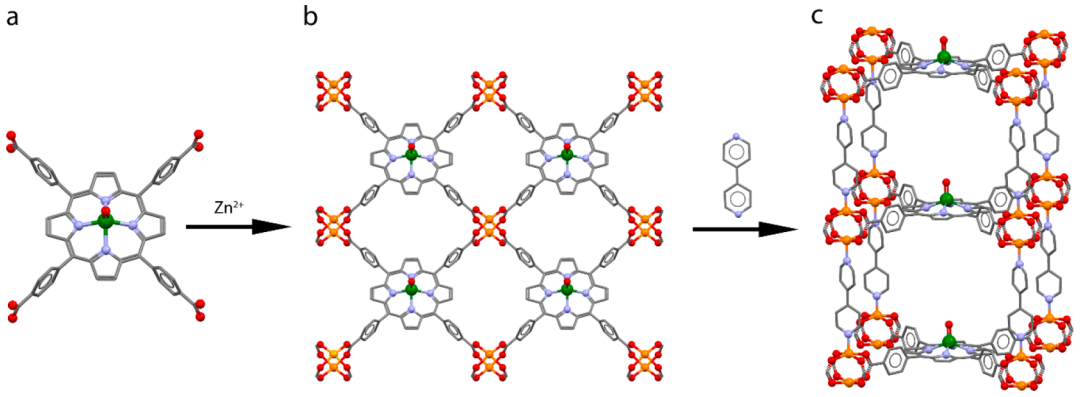

Figure 1. Schematic representation of the two-step self-assembly process responsible for the formation of the 3D MOFs **1** and **1′**. Color codes: green, vanadium; orange, zinc; red, oxygen; light blue, nitrogen; gray, carbon. Hydrogen atoms are omitted for graphical clarity.

Scheme 1. Reaction Schemes for the Synthesis of Vanadyl and Titanyl Tetraphenylporphyrin Derivatives (M = V, Ti; x = 1, 2)

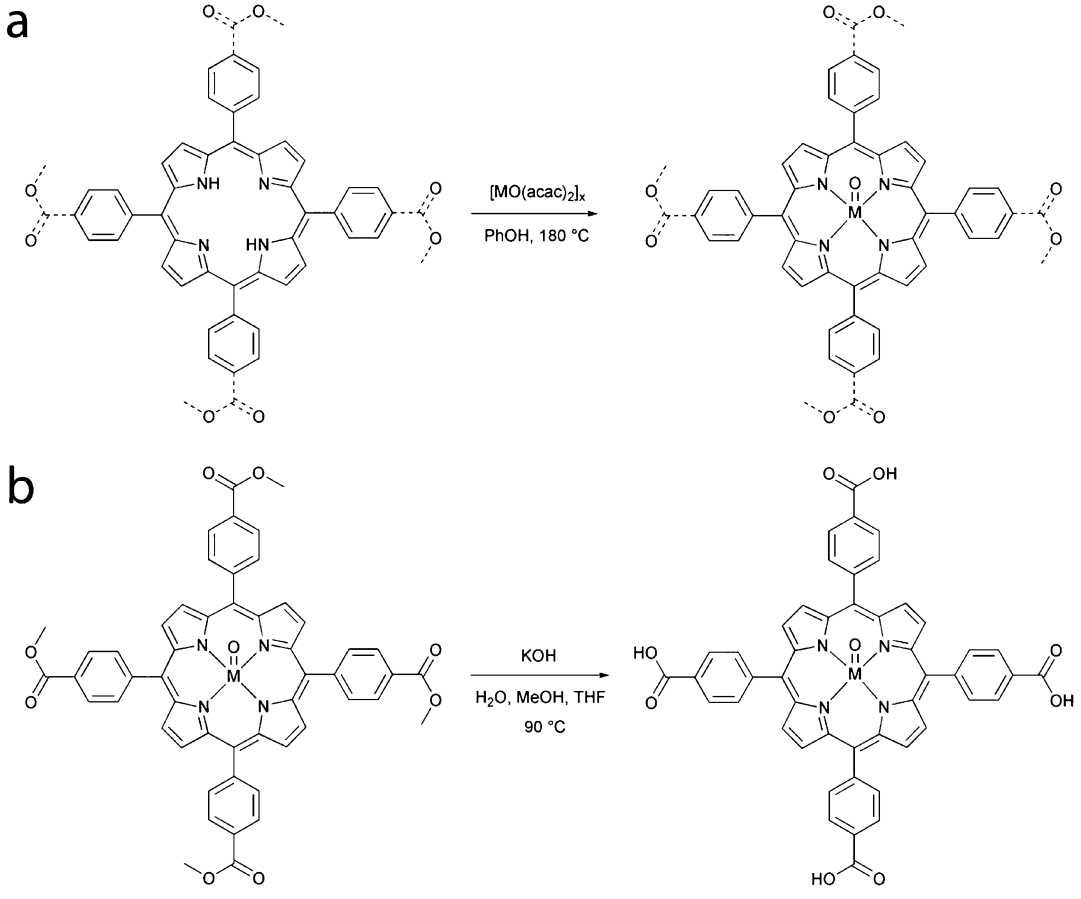

Zn^{2+} and bpy has been performed to obtain the 3D structure reported in Figure 1c.

The synthesis of the vanadyl tetracarboxylphenylporphyrinate [VO(TCPP)] building block has been achieved by following a reported procedure that has been adapted for the oxidovanadium(IV) ion.[37] It consists of the reaction between the vanadyl precursor $[VO(acac)_2]$ ($acac^-$ = acetylacetonate) and the tetrakis(4-carboxyphenyl)porphyrin ligand with carboxyl groups protected by ester functionalities, H_2TMeCPP (tetrakis(4-(methoxycarbonyl)phenyl)porphyrin), in PhOH at reflux temperature (Scheme 1a).

Subsequent deprotection of the ester groups through basic hydrolysis provides the [VO(TCPP)] molecular building block (Scheme 1b). The same reaction conditions have been used to prepare the 0D reference compound [VO(TPP)] (**2**) as well as the titanyl diamagnetic analogues [TiO(TCPP)] and [TiO(TPP)] (**3**) (Scheme 1). It should be highlighted that metalation of the tetracarboxylphenylporphyrin with the oxidovanadium(IV) moiety is easily accomplished within ca. 6 h of reaction, whereas metalation with the oxidotitanium(IV) ion appears to be more difficult, requiring longer reaction times (ca. 36 h) and a larger excess of the titanyl precursor $[TiO(acac)_2]_2$. This chemical inertness is reflected by the lack of titanyl porphyrinates reported so far in the literature with respect to other transition metal ion derivatives, including the vanadyl analogues.

DOI: 10.1021/jacs.8b06733
J. Am. Chem. Soc. XXXX, XXX, XXX−XXX

Self-assembly of vanadyl tetracarboxylphenylporphyrinate building blocks, Zn^{2+}, and bpy in DMF at 80 °C followed by slow cooling to room temperature provides air-stable red cubic single crystals of compound **1** suitable for X-ray diffraction analysis. The magnetically diluted sample **1′** was prepared by following the same synthetic procedure developed for the preparation of **1** by reacting a mixture of [VO(TCPP)] and [TiO(TCPP)] in 5:95 molar ratios with Zn^{2+} and bpy. Instead, the magnetically diluted samples **2′** and **2″** were prepared by recrystallization of [VO(TPP)] and [TiO(TPP)] in 2:98 and 30:70 molar ratios, respectively. The difference in the nominal concentration of paramagnetic species between the two lower concentrated materials has been designed to achieve similar spin concentrations in view of the presence of large voids for the 3D compound **1** with respect to the 0D compound **2** (vide infra).

Crystal Structures. Compound **1** crystallizes in the tetragonal *P*4 space group with one anionic complex, two Zn^{2+} ions, and one bpy molecule in the unit cell, the asymmetric unit being one-fourth of the molecule. The peripheral carboxyl substituents of the porphyrin macrocycle (Figure 1a) interact with Zn^{2+} to form 2D layers where the porphyrin units are connected in a 4-folded symmetry through $[Zn_2(COO)_4]$ subunits (Figure 1b), similarly to what has recently been reported for $[Cu(TCPP)-Zn_2(H_2O)_2]$.[29] The pillar-like bpy ligands then allow connection between the 2D layers to form a 3D MOF by further axial coordination between pairs of $[Zn_2(COO)_4]$ subunits (Figure 1c). The obtained structure has 3D channels with a pore dimension of 1.66 × 1.38 nm^2 along the *a* and *b* axes. The percentage of void volume in the structure of **1** was estimated to be ca. 74% (2842 $Å^3$) and 72.8% (2795 $Å^3$) of the total volume (3838 $Å^3$) considering H_2 and N_2 as probe gases, respectively (kinetic radii: H_2, *r* = 1.40 Å; N_2, *r* = 1.82 Å).[38]

The coordination geometry of the Zn^{2+} ions, which templates the formation of the overall crystal structure, consists of a square pyramid where pairs of Zn^{2+} ions are bridged in a μ-type binding mode by four carboxylate ligands. The resulting equatorial plane around each Zn^{2+} ion is thus formed by four oxygen donor atoms, while the axial position of the square pyramid is completed by the nitrogen donor of a bpy ligand, which bridges pairs of Zn^{2+} ions from adjacent 2D layers (Figure 2a).

The molecular structure of the anionic complex $[VO(TCPP)]^{4-}$ shows a vanadium(IV) ion in a square pyramidal coordination geometry with the metal ion slightly above the basal plane (ca. 0.59 Å) formed by the four nitrogen donor atoms of the porphyrin macrocycle (Figure 2a). The V═O moiety is sitting on the 4-fold symmetry axis and is disordered on two positions, symmetric with respect to the macrocycle ring, with 50:50 occupancy factors, leading to a nonpolar crystal structure. The V−O and V−N distances, 1.60 and 2.09 Å, respectively, are in agreement with what is usually encountered for similar vanadyl complexes. The planes of the phenyl substituents are 90° tilted with respect to the plane of the porphyrin macrocycle, in agreement with what is observed for analogous MOFs based on isostructural building blocks (Figure 2a). This leads to an overall crystal structure of tetragonal symmetry where all vanadyl moieties are oriented along the *c* axis (Figure S1, Supporting Information). The V···V shortest distances in the crystal structure of **1** correspond to the unit cell distances, i.e., 13.9 Å along the *c* axis and 16.6 Å in the *ab* plane. Finally, it should be noted that the pyridine rings of the bpy ligand appear disordered in two 90°-tilted orientations, with the orientation of the two independent rings 45°-tilted with respect to each other.

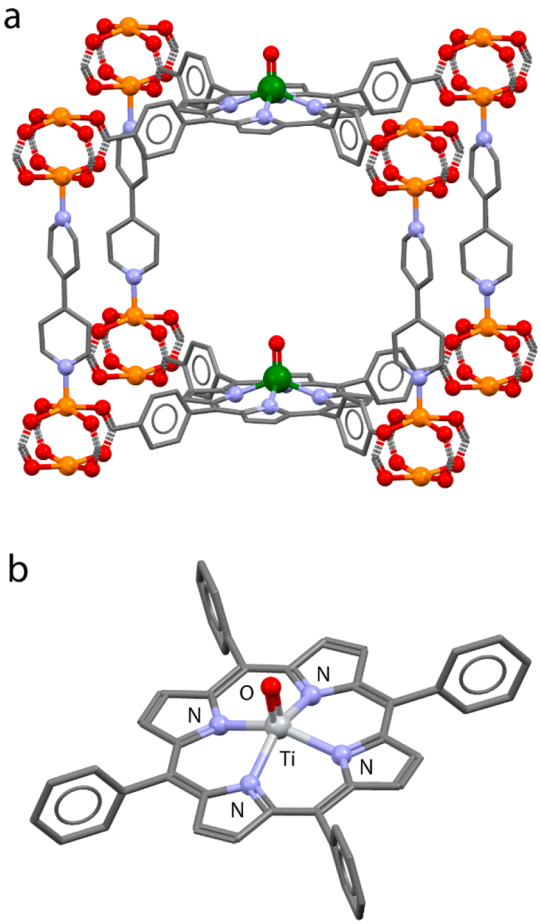

Figure 2. Molecular structures of compounds **1** (a) and **3** (b) with the coordination geometry of the metal ions highlighted. Color codes: green, vanadium; orange, zinc; silver, titanium; red, oxygen; light blue, nitrogen; gray, carbon. Hydrogen atoms and disordered fragments are omitted for graphical clarity.

Single crystals suitable for X-ray diffraction analysis of compounds **2** and **3** were obtained by slow evaporation of CH_2Cl_2 solutions. Both compounds crystallize in the tetragonal *I*4 space group with two neutral complexes in the unit cell; the asymmetric unit is one-fourth of the molecule also in this case. Due to the better quality of the collected diffraction data and the isostructurality between the two compounds, here we report only the data related to the [TiO(TPP)] compound **3**.

The crystal structure of **3** consists of neutral titanyl tetraphenylporphyrinate complexes with all Ti═O units lying on the 4-fold symmetry *c* axis (Figure S2, Supporting Information). The shortest M···M distance is 10.9 Å and involves metal complexes of adjacent layers. No significant intermolecular contacts involving the phenyl rings are present. The molecular structure of the complex is reported in Figure 2b. The coordination geometry around the Ti^{IV} ion is a square pyramid with a Ti−O distance of 1.58 Å and Ti−N distances of 2.11 Å. As already observed for **1**, the metal−oxido cationic moiety is disordered along the tetragonal axis on two positions with equal occupancy factors, with the metal center lying 0.58 Å from the basal plane of the porphyrin macrocycle.

Powder X-ray diffraction (PXRD) patterns were recorded on polycrystalline samples of all investigated systems, both pure

DOI: 10.1021/jacs.8b06733
J. Am. Chem. Soc. XXXX, XXX, XXX−XXX

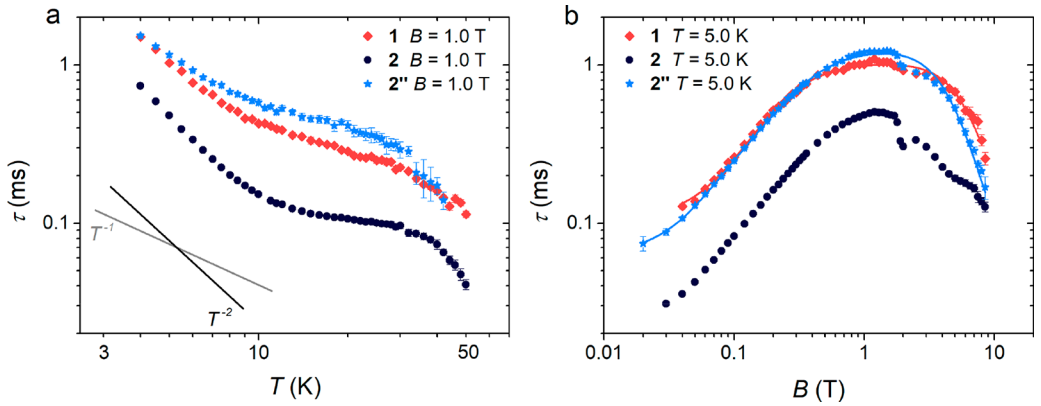

Figure 3. Temperature (a) and magnetic field (b) dependence of τ extracted from ac susceptibility measurements for microcrystalline samples of compounds **1**, **2**, and **2″** under an applied static magnetic field of 1.0 T (a) and in the 0.0−8.5 T range at 5.0 K (b). Solid lines are the best fit of the models (see the text).

compounds and crystalline dispersions, to ascertain their structural phase homogeneity. This is clearly evidenced by the good agreement between experimental and simulated patterns (Figures S3 and S4, Supporting Information).

Magnetization Dynamics. ac susceptibility measurements were performed on microcrystalline samples of compounds **1** and **2** and the crystalline dispersion **2″** to investigate their magnetization dynamics. The choice to study the dilution **2″** is due to the pronounced difference in the spin concentration between **1** and **2**. Indeed, the spin concentration for **1** is 0.26 spin nm^{-3}, whereas for **2** it is 1.1 spin nm^{-3}. **2″** provides a spin concentration of 0.34 spin nm^{-3}, which is closer to that of **1** and thus associated with a comparable dipolar internal magnetic field.

As commonly observed for $S = 1/2$ molecular spin qubit systems, the thermal variation of the complex magnetic susceptibility in zero static magnetic field reveals no out-of-phase component of the susceptibility (χ'') in the whole investigated temperature range. When a small static magnetic field (>40 mT) is applied, slow magnetic relaxation is observed for all samples, with appearance of a peak in the out-of-phase component of the susceptibility and a concomitant decrease of the in-phase part (χ') (Figures S5−S17, Supporting Information).[13,34] The relaxation time (τ), which is representative of the spin−lattice relaxation, was obtained by simultaneously fitting the real and imaginary components of the magnetic susceptibility with the generalized Debye model (see the Supporting Information).[39] The extracted values of τ for **1**, **2**, and **2″** obtained under a static magnetic field, $B = 1.0$ T, scanning the temperature, are reported in Figure 3a in a $\log(\tau)$ vs $\log(T)$ plot.

The absolute values of the spin−lattice relaxation times are comparable for **1** and **2″** in a wide temperature region, whereas those of **2** are lower, thus following the trend of the spin concentrations. The temperature dependence of τ shows a qualitatively similar behavior for the three compounds in the entire T range. At the lowest temperatures, between 4 and 10 K, the spin−lattice relaxation time shows a T^{-2} dependence, which suggests the presence of an important spin−phonon bottleneck effect.[40,41] This phenomenon affects the direct spin−lattice relaxation mechanism in magnetically concentrated samples and is particularly relevant in vanadyl-based molecules.[42] Figure 3a shows that, in the 10−30 K range, an unexpected remarkably weak temperature dependence of τ is observed, with an exponent significantly lower than the unity expected for a pure direct mechanism relaxation process.[43] For $T > 30$ K, the τ values of both compounds exhibit a faster decrease with increasing temperature.

To have a better understanding of the relaxation mechanisms involved in such compounds, the magnetization dynamics was also studied as a function of the static magnetic field in a wide magnetic field range (0.0−8.5 T) at different temperatures (5.0, 7.5, and 10.0 K) for each compound (Figures S9−S17, Supporting Information). The relaxation times at 5.0 K are shown in Figure 3b, while the data obtained at all investigated temperatures are reported in Figures S18−S20 (Supporting Information). All compounds show the expected nonmonotonous behavior of the relaxation time, with an increase of τ at low field, a plateau at intermediate fields, and then a decrease at high fields. In the low-field region, up to 1.0 T, spin−spin and spin−nucleus interactions, which promote spin relaxation by breaking the time-reversal symmetry of the Kramers doublet,[44,45] are suppressed by the increase of the magnetic field, resulting in a rapid growth of τ. Instead, in the high-field region, beyond 3.0 T, the strong field dependence of the direct mechanism causes the rapid decrease of τ. Indeed, the larger the Zeeman splitting of the two M_S states, the larger the number of phonons matching this energy difference.

The absolute values of the relaxation times of **1** and **2″**, as well as the magnetic field dependence, are again comparable, whereas **2** shows lower values of τ, in agreement with its temperature dependence (Figure 3a). A striking feature in the magnetic field dependence of the relaxation times is the dip shown by all compounds at 2.0 T. This feature is particularly pronounced for **2** (Figure S21, Supporting Information) and less pronounced for **2″**, suggesting that the presence of this dip might be related to the spin−phonon bottleneck effect. However, the reason why an acceleration of the relaxation rate at 2.0 T is observed, is, at the moment, unclear. To check if an anomalous temperature dependence of τ is also present at this field value, ac susceptibility data for compound **2** were recorded also at 2.0 T, showing a very similar behavior (Figure S22, Supporting Information).

The magnetic field dependence of τ for **1** is reproduced by the Brons−van Vleck model[45,46] with a slight modification (eq 1):

$$\tau^{-1} = d\left(\frac{1 + eB^2}{1 + fB^2}\right) + cB^m \quad (1)$$

The first term is related to the low-field region where τ increases due to the suppression of the internal fields, whereas the second term accounts for the direct relaxation mechanism.

DOI: 10.1021/jacs.8b06733
J. Am. Chem. Soc. XXXX, XXX, XXX−XXX

In the standard Brons–van Vleck model, the direct contribution to the spin–lattice relaxation rate in Kramers systems depends on the field as $\tau^{-1} \propto cB^4$. This has indeed been confirmed by previous studies on vanadium-based molecular spin qubits.[13,16,22,32,34,42] However, in this case, τ shows a weaker magnetic field dependence, and the best fits of the experimental data obtained for **1** assuming different integer values of m (Figures S23–S25 and Table S1, Supporting Information) clearly favor a cubic field dependence. This points to a nonconventional direct relaxation mechanism, in agreement with the observed anomalous weak temperature dependence of τ.

The extended Brons–van Vleck model[32] has been used to properly reproduce the data obtained for **2″**:

$$\tau^{-1} = d\left(\frac{1 + eB^2}{1 + fB^2}\right) + g\left(\frac{1 + eB^2}{1 + hB^2}\right) + cB^m \quad (2)$$

In this case, a second term accounting for the suppression of the internal fields due to the increase of the magnetic field is introduced. The use of the extended law is justified in Figure S26 (Supporting Information), where the data of **2″** are fitted with both models, while Table S1 (Supporting Information) contains the best fit parameters for the three different temperatures. Finally, it should be highlighted that the modeling of the magnetic field dependence of the spin–lattice relaxation time for **2** is not feasible because the distortions observed between 2.0 and 7.0 T do not allow for reasonable fits with either standard or extended Brons–van Vleck models.

Continuous Wave and Pulsed Electron Paramagnetic Resonance Spectroscopy. While ac susceptometry provides useful information about spin–lattice relaxation as a function of the applied static magnetic field in concentrated samples, pulsed EPR spectroscopy techniques allow determination of both spin–lattice and spin coherence relaxation times for magnetically diluted systems in a wide temperature range.

Continuous wave (CW) and echo-detected field-swept (EDFS) EPR spectra of the diluted compounds **1′** and **2′** recorded at T = 10 and 50 K, respectively, are reported in Figure 4 together with their simulations.

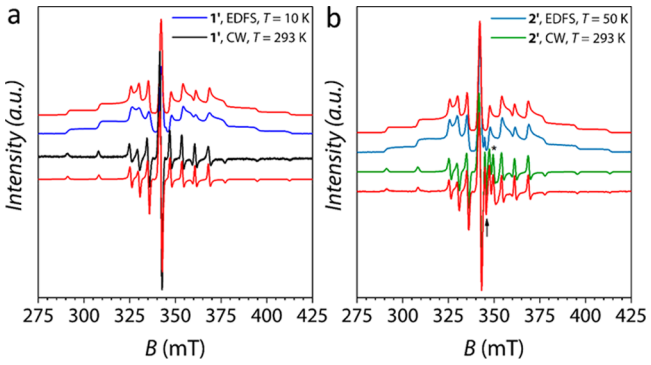

Figure 4. Experimental and simulated CW and EDFS EPR spectra for **1′** (a) and **2′** (b) at X-band frequency (9.7 GHz). Spectral simulations corresponding to the spin Hamiltonian parameters reported in Table 1 are shown in red. The asterisk and the arrow on the CW EPR spectrum of **2′** evidence the presence of unavoidable paramagnetic impurities that have been included in the simulation (see the text and Supporting Information for further details).

Both compounds show similar spectra that are characterized by the 8-fold hyperfine structure due to the coupling between the S = 1/2 electronic spin of V^{IV} and the I = 7/2 nuclear spin of its most abundant isotope (^{51}V, abundance 99.76%). The signals are further split by the anisotropic components of the hyperfine coupling in perpendicular and parallel directions. Spectral simulations[47] were then performed using the following spin Hamiltonian:

$$\mathcal{H} = \hat{\mathbf{I}}\cdot\mathbf{A}\cdot\hat{\mathbf{S}} + \mu_B\hat{\mathbf{S}}\cdot\mathbf{g}\cdot\mathbf{B} \quad (3)$$

to evaluate the anisotropy of the **g** factor as well as of the hyperfine coupling constant (**A**). The experimental spectra can be satisfactorily reproduced assuming an axial model (i.e., $x = y \neq z$) for both compounds, in agreement with the tetragonal site symmetry of the molecular systems. The best fit parameters are reported in Table 1. Such parameters agree with those expected for vanadyl porphyrinate derivatives[48,49] and correspond to a ground state with the unpaired electron in a d_{xy} orbital. It is evident that the EPR spectrum of **2′** also shows some weak features (<4% of the total signal and indicated in Figure 4b) which cannot be attributed to vanadyl species. On the basis of the best simulation parameters (Figure S27 and Table S2, Supporting Information), these were attributed to a radical monoanionic ligand and a residual Ti^{III} species.

Hyperfine sublevel correlation (HYSCORE) experiments have been performed on the two compounds to detect and determine the hyperfine interactions due to the ligand nitrogen atoms of the porphyrin ring and nearby hydrogens. The spectra of **1′** and **2′** (Figures S28 and S29, Supporting Information) are practically superimposable and typical for vanadyl porphyrin and phthalocyanine molecular systems.[49] Spectral simulation (Figure S30, Supporting Information) provided ^{14}N hyperfine and quadrupole splitting parameters that well compare with previously reported data on similar coordination environments (Table S3, Supporting Information).

The intense spin-echo-detected EPR spectra let us anticipate that quantum coherence could be measured for both compounds. Moreover, the spin Hamiltonian parameters obtained through the simulation of the CW spectrum provide good simulations of the EDFS spectra as well, hence indicating that the entire paramagnetic components are experiencing the detected coherence.

Inversion recovery experiments on **1′** and **2′** were performed in the 5.0–290 K temperature range at X-band frequency to investigate the temperature dependence of the spin–lattice relaxation time (T_1) at the resonant magnetic field corresponding to the hyperfine transition $M_I = -1/2 \rightarrow +1/2$. The resulting saturation recovery traces were fitted with a stretched-exponential equation:

$$I = I_0 + k_1 \exp\left[-\left(\frac{\tau_p}{T_1}\right)^{\beta_1}\right] \quad (4)$$

and the extracted T_1 values (Tables S4 and S5, Supporting Information) as a function of T are reported in Figure 5.

The temperature dependence of T_1 for the magnetically diluted samples **1′** and **2′** shows an increase of the slope on increasing the temperature, which is characteristic of the crossover from a dominating direct process of relaxation at low temperature to a Raman mechanism at high temperatures. T_1 values of **1′** at low temperature are ca. 1 order of magnitude lower than that of **2′** despite the similar spin concentration of the two compounds. As the temperature increases, the spin–lattice relaxation time for **2′** starts to decrease more abruptly above 30 K, whereas **1′**

DOI: 10.1021/jacs.8b06733
J. Am. Chem. Soc. XXXX, XXX, XXX–XXX

Table 1. Best Fit Parameters Extracted from Simulation of the Experimental Spectra of 1′ and 2′

compound	g_x	g_y	g_z	$\|A_x\|$ (MHz)	$\|A_y\|$ (MHz)	$\|A_z\|$ (MHz)
1′	1.9865(1)	1.9865(1)	1.963(1)	168(2)	168(2)	477(2)
2′	1.9865(1)	1.9865(1)	1.963(1)	169(2)	169(2)	480(2)

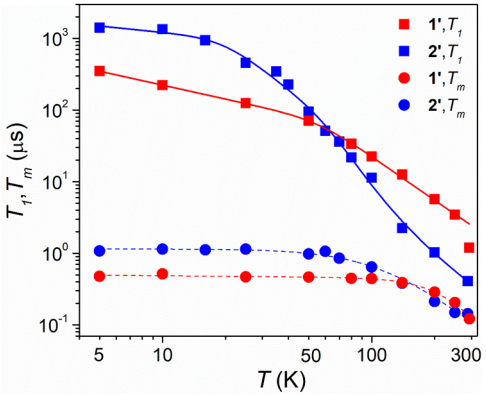

Figure 5. Temperature dependence of T_1 and T_m for **1′** and **2′** (see the legend) from pulsed EPR inversion recovery experiments at X-band frequency. Solid lines are the best fits considering local vibrational modes according to eq 7. Short-dashed lines represent a guide for the eyes. Error bars are within the size of the symbols.

shows such a behavior only at higher temperature and with a weaker temperature dependence. Consequently, the curves for the two compounds intersect around 60 K, and at room temperature, T_1 for **1′** reaches a value of ca. 1 μs vs 0.6 μs observed for **2**.

Different analytical functions are commonly used to reproduce the temperature dependence of T_1.[50] Here, the experimental data are well reproduced (Figure S31, Supporting Information) by the phenomenological relation:

$$T_1^{-1} = a_{dir}T^x + a_{Ram}T^n \quad (5)$$

where, unlike in previous reports, the exponent x of the temperature dependence of the direct process is left free to vary from the unitary value which is expected.[43] The best fit values for the direct process are x = 0.54(6) and 0.3(3) for **1′** and **2′**, respectively, thus deviating significantly from unity. On the other hand, the Raman process exponents, n = 2.5(1) and 3.4(1) for **1′** and **2′**, respectively, are within the usual range observed for vanadyl complexes (n ca. 3).[13,16,34,51] It is worth noting that replacement of the second term of eq 5 with the Debye transport integral function (eq S3, Supporting Information) does not significantly improve the overall fitting of data for **1** and worsens that for **2** (Figure S31 and Table S6, Supporting Information).

To investigate the quantum coherence in detail and to determine the phase memory time (T_m) for **1′** and **2′** as a function of the temperature, echo decay experiments were also performed. Because T_1 values, which limit the T_m values especially at high temperatures, are sufficiently long for both compounds in the whole investigated temperature range, echo decay traces were detected up to room temperature for both **1′** and **2′**. As usually done for transition metal systems,[50] echo decay traces were fitted using the stretched-exponential equation:

$$I = I_0 + k_m \exp\left[-\left(\frac{2\tau_p}{T_m}\right)^{\beta_m}\right] \quad (6)$$

where I indicates the echo intensity, $2\tau_p$ is the delay between the initial pulse and the echo detection and β_m is the stretch factor.

The thermal variations of T_m for **1′** and **2′** (reported in Figure 5) show an almost temperature independent behavior in the 5.0−100 K range for **1′** (ca. 0.5 μs) and in the 5.0−60 K range for **2′** (ca. 1.0 μs), with relative values that follow the corresponding T_1 values. These values are comparable to those recently reported for a 2D network formulated as [Cu(TCPP)−$Zn_2(H_2O)_2$] and the relative mononuclear building block [Cu(TPP)] in a frozen solution, although coherence time data were only measurable up to 90 K.[29] At 150 K, T_m assumes the same value for **1′** and **2′** (ca. 0.4 μs) and decreases to reach the lowest values at room temperature (ca. 0.14 μs). It is interesting to note that a crossover between the T_m values of **1′** and **2′** occurs in much the same way as observed for T_1 at slightly lower temperatures.

To prove that the observed coherence times for **1′** and **2′** allow coherent spin manipulations, i.e., placement of the spins in any arbitrary superposition of states, nutation experiments were performed at different microwave powers. Remarkably, Rabi oscillations were clearly observed with the expected linear dependence of the Rabi frequency (Ω_R) as a function of the microwave attenuation for both **1′** (Figure 6) and **2′** (Figure S32, Supporting Information).

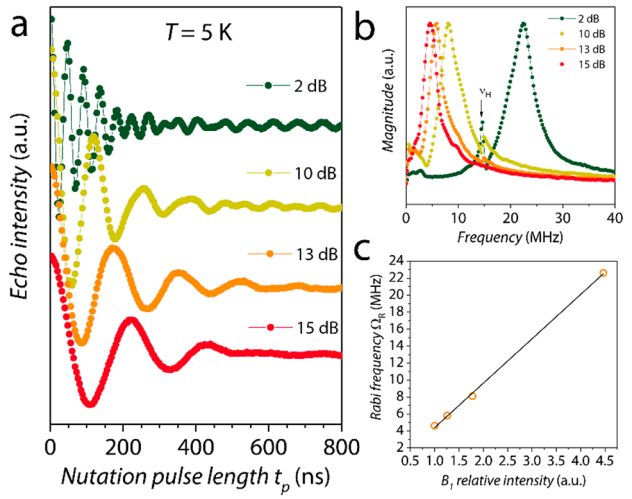

Figure 6. (a) Rabi oscillations recorded for **1′** at 5 K for different microwave attenuations (X-band). (b) Fourier transform of the Rabi oscillations. (c) Linear dependence of the Rabi frequency (Ω_R) as a function of the relative intensity of the oscillating field B_1.

Terahertz Vibrational Spectroscopy. Terahertz spectra, corresponding to the 10−110 cm^{-1} range, were recorded by time-domain transmission spectroscopy (THz-TD) on polycrystalline samples of **1** and **2** dispersed in polyethylene pellets.

A striking difference between the isolated [VO(TPP)] units of **2** and the extended structures of **1** is observed. Indeed, **2** shows a well-defined absorption band at ca. 67 cm^{-1}, which is absent in **1** (Figure 7).

Assignment of the low -energy absorption of **2** is not straightforward because porphyrinate complexes show metal−ligand

DOI: 10.1021/jacs.8b06733
J. Am. Chem. Soc. XXXX, XXX, XXX−XXX

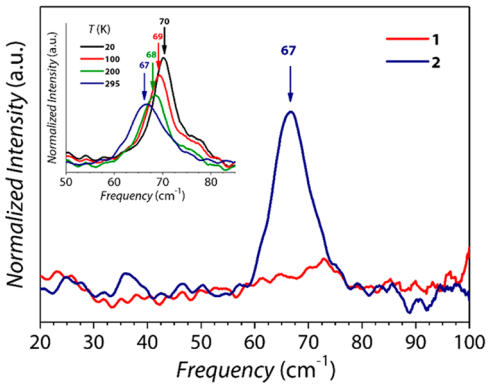

Figure 7. Vibrational spectra in the 0.6–3.0 THz range (20–100 cm^{-1}) of compounds **1** and **2** recorded at 295 K. The arrow indicates the frequency of the absorption. The inset shows the temperature dependence (20–295 K range) of the absorption spectra of **2**.

vibrations that are often mixed with porphyrin ring deformations.[52−54] Moreover, previous theoretical studies on simpler vanadyl-based potential molecular qubits showed that, in the terahertz frequency range, a strong admixing between local and collective degrees of freedom is present.[32]

The temperature dependence of the spectra of **2** (inset in Figure 7) shows a pronounced narrowing and shift to higher frequency of the absorption peak on lowering the temperature. According to the idea that structure stiffening at low temperature is expected to increase the vibration energy of collective modes, we can deduce that a significant contribution of collective vibrations to the nature of this mode is present. This is also in agreement with the lack of this mode in the covalent lattice of **1**, as well as its similar frequency in the titanyl derivative **3** (Figure S33, Supporting Information).

DISCUSSION

Our investigation proves the successful inclusion of paramagnetic vanadyl units in a structurally well characterized MOF, which is, to the best of our knowledge, unprecedented though not unexpected. More relevant is the preservation of spin coherence at room temperature, with comparable coherence times for the MOF and the mononuclear unit. This is a remarkable result because it allows the application of pulse EPR techniques at this temperature. These are known to provide more detailed information on the nature and the adsorption mode of guest molecules than CW techniques.[55,56]

The origin of this appealing behavior can be rationalized thanks to the comparative study that we have performed. First, it is important to stress that the electronic structures of the vanadyl unit are practically identical in the MOF and in the isolated molecule. This is clearly demonstrated by the very minor modifications of the spin Hamiltonian parameters, reported in Table 1, as well as of the hyperfine coupling values with neighboring nuclei detected by HYSCORE and listed in Table S3 (Supporting Information). It is also interesting to note that some characteristic features of the spin dynamics are preserved on increasing the material dimensionality, such as the field dependence of the magnetization relaxation time that shows a wide plateau extended up to several Tesla as reported in Figure 3b. This behavior, typical of the V^{IV} ion and much more pronounced than in analogous $S = 1/2$ systems based, for example, on Cu^{II},[29] allows high-field/high-frequency applications without significant acceleration of the spin dynamics.

Another feature common to the MOF and isolated molecule is the very weak temperature dependence of the spin–lattice relaxation time in the temperature range of 10–30 K, where magnetic relaxation is dominated by the direct mechanism and a linear dependence with temperature is expected. Such a behavior was also observed, though not highlighted, for a vanadyl phthalocyaninate complex.[34] As data for the latter system were collected on less concentrated samples with respect to those investigated here, we can safely exclude that an intermolecular process of relaxation is responsible for such a phenomenon. This leads us to associate this peculiarity with the macrocyclic coordination mode, although a rationale for it is still lacking.

In contrast to this remarkable similarity, **1** and **2** differ significantly in their low-energy vibrational spectra. The first IR-active vibrational mode, occurring at 67 cm^{-1} for **2**, exceeds our accessible range (110 cm^{-1}) in **1**. This originates remarkable differences in the temperature dependence of T_1 above 30 K. Local vibration modes have already been considered as sources of magnetic relaxation, but the support of optical investigations is uncommon.[57,58] We have therefore reproduced the temperature dependence of the spin–lattice dynamics through the already proposed phenomenological model[50]:

$$T_1^{-1} = a_{dir}T^x + a_{loc}\frac{\exp(\hbar\omega/k_BT)}{(\exp(\hbar\omega/k_BT) - 1)^2} \quad (7)$$

where ω is the frequency of the vibrational mode and a_{dir} and a_{loc} are coupling coefficients as in eq 5. The T_1 data of **1** are successfully simulated (Figure 5) with $x = 0.64$ and $\omega = 184(2)$ cm^{-1}, thus suggesting that the first active mode occurs at a frequency higher than our accessible spectral range. Data simulation of **2** was performed by fixing the frequency of the vibration mode to 67 cm^{-1}, accordingly to spectroscopic findings. The whole temperature range is well reproduced when including a second mode at higher frequency, 303(35) cm^{-1}, to the model. This is reasonable because an increasing number of active vibrational modes are expected to be present at higher frequencies. Notably, similar unusually low x exponents of the direct process are obtained independently of the model used to simulate the data (see Table S6, Supporting Information), confirming the robustness of the analysis.

CONCLUSIONS

In conclusion, we have successfully synthesized a 3D porous network embedding vanadyl spin units that retains spin coherence up to room temperature. This is a remarkable result for coherent magnetic sensing of potentially adsorbed species. Engineering of MOF structures with embedded vanadyl moieties acting as quantum spin sensors toward specific analytes seems indeed quite straightforward.

Our multitechnique investigation has also provided precious hints for a better understanding of the spin dynamics in molecular systems. In contrast to what could be intuitively expected, the inclusion of [VO(TPP)] units in an extended network does not affect the low-temperature regime. The $n < 1$ exponent in the $T_1 \propto T^{-n}$ law seems rather typical of the rigidity of the tetraphenylporphyrin coordination environment. On the contrary, linking the vanadyl units in the 3D network has pronounced effects on the infrared-active low-energy vibrational modes. This is reflected on the temperature dependence of T_1 in the intermediate temperature regime. The observed behavior is of paramount importance for quantum sensing as it warrants that spin coherence is not

DOI: 10.1021/jacs.8b06733
J. Am. Chem. Soc. XXXX, XXX, XXX−XXX

limited at room temperature by a rapid spin−lattice magnetic relaxation.

It also emerges from this study that the optimization of metal−organic framework performance through chemical design requires a deeper understanding of the role of intramolecular and intermolecular vibrations in the spin dynamics. The first step we can envisage in this direction is obtaining high-quality IR spectra on a continuous range to detect the lowest vibrational mode of **1**. Recording Raman spectra in the terahertz regime is also important as it will allow exclusion of relevant low-energy vibrational modes that might have remained undetected in the IR absorption spectra. The disorder in the V═O orientation indeed symmetrizes the otherwise acentric crystal structures of **1** and **2**. Theoretical analysis of the vibrational modes and their coupling to the spin system would also add significant information, although this is expected to be particularly challenging for **1**. Finally, the results presented here highlight the potentiality of vanadyl-based molecular units as highly coherent spin qubit units for quantum sensing applications despite a complex and nuclear-spin-rich crystal structure. This opens the door for further studies focused on the spin coherence measurements in the presence of guest solvents inside the MOF cavities, to probe its potential use as a molecule-based quantum sensor.

EXPERIMENTAL SECTION

General Remarks. All chemicals were purchased and used without further purification except for the tetrakis(4-(methoxycarbonyl)-phenyl)porphyrin (H_2TMeCPP), the precursor of tetrakis(4-carboxyphenyl)porphyrin (H_2TCPP), that was synthesized according to a previously reported study.[37]

Synthesis of [VO(TCPP)]·MeOH·2H_2O. H_2TMeCPP (1.00 g, 1.18 mmol) and [$VO(acac)_2$] (0.31 g, 1.18 mmol) were reacted at 180 °C in 5 mL of PhOH for 6 h. After that, the solvent was removed under vacuum, and the resulting solid of [VO(TMeCPP)] was washed with EtOH and dried under vacuum (yield 83%). [VO(TMeCPP)] (1.00 g, 1.10 mmol) was stirred in a mixture of THF (25 mL) and MeOH (25 mL). To this solution was added a solution of KOH (2.65 g, 47.2 mmol) in H_2O (25 mL). The mixture was refluxed for 12 h. After refluxing, THF and MeOH were removed under reduced pressure through rotary evaporation. Additional water was added to the solution, and then the solution was acidified with 1 M HCl until no further precipitation occurred. The solid was collected by filtration, washed with water, and dried in vacuum. Needle-shaped crystals of [VO(TCPP)]·MeOH·2H_2O were obtained by slow evaporation (1 week) of a MeOH solution of the crude [VO(TCPP)]. Yield: 95%. Anal. Calcd for $C_{49}H_{36}N_4O_{12}V$: C, 63.71; H, 3.93; N, 6.07. Found: C, 64.04; H, 3.89; N, 6.11. FT-IR ($\bar{\nu}_{max}$/cm^{-1}, KBr pellet): 3445m, 1696vs, 1606s, 1510vw, 1404m, 1276m, 1100w, 1005m, 803m.

Synthesis of [TiO(TCPP)]·H_2O. [TiO(TCPP)] was synthesized by following a slightly modified procedure with respect to that of [VO(TCPP)]. H_2TMeCPP (260 mg, 0.31 mmol) and [$TiO(acac)_2]_2$ (97 mg, 0.37 mmol) were reacted at 180 °C in 5 mL of PhOH for 63 h. After that, PhOH was removed under vacuum. The resulting solid was dissolved in a mixture of THF (15 mL) and MeOH (15 mL). To this solution was added a solution of KOH (0.7 g, 12.4 mmol) in H_2O (15 mL). The mixture was refluxed for 12 h. After refluxing, THF and MeOH were removed under reduced pressure through rotary evaporation. Additional water was added to the solution, and then the solution was acidified with 1 M HCl until no further precipitation occurred. The solid was collected by filtration, washed with water, and dried in vacuum. Yield: 45%. Anal. Calcd for $C_{48}H_{30}N_4O_{10}Ti$: C, 66.22; H, 3.47; N, 6.44. Found: C, 66.79; H, 3.66; N, 7.03. FT-IR ($\bar{\nu}_{max}$/cm^{-1}, KBr pellet): 2953m, 1692vs, 1603s, 1563vw, 1488vw, 1406w, 1248m, 1106w, 1004s, 941w, 798w.

Synthesis of [VO(TCPP-Zn_2-bpy)]·4DMF·4H_2O (1). [VO(TCPP)] (50 mg, 58 μmol), $Zn(NO_3)_2$·6H_2O (35 mg, 116 μmol), and 4,4′-bipyridyl (18.1 mg, 116 μmol) were dissolved in 7 mL of DMF, and the solution was placed in a glass capped vial. The solution was heated in an oven at 80 °C for 24 h. After cooling, purple cubic-shaped single crystals were obtained. They were collected by filtration and washed with DMF and MeOH. Yield: 65%. Anal. Calcd for $C_{70}H_{68}N_{10}O_{17}VZn_2$: C, 55.93; H, 4.56; N, 9.32. Found: C, 56.11; H, 5.06; N, 9.48. FT-IR ($\bar{\nu}_{max}$/cm^{-1}, KBr pellet): 3340w, 1630vs, 1548m, 1403vs, 1335w, 1204vw, 1180vw, 1069vw, 1007s, 806m, 779m, 713w.

Synthesis of $VO_{0.05}TiO_{0.95}$(TCPP-Zn_2-bpy)] (1′). [VO(TCPP)] (2.0 mg 2.34 μmol) and [TiO(TCPP)] (64.5 mg 75.66 μmol) were mixed in 6 mL of DMF by using ultrasonication for 30 min. To the solution were added $Zn(NO_3)_2$·6H_2O (46.4 mg, 156 μmol) and 4,4′-bipyridyl (29.2 mg, 187.2 μmol), and the resulting solution was placed in a glass capped vial. The solution was heated in an oven at 80 °C for 24 h, and after cooling, purple cubic crystals of **1′** were obtained. They were collected by filtration and washed with DMF and MeOH. Yield: 57%. Inductively coupled plasma atomic emission spectrometry (ICP-AES) was used to determine the effective concentration of V^{IV}:Ti^{IV}. This was found to be 4.94:95.06.

Synthesis of [VO(TPP)] (2). H_2TPP (0.25 g, 0.40 mmol) and [$VO(acac)_2$] (0.133 g, 0.50 mmol) were reacted at 180 °C in 6 mL of PhOH for 9 h. After that, the solvent was removed under vacuum, and the residual solid was solubilized in CH_2Cl_2. A small portion of MeOH was added to the CH_2Cl_2 solution, inducing precipitation of **2** as a red-purple microcrystalline powder. The precipitate was washed several times with MeOH and then with Et_2O and air-dried. Yield: 70%. Compound **2** was recrystallized by slow evaporation of a CH_2Cl_2 solution, which gave purple shiny crystals suitable for X-ray analysis. Anal. Calcd for $C_{44}H_{28}N_4OV$: C, 77.76; H, 4.15; N, 8.24. Found: C, 76.72; H, 4.36; N, 7.79. FT-IR ($\bar{\nu}_{max}$/cm^{-1}, KBr pellet): 3130vw, 3111vw, 3024vw, 1831vw, 1595m, 1506w, 1487m, 1439m, 1337m, 1204m, 1175s, 1157m, 1070s, 1005vs, 835w, 806s, 750s, 725m, 702s, 661m, 527w, 453m.

Synthesis of [TiO(TPP)] (3). H_2TPP (0.50 g, 0.81 mmol) and [$TiO(acac)_2]_2$ (0.260 g, 0.50 mmol) were reacted at 180 °C in 12 mL of PhOH for 3 days. After that, the solvent was removed under vacuum, and the residual solid was solubilized in CH_2Cl_2. A small portion of MeOH was added to the CH_2Cl_2 solution, inducing precipitation of **3** as a red-purple microcrystalline solid. The precipitate was washed several times with MeOH and then with Et_2O and air-dried. Yield: 74%. Compound **3** was recrystallized by slow evaporation of a CH_2Cl_2 solution, which gave purple shiny crystals suitable for X-ray analysis. Anal. Calcd for $C_{44}H_{28}N_4OTi$: C, 78.11; H, 4.17; N, 8.28. Found: C, 77.54; H, 4.41; N, 7.79. FT-IR ($\bar{\nu}_{max}$/cm^{-1}, KBr pellet): 3130vw, 3111vw, 3024vw, 1831vw, 1595m, 1506w, 1483m, 1439m, 1335m, 1200m, 1175s, 1069s, 1157m, 1009vs, 979s, 966s, 835w, 806s, 748s, 723m, 702s, 660m, 525w, 438m.

Synthesis of [$VO_{0.02}TiO_{0.98}$(TPP)] (2′). **2** (2.5 mg, 0.0037 mmol) and **3** (97.5 mg, 0.144 mmol) were dissolved in 50 mL of CH_2Cl_2. The solution was filtrated, and 5 mL of MeOH was added. Then the solvent was slowly evaporated under reduced pressure. **2′** precipitated as a red-purple microcrystalline solid that was washed with MeOH and then Et_2O and air-dried. Yield: quantitative. X-ray fluorescence (XRF) analysis was used to estimate the effective percentage of doping of V^{IV} by comparing the XRF intensity of the vanadium Kα emission of compound **2′** to a calibration curve obtained by mixing weighted amounts of the pure compounds (**2** and **3**) in the 1−20% concentration range. This was found to be 2(1)% VO^{2+} and 98(1)% TiO^{2+}.

Synthesis of [$VO_{0.30}TiO_{0.70}$(TPP)] (2″). Compound **2″** was prepared according to the method described above for **2′** by recrystallization of a mixture of **2** (30.0 mg, 0.044 mmol) and **3** (70.0 mg, 0.103 mmol) in 75 mL of CH_2Cl_2. Yield: quantitative. Magnetic measurements were used to estimate the effective percentage of V^{IV} doping. This was found to be in agreement with the nominal content of VO^{2+} paramagnetic species (30(2)%).

Characterization. C, H, N analyses were performed with a CHN-S Flash E1112 Thermofinnigan analyzer. FT-IR spectra were obtained on KBr pellets and collected with a Shimadzu-8400S spectrophotometer. X-ray fluorescence analyses were performed with a WD-XRF Rigaku

DOI: 10.1021/jacs.8b06733
J. Am. Chem. Soc. XXXX, XXX, XXX−XXX

PrimusII spectrophotometer. ICP-AES was performed at the Research and Analytical Centre for Giant Molecules, Graduate School of Science, Tohoku University, Japan, on a SHIMADZU ICPE-9000 spectrometer with 5% HNO_3 aqueous solution.

Single X-ray Crystallography. Single-crystal X-ray diffraction measurements for compound **1** were performed on an ADSC Quantum210 installed in the Pohang Accelerator Laboratory PLS-II beamlines. The synchrotron radiation was monochromated by using a double-crystal monochromator (λ = 0.8000 Å). Single-crystal X-ray diffraction measurements for **3** were performed on an Oxford Xcalibur PX Ultra-Onyx charge-coupled device (CCD) diffractometer using Enhance Ultra X-ray graphite-monochromated Cu Kα (λ = 1.540 Å) radiation. The structures were solved by direct methods (SHELXL)[59] and refined on F^2 with full-matrix least-squares (SHELXL) using the WinGX software package.[60] All non-H atoms were refined with anisotropic displacement parameters. Graphical material was prepared using Mercury CSD 3.9.[38] A summary of the crystallographic data and the structure refinement for compounds **1** and **3** is reported in Table 2.

Table 2. Summary of X-ray Crystallographic Data for 1 and 3

	1	3
empirical formula	$C_{58}H_{32}N_6O_9VZn_2$	$C_{44}H_{28}N_4OTi$
fw	1138.58	676.57
cryst size, mm	0.20 × 0.20 × 0.20	0.50 × 0.30 × 0.15
cryst syst	tetragonal	tetragonal
space group	*P*4	*I*4
a, *b*, Å	16.644(2)	13.3796(2)
c, Å	13.854(2)	9.7766(3)
α, β, γ, deg	90	90
V, Å^3	3837.9(9)	1750.15(7)
Z	1	2
T, K	100(2)	100(2)
ρ(calcd), Mg/m^3	0.493	1.284
μ, mm^{-1}	0.391	2.385
θ range, deg	0.81−50.00	5.61−72.51
GOF	1.074	1.037
R1[a]	0.0879	0.0503
wR2[a]	0.2547	0.1399

[a] $R1 = \sum||F_o| - |F_c||/\sum|F_o|$. $wR2 = [\sum[w(F_o^2 - F_c^2)^2]/\sum[w(F_o^2)^2]]^{1/2}$. $w = 1/[\sigma^2(F_o^2) + (aP)^2 + bP]$, where $P = [\max(F_o^2,0) + 2F_c^2]/3$.

Full crystallographic data for the solved structures have been deposited in the Cambridge Crystallographic Data Centre with CCDC numbers 1847868 (**1**) and 1849460 (**3**).

Powder X-ray Crystallography. Powder X-ray diffraction (PXRD) measurements on **1** and **1′** were performed on crushed polycrystalline samples by using an AFC-7R/LW (Rigaku, Akishima, Japan) operated at 50 kV and 300 mA at 293 K. The data were collected in the diffraction angle range of 3−60° in steps of 0.02° with an irradiation time of 2 s/step. To prevent evaporation of the crystal solvent, the samples were loaded into a capillary (diameter 0.8 mm, length 80 mm, Hilgenderg, Malsfeld, Germany) with the mother liquor. Wide-angle PXRD patterns on polycrystalline samples of **2**, **2′**, and **3** were recorded on a Bruker New D8 Advance DAVINCI diffractometer in a θ−θ configuration equipped with a linear detector. The scans were collected within the range 5−40° (2θ) using Cu Kα radiation (λ = 1.540 Å). Simulated patterns were generated from the atomic coordinates of the single-crystal structure solutions using the Mercury CSD 3.5 software[52] (copyright CCDC, http://www.ccdc.cam.ac.uk/mercury/) using an fwhm (full width at half-maximum) of 0.10 and a 2θ step of 0.025.

Magnetic Measurements. Magnetic susceptibility measurements were performed by using a quantum design physical property measurement system (PPMS). Alternate current susceptibility measurements were performed in the frequency (ν) range of 10−10000 Hz in the temperature range of 2.0−50 K by applying an oscillating field of 10 Oe and applied static magnetic fields up to 8.5 T. Measurements were performed on randomly oriented powder samples of **1** (37.12 mg), **2** (51.68 mg), and **2″** (45.38 mg). Susceptibility data were corrected for the sample holder previously measured using the same conditions and for the diamagnetic contributions as deduced by using Pascal's constant tables.[61]

Terahertz Time-Domain Spectroscopy Setup. Terahertz spectra were measured by time-domain transmission spectroscopy using a table-top experimental setup equipped with optical laser pulses (T-light 780 nm fiber laser, MenloSystems) and low-temperature GaAs photoconductive antennas. Low-temperatures measurements are allowed by means of a closed-cycle helium cryostat in the temperature range from 20 to 300 K. The developed acquisition procedure enables achievement of a signal-to-noise ratio higher than what is commonly achieved in standard far-infrared investigations. The accurate analysis of the data enables disentanglement of the signals from spurious contributions coming from multiple reflections. The detailed description of the experimental setup and the data analysis procedure is reported elsewhere.[62,63] The spectra were measured in pellets of 13.2 mm diameter and thickness of about 0.7 mm. These were made by pressing under a manual hydraulic press (∼0.8 GPa) a mixture of microcrystals and polyethylene powder (Merck).

Electron Paramagnetic Resonance. CW X-band EPR spectra of all samples were recorded on a Bruker Elexsys E500 spectrometer equipped with an SHQ cavity ($\nu \cong$ 9.70 GHz). Low-temperature measurements were obtained using an Oxford Instruments ESR900 continuous flow helium cryostat, and the temperature was controlled by an Oxford Instruments ITC503. Pulsed EPR measurements were carried out with a Bruker Elexsys E580 at X-band ($\nu \cong$ 9.70 GHz) equipped with a flexline dielectric ring ENDOR resonator (Bruker EN 4118X-MD4). Temperatures between 4.5 and 250 K were obtained with an Oxford Instruments CF935 continuous flow helium cryostat. Echo-detected field-swept EPR spectra were recorded by using the Hahn echo pulse sequence ($\pi/2-\tau-\pi-\tau-$echo) with fixed interpulse delay time τ = 200 ns, $t_{\pi/2}$ = 16 ns, and t_π = 32 ns. Phase memory times were measured by the Hahn echo sequence upon increasing the interpulse delay τ starting from τ = 98 ns. Typical pulse lengths were $t_{\pi/2}$ = 40 ns and t_π = 80 ns. Spin−lattice relaxation times were measured using the standard inversion recovery sequence ($\pi-t_d-\pi/2-\tau-\pi-\tau-$echo), with $t_{\pi/2}$ = 16 ns. The uncertainty in T_1 estimated from replicate measurements was 5−10% depending upon the signal-to-noise ratio at a given temperature−field combination. Nutation measurements were performed with a nutation pulse (t_p) of variable length followed by a Hahn echo sequence ($t_p-t_d-\pi/2-\tau-\pi-\tau-$echo) with $t_d \gg T_m$ (i.e., t_d = 7 μs for 4 K and 2 μs for room temperature measurements). The interpulse delay τ was 200 ns, and the pulse length of the detection sequence was adjusted depending on the attenuation level of B_1. Hyperfine sublevel correlation (HYSCORE) experiments[64] were carried out with the pulse sequence $\pi/2-\tau-\pi/2-\tau_1-\pi-\tau_2-\pi/2-\tau-$echo with the microwave pulse length $t_{\pi/2}$ = 16 ns and t_π = 16 ns. The time intervals t_1 and t_2 were varied in steps of 8 ns starting from 96 to 2704 ns. Spectra with two τ values (100 and 136 ns), which are specified in the figure captions, were recorded to avoid blind spot effects. An eight-step phase cycle was used for eliminating unwanted echoes. The time traces of the HYSCORE spectra were baseline corrected with a third-order polynomial, apodized with a Hamming window, and zero filled. After two-dimensional Fourier transformation, the absolute value spectra were calculated. The HYSCORE frequencies were computed for a three-spin system (S = 1/2; I_a = 1; I_b = 1) using the endorfrq function, implemented in the Easyspin program.[47]

■ ASSOCIATED CONTENT

Supporting Information

The Supporting Information is available free of charge on the ACS Publications website at DOI: 10.1021/jacs.8b06733.

Additional figures, PXRD patterns, magnetic susceptibility, and HYSCORE data (PDF)

X-ray crystallographic data for **1** (CIF)

X-ray crystallographic data for **3** (CIF)

DOI: 10.1021/jacs.8b06733
J. Am. Chem. Soc. XXXX, XXX, XXX−XXX

AUTHOR INFORMATION

Corresponding Authors

*roberta.sessoli@unifi.it

*yamasita.m@gmail.com

ORCID

Matteo Atzori: 0000-0003-1357-6159

Lorenzo Tesi: 0000-0003-4001-8363

Goulven Cosquer: 0000-0003-2692-1230

Fabio Santanni: 0000-0002-0506-8333

Marie-Emmanuelle Boulon: 0000-0003-1837-0803

Stefano Benci: 0000-0001-6492-1616

Renato Torre: 0000-0003-3182-9906

Mario Chiesa: 0000-0001-8128-8031

Lorenzo Sorace: 0000-0003-4785-1331

Roberta Sessoli: 0000-0003-3783-2700

Notes

The authors declare no competing financial interest.

ACKNOWLEDGMENTS

This work was performed with the financial support of the Italian MIUR through Project PRIN 2015-HYFSRT, Fondazione Ente Cassa di Risparmio di Firenze, European Project SUMO (QuantERA call 2017), and the Photon Factory Program Advisory Committee (Proposal No. 2016G040, beamline NW2A). European COST Action CA15128 MOLSPIN is also acknowledged. M.Y. acknowledges the support by the 111 project (Grant B18030) from China. We thank Sandra and Gareth Eaton (University of Denver, Colorado) for stimulating discussions.

REFERENCES

(1) Nielsen, M. A.; Chuang, I. L. *Quantum Computation and Quantum Information*; Cambridge University Press: Cambridge, U.K., 2010.

(2) Schirhagl, R.; Chang, K.; Loretz, M.; Degen, C. L. *Annu. Rev. Phys. Chem.* **2014**, *65*, 83−105.

(3) Wu, Y.; Jelezko, F.; Plenio, M. B.; Weil, T. *Angew. Chem., Int. Ed.* **2016**, *55*, 6586−6598.

(4) Degen, C. L.; Reinhard, F.; Cappellaro, P. *Rev. Mod. Phys.* **2017**, *89*, 035002.

(5) Knill, E.; Laflamme, R.; Milburn, G. J. *Nature* **2001**, *409*, 46−52.

(6) Blatt, R.; Wineland, D. *Nature* **2008**, *453*, 1008−1015.

(7) Mi, X.; Benito, M.; Putz, S.; Zajac, D. M.; Taylor, J. M.; Burkard, G.; Petta, J. R. *Nature* **2018**, *555*, 599−603.

(8) Clarke, J.; Wilhelm, F. K. *Nature* **2008**, *453*, 1031−1042.

(9) Kennedy, T. A.; Colton, J. S.; Butler, J. E.; Linares, R. C.; Doering, P. J. *Appl. Phys. Lett.* **2003**, *83*, 4190−4192.

(10) Balasubramanian, G.; Neumann, P.; Twitchen, D.; Markham, M.; Kolesov, R.; Mizuochi, N.; Isoya, J.; Achard, J.; Beck, J.; Tissler, J.; Jacques, V.; Hemmer, P. R.; Jelezko, F.; Wrachtrup, J. *Nat. Mater.* **2009**, *8*, 383−387.

(11) Bar-Gill, N.; Pham, L. M.; Jarmola, A.; Budker, D.; Walsworth, R. L. *Nat. Commun.* **2013**, *4*, 1743.

(12) Ardavan, A.; Rival, O.; Morton, J. J. L.; Blundell, S. J.; Tyryshkin, A. M.; Timco, G. A.; Winpenny, R. E. P. *Phys. Rev. Lett.* **2007**, *98*, 057201.

(13) Tesi, L.; Lucaccini, E.; Cimatti, I.; Perfetti, M.; Mannini, M.; Atzori, M.; Morra, E.; Chiesa, M.; Caneschi, A.; Sorace, L.; Sessoli, R. *Chem. Sci.* **2016**, *7*, 2074−2083.

(14) Troiani, F.; Affronte, M. *Chem. Soc. Rev.* **2011**, *40*, 3119.

(15) Aromí, G.; Aguilà, D.; Gamez, P.; Luis, F.; Roubeau, O. *Chem. Soc. Rev.* **2012**, *41*, 537−546.

(16) Atzori, M.; Morra, E.; Tesi, L.; Albino, A.; Chiesa, M.; Sorace, L.; Sessoli, R. *J. Am. Chem. Soc.* **2016**, *138*, 11234−11244.

(17) Warner, M.; Din, S.; Tupitsyn, I. S.; Morley, G. W.; Stoneham, A. M.; Gardener, J. A.; Wu, Z.; Fisher, A. J.; Heutz, S.; Kay, C. W. M.; Aeppli, G. *Nature* **2013**, *503*, 504−508.

(18) Bader, K.; Dengler, D.; Lenz, S.; Endeward, B.; Jiang, S.-D.; Neugebauer, P.; van Slageren, J. *Nat. Commun.* **2014**, *5*, 5304.

(19) Zadrozny, J. M.; Niklas, J.; Poluektov, O. G.; Freedman, D. E. *J. Am. Chem. Soc.* **2014**, *136*, 15841−15844.

(20) Zadrozny, J. M.; Niklas, J.; Poluektov, O. G.; Freedman, D. E. *ACS Cent. Sci.* **2015**, *1*, 488−492.

(21) Graham, M. J.; Yu, C.-J.; Krzyaniak, M. D.; Wasielewski, M. R.; Freedman, D. E. *J. Am. Chem. Soc.* **2017**, *139*, 3196−3201.

(22) Atzori, M.; Benci, S.; Morra, E.; Tesi, L.; Chiesa, M.; Torre, R.; Sorace, L.; Sessoli, R. *Inorg. Chem.* **2018**, *57*, 731−740.

(23) Gao, W.-Y.; Chrzanowski, M.; Ma, S. *Chem. Soc. Rev.* **2014**, *43*, 5841−5866.

(24) Furukawa, H.; Cordova, K. E.; O'Keeffe, M.; Yaghi, O. M. *Science* **2013**, *341*, 1230444.

(25) Huh, S.; Kim, S.-J.; Kim, Y. *Cryst. Eng. Comm.* **2016**, *18*, 345−368.

(26) Yi, F.-Y.; Chen, D.; Wu, M.-K.; Han, L.; Jiang, H.-L. *Chem. Plus Chem.* **2016**, *81*, 675−690.

(27) Kreno, L. E.; Leong, K.; Farha, O. K.; Allendorf, M.; Van Duyne, R. P.; Hupp, J. T. *Chem. Rev.* **2012**, *112*, 1105−1125.

(28) Chen, B.; Xiang, S.; Qian, G. *Acc. Chem. Res.* **2010**, *43*, 1115−1124.

(29) Urtizberea, A.; Natividad, E.; Alonso, P. J.; Andrés, M. A.; Gascón, I.; Goldmann, M.; Roubeau, O. *Adv. Funct. Mater.* **2018**, *28*, 1801695.

(30) Zadrozny, J. M.; Gallagher, A. T.; Harris, T. D.; Freedman, D. E. *J. Am. Chem. Soc.* **2017**, *139*, 7089−7094.

(31) Escalera-Moreno, L.; Suaud, N.; Gaita-Ariño, A.; Coronado, E. *J. Phys. Chem. Lett.* **2017**, *8*, 1695−1700.

(32) Atzori, M.; Tesi, L.; Benci, S.; Lunghi, A.; Righini, R.; Taschin, A.; Torre, R.; Sorace, L.; Sessoli, R. *J. Am. Chem. Soc.* **2017**, *139*, 4338−4341.

(33) Escalera-Moreno, L.; Baldoví, J. J.; Gaita-Ariño, A.; Coronado, E. *Chem. Sci.* **2018**, *9*, 3265−3275.

(34) Atzori, M.; Tesi, L.; Morra, E.; Chiesa, M.; Sorace, L.; Sessoli, R. *J. Am. Chem. Soc.* **2016**, *138*, 2154−2157.

(35) Barron, P. M.; Son, H.-T.; Hu, C.; Choe, W. *Cryst. Growth Des.* **2009**, *9*, 1960−1965.

(36) Goldberg, I. *Chem. Commun.* **2005**, 1243.

(37) Feng, D.; Gu, Z.-Y.; Li, J.-R.; Jiang, H.-L.; Wei, Z.; Zhou, H.-C. *Angew. Chem., Int. Ed.* **2012**, *51*, 10307−10310.

(38) Macrae, C. F.; Edgington, P. R.; McCabe, P.; Pidcock, E.; Shields, G. P.; Taylor, R.; Towler, M.; van de Streek, J. *J. Appl. Crystallogr.* **2006**, *39*, 453−457.

(39) Cole, K. S.; Cole, R. H. *J. Chem. Phys.* **1941**, *9*, 341−351.

(40) Van Vleck, J. H. *Phys. Rev.* **1941**, *59*, 724−729.

(41) Scott, P. L.; Jeffries, C. D. *Phys. Rev.* **1962**, *127*, 32−51.

(42) Tesi, L.; Lunghi, A.; Atzori, M.; Lucaccini, E.; Sorace, L.; Totti, F.; Sessoli, R. *Dalt. Trans.* **2016**, *45*, 16635−16643.

(43) Standley, K. J.; Vaughan, R. A. *Electron Spin Relaxation Phenomena in Solids*; Springer US: Boston, MA, 1969.

(44) Gómez-Coca, S.; Urtizberea, A.; Cremades, E.; Alonso, P. J.; Camón, A.; Ruiz, E.; Luis, F. *Nat. Commun.* **2014**, *5*, 4300.

(45) Van Vleck, J. H. *Phys. Rev.* **1940**, *57*, 426−447.

(46) De Vroomen, A. C.; Lijphart, E. E.; Prins, D. Y. H.; Marks, J.; Poulis, N. J. *Physica* **1972**, *61*, 241−249.

(47) Stoll, S.; Schweiger, A. *J. Magn. Reson.* **2006**, *178*, 42−55.

(48) Gourier, D.; Delpoux, O.; Bonduelle, A.; Binet, L.; Ciofini, I.; Vezin, H. *J. Phys. Chem. B* **2010**, *114*, 3714−3725.

(49) Moons, H.; Patel, H. H.; Gorun, S. M.; Van Doorslaer, S. *Z. Phys. Chem.* **2017**, *231*, 887−903.

(50) Eaton, S. S.; Eaton, G. R. Distance Measurements in Biological Systems by EPR. In *Biological Magnetic Resonance*; Berliner, L. J., Eaton, G. R., Eaton, S. S., Eds.; Springer US: Boston, MA, 2002; Vol. *19*.

DOI: 10.1021/jacs.8b06733
J. Am. Chem. Soc. XXXX, XXX, XXX−XXX

(51) Du, J.-L.; Eaton, G. R.; Eaton, S. S. *J. Magn. Reson., Ser. A* **1996**, *119*, 240−246.
(52) Domke, K. F.; Pettinger, B. *ChemPhysChem* **2009**, *10*, 1794−1798.
(53) Li, D.; Peng, Z.; Deng, L.; Shen, Y.; Zhou, Y. *Vib. Spectrosc.* **2005**, *39*, 191−199.
(54) Kincaid, J.; Nakamoto, K. *J. Inorg. Nucl. Chem.* **1975**, *37*, 85−89.
(55) Jee, B.; Eisinger, K.; Gul-E-Noor, F.; Bertmer, M.; Hartmann, M.; Himsl, D.; Pöppl, A. *J. Phys. Chem. C* **2010**, *114*, 16630−16639.
(56) Poryvaev, A. S.; Sheveleva, A. M.; Demakov, P. A.; Arzumanov, S. S.; Stepanov, A. G.; Dybtsev, D. N.; Fedin, M. V. *Appl. Magn. Reson.* **2018**, *49*, 255−264.
(57) Šimėnas, M.; Macalik, L.; Aidas, K.; Kalendra, V.; Klose, D.; Jeschke, G.; Mączka, M.; Völkel, G.; Banys, J.; Pöppl, A. *J. Phys. Chem. C* **2017**, *121*, 27225−27232.
(58) Müller, H.-E.; Völkel, G.; Brunner, W.; Cevc, P.; Kurkin, I. N. *Phys. Status Solidi B* **1987**, *141*, 343−349.
(59) Sheldrick, G. M. *Acta Crystallogr., Sect. C: Struct. Chem.* **2015**, *71*, 3−8.
(60) Farrugia, L. J. *J. Appl. Crystallogr.* **2012**, *45*, 849−854.
(61) Bain, G. A.; Berry, J. F. *J. Chem. Educ.* **2008**, *85*, 532.
(62) Tasseva, J.; Taschin, A.; Bartolini, P.; Striova, J.; Fontana, R.; Torre, R. *Analyst* **2017**, *142*, 42−47.
(63) Taschin, A.; Bartolini, P.; Tasseva, J.; Torre, R. *Measurement* **2018**, *118*, 282−288.
(64) Höfer, P.; Grupp, A.; Nebenführ, H.; Mehring, M. *Chem. Phys. Lett.* **1986**, *132*, 279−282.

DOI: 10.1021/jacs.8b06733
J. Am. Chem. Soc. XXXX, XXX, XXX−XXX

Acknowledgments

At the end of this looong dissertation I must acknowledge many people. However, unfortunately for the curious reader, I will do that in Italian.

Il mio più grande Grazie! va sicuramente a Roberta, che sotto la sua instancabile guida mi ha visto crescere dal punto di vista umano e scientifico. Potrei decantare per svariate pagine la fortuna che ho avuto nel poter lavorare con lei, ma preferisco soffermarmi su alcuni aspetti che mi hanno colpito in modo particolare. Il primo aspetto riguarda la sua profonda conoscenza scientifica e l'innata capacità di sapersi orientare anche in mezzo ad esperimenti complicati. In quattro anni non mi è mai riuscito di contraddirla su qualcosa. Anche quando pensavo di aver ragione, alla fine veniva fuori che se lei aveva detto A, era davvero A. Ho imparato molto da lei, e questo anche grazie alla pazienza che ha sempre avuto nel rispiegarmi le cose anche dieci volte. Il secondo aspetto è rivolto all'umiltà e la semplicità che ha sempre mantenuto nell'affrontare le situazioni, le discussioni e i problemi. A mio parere queste sono qualità fondamentali, che desidererei trovare sempre nelle persone. Ripensandoci un po', ancora mi stupisco del fatto che mai, e ripeto mai, abbia ignorato o interrotto il mio parere o agito in maniera arrogante, anche quando la mia era chiaramente una bischerata (e quante ne devo aver dette…). Questo parere è sempre stato prima ascoltato, osservato e nel caso accettato o rifiutato. In questo, ha ragione Carlo Rovelli nel dire che la scienza è democratica: le idee di tutti vengono accolte e valutate. O almeno così dovrebbe essere. L'ultimo aspetto che vorrei infine sottolineare, e che mi è rimasto radicato dentro, è la capacità di fare gruppo, di costruire e di tramandare. La Scuola Fiorentina di Magnetismo Molecolare vive e ancora cresce grazie a Roberta. Sono orgoglioso di essere stato parte di questa storia e spero di avervi contribuito anche io, nel mio piccolo. Per tutto questo, ancora una volta, Grazie!

Il secondo ringraziamento va interamente a Lorenzo Sorace, con cui sono felice di aver lavorato molto in questi anni, e con cui mi sono sempre trovato in grande sintonia. Provo profondo rispetto per Lorenzo, perché non si è mai tirato indietro quando si trattava di rimboccarsi le maniche, nonostante questo a volte significasse incastrare insieme mille cose. Questa sua grande umanità va poi unita ad una notevole conoscenza

a 360°, alla capacità di scovare errori di ogni sorta (anche i più nascosti), ad un'incredibile memoria e al talento di trovare equazioni improbabili (spesso di russi folli) e dimenticate ai più. E tutto questo avendo sempre il sorriso pronto! :) Lo ringrazio per tutto il tempo dedicatomi, per tutte le volte che "toc toc, scusa Lorenzo, posso disturbarti un attimo?", per il suo insostituibile aiuto in molti momenti di difficoltà (primo tra tutti la stesura di questo lavoro) e per altre mille cose per cui merita di essere ringraziato!

Ringrazio molto Matteo Atzori e Mauro Perfetti, con cui ho lavorato a stretto contatto e che mi hanno fortemente supportato (o forse dovrei dire sopportato?) in questo bellissimo, ma a volte faticoso, percorso. Due persone dalle capacità fuori dal comune, da cui spero di aver imparato almeno un decimo di quello che sanno fare loro. Le strade della ricerca certe volte dividono, ma mi auguro che i nostri percorsi si incontrino ancora molte volte in futuro. Grazie!

Quello del dottorato è stato un percorso bello, ricco di emozioni, di esperienze e di viaggi, in cui ho conosciuto persone da varie parti del mondo e visitato laboratori incredibili! Sono contento di quanto fatto in questi anni, dei risultati scientifici ottenuti, così come delle amicizie create. Questo è stato possibile grazie a Roberta, Lorenzo, Matteo e Mauro, ma un sincero grazie va anche a tutte le persone del LAMM che non solo hanno lavorato con me, ma con il quale ho avuto il piacere di condividere esperienze ed emozioni, conferenze, feste, scampagnate, braciate e sciate! Per questo ringrazio singolarmente (in ordine sparso ma ci tengo ad elencarli tutti) Eva, Irene, Alessandro, Andrea Caneschi e Andrea Guerrini, Matteo Mannini e Briganti, Claudia, Fabio, Beatrice, Sorre, Peppe, Gabba, Gaia, Elvira, Sara, Asma, Squillo, Giulia, Federico, Michele Serri, Pamela, Alberto, Guglielmo, Luca, Martin & Michele, Poggio, Beppe, Pone, Claudio, Brunetto, Niccolò, Marie e Maria, Donella, Pine, Andrea Dei e Dante Gatteschi.

Ringrazio in modo particolare per l'importante collaborazione che c'è stata in questi anni i colleghi del CRIST: Samuele Ciattini e Laura Chelazzi, ed i colleghi del LENS: Stefano Benci, Roberto Righini, Renato Torre, Paolo Bartolini e Andrea Taschin.

Devo ringraziare anche le persone al di fuori dell'accademia fiorentina che hanno contribuito a rendere questi tre anni di dottorato belli e densi. Ringrazio quindi i colleghi di Parma: Elena Garlatti, Alessandro Chiesa e Stefano Carretta; i colleghi di Torino: Mario Chiesa ed Elena Morra; i colleghi di Modena: Claudio Bonizzoni, Alberto Ghirri, Marco Affronte, Luca Rigamonti e Andrea Cornia; Zaher Salman del PSI;

i colleghi di Rennes: Kevin Bernot, Fabrice Pointillart, Thomas Lauwers, Maxime Pulcini, e Joanna Bcd di Nantes; i colleghi di Saragozza: Fernando Luis, Giulia Lorusso e Marco Evangelisti; Julia Mayans di Barcellona; i colleghi di Otago: Sally Brooker e Fabrice Karabulut; i colleghi di Londra: Sandrine Heutz e Peter Robaschik; i colleghi di ISIS: Tatiana Guidi e David Voneshen; Tsutomu Yamabayashi di Sendai, e i colleghi di New York: Giacomo Lovat, Bonnie Choi e Stella.

Ho voglia di continuare ancora un po' questi ringraziamenti, per cui ho deciso che menzionerò anche i miei amici, compagni di mille avventure. E poiché sto iniziando a detestare gli elenchi, ma ancora non abbastanza da risparmiarmene un altro, eccoli qua: Motta, Naomi, Franci, Damia, Costy, Ros, Chiara, Braccia, Mila, Laura, Simo, Iory, Bare, Chiara, Semo, Valeria, Martina, Wendy, Sore, Luci, Ele, Silvia, Tommy, Papi, Martino, Anna, Iacopo, Miriam, Matteo e anche Luca! Rigorosamente in ordine casuale. Belli vu'sieteeee!

Giunti a questo punto devo ringraziare assolutamente mia madre Annalisa e mia sorella Sofia. È quasi scontato descrivere l'affetto che provo per loro, per cui mi limiterò a queste due righe. Semplicemente grazie per ciò che siete e per tutto quello che quotidianamente mi donate!

Last but not least, voglio ringraziare Eleonora. Stella polare di questa mia vita vorticosa. La ringrazio per aiutarmi continuamente a camminare, a migliorare, a crescere. Insieme. E ringrazio ogni giorno il cielo per avermela messa accanto. Grazie.

Infine, ringrazio nuovamente ed in particolar modo coloro che hanno contribuito in qualsiasi modo nella scrittura di questa tesi di dottorato: Roberta Sessoli, Lorenzo Sorace, Matteo Atzori, Mauro Perfetti, Eleonora Lippi, Fabio Santanni, Giulia Serrano, Francesco Papi, Guglielmo F.Garcìa, Zaher Salman ed Eleonora Izzo. Ringrazio inoltre i referees Stefano Carretta e Joris van Slageren per i loro preziosi suggerimenti.

The classic circuit graphic in the thesis cover has been made by modifying vector graphics taken from the website Freepik. The same for the background waves that were designed by Harryarts.

In realtà un lavoro simile non termina mai.
Lo si deve dichiarare concluso
Quando, a seconda del tempo e delle circostanze,
si è fatto il possibile.

Johann Wolfgang von Goethe


LAMM
Laboratorio di Magnetismo Molecolare